FUNDPAR: A PROGRAM FOR DERIVING FUNDAMENTAL PARAMETERS FROM EQUIVALENT WIDTHS *C. Saffe* 3

THE PARKER INSTABILITY IN AXISYMMETRIC FILAMENTS: FINAL EQUILIBRIA WITH LONGITUDINAL MAGNETIC FIELD *F. J. Sánchez-Salcedo & A. Santillán* 15

MID-INFRARED OBSERVATIONS OF PLANETARY NEBULAE DETECTED IN THE GLIMPSE 3D SURVEY *J. A. Quino-Mendoza, J. P. Phillips, & G. Ramos-Larios* 31

PLANETARY NEBULAE IN THE INNER MILKY WAY II: THE BULGE-DISK TRANSITION *O. Cavichia, R. D. D. Costa, & W. J. Maciel* 49

UBVR POLARIMETRY OF HIGH-GALACTIC LATITUDE CARBON STARS *J. M. López & D. Hiriart* 63

RECALIBRATED TURBULENCE PROFILES AT SAN PEDRO MÁRTIR *R. Avila, L. Sánchez, I. Cruz-González, E. Carrasco, & V. M. Castaño* 75

MID- AND FAR-INFRARED PHOTOMETRY OF GALACTIC PLANETARY NEBULAE WITH THE AKARI ALL-SKY SURVEY *J. P. Phillips & R. A. Márquez-Lugo* 83

MASS AND METAL EJECTION EFFICIENCY IN DISK GALAXIES DRIVEN BY YOUNG STELLAR CLUSTERS OF NUCLEAR STARBURST *A. Rodríguez-González, A. Esquivel, A. C. Raga, & P. Colín* 113

TITLE FOR TOC *Author list for TOC* 127

H II REGIONS AND PROTOSOLAR ABUNDANCES IN GALACTIC CHEMICAL EVOLUTION *L. Carigi & M. Peimbert* 139

TEMPERATURE, BRIGHTNESS AND SPECTRAL INDEX OF THE CYGNUS RADIO LOOP *V. Borka Jovanović & D. Urošević* 159

A VARIANT OF THE TITIUS-BODE LAW *J. D. Flores-Gutiérrez & C. García-Guerra* 173

$UVBY-\beta$ PHOTOELECTRIC PHOTOMETRY OF THE OPEN CLUSTERS NGC 1647 AND NGC 1778 *C. A. Guerrero, J. H. Peña, & J. P. Sareyan* 185

ERRATUM *C. Neria, Y. Gómez, & L. F. Rodríguez* 193

AUTHOR INDEX 195

Revista Mexicana de Astronomía y Astrofísica, **47**, 3–14 (2011)

FUNDPAR: A PROGRAM FOR DERIVING FUNDAMENTAL PARAMETERS FROM EQUIVALENT WIDTHS

C. Saffe

Instituto de Ciencias Astronómicas, de la Tierra y del Espacio (ICATE), San Juan, Argentina

Received 2 July 2010; accepted 14 September 2010

RESUMEN

Implementamos un programa en Fortran que determina parámetros fundamentales de estrellas de tipo solar, a partir de anchos equivalentes del Fe. La solución debe verificar tres condiciones en el método estándar: equilibrio de ionización, equilibrio de excitación e independencia entre abundancias y anchos equivalentes. Calculamos modelos de atmósfera de Kurucz con opacidades NEWODF. Detalles como el parámetro de longitud de mezcla, el sobre impulso convectivo, etc. se calculan con un programa independiente. FUNDPAR calcula las incertezas por dos métodos: el criterio de Gonzalez & Vanture (1998) y utilizando la función χ^2. Los resultados derivados con FUNDPAR están de acuerdo con determinaciones previas en la literatura. En particular obtuvimos parámetros fundamentales de 58 estrellas con exoplanetas. El programa está disponible en la red[1].

ABSTRACT

We implemented a Fortran code that determines fundamental parameters of solar type stars from a list of Fe line equivalent widths. The solution should verify three conditions in the standard method: ionization equilibrium, excitation equilibrium and independence between metallicity and equivalent widths. Solar-scaled Kurucz model atmospheres with NEWODF opacities are calculated with an independent program. Parameter files control different details, such as the mixing-length parameter and the overshooting. FUNDPAR derives the uncertainties following two methods: the criterion of Gonzalez & Vanture (1998) and the dispersion using the $\chi 2$ function. The code uses the 2009 version of the MOOG program. The results derived with FUNDPAR are in agreement with previous determinations in the literature. The program is freely available from the web[1].

Key Words: stars: abundances — stars: fundamental parameters

1. INTRODUCTION

Different methods have been used in the literature to derive fundamental parameters and metallicities of solar type stars. For instance, some studies begin with a photometric estimation of temperature and gravity and then derive the metallicity using equivalent widths. Useful codes such as WIDTH9 (Kurucz 1993; Kurucz 1995, private communication) or BLACKWEL[2] (an implementation of the Blackwell method) are widely used in the literature (e.g., Saffe & Levato 2004). However, the temperature and gravity are usually considered as fixed parameters. The observed stellar spectra could be compared with a grid of previously calculated synthetic spectra (e.g., Fischer & Valenti 2005; Saffe et al. 2008) to determine fundamental parameters. However, in this case the instrumental broadening should be taken into account and the rotational velocity could be considered as another independent parameter.

Recently, Sousa et al. (2010) derived an effective temperature calibration based on line equivalent width ratios of different absorption lines. Also, the equivalent widths of Fe lines could be used to determine the parameters of solar type stars. The solution should verify three conditions in the standard

[1] `http://icate-conicet.gob.ar/saffe/fundpar/`.

[2] `http://www1.appstate.edu/dept/physics/spectrum/spectrum.html`.

method: [FeI/H]=[FeII/H] (i.e., ionization equilibrium), independence between the metallicity and both the excitation potential (i.e., excitation equilibrium) and the equivalent widths. This method has been applied to solar type stars, for instance, in the determination of metallicity of stars with and without low mass companions or exoplanets (e.g., Gonzalez 1997, 1998; Gonzalez, Wallerstein, & Saar 1999; Santos, Israelian, & Mayor 2000; Gonzalez & Laws 2000; Gonzalez et al. 2001; Laws & Gonzalez 2001; Laws et al. 2003). The process estimate initially the fundamental parameters ($T_{\rm eff}$, $\log g$, [Fe/H] and ξ, the microturbulence velocity). This information is used in the ATLAS program (Kurucz 1993; Kurucz 1995, private communication) to derive a model atmosphere in LTE (local thermodynamic equilibrium). The model atmosphere with the measured equivalent widths of the spectra, is introduced in the code MOOG[4] to derive a new metallicity. If the mentioned conditions are not satisfied, the process is restarted using new fundamental parameters calculated with the downhill method.

In this contribution, we present the Fortran code FUNDPAR (and their complement `atlas.launcher`) that implements the method explained above. The programs are available from the Web[5], including detailed installation instructions and some technical details such as the format of the input/output files (`install.txt`). As an example of practical use, we derived the fundamental parameters of 58 main sequence exoplanet host stars and verified the metal-rich nature of the group. The values derived are in agreement with previous determinations from the literature.

In § 2 we show the general idea and the logic of the program. The procedure of minimization of the χ^2 function is detailed in § 3. The estimation of the uncertainties in the parameters and the comparison with literature, are showed in §§ 4 and 5, respectively. Finally we present some concluding remarks in § 6.

2. THE LOGIC OF THE PROGRAM

The algorithm is organized in one main procedure and a number of sub-programs with specific tasks. The iterative process begins at one starting point in a 4D-space, where the variables are ($T_{\rm eff}$, $\log g$, [Fe/H], ξ). This starting point could be optionally given in the first line of the input file (see the file `install.txt` for details of input/output files). If this point is unknown, the program adopts (5000 K, 4.00 dex, −0.10 dex, 1.00 km s^{-1}) to begin the iteration. For example, Santos et al. (2000) estimate $T_{\rm eff}$ and $\log g$ from the *uvby* photometry and the calibration of Olsen (1984), while [Fe/H] and ξ are estimated following Schuster & Nissen (1989) and Edvarsson et al. (1993), respectively.

Then for each iteration step, i.e., for each group of 4 parameters ($T_{\rm eff}$, $\log g$, [Fe/H], ξ), the program should:

(a) Generate an appropriate ATLAS model atmosphere (through the `atlas.launcher` program). First, the code should select from the Kurucz grid the model atmosphere closest in the parameter space to those requested and take this as initial input model. Then the program executes ATLAS9 to derive the final model.

(b) Transform the model atmosphere to a format readable by MOOG (subroutine `kurucz2moog`). The format of the model atmosphere used by MOOG is not exactly the Kurucz model and should be rewritten accordingly.

(c) Call the MOOG program. At this point, the program takes the file containing the equivalent widths of the FeI and FeII lines of the star and the model atmosphere as input for the MOOG program. The MOOG program is executed using a driver called "abfind" which is selected for the abundance determination.

(d) Read the new metallicity values calculated by MOOG (subroutine `rmr, read-moog-results`); and finally,

(e) Determine the value of the χ^2 function. This step will be explained below.

We take into account the conditions mentioned in the introduction through a variable called χ^2. We adopt for χ^2 the expression $\chi^2 = w_1c_1^2+w_2c_2^2+w_3c_3^2+w_4c_4^2$, where w_1,...,w_4 are weight factors ($w_i \geq 0$), c_1 and c_2 are the slopes in the plots of [Fe/H] vs. $\log_{10}({\rm W}/\lambda)$ (logarithm of the reduced equivalent width) and [Fe/H] vs. excitation potential, c_3 = [FeI/H] − [FeII/H], and c_4 is the difference between the input ATLAS metallicity (Step a) and the resulting metallicity using equivalent widths (Step d). We added explicity the fourth condition: the input metallicity of the model atmosphere should be similar to the output metallicity derived from equivalent widths, i.e., the term with c_4. Then, the four conditions are quantified in the χ^2 function: the solution corresponds to the minimum value of χ^2.

[4] http://verdi.as.utexas.edu/moog.html.
[5] http://icate-conicet.gob.ar/saffe/fundpar/.

TABLE 1

SAMPLE OF THE FUNDPAR.PAR FILE WHICH CONTAINS THE WEIGHTS OF THE χ^2 FUNCTION

t1 = 200.00	# Characteristic length scale of Teff (K)
t2 = 0.10	# Characteristic length scale of Logg (dex)
t3 = 0.10	# Characteristic length scale of [Fe/H] (dex)
t4 = 0.10	# Characteristic length scale of Xita (km s^{-1})
w1 = 25000.00	# Chi2 Weight factor
w2 = 2500.00	# Chi2 Weight factor
w3 = 1111.00	# Chi2 Weight factor
w4 = 1111.00	# Chi2 Weight factor

The users are free to modify the values of the weights w_1,...,w_4 according to their own criteria. However, we show a simple example estimating aproximately the values of the weights. Adopting $\chi^2 = 1$ as the limiting case of a solution, each condition contributes, for example, with 0.25 to the sum $\chi^2 = 0.25 + ... + 0.25$. In this case the 4 conditions are taken equally important within χ^2, which is not always true. In the plot of abundance vs. excitation potential, we accept a maximum slope, for instance, of $c_1 \sim 0.015/4$ dex/eV, taking a difference of ∼0.015 dex in the abundance, for a total range of ∼4 eV in the excitation potential of Fe lines. Then, in the limiting case, $w_1 c_1^2 \sim 0.25$ and thus $w_1 \sim 18000$ eV^2/dex^2. The units of w_1 are forced so as to obtain a dimensionless product $w_1 c_1^2$. In the plot of abundance vs. $\log_{10}(W/\lambda)$ (where W and λ are the equivalent width and wavelength in Å, respectively), we accept a maximum slope (for example) of $c_2 \sim 0.015/1.5$, taking a difference of 0.015 dex in the abundance for a range of ∼1.5 in the $\log_{10}(W/\lambda)$ of Fe lines. Then, $w_2 c_2^2 \sim 0.25$ and thus $w_2 \sim 2500$. For the third condition, c_1 = [FeI/H] − [FeII/H] and we adopt a maximum difference of 0.015 dex. Then, $w_3 c_3^2 \sim 0.25$ and thus $w_3 \sim 1100$ dex^{-2}. Similarly, for w_4 result $w_4 \sim 1100$ dex^{-2}. In this estimation the weights w_1,...,w_4 turned out to be 18000 eV^2/dex^2, 2500, 1100 dex^{-2} and 1100 dex^{-2}, respectively, for a solution in which the four conditions contribute equally with 0.25 to the χ^2 function in the limiting case of $\chi^2 = 1$. In this example those solutions with $\chi^2 > 1$ do not verify the four conditions.

The user will probably have his/her own criteria for the values of w_1,...,w_4, instead of the values of the example explained the previous paragraph. The user is free to modify the values of w_1,...,w_4 (file `fundpar.par`) and this could result in more (or less) restrictive conditions. The code uses these values to define χ^2 and then search for the minimum of the function. Then, the user should read the values of the slopes and metallicities in the output files to verify if the four conditions are satisfied. The values of w_1,...,w_4 previously shown seem to verify in practice the requirements of minimization and verification of the four conditions. In Table 1 we show a sample of the file `fundpar.par` where the weights could be modified. Other parameters will be explained in the following sections.

According to the definition, χ^2 could be considered as a function that depends on the fundamental parameters $\chi^2 = \chi^2(T_{\rm eff},\ \log g,\ [Fe/H],\ \xi)$. If χ^2 is not a minimum, the algorithm should determine the next set of four possible values. These new variables are used in another iteration (following Steps a to e) to derive a new model atmosphere, metallicity and, finally, a new value of χ^2. The algorithm that determines the next group of four parameters is called the downhill method, and explained in the next section.

In Table 2 we show a list of the input and output files used by FUNDPAR. The format of the input/output files is detailed in the file `install.txt`. There are two main directories (`datain` and `dataout`) containing the input and output files of the stars. The equivalent widths should be stored in separate files (one file per star), and the names of these files should be listed in another file called `filenames.txt`. The files `atlas.par`, `batch.par` and `fundpar.par` contain the values of some parameters used in the model calculation and abundance determination and will be explained in the next sections. After the execution of FUNDPAR, three output files per star are created: the ATLAS model atmosphere of the solution and two output files directly from the MOOG abundance de-

TABLE 2

LIST OF THE INPUT AND OUTPUT FILES USED BY FUNDPAR

Filename	Directory	Comment
Input Files:		
`filenames.txt`	`datain`	List of files containing the equivalent widths
`hd001.txt`	`datain`	Equivalent widths of the star HD 001
...	...	...
`hd999.txt`	`datain`	Equivalent widths of the star HD 999
Parameter Files:		
`atlas.par`	`atlas.launcher`	Parameters used by ATLAS
`batch.par`	FUNDPAR	Parameters used by MOOG
`fundpar.par`	FUNDPAR	Parameters used by FUNDPAR
Output Files:		
`hd001.mod`	`dataout`	Model atmosphere of HD 001 from ATLAS9
`hd001.out1.txt`	`dataout`	Output file 1 from MOOG
`hd001.out2.txt`	`dataout`	Output file 2 from MOOG
...	...	...
`output1.screen`	`dataout`	Similar output to the screen
`output2.results`	`dataout`	Table of results for all the stars

termination. The file `output1.screen` displays similar information on the screen and `output2.results` lists the final parameters and their uncertainties.

3. THE DOWNHILL SIMPLEX METHOD: MINIMIZATION OF χ^2

In this section we briefly review the minimization procedure for χ^2 as a function of four independent variables, using a Numerical Recipes routine called `amoeba` (Press et al. 1992). The downhill simplex method is due to Nelder & Mead (1965) and requires only function evaluations, not derivatives. A simplex could be considered to be a geometrical figure of $N+1$ vertices in N-dimensional space (in our case, $N=4$). Taking any vertex as the origin, then the four other points define possible vector directions in the 4-dimensional volume.

The downhill simplex method starts with a group of $N+1$, i.e., 5 vertices rather than a single point or vertex. These vertices are displaced with a scale length characteristic of the problem. In our case, χ^2 is initially calculated adopting displacements of 200 K, 0.1 dex, 0.1 dex and 0.1 km s^{-1} for the variables $T_{\rm eff}$, $\log g$, [Fe/H] and ξ, respectively. The characteristic lengths could be modified in the file `fundpar.par` (see Table 1). FUNDPAR executes an initial calculation of χ^2 at the vertices of the simplex, before the iteration process begins. Then, the downhill method takes a series of steps, usually moving the highest point of the simplex, i.e., where χ^2 is maximum. Succesive steps could be visualized as reflections, expansions and contractions of the 4-dimensional object. When the simplex finds a valley, it contracts itself down the valley. An appropriate sequence of these steps will converge to the minimum of χ^2.

As explained by Press et al. (1992), the termination criterion is usually delicate in the minimization process. The program requires that the decrease in the function value in the terminating step be fractionally smaller that some tolerance (variable `ftol` within the `amoeba` subroutine). The method just described exactly follows Nelder & Mead (1965). However, in practice we found that for some stars the routine converges in a few iteration steps to a solution with $\chi^2 \gg 1$. In such cases the code decreases the tolerance and continues the iteration process from the last point. We verified that it is not necessary in this case to restart the process, because the effect of modifying the tolerance determines only at which iteration the program stops. We also note that decreasing the tolerance does not guarantee convergence of the solution: we are only modifying the termination step or the termination criterion.

With the adopted values of w_1,...,w_4, the program usually takes less than $\sim$200 iterations to reach a solution. The number of iterations is a known

TABLE 3

PARAMETERS ADOPTED IN DIFFERENT CASES (A,...,E) FOR 5 SAMPLE STARS (SEE TEXT FOR DETAILS)

Run	ML	W	D
A	1.25	1	2
B	1.25	0	2
C	1.32	1	2
D	1.25	1	1
E	1.25	1	0

problem of the downhill method. If the code reaches a solution with $\chi^2 > 1$, then the program restarts the iteration process using the last solution as a new initial condition. The restart is recomended by Press et al. (1992) in the downhill method to eliminate a probable local minimum of the function. The code restarts the iteration process only once. The user also could manually restart the process using the last solution, for instance, as the new initial condition and FUNDPAR will try to reach a solution with a smaller χ^2.

4. DERIVATION OF THE MODEL ATMOSPHERES

Together with the FUNDPAR code, we provide another independent program called `atlas.launcher`, which prepares and executes the Kurucz's ATLAS9 in LTE. As input of `atlas.launcher` the fundamental parameters $T_{\rm eff}$, $\log g$, [Fe/H] and ξ are used. The output is an ATLAS solar-scaled model atmosphere corresponding to these parameters. The program uses a parameter file called `atlas.par` that contains different parameters used by ATLAS, such as the mixing-length parameter (usually taken as 1.25), and the overshooting weight parameter W, defined in Castelli, Gratton, & Kurucz (1997). A list of files used by ATLAS (grid of precalculated models, Rosseland and ODFs, and a sample of `atlas.par`) is presented in the file `install.txt`.

Then, the model atmosphere and the equivalent widths are introduced in the MOOG program. We incorporated in this code the solar abundances of Grevesse & Sauval (1998) instead of the original from Anders & Grevesse (1989), except for Fe for which we adopted [Fe/H]=7.47 dex. The NEWODF opacities use these abundance values (Castelli & Kurucz 2003). MOOG use a parameter file (`batch.par`) where some options[6] could be modified, such as the molecular equilibrium and the van der Waals line damping options.

Literature authors have different preferences for the choice of ATLAS and MOOG parameters. The user is free to modify the parameters according to his/her own criteria, and then FUNDPAR will find the corresponding solution. To give an idea of the sensivity of the results, we rederived the fundamental parameters of 5 sample stars (HD 106252, HD 177830, HD 190228, HD 195019 and HD 202206) using different combinations of the parameters. In the Table 3 we show the values of the parameters adopted in different calculations A,...,E. The parameters shown are the mixing-length parameter (ML), the overshooting parameter (W) and the line damping option (D). We start the execution of case A adopting ML=1.25, W=1 and D=2. In case B we switched off the overshooting, while in case C we adopted a slightly higher ML. In cases D and E we used different options for the line damping.

The variation of $T_{\rm eff}$, $\log g$, [Fe/H] and ξ (adopting different ML, W and D) is different from star to star. For instance, varying W increases the $T_{\rm eff}$ for some stars, and decreases it for others. Probably the variation depends on the fundamental parameters of the stars. Then, in the Figure 1 we show the difference (called Δ) between the parameters derived for case A and the parameters derived for cases B, C, D and E. The differences are plotted vs. $T_{\rm eff}$ only for the 5 stars previously mentioned. All differences are derived with respect to case A. The symbols used in the panels are filled circles (results B-A), diagonal crosses (results C-A), empty circles (results D-A) and squares (results E-A). The panels seems to show a slight dependency on $T_{\rm eff}$. Switching on/off the overshooting (case B), $\Delta T_{\rm eff}$, $\Delta \log g$ and Δ[Fe/H] seem to show a dependency on $T_{\rm eff}$. Increasing ML from 1.25 to 1.32 (case C), we find no clear tendency and the differences are small. Using the damping option 1 instead of 2 (case D), $T_{\rm eff}$, $\log g$ and [Fe/H] increase by an average of $\sim$48 K, $\sim$0.14 dex and $\sim$0.05 dex, respectively. Using the damping option 0 (case E), $T_{\rm eff}$, $\log g$, [Fe/H] and ξ increase by an average of $\sim$70 K, $\sim$0.20 dex, $\sim$0.06 dex and $\sim$0.1 km s^{-1}, respectively. We caution that these preliminary differences have been derived using only 5 stars. A larger number of stars is needed to properly determine how the parameters ML, W and D modify the derived fundamental parameters.

[6]For a complete list of options, see the manual of the MOOG program, `http://verdi.as.utexas.edu/moog.html`.

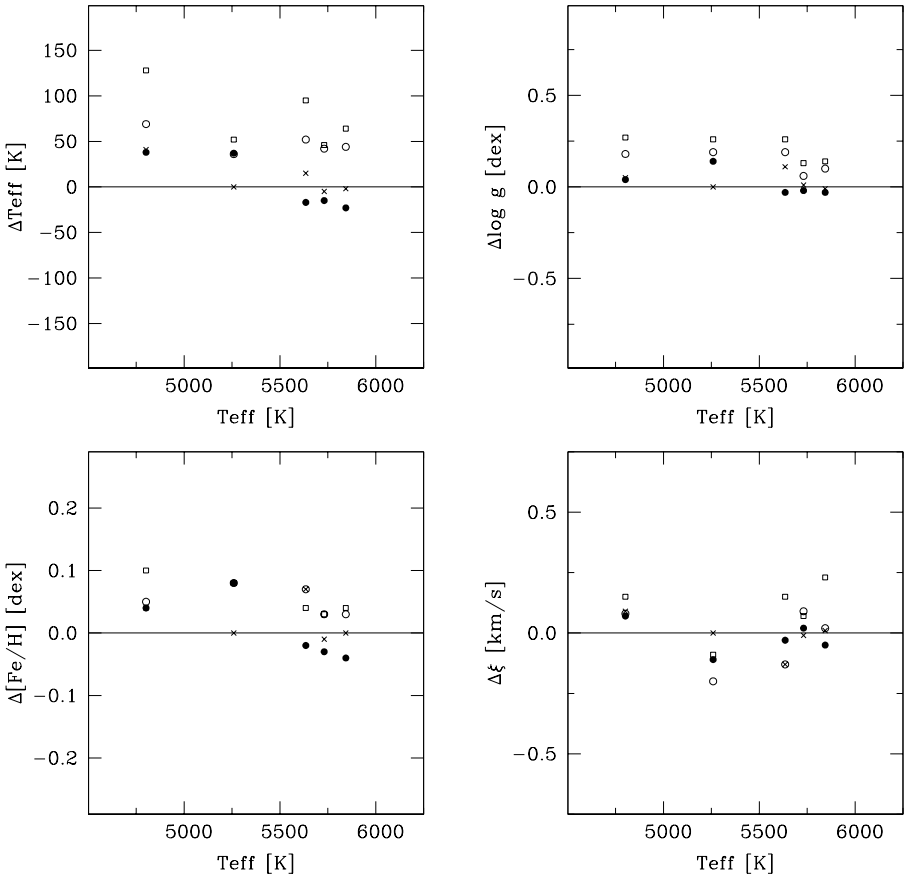

Fig. 1. Difference between the parameters derived in case A and the parameters derived in cases B, C, D and E. The differences are plotted vs. $T_{\rm eff}$ only for 5 stars. For instance, in the $T_{\rm eff}$ panel we ploted $\Delta T_{\rm eff} = T_{\rm eff}({\rm B}) - T_{\rm eff}({\rm A})$ with filled circles. The symbols used in the panels are filled circles (differences B-A), diagonal crosses (differences C-A), empty circles (differences D-A) and squares (differences E-A).

5. UNCERTAINTY ESTIMATION OF THE DERIVED PARAMETERS

The uncertainties in the atmospheric parameters were estimated following Gonzalez & Vanture (1998). The uncertainty in ξ was determined from the standard deviation of the slope of the least-squares fit of abundance vs. reduced equivalent width. Then, the dispersion of the effective temperature was determined from the uncertainty of the slope of the least-squares fit of abundance vs. excitation potential, in addition to the uncertainty of the slope due to the uncertainty of ξ. The uncertainty of the Fe abundance was derived combining the uncertainties of $T_{\rm eff}$, ξ and the scatter of the individual FeI abundances (standard deviation of the mean), all added in quadrature. In calculating the uncertainty of $\log g$, we include the contribution from the uncertainty of $T_{\rm eff}$ in addition to the scatter in the FeII line abundances.

We derive another estimation of the uncertainty of the solution using χ^2. As we explained previously, we select the values of the weights such that solutions with $\chi^2 > 1$ do not verify the four conditions. Then, we adopt the size of the region $\chi^2 = 1$ as another estimation of the uncertainty of the solution. FUNDPAR stores a record of the points with $\chi^2 < 1$ and uses them to estimate the size of the region. The range of the values of $T_{\rm eff}$, $\log g$, [Fe/H] and ξ is shown in the results along with the number n of solutions with $\chi^2 < 1$. These dispersion values should be taken with caution if n is small. This kind of uncertainty is comparable to those derived by the criteria of Gonzalez & Vanture (1998). In the next section we present a histogram comparing both uncertainties for a group of exoplanet host stars. The user is free to select among them, or to take the maximum value, for instance.

TABLE 4

FUNDAMENTAL PARAMETERS AND DISPERSIONS DERIVED WITH FUNDPAR

Star	$T_{\rm eff}$ [K]	$\log g$ [dex]	[Fe/H] [dex]	ξ [km s^{-1}]	e$T_{\rm eff}$ [K]	e$\log g$ [dex]	e[Fe/H] [dex]	eξ [km s^{-1}]	Ref[1]
14 Her	5294	4.33	0.50	0.71	40.60	0.19	0.07	0.05	R1
16 Cyg A_1	5704	4.29	−0.01	1.32	90.75	0.19	0.11	0.10	R2
16 Cyg A_2	5749	4.23	0.07	1.02	15.58	0.04	0.06	0.03	R3
16 Cyg B_1	5632	4.36	−0.05	1.21	83.68	0.25	0.10	0.09	R2
16 Cyg B_2	5690	4.30	0.05	0.91	14.16	0.04	0.06	0.03	R3
47 Uma	5720	4.26	−0.12	1.31	86.63	0.15	0.10	0.08	R2
51 Peg_1	5681	4.37	0.11	1.21	62.21	0.11	0.08	0.08	R2
51 Peg_2	5797	4.39	0.22	1.13	16.33	0.04	0.04	0.03	R4
70 Vir	5481	3.98	−0.08	1.10	92.16	0.15	0.09	0.07	R2
BD-10 3166	5275	4.36	0.32	0.69	42.70	0.05	0.09	0.05	R4
HD 106252	5844	4.50	−0.06	0.98	12.23	0.12	0.05	0.03	R5
HD 10697	5600	3.96	0.10	1.20	28.41	0.03	0.05	0.04	R4
HD 108147	6279	4.59	0.19	1.11	41.51	0.12	0.11	0.09	R5
HD 114783	5100	4.48	0.08	0.87	15.70	0.10	0.07	0.04	R5
HD 117176	5487	4.09	−0.06	1.00	10.86	0.10	0.06	0.02	R5
HD 1237_1	5537	4.50	0.22	1.19	30.76	0.15	0.07	0.05	R4
HD 1237_2	5468	4.50	0.05	1.38	23.27	0.18	0.07	0.04	R6
HD 12661_1	5670	4.41	0.38	0.91	19.18	0.06	0.05	0.03	R4
HD 12661_2	5719	4.48	0.38	0.84	24.28	0.04	0.05	0.04	R4
HD 13445	5080	4.43	−0.30	0.65	19.69	0.23	0.07	0.05	R6
HD 134987	5719	4.28	0.33	1.09	22.44	0.04	0.07	0.04	R4
HD 136118	6153	4.37	−0.09	2.00	21.82	0.15	0.08	0.11	R5
HD 141937	5832	4.50	0.12	0.97	12.63	0.10	0.05	0.03	R5
HD 160691	5788	4.49	0.24	1.12	22.03	0.08	0.06	0.04	R5
HD 16141_1	5768	4.24	0.17	1.10	22.07	0.04	0.04	0.04	R4
HD 16141_2	5751	4.28	0.16	1.00	12.18	0.05	0.05	0.03	R5
HD 168443	5549	4.13	0.08	1.04	17.06	0.02	0.06	0.03	R4
HD 168746	5566	4.43	−0.09	0.94	10.51	0.04	0.05	0.03	R5
HD 169830_1	6268	4.10	0.20	1.29	22.14	0.18	0.05	0.03	R6
HD 169830_2	6283	4.23	0.16	1.27	24.27	0.08	0.06	0.06	R5
HD 177830	4801	3.37	0.38	0.95	55.16	0.07	0.10	0.04	R4
HD 187123	5792	4.39	0.14	1.04	26.26	0.08	0.04	0.04	R1
HD 190228	5259	3.64	−0.32	1.13	11.79	0.11	0.05	0.02	R5
HD 192263	4905	4.38	−0.02	0.73	19.76	0.18	0.08	0.05	R4
HD 195019a	5731	4.17	0.00	1.20	13.09	0.13	0.05	0.03	R5
HD 19994.2	6147	4.35	0.12	2.03	23.94	0.10	0.08	0.09	R5
HD 202206_1	5635	4.55	0.28	0.88	24.27	0.14	0.06	0.04	R6
HD 202206_2	5713	4.45	0.30	1.07	14.42	0.04	0.06	0.03	R5
HD 209458	6065	4.43	0.02	1.14	18.56	0.13	0.06	0.04	R4
HD 210277	5517	4.34	0.24	0.84	26.56	0.12	0.05	0.04	R1
HD 217107	5602	4.42	0.42	0.87	17.64	0.03	0.05	0.03	R4
HD 22049	5083	4.47	−0.14	0.84	14.29	0.15	0.06	0.04	R5
HD 222582	5719	4.25	0.00	0.99	18.90	0.03	0.04	0.04	R4
HD 27442	4859	3.60	0.38	1.21	45.85	0.22	0.15	0.06	R5
HD 28185	5637	4.54	0.21	0.96	13.79	0.04	0.06	0.03	R5
HD 33636	5877	4.27	−0.13	0.95	14.81	0.10	0.06	0.04	R5
HD 37124_1	5579	4.60	−0.39	0.74	19.83	0.11	0.09	0.08	R5
HD 37124_2	5495	4.46	−0.42	0.71	22.54	0.04	0.05	0.07	R4
HD 38529	5600	3.82	0.34	1.25	38.21	0.05	0.06	0.03	R4
HD 4203	5667	4.43	0.43	1.08	29.95	0.06	0.15	0.06	R5
HD 4208	5592	4.33	−0.29	0.87	14.74	0.15	0.06	0.04	R5

TABLE 4 (CONTINUED)

Star	$T_{\rm eff}$ [K]	$\log g$ [dex]	[Fe/H] [dex]	ξ [km s^{-1}]	e$T_{\rm eff}$ [K]	e$\log g$ [dex]	e[Fe/H] [dex]	eξ [km s^{-1}]	Ref[1]
HD 46375$_1$	5210	4.37	0.24	0.65	35.26	0.10	0.06	0.04	R4
HD 46375$_2$	5252	4.50	0.26	0.68	21.15	0.09	0.10	0.06	R5
HD 50554	5978	4.51	−0.01	1.10	11.93	0.10	0.06	0.03	R5
HD 52265$_1$	6102	4.28	0.24	1.20	17.71	0.06	0.05	0.03	R4
HD 52265$_2$	6163	4.37	0.27	1.21	19.51	0.10	0.03	0.03	R4
HD 52265$_3$	5993	4.21	0.17	1.24	25.17	0.18	0.06	0.04	R6
HD 6434	5715	4.32	−0.54	0.70	23.11	0.16	0.11	0.10	R5
HD 68988	5936	4.49	0.32	1.19	19.40	0.02	0.09	0.05	R5
HD 75289$_1$	6138	4.52	0.27	1.50	20.96	0.10	0.07	0.05	R7
HD 75289$_2$	6070	4.44	0.23	1.42	30.93	0.16	0.06	0.05	R6
HD 75332	6277	4.47	0.22	1.03	24.73	0.11	0.05	0.04	R4
HD 82943$_1$	5950	4.45	0.28	1.10	25.37	0.07	0.05	0.03	R6
HD 82943$_2$	5987	4.46	0.24	1.11	17.85	0.04	0.05	0.03	R5
HD 83443$_1$	5389	4.31	0.33	1.00	27.40	0.18	0.08	0.04	R6
HD 83443$_2$	5427	4.40	0.34	0.99	22.07	0.13	0.07	0.05	R5
HD 8574	6029	4.34	0.00	1.19	13.29	0.16	0.05	0.03	R5
HD 89744	6315	4.16	0.27	1.67	28.06	0.07	0.04	0.05	R4
HD 92788	5755	4.43	0.29	1.02	26.37	0.04	0.05	0.04	R4
HD 95128	5832	4.31	0.02	1.08	13.83	0.10	0.05	0.02	R5
HR 810	6072	4.48	0.15	1.23	27.89	0.09	0.07	0.08	R4
ν And$_1$	6165	4.21	0.13	1.40	50.44	0.03	0.06	0.07	R8
ν And$_2$	6150	4.14	0.09	1.48	50.48	0.03	0.07	0.07	R7
ρ Cnc$_1$	5201	4.27	0.32	0.78	99.87	0.20	0.11	0.10	R2
ρ Cnc$_2$	5206	4.40	0.41	0.69	27.42	0.18	0.07	0.04	R7
ρ Crb	5751	4.15	−0.24	1.33	28.85	0.05	0.04	0.05	R2
τ Boo$_1$	6517	4.37	0.30	1.57	60.99	0.04	0.06	0.08	R8
τ Boo$_2$	6415	4.23	0.30	1.34	49.61	0.06	0.08	0.07	R7

[1]References for the equivalent widths (last column): R1: Gonzalez et al. (1999), R2: Gonzalez (1998), R3: Laws & Gonzalez (2001), R4: Gonzalez et al. (2001), R5: Laws et al. (2003), R6: Santos et al. (2000), R7: Gonzalez & Laws (2000), R8: Gonzalez (1997).

FUNDPAR include the uncertainty estimation of the parameters and they are shown in the ouput files. The size of the uncertainty depends on many factors, such as the number of lines involved (which is usually small for FeII), the measured equivalent widths and the laboratory data of the spectral lines. The $\log gf$ values (oscillator strength) and excitation potential of the lines are important because many derived values (Fe abundances, the slopes of abundance vs. equivalent widths and vs. excitation potential, etc.) depend on these quantities. We note that the inclusion of a line which (for one reason or another) implies an abundance very different from the average could modify the results and/or increase the uncertainty of the parameters. These lines should be eliminated from the list of measured equivalent widths. The abundances of individual lines are shown in the file `out2.txt` (`work.dir` directory).

6. COMPARISON WITH LITERATURE VALUES

There are small differences in the parameters derived using this method by different authors. Santos et al. (2000) derived surface gravities systematically larger than the ones obtained by other authors (e.g., Gonzalez et al. 2001) by 0.15 dex. To solve this problem, Santos, Israelian, & Mayor (2004) adopted new $\log gf$ values for the iron lines. Then the authors found a small average difference of +25 K in the temperature compared to the studies of Gonzalez et al. (2001) and Laws et al. (2003) (57 stars in common). Also their $\log g$ are +0.05 dex (on average) larger and the average differences in metallicity are between −0.10 and +0.10 dex. Ammler-von Eiff et al. (2009) derived the fundamental parameters of host stars with transiting planets using the 2002 version of the code MOOG and ATLAS model atmospheres. However, for the TrES and HAT objects the abundances determined by Sozzetti et al.

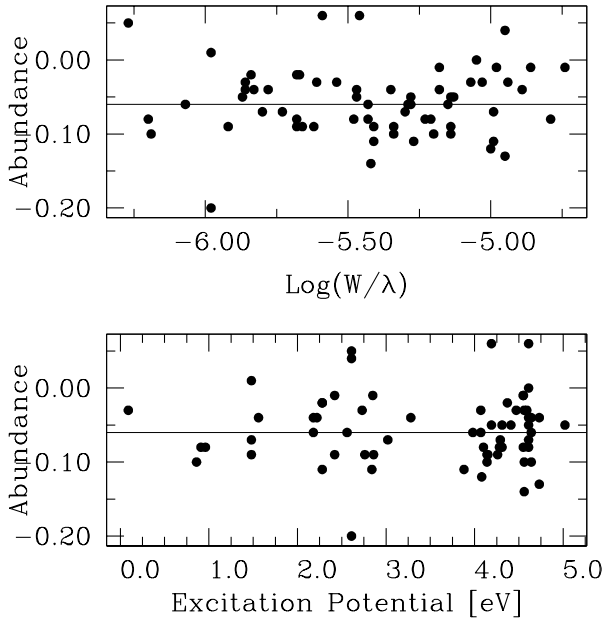

Fig. 2. Plots of abundance vs. excitation potential and abundance vs. $\log_{10}(W/\lambda)$ (logarithm of the reduced equivalent width) for HD 106252.

(2007) and Sozzetti et al. (2009) using essentially the same method are systematically lower (∼0.10 dex) than those derived by Ammler-von Eiff et al. (2009). The authors also mention differences in temperature (∼100 K) and gravity (∼0.15 dex) due to possible systematic differences between the works, and they note that the origin of the abundance discrepancies is usually unidentified.

We compare the parameters derived using FUNDPAR and those from the literature (Gonzalez 1997, 1998; Gonzalez et al. 1999; Santos et al. 2000; Gonzalez & Laws 2000; Gonzalez et al. 2001; Laws & Gonzalez 2001; Laws et al. 2003). We select these works in particular because they present the Fe equivalent widths: we use the same values with FUNDPAR. In the Table 4 we show the $T_{\rm eff}$, $\log g$, [FeI/H] and ξ obtained. Some stars in the table are listed twice (they are identified with a subscript) because we have different equivalent width sources in the literature. The sources of the equivalent widths are listed in the Table 4 as R1,...,R8.

We show in Figure 2 an example of plots of abundance vs. excitation potential and abundance vs. $\log_{10}(W/\lambda)$ (logarithm of the reduced equivalent width) for HD 106252. In Figure 3 we present the difference between FUNDPAR parameters and literature values (y axis, Δ=FUNDPAR-literature) vs. literature values (x axis). The empty point in Figure 3 corresponds to the star HD 38529, and shows that the slopes, metallicities and χ^2 values for this object should be taken with caution. The derived parameters of this star are based only on 3 FeII lines (and 24 FeI lines). In the literature, some values of $T_{\rm eff}$, $\log g$ and ξ have been rounded to within 50 K or 10 K, 0.05 dex and 0.1 km s^{-1}, respectively (see, for example, Gonzalez 1997, 1998; Gonzalez et al. 1999). There is a good agreement between FUNDPAR parameters and previous values from the literature, within the errors, which is expected since FUNDPAR uses a very similar method. However, Figure 3 shows that there is a dispersion in the values of the parameters (particularly $\log g$ and ξ) and probably a systematic trend for the metallicity (∼0.01 dex below literature values, see next discussion). The values of $\Delta T_{\rm eff}$ and $\Delta \log g$ also seem to slightly decrease with $T_{\rm eff}$ and $\log g$, respectively. The medians of the differences for the fundamental parameters compared to literature values are 24 K, 0.06 dex, 0.03 dex and 0.08 km s^{-1}, corresponding to $T_{\rm eff}$, $\log g$, [Fe/H] and ξ, respectively. The largest differences in the parameters amount to 118 K (16 Cyg B), 0.30 dex (HD 27442), 0.16 dex (16 Cyg B) and 0.31 km s^{-1} (47 Uma), corresponding to $T_{\rm eff}$, $\log g$, [Fe/H] and ξ, respectively.

Now we discuss the possible origin of the dispersions and probable trends observed in Figure 3. We tested FUNDPAR significantly modifying the values of the weights w_1,...,w_4 in the function χ^2 and verified that the difference in [Fe/H] compared with literature values and the dispersion of the other parameters change very slightly. Then the weights w_1,...,w_4 do not seem to be the cause. We use a method similar to that of the literature; however it is not totally identical. FUNDPAR uses Kurucz model atmospheres (Castelli & Kurucz 2003) different from those used in the literature (most of them date from before the creation of the ODFNEW models). The code uses model atmospheres derived by ATLAS with ODFNEW opacities and solar abundances from Grevesse & Sauval (1998) instead of Anders & Grevesse (1989). The new models present differences compared to older Kurucz models (Kurucz 1990), such as the solar abundances, the replacement of TiO and H_20 molecular lines, some HI quasi-molecular absorptions, etc. which are taken into account in the NEWODF opacities. Preliminary improvements are the $U-B$ and $u-b$ color indices for $T_{\rm eff} < 6750$ K, all color indices for cooler stars, and the better modeling for the upper layers of cool and giant stars (Castelli & Kurucz 2003). In this example, the model atmospheres are computed with con-

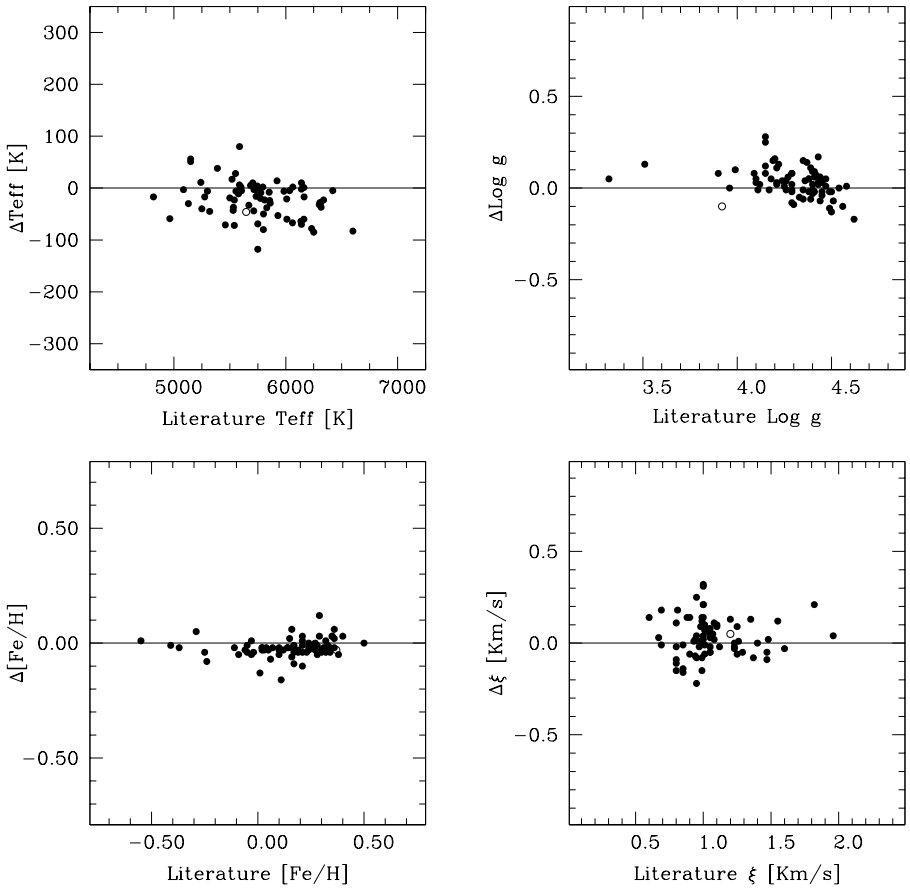

Fig. 3. Difference between FUNDPAR parameters and literature (y axis) vs. literature (x axis). The panels shows separately the effective temperature, gravity, metallicity and ξ. Filled and empty points correspond to solutions with $\chi^2 < 1$ and $\chi^2 > 1$, respectively.

vection (mixing-lenght parameter=1.25), overshooting (W=1) and damping in the Unsöld approximation, but multiplied by a factor as suggested by Blackwell, Lynas-Gray, & Smith (1995). The use of the fourth condition within the function χ^2 is (possibly) another difference from previous studies. Literature works surely take this into account, but it is not totally clear for us how they do so. Finally, we use the MOOG 2009 version[7] of the program instead of the 2002 version used in the literature, although we expect almost the same abundance values from both versions.

These differences, at least in part, produce the slightly dissimilar values showed in the Figure 3, which suggest that FUNDPAR probably uses a different metallicity scale than that of the literature. A complete comparison requires the exact knowledge of all involved details used in the literature calculations. Our intention is to clearly present all the asumptions used in FUNDPAR, in the model atmospheres and within the code.

In Figure 4 we show the histogram distributions of the uncertainties derived for $T_{\rm eff}$, $\log g$, [Fe/H] and ξ. The densely and slightly shaded histograms correspond to uncertaities derived following Gonzalez & Vanture (1998) and using the χ^2 function, respectively. Some distributions present a peak in a common uncertainty value, such as ∼0.05 dex in the [Fe/H] distribution and ∼30 K in the distribution of effective temperature. We see that the errors derived using both methods are comparable.

The metallicities presented in Table 4 correspond to a group of exoplanet host stars. The median of the group is 0.17 dex with a dispersion of 0.22 dex. In Figure 5 we present the histogram of the metallicity distribution. Then, as an example of the practical use of FUNDPAR, we verified the metal-rich nature of main sequence stars with low mass companions,

[7] `http://verdi.as.utexas.edu/moog.html`.

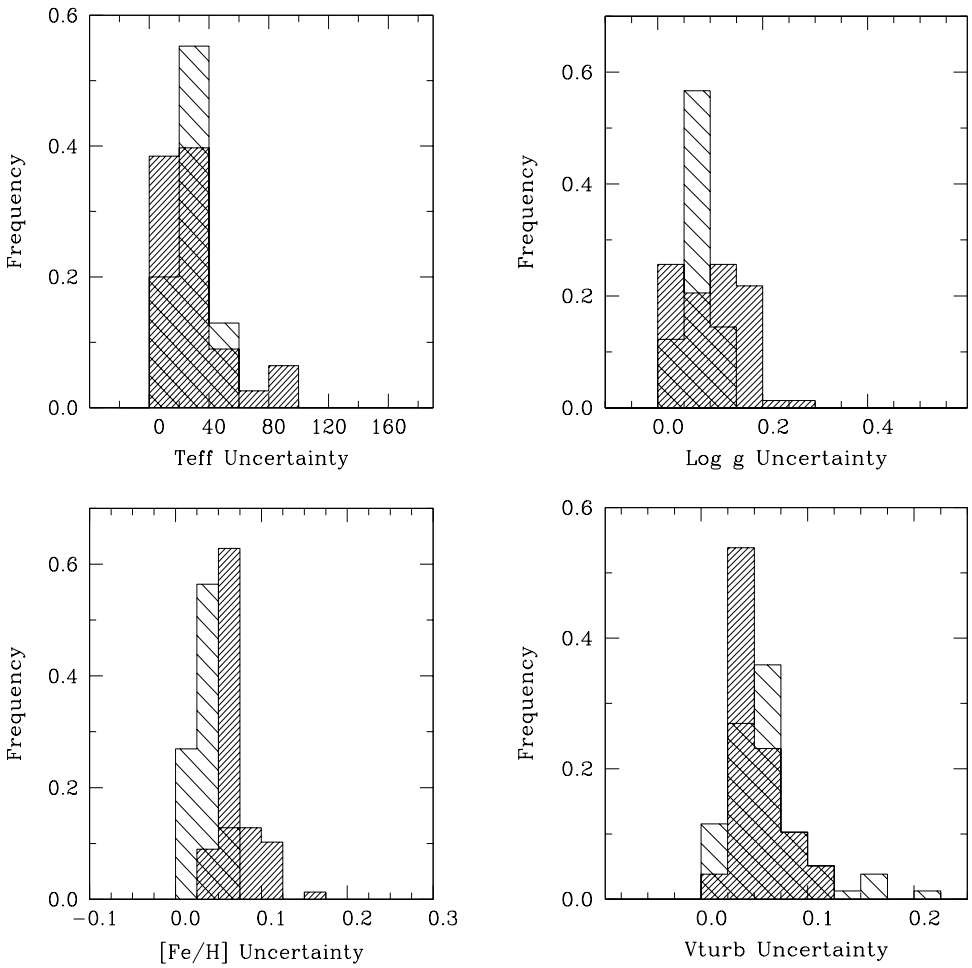

Fig. 4. Histogram distributions of the uncertainties in $T_{\rm eff}$, $\log g$, [Fe/H] and ξ derived with FUNDPAR. The densely and slightly shaded histograms correspond to uncertaities derived following Gonzalez & Vanture (1998) and using the χ^2 function, respectively.

a fact known from the literature (see, for example, Gonzalez 1997; Santos et al. 2000).

7. CONCLUDING REMARKS

We have implemented a Fortran algorithm available from the web that estimates fundamental parameters of solar type stars, requiring only the measurement of Fe equivalent widths. The final solution should verify the three conditions of the standard method: [FeI/H]=[FeII/H] (i.e., ionization equilibrium), independence of the metallicity from the excitation potential (i.e., excitation equilibrium) and from the equivalent widths. We also add another condition: the input metallicity used in the model atmosphere should be similar to the resulting metallicity from the equivalent widths. We taken into account these conditions in one variable called χ^2, adopting an expression which includes the weights w_1,...,w_4. FUNDPAR uses Kurucz model atmospheres with the NEWODF opacities (Castelli & Kurucz 2003), solar-scaled abundances from Grevesse & Sauval (1998) and the 2009 version of the MOOG program. Different details could be selected, such as the mixing-lenght parameter, the overshooting and the damping of the lines, for instance. We have planed a new version that includes the option of using the WIDTH9 program instead of MOOG.

The code includes the derivation of the uncertainty in the four parameters following the criteria of Gonzalez & Vanture (1998) and another uncertainty estimation using the χ^2 function. We verified the metal-rich nature of a group of exoplanet host stars. The parameters derived with FUNDPAR are in agreement with previous values in the literature.

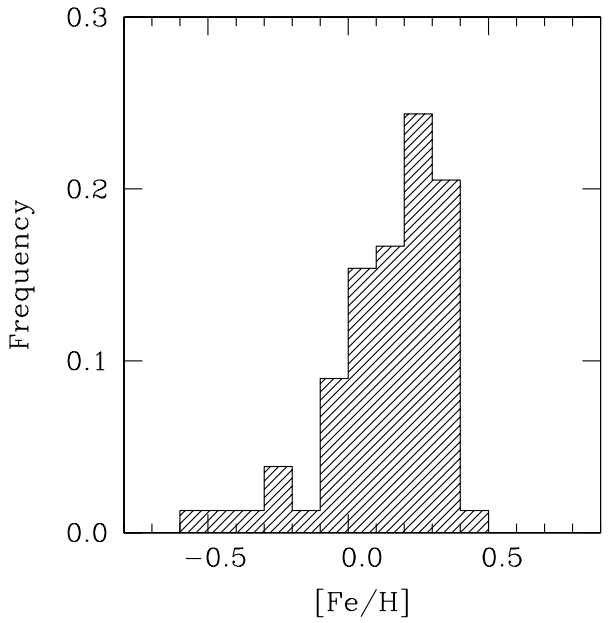

Fig. 5. Metallicity distribution of the sample stars derived by FUNDPAR.

The author thank R. L. Kurucz, C. Sneden, L. Sbordone, P. Bonifacio and F. Castelli for making their codes available to him. We also thank the anonymous referee whose suggestions improved the paper. This work was partially supported by a grant PIP 1153 from Consejo Nacional de Investigaciones Científicas y Técnicas de la República Argentina.

REFERENCES

Ammler-von Eiff, M., et al. 2009, A&A, 507, 523
Anders, E., & Grevesse, N. 1989, Geochim. Cosmochim. Acta, 53, 197
Blackwell, D. E., Lynas-Gray, A., & Smith, G. 1995, A&A, 296, 217
Castelli, F., Gratton, R., & Kurucz, R. 1997, A&A, 318, 841
Castelli, F., & Kurucz, R. 2003, in IAU Symp. 210, Modelling of Stellar Atmospheres, ed. N. Piskunov, W. W. Weiss, & D. F. Gray (San Francisco: ASP), A20
Edvarsson, B., Andersen, J., Gustafsson, B., Lambert, D. L., Nissen, P. E., & Tomkin, J. 1993, A&A, 275, 101
Fischer, D., & Valenti, J. 2005, ApJ, 622, 1102
Gonzalez, G. 1997, MNRAS, 285, 403
_____. 1998, A&A, 334, 221
Gonzalez, G., & Laws, C. 2000, AJ, 119, 390
Gonzalez, G., Laws, C., Tyagi, S., & Reddy, B. 2001, AJ, 121, 432
Gonzalez, G., & Vanture, A. D. 1998, A&A, 339, L29
Gonzalez, G., Wallerstein, G., & Saar, S. 1999, AJ, 511, L111
Grevesse, N., & Sauval, A. J. 1998, Space Sci. Rev., 85, 161
Kurucz, R. L. 1990, in Stellar Atmospheres: Beyond Classical Models, ed. L. Crivellari (Dordrecht: Kluwer), 441
_____. 1993, CD-ROM No. 13, ATLAS9 Stellar Atmosphere Programs and 2 km/s grid (Cambridge: SAO)
Laws, C., & Gonzalez, G. 2001, AJ, 553, 405
Laws, C., Gonzalez, G., Walker, K., Tyagi, S., Dodsworth, J., Snider, K., & Suntzeff, N. 2003, AJ, 125, 2664
Nelder, J. A., & Mead, R. 1965, Computer Journal, 7, 308
Olsen, E. H. 1984, A&AS, 57, 443
Press, W. H., Teukolsky, S. A., Vetterling, W. T., & Flannery, B. P. 1992, Numerical Recipes in Fortran: The Art of Scientific Computing, (2nd ed.; Cambridge: Cambridge Univ. Press)
Saffe, C., Gómez, M., Pintado, O., & Gonzalez, E. 2008, A&A, 490, 297
Saffe, C., & Levato, H. 2004, A&A, 418, 1083
Santos, N. C., Israelian, G., & Mayor, M. 2000, A&A, 363, 228
_____. 2004, A&A, 415, 1153
Schuster, W. J., & Nissen, P. E. 1989, A&A, 221, 65
Sousa, S. G., Alapini, A., Israelian, G., & Santos, N. C. 2010, A&A, 512, 13
Sozzetti, A., et al. 2007, ApJ, 664, 1190
Sozzetti, A., et al. 2009, ApJ, 691, 1145

C. Saffe: Instituto de Ciencias Astronómicas, de la Tierra y del Espacio (ICATE), C.C 467, 5400, San Juan, Argentina. Member of the Carrera del Investigador Científico, Consejo Nacional de Investigaciones Científicas y Técnicas (CONICET) de la República Argentina (csaffe@icate-conicet.gob.ar).

Revista Mexicana de Astronomía y Astrofísica, **47**, 15–29 (2011)

THE PARKER INSTABILITY IN AXISYMMETRIC FILAMENTS: FINAL EQUILIBRIA WITH LONGITUDINAL MAGNETIC FIELD

F. J. Sánchez-Salcedo[1] and A. Santillán[2]

Received 2010 August 4; accepted 2010 November 18

RESUMEN

En este trabajo se estudian los estados finales de equilibrio que surgen de la inestabilidad de Parker cuando partimos de una configuración cilíndrica de gas en equilibrio magnetohidrostático en un campo gravitacional radial y con un campo magnético longitudinal. Nuestro objetivo es comparar los estados de equilibrio no lineales con los que se obtienen en los sistemas con geometría Cartesiana. Se presentan los mapas de densidad y de las líneas de campo magnético en ambas geometrías para un campo gravitacional de intensidad constante. Encontramos que el flotamiento magnético es menos eficiente bajo simetría axial que en una atmósfera Cartesiana. Como consecuencia, las condensaciones que se forman en el modelo axisimétrico tienen menor densidad columnar. Por ende, el cociente entre la presión magnética y térmica en el estado final toma valores más extremos bajo simetría Cartesiana. Se discuten también algunos modelos en los que el campo gravitacional no es uniforme.

ABSTRACT

We study the final equilibrium states of the Parker instability arising from an initially unstable cylindrical equilibrium configuration of gas in the presence of a radial gravitational field and a longitudinal magnetic field. The aim of this work is to compare the properties of the nonlinear final equilibria with those found in a system with Cartesian geometry. Maps of the density and magnetic field lines, when the strength of the gravitational field is constant, are given in both geometries. We find that the magnetic buoyancy and the drainage of gas along field lines are less efficient under axial symmetry than in a Cartesian atmosphere. As a consequence, the column density enhancement arising in gas condensations in the axially-symmetric model is smaller than in a Cartesian geometry. The magnetic-to-gas pressure ratio in the final equilibrium state takes more extreme values in the Cartesian model. Models with non-uniform radial gravity are also discussed.

Key Words: instabilities — ISM — ISM: structure — magnetic fields — MHD

1. INTRODUCTION

Parker (1966) demonstrated that a layer supported against the vertical gravity by the pressure of interstellar gas, horizontal magnetic field and cosmic rays is always unstable to long wavelength deformations of the field lines because of the buoyancy of magnetic field and cosmic rays. Much work has been done to understand the role of the Parker instability in modeling the structure of the interstellar medium (ISM) and, more specifically, its role in gathering gas to trigger the formation of giant molecular clouds (e.g., Mouschovias, Shu, & Woodward 1974; Blitz & Shu 1980; Mouschovias, Kunz, & Christie 2009). Giz & Shu (1993), Kim, Hong, & Ryu (1997) and Kim & Hong (1998) examined how the non-uniform nature of the Galactic gravity might affect the length and timescales of the Parker instability. Many studies have been devoted to investigate the effect of other physical ingredients on the Parker instability (Shu 1974; Nakamura, Hanawa, & Nakano 1991; Hanawa, Matsumoto, & Shibata 1992; Hanasz & Lesch 2000; Kim et al. 2000; Santillán et al. 2000; Kim, Ryu, &

[1]Instituto de Astronomía, Universidad Nacional Autónoma de México, Mexico.

[2]DGTIC, Universidad Nacional Autónoma de México, Mexico.

Jones 2001; Franco et al. 2002; Kosiński & Hanasz 2006, 2007; Lee & Hong 2007; Mouschovias et al. 2009).

The structure of the final static state resulting from the Parker instability was derived by Mouschovias (1974, hereafter M74) in the Cartesian model, namely, for a non-rotating layer under a vertical gravity, with a horizontal magnetic field in the initial equilibrium state. In the unperturbed state, the gas is in hydrostatic equilibrium in a stratified layer, so that all the quantities depend only on the distance from the midplane y, and the magnetic field is plane-parallel and runs along the x-direction. In this *two-dimensional Cartesian* problem, one assumes that all the quantities are independent of the third dimension, z, at any time. In the final state, the magnetic field rises in certain regions and sinks in others forming bulges and valleys. Matter loads onto the field lines by draining down from the top region of the bulge and sinking into the valleys.

So far, the final states of the Parker instability have been discussed in Cartesian models. In various astrophysical systems, however, the gas tends to form structures with other symmetries, such as filaments or elongated structures (e.g., Genzel & Stutzki 1989; Alfaro, Cabrera-Caño, & Delgado 1992; Ryu, Kang, & Biermann 1998; Conselice, Gallagher, & Wyse 2001; Salomé et al. 2006; Jackson et al. 2010). Suppose now that we have a very elongated self-gravitating filamentary structure with a magnetic field traveling along the major axis of this structure, such that it has the effective geometry of a infinite cylinder. If the filament is supported against the radial self-gravity of the system by the pressure of gas and the longitudinal magnetic field, long wavelength deformations of the magnetic field lines will allow matter to slide radially along field lines under the action of the gravitational field towards the symmetry axis, whereas the magnetic field will tends to expand in radius, through a process of magnetic buckling (see Figure 1). If the disturbances are axisymmetric, we expect the alternate formation of magnetic bottlenecks in the condensations of gas separated by portions of inflated magnetic lines or arcades, resembling a sausage mode. The final state is expected to be different from than of a vertically stratified disk such as those models currently used to study the Parker instability in galactic disks. In fact, the response of the system and the final equilibrium state depend on the adopted model: Cartesian or axisymmetric.

In this paper, we study the nonlinear final equilibria of the Parker instability of a non-rotating,

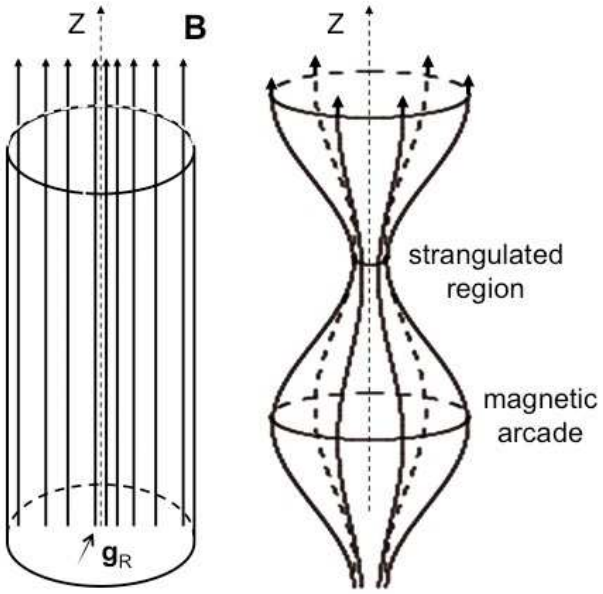

Fig. 1. Sketch of the magnetic field configuration in the initial (left panel) and final (right panel) equilibrium states in axial symmetry.

cylindrical initial state. In the initial state, the magnetic field is assumed to be parallel to the axis of the cylinder, which is taken to coincide with the z-axis. The cylinder is supported against the action of a radial gravitation field g_R by the thermal and magnetic pressures (see Figure 1). We will assume that the gas is isothermal and evolves under flux-freezing conditions. For axisymmetric perturbations, all the quantities depend only on z and R (not on the azimuthal angle ϕ) and hence the problem is also two-dimensional. The evolution of the Parker instability in the (z, R)-plane is expected to be qualitatively analogous, in the main features, to the evolution found in the (x, y)-plane for the case of a plane-parallel initial state by M74. Throughout the paper, we will use the coordinate z to denote the distance on the axis of symmetry in the axisymmetric model; it should not be confused with the third component of the Cartesian model.

The aim of this work is to compare in detail how the final distributions of density and magnetic field vary from Cartesian to axisymmetric geometry[3]. Accurate predictions of the nonlinear final states, an interesting problem in itself, can be very useful for the purpose of testing MHD codes. We will follow Mouschovias' procedure (1974, 1976) to construct the final equilibrium states. Nakano (1979)

[3]Note that the change in the geometry of the system is, by no means, equivalent to a coordinate transformation.

and Tomisaka, Ikeuchi, & Nakamura (1988) used the same technique to find the structure of axisymmetric magnetized clouds that can be reached from *nonequilibrium spherical* configurations. By contrast, we start from a cylindrical configuration in magnetohydrostatic equilibrium as those used to study the gravitational collapse and fragmentation of filamentary clouds (e.g., Nakamura, Hanawa, & Nakano 1995). In these simulations, however, the gravitational instabilities play a dominant role and not the Parker instability itself. In order to isolate the outcomes of the Parker instability, we will not consider self-gravity of the gas. In addition, we will also ignore the destabilizing influence of the interchange mode and the magnetic field curvature in the equilibrium states (Asséo et al. 1978, 1980; Lachièze-Rey et al. 1980), which could lead to the development of substructure. The study of these instabilities requires a full magnetohydrodynamical model and they will not be discussed further here.

Our paper is organized as follows. In § 2, we describe the initial equilibrium configurations. The elliptic differential equations that give the equilibrium states under flux-freezing conditions are provided in § 3. In § 4 we compare the resulting features of the final states arising from the Parker instability in Cartesian and axisymmetric models. A summary of the results is presented in § 5.

2. INITIAL STATES

We consider first the initial state in the Cartesian model, that is, a planar layer that is supported against the vertical gravity field by the gas pressure P and a horizontal magnetic field. We will use a Cartesian coordinate system (x, y), where x is the horizontal coordinate and y is the distance to the midplane of the layer, so that $\vec{B}_0 = (B_{0,x}(y), 0)$ in the initial state. Throughout the paper, the subscript 0 signifies the initial state. Magnetohydrostatic equilibrium is satisfied if

$$\vec{\nabla}\left(P_0 + \frac{B_{0,x}^2}{8\pi}\right) = -\rho\vec{\nabla}\psi, \tag{1}$$

where $\psi = \psi(y)$ is the gravitational potential. If the gas is isothermal with thermal sound speed c_s and the ratio of the magnetic to gas pressures, $\alpha \equiv B_0^2/8\pi P_0$, is constant, the equilibrium equation reads

$$(1+\alpha)c_s^2\vec{\nabla}\ln\rho_0 = -\vec{\nabla}\psi, \tag{2}$$

which has the solution

$$\rho_0(y) = \rho_0(0)\exp\left(-\frac{\psi}{(1+\alpha)c_s^2}\right), \tag{3}$$

with $\psi(0) = 0$. If the gravitational field $\vec{g} = -\vec{\nabla}\psi$ is taken to be vertical and constant (but it reverses its direction across the midplane), we have $\psi = g|y|$, with g = constant > 0. In this particular case, the mass density decays exponentially with a typical scale H of $(1+\alpha)c_s^2/g$, whereas the magnetic field strength decays with a characteristic scale $2H$.

If, instead of a planar atmosphere, we assume that the gas extends to infinity along a cylinder whose axis coincides with the z-axis, and is threaded by an axial magnetic field B_z, the density profile at equilibrium is:

$$\rho_0(R) = \rho_0(0)\exp\left(-\frac{\psi}{(1+\alpha)c_s^2}\right), \tag{4}$$

where R is the radial distance in cylindrical coordinates and $\psi(R)$ is the gravitational potential, with $\psi(0) = 0$. In fact, we assume that the gravitational acceleration has only a radial component. If the radial gravitational force is taken to be constant, it holds that $\psi = gR$. Therefore, the radial scalelength for the density is$H = (1+\alpha)c_s^2/g$, as in Cartesian geometry.

We see that if the gravitational potential $\psi(y)$ in the infinite planar layer is identical to the gravitational potential $\psi(R)$ in the cylindrical model, the profiles of density, magnetic field and gas pressure along y and R will be identical in both models. However, these systems are no longer equivalent when the Parker instability arises. In the Cartesian model, magnetic field lines are allowed to inflate only in the vertical direction, whereas the expansion of field lines as well as the contraction of matter occur radially in the axisymmetric model (see Figure 1). The question that arises is how the distributions of density, pressure and field lines in an azimuthal section [i.e. in the (z, R)-plane] will look like as compared to those found in a vertical section [i.e. in the (x, y)-plane] in the well-studied Cartesian model.

When studying the Parker instability at the solar neighborhood, it is common to use a local Cartesian frame where the azimuthal direction is identified with the horizontal coordinate x and the vertical direction in the Galaxy with y. In the two-dimensional approximation, the third (radial) direction is ignored. As a cautionary comment, our coordinate R used throughout the paper should not be confused with the radial direction in the Galaxy.

3. THE EQUILIBRIUM EQUATIONS

If a disturbance of sufficiently long wavelength is applied along the initial magnetic field to the initial equilibrium states described in the previous section,

the Parker instability develops in time and parts of the magnetic field lines bulge outward until the tension of the field lines increases sufficiently for an equilibrium state to be established. In the final states arising from the Parker instability, the magnetic field lines are curved and the magnetohydrostatic force equation is

$$-\vec{\nabla}P - \rho\vec{\nabla}\psi + \frac{1}{c}\vec{J}\times\vec{B} = 0, \tag{5}$$

where $\vec{J}$ is the current density. The coordinate symmetries of the unperturbed states (see § 2) reduce the problem to the (x, y)-plane in the Cartesian model and to the (z, R)-plane in the axisymmetric model. Under these symmetries, flux-freezing allows to transform the magnetostatic equations of equilibria into a second-order elliptic partial differential equation (Dungey 1953), conventionally called the Grad-Shafranov equilibrium equation. The beauty of this approach is that the final equilibrium states can be found with no need to solve a time-dependent problem (M74; Mouschovias 1976). In the following we give the Grad-Shafranov equilibrium equations and the boundary conditions. Details on its derivation can be found in M74, Mouschovias (1976) and Nakano (1979).

3.1. *The Cartesian model*

In the Cartesian layer with one ignorable coordinate, so that all quantities depend only on (x, y), the magnetic vector potential can be written as $\vec{A} = A(x, y)\hat{e}_z$ and then $B_x = \partial A/\partial y$ and $B_y = -\partial A/\partial x$. One can show that the scalar function $q(x, y)$, defined by

$$q = P\exp\left(\frac{\psi}{c_s^2}\right), \tag{6}$$

is constant on a field line *at magnetohydrostatic equilibrium*, and is given by:

$$q(A) = \frac{c_s^2}{2}\frac{d\tilde{m}}{dA}\left[\int_0^{\lambda_x/2} dx \frac{\partial y(x, A)}{\partial A}\exp\left(-\frac{\psi(x, A)}{c_s^2}\right)\right]^{-1}, \tag{7}$$

where λ_x is the perturbation wavelength along the initial magnetic field and $d\tilde{m}$ is the mass per unit length (along the ignorable coordinate) in a flux tube between field lines characterized by A and $A + dA$ and between $x = 0$ and $x = \lambda_x$ (i.e. the mass-to-flux ratio). Under flux-freezing conditions, the mass-to-flux ratio is a constant of motion and, therefore, can be determined from the initial equilibrium configuration:

$$\frac{d\tilde{m}}{dA} = \lambda_x\frac{\rho_0(A)}{B_0(A)}. \tag{8}$$

Finally, the magnetic equilibrium equation (5) may be written in terms of A as

$$\nabla^2 A = -4\pi\frac{dq}{dA}\exp\left(-\frac{\psi}{c_s^2}\right), \tag{9}$$

(Dungey 1953; M74). Once the boundary conditions are specified, equations (7) and (9) can be solved numerically by using an iterative scheme (M74).

The boundary conditions we take are the same as those in M74. The system is assumed to be periodic in x and symmetric about the x-axis so that equation (9) is solved in the rectangle $0 < x < X_{\max}$ with $X_{\max} = \lambda_x/2$ and $0 < y < Y_{\max}$, with the boundary conditions

$$\left.\frac{\partial A}{\partial x}\right|_{x=0, X_{\max}} = 0. \tag{10}$$

The upper boundary must be far enough from the midplane to not affect the evolution, since a small vertical size of the computational domain suppresses the instability (e.g., M74; Mouschovias 1996). At the upper boundary we impose the condition that the field lines are not deformed, $A(x, Y_{\max}) = A_0(Y_{\max})$. Due to the imposed reflection symmetry about the midplane, the field line originally coinciding with the x-axis remains undeformed.

In the following, we provide the equations for the particular case of a constant external field. Although a uniform acceleration is only realistic at high altitudes from the midplane, we will concentrate on this case for simplicity and to facilitate comparison with some previous work that uses a constant gravitational field (e.g., M74; Mouschovias et al. 2009). A realistic model of the gravitational potential is important to derive the growth rate of the instability and the most unstable wavelength, which determines the separation of the magnetic valleys (Kim & Hong 1998; § 4.2). For now, we are mainly interested in the main conceptual features that arise in the final equilibria states when the geometry of the problem is changed, even if the adopted spatial dependence of the gravitational field lacks a strong astrophysical motivation.

As said in § 2, if the external gravitational field is constant, the gravitational potential is $\psi = g|y|$, with g a positive and constant acceleration. The equations are put in dimensionless form by choosing the following natural units: c_s^2/g, c_s and $\rho_0(0)$, for length, velocity and density, respectively. The magnetic vector potential will be measured in units of $-2HB_0(0)$. Note that the dimensionless vertical scale is $H = (1+\alpha)$ in these units. The dimensionless equation (9) has the form

$$\nabla^2 A = \hat{Q}_{xy}(x, y; \alpha), \tag{11}$$

where

$$\hat{Q}_{xy} = -\frac{1}{8\alpha(1+\alpha)^2}\frac{dq}{dA}\exp(-y). \quad (12)$$

In these units,

$$q(A) = \frac{1}{2}\frac{d\tilde{m}}{dA}\left[\int_0^{\lambda_x/2} dx \frac{\partial y(x,A)}{\partial A}\exp[-y(x,A)]\right]^{-1}, \quad (13)$$

where

$$\frac{d\tilde{m}}{dA} = -2\lambda_x(1+\alpha)A. \quad (14)$$

Under a constant gravity condition, the vector potential in the plane-parallel unperturbed state is

$$A_0(y) = \exp\left(-\frac{y}{2(1+\alpha)}\right), \quad (15)$$

and the source term of equation (11) is

$$\hat{Q}^{(i)}_{xy} = \frac{1}{4(1+\alpha)^2}\exp\left(-\frac{y}{2(1+\alpha)}\right). \quad (16)$$

In this initial state, the relation between A and q is $A_0(q) = q^{-1/(2\alpha)}$ (see also M74).

3.2. *The axisymmetric model*

Now, we consider a three-dimensional geometry with axial symmetry about the z-axis and longitudinal magnetic field ($B_\phi = 0$). The magnetic field is related to the potential vector $\vec{A} = A(z,R)\hat{e}_\phi$ by $B_z = R^{-1}\partial(RA)/\partial R$ and $B_R = -\partial A/\partial z$. Under axisymmetric disturbances, the magnetic flux $\Phi(R,z) \equiv RA$ is constant on a magnetic surface and is also a constant of the motion. In this geometry, the function q defined in equation (7) is given by

$$q(\Phi) = \frac{c_s^2}{2\pi}\frac{dm}{d\Phi}\left[\int_0^{\frac{\lambda_z}{2}} dz \frac{\partial R^2(z,\Phi)}{\partial\Phi}\exp\left(-\frac{\psi(z,\Phi)}{c_s^2}\right)\right]^{-1}, \quad (17)$$

where λ_z is the longitudinal perturbation wavelength and dm is the mass in a flux tube between Φ and $\Phi + d\Phi$ and between $z = 0$ to $z = \lambda_z$. Again, q is a constant along field lines in equilibrium configurations. Under flux-freezing conditions, the mass-to-flux ratio is a constant of the motion, which can be determined from the initial configuration by:

$$\frac{dm}{d\Phi} = 2\pi\lambda_z\frac{\rho_0}{B_0}. \quad (18)$$

The balance of forces (equation 5) in the final magnetic configuration can be rewritten in terms of Φ as

$$\nabla^2\Phi - \frac{2}{R}\frac{\partial\Phi}{\partial R} = -4\pi R^2\frac{dq}{d\Phi}\exp\left(-\frac{\psi}{c_s^2}\right), \quad (19)$$

(Mouschovias 1976; Nakano 1979). Equation (19) together with equation (17) enable us to derive $\Phi(z,R)$ once the boundary conditions are specified. The magnetic field can be found just by simple derivation: $B_z = R^{-1}\partial\Phi/\partial R$ and $B_R = -R^{-1}\partial\Phi/\partial z$.

The computational domain is a rectangular box of $0 < z < Z_{\max}$ and $0 < R < R_{\max}$. Because of the symmetries of the initial and final states, the length of the computation box in the z-direction, $Z_{\max}$, is taken to be $\lambda_z/2$, half the wavelength of the perturbation. Periodicity in z translates into

$$\left.\frac{\partial\Phi}{\partial z}\right|_{z=0,Z_{\max}} = 0. \quad (20)$$

The definition of Φ means that $\Phi(0,z) = 0$ at any time. Assuming that the deformation of field lines can be neglected on the surface of the cylinder, we impose the condition that $\Phi(z,R_{\max}) = \Phi_0(R_{\max})$.

The equivalent condition of constant gravity is to assume that the radial gravitational field is constant, i.e. $\vec{g} = -g\hat{e}_R$, with g a positive constant acceleration. We may use the units for distance, velocity and density described in the previous subsection. The magnetic flux will be measured in units of $-4H^2B_0(0)$. Equation (19) in dimensionless form is:

$$\nabla^2\Phi - \frac{2}{R}\frac{\partial\Phi}{\partial R} = Q_{zR}(z,R;\alpha), \quad (21)$$

with

$$Q_{zR} = -\frac{R^2}{32\alpha(1+\alpha)^4}\frac{dq}{d\Phi}\exp(-R), \quad (22)$$

and

$$q(\Phi) = \frac{1}{2\pi}\frac{dm}{d\Phi}\left[\int_0^{\lambda_z/2} dz \frac{\partial R^2(z,\Phi)}{\partial\Phi}\exp[-R(z,\Phi)]\right]^{-1}, \quad (23)$$

where the dimensionless mass-to-flux is

$$\frac{dm}{d\Phi} = -8\pi(1+\alpha)^2\lambda_z\frac{\rho_0}{B_0} \quad (24)$$

$$= -8\pi(1+\alpha)^2\lambda_z\exp\left(-\frac{R(\Phi)}{2(1+\alpha)}\right). \quad (25)$$

By comparing equations (21)–(22) with equations (11)–(12), we see that the dynamical variable Φ also satisfies a nonlinear elliptical differential equation, but with a differential operator and source term different from those of the equation governing A in the Cartesian model.

In order to gain some physical insight, it is useful to compute the function $q(\Phi)$ in the initial equilibrium configurations which, of course, are solutions

of the differential equation (21). In a model with uniform radial gravitational field, the magnetic flux and the q-function in the unperturbed state are, respectively:

$$\Phi_0(R) = \left(1 + \frac{R}{2(1+\alpha)}\right) \exp\left(-\frac{R}{2(1+\alpha)}\right), \quad (26)$$

and

$$q_0(R) = \exp\left(\frac{\alpha R}{1+\alpha}\right). \quad (27)$$

At small enough R, say $R \ll 2(1+\alpha)$, they can be approximated by $\Phi_0(R) \approx \exp(-R/2[1+\alpha])$ and $q_0(\Phi_0) = \Phi_0^{-2\alpha}$. Interestingly, they have exactly the same forms as $A_0(y)$ and $q_0(A)$ in the Cartesian model, respectively (see equation 15 and the very end of § 3.1). At large radii, $R \gg 2(1+\alpha)$, or equivalently, $\ln q \gg 2\alpha$, the relationship between Φ_0 and q_0 is $\Phi_0 \simeq (2\alpha)^{-1} q_0^{-1/(2\alpha)} \ln q_0$. Therefore, at these large q values, q increases with Φ^{-1} slightly faster than the rate at which q increases with A^{-1} in the Cartesian model ($q = A^{-2\alpha}$). In § 4, we will calculate the dependence of the function q on Φ in the final axially-symmetric equilibrium state. The shape of $q(\Phi)$ as compared to $q(A)$ in the Cartesian model will be also discussed.

The source term of the differential equation in the initial cylindrical configuration with constant g_R is:

$$Q_{zR}^{(i)} = \frac{1}{8(1+\alpha)^3} R \exp\left(-\frac{R}{2(1+\alpha)}\right). \quad (28)$$

By comparing equations (16) and (28), we see that $Q_{zR}^{(i)}$ has a similar dependence on R as $\hat{Q}_{xy}^{(i)}$ on y, except by the factor $R/(2+2\alpha)$. As a consequence, $Q_{zR}^{(i)}$ has a maximum at $2(1+\alpha) = 2H$, whereas $\hat{Q}_{xy}^{(i)}$ is a monotonically decreasing function of y. In order to facilitate comparison between both cases, it is convenient to use Q_{xy} defined as $Q_{xy} \equiv y\hat{Q}_{xy}/(2+2\alpha)$ because both Q_{xy} and Q_{zR} are identical at the initial state. However, they are expected to depart from each other in the nonlinear equilibrium state because of the changes introduced by the different geometries. The form of Q_{xy} and Q_{zR} in the final equilibrium states will be discussed in the next section.

4. FINAL EQUILIBRIUM STATES

The final equilibrium state can be reached from the initial configuration through continuous deformations of field lines using an iterative method as described in M74. To do so, we add a perturbation to the magnetic variables in the initial equilibrium state,

$$\delta A(x,y) = -\mu A_0(y) \sin\left(\frac{\pi y}{Y_{\max}}\right) \cos\left(\frac{\pi x}{X_{\max}}\right), \quad (29)$$

for the Cartesian model and

$$\delta\Phi(z,R) = -\mu \Phi_0(R) \sin\left(\frac{\pi R}{R_{\max}}\right) \cos\left(\frac{\pi z}{Z_{\max}}\right), \quad (30)$$

for the axisymmetrical model. Here μ is the amplitude of the perturbation which we chose between 0.02 and 0.06. Note that the perturbations are symmetric about $y = 0$ in the Cartesian model[4].

Our main interest is to compare the final equilibrium states in Cartesian and axisymmetrical models using the same external gravitational potential along y and R, respectively. In this way, the comparison can be done on a common ground. In the next subsection, we will do so for models with constant gravitational acceleration. A more realistic gravitational potential will be studied in § 4.2 in order to examine how it might affect the final nonlinear states.

4.1. *Constant gravitational acceleration*

Parker (1966) showed that a plane-parallel atmosphere with uniform gravity and a horizontal magnetic field is unstable to the undular mode if the horizontal wavelength of the perturbation is larger than a critical value, namely, $\lambda_x > \lambda_{\rm crit} \equiv 4\pi(1+\alpha)(2\alpha+1)^{-1/2}$. For the reference value $\alpha = 1$, the dimensionless critical wavelength is 14.5 or, equivalently, $7.26H$. Magnetic tension can stabilize disturbances with shorter wavelengths. The horizontal wavelength of the mode with the maximum growth rate depends on the vertical wavelength. For a typical value of $Y_{\max} = 24$, the maximum growth rate occurs at $X_{\max} = 12$ (i.e. $\lambda_x = 24$).

The stability of magnetized cylinders has been considered in the past (e.g., Stodolkiewicz 1963; Nagasawa 1987) but, to our knowledge, none derived the dispersion relation under the assumption of a constant gravitational field. Nevertheless, the linearized equations of motion under axial geometry and axisymmetric perturbations are identical to equations (III-3)–(III-6) quoted in Parker (1966), once the subscripts y and z in Parker's notation are replaced by z and R, except for the curvature term v_R/R that appears as an extra term in the continuity and energy equations. Since the curvature term

[4]The Cartesian model allows also solutions where field lines cross the midplane. They are called odd-parity solutions or midplane antisymmetric modes.

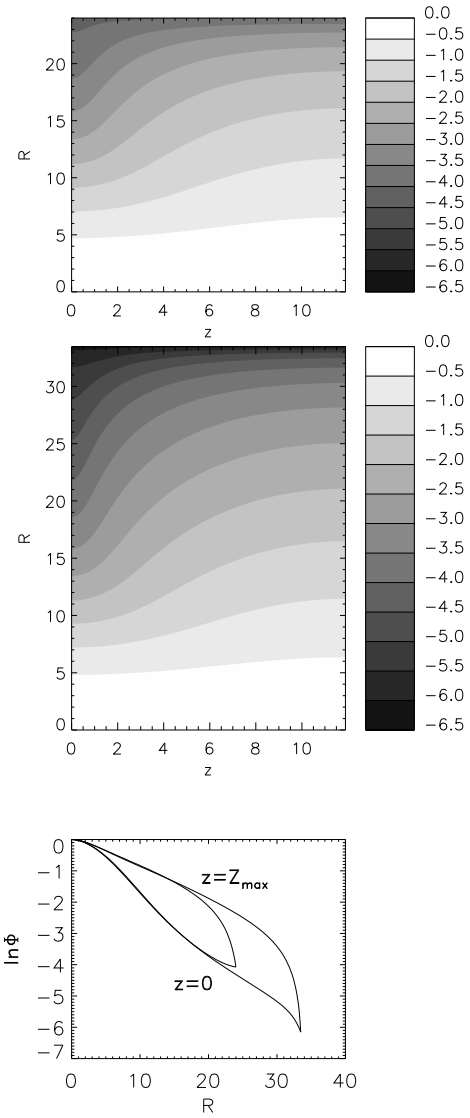

Fig. 2. Azimuthal section of the magnetic flux $\Phi(z, R)$ in the axially-symmetric final state for $\alpha = 1$ and $g_R = g =$ const, when the upper boundary is placed at $R_{\max} = 24$ (top) and at $R_{\max} = 33.5$ (middle). Magnetic field lines coincide with the isocontours of Φ. The grayscale bar is shown in a natural logarithmic scale. The unit length is c_s^2/g. A comparison of the radial profile of the magnetic flux along cuts at $z = 0$ and $z = Z_{\max}$ is given in the lower panel when the boundary is located at $R_{\max} = 24$ and $R_{\max} = 33.5$.

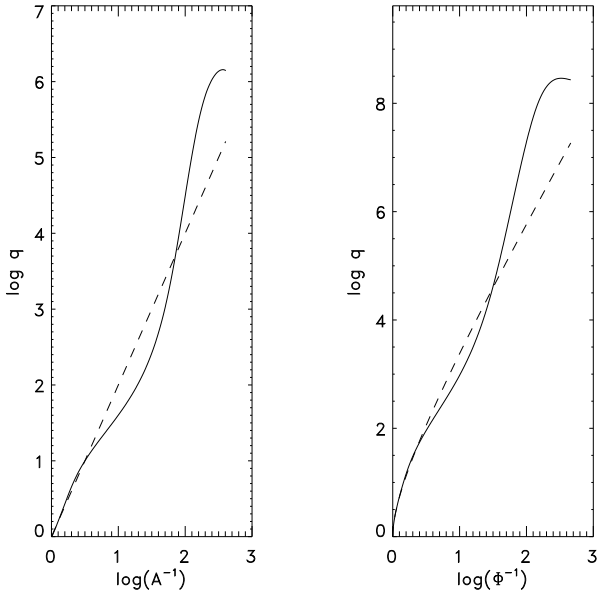

Fig. 3. The shape of the function $q(A)$ (left panel) and $q(\Phi)$ (right panel) in the initial state (dashed lines) and in the final state (solid lines), with $\alpha = 1$ and constant gravity, for $X_{\max} = 15$ and $Z_{\max} = 15$, respectively. Note that the range of the q-axis is different.

becomes small at scales comparable or larger than $\lambda_{\rm crit}$, the critical wavelength is essentially the same in both geometries. In fact, we have checked that our iterative scheme converges to the initial state as long as $\lambda_z \lesssim 7.5H$ (when $\alpha = 1$ is used), indicating that they are stable.

In the Cartesian atmosphere, M74 found that if the upper boundary is far enough from the galactic plane, i.e. $Y_{\max} \gg (1 + \alpha)$ in dimensionless units, the evolution of most of the matter in the domain is not affected by the location of the upper boundary. The reason is that more than 90% of the energy of the initial state resides under $y < 3.5(1 + \alpha)$ (see M74). In the axisymmetrical model, we can apply the same reasoning to expect that the solution is not significantly altered as long as the box size is much larger than the effective scaleheight, defined as the radius R at which Φ_0 decays by a factor e, namely, $4.3(1+\alpha)$ [note that the effective scaleheight of A_0 in the Cartesian model is $2(1 + \alpha)$]. In Figure 2 we compare the the magnetic flux of the final state in the axisymmetrical model using $\alpha = 1$ and $\lambda_z/2 = 12$, when the upper boundary, $R_{\max}$, is located at 24 and at 33.5. We see that both maps are almost identical at $R < 20$. The main difference is that the upper magnetic field lines in the magnetic bulge region inflate further out when the boundary is far away, because a larger column of material is unloaded and brought down to the valley of the curved magnetic field lines. Therefore, this upper region becomes lighter and more buoyant. By contrast, cuts of Φ along the valley $z = 0$ are very similar in both cases (see the lower panel of Figure 2). This means

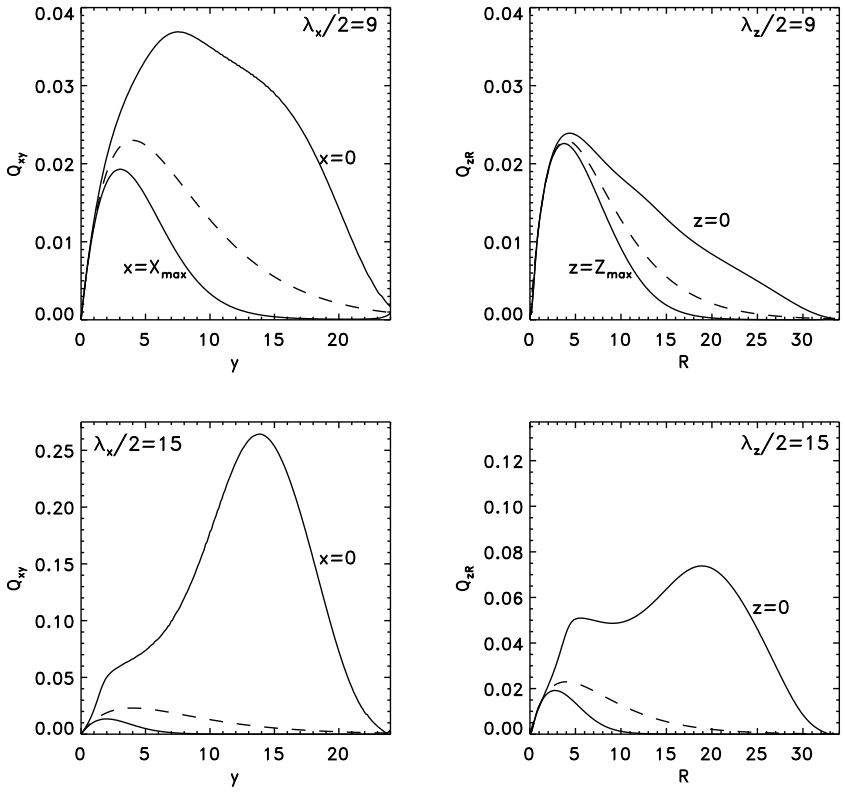

Fig. 4. The dependence of the functions Q_{xy} and Q_{zR} on y and R, respectively in the initial states (dashed lines) and in the final states (solid lines), with $\alpha = 1$ and constant gravity. In the left panels, Q_{xy} is shown along the lines $x = 0$ and $x = X_{\max}$ for two different wavelengths: $\lambda_x/2 = 9$ and 15. The right panels display Q_{zR} along the lines $z = 0$ and $z = Z_{\max}$ for $\lambda_z/2 = 9$ and 15, as quoted in the corners of these panels.

that the extra material that has been loaded into the valley when the upper boundary is placed at 33.5, does not cause significant additional compression in the radial direction.

In order to have the same dynamical range in all our calculations, we will place our upper boundary at the distance at which the variable of interest (A for the Cartesian model and Φ for the axisymmetric case) decreases to $\exp(-6.12) = 0.0022$ of its maximum value. With this convention, $Y_{\max} = 12.2(1+\alpha)$ and $R_{\max} = 16.7(1+\alpha)$. Interestingly, in the axisymmetric case, the corresponding density at $R_{\max}$ is only 5.4×10^{-8} of its value at $R = 0$.

Different magnetostatic equilibrium configurations can be found by choosing the function $q(A)$ for the Cartesian model and $q(\Phi)$ for the axisymmetric one. Parker (1966) explored the cases in which $q(A)$ is either a linear or quadratic function of A. In practice, these functions are not free because they are defined by the initial conditions. M74 emphasized that q increases when A decreases in the Cartesian model. In Figure 3, the functions $q(A)$ for the Cartesian layer and $q(\Phi)$ for the axially-symmetric configuration are plotted for $\alpha = 1$ and $\lambda_x/2 = \lambda_z/2 = 15$. In the initial state, the function $q_0(A)$ follows a power-law with index -2α (see § 3.1 and Figure 3). In the final equilibrium state, the power-law index varies with A, but $q(A)$ is always a monotonically decreasing function. As discussed in § 3.2 and shown in Figure 3, the slope of q in the initial state of the axisymmetric model is steeper than in the Cartesian model. In fact, q_0 reaches a maximum value of $10^{7.3}$ in the axisymmetric model, but only $10^{6.2}$ in the Cartesian model. Note that the range of the q-axis in Figure 3 spans somewhat different values in order to facilitate comparison of the shape of the curves. The behavior of q versus Φ in the final equilibrium state is similar to that of q versus A (see Figure 3), although the new geometry introduces some remarkable differences in the shape of the function $q(\Phi)$. For instance, the change of q, relative to its initial value, in the range $0.6 < \log_{10} \Phi^{-1} < 1.5$ is smaller than in the same range of A in the Cartesian model. The similar appearance of the functions

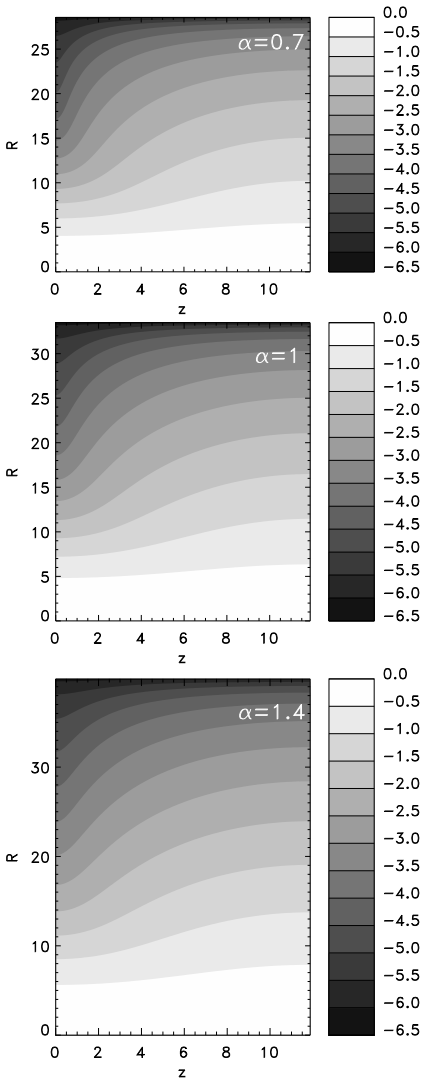

Fig. 5. Grayscale map of the magnetic flux $\Phi(z, R)$ in a natural logarithmic scale for the final state for $\lambda_z/2 = 12$ (in dimensionless units) and different values of α. The radial gravitational acceleration g_R was assumed to be constant.

$q(A)$ and $q(\Phi)$ should not lead us to the false conclusion that the source terms of the elliptic differential equations, namely $Q_{xy}(x, y)$ and $Q_{zR}(z, R)$, are also similar. Figure 4 displays Q_{xy} at two different cuts along $x = 0$ and $x = X_{\max}$, and Q_{zR} along $z = 0$ and $z = Z_{\max}$. The fractional change of Q_{xy} from its initial value is always larger than the change of Q_{zR}. Both Q_{xy} and Q_{zR} may present two local maxima along a cut through the maximum heights of the magnetic field lines, i.e., along $x = X_{\max}$ and $z = Z_{\max}$. The relative amplitude of these maxima varies with the wavelength of the perturbation.

Figure 5 shows contour plots of the magnetic flux in the final axisymmetric state for a disturbance with $\lambda_z/2 = 12$ and three different α values ($\alpha = 0.7, 1.0$ and 1.4). We see that the maps are a scaled version of each other by the factor $1+\alpha$. Since it is common for astrophysical purposes to assume equipartition between magnetic field and gas pressures, we will restrict ourselves to the case $\alpha = 1$ hereafter.

Figure 6 exhibits contour plots of the density (grayscale image) and magnetic field lines in the final stable state of the axisymmetric model for three different horizontal wavelengths ($\lambda_z/2 = 9, 12$ and 24). For comparison, density and magnetic field lines are also shown for the Cartesian model. Although the vertical size of the computational domain is larger in the axisymmetric case, we show the same box in all the cases for ease in visualization. When the systems are disturbed with the same wavelength, it is clear from Figure 6 that the field lines and the density contours become more deformed in the Cartesian model than under axial symmetry. It turns out that a cylindrical initial configuration is more rigid to perturbations and the magnetic field is less buoyant than a plane-parallel layer. Interestingly, the same degree of deformation of magnetic field lines found for $\lambda_x/2 = 9$ in the Cartesian model, can be achieved in the axisymmetric case but for a longer wavelength of $\lambda_z/2 = 12$. Likewise, the level of radial buoyancy of the magnetic field for $\lambda_z/2 = 15$ is comparable to the level of vertical buoyancy for $\lambda_x/2 = 12$ in the Cartesian model.

The column density map of a filament with $\alpha = 1$ and whose axis of symmetry lies in the plane of the sky is given in Figure 7 in the initial and final equilibrium states with $\lambda_z/2 = 15$. The scaleheight of the column density along a condensation in the direction perperdicular to z is about twice the scaleheight in the wings of the condensations. As a consequence of the less efficient drainage of gas into the magnetic valleys, the column density enhancement in the gas condensations is rather modest. In fact, the maximum enhancement in the column density over a line of sight with zero impact parameter is smaller than in the Cartesian model (see Figure 8). The column density may increase up to a factor of 7/4 in Cartesian geometry (see also Kim, Ryu, & Hong 2004) but only by a factor of 5/4 in the axisymmetric model.

The result that a cylindrical configuration is more rigid than a plane-parallel layer has, *a posteriori*, a simple geometrical explanation, as follows. Since magnetic forces act only perpendicular to the field lines, gas pressure gradients must balance the gravitational forces along a field line regardless the ge-

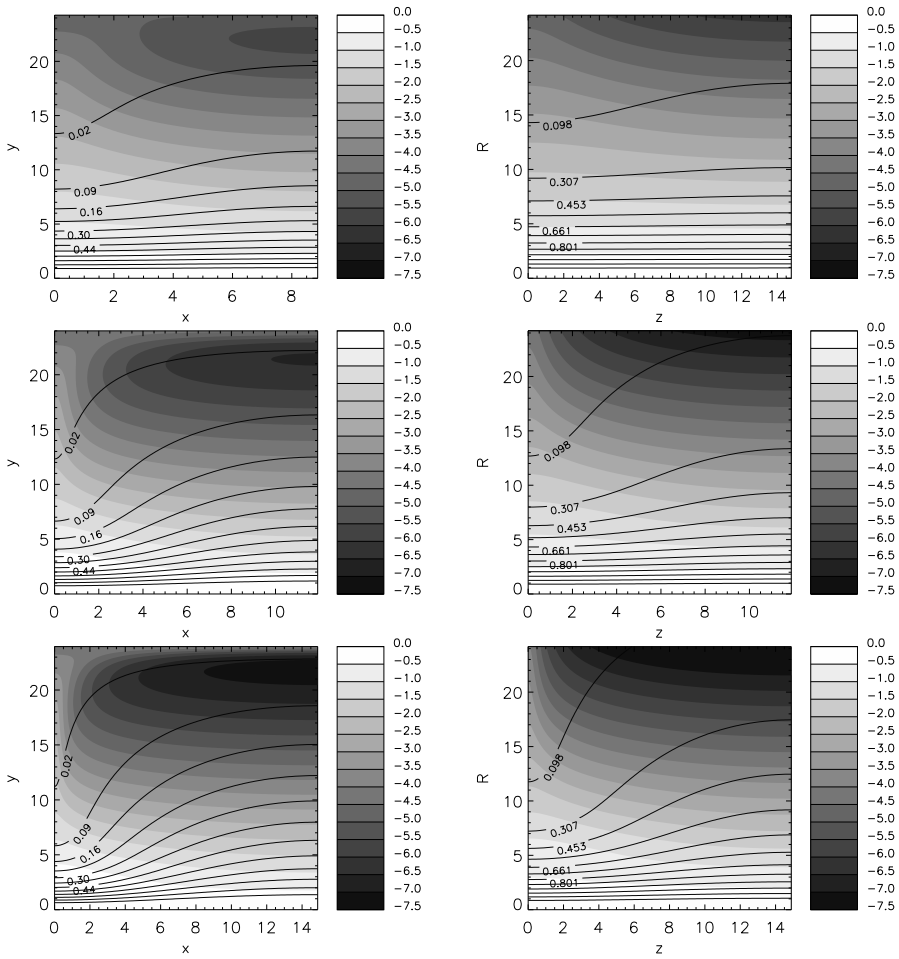

Fig. 6. Grayscale contour plots of the density and magnetic field lines (solid lines) for the Cartesian model (left) and the axisymmetric model (right), under constant gravity, for half the wavelength of 9, 12 and 15 in units of c_s^2/g (from top to bottom) and $\alpha = 1$. The bar gives the correlation between the grayscale and the natural logarithm of the density. The number on some curves is the value of A in the Cartesian model or the value of Φ in the axisymmetric model. To make the comparison of the deformation of the magnetic field lines easier, we plot the same magnetic lines in both models.

ometry of the problem. The plasma must slide down along the magnetic field lines until it reaches a new configuration of pressure equilibrium. The point is that, because of the radial convergence of the flow streamlines in the axisymmetrical model, we need less displacement of gas in the axisymmetric case than in the Cartesian model to achieve the same pressure gradient, as soon as the gas is isothermal, and, henceforth, less deformation of the magnetic field lines.

Since the separation between magnetic field lines in azimuthal sections do not reflect the magnetic strength in the axisymmetric case, it is illustrative to compare the magnetic pressure to make a fair comparison between the results in Cartesian and axial geometries (see Figure 9). Given a certain wavelength of the perturbation, the magnetic pressure maps depend on the geometry. Because of the stronger deformation in the Cartesian scenario, the magnetic pressure force and the magnetic stresses along the valleys of the magnetic field lines, i.e. at the cut $x = 0$, are larger than along $z = 0$. The distribution of magnetic pressure in the axial model with $\lambda_z/2 = 12$ is quite similar to the magnetic pressure configuration in the Cartesian case with $\lambda_x/2 = 9$.

The ratio of the magnetic to gas pressures is an indicator of the efficiency with which gas flows along field lines. As the increase of gas density in the magnetic field valleys is due primarily to the drainage along the field lines (see also M74), we expect that if the drainage is less efficient in the axisymmetri-

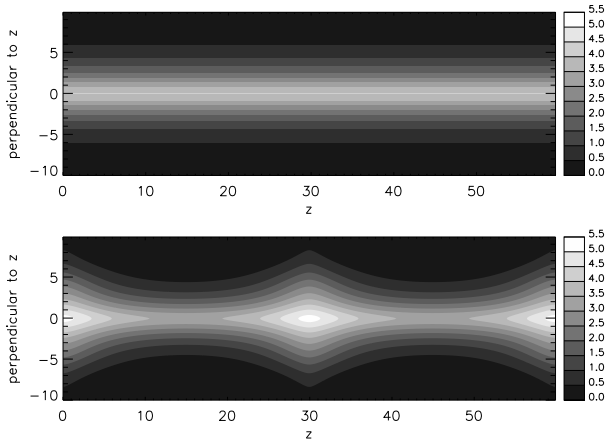

Fig. 7. Column density map for the initial (top panel) and final axisymmetric state (bottom panel) along a line of sight perpendicular to the axis of symmetry (z-axis). We used $\alpha = 1$, $\lambda_z/2 = 15$ and uniform radial gravity. The units of surface density and length are $\rho_0(0)c_s^2/g$ and c_s^2/g, respectively. Note that the scale is linear.

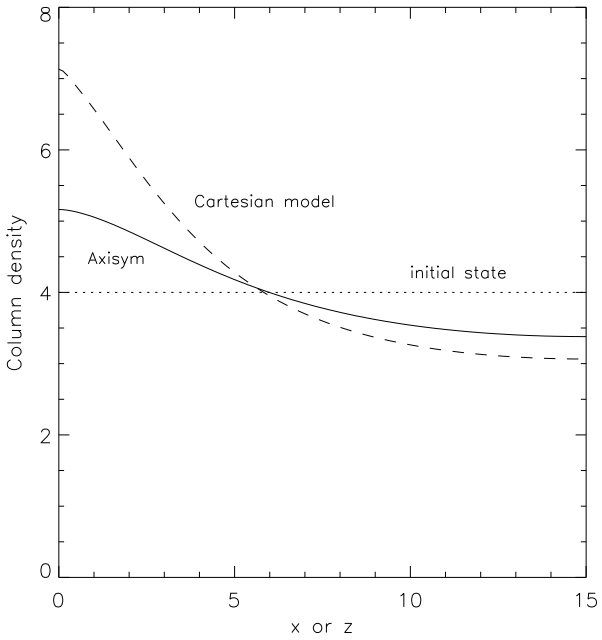

Fig. 8. Column density for the final states as a function of the horizontal coordinate for $\lambda/2 = 15$ and constant gravity. In the Cartesian model, the column density is $\Sigma(x) = \int_{-\infty}^{\infty} \rho(x, y)dy$. In the axisymmetric model, we plot the column density along a line of sight perpendicular to the axis of symmetry and with null impact parameter, i.e. $\Sigma(z) = \int_{-\infty}^{\infty} \rho(z, R)dR$. The column density at the initial states is drawn as a dotted line.

cal case, the variation of α in the final state relative to the initial values should be also smaller. In Figure 10, we plot the distribution of the magnetic-to-gas pressure ratio along $x = 0$ and $x = X_{\max}$ for the Cartesian model, and along the same cuts $z = 0$ and $z = Z_{\max}$ for the axisymmetric model in the final state, for a perturbation with half the wavelength of 15. Although the general shape of the curves is rather similar in both geometries, the α values in the range $10 < y < 22$ at $x = X_{\max}$ are almost a factor of 10 larger than in the axisymmetric model at the same region (i.e. $10 < R < 22$ and $z = Z_{\max}$).

4.2. *Non-uniform gravitational acceleration*

In an infinite self-gravitating isothermal filament, the gravitational acceleration g_R at large R decays as $1/R$, whereas it increases linearly at small R. Therefore, the assumption that g_R is constant is only valid at some intermediate range in R. To close our analysis, in this subsection we present the final equilibria for axially-symmetric configurations in a more realistic external gravitational field.

According to the results of Kim & Hong (1998) for a Cartesian model, the growth time is reduced by almost an order of magnitude and the length scale of the most unstable mode by factors of $4 - 8$ when a more realistic gravity model is used, because in such a realistic disk the magnetic field strength decreases rapidly with vertical distance which promotes the development of strong magnetic buoyancy. We expect, therefore, that the length and timescales of the Parker instability in a filament will be modified if a more realistic gravity model is adopted.

In order to have a model as self-consistent as possible, we will assume that the external gravitational potential is dominated by a collisionless (stellar or dark matter) component with isothermal one-dimensional velocity dispersion $\sigma_\star$. The gravitational potential created by an isothermal filament is given by

$$\psi(R) = 2\sigma_\star^2 \ln\left(1 + \frac{R^2}{8H_\star^2}\right), \qquad (31)$$

where $H_\star$ is a parameter that specifies the scale height of the collisionless component satisfying $4\pi G\rho_{0,\star}(0)H_\star^2 = \sigma_\star^2$, where $\rho_{0,\star}(0)$ is the density of collisionless matter at $R = 0$ (e.g., Ostriker 1964). As already anticipated, the gravitational acceleration $g_R(R)$ increases linearly with R at $R \ll \sqrt{8}H_\star$, reaches a maximum at $\sqrt{8}H_\star$ and decreases as $1/R$ at $R \gg \sqrt{8}H_\star$. Under this gravitational field, the density and magnetic field in the unperturbed state

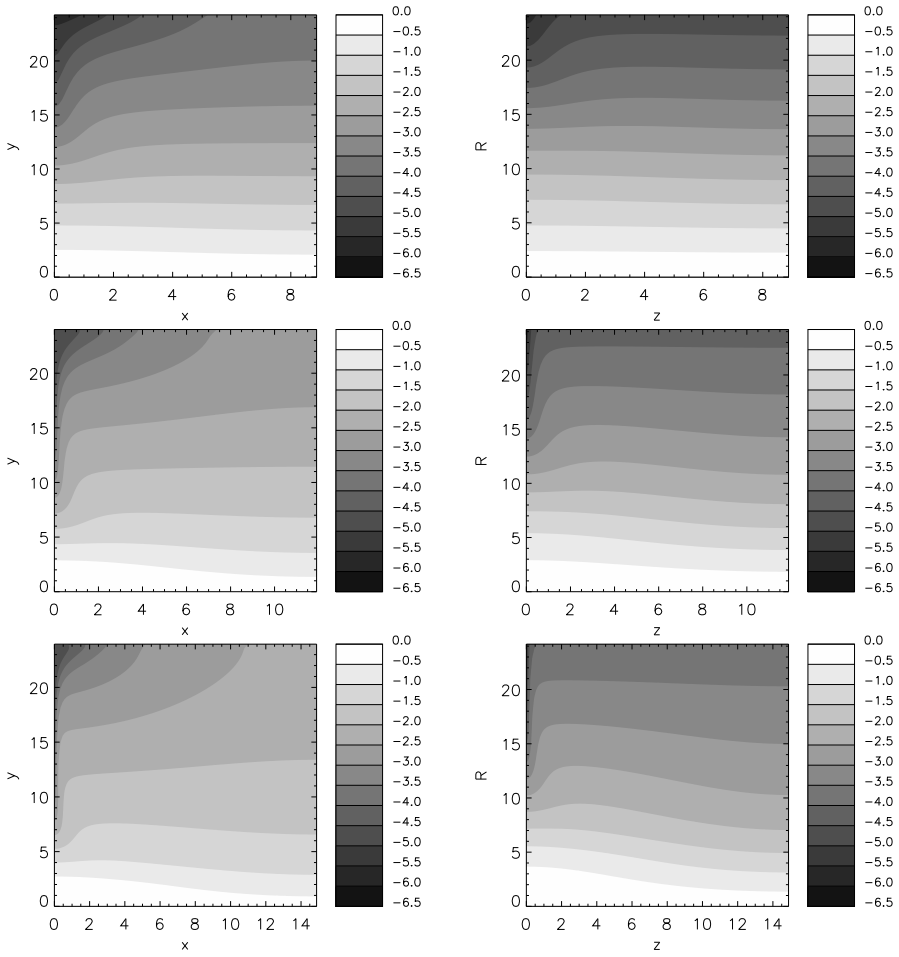

Fig. 9. Magnetic pressure maps, normalized to their value on the z-axis at the initial state, in the six final states of Figure 6.

are:

$$\frac{\rho_0(R)}{\rho_0(0)} = \frac{B_0^2(R)}{B_0^2(0)} = \left(1 + \frac{R^2}{8H_\star^2}\right)^{-s}, \qquad (32)$$

where s is defined by $s \equiv 2\sigma_\star^2/[(1+\alpha)c_s^2]$. If we define the scale height of the gas, H, as the radial distance at which the density of the gas is reduced to $1/e$ of its value at $R = 0$, then $H^2 = 8(\exp(1/s) - 1)H_*^2$.

To illustrate the effect of using a non-constant gravitational acceleration, we useed $\alpha = 1$ but different values of s. We ran models where the upper cap was located at the distance $R_{\rm max}$ at which the density decreases to $(1-5) \times 10^{-6}$ of its value at $R = 0$. We have empirically derived that the larger the s-value is, the smaller the critical wavelength becomes. For $s = 4$, perturbations with $\lambda_z/2 = 3.85H_\star = 2.55H$ are marginally unstable, whereas they become marginally unstable at $\lambda_z/2 = 1.5H$ when $s = 8$. In terms of H, this result implies that the critical wavelength for $s = 4 - 8$ is smaller by almost a factor of $1.5 - 2.5$ than that for the model with constant gravity (see § 4.1) and, therefore, the growth timescale is shorter for larger s-values. Figure 11 shows the final equilibrium state for $s = 4$ and $\lambda_z/2 = 5.3H$. This λ_z-value is close to the horizontal wavelength with maximum growth rate. By comparing with Figure 6, we note that although the global appearance is similar to the case with constant gravity and $\lambda_z/2 = 15$, the field lines appear slightly more deformed. The main effect of a non-constant gravitational acceleration strength is to shorten the separation of the magnetic valleys. The projected surface density that an observer would see if the axis of the filament lies in the plane of the sky is shown in Figure 12 for a model with $s = 4$. The enhancement in the column density over a line of sight passing through the core of a condensation is 2.1 in this model. This factor is appreciably larger than

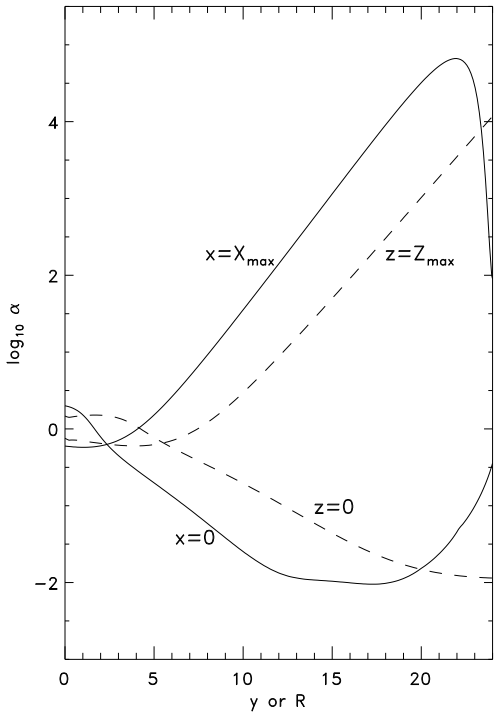

Fig. 10. Decadic logarithm of the ratio between the magnetic and gas pressures in the final state under constant gravity condition. The two solid lines give α values along the lines $x = 0$ and $x = X_{\max} = 15$ for the Cartesian model and the dashed lines give α along $z = 0$ and $z = Z_{\max} = 15$ in the axisymmetric case.

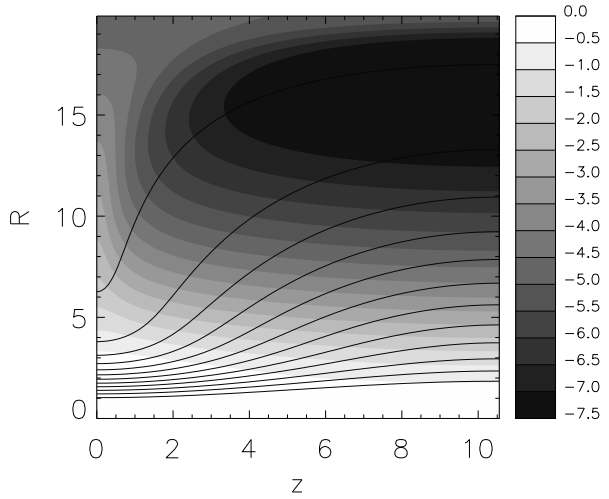

Fig. 11. Distribution of the volume density and magnetic field lines in the axisymmetric final equilibrium state in a non-uniform radial gravitational field with $s = 4$. In order to facilitate comparison with Figure 6 in which $H = 2$, distance is measured in units of $H/2$. Field lines (solid curves) were chosen so that they have the same magnetic strength in the initial state as those displayed in Figure 6.

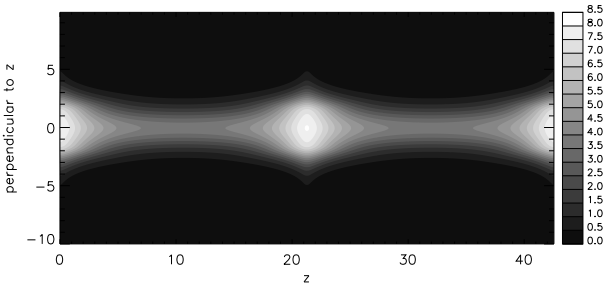

Fig. 12. Column density map for the final axisymmetric state along a line of sight perpendicular to the axis of symmetry (z-axis). We used $\alpha = 1$, $s = 4$ and $\lambda_z = 21.3$. The units of density and length are $\rho_0(0)$ and $H/2$, respectively. Note that the scale is linear.

that obtained in axisymmetric models with constant gravity but similar to that found in Cartesian models with uniform gravity.

5. DISCUSSION AND CONCLUSIONS

The Parker instability dictates that longitudinal magnetic field lines that give some support against gravity are always unstable to undular perturbations. It has long been realized that the Parker instability, which is interesting in itself, may play a significant role in understanding the formation of massive clouds in the interstellar medium, probably aided by thermal and gravitational instabilities (Mouschovias et al. 2009). The Parker instability can also play a role in the evolution of filamentary structure, such as filamentary clouds, at least at the early stages of the instability. While the properties of the final states are well documented for Cartesian models (e.g., M74; Basu, Mouschovias, & Paleologou 1997; Kim et al. 2001), it was unclear how they depend on the adopted geometry. In order to fill this gap, our primary goal was to investigate the nonlinear outcome of such an instability in an axisymmetric model where the initial equilibrium configuration consists of a infinite cylinder in the presence of a longitudinal magnetic field. We quantified the level of buoyancy of the magnetic field and drainage of the gas to promote density enhancements, as compared to the Cartesian models, which are currently being used to study the formation of substructure in the interstellar medium. We focused on understanding the physics of the Parker instability in filaments, rather than on making detailed comparisons with ob-

servations. This may be very useful as a first step to interpret full numerical simulations.

In the Cartesian model, the potential vector function A obeys a nonlinear elliptic equation, while for the axisymmetric model it is the magnetic flux Φ that obeys such equation. However, the differential operator as well as the source terms are different. In order to gain some insight on the different nature of the equations, we have compared the form of $q(A)$ and $q(\Phi)$ at the initial and final states in each model. The source terms depend directly on the derivatives of these functions. However, despite the fact that the aspect of these functions looks similar at a glance, the source terms Q_{xy} and Q_{zR} turn out to be absolutely different in the final state. This is a consequence of the nonlinearity of the differential equations.

We have focused first on models with uniform external gravity. We found that the axial model is more rigid than the Cartesian layer, in the sense that the magnetic field is less buoyant and the drainage of gas less efficient. In fact, in the axisymmetric model the matter shrinks in radius and generates a convergent flow that facilitates the achievement of pressure equilibrium with less deformation of the field lines. In order to have the same level of deformation of the field lines as in the Cartesian model with half the wavelength of $9c_s^2/g$, we need a perturbation of half the wavelength of $12c_s^2/g$, for $\alpha = 1$. Under uniform gravity, we find that a factor 5/4 enhancement in column density can be obtained in the axisymmetric model for the more unstable wavelength, which is modest as compared to the factor of 7/4 found in the Cartesian model. At the position of the wings of the condensations, the ratio of the magnetic-to-gas pressure becomes larger than 1 beyond a certain radius, because of the evacuation of gas in these regions. However, it is still approximately 10 times smaller than in Cartesian geometry.

We have examined a more realistic choice to describe the variation of the external gravitational potential in axisymmetric models. The main effects of a non-uniform gravitational acceleration is to modify the separation of magnetic valleys and therefore the timescale of the Parker instability. A factor of 2 enhancement in column density over its initial equilibrium value can be found in axisymmetric models with non-uniform radial gravity. Hence, unless this density enhancement is sufficient to initiate thermal or gravitational instabilities, the Parker instability should be thought of as setting the stage upon which other small-scale processes will be modeling the structure and evolution of the filament.

We would like to thank José Franco and Jongsoo Kim for helpful comments and the anonymous referee for very valuable suggestions, which have led to substantial improvements to the manuscript. The authors acknowledge financial support from Conacyt project CB-2006-60526 and PAPIIT project IN121609.

REFERENCES

Alfaro, E. J., Cabrera-Caño, J., & Delgado, A. J. 1992, ApJ, 399, 576
Asséo, E., Cesarsky, C. J., Lachièze-Rey, M., & Pellat, R. 1978, ApJ, 225, L21
_____. 1980, ApJ, 237, 752
Basu, S., Mouschovias, T. Ch., & Paleologou, E. V. 1997, ApJ, 480, L55
Blitz, L., & Shu, F. H. 1980, ApJ, 238, 148
Conselice, C. J., Gallagher, III, J. S., & Wyse, R. F. G. 2001, AJ, 122, 2281
Dungey, J. W. 1953, MNRAS, 113, 180
Franco, J., Kim, J., Alfaro, E. J., & Hong, S. S. 2002, ApJ, 570, 647
Genzel, R., & Stutzki, J. 1989, ARA&A, 27, 41
Giz, A. T., & Shu, F. H. 1993, ApJ, 404, 185
Hanasz, M., & Lesch, H. 2000, ApJ, 543, 235
Hanawa, T., Matsumoto, R., & Shibata, K. 1992, ApJ, 393, L71
Jackson, J. M., Finn, S. C., Chambers, E. T., Rathborne, J. M., & Simon, R. 2010, ApJ, 719, L185
Kim, J., Franco, J., Hong, S. S., Santillán, A., & Matos, M. A. 2000, ApJ, 531, 873
Kim, J., & Hong, S. S. 1998, ApJ, 507, 254
Kim, J., Hong, S. S., & Ryu, D. 1997, ApJ, 485, 228
Kim, J., Ryu, D., & Hong, S. S. 2004, Ap&SS, 292, 255
Kim, J., Ryu, D., & Jones, T. W. 2001, ApJ, 557, 464
Kosiński, R., & Hanasz, M. 2006, MNRAS, 368, 759
_____. 2007, MNRAS, 376, 861
Lachiéze-Rey, M., Cesarsky, C. J., Asséo, E., & Pellat, R. 1980, ApJ, 238, 175
Lee, S. M., & Hong, S. S. 2007, ApJS, 169, 269
Mouschovias, T. Ch. 1974, ApJ, 192, 37 (M74)
_____. 1976, ApJ, 206, 753
_____. 1996, in Solar and Astrophysical Magnetohydrodynamic Flows, ed. K. Tsinganos (Dordrecht: Kluwer), 475
Mouschovias, T. Ch., Kunz, M. W., & Christie, D. A. 2009, MNRAS, 397, 14
Mouschovias, T. Ch., Shu, F. H., & Woodward, P. R. 1974, A&A, 33, 73
Nagasawa, M. 1987, Prog. Theor. Phys., 77, 635
Nakamura, F., Hanawa, T., & Nakano, T. 1991, PASJ, 43, 685
_____. 1995, ApJ, 444, 770
Nakano, T. 1979, PASJ, 31, 697
Ostriker, J. P. 1964, ApJ, 140, 1056

Parker, E. N. 1966, ApJ, 145, 811
Ryu, D., Kang, H., & Biermann, P. L. 1998, A&A, 335, 19
Salomé, P., et al. 2006, A&A, 454, 437
Santillán, A., Kim, J., Franco, J., Martos, M., Hong, S. S., & Ryu, D. 2000, ApJ, 545, 353
Shu, F. H. 1974, A&A, 33, 55
Stodolkiewicz, J. S. 1963, Acta Astron., 13, 30
Tomisaka, K., Ikeuchi, S., & Nakamura, T. 1988, ApJ, 335, 239

F. Javier Sánchez-Salcedo: Instituto de Astronomía, Universidad Nacional Autónoma de México, Apdo. Postal 70-264, México D. F., C. P. 04510, Mexico (jsanchez@astroscu.unam.mx).
Alfredo Santillán: Dirección General de Cómputo y Tecnologías de la Información y Comunicación, Universidad Nacional Autónoma de México, Zona Cultural, México D. F., C. P. 04510, Mexico (alfredo@astro.unam.mx).

Revista Mexicana de Astronomía y Astrofísica, **47**, 31–48 (2011)

MID-INFRARED OBSERVATIONS OF PLANETARY NEBULAE DETECTED IN THE GLIMPSE 3D SURVEY

J. A. Quino-Mendoza, J. P. Phillips, and G. Ramos-Larios

Instituto de Astronomía y Meteorología, Universidad de Guadalajara, Mexico

Received 2010 September 23; accepted 2010 December 13

RESUMEN

Presentamos mapas, perfiles y fotometría de 24 nebulosas planetarias (NPs) detectadas en el estudio del plano galáctico en el infrarrojo medio (MIR) de GLIMPSE 3D. Las NPs muestran muchas de las propiedades observadas en estudios previos de estas fuentes, incluyendo la evidencia de emisión a mayores longitudes de onda afuera de las zonas ionizadas, una consecuencia probable de la emisión de hidrocarburos aromáticos policíclicos (PAHs) dentro de las regiones de fotodisociación (PDRs). Notamos también variaciones en los cocientes de flujo 5.8 μm/4.5 μm y 8.0 μm/4.5 μm con respecto a la distancia del núcleo; presentamos evidencia de un aumento en la emisión MIR en los halos de las fuentes y encontramos evidencia de variaciones en color respecto de la evolución nebular.

ABSTRACT

We present mapping, profiles and photometry for 24 planetary nebulae (PNe) detected in the GLIMPSE 3D mid-infrared (MIR) survey of the Galactic plane. The PNe show many of the properties observed in previous studies of these sources, including evidence for longer wave emission from outside of the ionised zones, a likely consequence of emission from polycyclic aromatic hydrocarbons (PAHs) within the nebular photo-dissociation regimes (PDRs). We also note variations in 5.8 μm/4.5 μm and 8.0 μm/4.5 μm flux ratios with distance from the nuclei; present evidence for enhanced MIR emission in the halos of the sources; and note evidence for variations in colour with nebular evolution.

Key Words: infrared: ISM — ISM: jets and outflows — planetary nebulae: general

1. INTRODUCTION

The late evolution of moderate mass stars is known to lead to appreciable loss of mass, and to the formation of planetary nebular shells. Whilst these envelopes are mostly neutral during the earliest phases of expansion, subsequent evolution of the central star leads to increased HII/HI mass ratios.

Much of the prior investigation of these sources in the radio and visible has concentrated on defining the physical properties and kinematics of the ionised shells. More recent observations in the infrared, however, have also extended our understanding of the neutral and dust emission regimes. Early bolometric observations, for instance, resulted in the detection of emission excesses attributable to hot and warm dust (see e.g., Barlow (1983) for a listing of earlier ground-based photometry). Subsequent advances in technology, and in the sensitivity of detector systems, have also enabled spectroscopy and mapping using ground- and space-based observatories. These include low resolution photometry and mapping undertaken with the *Infrared Astronomical Satellite* (*IRAS*, e.g., Leene, Zhang, & Pottasch 1987), and spectroscopy of a broad range of sources using the *Infrared Space Observatory* (*ISO*; e.g., Liu et al. 2001; Szczerba, Górny, & Tylenda 1998; Beintema 1997).

Perhaps the greatest advance to have occurred in recent years has been through near-to-far infrared observations with the *Spitzer Space Telescope* (*Spitzer*; Werner et al. 2004), however, which has enabled spectroscopy and mapping at high spatial and spectral resolutions. Individually pointed observations have been reported by Hora et al. (2004), Guiles et al. (2007), Su et al. (2007), Ueta (2006), Phillips & Ramos-Larios (2010), and Ramos-Larios,

Phillips, & Cuesta (2008), among many others. Similarly, the results of the more extended GLIMPSE and MIPSGAL surveys are reported by Phillips & Ramos-Larios (2008a), Cohen et al. (2007), Ramos-Larios & Phillips (2008), Zhang & Kwok (2009), Phillips & Marquez-Lugo (2010), Chu et al. (2009) and Mizuno et al. (2010). These show that much of the MIR emission is attributable to polycyclic aromatic hydrocarbons (PAHs) and a broad variety of ionic and molecular transitions, whilst much of the longer wave emission appears to arise from cool dust continua, as well as transitions such as [ArII] 6.985 μm, [NeVI] 7.643 μm, [ArIII] 8.991 μm, [Ne V] 24.32 μm, [OIV] 25.87 μm and so forth. The extension of PAH and dust emission components outside of the ionised shells suggests the presence of enveloping photo-dissociation regimes (PDRs), likely associated with neutral gas in the AGB mass-loss halos. Individual structures in these halos have been investigated by Phillips et al. (2009), Ramos-Larios & Phillips (2009), Phillips & Ramos-Larios (2010), and Ramos-Larios, Phillips, & Cuesta (2010).

Whilst much of the MIPSGAL survey material is available for public use, the 70 μm data is inaccessible at present, and the associated catalogues are in process of being compiled. Similarly, although the GLIMPSE I and II data are fully available, only $\sim$75% of the GLIMPSE 3D survey is accessible at present. Nevertheless, although interesting portions of the Galactic plane are still missing from the latter survey, we are in a position to analyse the properties of the PNe which have been detected so far. The coordinates of these sources are taken from Acker et al. (1992), Parker et al. (2006) and Miszalski et al. (2008), the latter two of which are referred to as the MASH I and II catalogues. These catalogues include the majority of Galactic PNe to have been identified so far, although the sampling of bulge PNe is less complete. A fuller discussion of the latter component can be found in Phillips & Ramos-Larios (2009).

We shall here concentrate upon extended nebular shells having reasonably high S/N detections. This will permit us to provide mapping, profiles and photometry for 24 PNe in the 3.6, 4.5, 5.8 and 8.0 μm photometric channels. It will become apparent that the sources have interesting characteristics in the MIR which are often at variance with what is observed in other wavelength regimes, and are attributable to the combined influence of neutral and ionised gas and dust components.

2. OBSERVATIONS

One of the major legacy programs of Spitzer was to map the inner region of the Galactic plane, a program which was undertaken using the Infrared Array Camera (IRAC; Fazio et al. 2004) in four photometric channels. The first results of this survey (denominated GLIMPSE I) covered the longitude and latitude ranges $l = 10^\circ - 65^\circ$, $295^\circ - 350^\circ$, $b = \pm 1^\circ$, and data products were delivered between April 2005 and August 2006. The second extension of this survey (GLIMPSE II) covered regions close to the Galactic centre (GC), including the longitude range $10^\circ < l < 350^\circ$, and latitudes extending up to $b = \pm 2^\circ$ – although it excluded the region about the G.C. itself (i.e. $l = \pm 1^\circ$, $b = \pm 0.75^\circ$). Products for this survey became available in May 2007. Finally, the GLIMPSE 3D survey represents a vertical extension of the GLIMPSE I & II surveys, and covers higher Galactic latitudes in selected longitude ranges. For the most part, latitudes $|b|$ are < 3 deg, but this extends to $|b| < 4.2$ deg in the centre of the Galaxy. The data have been delivered in several tranches between 2007 and the present date, and will (when fully available) cover an area of 199.6 deg^2; although data for $b > 1^\circ$, $8^\circ < l < 355^\circ$, and $5^\circ < l < 8^\circ$, $b < -1^\circ$ are still not available for general use – a region which corresponds to 25% of the final survey area. We shall be investigating the properties of planetary nebulae detected in the available 3D regime.

The IRAC employed filters having isophotal wavelengths (and bandwidths $\Delta\lambda$) of 3.550 μm ($\Delta\lambda$ = 0.75 μm), 4.493 μm ($\Delta\lambda$ = 1.9015 μm), 5.731 μm ($\Delta\lambda$ = 1.425 μm) and 7.872 μm ($\Delta\lambda$ = 2.905 μm). The normal spatial resolution for this instrument varied between $\sim$1.7 and $\sim$2 arcsec (Fazio et al. 2004), and was reasonably similar in all of the bands, although there was a stronger diffraction halo at 8 m than in the other IRAC bands. This leads to differences between the point source functions (PSFs) at $\sim$0.1 peak flux. The observations have a spatial resolution of 0.6 arcsec/pixel.

We have used these data to produce colour-coded combined images in three of the IRAC bands, where 3.6 μm results are represented as blue, 4.5 μm emission is green, and the 8.0 μm results are indicated by red. We have also undertaken contour mapping in all four of the IRAC bands, where the lowest contours correspond to $3\sigma_{\rm rms}$ background noise levels or greater, and the intrinsic flux E_n for contour n has a value

$$E_n = A10^{(n-1)C} - B, \qquad (\text{M Jy sr}^{-1}) \qquad (1)$$

TABLE 1

MIR PHOTOMETRY FOR EXTENDED GLIMPSE 3D PLANETARY NEBULAE

PN G	NAME	CAT	3.6 mag	4.5 mag	5.8 mag	8.0 mag
002.8–02.2	Pe 2-12	ACK	8.59	8.13	6.44	4.75
003.5–02.4	IC 4673	ACK	9.47	7.66	8.45	5.64
003.6–02.3	M 2-26	ACK	10.3	9.54	9.95	7.27
003.9–02.3	M 1-35	ACK	9.06	8.02	7.85	5.17
004.2–02.5	PHR1805-2631	M1	11.68	10.43	11.09	9.64
009.4–01.2	PHR1811-2123	M1	9.27	9.1	9.28	7.88
009.7–01.1	PHR1811-2102	M1	11.9	11.35	10.73	9.53
009.8–01.1	PHR1811-2100	M1	10.11	9.28	8.79	7.75
010.8–01.8	NGC 6578	ACK	7.81	6.99	7.43	5.06
025.9–02.1	Pe 1-15	ACK	11.17	9.83	10.29	7.51
330.6–02.1	He 2-153	ACK	9.63	8.76	8.57	6.86
335.4–01.9	PHR1637-4957	M1	9.83	9.1	9.22	7.86
336.2+01.9	Pe 1- 6	ACK	10.39	9.19	9.78	6.91
344.2–01.2	H 1- 6	ACK	9.36	8.02	7.65	6.01
344.4+01.8	MPA1654-4041	M2	11.2	10.41	11.21	9.2
345.2–01.2	H 1- 7	ACK	6.67	6.18	4.79	2.81
350.4+02.0	PHR1712-3543	M1	10.92	9.75	10.14	8.2
356.0–01.4	PPA1741-3302	M1	11.29	10.63	11.09	8.42
356.5–02.3	M 1-27	ACK	8.09	7.36	6.67	4.39
356.5–01.8	PPA1744-3252	M1	10.5	10.15	10.82	8.82
357.3–02.0	PPA1747-3215	M1	9.77	9.65	8.62	7.2
357.5–02.4	PPA1749-3216	M1	10.19	9.87	10.61	8.45
359.1–01.7	M 1-29	ACK	8.19	6.99	6.93	4.57
359.4–03.4	H 2-33	ACK	11.3	10.17	10.6	7.57

where A is a constant, $n = 1$ corresponds to the lowest (i.e. the outermost) contour level, B is the background, and C is the logarithmic separation between contours. Contour parameters A, B and C are indicated in the relevant figure captions.

We have additionally produced profiles through the sources after the elimination of background emission (particularly strong in the 5.8 and 8.0 μm IRAC channels), and the removal of linear spatial gradients. These results were then processed to indicate the variation of 3.6 μm/4.5 μm, 5.8 μm/4.5 μm and 8.0 μm/4.5 μm ratios with distance from the nebular nuclei. The rationale behind this is based on the fact that many PNe possess strong polycyclic aromatic hydrocarbon (PAH) emission bands at 3.3, 6.2, 7.7 and 8.6 μm, located in the 3.6, 5.8 and 8.0 μm IRAC bands. Given that the 4.5 μm band is usually dominated by the bremsstrahlung continuum, as well as by a variety of molecular and ionic transitions, such ratios enable us to gain an insight into the distribution of PAHs within the nebular shells (see e.g., Phillips & Ramos-Larios 2008a,b).

Contour mapping of the 3.6 μm/4.5 μm, 5.8 μm/4.5 μm and 8.0 μm/4.5 μm flux ratios was undertaken by estimating levels of background emission, removing these from the images, and subsequently setting values at < 3 rms noise levels to zero. The maps were then ratiod on a pixel-by-pixel basis, and the results contoured using standard IRAF programs. Contour levels are given through $R_n = D10^{(n-1)E}$, where the parameters (D, E) are again detailed in the figure captions.

The IRAC fluxes of extended sources are open to errors deriving from instrumental scattering, and require to be corrected by factors of 0.91 at 3.6 μm, 0.94 at 4.5 μm, 0.66–0.73 at 5.8 μm (we take a mean value of 0.70), and 0.74 at 8.0 μm – although this correction also depends upon the surface brightness

distribution of the source under consideration. A discussion of this question is to be found in § 4.11 of the IRAC Instrument Handbook[1] (version 1.0, 2010).

We have, in the face of these uncertainties, chosen to leave the flux ratio mapping and profiles unchanged. The maximum correction factors for the ratios are likely to be > 0.74, but less than unity, and ignoring this correction has little effect upon our interpretation of the results.

We have, finally, provided photometry for all of these sources, where the values were estimated by integrating within circular or polygonal apertures centred upon the nebulae; estimating the levels of background at various regions about the nebulae; applying the instrumental scattering corrections described above; and determined magnitudes using the α Lyrae calibration of Reach et al. (2006). The results are presented in Table 1.

3. DISCUSSION OF INDIVIDUAL PNE DETECTED IN THE GLIMPSE 3D SURVEY

We have obtained mapping and profiles for 14 PNe detected in the GLIMPSE 3D survey, and we shall present details of these sources in our analysis below. Images of six of the regions are also plotted in Figure 1, where we have combined 3.6 μm (blue), 4.5 μm (green) and 8.0 μm (red) IRAC imaging of the sources. It will be seen that most of the nebulae are relatively compact and ill-defined, although we see evidence for ring-like structures in IC 4674, H 1-6 and M 1-29, and for bipolarity in G009.8-01.1 (otherwise known as PHR1811-2100).

Although the range of bright high S/N sources is therefore less extensive than for GLIMPSE I & II (see e.g., Phillips & Ramos-Larios 2008a; Ramos-Larios & Phillips 2008), we are able to draw interesting conclusions concerning the properties of these nebulae.

3.1. *Pe 2–12*

This is a relatively little studied PN which appears to have an elliptical morphology (Figure 1), and an optical diameter of ∼5 arcsec (Cahn & Kaler 1971). Shell densities appear to be of order 1.1×10^3 cm^{-3} (although this value has a large range of uncertainty; see Chiappini et al. 2009), whilst the He/H abundance ratio is ≅ 0.072, and N/O ≅ 0.714 (Chiappini et al. 2009).

It is apparent that whilst the optical dimensions are comparable to those at 3.6 and 4.5 μm (see Figure 2), they are significantly less than those observed at larger MIR wavelengths. Such trends are partly affected by the differing instrumental sensitivities in the various IRAC channels, the values of contour level cut-off, and variation of source flux with wavelength, all of which may influence the apparent size of the envelope.

There is nevertheless clear evidence that this increase in size reflects a real trend in source dimensions. Logarithmic profiles through the centre of the source permit integration over several pixels, for instance, and lead to higher levels of S/N. These also show an increase in width with increasing IRAC wavelength. Where one ignores the trends observed at 3.6 μm (background field star contamination is extremely high in this channel), then we

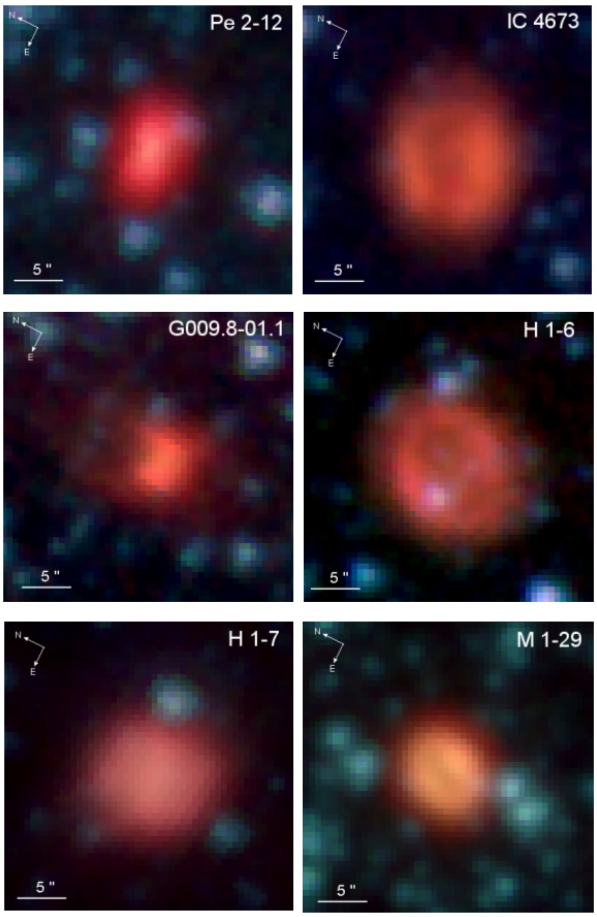

Fig. 1. Images of six planetary nebulae observed during the *Spitzer* GLIMPSE 3D survey, where 3.6 μm emission is represented as blue, 4.5 μm emission as green, and 8.0 μm emission as red. Three of the sources appear to have internal ring-like structures (viz. IC 4673, H 1-6 and M 1-29), whilst the MASH I source G009.8-01.1 (PHR1811-2100) has a bipolar morphology. The color figure can be viewed online.

[1] http://ssc.spitzer.caltech.edu/irac/iracinstrumenthandbook/IRAC_Instrument_Handbook.pdf.

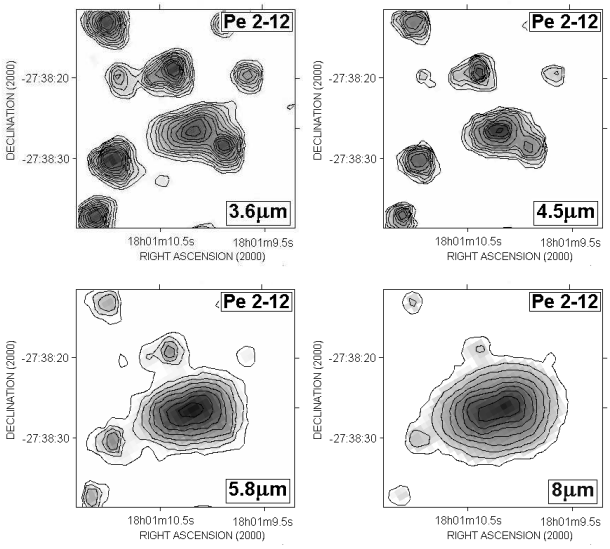

Fig. 2. Contour maps of Pe 2-12, where contour levels [A, B, C] are given by [9, 3.65, 0.1780] at 3.6 μm, [10, 2.58, 0.1111] at 4.5 μm, [10, 4.44, 0.1780] at 5.8 μm, and [17.5, 10.33, 0.1780] at 8.0 μm. It will be noted that the dimensions of the source appear to increase with increasing MIR wavelength, and that the internal contours are highly elliptical, perhaps indicative of a barely resolved bipolar structure.

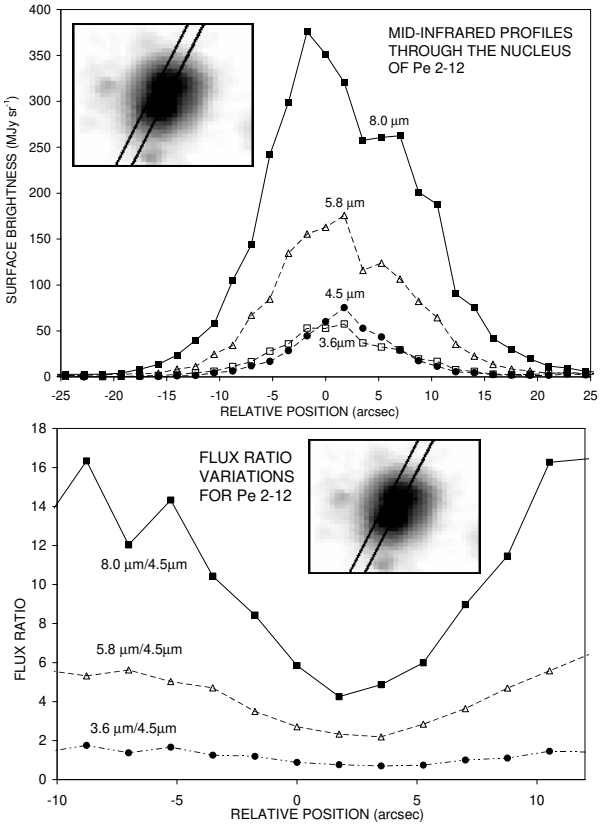

Fig. 3. Profiles along the major axis of Pe 2-12, where we show the variation in surface brightness with nebular position (upper panel), and of the flux ratios 3.6 μm/4.5 μm, 5.8 μm/4.5 μm, and 8.0 μm/4.5 μm (lower panel). The inserted images show the directions and widths of the traverses used for these trends. It will be noted that the longer wave profiles have a somewhat double-humped appearance, as might be expected where we are observing the two lobes of a bipolar structure – and there is indeed some further indication of this structure in the inserts, and in the contour maps in Figure 2. Note the evidence for an increase in flux ratios with distance from the nucleus.

find $1/10^{\rm th}$ peak emission widths of 10.0 arcsec at 4.5 μm, 13.0 arcsec at 5.8 μm, and 14.7 arcsec at 8.0 μm. Such a trend is closely comparable to what has been seen in other PNe (e.g., Phillips & Ramos-Larios 2008a; Ramos-Larios & Phillips 2008), and may be attributable to PAH band emission within the nebular PDR; the ν=0-0 S(4)-S(7) transitions of H_2; and warm dust continua arising from stochastic heating of small grains (Phillips & Ramos-Larios 2008a).

It is also conceivable, although perhaps less likely, that lower excitation ionic lines contribute to these trends, including the λ8.99 μm transition of [ArIII]. The absence of spectra for the exterior regions of this source precludes us from constraining these mechanisms, or defining which is the most dominant – and a similar situation applies for other nebulae as well. However, the presence of PAH band emission in PNe such as NGC 40 (Ramos-Larios et al. 2010), and in the PDRs about compact HII regions (Phillips & Ramos-Larios 2008c), suggests that the increase in MIR fluxes to longer wavelengths, and the extended emission in the 5.8 and 8.0 μm channels may arise from small PAH molecules within the nebular PDRs. This is perhaps the primary mechanism where C/O > 1.

The evolutionary status of this source is quite uncertain, although one might envisage that where the PN is relatively young (and the dimensions of the ionised regime are small), then we may be observing an envelope which is largely neutral and emerging from the proto-planetary phase of evolution. Having said this, we note that Zhang (1995) quotes a statistical distance of 15.4 kpc, which would place Pe 2-12 well on the other side of the Galactic centre. The corresponding physical size (for an optical diameter of $\Theta = 5$ arcsec) would then be of the order of $\sim$0.37 pc, making the source reasonably evolved.

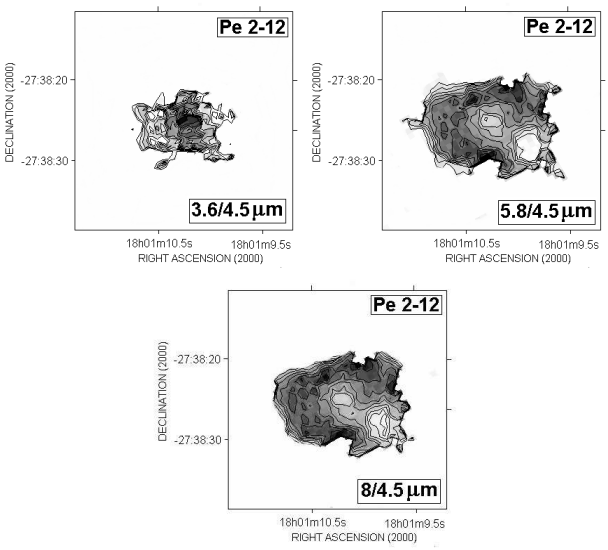

Fig. 4. Mapping of IRAC flux ratios over the projected envelope of Pe 2-12, where the contour parameters [D, E] are given by [0.5, 0.0618] for 3.6 μm/4.5 μm, [1.6, 0.0972] for 5.8 μm/4.5 μm, and [2.0, 0.1307] for 8.0 μm/4.5 μm. Notice how ratios are lowest (lighter grey colouration) at the centre of the source, and increase outwards towards the perimeter. The region of lower ratios to the south-west (lower right-hand side) results from contamination by an unrelated field star.

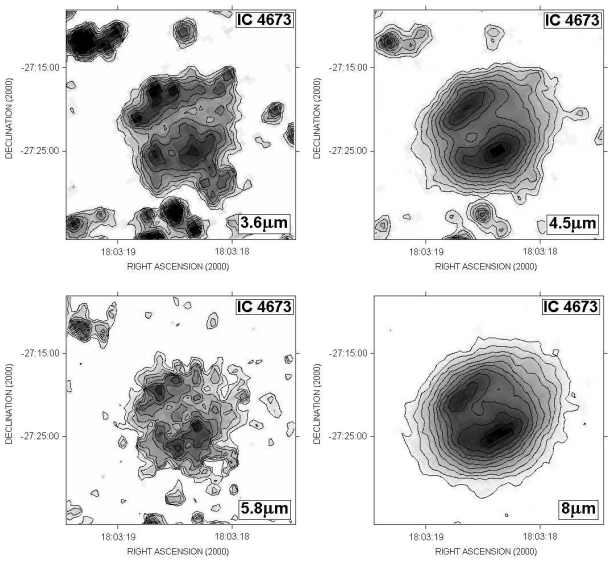

Fig. 5. Contour mapping of IC 4673 in the MIR, where the contour parameters [A, B, C] are given by [3.9, 2.48, 0.0478] at 3.6 μm, [3.2, 1.50, 0.0972] at 4.5 μm, [5.7, 3.57, 0.0450] at 5.8 μm, and [17, 13.04, 0.0521] at 8.0 μm. The shell is seen to have an elliptical morphology, with higher levels of surface brightness along the minor axis of the source. The fragmentary appearance of the envelope at 3.6 and 5.8 μm is due to lower levels of S/N.

There appears to be an increase in ratios 5.8 μm/4.5 μm and 8.0 μm/4.5 μm over the central portions of the source (Figure 3); a trend which is also confirmed through the IRAC band ratio mapping illustrated in Figure 4, whence it would seem that nuclear 5.8 μm/4.5 μm and 8.0 μm/4.5 μm ratios are low, and surrounded by a collar of higher ratio material. This may arise, yet again, as a result of more extended PAH band emission.

We finally note evidence for a dip in the profiles at the centre of the source, suggesting the possible presence of a central cavity in the longer wave (5.8 and 8.0 μm) emission (see Figure 3), or a narrowing of the structure associated with a nebular waist. On the other hand, the high ellipticity of the central 8.0 μm contours (see Figure 2) suggests aspect ratios which are relatively large (and of order $\sim$2). Both of these results may imply that the nebula is a barely resolved bipolar source.

3.2. *IC 4673*

Early optical observations of this source quoted by Cahn & Kaler (1971) and Chu, Jacoby, & Arendt (1987) showed it to have a diameter of 14.8 arcsec, compared to radio dimensions of 17 arcsec (Zijlstra, Pottasch, & Bignell 1989) Patriarchi & Perinotto (1994) used an ESO B survey plate to determine a size of 18×15 arcsec^2, whilst imaging by Schwarz, Corradi, & Melnick (1992) appeared to show a halo extending to 25×16 arcsec^2. The results of the latter authors have been combined in the Planetary Nebula Image Catalogue (Bruce Balick & collaborators[2]) to make an excellent false-colour image of the source which is similar to that in Figure 1. Patriarchi & Perinotto (1994) suggest that IC 4673 is a Type I source, and their abundances He/H $\cong$ 0.15 and N/O $\cong$ 5.57 are certainly consistent with this presumption. However, we note that values [He/H, N/O] of [0.0869, 0.565], [0.132, 0.424] and [0.146, 0.281] have been quoted by Chiappini et al. (2009), Exter, Barlow, & Walton (2004) and Kingsburgh & Barlow (1994), and it is possible that the Type I designation may have to be revised.

Phillips (2003) points out that the mean HeII Zanstra is 113.3 kK, whilst the corresponding H Zanstra value is 63.5 kK, perhaps implying a significant loss of H ionising photons by the nebular shell. This may suggest that the nebula is density bound, and that there is little neutral material outside of the ionised regime. Such an analysis would

[2]Available at `http://www.astro.washington.edu/users/balick/PNIC/`.

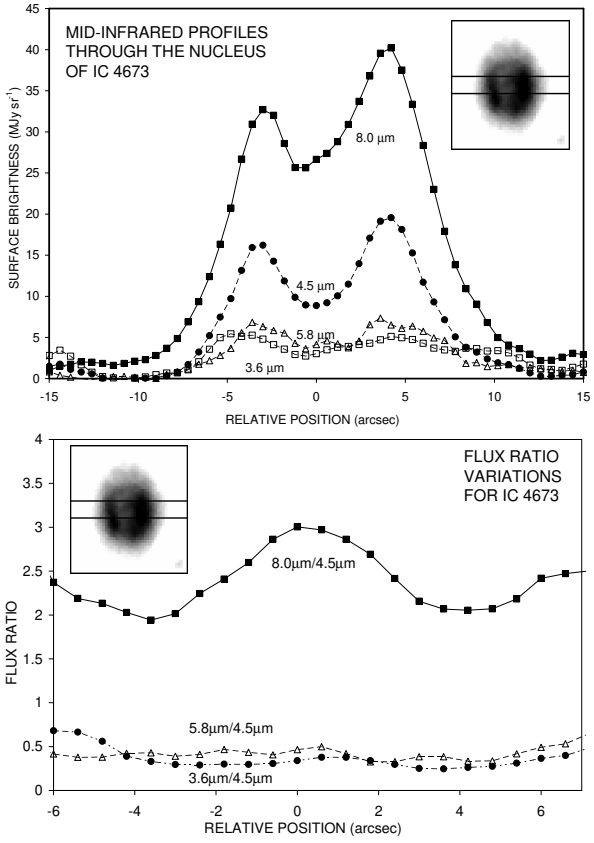

Fig. 6. As for Figure 3, but for the case of IC 4673. The profiles are taken along the major axis of the source, and show a double-humped profile. There is also evidence for lower 3.6 μm/4.5 μm and 8.0 μm/4.5 μm ratios at the positions of peak surface brightness.

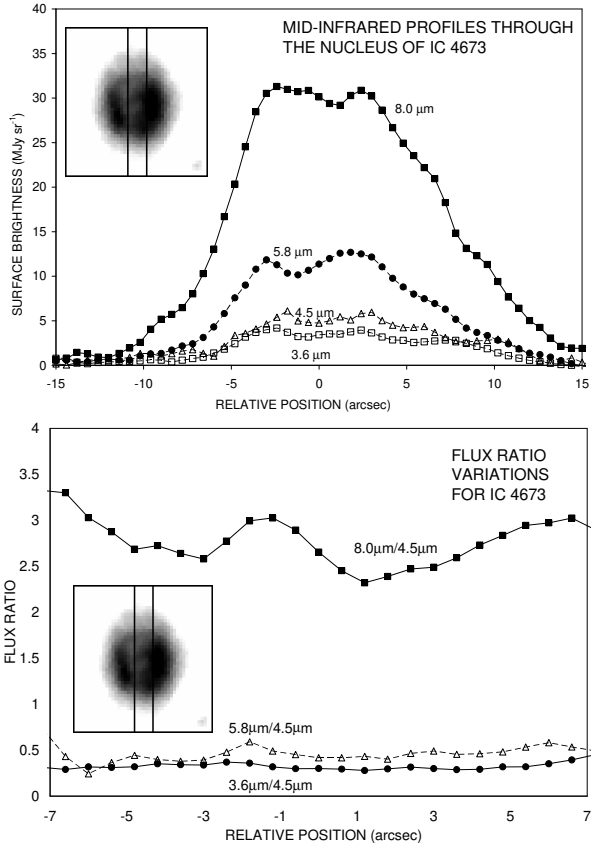

Fig. 7. As for Figure 6, but for an orthogonal direction through the nucleus of the source.

be inconsistent with the assumptions of Patriarch & Perinotto (1994), who proposed that the shell was mostly ionisation bound, although it is consistent with the results in Figure 5.

It is apparent, in the latter case, that the 3.6 and 5.8 μm results are noisier than at 4.5 and 8.0 μm, with the latter emission showing dimensions of 19.6$\times$ 17.0 arcsec^2. These values are comparable to the visual sizes noted above, suggesting that very little of the longer wave emission arises outside of the ionised shell – and that any PDR makes a modest overall contribution.

Profiles through the centre of the source (Figures 6 and 7, upper panels), show evidence for the minor axis surface brightness enhancements seen in the visible (Figure 6 and Figure 1), whilst there is also evidence for a sinusoidal variation in the 8.0 μm/4.5 μm ratio (Figure 6, lower panel). It will be noted however that there is little evidence for the radial increase in ratios noted in many other PNe (see e.g., Phillips & Ramos-Larios 2008a, 2010, and sources Pe 2-12 and M 1-29 in the present study), whereby 8.0 μm/4.5 μm and 5.8 μm/4.5 μm increase with increasing distance from the nucleus. On the contrary, our ratio mapping (Figure 8) shows that much of the variation is due to a decrease in ratios at the positions of peak surface brightness. A similar decrease is also noted for the 3.6 μm/4.5 μm mapping, but appears to be absent from the 5.8 μm/4.5 μm results.

The fact that such variations are present for 3.6 μm/4.5 μm and 8.0 μm/4.5 μm, but absent in the 5.8 μm/4.5 μm map, suggests that the trends are unlikely to be due to PAH emission bands. It is possible however that ionic lines (such as [ArII] λ6.985 μm and [ArIII] λ8.991 μm) are preferentially enhancing 8.0 μm fluxes.

It would therefore appear likely that IC 4673 possesses a highly ionised envelope with little evidence for a PDR or PAH emission bands, leading to a shell morphology and dimensions similar to those observed in the visible.

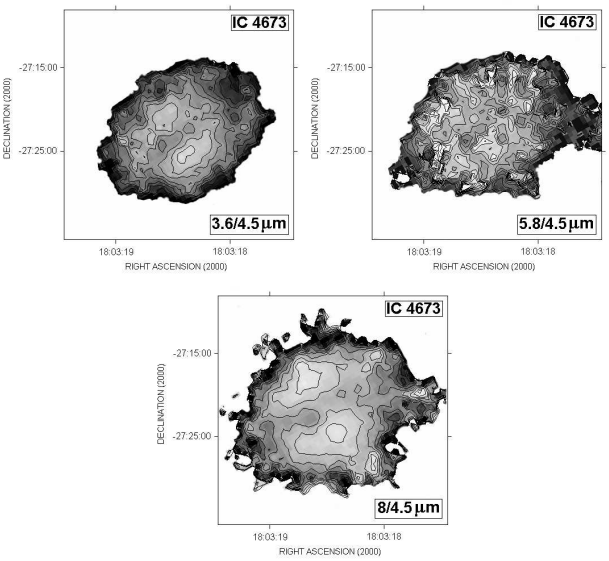

Fig. 8. IRAC band ratio mapping for IC 4673, where the parameters [D, E] are given by [0.2, 0.0865] for 3.6 μm/4.5 μm, [0.2, 0.0777] for 5.8 μm/4.5 μm, and [1.7, 0.0943] for 8.0 μm/4.5 μm. The structure of the 5.8 μm/4.5 μm map is highly complex, and shows little evidence for systematic changes with position in the shell. The 3.6 μm/4.5 μm and 8.0 μm/4.5 μm maps, on the other hand, show evidence for ratio minima along the minor axis of the source, at the positions of maximum surface brightness.

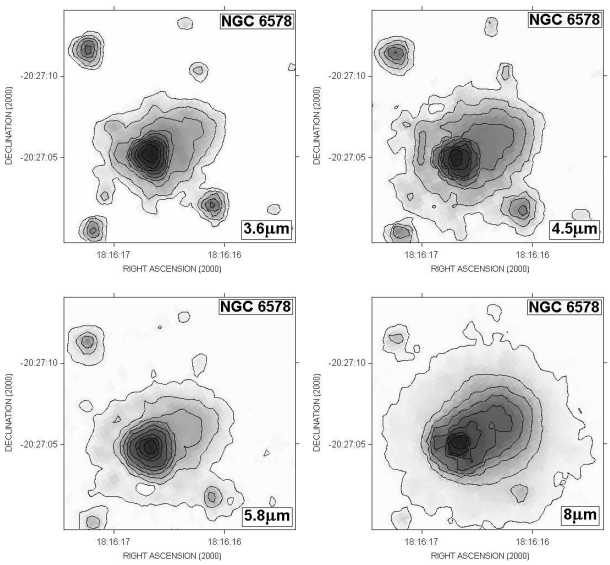

Fig. 9. IRAC contour mapping of NGC 6578, where parameters [A, B, C] are given by [11, 2.56, 0.2680] at 3.6 μm, [6, 1.56, 0.3051] at 4.5 μm, [12.5, 6.50, 0.2513] at 5.8 μm, and [25, 19.67, 0.1947] at 8.0 μm. The map shows evidence for a bright interior elliptical shell, and a more circular halo at longer wavelengths. The point source close to $\alpha = 18^h16^m16^s.65$, $\delta = -20°27'04''.7$ is likely to correspond to an unrelated field star.

3.3. *NGC 6578*

NGC 6578 has an elliptical shell with dimensions $\cong 7.5 \times 25$ arcsec^2 (see e.g., the imaging of Corradi et al. (2003), and the HST [OIII] image illustrated by Hajian et al. (2007), surrounded by an irregular outer halo with size 14×60 arcsec^2 (Corradi et al. 2003). Modelling of the spectral lines in the source has been undertaken by Hajian et al. (2007), whilst Perinotto et al. (1994) determine abundance ratios He/H $\cong$ 0.14, N/O $\cong$ 0.2; values which are also similar to those estimated by Perinotto, Morbidelli, & Scatarzi (2004) (He/H $\cong$ 0.198, N/O $\cong$ 0.21). It would therefore appear that whilst the helium abundance is high, the nebula is not a Type I source.

The mapping in Figure 9 doesn't bear much relation to the symmetric structure noted in the visible, partially because of the presence of a bright point source close to $\alpha = 18^h16^m16^s.65$, $\delta = -20°27'04''.7$. It is possible that this corresponds to a rather red (peaking at $\lambda \sim 6$ μm) background object which is unrelated to NGC 6578, and is appreciably contaminating the inner source structure.

We have therefore attempted to side-step this feature in our profiles in Figure 10, where it is clear that trends in all of the channels are very much the same. This results in relatively modest variations in the IRAC band ratios (Figure 10, lower panel), although there is some evidence for peaks in 5.8 μm/4.5 μm and 8.0 μm/4.5 μm close to the limits of the interior shell (i.e. at relative positions $\pm$5 arcsec). It is fascinating to note that the visual halo about the source has its counterpart at 8.0 μm as well, where we see evidence for a circular region with size 11×12 arcsec^2. This is, in fact, a lower limit dimension, and profiles show that the halo extends to distances of at least $\sim$17 arcsec from the centre.

Such a result is somewhat surprising, given the weakness of the halo in the visible. Corradi et al. (2003) find that the halo trends for H + [NII] and [OIII] are very closely similar, and imply intensities of $\sim$0.15 at RP = 5 arcsec, $\sim 5 \times 10^{-3}$ at 10 arcsec, and $\sim 10^{-3}$ at 20 arcsec when compared to peak strengths within the nucleus of the source. This is well below what would ordinarily be detectable with *Spitzer*. The reason why we are detecting the halo in the present observations is because it is relatively very much brighter in the MIR, and has a relative intensity $\sim 2 \times 10^{-2}$ at distances of 15 arcsec from the centre.

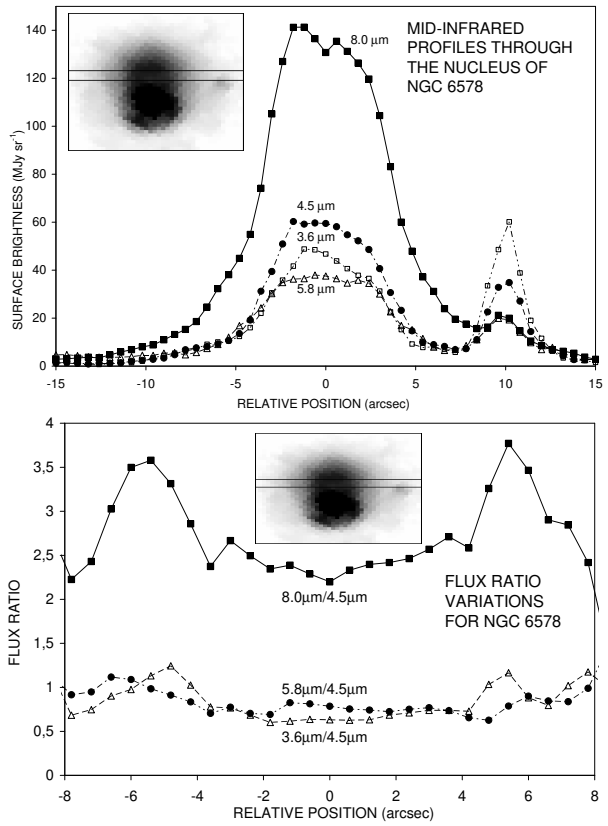

Fig. 10. As for Figure 3, but for the case of NGC 6578. The profiles avoid the region of contamination by the MIR point source. Note the increase in 5.8 μm/4.5 μm and 8.0 μm/4.5 μm close to the limits of the bright interior shell.

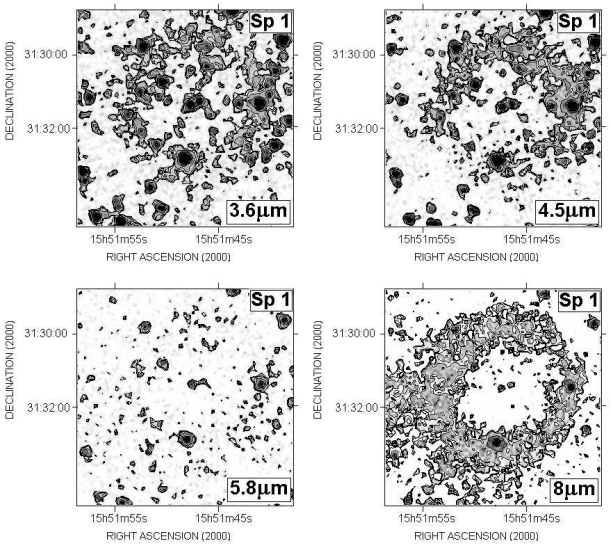

Fig. 11. Mapping of Sp 1 in the four IRAC bands, where the contour parameters [A, B, C] are given by [1.18, 0.74, 0.1119] at 3.6 μm, [1, −0.05, 0.0939] at 4.5 μm, [6, 3.89, 0.0442] at 5.8 μm, and [19, 17.33, 0.0048] at 8.0 μm. This source is close to the limits of detection for the GLIMPSE 3D survey, and levels of S/N are extremely low. Most of the fragmentary appearance can be attributed to noise. The apparent extension of the 8.0 μm shell to the east results from contamination by background emission.

So, the halo surface brightness in the MIR, when compared to peak values in the nucleus, is > 10 times greater than observed in the visual. This unusual behaviour appears typical of many PNe (see e.g., Phillips et al. 2009; Ramos-Larios & Phillips 2009), and may presumably arise due to H_2 emission, PAH emission bands, or as a result of exceptionally strong low excitation transitions such as [ArII] λ6.985 μm or [ArIII] λ8.991 μm. Much depends, in this interpretation, on whether the halo is ionised or neutral, or perhaps even composed of a mixture of the two, and it is still far from clear what the primary emission mechanisms might be.

3.4. *Sp 1*

Sp 1 is one of the most interesting of the sources to fall within the limits of the GLIMPSE 3D survey. The nebula has a closely circular structure with diameter ∼120 arcsec (e.g., Miszalski et al. 2009); a large [OIII] expansion velocity of ∼60 km s^{-1} (Meatheringham, Wood, & Faulkner 1988); and moderate H and HeII Zanstra temperatures of ∼32.5 and 82.0 kK (Phillips 2003). The difference between these values may indicate the escape of H ionising photons, and a nebular structure which is density bound. An image of the source (taken by D. Malin) is available at `http://www.aao.gov.au/images/captions/aat095.html`.

By far the most interesting characteristic of this angularly large PN, however, is that it appears to be centred on a close binary system with period 2.91 days, having an amplitude variation of 0.1 mag in B (e.g., Bond & Livio 1990). Although the binary is a non-eclipsing system, it may be exhibiting radiation effects (e.g., Mendez et al. 1988).

It has popularly been supposed that close binary systems result in bipolar outflows, and Sp 1 would therefore appear to be in conflict with this presumption; a problem which also occurs for SuWt 2 and WeBo 1 (Bond, Ciardullo, & Webbink 1996), both of which are non-bipolar sources centred upon close binary systems. One way out of this predicament has been to suppose that Sp 1 may be being viewed head-on, and that the ring corresponds to the toroidal waist of the bipolar PN (Bond & Livio 1990). Similar hypotheses have also been proposed

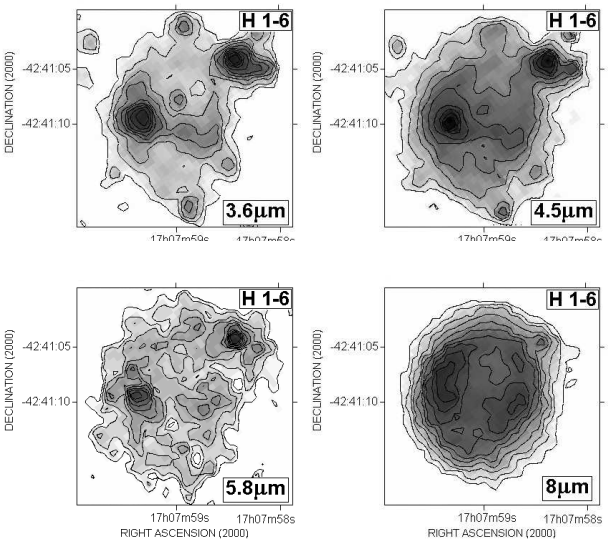

Fig. 12. Mapping of H 1-6 in the four IRAC bands, where the contour parameters [A, B, C] are given by [3.3, 1.64, 0.1126] at 3.6 μm, [2.4, 0.63, 0.1250] at 4.5 μm, [9.5, 6.40, 0.0427] at 5.8 μm, and [30, 25.62, 0.0227] at 8.0 μm.

for NGC 6720 (Bryce, Balick, & Meaburn 1994) and NGC 6781 (Ramos-Larios, Phillips, & Guerrero, in preparation).

The present contour results are shown in Figure 11, where it is clear that emission from the source is very faint indeed, and barely detected in the MIR. The apparent extension of the 8.0 μm shell to the left-hand side is a result of the contaminating effects of background emission. Excluding this factor, and taking into account the extreme noisiness of the results, it is clear that the MIR and optical results are likely to be reasonably consistent.

3.5. *H 1−6*

H 1-6 appears to be a reasonably bright PN at infrared wavelengths, although it has been very little studied in other wavelength regimes. The elliptical shell (Figures 1 and 12) has dimensions of 16.3×14.4 arcsec^2. Profiles through the source are illustrated in Figure 13, and show a double-humped structure arising from an internal ring. The 3.6–5.8 μm profiles are strongly dominated by a star at RP $\sim$–5 arcsec, however, and this causes some distortion of the IRAC band ratios (Figure 13, lower panel).

3.6. *H 1−7*

This nebula appears to have a rather irregular morphology at optical wavelengths (Schwarz et al. 1992), and has [SII] densities which are moderately

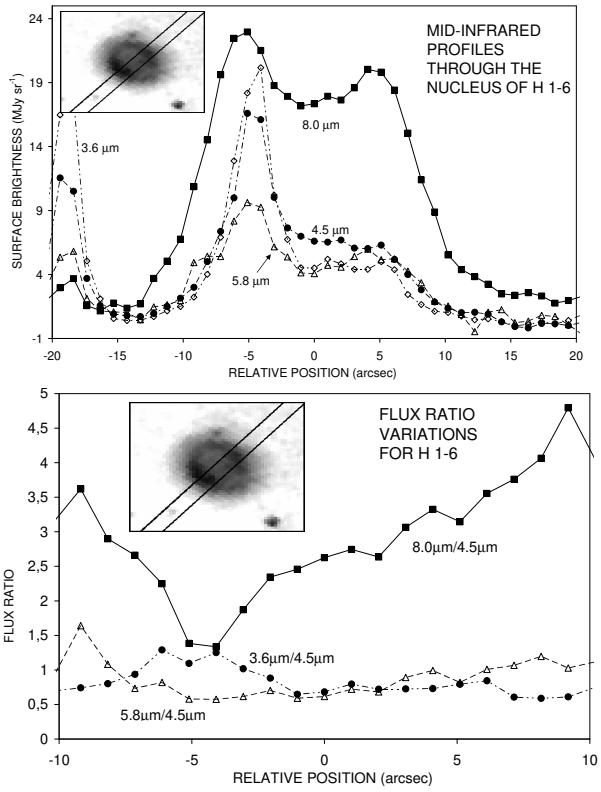

Fig. 13. As for Figure 3, but for the case of H 1-6. The peaks in the 3.6–5.8 μm channels close to RP $\sim$–5 arcsec are mostly attributable to an unrelated field star. This also leads to minima in the 8.0 μm/4.5 μm and 5.8 μm/4.5 μm ratios (lower panel), and a corresponding maximum in 3.6 μm/4.5 μm. There is, apart from this component, not too much evidence for variations in the IRAC ratios.

high ($\sim 4.2 \times 10^3$ cm^{-3}; Chappini et al. 2009). The N/O ratio of $\cong$ 0.56, and a value He/H $\cong$ 0.12 may imply that the source is a Type I PN (Chiappini et al. 2009). The optical diameter is quoted as 8.5 arcsec (Perek & Kohoutek 1967), which is significantly smaller than any of the contour maps in Figure 14, and less than half of the size observed at 8.0 μm ($\sim$22 arcsec). This, and the tendency of the source to become larger towards longer IRAC wavelengths, may suggest that much of the longer wave emission is associated with the nebular PDR.

Further evidence for this is provided in Figure 15, where we show logarithmic profiles through the centre of the source (upper panel), and IRAC band ratios in the central portion of the envelope (lower panel). It is apparent from this that the shorter wave profiles (3.6 and 4.5 μm) cut-off close to RP $\cong -15$ arcsec and +19 arcsec (an extension to RP ~ -25 arcsec is likely to be due to an unrelated

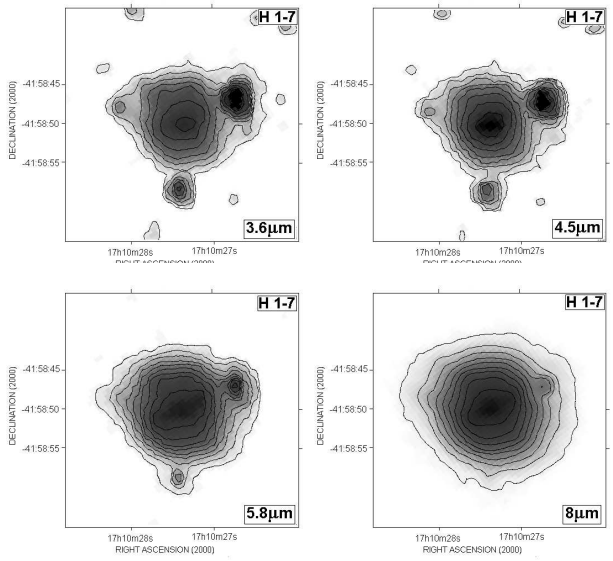

Fig. 14. IRAC mapping of H 1-7, where the contour parameters [A, B, C] are given by [5.8, 1.75, 0.2313] at 3.6 μm, [4.3, 0.57, 0.2150] at 4.5 μm, [12, 5.71, 0.1592] at 5.8 μm, and [30.6, 17.23, 0.1720] at 8.0 μm. Although the innermost contours are elliptical, the outer structure appears to be more circular. Note the strong variation in dimensions between shorter and longer MIR wavelengths.

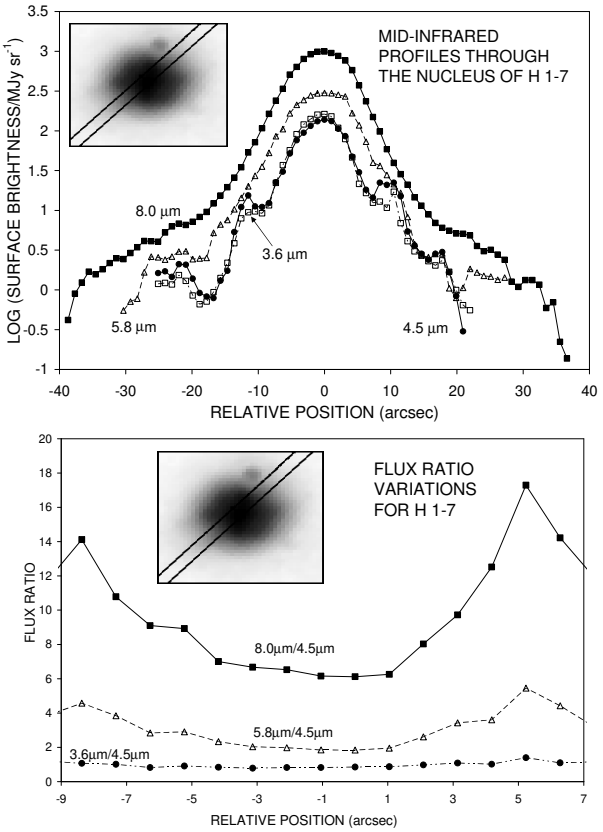

Fig. 15. As for Figure 3, but for the case of H 1-7; where in this case, the upper profiles are represented in terms of logarithmic surface brightness. The profiles have a mostly Gaussian emission fall-off, whilst there is evidence for an increase in 8.0 μm/4.5 μm and 5.8 μm/4.5 μm ratios towards the limits of the interior shell.

field star, having as it does stronger emission in the shorter wave IRAC channels), whilst the 8.0 μm profile extends to RP $\cong -36$ arcsec and +32 arcsec. There is, apart from this, very little discernible structure, and the appearance is similar to those of many other PNe observed in this survey. Examples of these (mostly more compact) sources are discussed in § 3.11.

Finally, the differing IRAC band ratios are shown in the lower panel of Figure 15. It is again clear, as for Pe 2-12 (§ 3.1), that there is a marked increase in 5.8 μm/4.5 μm and 8.0 μm/ 4.5μm ratios close to the edges of the central shell, perhaps arising from an increase in PAH emission within an enveloping PDR. There is little comparable variation for 3.6 μm/4.5 μm, however, which remains (for the most part) close to unity.

3.7. *M 1−29*

M 1-29 is an interesting PN with optical dimensions of ∼7.6 arcsec (Cahn & Kaler 1971; Moreno et al. 1988). The kinematics of the shell appear complex, with evidence for velocities of up to ±50 km s^{-1} (Gesicki, Acker, & Zijlstra 2003), and this, together with the VLA mapping of Zijlstra et al. (1989), has been used to suggest that it may be a poorly resolved bipolar outflow. Perusal of the VLA mapping suggests that it is more likely to have an elliptical structure, however, with higher levels of surface brightness at the minor axis limits of the shell. The size of the envelope at radio wavelengths appears to be $\cong 11.3 \times 6.5$ arcsec^2. Estimates of the ratios [He/H, N/O] have varied between [0.15, 0.93] (Chiappini et al. 2009), [0.145, 0.68–0.7] (Wang & Liu 2007), and [0.14, 0.32] (Perinotto 1991). It would seem clear, from the more recent estimates, that the nebula should be classified as a Type I source. The only previous analysis of the object in the infrared appears to have been undertaken by Cassasus et al. (2001), who find that the spectrum is flat between 7 and 14 μm, and shows no evidence for dust emission continua.

It appears clear, from our contour mapping (Figure 16), that there is a marked increase in dimensions between 3.6 and 8.0 μm, with the overall dimensions at the latter wavelength being of order

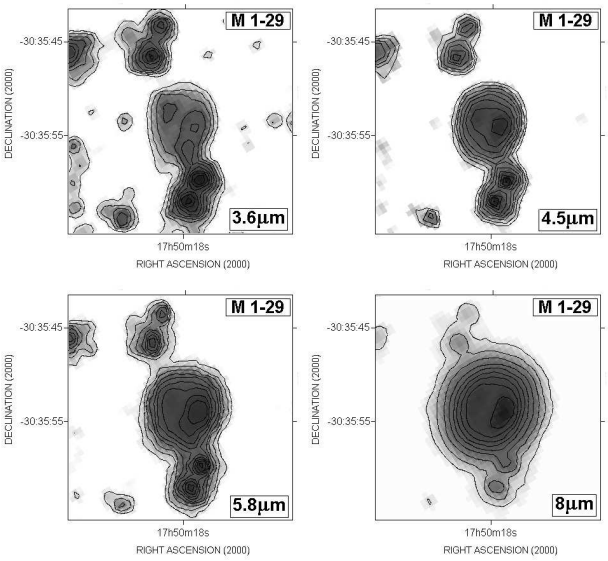

Fig. 16. Mapping of M 1-29 in the four IRAC channels, where the contour parameters [A, B, C] are given by [12, 5.12, 0.1502] at 3.6 μm, [12, 3.10, 0.1192] at 4.5 μm, [12, 6.55, 0.0950] at 5.8 μm, and [25, 17.32, 0.1242] at 8.0 μm. Note again how the dimensions of the source increase as the wavelength of observation becomes larger.

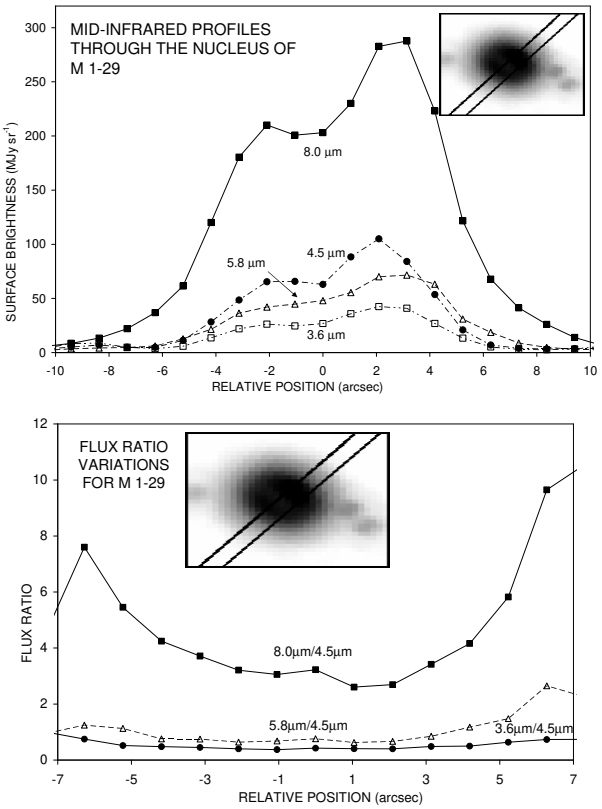

Fig. 17. As for Figure 3, but for the case of M 1-29, where it is seen that the longer wave profiles have a double-humped appearance. The 8.0 μm/4.5 μm ratio in the inner portions of the shell increases with increasing distance from the nucleus.

$\sim$13 arcsec; a value which is rather larger than is determined for the radio and optical regimes. This is confirmed through logarithmic profiles through the centre of the source, which show a $1/10^{\rm th}$ peak width of $\sim$11.3 arcsec at 3.6 μm, of 13.7 arcsec at 5.8 μm, and of $\sim$15 arcsec at 8.0 μm. The overall 8.0 μm dimensions at 0.6% peak height –the lowest level at which it appears possible to detect the envelope above background fluctuations and noise– are of the order of $\sim$39.7 arcsec.

The 8.0 μm/4.5 μm ratio also increases from a value $\sim$2.6 at the centre, to $\approx$8–10 at RP $\sim$7 arcsec (Figure 17), a tendency which is confirmed in the ratio maps illustrated in Figure 18. It is therefore likely that much of the longer wave emission arises from outside of the ionised shell.

3.8. *MeWe 1−6*

This is a recently discovered example of an old PN with extremely low levels of surface brightness in the visible (Melmer & Weinberger 1990). The structure seems to take the form of a thick-ringed shell with dimensions of order 16 arcsec. There have however, apart from this, been no other studies of this source.

Our IRAC contour maps are illustrated in Figure 19, whence it is again evident that surface brightnesses are low, and that the object is located in a region of high field star densities. This makes it difficult to discern the shell at 3.6 and 5.8 μm. Profiles through the envelope (Figure 20) reveal the expected double-humped structure, and suggest 8.0 μm dimensions $\sim$21.6 arcsec which are slightly larger than in the visible.

3.9. *PN G009.8−01.1 (PHR1811−2100)*

This source represents one of the many new PNe detected in the MASH I survey, where Hα images show the presence of a bright rectangular band surmounted by orthogonal fainter wing-like structures. The source is classified as a bipolar PN. The published spectrum appears to be extremely noisy, although Parker et al. (2006) suggest that [NII] > 4Hα, and [OIII] > Hα.

Our present contour maps (Figure 21) are dominated by the bright interior emission regime, with evidence for 8.0 μm extensions to $\sim$25 arcsec. The minor axis width is $\sim$12 arcsec. This compares to dimensions 32×12 arcsec^2 quoted for the Hα image.

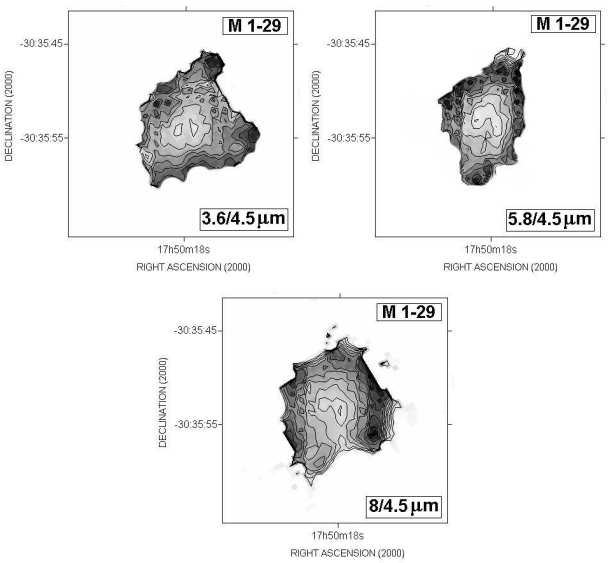

Fig. 18. IRAC band ratio mapping over the projected envelope of M 1-29, where the contour parameters [D, E] are given by [0.2, 0.0930] for 3.6 μm/4.5 μm, [0.5, 0.0669] for 5.8 μm/4.5 μm, and [2.4, 0.0884] for 8.0 μm/4.5 μm. There is evidence for an increase in ratios with radial distance from the nucleus, in conformity with the profiles illustrated in Figure 17.

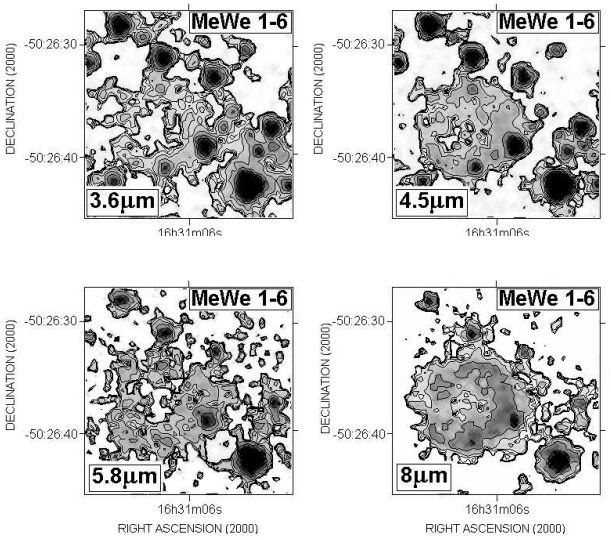

Fig. 19. IRAC mapping of MeWe 1-6, where the contour parameters [A, B, C] are given by [2.28, 1.33, 0.1094] at 3.6 μm, [2.0, 1.00, 0.1179] at 4.5 μm, [7.8, 5.83, 0.0528] at 5.8 μm, and [23.0, 19.62, 0.0128] at 8.0 μm. It is clear that the source has a ring-like morphology at 4.5 and 8.0 μm which is closely comparable to that observed in the visible. However, the high field star densities, and low surface brightness of the envelope make it much more difficult to discern at 3.6 and 5.8 μm.

It would therefore appear that we are detecting most of the region defined through optical imaging.

Profiles through the source are illustrated in Figures 22 and 23, from which it is clear that there is a small dip in 8.0 μm emission close to the centre of the minor axis traverse (Figure 23). This may indicate barely resolved evidence for a central, inclined toroidal structure. The fact that this dip is evident 8.0 μm, but absent at shorter wavelengths may arise where 8.0 μm fluxes are enhanced within the toroid – perhaps as a result of warm dust emission or fluorescently or shock excited H_2. The 3.6 and 4.5 μm fluxes, by contrast, are more likely to arise from ionic transitions, and to trace components of gas within the limits of this structure.

The IRAC band ratios in the lower panels are highly variable with relative position, and show evidence for lower 8.0 μm/4.5 μm and 5.8 μm/4.5 μm ratios close to the centre of the source. These trends are also evident in our contour mapping in Figure 24, where we see a minimum in 5.8 μm/4.5 μm and 8.0 μm/4.5 μm ratios close to the centre of the source, and larger values towards the periphery. There is a great deal of similarity between the longer wave ratio maps, suggesting that their fragmentary appearance is real, and corresponds to actual variations in the ratios. A similarly high level of complexity is also noted in the 3.6 μm/4.5 μm map, although the central minimum is less strong.

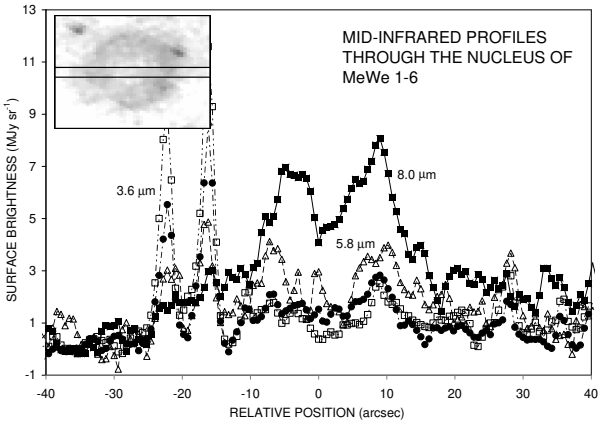

Fig. 20. As for Figure 3, but for profiles through MeWe 1-6. The double-humped structure arises from the ring-like morphology of the source.

3.10. *PN G344.4+01.8 (MPA1654−4041)*

This source was first detected in the MASH II survey, and is quoted as having an elliptical morphology with dimensions $\cong 15 \times 9$ arcsec^2 (Miszalski

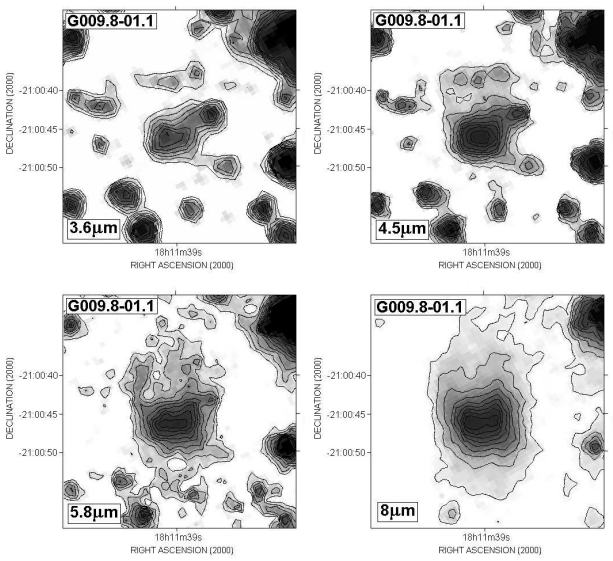

Fig. 21. IRAC band mapping of the MASH I source PN G009.8-01.1 (PHR1811-2100), where the contour parameters [A, B, C] are given by [2.8, 2.35, 0.0995] at 3.6 μm, [3.8, 1.57, 0.0909] at 4.5 μm, [12.9, 11.00, 0.0374] at 5.8 μm, and [39, 34.77, 0.0398] at 8.0 μm. The nebula has a highly elongated appearance at 8.0 μm, and an orthogonal bright interior band. Both of these features are consistent with a bipolar structure.

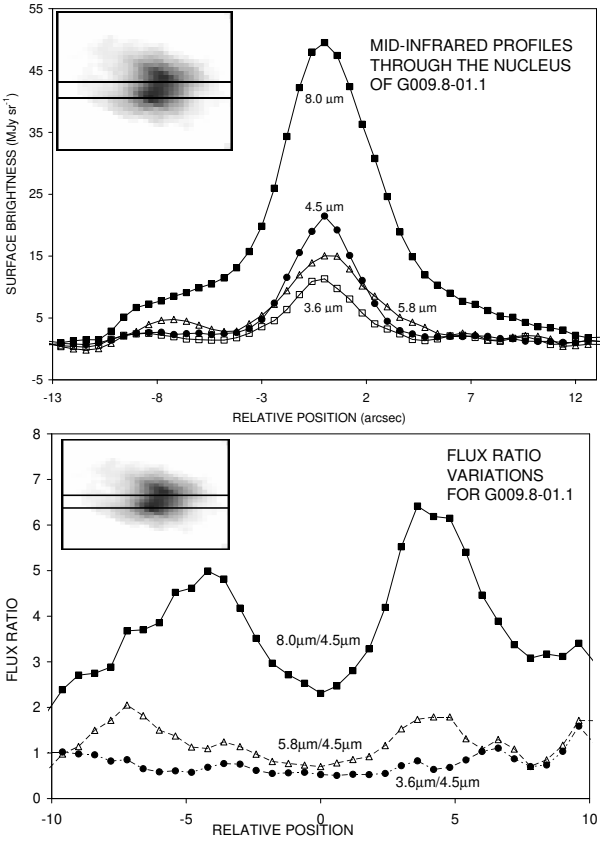

Fig. 22. As for Figure 3, but for the major axis of PN G009.8-01.9 (PHR1811-2100). The centre of the source has a Gaussian emission fall-off, whilst ratios 8.0 μm/4.5 μm and 5.8 μm/4.5 μm have maxima at $\pm$4 arcsec from the nucleus.

et al. 2008). It is also defined as being a "likely" PN, through there is no visual spectrum by which this identification can be assessed.

The dimensions of the 8.0 μm mapping (15.6 $\times$ 11 arcsec^2; see Figure 25) are closely similar to those determined in the visual, and although there appears to be an increase in dimensions between 3.6 and 8.0 μm, it is likely that much of this is due to the low S/N of our results. Profiles along the major and minor axes of the source are illustrated in Figure 26, from which it is clear that there is a bright unresolved nucleus at 3.6–5.8 μm, and a somewhat broader structure at 8.0 μm. The minor axis variation is of particular interest, in that it shows a systematic fall-off with distance from the nucleus. This is untypical of what is observed in most other PNe, where we normally see evidence for well defined central shells, rather than continuous stellar-wind type fall-offs. Such variations have only previously been noted in bipolar flows (see e.g., Phillips & Ramos-Larios 2008a, 2010), where CS winds are important in defining the kinematics. This trend may therefore place the identification of the source in doubt.

3.11. *Other PNe Detected in the GLIMPSE 3D survey*

It is apparent that the haul of extended, higher surface-brightness PNe is rather slim – particularly when compared to what has been observed in previous surveys (e.g., Phillips & Ramos-Larios 2008a; Ramos-Larios & Phillips 2008). This was, in general, broadly to be expected, given that the 3D survey covers regions which are further away from the Galactic plane, and at larger positive and negative latitudes. The spatial density of PNe is very much reduced compared to those observed at lower Galactic latitudes

It is finally worth noting that a good fraction of the PNe detected in this survey were either extremely compact and unresolved, or had a size which was too modest to permit a useful analysis. Four examples of the latter sources are shown in Figures 27 and 28, where we illustrate profiles through the cen-

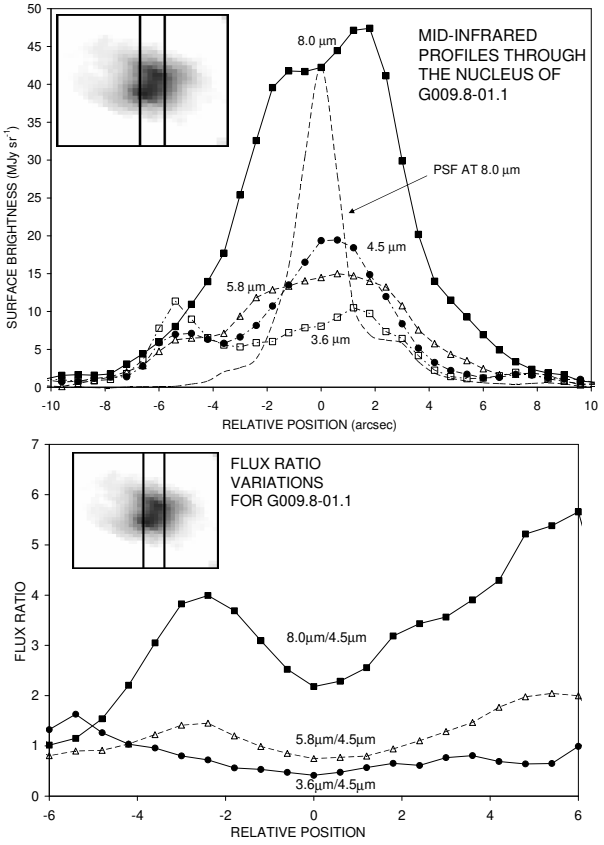

Fig. 23. As for Figure 20, but for a minor axis traverse through the nucleus. The longer-wave profiles have a slightly double-humped appearance, perhaps indicating a toroidal internal structure.

tres of M 1-27, M 1-35, Pe 1-6 and Pe 1-15. The most extended of these sources are M 1-27 and Pe 1-6, both of which have circular/elliptical morphologies. It is clear however that it would be difficult to reliably assess their properties, and/or assess spatial trends in their emission.

4. PHOTOMETRY OF THE GLIMPSE 3D SOURCES.

We have finally assessed fluxes for the more extended sources detected in the GLIMPSE 3D survey, and results are provided in Table 1. This represents the first part of a more extended program of photometry which will encompass extended and compact sources alike. Columns 1 and 2 of the table give the Galactic coordinates and normally recognised names, whilst Column 3 indicates the catalogue from which the positions were acquired (MI corresponds to MASH I (Parker et al. 2006), MII is MASH II (Miszalski et al. 2008), and Ack corresponds to Acker et al. (1992). The remaining four

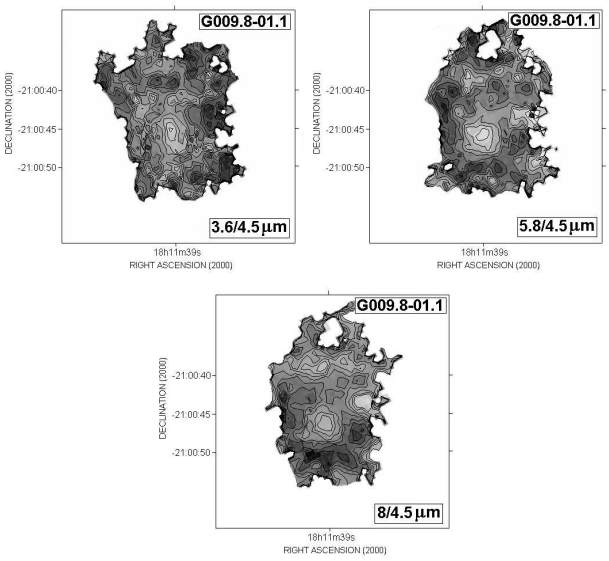

Fig. 24. IRAC band ratio mapping over the envelope of PN G009.8-01.1 (PHR1811-2100), where the contour parameters [D, E] are given by [0.4, 0.0569] for 3.6 μm/4.5 μm, [0.5, 0.0865] for 5.8 μm/4.5 μm, and [2.0, 0.0752] for 8.0 μm/4.5 μm. It would seem that ratios vary over quite small spatial scales, with little systematic variation from one part of the shell to the other. The central ratio values are in all cases low.

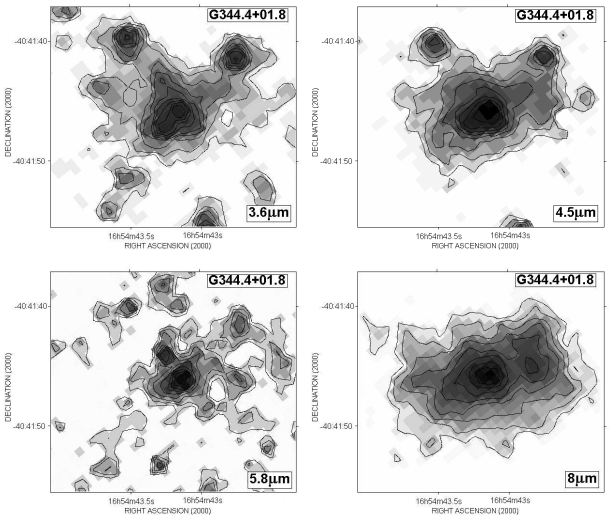

Fig. 25. IRAC mapping of the MASH II PN G344.4+01.8 (MPA1654-4041), where the contour parameters [A, B, C] are given by [1.7, 0.65, 0.0777] at 3.6 μm, [1.5, 0.59, 0.0854] at 4.5 μm, [4.27, 2.92, 0.0409] at 5.8 μm, and [15.8, 13.29, 0.0231] at 8.0 μm. This is an extremely low surface brightness structure in most of the bands, although the elliptical morphology is clearly visible at 8.0 μm.

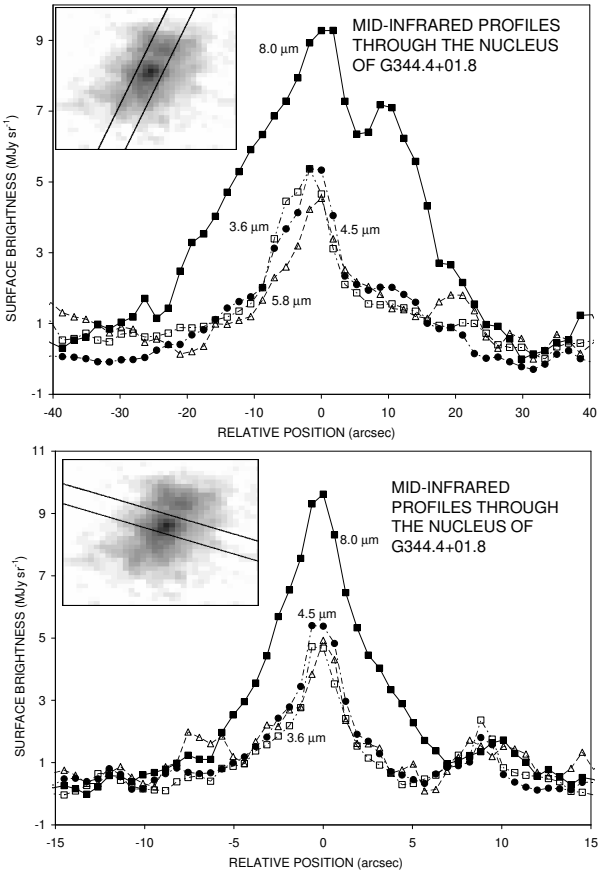

Fig. 26. Major and minor axis profiles though PN G344.4+01.8 (MPA1654-4041). Note the presence of a bright and unresolved core source, and the steep and monotonic fall-off in emission along the minor axis (lower panel). This latter variation is untypical of elliptical PNe.

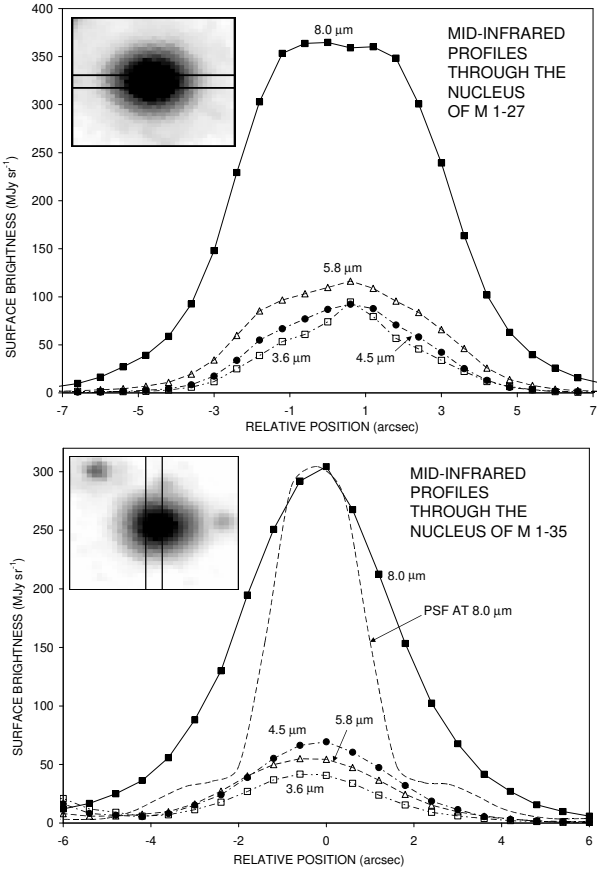

Fig. 27. Profiles through the nuclei of two compact PNe. These sources have an elliptical/circular appearance, and are typical of a large fraction of the PNe detected in the GLIMPSE 3D survey.

columns give the magnitude in each of the IRAC bands, determined using the zero magnitude calibration of Reach et al. (2006) and the techniques described in § 2. Typical errors range from 0.03 mag for the fainter sources through to 0.01 or less for the brightest.

It is of interest to compare the present results with photometry of other PNe, and this is undertaken in the [3.6]−[4.5]/[5.8]−[8.0] colour plane in Figure 29. In this latter case, MASH I sources are indicated by squares, the Acker et al. (1992) PNe are identified through disks, and the single MASH II PN is represented by a triangle. The solid lines indicate the limits for PNe detected through previous photometry, and are taken from the compilation of results by Phillips & Ramos-Larios (2010).

It is finally worth noting that previous photometry of PNe has sometimes used slightly differing correction factors for the diffuse background scattering (see § 2). These correction factors have proven extremely difficult to pin down, and officially quoted estimates have varied over time. It follows that care must be taken when comparing differing sets of data.

For the most part, it is clear that the 3.6 and 4.5 μm correction factors are similar, however, and the same applies for the 5.8 and 8.0 μm factors as well. Changes in the values of these factors therefore lead to only minor variations in colour, and a comparison between differing sets of data is expected to be reliable.

It is clear that our present results fall neatly within the range for other PNe, although they occupy a region which is somewhat more restricted. In particular, it would seem that there is a paucity of indices $[5.8]-[8.0] < 1$. This may, in part, testify to lower levels of stellar contamination, whether this occurs due to unrelated field stars or the PN central stars themselves. It can also however occur where

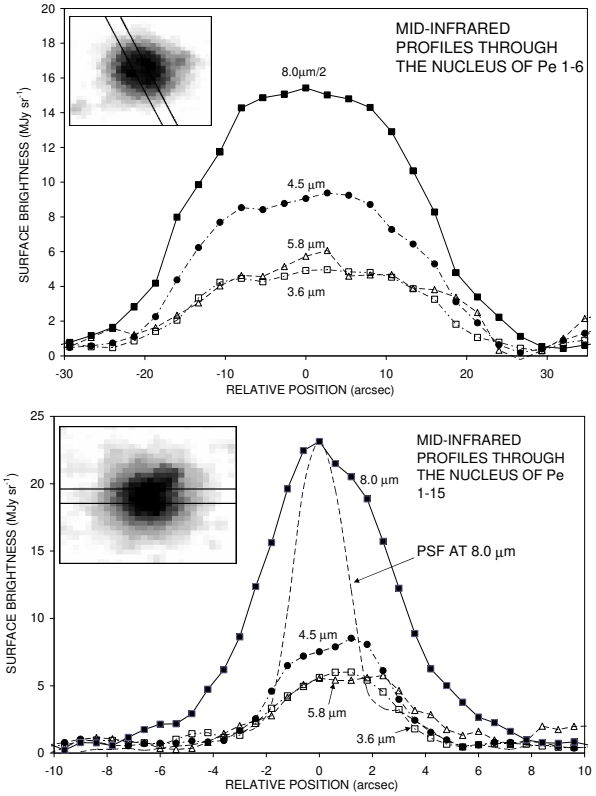

Fig. 28. As for Figure 27, but for Pe 1-6 and Pe 1-15.

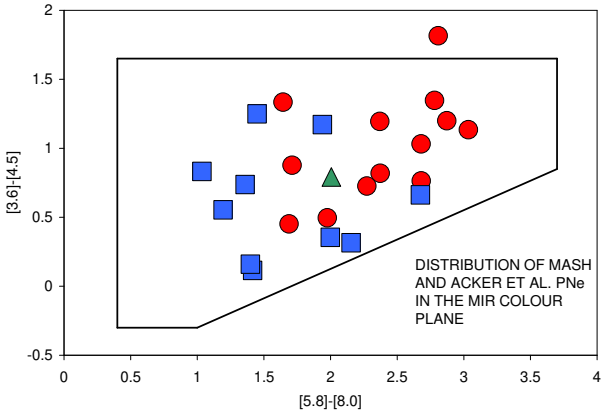

Fig. 29. The distribution of GLIMPSE 3D sources in the [3.6]–[4.5]/[5.8]–[8.0] colour plane, where the Acker et al. (1992) sources are represented as disks, MASH I sources are squares, and the sole MASH II PN is represented by a triangle. The solid lines indicate the approximate limits for Galactic PNe deduced from previous photometry of these sources. There is a tendency for MASH I sources to have somewhat lower indices [5.8]–[8.0], and for the Acker et al. (1992) sources to have larger values for these parameters; a situation which, if confirmed, might indicate a secular evolution in MIR colours.

there is strong shock-excited H_2 emission, higher excitation gas thermal emission, and/or strong dust continua or PAH emission bands. A further interesting aspect of the results is that there appears to be a tendency for the Acker et al. (1992) sources (disks) to have higher values of [5.8]−[8.0]. Specifically, whilst 80% of MASH I sources have indices smaller than [5.8]−[8.0] = 2.05 mag, the corresponding fraction for the Acker et al. (1992) nebulae is closer to 25%. Since the MASH I sources (squares) are normally regarded as being larger, more evolved, and to have lower levels of surface brightness, this may imply that there is an evolutionary trend within the colour plane – a trend which is related to a variation in the strength of the emission mechanisms cited above. It is possible, for instance, that ionic transitions (such as [ArII] λ6.985 μm and [ArIII] λ8.991 μm) become weaker as nebulae evolve, although the reduction of nebular excitation with increasing size, and evolution of the central stars to lower temperatures might be expected to have precisely the reverse effect. It is also conceivable that PAH band excitation becomes less strong as nebulae expand, and that radiative excitation of the molecules decreases. This would affect 8.0 μm band fluxes more than those at 5.8 μm, and lead to decreases in the [5.8]–[8.0] indices. Finally, the paucity of lower [5.8]–[8.0] sources may reflect a bias in the sample, such that the proportion of more evolved PNe is less than in previous studies of these nebulae.

It is clear however that these various mechanisms are no more than possible explanations, and further spectroscopy is required before we can understand such trends.

5. CONCLUSIONS

We have undertaken a provisional survey of PNe detected in the GLIMPSE 3D survey. This has involved mapping the shells in the 3.6, 4.5, 5.8 and 8.0 bands, as well as obtaining profiles through the nuclei, and maps of flux ratio parameters. We have detected many of the signatures discovered in previous mapping of such sources, including increases in the 5.8 μm/4.5 μm and 8.0 μm/4.5 μm ratios with distance from the nuclei, and emission from enveloping PDRs (Pe 2-12, H1-7, M 1-29). We have also detected enhanced levels of emission in the halos of the sources (NGC 6578) when compared to trends observed in the visual wavelength regime. It is therefore clear that the MIR characteristics of the PNe are sometimes radically different from those observed in other wavelength regimes.

We have also presented the first phase of photometry for GLIMPSE 3D sources, limited (in this case) to PNe having evidence for spatial extension. The colour-colour mapping of these results appears similar to what has been observed for other PNe, although we also note evidence for a possible secular evolution in the [5.8]−[8.0] indices. The more evolved GLIMPSE I sources appear to have lower mean colours, whilst the (mostly) less evolved Acker et al. (1992) nebulae have larger values of this parameter. This may reflect corresponding variations in nebular emission mechanisms.

This work is based, in part, on observations made with the Spitzer Space Telescope, which is operated by the Jet Propulsion Laboratory, California Institute of Technology under a contract with NASA. GRL acknowledges support from Conacyt (Mexico) grant 132671 and PROMEP (Mexico).

REFERENCES

Acker, A., Marcout, J., Ochsenbein, F., Stenholm, B., & Tylenda, R. 1992, Strasbourg-ESO Catalogue of Galactic Planetary Nebulae (Part 1 and 2; Garching: ESO)
Barlow, M. J. 1983, in IAU Symp. 103, Planetary Nebulae, ed. D. R. Flower (Dordrecht: Kluwer), 105
Beintema, D. A. 1997, in IAU Symp. 180, Planetary Nebulae, ed. H. J. Habing & H. J. G. L. M. Lamers (Dordrecht: Kluwer), 145
Bond, H. E., Ciardullo, R., & Webbink, K. 1996, BAAS, 28, 1401
Bond, H. E., & Livio, M. 1990, ApJ, 355, 568
Bryce, M., Balick, B., & Meaburn, J. 1994, MNRAS, 266, 721
Cahn, J. H., & Kaler, J. B. 1971, ApJS, 22, 319
Casassus, S., Roche, P. F., Aitken, D. K., & Smith, C. H. 2001, MNRAS, 327, 744
Chiappini, C., Górny, S. K., Stasinska, G., & Barbuy, B. 2009, A&A, 494, 591
Chu, Y. H., Jacoby, G. H., & Arendt, R. 1987, ApJS, 64, 529
Chu, Y.-H., et al. 2009, AJ, 138, 691
Cohen, M., et al. 2007, ApJ, 669, 343
Corradi, R. L. M., Schönberner, D., Steffen, M., & Perinotto, M. 2003, MNRAS, 340, 417
Exter, K. M., Barlow, M. J., & Walton, N. A. 2004, MNRAS, 349, 1291
Fazio, G., et al. 2004, ApJS, 154, 10
Gesicki, K., Acker, A., & Zijlstra, A. A. 2003, A&A, 400, 957
Guiles, S., Bernard-Salas, J., Pottasch, S. R., & Reillig, T. L. 2007, ApJ, 660, 1282
Hajian, A. R., et al. 2007, ApJS, 169, 289
Hora, J. L., Latter, W. B., Allen, L. E., Marengo, M., Deutsch, L. K., & Pipher, J. L. 2004, ApJS, 154, 296
Kingsburgh, R. L., & Barlow, M. J. 1994, MNRAS, 271, 257
Leene, A., Zhang, C. Y., & Pottasch, S. R. 1987, in Planetary and Proto-Planetary Nebulae: From IRAS to ISO, ed. A. Preite-Martinez (Dordrecht: Reidel), 39
Liu, X.-W., et al. 2001, MNRAS, 323, 343
Meatheringham, S. J., Wood, P. R., & Faulkner, D. J. 1988, ApJ, 334, 862
Melmer, D., & Weinberger, R. 1990, MNRAS, 243, 236
Mendez, R. H., Kudritzki, R. P., Herrero, A., Husfeld, D., & Groth, H. G. 1988, A&A, 190, 113
Miszalski, B., Acker, A., Parker, Q. A., & Moffat, A. F. J. 2009, A&A, 505, 249
Miszalski, B., Parker, Q. A., Acker, A., Birkby, J. L., Frew, D. J., & Kovacevic, A. 2008, MNRAS, 384, 525
Mizuno, D. R., et al. 2010, AJ, 139, 1542
Moreno, H., Gutiérrez-Moreno, A., Torres, C., & Lasker, B. M. 1988, PASP, 100, 604
Parker, Q. A., et al. 2006, MNRAS, 373, 79
Patriarchi, P., & Perinotto, M. 1994, A&A, 287, 585
Perek, L., & Kohoutek, L. 1967, Catalogue of Galactic Planetary Nebulae (Prague: Publ. House Czech Acad. Sci.)
Perinotto, M. 1991, ApJS, 76, 687
Perinotto, M., Morbidelli, L., & Scatarzi, A. 2004, MNRAS, 349, 793
Perinotto, M., Purgathofer, A., Pasquali, A., & Patriarch, P. 1994, A&AS, 107, 481
Phillips, J. P. 2003, MNRAS, 344, 501
Phillips, J. P., & Márquez-Lugo, R. M. 2011, MNRAS, in press*****
Phillips, J. P., & Ramos-Larios, G. 2008a, MNRAS, 383, 1029
_____. 2008b, MNRAS, 386, 995
_____. 2008c, MNRAS, 391, 1572
_____. 2009, MNRAS, 396, 1915
_____. 2010, MNRAS, 405, 2179
Phillips, J. P., Ramos-Larios, G., Schröder, K.-P., & Verbena-Contreras, J. L. 2009, MNRAS, 399, 1126
Ramos-Larios, G., & Phillips, J. P. 2008, MNRAS, 390, 1014
_____. 2009, MNRAS, 400, 575
Ramos-Larios, G., Phillips, J. P., & Cuesta, L. 2008, MNRAS, 391, 52
_____. 2011, MNRAS, in press*****
Reach, W. T., et al. 2006, AJ, 131, 1479
Schwarz, H. E., Corradi, R. C. M., & Melnick, J. 1992, A&AS, 96, 23
Su, K. Y. L., et al. 2007, ApJ, 657, 41
Szczerba, R., Górny, S. K., & Tylenda, R. 1998, Ap&SS, 255, 515
Ueta, T. 2006, ApJ, 650, 228
Wang, W., & Liu, X.-W. 2007, MNRAS, 381, 669
Werner, M., et al. 2004, ApJS, 154, 1
Zhang, C. Y. 1995, ApJS, 98, 659
Zhang, C. Y., & Kwok, S. 2009, ApJ, 706, 252
Zijlstra, A. A., Pottasch, S. R., & Bignell, C. 1989, A&AS, 79, 329

J. A. Quino-Mendoza, J. P. Phillips, and G. Ramos-Larios: Instituto de Astronomía y Meteorología, Av. Vallarta No. 2602, Col. Arcos Vallarta, C.P. 44130 Guadalajara, Jalisco, Mexico (jpp@astro.iam.udg.mx).

Revista Mexicana de Astronomía y Astrofísica, **47**, 49–61 (2011)

PLANETARY NEBULAE IN THE INNER MILKY WAY II: THE BULGE-DISK TRANSITION

O. Cavichia, R. D. D. Costa, and W. J. Maciel

Instituto de Astronomia, Geofísica e Ciências Atmosféricas
Universidade de São Paulo, Brazil

Received 2010 November 29; accepted 2011 January 14

RESUMEN

En este trabajo se usa una muestra de nebulosas planetarias localizadas en el disco interno y en el bulbo de la Galaxia con objeto de encontrar la distancia galactocéntrica que mejor separa estas dos poblaciones desde el punto de vista de las abundancias. Se utilizan escalas de distancias estadísticas para estudiar la distribución de abundancias en la interfase disco-bulbo. Mediante una prueba de Kolmogorov-Smirnov se encuentra la distancia a la cual las propiedades químicas de estas regiones mejor se separan.

El resultado del análisis estadístico indica que, en promedio, la población interior tiene menores abundancias que la exterior. Además, la población interior no sigue el gradiente radial del disco hacia el centro galáctico. Basados en nuestros resultados, sugerimos que la interfase disco-bulbo está situada a 1.5 kpc del centro, y marca la transición entre la población del bulbo y la del disco interno, definida como la población de masas intermedias.

ABSTRACT

In this work, a sample of planetary nebulae located in the inner-disk and bulge of the Galaxy is used in order to find the galactocentric distance which better separates these two populations, from the point of view of abundances. Statistical distance scales are used to study the distribution of abundances across the disk-bulge interface. A Kolmogorov-Smirnov test is used to find the distance at which the chemical properties of these regions better separate.

The results of the statistical analysis indicate that, on the average, the inner population has lower abundances than the outer. Additionally, for the α-element abundances, the inner population does not follow the disk radial gradient towards the galactic center. Based on our results, we suggest a bulge-disk interface at 1.5 kpc, marking the transition between the bulge and inner-disk of the Galaxy as defined by the intermediate mass population.

Key Words: Galaxy: abundances — Galaxy: evolution — planetary nebulae: general — techniques: spectroscopic

1. INTRODUCTION

Chemical abundances of Planetary Nebulae (PNe) are an important tool to investigate the chemical evolution of the Galaxy. As a final stage of evolution of low and intermediate-mass stars ($\sim$1–8 $M_{\odot}$), the abundances of α-elements found in PNe usually are not modified by the evolution of the progenitor star. In this sense, chemical abundances of PNe can be used to study the chemical evolution of galaxies as done by Maciel, Lago, & Costa (2005, 2006), Fu et al. (2009), Stanghellini & Haywood (2010).

The chemical abundances obtained from PNe are relatively accurate and the nebulae can be observed at large distances in the Galaxy, even in regions obscured by the dust in the galactic disk, since they have bright emission lines, such as [O III]λ500.7 nm and Hα. Therefore PNe are useful to study the pattern of abundances in the inner-disk and bulge of the

Galaxy, where the extinction in the optical range is very severe (see for example Escudero & Costa 2001; Escudero, Costa, & Maciel 2004; Chiappini et al. 2009; Cavichia, Costa, & Maciel 2010). On the other hand, PNe distances are still subject to discussion. Only in a few cases can the distances be determined by a direct method, such as for nearby PNe, which have the distances determined by trigonometric parallax, or in cases where there is a main sequence binary companion. In the cases were accurate individual distances cannot be determined, alternative methods have been developed in order to obtain reliable distances. In these cases, distances are derived from nebular properties (see e.g., Maciel & Pottasch 1980; Cahn, Kaler, & Stanghellini 1992; Stanghellini, Shaw, & Villaver 2008). These methods are called statistical methods and the distances so obtained are called statistical distances. In spite of the uncertainties, statistical distance scales are still the best tool to study the chemical abundance patterns in the Galaxy from the point of view of PNe, as done by Maciel & Quireza (1999), Maciel et al. (2006), Perinotto & Morbidelli (2006), and recently by Gutenkunst et al. (2008), Stanghellini & Haywood (2010), Henry et al. (2010).

From the point of view of the chemical evolution of the Galaxy, the bulge and the disk display different chemical abundance patterns such as the radial abundance gradients in the disk (Carigi et al. 2005; Daflon & Cunha 2004; Andrievsky et al. 2004; Maciel et al. 2005, 2006), or the wide abundance distribution in the bulge (Rich 1988; Zoccali et al. 2003, 2006). Also, the bulge and the disk may have different evolution histories, as described for example by the multiple infall scenario (Costa, Escudero, & Maciel 2005; Costa, Maciel, & Escudero 2008) or by the inside out formation model (Chiappini, Matteucci, & Romano 2001), respectively. As a consequence, we expect these differences to be reflected on the chemical properties of each component.

Additionally, the gas density, and consequently the star formation rate (SFR), also decrease in the inner Galaxy as found by Portinari & Chiosi (1999). They attribute this result to the influence of the galactic bar in the first 3 kpc of the Galaxy (see for example Gerhard 2002; Binney 2009). The decrease of the SFR is reflected on the α-element abundances in PNe, since a lower SFR limits the total mass ejected by the progenitor star, and consequently the chemical enrichment of the ISM decreases throughout the succeeding stellar generations. The galactic evolution models also point to a severe decrease in the SFR and chemical abundances at radii smaller than 3 kpc (Portinari & Chiosi 2000). Other chemical evolution models also predict a flatter abundance gradient in the inner-disk, such as those by Hou, Prantzos, & Boissier (2000) and Mollá & Díaz (2005).

Some recent work seems to support this scenario, based on the fact that towards the galactic center, stars do not follow the chemical abundance gradient found in the disk (Cunha et al. 2007). Davies et al. (2009) studying the chemical abundance patterns of the Scutum red supergiant clusters, located at the end of the galactic bar, find that there is a minimum in the abundances in this region, compared to other azimuthal angles.

From the point of view of PNe, the results of Gutenkunst et al. (2008) also point to a discontinuity in the abundance gradient towards the galactic center, in the sense that the abundances of bulge PNe do not follow the trend of those from the disk, as can be seen in their Figure 4. Górny et al. (2004) also notice that the oxygen gradient of the PNe population in the galactic disk flattens in the most internal parts of the Galaxy, and may even change sign. On the other hand, Chiappini et al. (2009) compared the abundances of PNe located in the bulge, inner-disk and Large Magellanic Cloud. Their results do not show any clear difference between bulge and inner-disk objects.

Other previous studies of the galactic bulge based on abundances of PNe such as Ratag et al. (1992), Cuisinier et al. (2000), Escudero & Costa (2001), Escudero et al. (2004), Exter, Barlow, & Walton (2004), find that bulge PNe have an abundance distribution similar to disk PNe, showing that He, O, Si, Ar, and Ca have a normal abundance pattern, and favoring therefore a slower galactic evolution than that indicated by stars. In conclusion, the distribution of chemical abundances in the inner region of the Galaxy is still an open question, especially regarding the bulge-disk connection. On the other hand, a detailed comparison of the bulge and inner-disk populations is important in order to characterize the galactic bulge as a "pseudobulge", as suggested by photometric and kinematic evidences (Howard et al. 2009; Shen et al. 2010), in opposition to a classical bulge as suggested by Binney (2009).

Both from modelling and from observational results, we expect a galactocentric distance to exist which better separates the populations of the bulge and inner-disk from the point of view of chemical abundances. However, such transition is still to be determined from the point of view of chemical abundances. The goal of this paper is to perform a

statistical analysis using the new data provided by Cavichia et al. (2010, hereafter Paper I), and additional data from the literature, in order to characterize the interface between the bulge and inner-disk of the Galaxy, as defined by the PNe population. Taking into account both the abundance distributions and the individual distances for a sample of PNe, we are able to characterize the interface by establishing at which galactocentric distance bulge and disk characteristics better separate.

This paper is organized as follows: in § 2 the details of the sample and the new distances to our objects are presented. In § 3 the method used in order to characterize the bulge-disk transition is described. In § 4 we discuss the results and compare them with other results in the literature. Finally, in § 5 the main conclusions are presented.

2. THE SAMPLE AND NEW DISTANCES

2.1. *The Sample*

An extensive number of statistical scales have been proposed in the literature, and two of them have been adopted in order to study the chemical abundance distribution in the inner Galaxy: the Stanghellini et al. (2008, hereafter SSV08), and the Zhang (1995, hereafter Z95), distance scales. These scales are based on the Shklovsky method but with the introduction of a relationship between the ionized mass and the radius of the nebula, as proposed by Maciel & Pottasch (1980). SSV08 is a recent revision of the Cahn et al. (1992, hereafter CKS92), scale based on the physical properties of the PNe in the Magellanic Clouds, whose distances are accurately known. As the authors argue, this new distance scale is the most reliable to date.

The selection criteria applied to search for objects in the two catalogues (SSV08 and Z95) were the following: we selected those PNe which had 5 GHz fluxes lower than 100 mJy, optical diameters smaller than 12 arcsec, and galactic coordinates within the range $|\ell| \leq 10^\circ$ and $|b| \leq 10^\circ$. The galactic coordinates were used to take into account only the PNe which are in the galactic center direction. The combination of the other two criteria leads to the rejection of about 90–95% of the PNe which are in the galactic center direction, but have heliocentric distances of less than 4 kpc (cf. Stasińska, Richer, & McCall 1998). These criteria are commonly used by other authors to select bulge PNe (e.g., Exter et al. 2004 and Chiappini et al. 2009), so that most of the objects considered in this work should be at or near the bulge.

In order to study the chemical abundance distribution in the inner Galaxy, we have made use of the data published by our group (Cavichia et al. 2010; Escudero et al. 2004; Escudero & Costa 2001). We also searched for chemical abundances of PNe located in the bulge and inner-disk of the Galaxy in the following works: Ratag et al. (1997), Exter et al. (2004), Górny et al. (2004), Perinotto, Morbidelli, & Scatarzi (2004), de Freitas Pacheco, Maciel, & Costa (1992), Köppen, Acker, & Stenholm (1991), Samland et al. (1992), Cuisinier et al. (2000). All these works deal with the same region of interest, and, besides that, they contain significant and homogeneous samples, which is very important in multi-object study, as we propose in this work. For more details on these works see Paper I. Adding these objects to our original sample in Paper I, our database contains 140 objects, as given in Table 1. In this table, the columns give the PN G number, the name of the nebula, the galactocentric distance in kpc for the SSV08 and the Z95 distance scales, respectively. An asterisk marks those PNe whose distances were derived in the present work. The galactocentric distances of the objects located beyond the galactic bulge are given with a negative sign in Table 1. The extinction in this region is very high, and the uncertainties in the distances are large, reaching 30% in some cases. For example, an object with a heliocentric distance of 8 kpc in this direction according to both scales will have a true heliocentric distance between 5.6 and 10.4. Therefore, it is unlikely that these objects are really located far beyond the galactic bulge, so that we assume that they actually belong to the bulge population. The implications of this assumption will be further discussed in § 3.3. More details on the new distances and the determination of the galactocentric distances are given in § 2.2.

2.2. *New distances to the Planetary Nebulae*

Several of the objects for which the chemical abundances were determined in Paper I, do not have distances published by SSV08. In order to include these PNe in our analysis, their distances were estimated from equations (8a) and (8b) of SSV08. In cases where the 5 GHz flux was not available, their equivalent 5 GHz flux from Hβ flux was derived using equation (6) in CKS92. The optical thickness parameter was derived from equation (2) in SSV08. Angular radii were obtained from the literature, most of them from Acker et al. (1992), and some from more recent works such as Tylenda et al. (2003) and Ruffle et al. (2004). The objects with new distances are marked with an asterisk in Table 1, and the data

TABLE 1

GALACTOCENTRIC DISTANCES OF PNE IN THE SAMPLE

PN G	Name	R_{SSV08} (kpc)	R_{Z95} (kpc)	PN G	Name	R_{SSV08} (kpc)	R_{Z95} (kpc)
000.1–01.1	M3-43	–	1.81	009.4–09.8	M3-32	1.85	1.57
000.2–01.9	M2-19	−0.30	0.63	009.6–10.6	M3-33	−1.45	–
000.3–04.6	M2-28	–	−0.70	009.8–04.6	H1-67	0.64	0.80
000.4–02.9	M3-19	0.31	−0.73	010.4+04.5	M2-17	–	0.85
000.7–02.7	M2-21	−2.20	–	010.7–06.4	IC4732	1.51	3.22
000.7–03.7	M3-22	0.50	−0.63	010.7–06.7	Pe1-13	−1.37	–
000.7+03.2	Hen 2-250	–	1.07	010.7+07.4*	Sa2-230	1.41	–
000.9–04.8	M3-23	3.78	3.45	010.8–01.8	NGC 6578	4.42	–
001.0+01.9	K1-4	6.06	–	011.0+05.8	NGC 6439	1.89	–
001.2–03.0	H1-47	–	−2.07	350.5–05.0*	H1-28	−1.93	–
001.2+02.1	Hen 2-262	−1.57	1.39	350.9+04.4	H2-1	2.45	–
001.4+05.3	H1-15	−1.29	0.73	351.1+04.8	M1-19	−2.75	0.71
001.7–04.6	H1-56	–	−3.06	351.2+05.2	M2-5	–	0.80
001.7+05.7	H1-14	1.73	2.24	351.6–06.2*	H1-37	−1.81	–
002.0–02.0*	H1-45	−7.12	−0.36	352.0–04.6	H1-30	–	2.88
002.0–06.2	M2-33	−1.09	−1.02	352.1+05.1	M2-8	−1.39	1.05
002.1–02.2	M3-20	0.44	2.71	352.6+03.0	H1-8	−0.91	–
002.1–04.2	H1-54	−4.39	−0.57	353.7+06.3	M2-7	1.19	−1.00
002.2–02.7	M2-23	3.75	−0.51	354.2+04.3	M2-10	–	−2.73
002.2–09.4	Cn1-5	2.83	3.70	355.1–02.9	H1-31	–	−3.78
002.4+05.8	NGC 6369	6.92	–	355.1–06.9	M3-21	–	2.55
002.6–03.4	M1-37	–	−0.62	355.4–02.4	M3-14	2.33	1.58
002.6+08.1	H1-11	1.19	1.30	355.4–04.0	Hf2-1	1.92	–
002.7–04.8	M1-42	2.53	3.15	355.7–03.0	H1-33	−4.05	−1.23
002.7+01.6	H2-20	–	0.53	355.7–03.4*	H1-35	2.15	2.03
002.8–02.2	Pe2-12	–	−4.12	355.9–04.2	M1-30	–	2.18
003.1+02.9	Hb4	2.98	–	355.9+03.6*	H1-9	2.19	–
003.1+03.4	H2-17	–	−0.98	356.2–04.4	Cn2-1	−0.56	1.91
003.2–06.1	M2-36	2.03	1.29	356.3–06.2*	M3-49	−5.33	–
003.3–04.6	Ap1-12	3.42	–	356.5–02.3	M1-27	3.41	4.27
003.4–04.8	H2-43	–	3.03	356.5–03.9	H1-39	−7.28	−2.08
003.5–04.6	NGC 6565	3.37	3.68	356.7–04.8	H1-41	2.37	1.51
003.6–02.3	M2-26	−0.40	−1.46	356.8–05.4*	H2-35	1.86	–
003.7–04.6	M2-30	−1.55	−0.68	356.9–05.8	M2-24	−1.52	−3.86
003.8–04.3	H1-59	−1.53	−3.18	356.9+04.4	M3-38	−6.07	−0.65
003.8–04.5	H2-41	−0.85	−6.23	356.9+04.5	M2-11	–	1.08
003.8+05.3	H2-15	−7.40	−8.96	357.1–04.7	H1-43	−5.33	−3.59
003.9–02.3	M1-35	1.93	3.38	357.1+03.6	M3-7	1.73	2.62
004.0–03.0	M2-29	−0.75	−2.01	357.2–04.5	H1-42	1.94	3.22
004.0–05.8	Pe1-12	1.66	−2.33	357.2+07.4	M4-3	–	−0.37
004.1–04.3	H1-60	−2.24	−0.82	357.3+03.3	M3-41	–	3.87
004.6+06.0	H1-24	–	0.89	357.3+04.0	H2-7	–	−1.32
004.8–05.0	M3-26	0.82	−0.82	357.4–03.2	M2-16	1.05	2.18
004.8+02.0	H2-25	−3.45	−4.22	357.4–03.5	M2-18	−7.74	−1.48
004.9+04.9	M1-25	1.50	3.11	357.4–04.6	M2-22	−0.79	−1.97
005.0+04.4	H1-27	0.65	−2.94	357.5+03.2	M3-42	1.17	−1.78
005.2+05.6	M3-12	–	1.24	357.6+01.7	H1-23	−1.74	1.89
005.5–02.5*	M3-24	1.34	–	357.6+02.6	H1-18	–	0.72
005.7–05.3	M2-38	1.24	−1.01	357.9–05.1	M1-34	–	2.15
005.8–06.1	NGC 6620	−1.19	1.61	358.2+03.5	H2-10	−5.35	−0.50
005.8+05.1	H2-16	2.81	–	358.2+03.6	M3-10	−1.40	1.72
006.0–03.6	M2-31	–	3.14	358.2+04.2	M3-8	0.96	0.78
006.1+08.3*	M1-20	−1.12	2.34	358.3–02.5	M4-7	1.66	2.81
006.4–04.6*	Pe2-13	1.92	–	358.3+03.0*	H1-17	0.42	−0.59
006.4+02.0	M1-31	2.94	4.10	358.5–04.2*	H1-46	−0.75	1.04
006.8–03.4*	H2-45	1.89	–	358.6+01.8	M4-6	–	1.76
006.8+04.1	M3-15	–	3.94	358.6+07.8	M3-36	–	−6.05
007.0–06.8	VY2-1	0.86	2.57	358.7–05.2*	H1-50	−3.03	0.79
007.0+06.3*	M1-24	−1.00	–	358.8+03.0	Th3-26	0.66	–
007.1–06.0	H1-66	–	−1.70	358.9+03.2	H1-20	0.64	2.91
007.2+01.8*	Hb6	3.78	–	358.9+03.3*	H1-19	−2.95	−0.51
007.5+07.4	M1-22	–	−4.02	359.1–01.7	M1-29	–	4.70
007.8–04.4	H1-65	–	−2.25	359.1–02.3	M3-16	1.30	1.50
008.0+03.9	NGC 6445	6.64	–	359.3–03.1	M3-17	−3.60	−1.10
008.1–04.7	M2-39	−4.02	−2.21	359.4–03.4	H2-33	0.54	−1.78
008.2–04.8	M2-42	−1.48	0.66	359.7–02.6	H1-40	0.84	0.36
008.2+06.8*	Hen 2-260	−12.23	−3.62	359.8+03.7	Th3-25	-6.52	–
008.3–07.3*	NGC 6644	2.18	4.01	359.8+06.9	M3-37	−8.69	−5.50
009.0+04.1	Th4-5	–	1.69	359.9–04.5	M2-27	−4.45	2.68
009.4–05.0	NGC 6629	5.67	–	359.9+05.1	M3-9	4.70	–

TABLE 2

NEW DISTANCES

PN G	Name	θ (arcsec)	F (mJy)	τ	d (kpc)
002.0–02.0	H1-45	0.8	20	2	15.1
005.5–02.5	M3-24	5.1	4.9	4.3	6.7
006.1+08.3	M1-20	0.8	50	1.7	8.1
006.4-04.6	Pe2-13	6.6	3.4	4.7	6.2
006.8–03.4	H2-45	4.6	9.7	3.9	6.2
007.0+06.3	M1-24	3.2	6.2	3.8	8.5
007.2+01.8	Hb6	2.5	240	2	4.3
008.2+06.8	Hen 2-260	0.5	10	1.9	20.4
008.3–07.3	NGC6644	1.3	100	1.8	6.1
010.7+07.4	Sa2-230	5	4	4.4	7.1
350.5–05.0	H1-28	3.9	1.5	4.6	9.9
351.6–06.2	H1-37	4.3	1.3	4.7	9.7
355.7–03.4	H1-35	1	90	1.7	5.9
355.9+03.6	H1-9	3.5	30	3.2	5.9
356.3–06.2	M3-49	4.9	0.2	5.7	13.2
356.8–05.4	H2-35	5.4	0.9	5.1	9.1
358.3+03.0	H1-17	0.5	40	1.4	7.9
358.5–04.2	H1-46	0.6	40	1.5	8.5
358.7–05.2	H1-50	0.7	30	1.8	10.9
358.9+03.3	H1-19	0.7	30	1.9	10.9

used in the determination are shown in Table 2. In this table, Column 1 gives the PN G number, Column 2, the name, Column 3, the angular diameter, Column 4, the 5 GHz flux, Column 5, the optical thickness parameter, and Column 6 lists the new distances derived for these objects.

2.3. *Galactocentric distances and distribution*

Heliocentric distances were converted into galactocentric distances using equation 1, where d is the heliocentric distance, b and ℓ the galactic latitude and longitude, respectively, and R_0 the solar distance to the galactic center. In this work we adopted $R_0 = 8$ kpc, as suggested by recent studies (Gillessen et al. 2009; Nishiyama et al. 2006).

$$R = \sqrt{R_0^2 + (d\cos\ b)^2 - 2\ R_0\ d\cos\ b\cos\ \ell}, \quad (1)$$

In order to check the distribution of distances for the PNe in our database, Figure 1 shows the distribution of the PNe with respect to the galactocentric distance for both distance scales used in this work, Z95 (left) and SSV08 (right), including the new distances derived in this work. The figure also shows a Gaussian fit to each histogram. The mean and standard deviation are (0.6 ± 0.3) kpc and (2.6 ± 0.3) kpc for the SSV08 scale, and (0.6 ± 0.2) kpc and (2.5 ± 0.2) kpc for the Z95 scale. For both scales, the mean is consistent with the most recent determinations of the solar distance to the galactic center, which are all near 8 kpc, while the widths are larger than the standard deviation expected of 1.2 kpc for the bulge. As discussed by Z95, this dispersion is a convolution of the probably real Gaussian distribution of the bulge, with the extra spread introduced by the mass-radius relationship.

3. DETERMINATION OF THE BULGE-DISK INTERFACE

3.1. *Abundance differences between bulge and inner-disk PNe*

In order to study the chemical abundance distribution in the inner Galaxy and to determine the bulge-disk interface, we made use of a method similar to that suggested by Maciel et al. (2006). First, a galactocentric distance (R_L) is chosen, which defines a limit for the sample. Then the sample is divided into two groups: Group I is composed by PNe with galactocentric distances smaller than the limit previously settled, and Group II, is composed by PNe with galactocentric distances larger than this limit. For each group, the average abundances and the standard error of the mean are calculated for the available elements, namely He, O, N, S, and Ne. Then, the limiting radius R_L is varied, considering distances in the interval from 0.1 to 3.6 kpc, in 0.7 kpc steps for each distance scale.

The results are shown in Figures 2 and 3 for the SSV08 and Z95 distance scales, respectively. In each figure, Group I is represented by filled circles joined by continuous lines and Group II by squares joined by dashed lines. Each pair of circle/square points in each plot represents the average abundance for that element adopting a given limit for the bulge-disk interface, as a function of the limiting distance. Therefore, each plot shows how the differences between the groups evolve adopting distinct limits to define them. Considering elements heavier than He, it can be seen that, on average, abundances of Group I are lower than those of Group II objects for both distance scales. That is, in most cases the objects of Group I, which are closer to the galactic center, have systematically lower abundances compared with the objects of Group II, for all chosen values of the limiting radius (R_L). The main exceptions are the helium abundances for both distance scales and argon for the Z95 scale, which present similar distributions for both groups. In the case of helium, these results are not surprising, as (a) this element is equally contaminated by the PN progenitor stars, both in the bulge

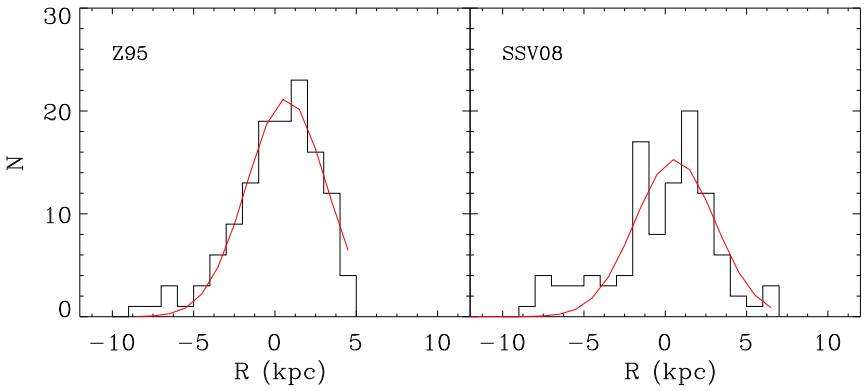

Fig. 1. Galactocentric distance distribution for the Z95 distance scale (left) and for the SSV08 distance scale (right). For each histogram a Gaussian fit is shown (see the text for more details).

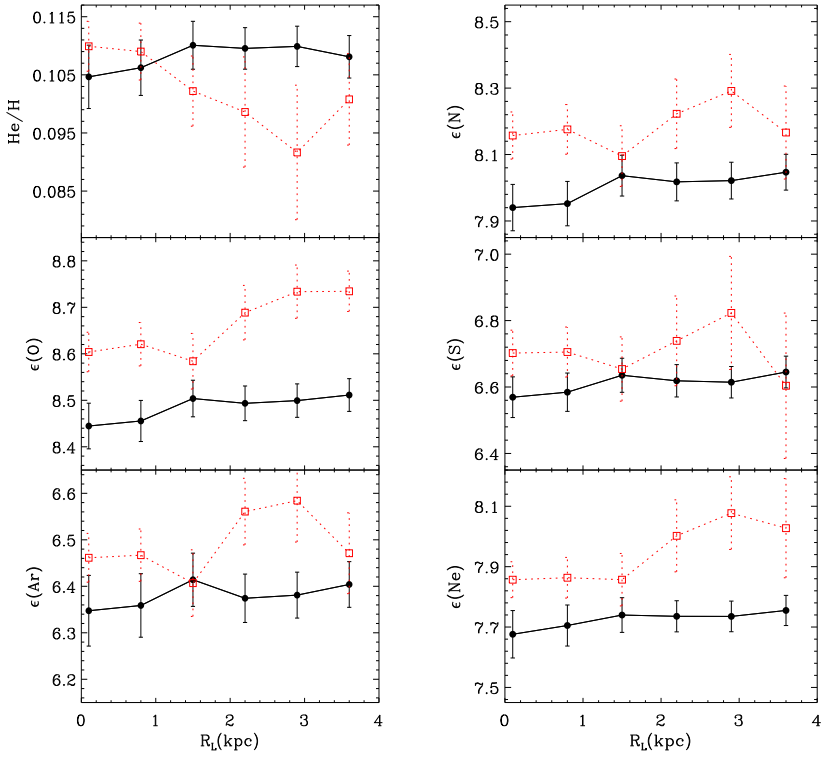

Fig. 2. Average abundances of PNe of Group I (circles joined by continuous lines) and Group II (squares joined by dashed lines) for the SSV08 distance scale. The abscissa gives the limiting galactocentric distance R_L, considered to be in the range 0–4 kpc. Error bars indicate the standard error of the mean for each subsample.

and in the galactic disk, and (b) helium does not show any measurable radial abundance gradient, in contrast with the remaining elements considered in this paper. (See a detailed discussion of the helium gradient in Maciel 2000).

Examining Figure 2 we see that for the α-elements oxygen, sulfur and argon the differences between both samples reach a minimum between 1.5 and 2.5 kpc, where it is of the order of 0.1 dex or lower. In Figure 3, examining now the α-elements, we see that a minimum difference appears around 1.5 or 2 kpc. For neon, the abundance difference between the groups is of the order of 0.2 dex, while for the other elements this difference is of the order

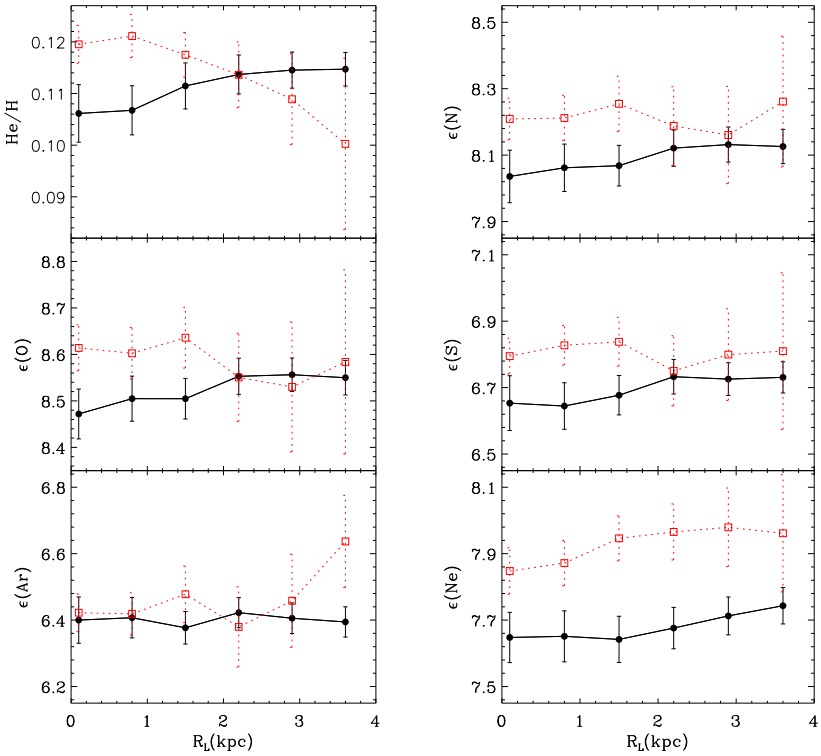

Fig. 3. The same as Figure 2 for the Z95 scale.

of 0.15 dex. For argon this difference is not clear, which is already expected since the ionization correction factor used to derive its abundance can lead to uncertainties larger than those for other elements.

3.2. *Kolmogorov-Smirnov test*

Our goal in this section is to find the distance that best characterizes the separation of the two groups, in the sense that the populations of each group should be as distinct as possible. In this case, we will be able to ascertain a value for the galactocentric distance of the bulge-disk interface based on the intermediate mass population represented by the PNe sample. In order to find such distance, we performed a Kolmogorov-Smirnov test for Groups I and II at each step of the procedure described above. The test returns the probabilities that the two groups are drawn from the same distribution. Small probabilities show that the cumulative distribution function of Group I is significantly different from Group II. The results are displayed in Figure 4. For each element the probability is shown as function of the limiting distance R_L. For each distance step, the left filled bar represents the SSV08 scale and the right empty bar the Z95 scale. Since we are looking for small probabilities, we can see from the figure that the lowest probabilities are achieved at 1.5 kpc for the Z95 distance scale for the elements O, S, Ar, and Ne. The probabilities for each element and distance are listed in Table 3 and the lowest values are highlighted in black. Again, it is clear that for the Z95 distance scale the lowest probabilities are achieved at 1.5 kpc for all the α-elements. On the other hand, SSV08 does not show a unique distance for the lowest probabilities. Indeed, considering only the α-elements, no distances are alike. Nevertheless, examining Figure 2 in detail, we can see that there is a step in the abundance radial distributions for the α-elements concerning the distance of 2.2 kpc. So that the safest conclusion we can draw is that $R_L < 2.9$ kpc based on the SSV08 distance scale.

3.3. *Resulting abundance distributions*

Adopting the separation distances obtained for each element and distance scale, namely 1.5 kpc for Z95 and 2.2 kpc for SSV08, the distribution of the abundances for each group are shown in Figures 5 and 6 for the Z95 and SSV08 distance scales, respectively. Empty histograms represent Group I objects, while filled histograms represent Group II objects. The number of objects used is also given for each plot.

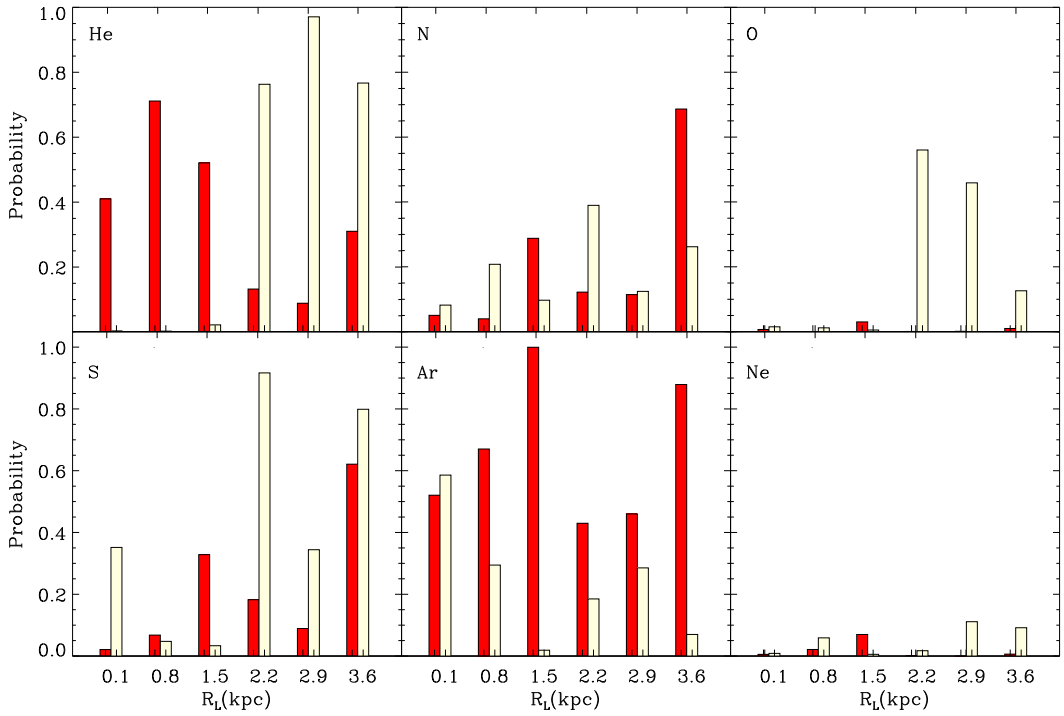

Fig. 4. Kolmogorov-Smirnov probability bar plot for each element as a function of the limiting radius of Groups I and II. Left filled bars correspond to the SSV08 scale and empty right bars to the Z95 scale.

TABLE 3

KOLMOGOROV-SMIRNOV PROBABILITIES

	$P(R_L)$ SSV08						$P(R_L)$ Z95					
R_L (kpc)	0.1	0.8	1.5	2.2	2.9	3.6	0.1	0.8	1.5	2.2	2.9	3.6
He	0.574	0.865	0.379	0.118	**0.080**	0.293	0.003	**0.0026**	0.022	0.763	0.971	0.767
N	**0.053**	0.075	0.335	0.103	0.099	0.647	**0.0819**	0.208	0.097	0.390	0.124	0.262
O	0.014	**0.001**	0.058	**0.001**	**0.001**	0.008	0.015	0.012	**0.0051**	0.560	0.459	0.126
S	**0.022**	0.074	0.370	0.154	0.077	0.583	0.352	0.047	**0.0334**	0.917	0.344	0.799
Ar	0.720	0.864	0.989	**0.394**	0.508	0.845	0.586	0.295	**0.0188**	0.185	0.285	0.070
Ne	0.014	0.046	0.128	0.001	**0.000**	0.007	0.009	0.059	**0.0056**	0.017	0.111	0.092

In Figure 5 the oxygen distribution for Group I is wider than that for Group II, while most objects from Group II have abundances centered at 8.5 dex. The other α-elements also show this pattern according to which Group II objects favor higher abundances than those from Group I. However, these differences are not larger than the individual errors in abundances. Among the α-elements, neon displays the largest difference between the two distributions. Nevertheless, some caution must be taken here. In a recent study by Milingo et al. (2010), there are some evidences that neon enhancement is present in a significant portion of PNe. This enhancement could be explained considering the charge exchange reaction $O^{++} + H^0 \rightarrow O^+ + H^+$ (see Peimbert, Luridiana, & Torres-Peimbert 1995, and references therein). Since the neon ICF depends inversely on the O^{++} abundance, the charge exchange reaction could increase the neon elemental abundance. If the neon enhancement is real, it does not represent the abundance of the interstellar medium at the time of the formation of the progenitor star. Thus, the neon distribution in Figure 5 must be interpreted carefully.

In Figure 6, showing the distribution of the abundances for the SSV08 scale, the oxygen distribution for Group I objects is wider than for Group II and the

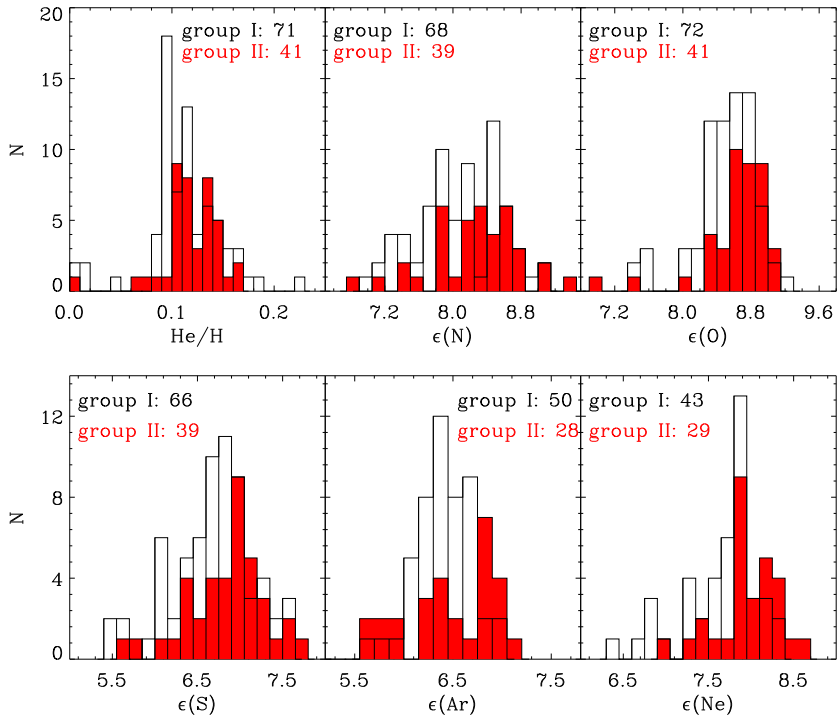

Fig. 5. Abundance distributions for Groups I and II using the Z95 distance scale. Unfilled histograms represent Group I objects and filled histograms are for Group II. The number of objects in each distribution is shown at the top.

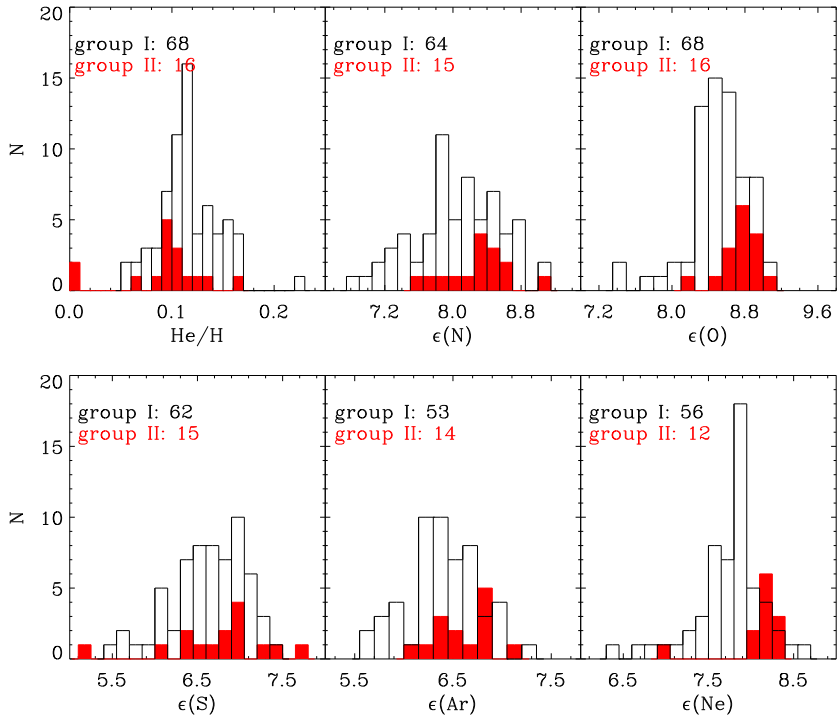

Fig. 6. The same as Figure 5 for the SSV08 distance scale.

TABLE 4

AVERAGE ABUNDANCES OF GROUPS I AND II FOR EACH DISTANCE SCALE

	SSV08		Z95	
Element	Group I	Group II	Group I	Group II
He/H	0.110 ± 0.004	0.099 ± 0.009	0.111 ± 0.004	0.117 ± 0.004
ϵ(N)	8.02 ± 0.06	8.22 ± 0.10	8.07 ± 0.06	8.25 ± 0.08
ϵ(O)	8.49 ± 0.04	8.69 ± 0.06	8.50 ± 0.04	8.64 ± 0.07
ϵ(S)	6.62 ± 0.05	6.74 ± 0.14	6.68 ± 0.06	6.84 ± 0.07
ϵ(Ar)	6.37 ± 0.05	6.56 ± 0.07	6.38 ± 0.05	6.48 ± 0.08
ϵ(Ne)	7.74 ± 0.05	8.00 ± 0.12	7.64 ± 0.07	7.95 ± 0.07

values are between 8.0 and 9.3 dex. The same trend is seen in the distributions for the SSV08 scale when compared with the Z95 scale: compared to Group I objects, the α-element distributions for Group II show a tendency to higher abundances.

Table 4 shows the average abundances and the standard error of the mean for Group I and II objects, adopting the distances 1.5 and 2.2 kpc for the Z95 and SSV08 scales as the limit between the two groups. Although these abundances are similar, reflecting the large dispersion of abundances found in these regions of the Galaxy, some important differences are apparent. In particular, the N, O, S, Ar, and Ne abundances are *smaller* for Group I compared to Group II for both distance scales. For N and O the difference between the two groups is 0.20 dex. For S, Ar, and Ne it is 0.12, 0.19 and 0.26 dex, respectively. In spite of the fact that these differences are not larger than the individual errors in the abundances, we can draw important conclusions about these results. The standard error of the mean is small since both groups have several objects and therefore the difference between both groups is statistically significant. This can be seen considering the lower and upper 90% and 68% confidence limits of each group. Although there are some overlaps between the distributions, for N, O, Ar, and Ne they are statistically significantly different considering the 68% confidence limit of each group for the SSV08 distance scale. Only the S distributions are not statistically different considering this method. For the Z95 distance scale, the distributions of N, O, and S of each group are significantly different considering the same confidence limit. The Ne distributions are statistically different considering the 90% confidence limit for this scale. These results are an important indication that bulge nebulae (Group I) do not follow the trends observed in the inner-disk (Group II), as we will discuss in § 4.

Relaxing the assumption that objects with adopted negative galactocentric distances belong to the bulge would not change the derived conclusions. We performed some tests excluding these objects, and the main conclusions are unchanged: bulge objects have lower α-element abundances than those in the inner disk. Adopting positive distances for these objects makes the group separation less clear, as the mixing of both populations is enhanced, but even in this case bulge objects still have lower abundances compared to inner disk objects.

The galactocentric distance of 1.5 kpc for the Z95 distance scale marks the limit at which the Groups I and II are more likely to separate from the point of view of the chemical abundances, as shown by the Kolmogorov-Smirnov test. On the other hand, the galactocentric distance of 2.2 kpc for the SSV08 scale was chosen from eye inspection in the radial abundances distributions, marking the limit in the α-elements abundances. In this case too, objects from Group II, whose galactocentric distances are greater than 2.2 kpc, have higher abundances than those from Group I, whose distances are lower than this limit.

Since the bulge and the disk display different chemical abundance characteristics, such as for example the radial abundance gradients found in the disk, or the large abundance distribution found in the bulge, as we discussed in § 1, we expect the existence of a galactocentric distance which better separates the two populations. Our analysis point to a separation at $R_L = 1.5$ kpc for the Z95 distance scale and $R_L < 2.9$ kpc for the SSV08 scale. Therefore, we can assign to Group I those objects that pertain to the bulge, and to Group II those that pertain to the inner-disk.

4. DISCUSSION

There are other evidences that point to a transition from the bulge to the inner-disk at a galactocen-

tric distances similar to the distances found in this work. Indeed, infrared observations of the bulge, like those from the COBE/DIRBE satellite (Weiland et al. 1994), support these results. From their Figure 1, it is clear that the nuclear radius of the bulge is between 10° and 15°. For the canonical solar distance to the galactic center of 8 kpc adopted in this work, the bulge longer radius is between 1.4 and 2.1 kpc.

From the point of view of giant stars, Tiede & Terndrup (1999) performed photometric and spectroscopic observations of 503 stars in four windows toward the bulge, with coordinates (ℓ,b) of (−28.8°,−6°), (−8.7°,6.0°), (8.4°,−6.0°) and (24.4°, 6.1°). According to their results, the abundance distribution in the inner Galaxy presents a discontinuity. The authors argue that such a difference is larger than any bias in the sample selection and not due to errors in the abundances. As we are suggesting, they assign the difference found to the different populations in the line of sight.

Smartt et al. (2001) observed type-B stars located between 2.5 and 5 kpc from the galactic center. Due to the young nature of these stars, their photospheric abundances reflect the present day abundances of the ISM. Their results agree with ours in the sense that the oxygen abundance decreases for distances smaller than 3 kpc, as can be seen from their Figure 3. However, the error bars are large and it is only possible to say that the oxygen abundances do not follow the radial gradient of the disk toward the galactic center, since they are 0.3 to 0.4 dex lower than what we expected from the Rolleston et al. (2000) radial gradient, given their position.

In the light of recent studies using PNe, Gutenkunst et al. (2008) point to a discontinuity in the abundance gradient towards the galactic center, in the sense that the abundances of bulge PNe do not follow the trend of those from the disk, as can be seen in their Figure 4. The same trend can be seen in Figure 3 of Stanghellini & Haywood (2010). Considering PNe type III as defined by Peimbert (1978), which represent the old disk population, it is possible to note from their figure that oxygen abundances are smaller for galactocentric distances of less than 4 kpc.

Finally, Mishurov, Lépine, & Acharova (2002) proposed a galactic formation model where the spiral arms are inductors of stellar formation and they can exist only between the internal and external Lindblad resonances. As a consequence, the SFR decreases strongly outside these limits, and the chemical abundances are depleted in these regions. Combining these evidences with our results, we can point out to a bulge-disk interface for the intermediate mass population, marking therefore the transition between the disk and the bulge populations, at a galactocentric distance of 1.5 for the Z95 distance scale. On the other hand, for the SSV08 distance scale the Kolmogorov-Smirnov test was not conclusive, and we can point out that, for galactocentric distances smaller than 2.9 kpc, the α-elements abundances do not follow the disk radial gradient towards the center of the Milky Way galaxy.

5. SUMMARY AND CONCLUSION

This work reports an important result concerning PNe and the chemical evolution of the Galaxy. In addition to our previous work (Cavichia et al. 2010, Paper I), where we presented the chemical abundances and the analysis of these abundances for a sample of 56 PNe in the direction of the galactic bulge, among which 35 PNe have their abundances derived for the first time, we extended our data base to 140 PNe in order to study the chemical abundance distribution in the inner disk and bulge of the Galaxy.

In this work, a statistical analysis was performed in order to find the galactocentric distance where bulge and disk characteristics intersect. Two distance scales were used: Zhang (1995) and Stanghellini et al. (2008). Applying the Kolmogorov-Smirnov test, the former results in a distance of 1.5 kpc, while for the latter the test was not conclusive. Nevertheless, the radial α-elements abundance distributions for both scales indicate that they do not follow the trend of the disk. On average, the abundances for objects with galactocentric distances smaller than 1.5 and 2.2 kpc for the Z95 and SSV08 distance scales, respectively, are lower than for objects with distances greater than this limit, although this difference is not larger than the errors in individual abundances. Considering the SSV08 distance scale, the abundance difference between the two groups of PNe is based on 68, 62, 53, and 56 PNe of Group I (bulge) for O, S, Ar, and Ne, respectively, and 16, 15, 14, 12 PNe of Group II (inner disk) for the same elements. For the Z95 distance scale, the abundance difference is based on 72, 66, 50, and 43 PNe of Group I, and 41, 39, 28, 29 of Group II, for the same elements. Furthermore the combined error of the four elements (O, S, Ar, Ne) of each group is considerably smaller than the abundance difference between the two groups derived from the average difference of the four elements.

Taking into account the results derived in this work as well as other evidences from the literature, we propose the galactocentric distance of 1.5 kpc (for

the Z95 distance scale) as the mark of the transition between the bulge and the inner-disk of the Galaxy.

Part of this work was supported by the Brazilian agencies *FAPESP* and *CNPq*. O.C. would like to acknowledge FAPESP for his graduate fellowship (processes 05/03194-4 and 07/07704-2). We also thank the referee for his/her comments and suggestions.

REFERENCES

Acker, A., Marcout, J., Ochsenbein, F., Stenholm, B., & Tylenda, R. 1992, Strasbourg-ESO Catalogue of Galactic Planetary Nebulae (Part 1 and 2; Garching: ESO)

Andrievsky, S. M., Luck, R. E., Martin, P., & Lépine, J. R. D. 2004, A&A, 413, 159

Binney, J. 2009, in IAU Symp. 254, The Galaxy Disk in Cosmological Context, ed. J. Andersen, J. Bland-Hawthorn, & B. Nordström (Cambridge: Cambridge Univ. Press), 145

Cahn, J. H., Kaler, J. B., & Stanghellini, L. 1992, A&AS, 94, 399 (CKS92)

Carigi, L., Peimbert, M., Esteban, C., & García-Rojas, J. 2005, ApJ, 623, 213

Cavichia, O., Costa, R. D. D., & Maciel, W. J. 2010, RevMexAA, 46, 159 (Paper I)

Chiappini, C., Górny, S., Stasińska, G., & Barbuy, B. 2009, A&A, 494, 591

Chiappini, C., Matteucci, F., & Romano, D. 2001, ApJ, 554, 1044

Costa, R. D. D., Escudero, A. V., & Maciel, W. J. 2005, in AIP Conf. Proc. 804, Planetary Nebulae as Astronomical Tools, ed. R. Szczerba, G. Stasińska, & S. K. Górny (Melville: AIP), 252

Costa, R. D. D., Maciel, W. J., & Escudero, A. V. 2008, Baltic Astron., 17, 321

Cuisinier, F., Maciel, W. J., Köppen, J., Acker, A., & Stenholm, B. 2000, A&A, 353, 543 (CMKAS00)

Cunha, K., Sellgren, K., Smith, V. V., Ramirez, S. V., Blum, R. D., & Terndrup, D. M. 2007, ApJ, 669, 1011

Daflon, S., & Cunha, K. 2004, ApJ, 617, 1115

Davies, B., et al. 2009, ApJ, 696, 2014

de Freitas Pacheco, J. A., Maciel, W. J., & Costa, R. D. D. 1992, A&A, 414, 211

Escudero, A. V., & Costa, R. D. D. 2001, A&A, 380, 300

Escudero, A. V., Costa, R. D. D., & Maciel, W. J. 2004, A&A, 414, 211

Exter, K. M., Barlow, M. J., & Walton, N. A. 2004, MNRAS, 349, 1291

Fu, J., Hou, J. L., Yin, J., & Walton, N. A. 2009, ApJ, 696, 668

Gerhard, O. 2002, in ASP Conf. Ser. 273, The Dynamics, Structure and History of Galaxies, ed. G. S. Da Costa & H. Jerjen (San Francisco: ASP), 73

Gillessen, S., Eisenhauer, F., Trippe, S., Alexander, T., Genzel, R., Martins, F., & Ott, T. 2009, ApJ, 692, 1075

Górny, S. K., Stasińska, G., Escudero, A. V., & Costa, R. D. D. 2004, A&A, 427, 231

Gutenkunst, S., Bernard-Salas, J., Pottasch, S. R., Sloan, G. C., & Houck, J. R. 2008, ApJ, 680, 1206

Henry, R. B. C., Kwitter, K. B., Jaskot, A. E., Balick, B., Morrison, M. A., & Milingo, J. B. 2010, ApJ, 724, 748

Hou, J. L., Prantzos, N., & Boissier, S. 2000, A&A, 362, 921

Howard, C. D., et al. 2009, ApJ, 702, L153

Köppen, J., Acker, A., & Stenholm, B. 1991, A&A, 248, 197

Maciel, W. J. 2000, in IAU Symp. 198, The Light Elements and their Evolution, ed. L. da Silva, R. De Medeiros, & M. Spite (San Francisco: ASP), 204

Maciel, W. J., Lago, L. G., & Costa, R. D. D. 2005, A&A, 433, 127

———. 2006, A&A, 453, 587

Maciel, W. J., & Pottasch, S. R. 1980, A&A, 88, 1

Maciel, W. J., & Quireza, C. 1999, A&A, 345, 629

Milingo, J. B., Kwitter, K. B., Henry, R. B. C., & Souza, S. P. 2010, ApJ, 711, 619

Mishurov, Y. N., Lépine, J. R. D., & Acharova, I. A. 2002, ApJ, 571, L113

Mollá, M., & Díaz, A. I. 2005, MNRAS, 358, 521

Nishiyama, S., et al. 2006, ApJ, 647, 1093

Peimbert, M. 1978, in IAU Symp. 76, Planetary Nebulae, ed. Y. Terzian (Dordrecht: Reidel), 215

Peimbert, M., Luridiana, V., & Torres-Peimbert, S. 1995, RevMexAA, 31, 147

Perinotto, M., & Morbidelli, L. 2006, MNRAS, 372, 45

Perinotto, M., Morbidelli, L., & Scatarzi, A. 2004, MNRAS, 349, 793

Portinari, L., & Chiosi, C. 1999, A&A, 350, 827

———. 2000, A&A, 355, 929

Ratag, M. A., Pottasch, S. R., Dennefeld, M., & Menzies, J. W. 1992, A&A, 255, 255

———. 1997, A&AS, 126, 297

Rich, R. M. 1988, AJ, 95, 828

Rolleston, W. R. J., Smartt, S. J., Dufton, P. L., & Ryans, R. S. I. 2000, A&A, 363, 537

Ruffle, P. M. E., Zijlstra, A. A., Walsh, J. R., Gray, M. D., Gesicki, K., Minniti, D., & Comeron, F. 2004, MNRAS, 353, 796

Samland, M., Köppen, J., Acker, A., & Stenholm, B. 1992, A&A, 264, 184

Shen, J., Rich, R. M., Kormendy, J., Howard, C. D., De Propris, R., & Kunder, A. 2010, ApJ, 720, L72

Smartt, S. J., Venn, K. A., Dufton, P. L., Lennon, D. J., Rolleston, W. R. J., & Keenan, F. P. 2001, A&A, 367, 86

Stanghellini, L., & Haywood, M. 2010, ApJ, 714, 1096
Stanghellini, L., Shaw, R. A., & Villaver, E. 2008, ApJ, 689, 194 (SSV08)
Stasińska, G., Richer, M. G., & McCall, M. L. 1998, A&A, 336, 667
Tiede, G. P., & Terndrup, D. M. 1999, AJ, 118, 895
Tylenda, R., Siódmiak, N., Górny, S., Corradi, R. L. M., & Schwarz, H. E. 2003, A&A, 405, 627
Weiland, J. L., et al. 1994, ApJ, 425, L81
Zhang, C. Y. 1995, ApJS, 98, 659 (Z95)
Zoccali, M., et al. 2006, A&A, 457, L1
Zoccali, M., et al. 2003, A&A, 399, 931

O. Cavichia, R. D. D. Costa, and W. J. Maciel: Departamento de Astronomia, Instituto de Astronomia, Geofísica e Ciências Atmosféricas Universidade de São Paulo, Rua do Matão, 1226, Cidade Universitária, 05508-900 São Paulo-SP, Brazil (cavichia, roberto, maciel@astro.iag.usp.br).

Revista Mexicana de Astronomía y Astrofísica, **47**, 63–73 (2011)

UBVR POLARIMETRY OF HIGH-GALACTIC LATITUDE CARBON STARS

J. M. López and D. Hiriart

Instituto de Astronomía
Universidad Nacional Autónoma de México, Ensenada, B. C., Mexico

Received 2010 October 20; accepted 2011 January 17

RESUMEN

Presentamos polarimetría y fotometría en las bandas *UBVR*, en el periodo de un año, de ocho estrellas de carbón de alta latitud galáctica: V Hya, CZ Hya, R For, R Lep, Y Cvn, T Dra, RV Aqr y RT Cap. La polarización observada alcanza su máximo valor en la banda U y es muy variable en el tiempo. Similarmente, la polarización en la banda B es muy variable pero sus valores son siempre inferiores a los obtenidos en la banda U. El origen y la variabilidad de la polarización en estas bandas puede explicarse como el resultado de la dispersión de la radiación de la estrella central en las regiones interiores de la envolvente circunestelar donde los granos de polvo y las moléculas son creados, destruidos y mezclados por ondas de choque.

ABSTRACT

We present *UBVR* polarimetry and photometry obtained over a period of one year of eight high-galactic latitude carbon stars: V Hya, CZ Hya, R For, R Lep, Y Cvn, T Dra, RV Aqr, and RT Cap. The observed polarization is highest in the U band and highly variable with time. Similarly, the polarization in the B band is highly variable but the values are always lower than those in the U band. The origin and variability of the linear polarization in these bands may be explained as dispersion of radiation from the central star at the inner regions of the circumstellar envelope, where grains and molecules are created, destroyed, and stirred by shock waves.

Key Words: circumstellar matter — polarization — stars: carbon — stars: variables: general

1. INTRODUCTION

It is known that some evolved stars present circumstellar envelopes of dust and gas. These envelopes are the result of mass loss from the star driven by a strong wind. The spectral energy distribution emerging from the circumstellar envelope presents a double peak with the one at the longest wavelength produced by dust emission. Also, some of these stars have strong emission of molecular lines associated with the envelope.

The geometry of these envelopes is a fundamental parameter assumed to be responsible for the observed morphologies of planetary nebulae (Johnson & Jones 1991; Trammell, Dinerstein, & Goodrich 1994). Some models used to reproduce the observed morphologies in planetary nebulae take into account the geometry of the original circumstellar envelope (Kahn & West 1985; Habing, te Lintel Hekkert, & van der Veen 1989).

Circumstellar envelopes are usually not resolved. Therefore photometry is not an appropriate technique to study their morphology since it is not possible to determine their evolution by photometric monitoring over the medium to long term, because a change in the shape of the envelope does not necessarily imply a variation in the integrated flux of the object. Polarimetry is the proper technique to study their morphology since modifications in the geometry may be related to variations in the position angle of the polarization vector.

Starlight is not polarized due to the thermal nature of the radiation. However, an evolved star surrounded by an envelope will produce a certain amount of polarization if the shape of the envelope

TABLE 1

BASIC DATA OF THE PROGRAM STAR

Star	Variability Type	Galactic longitude $l^{\rm II}(^\circ)$	Galactic latitude $b^{\rm II}(^\circ)$	Spectral Type	Period (days)
V Hya	SRa	269	+33.6	C7.5,E	531
CZ Hya	Mira	266	+29.9	Nev,C	442
R For	Mira	215	−68.1	C0,E	389
R Lep	Mira	214	−31.3	C7,6E	430
Y Cvn	SRb	126	+71.6	C7,I	157
T Dra	Mira	86	+29.9	N0,E	422
RV Aqr	Mira	49	−29.6	C0,E	454
RT Cap	SRb	22	−27.9	C6,II	393

departs from spherical symmetry (Trammell et al. 1994). Polarimetric monitoring of evolved stars will provide us with information about their evolution because the degree of polarization and the polarization position angle are related to changes in their morphology. Evolved stars are variables, but flux variations do not necessarily imply changes in the degree of polarization of its envelope. At low polarization values, the observations might be contaminated by interstellar polarization. The contribution of this effect is enhanced towards the galactic disc and decreases with galactic latitude.

There are strong reasons to believe that the main mechanism for polarization of stellar flux from these envelopes is light dispersion, either by dust grains ($\propto \lambda^{-1}$) or molecules ($\propto \lambda^{-4}$) formed in the cold envelope. Multi-wavelength polarimetry observations could provide us with better information to determine which of these mechanisms dominates according to its wavelength dependence. Also, a polarimetric study can give us information on the size and chemical composition of the dust grains, since polarization is a function of the refractive index.

In this paper we present *UBVR* polarimetry and photometry for a sample of eight high-galactic latitude evolved carbon stars over a period of one year. The wavelength and time dependence of their degree of polarization, the position angles, and brightnesses are presented. Four of the objects have no previously reported values for these parameters. All but one of the objects have no previously reported polarization measurements in the U band.

2. OBSERVATIONS

The basic data for the observed carbon stars are listed in Table 1. They were selected from the list of Hiriart & Kwan (2000) and Hiriart (1998) where model results for gas and dust emission from their circumstellar envelopes are available. All the selected objects have galactic latitude $|b^{\rm II}| \geq 20^\circ$ to minimize contamination by polarization from the galactic plane. The envelopes of these stars are optically thin so they can be observed at optical wavelengths. All the stars have been observed in the infrared and molecular gas emission, from which the mass loss rates have been determined (Oloffson et al. 1993).

Linear polarization measurements were made at the 0.84 m, f/15, telescope of the Observatorio Astronómico Nacional in the Sierra de San Pedro Mártir, Mexico, using a CCD camera and the POLIMA polarimeter (Hiriart et al. 2005). The CCD camera employed an e2V chip with 2048×2048 pixels and a 13 μm pixel size, which provides a plate scale of 0.44 arc-sec pixel^{-1}. POLIMA consists of a rotating Glan-Taylor prism driven by a step motor. Since the polarimeter is a single-beam device with a very slow modulation, photometric conditions are required for accurate polarimetry. The U, B, V, and R measurements were obtained between January and December 2009 at or near the new moon phase in all cases. Only data from photometric nights were considered.

Separate images were obtained for all four wavelengths and at relative position angles of the prism of 0°, 45°, 90°, and 135°. The zero position angle was established from observations of polarized standards and it was found to be $(-91 \pm 2)^\circ$. The instrumental polarization was determined by observing unpolarized standard stars and it was found to be $(0.6 \pm 0.5)\%$. The error quoted for the instrumental polarization is relatively high because single-beam polarization measurements are affected by sky variations during data acquisition at the four position angles of the prism. We used polarized and unpolar-

ized standard stars from Schmidt, Elston, & Lupie (1992).

Data were reduced using IRAF tasks. Observations of nearby blank sky were obtained at different prism orientations using the same on-chip exposures times as for the on-source observation. Dark-current frames were not taken because of the low noise of the detector. Flat fields were taken at the four positions of the polarizer and for all the filters at dusk and dawn. Bias frames were also taken at the middle of the night. For each filter and prism position, bias frames were subtracted from the flat field images; the flat field images corrected for bias were combined to form an average flat field for each filter and prism position. The bias frame was also subtracted from each object image and the resulting frames were multiplied by the mean value of the combined bias-corrected flats. Finally, the object image was divided by the combined flat field.

The flux of the object may be determined from two orthogonal measurements $f_1 = f(0^\circ) + f(90^\circ)$ and $f_2 = f(45^\circ) + f(135^\circ)$ where $f(\theta)$ is the flux of the object at image taken at polarizer position θ. The instrumental flux is the average of these two fluxes, from which instrumental magnitudes for each object were obtained. A number of photometric standard stars were observed to determine the photometric zero points. The conversion to standard magnitudes was made using the standard photometric stars from Landolt (1992).

We calculated the normalized Stokes parameters q and u for each object as

$$q = \frac{f(0^\circ) - f(90^\circ)}{f(0^\circ) + f(90^\circ)}\,, \tag{1}$$

and

$$u = \frac{f(45^\circ) - f(135^\circ)}{f(45^\circ) + f(135^\circ)}\,. \tag{2}$$

The q and u parameters are related to the fractional polarization p and the position angle of polarization θ by

$$p = \sqrt{q^2 + u^2}\,, \tag{3}$$

and

$$\theta = \frac{1}{2}\arctan\left(\frac{u}{q}\right)\,. \tag{4}$$

By defining the fractional polarization in this way, we are assuming that the circular polarization is negligible.

2.1. *Error calculations*

The uncertainty of the flux measurement of the star is given by

$$\sigma_f = \sqrt{f_{\rm star} + 2f_{\rm sky}}\,, \tag{5}$$

where $f_{\rm star}$ and $f_{\rm sky}$ are the fluxes from the star and sky from the same image, respectively.

From equations (1) and (2), we use Gaussian propagation to obtain the errors for u and q

$$\sigma_u = \sqrt{\left[\frac{2f_{135}}{(f_{45}+f_{135})^2}\sigma_{f_{45}}\right]^2 + \left[\frac{2f_{45}}{(f_{45}+f_{135})^2}\sigma_{f_{135}}\right]^2}\,, \tag{6}$$

and

$$\sigma_q = \sqrt{\left[\frac{2f_{90}}{(f_0+f_{90})^2}\sigma_{f_0}\right]^2 + \left[\frac{2f_0}{(f_0+f_{90})^2}\sigma_{f_{90}}\right]^2}\,, \tag{7}$$

where σ_f is the error in the flux and f_x is the flux at orientation x of the polarization analyzer.

Similarly, the errors in the polarization degree, ϵ_P, and polarization position angle, ϵ_θ, follow from equations (3) and (4). Using Gaussian propagation we get

$$\epsilon_P = \sqrt{\sigma_u^2 + \sigma_q^2}\,, \tag{8}$$

and

$$\epsilon_\theta = \frac{1}{2p}\sqrt{(q\sigma_u)^2 + (u\sigma_q)^2}\,, \tag{9}$$

where σ_u y σ_q are given by equations (6) and (7), respectively, and p is the measured polarization.

3. RESULTS AND ANALYSIS

The observed polarization values are shown in Table 2. For each object, this table shows: the Julian date; linear polarization, p; position angle, θ, and errors of the measurements of p and θ (ϵ_p and ϵ_θ, respectively). Except for V Hya, all the stars were observed on more than one night.

For each star two total fluxes, f_1 and f_2, can be derived from the measurements from a couple of object images separated by 90 degrees of the polarizer prism: $f_1 = f(0^\circ) + f(90^\circ)$ and $f_2 = f(45^\circ) + f(135^\circ)$. The difference between these two fluxes expressed in percent, Dif(%), is also shown in Table 2. A low value of Dif(%) indicates sky stability during the observations assuming that star flux does not change during the observing time.

The values of p and θ as a function of wavelength are plotted from Figures 1 to 8 for each object. The polarization measurements in the U band, in general, have large errors because of the low photon flux in this band. The results of polarization measurements for each object are described in the following sections, and comparisons with previously published results are made whenever possible. A summary of these comparisons is presented in Table 3.

TABLE 2

UBVR POLARIMETRY AND PHOTOMETRY OF CARBON STARS

Name	JD (2450000.00+)	Filter	Magnitude	Dif (%)	$p \pm \epsilon_p$ (%)	$\theta \pm \epsilon_\theta$ (deg)
V Hya	4951.64	*U*	14.15±0.02	1.53	5.7±0.3	59±1
		B	12.83±0.01	0.11	3.6±0.1	59±1
		V	8.25±0.01	0.81	2.2±0.1	124±1
		R	6.02±0.01	0.07	2.8±0.1	134±1
CZ Hya	4860.97	*B*	16.14±0.02	0.28	5.0±0.5	57±2
		V	11.57±0.02	0.21	2.1±0.2	139±2
	4891.89	*B*	15.33±0.02	1.25	4.8±0.3	53±1
		V	11.00±0.02	0.37	3.2±0.1	47±1
	4913.74	*B*	14.10±0.01	1.73	8.1±0.1	78±1
		V	10.44±0.01	0.92	4.4±0.1	58±1
		R	8.81±0.01	1.05	3.0±0.1	126±1
	4952.73	*U*	15.70±0.02	0.63	10.1±0.6	49±1
		B	12.85±0.01	0.24	2.2±0.1	131±1
		V	9.71±0.01	0.01	1.4±0.1	123±1
		R	8.21±0.01	0.29	1.1±0.1	114±1
R For	4855.66	*B*	14.70±0.02	0.50	0.9±0.3	94±6
		V	10.01±0.02	0.25	0.3±0.2	77±10
	5099.91	*B*	14.17±0.02	0.15	0.4±0.1	64±7
		V	9.32±0.02	0.10	1.7±0.1	54±1
		R	7.25±0.02	0.30	2.9±0.1	60±1
	5126.82	*U*	15.35±0.02	0.72	6.0±0.5	83±2
		B	13.55±0.01	0.01	0.2±0.2	136±20
		V	8.93±0.01	0.35	2.0±0.1	61±1
		R	7.04±0.01	0.30	2.9±0.1	60±1
	5155.69	*U*	15.42±0.02	1.30	2.3±0.6	94±5
		B	13.51±0.01	0.12	0.8±0.2	75±4
		V	8.93±0.01	0.06	2.1±0.1	71±1
		R	3.00±0.01	0.08	3.0±0.1	68±1
R Lep	4860.73	*U*	12.53±0.04	1.47	4.7±0.5	102±2
		B	11.62±0.02	0.15	0.7±0.3	62±7
		V	6.98±0.02	0.58	0.8±0.2	101±4
	4891.69	*U*	12.80±0.04	1.38	3.1±0.5	55±4
		B	12.06±0.02	1.02	2.5±0.5	42±4
		V	7.34±0.02	0.03	1.7±0.2	48±2
	5067.97	*B*	14.88±0.02	0.20	2.3±0.3	76±2
		V	10.20±0.01	0.23	1.8±0.1	70±1
		R	7.70±0.01	0.05	2.8±0.1	49±1
	5155.87	*U*	14.11±0.02	0.73	5.9±0.4	102±1
		B	12.60±0.01	0.02	1.0±0.1	109±3
		V	7.70±0.01	0.20	1.0±0.1	134±2
		R	5.56±0.01	0.58	1.3±0.1	135±1
Y Cvn	4856.02	*U*	12.12±0.04	0.30	8.1±0.4	93±1
		B	8.12±0.02	0.45	0.2±0.1	103±12
		V	5.01±0.02	0.24	0.6±0.1	61±4
	4891.95	*U*	11.71±0.04	0.17	4.0±0.3	65±1
		B	8.11±0.02	0.24	0.5±0.1	102±5
		V	4.99±0.02	0.08	0.5±0.1	93±3
	4913.83	*U*	12.82±0.01	0.23	0.8±0.2	64±5
		B	7.94±0.01	0.22	1.2±0.1	115±1
		V	5.01±0.01	0.08	1.3±0.1	98±1
		R	3.64±0.01	0.28	1.6±0.1	131±1
	4925.74	*U*	12.81±0.01	0.19	1.3±0.2	48±4
		B	7.87±0.01	0.25	0.8±0.1	50±2
		V	4.97±0.01	0.88	1.5±0.1	49±1
	5001.72	*U*	12.83±0.01	1.37	5.1±0.2	97±1
		B	8.06±0.01	0.35	0.6±0.1	138±3
		V	5.06±0.01	0.06	0.7±0.1	92±3
		R	3.47±0.01	0.48	1.7±0.1	75±1

TABLE 2 (CONTINUED)

Name	JD (2450000.00+)	Filter	Magnitude	Dif (%)	$p \pm \epsilon_p$ (%)	$\theta \pm \epsilon_\theta$ (deg)
T Dra	4913.93	*B*	13.86±0.01	0.71	4.4±0.1	95±3
		V	9.67±0.01	0.41	2.6±0.1	106±1
		R	7.94±0.01	0.18	2.3±0.1	104±1
	4951.88	*U*	16.17±0.02	1.91	5.7±0.7	113±3
		B	13.21±0.08	0.09	4.0±0.2	112±1
		V	9.24±0.01	0.02	3.5±0.1	100±1
		R	7.59±0.01	0.36	2.4±0.1	104±1
	5000.77	*U*	16.21±0.02	0.27	2.3±0.7	102±7
		B	13.30±0.01	0.40	6.1±0.1	116±3
		V	9.40±0.01	0.01	3.5±0.1	108±1
		R	7.64±0.01	0.27	3.2±0.1	103±1
	5039.72	*U*	16.33±0.03	0.29	8.2±0.8	114±1
		B	13.76±0.01	0.59	6.5±0.2	116±1
		V	9.78±0.01	0.16	3.8±0.1	117±1
		R	7.91±0.01	0.02	2.7±0.1	108±1
	5067.69	*U*	16.59±0.04	1.05	7.2±0.8	100±2
		B	14.17±0.02	0.12	4.2±0.2	113±3
		V	10.19±0.01	0.17	3.6±0.1	114±1
		R	8.11±0.01	0.09	2.4±0.1	109±1
RV Aqr	5000.97	*V*	11.65±0.01	0.05	7.41±0.31	106±1
		R	9.41±0.01	0.16	5.18±0.18	114±1
	5038.87	*B*	16.94±0.01	0.75	8.22±0.49	107±1
		V	12.13±0.01	0.17	7.81±0.19	111±1
		R	9.73±0.01	0.12	6.22±0.12	113±1
	5096.64	*B*	17.51±0.02	0.68	7.68±0.49	115±1
		V	12.45±0.02	0.02	7.36±0.16	114±1
		R	9.90±0.02	0.16	6.22±0.11	120±1
	5126.63	*B*	16.98±0.02	0.07	5.67±0.45	120±2
		V	12.11±0.01	0.15	6.66±0.19	117±1
		R	9.75±0.01	0.51	6.47±0.12	121±1
RT Cap	5003.9	*U*	14.06±0.02	1.60	4.14±0.48	106±2
		B	10.80±0.01	0.43	1.23±0.13	107±2
		V	6.93±0.01	0.01	2.24±0.09	88±1
		R	5.27±0.01	0.54	2.69±0.08	107±1
	5038.85	*U*	13.89±0.03	0.29	3.61±0.40	105±2
		B	10.40±0.01	0.07	1.47±0.13	100±2
		V	6.78±0.01	0.37	1.11±0.10	135±2
		R	5.11±0.01	2.19	3.64±0.13	102±1
	5067.76	*U*	14.17±0.03	0.09	9.90±0.36	91±1
		B	10.63±0.02	0.04	1.84±0.12	89±1
		V	7.05±0.01	0.40	1.04±0.11	107±2
		R	5.22±0.01	0.13	1.81±0.13	92±1
	5095.63	*U*	14.55±0.03	2.15	5.40±0.32	112±1
		B	11.07±0.02	0.13	0.46±0.11	134±5
		V	7.07±0.02	0.11	1.13±0.09	109±2
		R	5.55±0.02	0.49	1.74±0.12	77±1
	5127.58	*U*	14.34±0.02	0.32	5.14±0.43	105±2
		B	11.33±0.01	0.22	1.74±0.17	98±2
		V	7.61±0.01	0.24	1.85±0.10	92±1
		R	5.63±0.01	0.65	1.61±0.10	78±1

3.1. *V Hya*

Figure 1 shows the polarization and position angle of V Hya in the *UBVR* bands. This star was observed only once at JD=2454951.64. Spectropolarimetry of V Hya was performed by Trammell et al. (1994) in the range of $\lambda\lambda 5000 - 7000$, who obtained an average polarization of 3.01 ± 0.01 and $10.06 \pm 0.05\%$ at position angles of $124 \pm 1^\circ$ and $94 \pm 1^\circ$ for April 1992 and January 1993, respectively. The ranges of these values are in agreement with the ones presented in this work. Kruszewski, Gehrels, & Serkowski (1968) report polarization in the *B* filter of 2.73 to 3.17% over a span of 169 days, while the polarization in the yellow filter varied from 1.78 to 2.25% over the same period of time. Serkowski & Shawl (2001) obtain values of the degree of polarization in the following ranges for each filter: $U =$ (1.52 to 1.66)% during 76 days; $B =$ (1.31, 3.14)%

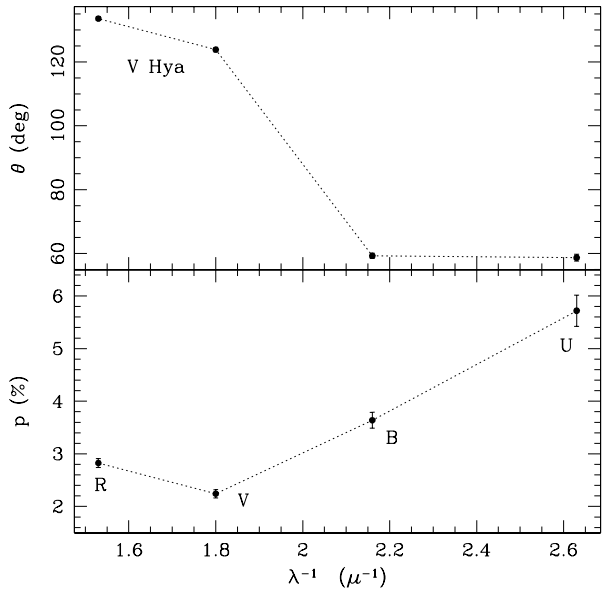

Fig. 1. Polarimetric observations of V Hya obtained on JD=2454951.64 for degree of polarization (lower panel) and position angle (upper panel) as a function of wavelength.

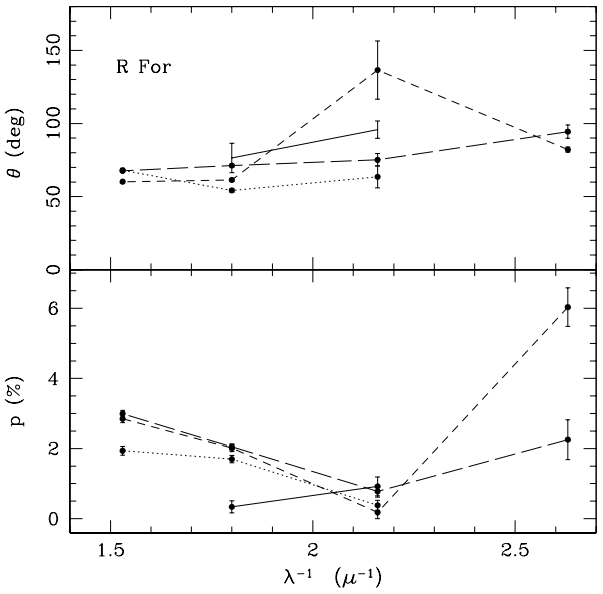

Fig. 2. Same as Figure 1, but for R For on JD=2454855.66 (solid line), 2455099.91 (dotted line), 2455126.82 (short-dashed line), and 2455155.69 (long-dashed line).

over 12,517 days; $V = (0.68, 2.26)\%$ for a period extending from JD=2439499 to 24352016. Our polarization value in the U band, 5.7%, is much higher than theirs, but their polarization values in the B and V bands are similar to the ones we find.

3.2. *R For*

Polarization observations of R For in the U and B bands by Serkowski & Shawl (2001) show values of $1.95 \pm 1.64\%$ and $0.92 \pm 0.2\%$ with position angles of 121° and 172°, respectively, for JD=2439500. For the U band we obtained a polarization of $6.0 \pm 0.5\%$ on JD=2455126.82, and $2.3 \pm 0.6\%$ on JD=24455155.69, with a polarization position angle of 82° and 94°, respectively. Our U polarization values are higher than those reported by Serkowski & Shawl (2001). Our values for the polarization in the B band are in the range of 0.18 to 0.923% with position angles in the range of 63 to 136° which are consistent with the ones reported by Serkowski & Shawl (2001).

3.3. *R Lep*

Polarimetric observations of R Lep extend back for 40 years (Kruszewski et al. 1968; Serkowski 1971; Dyck & Sandford 1971; Raveendran & Kameswara Rao 1989; Serkowski & Shawl 2001; Raveendran 2002). All the reported B and V polarization values are in agreement with the data presented in this paper. Our U-band measurements are the first published for this object.

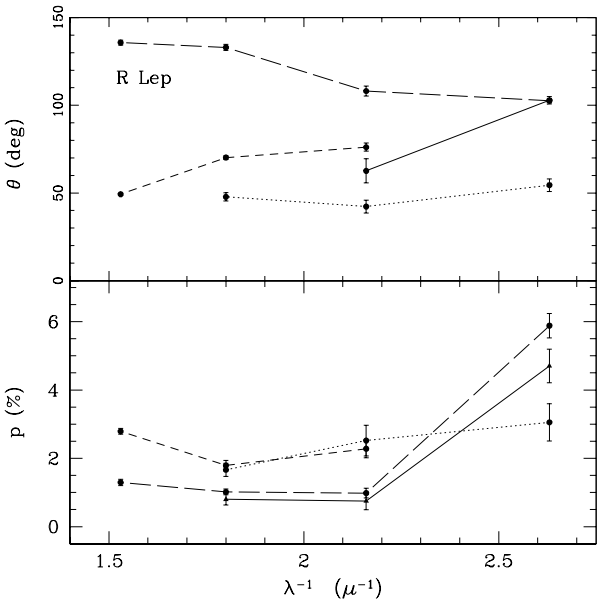

Fig. 3. Same as Figure 1, but for R Lep on JD=2454860.73 (solid line), 2454891.69 (dotted line), 2455067.97 (short-dashed line), and 2455155.87 (long-dashed line).

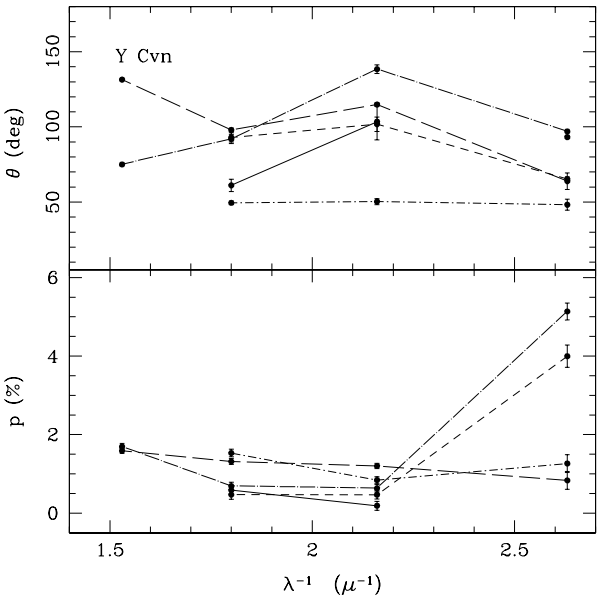

Fig. 4. Same as Figure 1, but for Y Cvn on JD=4856.02 (solid line), 4891.95 (dotted line), 4913.83 (short-dashed line), 4952.74 (long-dashed line), and 5001.72 (dot short-dashed line).

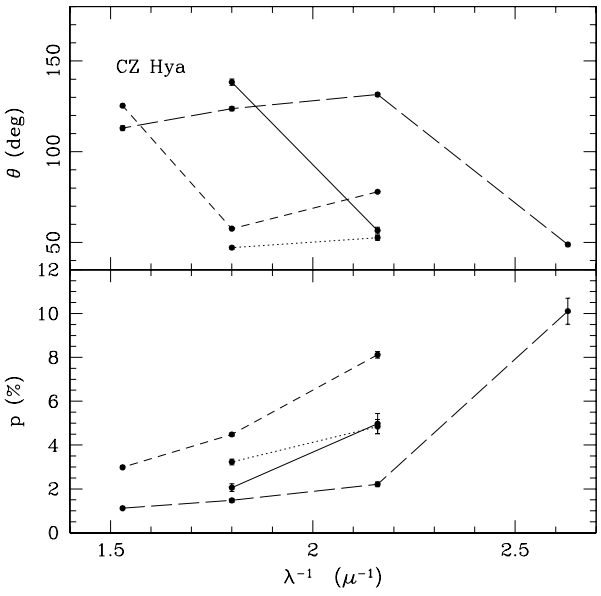

Fig. 5. Same as Figure 1, but for CZ Hya on JD=2454860.97 (solid line), 2454891.89 (dotted line), 2454913.74 (short-dashed line), and 2454952.73 (long-dashed line).

Raveendran (2002) presents polarimetry for R Lep in the *BVR* bands during 1991–2002 when the star went through an episode of fading brightness at light maximum after an interval of 3 yr. The percentage of linear polarization increased as the fading progressed and attained a maximum of 3% in the *V* band, close to the minimum; it remained more or less at the same level during and well after the star returned to normal brightness. Raveendran suggests that the physical mechanism that causes the rather large polarization is perhaps selective extinction by aligned foreground grains produced by the passage of shock waves through the circumstellar envelope.

3.4. *Y Cvn*

Raveendran (1991) carried out polarimetric observations of Y Cvn close to a light maximum and obtained values close to zero in the *BVRI* bands on JD=2446117.48. Serkowski (1971) reported a value of ∼0.25% for Y Cvn in the blue region. We have found a polarization of about ∼1.0% in the *BVR* bands and a relatively high and variable polarization in the *U* band for this star. Y Cvn is a high galactic latitude object ($b^{\rm II} = 72°$). The low polarization listed in Table 2 for the *BVR* bands indicates that the interstellar component of the polarization is almost zero.

3.5. *Other objects*

As far as we know, our polarization measurements are the first for the remaining objects: CZ Hya, T Dra, RV Aqr, and RT Cap.

4. DISCUSSION

4.1. *Wavelength dependence of polarization*

Even though the emission from evolved carbon stars is relatively dim at short wavelengths, we were able to measure linear polarization in the *B* and *U* bands. When both were measured for each object, the highest value was always found for the *U* band.

Among the eight observed carbon stars with significant linear polarization, only CZ Hya presents a polarization that increases systematically towards the ultraviolet. In general, T Dra also shows a systematical increase to the ultraviolet, but during one observing run (JD=2455000.77) it showed a drop in the ultraviolet polarization.

V Hya, R For, Y Cvn, R Lep, and RT Cap show a dip in their degree of polarization in the *V* or *B* bands. This dip has been observed previously by Raveendran (1991) for UU Aur and for SS Vir by Kruszewski et al. (1968). In all these cases, the polarization is larger in the *R* band than in the *V* or *B* bands. At low levels of polarization, distortion of the intrinsic polarization by the interstellar component could be significant. For our stars, interstellar

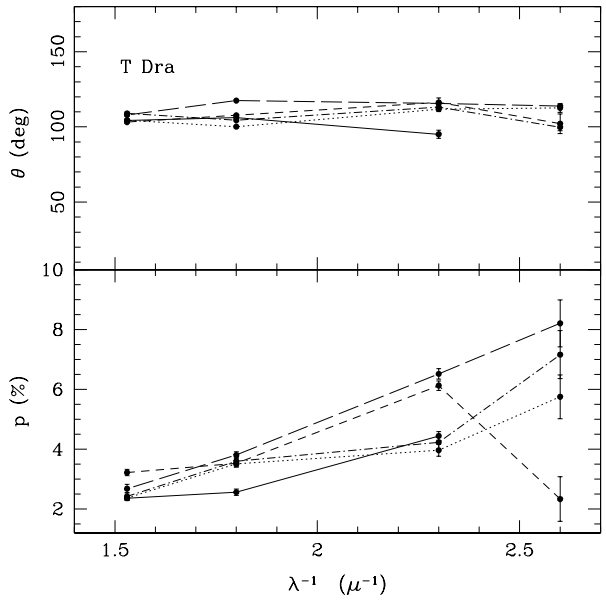

Fig. 6. Same as Figure 1, but for T Dra on JD=2454913.93 (solid line), 2454951.88 (dotted line), 2455000.77 (short-dashed line), 245503972 (long-dashed line), and 2455067.69 (dot-short-dashed line).

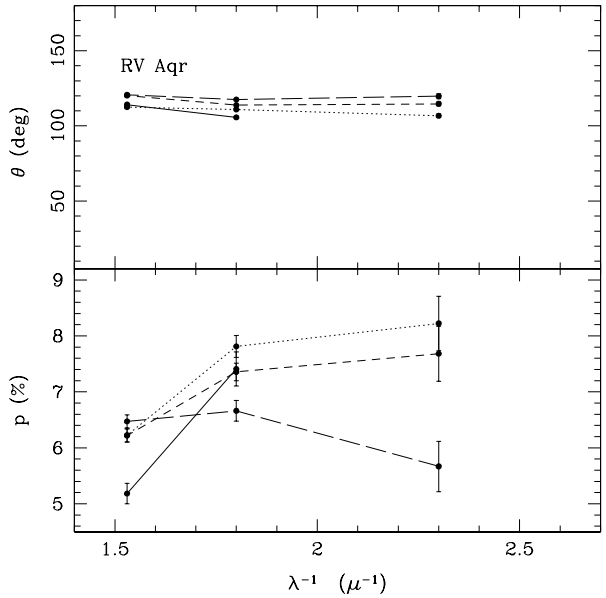

Fig. 7. Same as Figure 1, but for RV Aqr on JD=2455000.97 (solid line), 2455038.87 (dotted line), 2455096.64 (short-dashed line), and 2455126.63 (long-dashed line).

polarization was presumed to be negligible because of their high galactic latitude ($|b^{\rm II}| \geq 20°$).

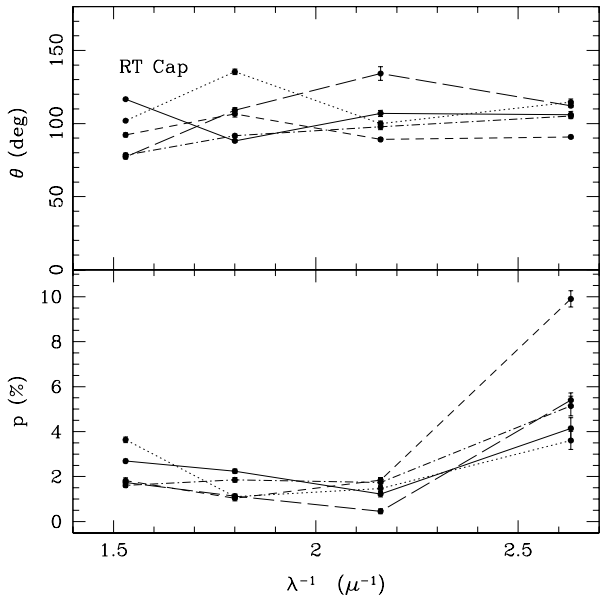

Fig. 8. Same as Figure 1, but for RT Cap on JD=2455003.90 (solid line), 2455038.85 (dotted line), 2455067.76 (short-dashed line), 2455095.63 (long-dashed line), and 2455127.58 (dot short-dashed line).

4.2. *Polarization mechanism*

Harrington (1969) has shown that light emerging from the limb of a star would be highly polarized due to Raleigh scattering by molecules or atoms, if the Planck function has a steep gradient in the atmosphere. However, for a net observable polarization, a photospheric asymmetry should be present and the proposed sources of asymmetry are non-radial pulsation of the star, variation of the temperature over the surface, and the presence of giant convection cells (Harrington 1969; Schwarzschild 1975).

Another suggested mechanism is the scattering by molecules or dust grains in an extended asymmetric circumstellar envelope (Kruszewski et al. 1968; Shawl 1975; Daniel 1978). This is the main mechanisms usually invoked to explain the intrinsic linear polarization of late-type stars in general.

4.3. *Time dependence*

The observed carbon stars show large variations of the degree of polarization and of the position angle over time. Some stars show a large swing from being highly polarized to being almost unpolarized.

T Dra and RV Aqr show an almost constant position angle during the period of observation: their spread is about 30 degrees. This suggests that the formation and destruction of dust and molecules proceeds without changes of the geometry of the inner

TABLE 3

POLARIZATION RESULTS COMPARISON

Name	Filter	p (deg)[a]	θ (deg)[a]	Reference
V Hya	U	5.7 ± 0.3	59 ± 1	This paper
	...	(1.52, 1.66)	(6, 9)	Serkowski & Shawl (2001)
	B	3.6 ± 0.1	59 ± 1	This paper
	...	(1.31, 3.14)	(173, 14)	Serkowski & Shawl (2001)
	V	2.2 ± 0.1	124 ± 1	This paper
	...	(0.68, 2.26)	(172, 13)	Serkowski & Shawl (2001)
R For	V	(0.3, 2.1)	(54,77)	This Paper
	...	1.57 ± 0.02	148	Serkowski & Shawl (2001)
R Lep	B	(0.7, 2.5)	(42,109)	This Paper
	...	(1.2, 3.00)	(37, 59)	Raveendran (2002)
	...	(0.3, 3.46)	(4, 173)	Serkowski & Shawl (2001)
	...	(1.4, 2.71)	(19, 45)	Dyck & Sandford (1971)
	...	(1.7, 1.93)	(27, 44)	Kruszewski et al. (1968)
	V	(0.8, 1.8)	(48, 134)	This Paper
	...	(1.1, 1.94)	(28, 48)	Raveendran (2002)
	...	(0.55, 2.48)	(13, 72)	Serkowski & Shawl (2001)
	...	(1.53, 1.78)	(30, 33)	Dyck & Sandford (1971)
	...	(2.15, 2.21)	(22, 32)	Kruszewski et al. (1968)
	...	2.7	25	Serkowski (1966)
	R	(1.3,2.8)	(50, 135)	This Paper
	...	(1.65, 1.75)	(16, 49)	Raveendran (2002)
Y Cvn	B	(0.2, 1.2)	(50, 138)	This Paper
	...	0.57 ± 0.37	37 ± 18	Raveendran (1991)
	...	0.25	...	Serkowski (1971)
	V	(0.5, 1.5)	(49, 98)	This Paper
	...	0.58 ± 0.04	70 ± 2	Raveendran (1991)
	R	(1.6, 1.7)	(75, 131)	This Paper
	...	0.44 ± 0.04	62 ± 3	Raveendran (1991)

[a]The range of published values are indicated in parenthesis.

regions, where most of the linear polarization is produced.

Figures 9, 10, and 11 show the brightness and polarization as a function of time for RT Cap, T Dra, and Y Cvn, respectively. In general, ultraviolet polarization shows the largest time variations in degree of polarization and position angle. In all three cases, the brightness of the star in the *UBVR* bands was almost constant.

Serkowski (1966) found that some stars exhibit a well-defined relation between light and polarization variations such that the polarization achieves the largest value at minimum light and the smallest value at maximum light. However, Zappala (1967) has concluded, based on his observations of 12 stars, that there is no correlation between luminosity and polarization changes. Clearly, more observations covering a longer time base and a closer follow-up are needed to decide whether such correlation exists.

The rather weak wavelength dependence of linear polarization indicates that circumstellar grain scattering is the main mechanism responsible for the continuum polarization in carbon stars. The identification of grains in the envelope presents a major difficulty, because of the inverse nature of the problem involved. Polarization models of circumstellar grain scattering by Raveendran (1991) show that graphite does not adequately explain the mean polarimetric behavior of carbon stars. Furthermore, graphite grains do not explain the IR spectra of the

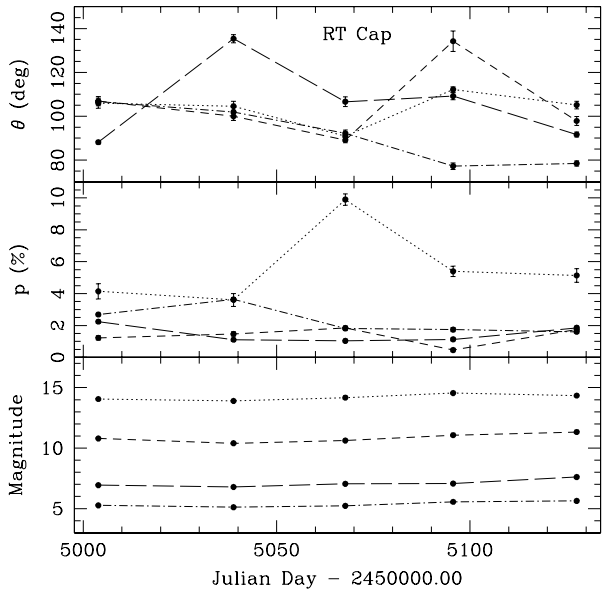

Fig. 9. RT Cap. Brightness, degree, and position angle of polarization as a function of time for U (dotted line), B (short-dashed line), V (long-dashed line), and R (dot short-dashed line) bands.

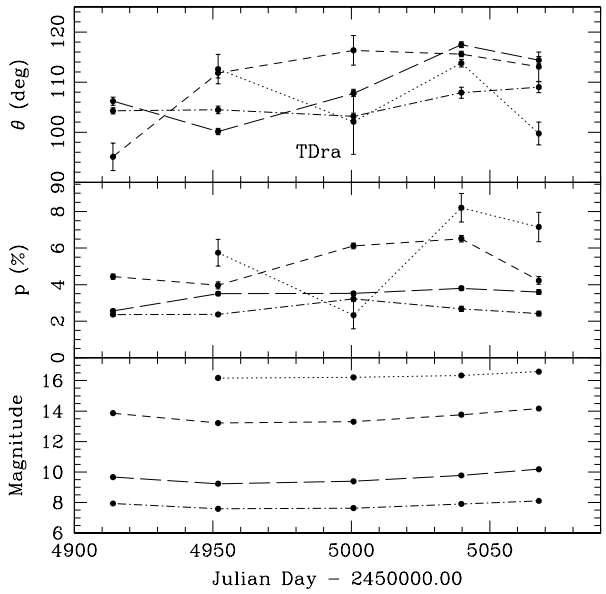

Fig. 10. Same as Figure 9, but for T Dra.

circumstellar dust envelopes around the carbon-rich objects either (Rowan-Robison & Harris 1983). It has been pointed out by Czyzak, Hirth, & Tabak (1982) that graphite formation in circumstellar envelopes is very unlikely and that carbon grains exist, most likely, in some other form, such as amorphous

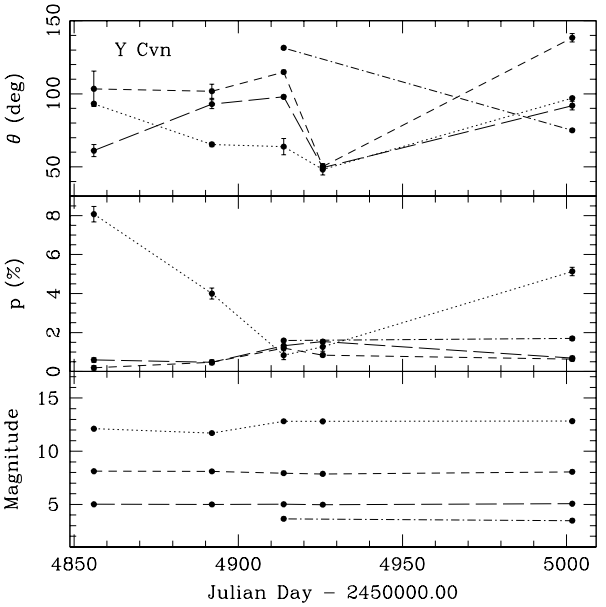

Fig. 11. Same as Figure 9, but for Y Cvn.

carbon. Dust and gas emission models for circumstellar envelopes of evolved carbon stars by Hiriart & Kwan (2000) also show that amorphous carbon grains can better reproduce the observed spectrum in these envelopes.

For Rayleigh scattering, a saturation of the amount of polarization occurs at the wavelength at which multiple scattering becomes important, and is controlled by the optical thickness of the scattering medium. Therefore, Rayleigh scattering may produce a plateau in the polarization as a function of wavelength due to the changes in the local conditions. This effect may explain the wavelength dependence of polarization for RV Aqr, which shows a plateau between the V and B bands.

5. SUMMARY

1. We have presented measurements of linear polarization for eight high-latitude carbon-rich stars in the *UBVR* bands and analyzed the polarimetric variability over time scales of months. Since the observed stars are located at high galactic latitudes, there is evidence for intrinsic linear polarization produced by their circumstellar envelopes, and negligible contribution from the interstellar medium.

2. Although the emission from evolved stars at short wavelengths is very dim, we were able to measured a quite large linear polarization from these stars in the blue and ultraviolet bands.

3. The wavelength dependence seems to be different for each star. However, a common characteristic

for all of them is the increase in the degree of linear polarization towards short wavelengths, reaching the highest values in the ultraviolet.

4. The large changes in the degree of linear polarization in the U and B bands may be explained as a result of formation and destruction processes of dust and molecules at the complex inner regions of the circumstellar envelope. Variations in the position angle may be interpreted as changes of the geometry at these inner regions produced by shock waves there.

5. The evolved stars in our study show variations in the degree of polarization over different time scales and these variations do not seem to be related to the photometric period.

The authors are very grateful to the staff of the OAN-SPM during several observing runs. J. M. López thanks to Conacyt for a graduate student fellowship. We thank Jorge Valdéz, Fernando Quirós, Benjamín García, and Esteban Luna for their contributions to the design and construction of POLIMA.

REFERENCES

Czyzak, S. J., Hirth, J. P., & Tabak, R. G. 1982, Vistas Astron., 25, 337
Daniel, J. Y. 1978, A&A, 67, 345
Dyck, H. M., & Sandford, M. T. 1971, AJ, 76, 43
Habing, H. J., te Lintel Hekkert, P., & van der Veen, W. E. C. J. 1989, in IAU Symp. 131, Planetary Nebulae, ed. S. Torres-Peimbert (Dordrecht: Kluwer), 359
Harrington, J. P. 1969, Astrophys. Lett., 3, 165
Hiriart, D. 1998, PhD Thesis, Univ. of Massachusetts, USA
Hiriart, D., & Kwan, J. 2000, ApJ, 532, 1006
Hiriart, D., Valdez, J., Quiros, F., García, B., & Luna, E. 2005, POLIMA Manual de Usuario, MU-2005-08 (México: Instituto de Astronomía, Universidad Nacional Autónoma de México)
Johnson, J., & Jones, T. 1991, AJ, 101, 1735
Kahn, F. D., & West, K. A. 1985, MNRAS, 212, 837
Kruszewski, A., Gehrels, T., & Serkowski, K. 1968, AJ, 73, 677
Landolt, A. U. 1992, AJ, 104, 340
Oloffson, H., Eriksson, K., Gustafsson, B., & Carlström, U. 1993, ApJS, 87, 267
Raveendran, A. V. 1991, A&A, 243, 453
_____. 2002, MNRAS, 336, 992
Raveendran, A. V., & Kameswara Rao, N. 1989, A&A, 215, 63
Rowan-Robison, M., & Harris, S. 1983, MNRAS, 202, 797
Schmidt, G. D., Elston, R., & Lupie, O. L. 1992, AJ, 104, 1563
Schwarzschild, M. 1975, ApJ, 195, 137
Serkowski, K. 1966, ApJ, 144, 857
_____. 1971, Kitt Peak Obs. Contr., 554, 107
Serkowski, K., & Shawl, S. J. 2001, AJ, 122, 2017
Shawl, S. J. 1975, AJ, 80, 602
Trammell, S., Dinerstein, H., & Goodrich, R. 1994, AJ, 108, 984
Zappala, R. R. 1967, ApJ, 148, L81

José Manuel López and David Hiriart: Instituto de Astronomía, Universidad Nacional Autónoma de México, Apdo. Postal 877, 22830 Ensenada, B. C., Mexico (jmlopez, hiriart@astrosen.unam.mx).

Revista Mexicana de Astronomía y Astrofísica, **47**, 75–82 (2011)

RECALIBRATED TURBULENCE PROFILES AT SAN PEDRO MÁRTIR

R. Avila,[1,2] L. J. Sánchez,[3] I. Cruz-González,[3] E. Carrasco,[4] and V. M. Castaño[5,6]

Received 2010 December 1; accepted 2011 January 21

RESUMEN

La calibración de perfiles de turbulencia óptica (C_N^2) medidos con el método SCIDAR generalizado ha sido recientemente revisada y corregida por Avila & Cuevas (2009). Basándonos en ese trabajo, aquí presentamos la corrección de todos los perfiles de C_N^2 medidos con el SCIDAR generalizado en el Observatorio Astronómico Nacional de San Pedro Mártir. El perfil de C_N^2 mediano corregido conserva su estructura vertical general. El cociente promediado en altura de la mediana de los valores de C_N^2 corregidos sobre la mediana de los valores no corregidos es igual a 0.87. La mediana del *seeing* corregido en el sitio es $0\farcs68 \pm 0\farcs03$, 4.2% menor que la mediana no corregida. Las medianas del *seeing* producido por turbulencia en los dos primeros kilómetros de altura sobre los telescopios de 1.5 m y 2.1 m de diámetro decrecen en un 15.8% y 13.6%, respectivamente. El ángulo isoplanático corregido tiene una mediana de $1\farcs96 \pm 0\farcs04$.

ABSTRACT

The calibration of optical turbulence (C_N^2) profiles measured with the generalized SCIDAR technique has been recently reviewed and corrected by Avila & Cuevas (2009). Based on that work, here we present the correction of all the C_N^2 profiles measured with a generalized SCIDAR at the Observatorio Astronómico Nacional of San Pedro Mártir. The median corrected C_N^2 profile conserves its overall vertical shape. The altitude-averaged ratio of the corrected median C_N^2 values over the uncorrected ones equals 0.87. The corrected median value of seeing at the site is $0\farcs68 \pm 0\farcs03$, 4.2% lower than the median value obtained with the uncorrected profiles. The median values of the seeing produced by turbulence in the first 2 km above the 1.5 m and the 2.1 m telescopes decrease by 15.8% and 13.6%, respectively. The corrected isoplanatic angle has a median value of $1\farcs96 \pm 0\farcs04$.

Key Words: atmospheric effects — instrumentation: high angular resolution — site testing

1. INTRODUCTION

Scintillation detection and ranging (SCIDAR) is an efficient technique to measure optical turbulence profiles, that is, the vertical distribution of the refractive-index structure constant, $C_N^2(h)$. The method is based on the determination of the normalized spatial autocovariance of the intensity distribution (scintillation) detected on the pupil plane of a telescope. The first version of this technique (Rocca, Roddier, & Vernin 1974) –known as Classical SCIDAR– was only sensitive to turbulence located higher than one kilometer above the ground, thus failing to detect turbulent layers near the ground, which are now known to be the most intense (Avila, Vernin, & Cuevas 1998; Egner, Masciadri, & McKenna 2007; Fuensalida et al. 2007; Chun et al. 2009; García-Lorenzo et al. 2009; Masciadri et al. 2010). Fuchs, Tallon, & Vernin (1994) proposed that turbulence near the ground would be measurable if instead of recording the scintillation on the telescope pupil plane, the detector was made the

[1]Centro de Física Aplicada y Tecnología Avanzada, Universidad Nacional Autónoma de México, Mexico.

[2]On leave from Centro de Radioastronomía y Astrofísica, Universidad Nacional Autónoma de México, Mexico.

[3]Instituto de Astronomía, Universidad Nacional Autónoma de México, Mexico.

[4]Instituto Nacional de Astrofísica Óptica y Electrónica, Mexico.

[5]Universidad Autónoma de Querétaro, Campus Cerro de las Campanas, Mexico.

[6]On sabatical leave from Centro de Física Aplicada y Tecnologá Avanzada, Universidad Nacional Autónoma de México, Mexico.

conjugate of a virtual plane located a few kilometers below the pupil (analysis plane). Avila, Vernin, & Masciadri (1997) put that idea in practice for the first time, showing its efficiency. This new configuration, called Generalized SCIDAR (GS), has been vastly used to characterize astronomical sites (Avila et al. 1997; Fuchs, Tallon, & Vernin 1998; Klückers et al. 1998; Avila et al. 1998; Kern et al. 2000; Avila, Vernin, & Sánchez 2001; Prieur, Daigne, & Avila 2001; Wilson et al. 2003; Avila et al. 2004; Tokovinin et al. 2005; García-Lorenzo & Fuensalida 2006; Egner et al. 2007; Vernin et al. 2007; Egner & Masciadri 2007; Avila et al. 2008; Fuensalida, García-Lorenzo, & Hoegemann 2008; García-Lorenzo & Fuensalida 2011; Masciadri et al. 2010). The method and the physics involved in either version of the SCIDAR technique have thoroughly been treated by a number of authors (Rocca et al. 1974; Vernin & Azouit 1983a,b; Klückers et al. 1998; Prieur et al. 2001).

Recently, Avila & Cuevas (2009) –inspired by Johnston et al. (2002)– demonstrated that the algebraic method customarily used in GS for the normalization of the scintillation autocovariance leads to overestimated C_N^2values, and proposed a procedure for the correct recalibration of the turbulence profiles. The relative error can take values from zero to a factor of 4, depending on the telescope size, the double star used as source, the position of the analysis plane and the turbulence altitude. Until now, turbulence profiles at Mt Graham (Masciadri et al. 2010) and El Teide (García-Lorenzo & Fuensalida 2011) observatories have been recalibrated using that procedure.

In 1997 and 2000, GS measurements were carried out at the Observatorio Astronómico Nacional de San Pedro Mártir (OAN-SPM), Baja California, Mexico. Avila et al. (2004, hereafter A04) report a statistical analysis of the $C_N^2(h)$ measured in both campaigns. Avila et al. (1998) present the results of the 1997 campaign and Avila et al. (2006) give a statistical analysis of wind speed profiles and wavefront coherence time. In view of the newly discovered calibration issue, a reanalysis of the GS results at the OAN-SPM is in order. Here we present the correction of the C_N^2 values and its implications on the statistical description of the seeing and isoplanatic angle. In § 2 the observation campaigns and original data are described. § 3 is devoted to the description of the C_N^2 values correction and the statistical analysis of the corrected turbulence profiles is presented in § 4. Finally the discussion and conclusions are given in § 5.

TABLE 1

TELESCOPES WHERE THE GS WAS INSTALLED

	Diameter (D)[a]	Secondary over Primary (e)
SPM2.1	2.1	0.27
SPM1.5	1.5	0.26

[a]In meters.

2. OBSERVATION CAMPAIGN AND DATA OVERVIEW

Two GS observation campaigns have been carried out at the OAN-SPM in 1997 and 2000, respectively. In 1997, the GS was installed at the 1.5 m and 2.1 m telescopes (SPM1.5 and SPM2.1) for 8 and 3 nights (1997 March 23–30 and April 20–22 UT), whereas in 2000 the instrument was installed for 9 and 7 nights (May 7–15 and 16–22 UT) at SPM1.5 and SPM2.1. It is fair to mention that in the 2000 campaign additional instruments (Masciadri, Avila, & Sánchez 2004) were deployed, even though they have no impact on the present article.

The numbers of $C_N^2(h)$ samples obtained in 1997 and 2000 were 3398 and 3016, respectively, making a total of 6414. The altitude scale of the profiles refers to altitude above sea level (2800 m at OAN-SPM). In GS data, part of the turbulence measured at the observatory altitude is produced inside the telescope dome. For site characterization, this contribution must be subtracted. In all the analyses presented here, dome turbulence has been removed using the procedure explained in A04. Almost all the time the most intense turbulence was located at the observatory altitude.

3. C_N^2VALUES CORRECTION

The GS technique is based on the estimation of the normalized spatial autocovariance $\mathcal{C}$ of a double-star scintillation recorded on a virtual plane located a distance d below the ground (of the order of a few kilometers). The procedure to estimate the scintillation autocovariance is to compute the mean autocorrelation of double-star scintillation images, normalized by the autocorrelation of the mean image. In the classical SCIDAR –where images are taken at the telescope pupil– this computation leads analytically to $\mathcal{C}$ (Rocca et al. 1974). However for the GS, Johnston et al. (2002) show that the result of this procedure is not equal to $\mathcal{C}$. The discrepancy is due to the shift of the out-of-focus pupil images pro-

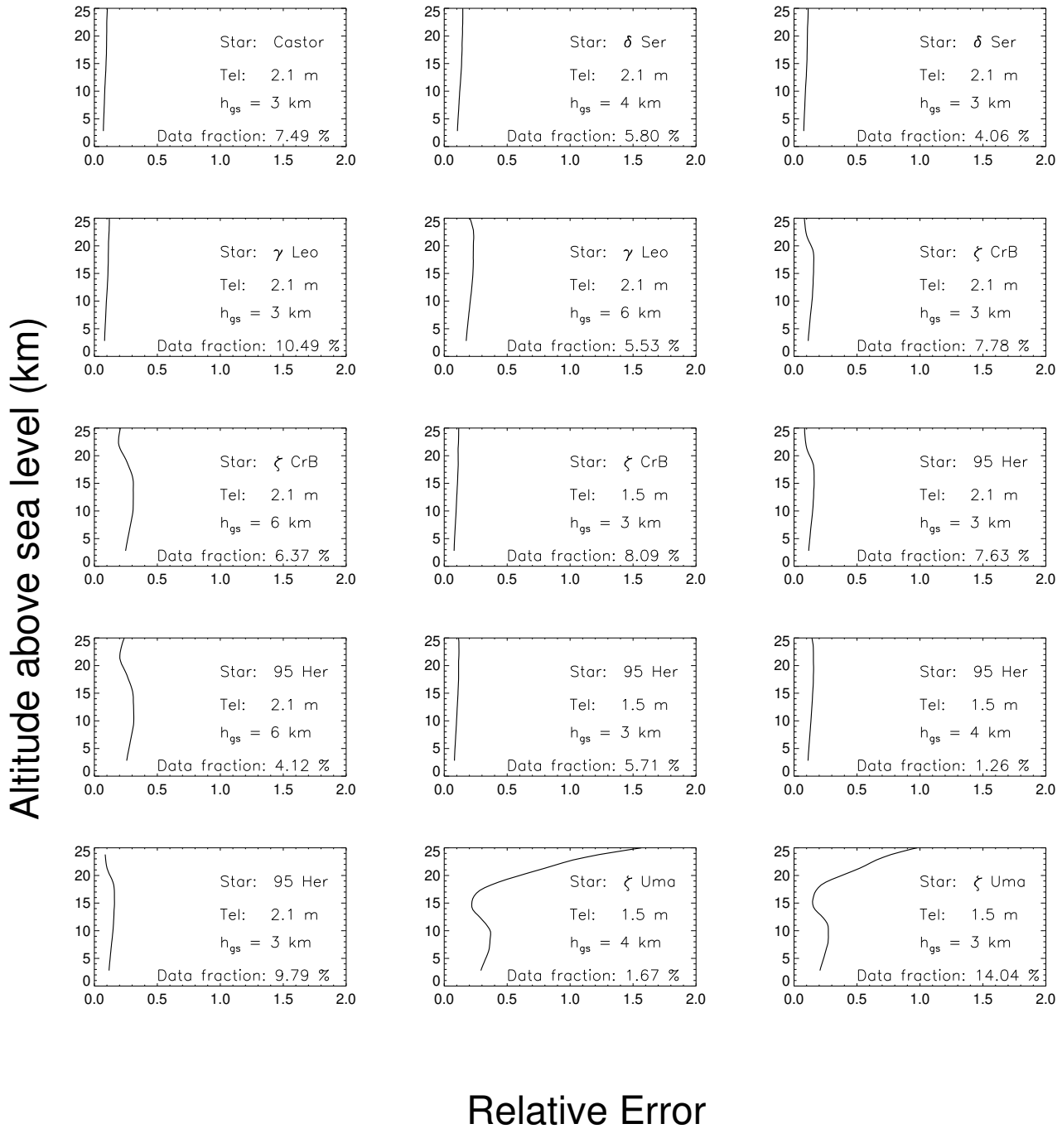

Fig. 1. Vertical profiles of the relative error. Each plot corresponds to a different combination of the parameters that define the relative error. Those parameters are indicated in each plot box together with the fraction of the data that was taken with the corresponding parameter set.

duced by each star on the detector. Those authors analyze this effect only for turbulence at ground level ($h = 0$). Avila & Cuevas (2009, hereafter AC09) generalize the analysis to turbulence at any height and provide an analytical formula for the calculation of the relative error ϵ induced on the C_N^2 values by the wrong normalization. AC09 provide exact and approximate –easier to compute– formulae for ϵ. In this paper, only the exact expression (equation 32 in AC09) is used. The general dependence of ϵ upon

TABLE 2

STELLAR SOURCES USED FOR GS MEASUREMENTS

Name	α_{2000}[a]	δ_{2000}[b]	Δm[c]	b[d]	θ[e]
Castor	7 34	31 53	2.1	0.19	4.0
γ Leo	10 20	19 50	1.3	0.16	4.5
ζ Uma	13 24	54 56	1.6	0.15	14.4
δ Ser	15 35	10 32	0.9	0.20	4.0
ζ Cbr	15 39	36 38	0.9	0.20	6.4
95 Her	18 01	21 36	0.4	0.25	6.3

[a]Right ascension in hours and minutes.

[b]Declination in degrees and arc minutes.

[c]Visible magnitude difference.

[d]See text and equation (24) in AC09.

[e]Angular separation in seconds of arc.

the observational parameters is as follows: the relative error is an increasing function of the turbulence altitude h, the double star separation θ, the conjugation distance d and the magnitude difference Δm of the double-star components. The relative error decreases as the telescope diameter D increases. The ratio e of the secondary over the primary mirror diameters has an influence on the shape of the plot ϵ vs. h, as can be seen in Figure 5 of AC09. For the sake of consistency with AC09, the magnitude difference of the stellar components is expressed through the parameter b defined by equation 24 in AC09. The values of D and e for the telescopes used in the OAN-SPM GS measurements are given in Table 1 and the stellar sources in Table 2.

The vertical profile of the relative error, $\epsilon(h)$, has been computed for the corresponding parameter values of the campaigns. The profiles are plotted in Figure 1. The percentage of data taken with each parameter set is indicated in the corresponding frame. The relative error is most of the time between 0.05 and 0.25 (5% to 25%). However, when ζ Uma is used (last two frames), ϵ reaches very high values at high altitude.

The correct $C_{\rm N}^2(h)$ are obtained by multiplying the original profiles by $1/(1+\epsilon(h))$. Each of the 6414 $C_{\rm N}^2$ profiles was so corrected.

The uncertainty of the statistical values given throughout the paper was estimated using the bootstrap method (Efron 1982), as explained in Appendix A of A04.

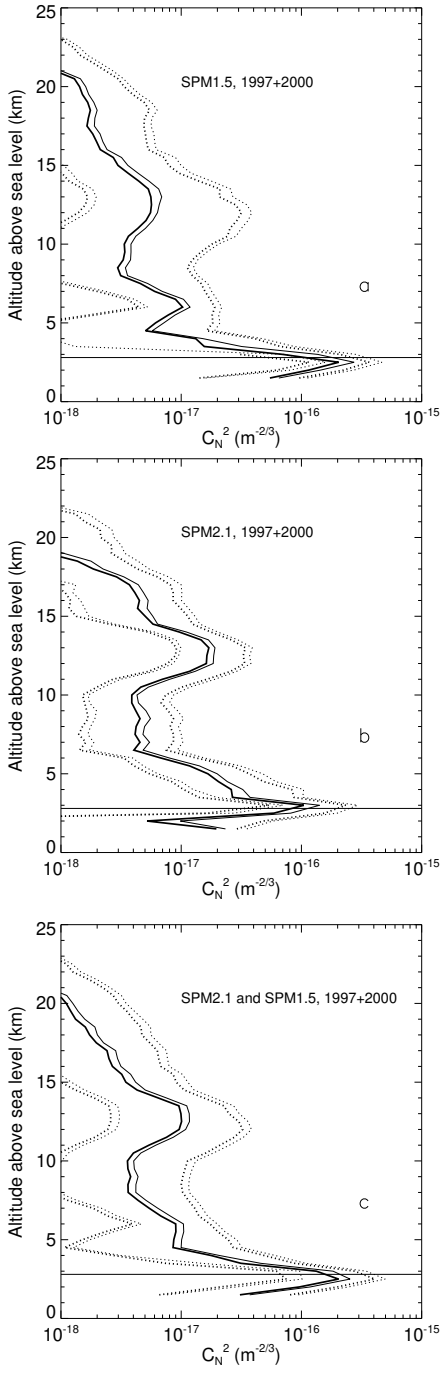

Fig. 2. Median (full line), 1st and 3rd quartiles (dashed lines) of the $C_{\rm N}^2(h)$ values obtained with the GS at the (a) 1.5mT, (b) 2.1mT and (c) both telescopes, during the 1997 and 2000 campaigns. Bold and thin lines correspond the corrected and non-corrected values, respectively. The horizontal axis represents $C_{\rm N}^2$ values, on a logarithmic scale, and the vertical axis represents the altitude above sea level. The horizontal lines indicate the observatory altitude. Dome seeing has been removed.

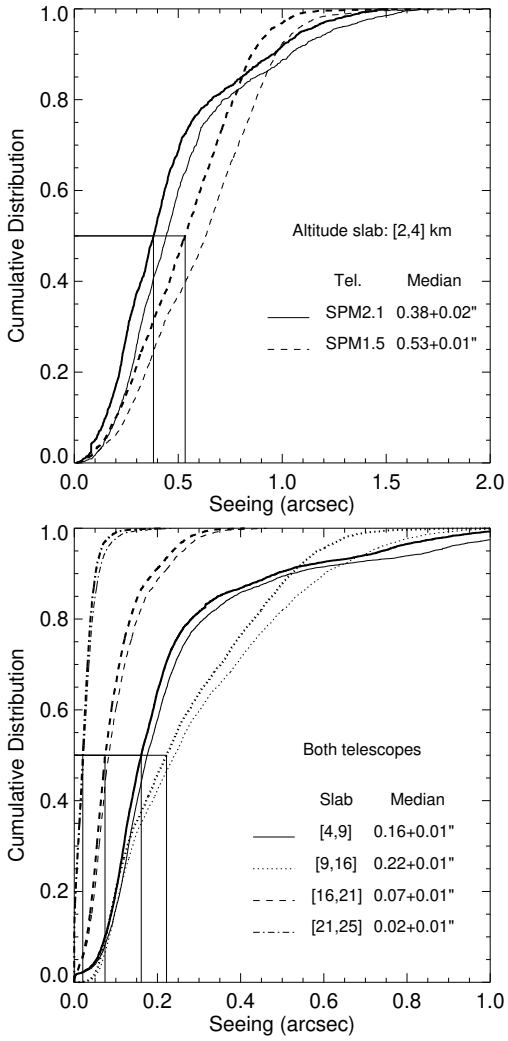

Fig. 3. Cumulative distributions of the seeing generated in different atmosphere slabs: (top)]2, 4] km for the 2.1mT (full line) and the 1.5mT (dashed line) without dome seeing; (bottom)]4, 9] km (full line),]9, 16] km (dotted line),]16, 21] km (dashed line),]21, 25] km (dash-dotted line). Data used: 1997 and 2000 campaigns. Bold and thin lines correspond the corrected and non-corrected values, respectively. Horizontal and vertical lines indicate corrected median values, which are reported in Table 3 together with the 1st and 3rd quartiles.

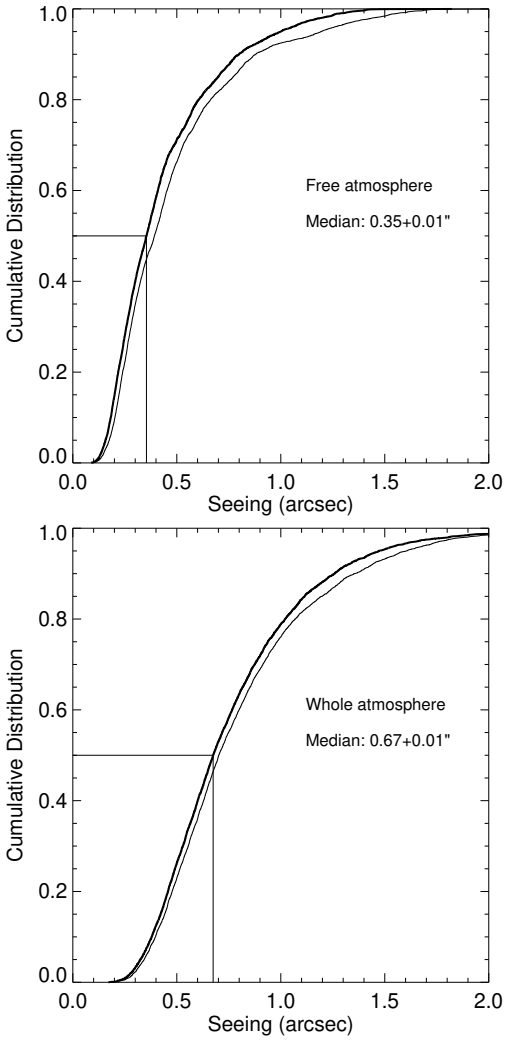

Fig. 4. Cumulative distributions of the seeing generated in (top) the free atmosphere (altitude higher than 4 km) and (bottom) the whole atmosphere, without dome seeing. Data from both telescopes and both campaigns are included.Bold and thin lines correspond the corrected and non-corrected values respectively. The horizontal and vertical lines indicate the corrected median values, which are reported in Table 3 together with the 1st and 3rd quartiles.

4. STATISTICAL ANALYSIS OF CORRECTED PROFILES

The median, first and third quartile profiles of the $C_N^2(h)$ data measured with SPM1.5 and SPM2.1 are shown in Figures 2a and 2b, respectively. In Figure 2c, the same kind of profiles are shown for the complete GS data set. It can be seen that the shape of those profiles is not altered by the correction. All the plots are basically only shifted towards lower values by a similar amount, which on a logarithmic scale corresponds to being multiplied by a factor. The average shift factor of all the quartile profiles shown in Figure 2 is 0.87.

As explained in A04, at ground level the turbulence at the 1.5 m telescope is more intense than that at the 2.1 m telescope, presumably because the later

TABLE 3

SEEING FOR DIFFERENT ATMOSPHERE SLABS AND VARIATION

Slab (km)	First Quartile (arcsec)	Median (arcsec)	Third Quartile (arcsec)
[2, 4] @ SPM2.1[a]	0.24[b] (−20.0%)	0.38[c] (−13.6%)	0.55[d] (−12.7%)
[2, 4] @ SPM1.5[a]	0.32[b] (−15.8%)	0.53[b] (−15.8%)	0.71[b] (−14.5%)
[4, 9]	0.11[b] (−8.3%)	0.16[b] (−5.9%)	0.24[b] (−11.1%)
[9, 16]	0.11[b] (−8.3%)	0.22[b] (−8.3%)	0.39[b] (−9.3%)
[16, 21]	0.04[b] (−20.0%)	0.07[b] (−12.5%)	0.12[b] (−14.3%)
[21, 25]	0.01[b] (0.0%)	0.02[b] (0.0%)	0.03[b] (−25.0%)
Free atmosphere: [4, 25]	0.24[b] (−7.7%)	0.35[b] (−10.2%)	0.55[b] (−6.8%)
Whole atmosphere.: [2, 25][e]	0.50[b] (−3.8%)	0.68[b] (-4.2%)	0.97[c] (−2.0%)

[a]Without dome seeing.

[b]Uncertainty: ±0.01.

[c]Uncertainty: ±0.02.

[d]Uncertainty: ±0.03.

[e]As if measured at the SPM2.1 and without dome seeing.

is on top of a 20 m high building whereas the former is at ground level. The general vertical structure of the turbulence distribution from the whole data set can be summarized as a strong layer at the ground, and two thick layers centered at 6 and 13 km. The mean relative difference of the corrected and uncorrected median C_N^2 values is 15.2%, 19.3% and 15.4% for the data obtained at SPM1.5, SPM2.1 and for the complete data set.

The cumulative distribution of the corrected and uncorrected measurements of seeing generated within different altitude slabs is shown in Figure 3. For the 2–4 km slab, which includes ground turbulence, the data obtained at SPM2.1 and SPM1.5 are separated into two different cumulative distributions as ground contributions are different for each telescope. Similar plots are exhibited in Figure 4 for the free (above 4 km) and the whole atmosphere. Differences between the corrected and uncorrected cumulative distributions seem to be basically driven by seeing values. The larger the seeing value, the larger the difference. This is an expected behavior, since corrected and uncorrected C_N^2 are proportional to each other. The corrected values of median, first and third quartile of the seeing generated in the different slabs are summarized in Table 3. The variation of the corrected relative to the uncorrected values (reported in Table 3 of A04) is given in parentheses. Note that the vertical distribution of those relative variations does not follow any of the individual altitude profiles of the relative error $\epsilon(h)$, shown in Figure 1. This is due to the fact that the statistical values reported in Table 3 were obtained from a combination of different functions $\epsilon(h)$.

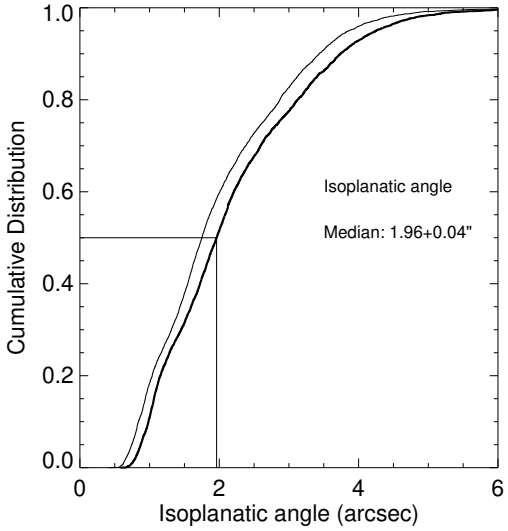

Fig. 5. Cumulative distribution of the isoplanatic angle θ_0 computed from each turbulence profile of both campaigns and both telescopes. Bold and thin lines correspond to the corrected and non-corrected values respectively. The corrected median value of θ_0 is $1\farcs96 \pm 0\farcs04$ and the 1st and 3rd quartiles are $1\farcs31 \pm 0\farcs04$ and $2\farcs86 \pm 0\farcs04$.

The isoplanatic angle θ_0 depends on C_N^2 and on its vertical distribution (see e.g. equations 5 and 6

from A04):

$$\theta_0 = \left[0.423 \left(\frac{2\pi}{\lambda} \right)^2 \int \mathrm{d}h \, h^{5/3} C_\mathrm{N}^2(h) \right]^{-3/5}, \quad (1)$$

where λ is the wavelength. Therefore, the correction of the C_N^2 profiles can have a strong impact on the values of θ_0. From each corrected $C_\mathrm{N}^2(h)$ one corrected value of the isoplanatic angle is obtained. The cumulative distribution of the corrected θ_0 is shown in Figure 5. The median value increased by the modest amount of 4.8% with respect to the median value of θ_0 obtained with the uncorrected turbulence profiles. However, under certain observation parameters and turbulence conditions, the isoplanatic angle increased significantly after the C_N^2 correction: in 10% of the cases, the increase was higher than 25%, and reached 40% in a few cases.

5. CONCLUSIONS

Although the impact on individual estimates of turbulence profiles caused by the correction of the normalization error may be very strong depending on the observational parameters – as deduced for example from the bottom right plot in Figure 1, the statistical parameters that describe the optical turbulence profiles measured at the OAN-SPM vary by a relatively small amounts after the correction. The vertical distribution of the median C_N^2 (on a logarithmic scale) remains basically the same as before the correction, the values being only multiplied by an average factor of 0.87. After correction, the median whole-atmosphere and free-atmosphere seeing diminished by 4.2% and 10.2% respectively, the correct values being 0.68 and 0.35 arc seconds. The altitude slab where the correction has the strongest impact is from 2 to 4 km, with a decrease in median seeing of 15.8% and 13.6% for measurements at SPM1.5 and SPM2.1. The corrected median value of the isoplanatic angle is $1\farcs96$ which represents an increase of 4.8% relative to the uncorrected value.

We are grateful to the OAN-SPM staff for their valuable support during the observation campaigns. This work was financially supported by Conacyt and PAPIIT through grants number 58291 and IN107109.

REFERENCES

Avila, R., Avilés, J. L., Wilson, R. W., Chun, M., Butterley, T., & Carrasco, E. 2008, MNRAS, 387, 1511

Avila, R., Carrasco, E., Ibáñez, F., Vernin, J., Prieur, J., & Cruz, D. 2006, PASP, 118, 503

Avila, R., & Cuevas, S. 2009, Optics Express, 17, 10926 (AC09)

Avila, R., Masciadri, E., Vernin, J., & Sánchez, L. 2004, PASP, 116, 682 (A04)

Avila, R., Vernin, J., & Cuevas, S. 1998, PASP, 110, 1106

Avila, R., Vernin, J., & Masciadri, E. 1997, Appl. Opt., 36, 7898

Avila, R., Vernin, J., & Sánchez, L. J. 2001, A&A, 369, 364

Chun, M., Wilson, R., Avila, R., Butterley, T., Aviles, J.-L., Wier, D., & Benigni, S. 2009, MNRAS, 394, 1121

Efron, B. 1982, The Jackknife, the Bootstrap and Other Resampling Plans (Philadelphia: The Society for Industrial and Applied Mathematics)

Egner, S. E., & Masciadri, E. 2007, PASP, 119, 1441

Egner, S. E., Masciadri, E., & McKenna, D. 2007, PASP, 119, 669

Fuchs, A., Tallon, M., & Vernin, J. 1994, Proc. SPIE, 2222, 682

———. 1998, PASP, 110, 86

Fuensalida, J. J., García-Lorenzo, B., Delgado, J. M., Rodríguez-Hernández, M. A. C., & Vernin, J. 2007, RevMexAA (SC), 31, 86

Fuensalida, J. J., García-Lorenzo, B., & Hoegemann, C. 2008, MNRAS, 389, 731

García-Lorenzo, B., Eff-Darwich, A., Fuensalida, J. J., & Castro-Almazán, J. 2009, MNRAS, 397, 1633

García-Lorenzo, B., & Fuensalida, J. J. 2006, MNRAS, 372, 1483

———. 2011, MNRAS, 410, 934

Johnston, R. A., Dainty, C., Wooder, N. J., & Lane, R. G. 2002, Appl. Opt., 41, 6768

Kern, B., Laurence, T. A., Martin, C., & Dimotakis, P. E. 2000, Appl. Opt., 39, 4879

Klückers, V. A., Wooder, N. J., Nicholls, T. W., Adcock, M. J., Munro, I., & Dainty, J. C. 1998, A&AS, 130, 141

Masciadri, E., Avila, R., & Sánchez, L. J. 2004, RevMexAA, 40, 3

Masciadri, E., Stoesz, J., Hagelin, S., & Lascaux, F. 2010, MNRAS, 404, 144

Prieur, J.-L., Daigne, G., & Avila, R. 2001, A&A, 371, 366

Rocca, A., Roddier, F., & Vernin, J. 1974, J. Opt. Soc. Am., 64, 1000

Tokovinin, A., Vernin, J., Ziad, A., & Chun, M. 2005, PASP, 117, 395

Vernin, J., & Azouit, M. 1983a, J. Optics (Paris), 14, 5

———. 1983b, J. Optics (Paris), 14, 131

Vernin, J., Trinquet, H., Jumper, G., Murphy, E., & Ratkowski, A. 2007, Environmental Fluid Mech., 7, 371

Wilson, R. W., Wooder, N. J., Rigal, F., & Dainty, J. C. 2003, MNRAS, 339, 491

Remy Avila: Centro de Física Aplicada y Tecnología Avanzada, Universidad Nacional Autónoma de México, Apdo. Postal 1-1010, 76000 Santiago de Querétaro, Querétaro, México (r.avila@crya.unam.mx).
Esperanza Carrasco: Instituto Nacional de Astrofísica, Óptica y Electrónica, Luis Enrique Erro 1, 72840 Tonantzintla, Puebla, Mexico (bec@inaoep.mx).
Víctor M. Castaño: Universidad Autónoma de Querétaro, Campus Cerro de las Campanas, 76010 Querétaro, Querétaro, Mexico (castano@fata.unam.mx).
Irene Cruz-González and Leonardo J. Sánchez: Instituto de Astronomía, Universidad Nacional Autónoma de México, Apdo. Postal 70-264, 04510, México, D. F. Mexico (irene,leonardo@astroscu.unam.mx).

Revista Mexicana de Astronomía y Astrofísica, **47**, 83–112 (2011)

MID- AND FAR-INFRARED PHOTOMETRY OF GALACTIC PLANETARY NEBULAE WITH THE AKARI ALL-SKY SURVEY

J. P. Phillips and R. A. Márquez-Lugo

Instituto de Astronomía y Meteorología
Universidad de Guadalajara, Mexico

Received 2010 December 14; accepted 2011 January 28

RESUMEN

Presentamos fotometría en el medio y lejano infrarrojo de 857 nebulosas planetarias (NPs) galácticas utilizando datos provenientes del AKARI All-Sky Survey. Se incluyen flujos a 9 y 18 μm obtenidos con la Infrared Camera (IRC), y a 65, 90, 140 y 160 μm producto de la far-Infrared Surveyor (FIS). Se nota que la luminosidad IR de las NPs más jóvenes es comparable a la luminosidad total la estrella central y que posteriormente decrece hasta $\sim5\times10^2$ $L_\odot$ cuando $D > 0.08$ pc, lo cual es congruente con la evolución de la opacidad del polvo de las NPs y la apreciable absorción en las NPs jóvenes y en las proto NPs. Además notamos que hay poca evidencia de la evolución en los cocientes de los flujos IR/radio sugerida por autores previos. También hacemos notar que la disminución de la temperatura del polvo al aumentar el diámetro nebular es similar a la obtenida en estudios previos, mientras que los niveles de calentamiento por fotones de Lyα son <0.5 de la energía disponible para los granos. Parece haber una evolución del exceso infrarrojo (IRE) con la expansión de las nebulosas, el cual adquiere sus valores máximos cuando las NPs son más compactas.

ABSTRACT

We provide mid- and far-infrared photometry of 857 Galactic planetary nebulae (PNe) using data derived from the AKARI All-Sky Survey. These include fluxes at 9 and 18 μm obtained with the Infrared Camera (IRC), and at 65, 90, 140 and 160 μm using the far-Infrared Surveyor (FIS). It is noted that the IR luminosities of the youngest PNe are comparable to the total luminosities of the central stars, and subsequently decline to $\sim5\times10^2$ $L_\odot$ where $D > 0.08$ pc. This is consistent with an evolution of PNe dust opacities, and appreciable absorption in young and proto-PNe. We also note that there is little evidence for the evolution in IR/radio flux ratios suggested by previous authors. The fall-off of dust temperatures with increasing nebular diameter is similar to that determined in previous studies, whilst levels of Lyα heating are <0.5 of the total energy budget of the grains. There appears to be an evolution in the infrared excess (IRE) as nebulae expand, with the largest values occurring in the most compact PNe.

Key Words: dust, extinction — infrared: ISM — ISM: jets and outflows — planetary nebulae: general

1. INTRODUCTION

Several large-scale surveys at infrared wavelengths have been undertaken in the last thirty or so years, permitting a clearer understanding of the properties of dust in planetary nebulae (PNe). Thus for instance, Pottasch et al. (1984) investigated the thermal and physical characteristics of grains using photometry taken with the *Infrared Astronomical Satellite* (*IRAS*; Neugebauer et al. 1984). They found that dust temperatures decline with increasing nebular radius R, and that dust/gas mass ratios decrease with expansion of the shells. A further analysis by Lenzuni, Natta, & Panagia (1989) found that grain radii also decreased with radius,

whilst the volume density of particles increased as $\propto R^{4.19}$; tendencies which were attributed to grain-grain collisions, sputtering by stellar winds, or the selective destruction of larger grains. A further analysis by Stasinska & Szczerba (1999), however, found no change in either of the latter two parameters.

A subsequent survey of PNe has been undertaken in the near infrared (NIR) using the 2MASS all-sky survey (Ramos-Larios & Phillips 2005), whilst a more restrictive survey, taken with the *Spitzer Space Telescope* (*Spitzer*; Werner et al. 2004), has enabled mid-infrared (MIR) observations of PNe close to the Galactic plane (see e.g., Cohen et al. 2005; Phillips & Ramos-Larios 2008; Ramos-Larios & Phillips 2008; Zhang & Kwok 2009; Phillips & Márquez-Lugo 2011). These latter results have shown the importance of polycyclic aromatic hydrocarbons (PAHs) in enhancing MIR emission at 5.8 and 8.0 μm, and revealed the presence of extensive emission outside of the ionized regimes, likely arising from photo-dissociation regimes (PDRs).

A more recent AKARI infrared survey has now completed the major phase of its observational program, and the point source catalogue (PSC) was made available in March 2010. This represents an updated version of the IRAS project, containing as it does more photometric channels, higher levels of spatial resolution, and higher sensitivity detectors. We present photometry for 857 Galactic PNe taken with the infrared camera (IRC) and far-infrared surveyor (FIS), and use this to analyse the evolution in grain temperatures and FIR luminosities.

2. OBSERVATIONS

The AKARI space mission (Murakami et al. 2007) was launched in 2006, and contains the IRC (Onaka et al. 2007) for observations in the range 2–26 μm, and the FIS (Kawada et al. 2007) for the 50–200 μm regime. The Ritchey-Chretien type telescope has a 0.685 m primary mirror, cooled to 6 K by liquid helium and mechanical coolers. One of the primary objectives of this mission was an all sky IRC/FIS survey, undertaken between 2006 May and 2007 August. The resulting PSCs [Kataza et al. 2010 (IRC); Yamamura et al. 2010 (FIS)] were published in 2010 March.

The IRC filter profiles extend between 6.76 and 11.6 μm (in the case of MIR-S), with an effective wavelength of 9 μm, and between 13.9 and 25.6 μm (MIR-L) with an effective wavelength of 18 μm. The camera field of view (FOV) was 10×9.6 arcmin^2 for MIR-S, and 10.7×10.2 arcmin^2 for MIR-L, whilst the pixel scales were 2.34×2.34 arcsec^2 (MIR-S) and 2.31×2.39 arcsec^2 (MIR-L). Each of four adjacent pixels were subsequently binned to create so-called "virtual" pixels, with areas 4×4 times greater than those of the original pixels. However, subsequent processing of two independent survey grids resulted in an improvement in spatial resolution, and point spread functions (PSFs) with FWHM ∼5.5 arcsec at 9 μm, and 5.7 arcsec for the 18 μm channel.

The FIS survey, by contrast, permitted observations at effective wavelengths of 65 μm (filter N60, bandwidth $\Delta\lambda = 21.7$ μm), 90 μm (Wide-S, $\Delta\lambda = 37.9$ μm), 140 μm (Wide-L, $\Delta\lambda = 52.4$ μm) and 160 μm ($\Delta\lambda = 34.1$ μm). The 65 and 90 μm results were taken with a monolithic Ge:Ga detector having a pixel size 26.8 arcsec, whilst the longer wave (140 and 160 μm) data were acquired using a stressed Ge:Ga detector, and pixel scale of 44.2 arcsec. The FOVs were in all cases ∼1 arcmin, whilst the FWHM of the PSFs were 37 arcsec (at 65 μm), 39 arcsec (90 μm), 58 arcsec (140 μm) and 61 arcsec (160 μm). Detector sensitivities are important in determining the rates of source detection, and quoted values range between 0.55 Jy at 90 μm to as high as 25 Jy for the 160 μm results. This question is further examined in § 3.4, where we consider its importance in determining nebular emission trends.

Details of the source selection procedure are provided in the following sections, together with a description of the catalogue results, the infrared dimensions of the PNe, and a comparison of the AKARI and IRAS photometry.

2.1. *Planetary Nebula Data Base and Search Radius*

The positions of the PNe investigated in this present study are taken from the listing of coordinates by Kerber et al. (2003). This provides positions for 1086 sources based on the 2$^{\rm nd}$ generation General Star Catalogue. The coordinates for sources which are compact (or have central stars) are quoted as being accurate to 0.35 arcsec, whilst the positions for 226 more extended PNe are accurate to ∼5 arcsec.

By contrast, the AKARI/IRC All-Sky Survey Release Point Source Catalogue - Release Note (Rev. 1) (Kataza et al. 2010) suggests that the mean angular separation of the AKARI and 2MASS sources is of order ≅0.77 arcsec, with 95% of the sources having angular separations of <2 arcsec. Similarly, the positional errors of the longer wave FIS sources (Yamamura et al. 2010) are determined through a comparison with the SIMBAD database, yielding flux independent uncertainties of order ∼6 arcsec.

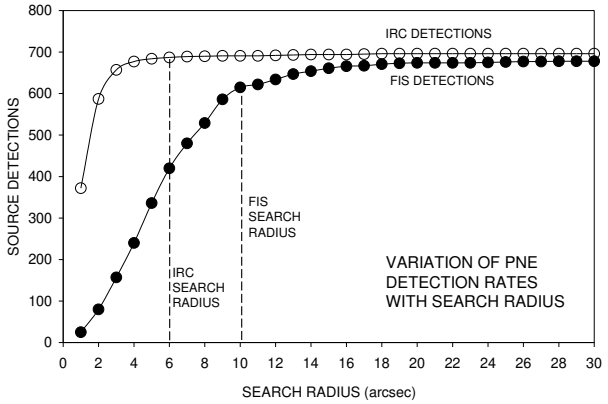

Fig. 1. The variations in the numbers of PNe with size of the search radius θ_S. Note how the numbers of IRC detections achieve a maximum within ∼2 arcsec of the nominal PNe positions, whilst the number of FIS detections increases more slowly, and peaks at radii close to 15–20 arcsec. This difference in detection rates reflects the difference in the positional accuracies of the surveys. Finally, the flattening of detection rates towards larger search radii confirms the low levels of contamination by background sources.

Given that the PNe data base is identical for the FIS and IRC searches, it follows that search radii need to be larger for FIS than for the IRC results.

That this is the case is apparent from Figure 1, where it is seen that the rates of source detection increase with increasing search radius, eventually reaching plateau values of 696 sources for the IRC detections, and 678 sources for the FIS results. It is also apparent that whilst most of the PNe are detected within radii $\theta_S \sim 3$ arcsec for the IRC results, a radius of order $\theta_S \sim 14$ arcsec is required for comparable rates of FIS detection. We have adopted a search radius $\theta_S = 6$ arcsec for the IRC results, and $\theta_S = 10$ arcsec for the FIS photometry.

There are two reasons to suspect that background contamination is extremely modest. It is apparent, for instance, that rates of source detection are flat as θ_S increases from ∼15 arcsec to 30 arcsec, implying that any field source contamination is likely to be $< 2\%$. We also note that the AKARI FIS catalogue includes a parameter NDENS, corresponding to the number of sources within 5 arcmin of the central (PNe) positions. This takes a mean value of ∼2.2 for 415 estimates of the parameter in the most sensitive (90 μm) channel, suggesting again that background contamination is extremely low. A similar conclusion applies for the NDENS parameters at 9 and 18 μm, corresponding to the numbers of sources within 45 arcsec of the search positions. We determine mean values NDENS09 = 0.068 (for 396 estimates of the parameter), and NDENS18 = 0.020 (for 612 estimates of NDENS), implying that very few of our identifications are likely to be spurious.

2.2. *Catalogue Results for Galactic PNe*

Photometric results for 857 PNe detected in the IRC catalogue are presented in Table 1, where all of the fluxes have FQUAL values of 3 (i.e. all of the data are classified as being valid). An analysis by the AKARI team of trends in photometric errors shows that the most probable uncertainties are of the order of ∼2–3%, with 80% of the data having errors of $< 15\%$. It is found that the signal to noise ratio (S/N) for the 9 μm data is of order ∼19 for sources having $F(9\ \mu\mathrm{m}) > 0.5$ Jy, and falls as approximately S/N ∼32 $F_\nu(9\ \mu\mathrm{m}) + 4$ for smaller flux levels. Similarly, it is found that the S/N for 18 μm results is ∼15 where $F(18\ \mu\mathrm{m}) > 0.8$ Jy, and decreases as ∼17 $F_\nu(18\ \mu\mathrm{m}) + 3$ below this limit.

We have, apart from this, specified the numbers of the PNe in the Kerber et al. (2003) list of coordinates (Column 1); the commonly accepted names of the sources (Column 2); and the right ascensions and declinations of the nebulae (Columns 3 and 4). The angular diameter θ is based upon radio and optical results, where we have taken values from Acker et al. (1992), Zhang (1995), Cahn & Kaler (1971), Tylenda et al. (2003), Perek & Kohoutek (1967), and Siodmiak & Tylenda (2001). Where maximal and minimal diameters θ_{MAX} and θ_{MIN} are quoted, then we have employed harmonic mean values $\theta = (\theta_{\mathrm{MAX}}\theta_{\mathrm{MIN}})^{0.5}$. Similarly, the AKARI mean radii at 18 μm (denoted in the catalogue by MEAN_AB18) are provided in Column 8, and labeled MN_18. The 1.4 GHz results (Column 9) are taken from the uniform data base of Condon et al. (1998), whilst the 5 GHz measures (Column 10) derive from the compilations of Acker et al. (1992), Zhang (1995) and Siodmiak & Tylenda (2001). Finally, the distances of PNe remain notoriously uncertain, and the numbers of more reliable distances (i.e. those based on trigonometric, reddening, gravitational and kinematic measures, among others) are still pitifully small. We have therefore quoted distances based on larger-scale statistical measures, whilst recognizing that these are prone to systematic and random errors. Typical uncertainties in distance are probably of the order ≈30%. We have used values quoted by Phillips (2004) and Zhang (1995) in that order of priority, and these are listed in Column 11 of Table 1. These estimates are also combined with the angular diameters in Column 7 to determine the physical diameters in Column 12.

TABLE 1

GALACTIC PNE IDENTIFIED IN THE AKARI IRC CATALOGUE

KN	NAME	R.A. (2000)	DEC (2000)	F (9 μm)	F (18 μm)	θ	MN_18	F(1.4 GHz)	F(5 GHz)	DIST	DIAM
		H:M:S	D:M:S	Jy	Jy	arcsec	arcsec	mJy	mJy	kpc	pc
4	010.2+02.7	17 58 14.415	−18 41 26.15	–	0.844	–	3.53	18.3	–	–	–
5	021.9+02.7	18 21 21.115	−08 31 42.30	0.285	4.516	–	4.12	36.2	–	–	–
6	050.6+19.7	18 08 20.083	+24 10 43.26	2.483	13.329	–	4.8	–	–	–	–
7	099.3−01.9	22 04 12.301	+53 04 01.36	0.46	11.917	–	4.74	–	–	–	–
9	19W32	17 39 02.870	−28 56 35.10	–	6.588	24	4.46	13.5	21.3	–	–
10	341.4−09.0	17 35 02.502	−49 26 26.38	5.541	77.831	–	6.67	–	–	–	–
27	A 30	08 46 53.514	+17 52 45.47	0.548	18.039	4.47	6.04	–	2.3	2.55	0.055
31	A 35	12 53 32.792	−22 52 22.57	0.114	–	772	–	–	255	0.74	2.77
42	A 47	18 35 22.569	−00 13 49.68	–	0.143	17	2.13	7.3	–	–	–
43	A 48	18 42 46.908	−03 13 17.30	–	3.342	40	6.97	159.4	–	–	–
48	A 53	19 06 45.910	+06 23 52.47	–	1.043	31	5.16	33.6	85.7	1.68	0.252
53	A 58	19 18 20.476	+01 46 59.62	2.846	15.29	–	4.95	–	–	–	–
73	A 78	21 35 29.410	+31 41 45.39	0.986	30.5	107	7.23	3.7	4.9	2.22	1.152
83	Al 2-E	17 30 14.398	−27 30 19.41	–	0.873	–	3.44	14.7	–	–	–
85	Al 2-G	17 32 22.670	−28 14 27.32	–	1.013	–	3.39	–	–	–	–
90	Al 2-0	17 51 44.663	−31 36 00.18	–	0.775	5.7	3.18	38	33	–	–
92	Al 2-R	17 53 36.431	−31 25 25.19	–	0.306	–	3.17	–	–	–	–
94	Ap 1-12	18 11 35.088	−28 22 37.02	0.207	3.286	12	4.03	6.6	18.7	5.34	0.311
96	BD+30 3639	19 34 45.235	+30 30 58.94	47.546	148.573	7.6	7.65	235.2	630	–	–
102	Bl 2-1	22 20 16.638	+58 14 16.59	1.554	4.116	1.6	3.99	21.6	54	6.94	0.054
103	Bl 3-10	17 55 20.537	−29 57 36.13	–	0.357	–	3.01	4.7	–	–	–
104	Bl 3-13	17 56 02.759	−29 11 16.21	–	0.809	–	3.31	4.7	10	–	–
105	Bl 3-15	17 52 35.947	−29 06 38.97	–	0.372	–	2.67	–	–	–	–
106	Bl B	17 36 59.836	−29 40 08.93	–	1.641	–	3.65	8.9	–	–	–
108	Bl M	17 53 47.180	−28 27 16.88	–	1.249	4.5	3.61	9.3	17	7.03	0.153
109	Bl O	17 53 49.717	−28 59 11.26	0.149	1.534	–	3.7	3.6	–	–	–
110	Bl Q	17 54 34.866	−28 12 43.04	0.195	1.65	–	3.76	18.2	–	–	–
112	CRBB 1	20 19 28.702	−41 31 27.46	–	0.647	–	3.37	–	–	–	–
113	CRL 618	04 42 53.672	+36 06 53.17	189.266	–	12	–	4	67	2.72	0.158
119	Cn 1-1	15 51 15.936	−48 44 58.67	13.024	27.81	–	5.27	–	10	–	–
120	Cn 1-3	17 26 12.392	−44 11 24.52	0.525	–	–	–	–	–	–	–
122	Cn 1-5	18 29 11.653	−31 29 59.21	–	4.672	7	4.16	51	44	4.43	0.15
123	Cn 2-1	17 54 32.978	−34 22 20.84	–	3.665	2.2	3.84	25.2	49	6.17	0.066
124	Cn 3-1	18 17 34.133	+10 09 03.99	0.239	6.365	4.5	4.33	59.5	75	4	0.087
126	DdDm 1	16 40 18.156	+38 42 19.92	–	0.233	1	2.69	5.7	6	15.85	0.077
150	Fg 1	11 28 36.205	−52 56 04.01	0.416	0.92	16	5.32	–	55	2.02	0.157
151	Fg 2	17 39 19.847	−44 09 37.14	0.227	1.226	–	3.66	–	–	–	–
152	Fg 3	18 00 11.819	−38 49 52.73	1.441	16.842	2	5.1	42	107	–	–
154	G001.1+00.8	17 45 11.085	−27 32 38.00	1.182	4.009	–	4.48	73	–	–	–
155	G001.5−00.7	17 52 08.717	−28 02 16.56	0.394	3.804	–	4.32	17.2	–	–	–
158	G002.5+05.1	17 32 12.788	−24 04 59.56	1.138	9.218	–	4.56	–	–	–	–
163	G009.3+05.7	17 45 14.155	−17 56 46.57	–	13.562	–	4.75	–	–	–	–
164	G010.2+07.5	17 41 00.035	−16 18 12.50	–	3.076	–	3.83	–	–	–	–
165	G011.1−07.9	18 40 19.914	−22 54 29.23	–	2.813	–	3.75	–	–	–	–
168	G013.1−13.2	19 04 43.548	−23 26 08.82	7.78	–	–	–	–	–	–	–
170	G014.2+03.8	18 02 38.257	−14 42 03.22	0.421	7.042	–	4.29	–	–	–	–
172	G014.5−36.1	20 42 45.967	+30 04 06.51	3.74	37.172	–	5.88	–	–	–	–
175	G017.0+11.1	17 42 14.430	−08 43 18.61	–	2.126	–	4.32	23.4	–	–	–
179	G019.2−04.4	18 42 24.770	−14 15 11.81	–	0.495	–	3.76	7.3	–	–	–
180	G020.4+00.6	18 25 58.081	−10 45 28.49	0.447	5.891	–	4.2	48.7	–	–	–
182	G032.0−01.7	18 56 15.684	−01 34 00.31	–	0.485	–	2.89	10.7	–	–	–
184	G033.7−02.0	19 00 16.133	−00 14 32.59	–	0.347	–	2.89	3.5	–	–	–
185	G034.5−11.7	19 36 17.531	−03 53 25.26	0.151	3.996	–	3.98	8.8	–	–	–
186	G038.4+01.8	18 54 54.139	+05 48 11.29	0.211	2.773	–	3.92	20.5	–	–	–
188	G039.1−02.2	19 10 53.284	+04 27 28.50	–	0.439	–	3.26	11	–	–	–
191	G044.1+01.5	19 06 32.146	+10 43 23.93	–	0.815	–	3.24	19.4	–	–	–
193	G047.2+01.7	19 11 35.828	+13 31 11.58	0.78	3.869	–	4.07	–	–	–	–
195	G051.5+00.2	19 25 40.679	+16 33 05.56	–	3.863	–	4.38	77	–	–	–
200	G059.4−00.7	19 45 34.244	+22 58 34.41	–	0.958	–	3.35	26.5	–	–	–
202	G069.2+01.2	20 00 41.998	+32 27 41.23	–	0.516	–	3.6	17	–	–	–
204	G076.6−05.7	20 48 16.627	+34 27 24.36	0.11	6.21	–	4.27	–	–	–	–
207	G095.0−05.5	21 56 32.945	+47 36 13.40	0.369	1.764	–	3.67	–	–	–	–
219	G199.4+14.3	07 20 01.614	+18 17 26.47	0.147	0.689	–	3.09	–	–	–	–
221	G222.8−04.2	06 54 13.406	−10 45 38.27	0.204	1.727	–	4	2.7	–	–	–
226	G255.3−03.6	08 06 28.339	−38 53 23.93	0.091	1.275	–	3.56	2.8	–	–	–
228	G260.1+00.2	08 37 24.599	−40 38 07.46	0.318	2.612	–	4.41	–	–	–	–
229	G270.1−02.9	08 59 02.971	−50 23 39.68	0.262	1.373	–	3.64	–	–	–	–
231	G277.1−01.5	09 37 51.861	−54 27 08.59	0.724	3.141	–	3.94	–	–	–	–
232	G279.1−00.4	09 53 27.058	−54 52 39.60	0.059	0.866	–	3.46	–	–	–	–
234	G282.6−00.4	10 13 19.673	−56 55 32.24	0.313	3.065	–	3.99	–	–	–	–
235	G285.1−02.7	10 19 32.466	−60 13 29.41	3.022	17.044	–	5.16	–	–	–	–
238	G301.1−01.4	12 34 35.968	−64 18 16.99	2.012	17.086	–	5.08	–	–	–	–
241	G308.5−03.5	13 46 25.712	−65 46 24.26	0.176	2.768	–	3.93	–	–	–	–
243	G313.1+02.1	14 16 51.803	−58 53 10.01	0.136	1.979	–	3.72	–	–	–	–
244	G313.3+01.1	14 15 53.284	−60 01 37.31	0.948	9.663	–	4.49	–	–	–	–
245	G314.4+02.2	14 21 19.909	−58 38 22.10	0.543	5.337	–	4.08	–	–	–	–
246	G316.2+00.8	14 38 19.980	−59 11 46.12	1.053	10.213	–	4.51	–	–	–	–
251	G328.4−02.8	16 09 20.143	−55 36 09.84	0.301	2.054	–	3.85	–	–	–	–
253	G331.3−12.1	17 16 21.107	−59 29 23.35	0.089	2.566	–	3.9	–	–	–	–
254	G336.1+04.1	16 15 02.803	−45 11 54.10	0.314	2.13	–	3.98	–	–	–	–
255	G340.3−03.2	17 03 10.027	−47 00 27.68	18.997	158.829	–	7.92	–	–	–	–
259	G342.2−00.3	16 56 33.989	−43 46 13.55	0.793	9.718	–	4.45	–	–	–	–
261	G343.7−09.6	17 45 33.415	−47 43 50.31	2.362	2.236	–	3.78	–	–	–	–

TABLE 1 (CONTINUED)

KN	NAME	R.A. (2000)	DEC (2000)	F (9 μm)	F (18 μm)	θ	MN_18	F(1.4 GHz)	F(5 GHz)	DIST	DIAM
		H:M:S	D:M:S	Jy	Jy	arcsec	arcsec	mJy	mJy	kpc	pc
263	G344.9−01.9	17 12 22.022	−42 30 41.24	0.487	9.329	–	4.58	–	–	–	–
264	G347.9−06.0	17 40 03.329	−42 24 05.58	–	0.202	–	3.04	–	–	–	–
267	G351.5−06.5	17 52 09.386	−39 32 14.52	–	0.229	–	2.45	–	–	–	–
273	G353.4−02.4	17 39 17.147	−35 46 58.88	0.248	–	–	–	–	–	–	–
276	G353.8−01.2	17 35 27.372	−34 47 42.22	–	0.474	–	2.83	8.2	–	–	–
286	G355.4+02.3	17 25 03.470	−31 28 38.50	–	0.533	–	3.2	10.4	–	–	–
287	G355.4−01.4	17 40 00.347	−33 35 32.29	–	0.34	–	3	8.7	–	–	–
294	G356.8−03.0	17 50 10.734	−33 14 17.97	–	0.436	–	3.03	4.2	–	–	–
295	G357.1+01.2	17 33 50.871	−30 42 36.75	0.206	0.967	–	3.38	11.3	–	–	–
300	G358.4+01.6	17 35 22.745	−29 22 17.40	–	0.452	–	2.91	5.5	–	–	–
301	G358.6−02.4	17 52 00.342	−31 17 49.92	–	0.665	–	3.37	12	–	–	–
308	G359.8+08.9	17 11 38.912	−24 07 32.87	0.755	6.889	–	4.13	–	–	–	–
310	G000.5+01.9	17 39 31.219	−27 27 46.77	–	0.53	–	3.11	6.8	–	–	–
316	G001.5+03.6	17 35 22.074	−25 42 46.48	–	0.934	–	3.45	12.2	–	–	–
318	G001.6+01.5	17 43 16.950	−26 44 17.54	–	0.539	–	3.14	9.8	–	–	–
326	G003.6+04.9	17 35 31.198	−23 11 47.62	–	0.213	–	2.57	4.6	–	–	–
333	G070.9+02.2	20 00 52.927	+34 28 22.18	0.153	3.084	–	4.04	–	–	–	–
335	G000.1−01.2	17 50 24.297	−29 25 18.70	–	2.05	–	3.64	–	–	–	–
339	G000.2−01.4	17 51 53.546	−29 30 53.18	3.23	3.541	–	3.75	–	–	–	–
340	G000.4+01.1	17 42 25.108	−27 55 35.95	–	1.157	–	4.13	23.6	–	–	–
341	G000.6−01.0	17 51 11.504	−28 56 26.16	0.493	–	–	–	–	–	–	–
345	G000.0+02.0	17 37 42.929	−27 49 09.55	–	1.557	–	3.61	6.2		–	–
359	H 1-11	17 21 17.693	−22 18 35.32	–	1.044	6	3.59	20.7	13	7.27	0.211
360	H 1-12	17 26 24.239	−35 01 41.26	–	30.05	<25	6.4	372	719	1.4	–
361	H 1-13	17 28 27.537	−35 07 31.63	–	27.492	14	6.16	474	620	1.39	0.094
363	H 1-15	17 28 37.616	−24 51 06.60	–	1.414	4.3	3.88	13.6	13	7.9	0.165
364	H 1-16	17 29 23.358	−26 26 04.39	0.272	–	2	–	34.7	58	–	–
366	H 1-18	17 29 42.759	−29 32 50.21	0.336	2.667	1.5	3.81	17.6	33	7.37	0.054
368	H 1-2	16 48 54.091	−35 47 09.01	2.425	15.806	1	4.94	14.3	62	–	–
369	H 1-20	17 30 43.799	−28 04 06.68	–	1.924	3.3	3.72	26.9	44	5.12	0.082
371	H 1-22	17 32 22.138	−37 57 23.81	–	1.517	<25	3.6	18.4	–	–	–
373	H 1-24	17 33 37.565	−21 46 24.78	–	1.172	5	3.67	5.1	15	7.32	0.177
374	H 1-26	17 36 29.743	−39 21 56.95	0.385	2.345	<25	5.18	67.1	–	–	–
375	H 1-27	17 40 17.926	−22 19 17.64	–	2.859	5.2	3.88	–	18	10.9	0.275
377	H 1-29	17 44 13.819	−34 17 33.05	0.174	–	<10	–	10.6	–	–	–
379	H 1-30	17 45 06.782	−38 08 49.48	–	0.556	<5	2.97	7	81	5.21	–
381	H 1-32	17 46 06.291	−34 03 46.25	0.266	–	1.1	–	3.4	37	9.09	0.048
382	H 1-33	17 47 49.387	−34 08 05.44	–	0.958	<10	3.5	15.8	12	–	–
383	H 1-34	17 48 07.572	−22 46 47.33	0.352	–	2	–	–	13	–	–
384	H 1-35	17 49 13.940	−34 22 52.96	1.709	19.148	2	4.86	18.4	72	6.03	0.058
385	H 1-36	17 49 48.172	−37 01 29.47	–	20.615	0.8	5.25	11.8	50	–	–
386	H 1-37	17 50 44.569	−39 17 25.98	–	0.508	–	3.56	8.5	–	–	–
388	H 1-39	17 53 21.003	−33 55 58.42	–	1.308	1.7	3.62	10.8	13	10.04	0.083
390	H 1-40	17 55 36.049	−30 33 32.08	1.255	10.494	3	4.48	8.1	31	7.84	0.114
391	H 1-41	17 57 19.145	−34 09 49.12	–	0.557	9.6	3.33	16.6	12	6.6	0.307
392	H 1-42	17 57 25.169	−33 35 42.94	–	1.769	5.8	3.77	34.5	40	4.82	0.136
393	H 1-43	17 58 14.430	−33 47 37.51	0.309	3.571	3	4.03	4	6	11.56	0.168
394	H 1-44	17 58 10.641	−31 42 56.08	–	0.484	<5	2.98	8	–	–	–
395	H 1-45	17 58 21.865	−28 14 52.20	5.23	2.443	<10	3.94	–	23.5	8.2	–
396	H 1-46	17 59 02.490	−32 21 43.42	0.303	3.205	1.2	3.94	18.3	43	7.11	0.041
397	H 1-47	18 00 37.596	−29 21 50.22	0.137	2.257	2.5	3.88	8.1	10	10.01	0.121
398	H 1-5	16 57 23.740	−41 37 57.88	1.631	–	–	–	–	–	–	–
399	H 1-50	18 03 53.461	−32 41 42.15	0.189	2.078	1.4	3.69	19.6	31	7.68	0.052
402	H 1-53	18 05 57.404	−26 29 41.50	–	0.651	<25	3.15	7.2	–	–	–
403	H 1-54	18 07 07.239	−29 13 06.35	0.192	3.092	2.5	3.87	12.7	31	8.01	0.097
404	H 1-55	18 07 14.542	−29 41 24.51	0.176	0.518	10	3.06	2.5	5.3	–	–
405	H 1-56	18 07 53.880	−29 44 34.26	–	0.894	3	3.37	8.3	7.8	10.98	0.16
407	H 1-58	18 09 13.835	−26 02 28.78	0.638	5.951	–	4.24	2.7	–	–	–
408	H 1-59	18 11 29.263	−27 46 15.69	–	0.317	6	2.99	3.4	4.2	11.12	0.323
410	H 1-60	18 12 25.155	−27 29 12.96	–	0.411	3.46	2.73	–	11.3	8.59	0.144
411	H 1-61	18 12 33.977	−24 50 00.28	0.427	–	<25	–	4.7	–	–	–
412	H 1-62	18 13 17.951	−32 19 42.74	0.123	1.979	–	3.78	11.9	–	–	–
413	H 1-63	18 16 19.336	−30 07 35.98	0.578	4.882	–	4.02	2.5	9	–	–
414	H 1-64	18 18 23.908	−23 24 57.15	–	0.297	<25	2.71	8.1	–	–	–
415	H 1-65	18 20 08.847	−24 15 05.09	0.195	2.52	2.5	3.75	5.9	10	10.23	0.124
416	H 1-66	18 24 57.539	−25 41 55.76	–	0.419	<10	3.53	10.4	6	9.5	–
417	H 1-67	18 25 04.976	−22 34 52.64	0.1	–	6	–	12.2	11.9	7.51	0.218
418	H 1-7	17 10 27.389	−41 52 49.42	1.893	13.029	–	4.72	–	–	–	–
419	H 1-8	17 14 42.902	−33 24 47.21	0.292	2.295	3.4	3.99	22.2	–	–	–
421	H 2-1	17 04 36.257	−33 59 18.75	0.967	8.184	2.4	4.23	51.5	61	5.84	0.068
422	H 2-10	17 27 32.848	−28 31 06.90	–	1.045	2	3.44	13.4	20	8.21	0.08
423	H 2-11	17 29 25.947	−25 49 06.64	0.248	–	1.5	–	11.5	27.7	–	–
425	H 2-13	17 31 08.084	−30 10 28.00	–	1.052	–	3.38	17.2	–	–	–
426	H 2-14	17 32 20.093	−39 51 25.60	–	0.326	15	3.7	5.2	4.9	–	–
430	H 2-18	17 43 28.751	−21 09 51.29	–	0.428	3.5	3.26	10.1	11	–	–
431	H 2-20	17 45 39.767	−25 40 00.04	–	1.474	3.5	3.66	13.1	16.3	7.5	0.127
432	H 2-22	17 47 33.926	−21 47 23.11	–	0.236	<8	2.3	5.4	–	–	–
433	H 2-23	17 48 57.994	−34 21 53.28	–	0.269	–	2.48	5.3	–	–	–
434	H 2-24	17 48 36.494	−24 16 34.26	–	3.535	4.9	4	4.5	13	7.77	0.185
437	H 2-27	17 51 50.576	−33 47 35.59	0.098	0.541	–	3	7.9	–	–	–
440	H 2-31	17 56 02.350	−28 14 11.36	–	0.877	–	3.37	5.3	–	–	–
442	H 2-33	17 58 12.535	−31 08 05.99	–	0.393	8	3.25	8.1	5	9.71	0.377
446	H 2-39	18 08 05.759	−28 26 10.50	–	0.208	–	2.43	4.9	–	–	–
450	H 2-43	18 12 47.953	−28 19 59.67	0.802	0.702	9	3.28	–	26.4	5.03	0.219
452	H 2-45	18 14 28.844	−24 43 38.35	–	0.317	4.447	2.82	13.2	–	–	–
454	H 2-48	18 46 35.149	−23 26 48.24	0.65	9.835	2	4.26	31.6	66	6.23	0.06

TABLE 1 (CONTINUED)

KN	NAME	R.A. (2000)	DEC (2000)	F (9 μm)	F (18 μm)	θ	MN_18	F(1.4 GHz)	F(5 GHz)	DIST	DIAM
		H:M:S	D:M:S	Jy	Jy	arcsec	arcsec	mJy	mJy	kpc	pc
455	H 2-7	17 23 24.936	−28 59 06.05	–	0.702	4.2	3.47	11.3	9	9.18	0.187
457	H 3-29	04 37 23.484	+25 02 40.94	0.087	0.711	21	4.06	18.3	18	3.4	0.346
462	HaTr 11	19 02 59.373	+03 02 20.77	–	0.566	–	3.74	17	83	–	–
465	HaTr 2	15 30 18.542	−61 01 38.79	–	0.199	–	2.95	–	–	–	–
474	Hb 12	23 26 14.814	+58 10 54.65	11.885	40.599	0.8	6.06	–	45	10.46	0.041
476	Hb 5	17 47 56.187	−29 59 41.91	–	41.232	3.4	6.43	179.5	548	1.32	0.022
477	Hb 6	17 55 07.023	−21 44 39.98	1.144	–	6	–	190.5	243	2.45	0.071
478	Hb 7	18 55 37.950	−32 15 47.07	0.161	2.143	4	3.78	25.4	30	5.9	0.114
479	He 1-1	19 23 46.875	+21 06 38.60	–	0.611	8	3.4	16	14	–	–
480	He 1-2	19 26 37.757	+21 09 27.04	0.125	2.281	4.7	4.01	14.6	15	–	–
481	He 1-3	19 48 26.422	+22 08 37.62	0.12	–	8	–	53.5	–	–	–
483	He 1-5	20 11 56.057	+20 20 04.43	14.057	5.46	36	4.07	4.8	5.2	6.71	1.171
485	He 2-101	13 54 55.721	−58 27 16.46	1.096	1.054	<10	3.55	–	–	–	–
486	He 2-102	13 58 13.866	−58 54 31.78	0.215	1.276	9	4.09	–	33	3.77	0.164
487	He 2-104	14 11 52.077	−51 26 24.18	7.077	7.358	5	4.24	–	15	–	–
489	He 2-107	14 18 43.339	−63 07 09.48	0.155	4.631	10	4.49	–	65	2.97	0.144
490	He 2-108	14 18 08.889	−52 10 39.76	0.179	4.04	11	4.76	–	32	3.49	0.186
494	He 2-112	14 40 30.924	−52 34 56.66	0.271	3.3	14.6	3.93	–	82	2.36	0.167
495	He 2-113	14 59 53.523	−54 18 07.20	62.991	209.197	–	7.79	–	115	–	–
499	He 2-117	15 05 59.193	−55 59 16.53	1.558	20.941	5	5.32	–	267	2.69	0.065
500	He 2-118	15 06 13.731	−42 59 56.46	–	0.87	5	3.5	–	10	–	–
502	He 2-120	15 11 56.388	−55 39 46.67	–	0.567	27	4.07	–	26	2.51	0.329
503	He 2-123	15 22 19.360	−54 08 12.77	0.419	2.327	4.6	3.88	–	110	3.59	0.08
504	He 2-125	15 23 36.326	−53 51 27.95	0.109	1.87	3	3.84	–	20.4	6.96	0.101
505	He 2-128	15 25 07.841	−51 19 42.29	0.201	2.529	5	3.86	–	40	–	–
506	He 2-129	15 25 32.677	−52 50 37.96	0.143	1.474	1.6	3.59	–	35	7.85	0.061
507	He 2-131	15 37 11.210	−71 54 52.89	2.586	50.505	6	6.43	–	325	2.2	0.064
508	He 2-132	15 38 01.182	−58 44 42.07	0.232	1.382	17.8	4.82	–	25	3.02	0.261
509	He 2-133	15 41 58.788	−56 36 25.72	1.254	16.766	<10	5.03	–	210	3.18	–
510	He 2-136	15 52 10.666	−62 30 46.94	0.137	0.588	10	3.14	–	23	–	–
511	He 2-138	15 56 01.694	−66 09 09.23	1.015	21.099	7	5.5	–	76	3.61	0.123
512	He 2-140	15 58 08.063	−55 41 50.13	0.309	6.339	2.6	4.32	–	80	5.03	0.063
513	He 2-141	15 59 08.762	−58 23 53.15	0.151	1.255	13.8	4.26	–	51	2.77	0.185
514	He 2-142	15 59 57.608	−55 55 32.89	4.033	15.811	3.6	4.89	–	65	4.75	0.083
515	He 2-143	16 00 59.125	−55 05 39.74	0.854	8.233	5.2	4.34	–	120	3.32	0.084
516	He 2-145	16 08 58.902	−51 01 57.74	–	0.713	<25	5.98	–	–	–	–
518	He 2-147	16 14 01.045	−56 59 27.78	5.208	2.678	–	3.65	–	–	–	–
519	He 2-149	16 14 24.266	−54 47 38.82	–	0.542	3	2.96	–	10	8.52	0.124
520	He 2-15	08 53 30.701	−40 03 42.08	0.227	1.209	23.8	4.64	94.5	105	1.92	0.222
521	He 2-151	16 15 42.269	−59 54 00.96	0.616	12.148	5	4.62	–	10	–	–
522	He 2-152	16 15 20.031	−49 13 20.76	1.234	7.995	11	4.64	–	196	2.09	0.111
524	He 2-155	16 19 23.101	−42 15 35.98	0.223	0.721	14.6	3.72	–	70	2.47	0.175
525	He 2-157	16 22 14.264	−53 40 54.09	–	1.951	<5	3.89	–	30	6.24	–
526	He 2-158	16 23 30.605	−58 19 22.64	–	0.455	2	3.37	–	2.7	14.71	0.143
527	He 2-159	16 24 21.417	−54 36 02.82	–	0.303	10	2.52	–	25	3.9	0.189
528	He 2-161	16 24 37.786	−53 22 34.14	0.113	0.717	10	3.43	–	32	3.64	0.176
529	He 2-162	16 27 50.914	−54 01 28.36	0.25	0.927	<5	3.78	–	28	–	–
531	He 2-164	16 29 53.255	−53 23 15.37	0.226	1.529	16	4.6	–	97	2.17	0.168
533	He 2-169	16 34 13.328	−49 21 13.20	0.338	1.699	21.8	4.6	–	128	2.7	0.285
534	He 2-170	16 35 21.170	−53 50 11.11	0.16	1.675	5	3.8	–	15	–	–
535	He 2-171	16 34 04.240	−35 05 26.93	4.775	3.186	10	3.75	–	10	–	–
536	He 2-175	16 39 28.112	−36 34 16.41	0.183	–	6.6	–	19.2	26.8	4.58	0.147
538	He 2-182	16 54 35.167	−64 14 28.43	0.365	4.408	10	4.21	–	62	–	–
539	He 2-185	17 01 17.254	−70 06 03.35	–	0.506	10	3.17	–	18	–	–
540	He 2-186	16 59 36.064	−51 42 06.46	0.091	0.752	3	3.44	–	21	6.9	0.1
541	He 2-187	17 01 36.976	−50 22 57.49	–	0.549	6	3.65	–	–	–	–
543	He 2-21	09 13 52.823	−55 28 16.80	–	0.237	<10	2.46	–	16	8.21	–
545	He 2-25	09 18 01.308	−54 39 29.01	1.781	3.827	4.4	3.95	–	827.9	2.07	0.044
546	He 2-250	17 34 54.710	−26 35 56.92	–	0.728	5	3.4	15.3	15	7.01	0.17
547	He 2-26	09 19 27.476	−59 12 00.39	0.171	1.109	<10	3.54	–	40	1.91	–
548	He 2-262	17 40 12.814	−26 44 21.37	–	1.082	<10	3.46	24.1	26	6.64	–
549	He 2-28	09 22 06.825	−54 09 38.60	–	0.123	10	1.95	–	20	4.15	0.201
550	He 2-29	09 24 45.834	−54 36 15.45	–	0.326	14	3.07	–	24	3.41	0.231
551	He 2-306	17 56 33.706	−43 03 18.90	–	0.83	–	3.32	–	–	–	–
553	He 2-34	09 41 13.997	−49 22 47.18	8.941	6.16	<10	4.19	–	–	–	–
554	He 2-35	09 41 37.504	−49 57 58.71	–	1.009	5	3.61	–	20	5.61	0.136
555	He 2-36	09 43 25.538	−57 16 55.44	0.192	1.686	22	4.25	–	90	3.1	0.331
559	He 2-41	10 07 23.611	−63 54 30.06	–	0.393	<10	2.94	–	41	3.39	–
561	He 2-428	19 13 05.239	+15 46 39.80	–	0.331	8	2.99	26.7	7	6.16	0.239
562	He 2-429	19 13 38.422	+14 59 19.21	0.271	2.24	4.2	3.96	58.5	64.9	4.33	0.088
563	He 2-430	19 14 04.197	+17 31 32.92	0.255	–	1.7	–	18.2	40	7.36	0.061
564	He 2-432	19 23 24.821	+21 08 00.50	0.152	1.286	2.3	3.61	21.3	32	6.88	0.077
565	He 2-434	19 33 49.420	−74 32 58.66	–	1.035	10	3.42	–	–	–	–
566	He 2-436	19 32 06.701	−34 12 57.43	0.327	0.457	10	2.86	–	23	–	–
567	He 2-437	19 32 57.657	+26 52 43.35	2.839	5.478	–	4.11	6.6	–	–	–
568	He 2-440	19 38 08.403	+25 15 40.98	0.233	2.995	2.2	3.98	26.4	43	6.45	0.069
569	He 2-442	19 39 43.376	+26 29 33.05	14.02	7.485	<10	4.24	–	6	–	–
570	He 2-447	19 45 22.164	+21 20 04.03	0.951	6.286	1.2	4.21	22.9	60	7.63	0.044
571	He 2-459	20 13 57.898	+29 33 55.94	2.042	17.276	1.3	5.12	13.9	64	7.24	0.046
572	He 2-47	10 23 09.143	−60 32 42.21	1.4	22.347	5	5.53	–	170	–	–
574	He 2-5	07 47 20.022	−51 15 03.42	0.08	1.011	3	3.51	–	29	6.3	0.092
577	He 2-55	10 48 43.168	−56 03 10.21	–	0.324	<25	3.58	–	–	–	–
579	He 2-62	11 17 43.157	−70 49 32.41	0.075	0.692	<10	3.36	–	–	–	–
582	He 2-67	11 28 47.369	−60 06 37.28	0.224	1.375	5	3.64	–	41	–	–
583	He 2-68	11 31 45.427	−65 58 13.67	0.369	2.549	10	3.9	–	34	–	–
584	He 2-7	08 11 31.890	−48 43 16.71	0.102	0.596	44.6	3.27	–	47	2.91	0.629

TABLE 1 (CONTINUED)

KN	NAME	R.A. (2000)	DEC (2000)	F (9 μm)	F (18 μm)	θ	MN_18	F(1.4 GHz)	F(5 GHz)	DIST	DIAM
		H:M:S	D:M:S	Jy	Jy	arcsec	arcsec	mJy	mJy	kpc	pc
586	He 2-71	11 39 11.198	−68 52 09.14	0.298	3.484	5	3.95	–	12	–	–
588	He 2-73	11 48 38.191	−65 08 37.33	0.378	3.875	4	3.99	–	76	4.23	0.082
589	He 2-76	12 08 25.433	−64 12 09.32	–	0.467	–	3.43	–	–	–	–
590	He 2-78	12 09 10.196	−58 42 37.44	–	0.717	–	3.4	–	–	–	–
591	He 2-81	12 23 01.237	−64 01 45.96	–	0.308	<25	2.7	–	–	–	–
593	He 2-83	12 28 43.997	−62 05 35.05	0.357	6.569	–	4.27	–	–	–	–
594	He 2-84	12 28 46.822	−63 44 37.22	–	0.261	–	2.56	–	–	–	–
595	He 2-85	12 30 07.567	−63 53 00.32	0.463	3.29	10.2	4.26	–	111.7	2.53	0.125
596	He 2-86	12 30 30.426	−64 52 05.58	1.102	12.943	3.6	4.81	–	125	3.85	0.067
598	He 2-9	08 28 27.988	−39 23 40.27	0.754	6.989	4.4	4.37	135.6	194.8	3.11	0.066
599	He 2-90	13 09 36.252	−61 19 35.96	32.451	62.806	10	6.59	–	25	–	–
600	He 2-96	13 42 36.150	−61 22 29.18	0.762	7.397	–	4.25	–	–	–	–
601	He 2-97	13 45 22.394	−71 28 56.13	0.419	4.989	5	4.03	–	30	–	–
602	He 2-99	13 52 30.683	−66 23 26.49	0.366	5.097	17	5.04	–	18	3.4	0.28
603	He 3-1333	17 09 00.932	−56 54 48.25	118.338	165.011	–	7.72	–	26	–	–
605	Hf 2-2	18 32 30.935	−28 43 20.47	–	0.3	–	2.31	4.4	–	–	–
606	Hf 39	10 53 59.586	−60 26 44.31	1.092	8.06	–	10.32	–	–	–	–
607	Hf 48	11 03 55.979	−60 36 04.57	–	0.416	–	3.26	–	–	–	–
608	Hu 1-1	00 28 15.614	+55 57 54.71	0.2	0.665	10	3.59	28	26	3.86	0.187
609	Hu 1-2	21 33 08.349	+39 38 09.57	0.211	1.849	6.5	4.21	107	155	2.53	0.08
610	Hu 2-1	18 49 47.562	+20 50 39.46	0.782	5.679	1.8	4.24	42.6	110	4.52	0.039
612	IC 1297	19 17 23.459	−39 36 46.40	0.32	1.45	7	3.93	59.4	68.9	3.75	0.127
614	IC 1747	01 57 35.896	+63 19 19.36	0.499	2.162	13	4.28	85.8	124	2.23	0.141
615	IC 2003	03 56 21.984	+33 52 30.59	0.245	1.539	10	3.93	54.8	30	3.89	0.189
616	IC 2149	05 56 23.908	+46 06 17.32	0.786	9.271	8.4	5.48	177	280	2.03	0.083
617	IC 2165	06 21 42.775	−12 59 13.96	0.485	4.793	9	4.21	180	188	2.47	0.108
618	IC 2448	09 07 06.261	−69 56 30.74	0.417	1.94	10	5.02	–	73	3.41	0.165
619	IC 2501	09 38 47.213	−60 05 30.92	1.939	13.312	2	4.99	–	261	2.09	0.02
620	IC 2553	10 09 20.856	−62 36 48.40	0.817	5.105	9	4.38	–	92	2.85	0.124
621	IC 2621	11 00 20.111	−65 14 57.77	2.614	15.35	5	4.89	–	195	2.94	0.071
622	IC 289	03 10 19.273	+61 19 00.91	–	5.7	36.8	7.95	152	170	1.18	0.211
623	IC 351	03 47 33.143	+35 02 48.50	–	0.637	7	3.51	31.9	27	4.45	0.151
624	IC 3568	12 33 06.834	+82 33 50.29	0.34	3.57	18	5.27	94.1	95	2.47	0.216
626	IC 4191	13 08 47.343	−67 38 37.67	0.961	9.494	14	4.67	–	172	1.95	0.132
627	IC 4406	14 22 26.278	−44 09 04.35	–	1.841	20	5.83	–	110	1.5	0.145
628	IC 4593	16 11 44.545	+12 04 17.06	0.375	9.95	12.8	5.16	90.6	92	2.42	0.15
629	IC 4634	17 01 33.572	−21 49 32.77	0.505	6.146	5.5	4.38	116	100	3.47	0.093
630	IC 4637	17 05 10.506	−40 53 08.44	–	9.044	18.6	5.7	–	132.5	2.29	0.207
631	IC 4642	17 11 45.025	−55 24 01.47	–	2.797	16.6	5.51	–	60	2.52	0.203
633	IC 4673	18 03 18.408	−27 06 22.61	0.692	3.057	16	5.02	53.4	62	3.12	0.242
634	IC 4699	18 18 32.024	−45 59 01.70	–	0.283	5	2.86	–	20	4.91	0.119
635	IC 4732	18 33 54.633	−22 38 40.91	0.203	–	3	–	12.2	49	4.79	0.07
636	IC 4846	19 16 28.220	−09 02 36.57	0.131	2.038	2.9	3.85	38.7	43	5.72	0.08
637	IC 4997	20 20 08.741	+16 43 53.71	1.143	16.078	2	4.97	30.1	127	5.45	0.053
638	IC 5117	21 32 31.027	+44 35 48.53	6.448	26.937	1.5	5.6	34.1	210	5.01	0.036
639	IC 5217	22 23 55.725	+50 58 00.43	0.278	1.772	6.5	3.89	50.4	163	2.71	0.085
643	J 320	05 05 34.313	+10 42 22.73	–	0.545	7.1	3.32	29.6	23	4.63	0.159
644	J 900	06 25 57.275	+17 47 27.19	1.467	4.976	6	4.24	107.8	100	3.29	0.096
653	KFL 15	18 14 19.324	−25 20 51.22	–	0.451	8.5	3.31	11	11.2	–	–
681	K 2-16	16 44 49.050	−28 04 04.56	2.535	–	–	–	–	–	–	–
687	K 3-11	18 41 07.311	−08 55 58.97	0.154	3.265	3	3.99	14.5	17	7.33	0.107
688	K 3-13	18 45 24.582	+02 01 23.85	–	1.335	3.7	3.54	30.6	34	5.5	0.099
689	K 3-14	18 48 32.821	+10 35 50.74	–	0.667	1	3.31	–	4.8	16.89	0.082
690	K 3-15	18 51 41.522	+09 54 53.06	0.478	–	0.3	–	–	4	–	–
692	K 3-17	18 56 18.171	+07 07 26.31	1.967	18.124	8	5.47	319.5	345	2.04	0.079
693	K 3-18	19 00 34.829	−02 11 57.62	–	9.729	3.5	4.82	–	11	13.98	0.235
694	K 3-19	19 01 36.575	−01 19 07.85	0.131	1.262	1.2	3.56	11.8	23	8.93	0.052
695	K 3-2	18 25 00.576	−01 30 52.64	0.082	2.431	2.8	3.77	25.9	31	6.37	0.086
698	K 3-22	19 09 26.658	+12 00 44.05	0.832	0.715	–	3.21	–	–	–	–
699	K 3-24	19 12 05.820	+15 09 04.47	–	0.268	6.2	2.7	8.5	–	–	–
700	K 3-26	19 14 39.178	+00 13 36.29	–	0.286	–	3.03	6.4	0.5	–	–
702	K 3-29	19 15 30.561	+14 03 49.83	0.869	7.708	1	4.29	13.9	65	8.07	0.039
703	K 3-3	18 27 09.338	+01 14 26.88	0.321	1.614	10	4.05	35.9	34	3.43	0.166
704	K 3-30	19 16 27.691	+05 13 19.47	0.11	0.662	3.3	3.23	12.1	23	6.46	0.103
705	K 3-31	19 19 02.666	+19 02 20.85	0.269	2.394	1.5	3.86	16.8	39	7.83	0.057
706	K 3-33	19 22 26.670	+10 41 21.39	–	1.613	1.1	3.83	8.6	17	11.33	0.06
708	K 3-35	19 27 44.036	+21 30 03.83	0.37	6.017	1.7	4.35	14.5	60	6.56	0.054
709	K 3-36	19 32 39.557	+07 27 51.57	–	0.164	–	1.88	3.1	0.2	–	–
710	K 3-37	19 33 46.749	+24 32 27.09	–	0.466	2.5	2.97	14.4	17	7.93	0.096
711	K 3-38	19 35 18.354	+17 13 00.71	0.236	1.362	5	3.81	28.7	31	5.09	0.123
712	K 3-39	19 35 54.469	+24 54 48.20	0.393	4.122	1	4.15	3.6	11	13.35	0.065
713	K 3-4	18 31 00.227	+02 25 27.35	–	0.18	21	2.84	17	21	–	–
714	K 3-40	19 36 21.828	+23 39 47.93	0.216	1.597	4	3.76	17.1	20	6.18	0.12
720	K 3-49	19 54 00.702	+33 22 12.95	0.227	2.631	–	3.87	5.5	7	34.5	–
721	K 3-5	18 31 45.833	+04 05 09.12	0.109	0.276	10	2.86	6.7	3	7.11	0.345
723	K 3-52	20 03 11.435	+30 32 34.15	0.877	7.924	0.7	4.28	16.9	65	9.42	0.032
724	K 3-53	20 03 22.475	+27 00 54.73	1.36	7.328	0.9	4.31	10	69	9.27	0.04
725	K 3-54	20 04 58.639	+25 26 37.36	0.155	0.638	0.8	3.29	4.8	7.5	16.39	0.064
726	K 3-55	20 06 56.210	+32 16 33.60	0.325	2.551	8.2	4.05	86.6	90	2.96	0.118
728	K 3-57	20 12 47.679	+34 20 32.52	0.245	1.861	6.3	3.96	46.8	60	3.72	0.114
731	K 3-60	21 27 26.477	+57 39 06.45	0.962	3.113	1.9	3.92	28	43	6.87	0.063
732	K 3-61	21 30 00.710	+54 27 27.45	0.118	0.606	6	3.25	16.6	14	5.73	0.167
733	K 3-62	21 31 50.203	+52 33 51.64	0.748	6.41	2.5	4.29	59.5	115	4.62	0.056
734	K 3-63	21 39 11.976	+55 46 03.94	–	0.443	7	3.18	8.5	29	–	–
737	K 3-66	04 36 37.243	+33 39 29.87	–	0.91	2.1	3.24	15.4	18	8.42	0.086
738	K 3-67	04 39 47.905	+36 45 42.85	0.119	1.456	2.2	3.74	33.3	42	6.49	0.069

TABLE 1 (CONTINUED)

KN	NAME	R.A. (2000)	DEC (2000)	F (9 μm)	F (18 μm)	θ	MN_18	F(1.4 GHz)	F(5 GHz)	DIST	DIAM
		H:M:S	D:M:S	Jy	Jy	arcsec	arcsec	mJy	mJy	kpc	pc
740	K 3-69	05 41 22.147	+39 15 08.09	0.162	0.838	0.46	3.4	2.9	0.4	13.87	0.031
741	K 3-7	18 34 13.601	−02 27 36.41	0.287	1.77	6.3	3.85	29.5	30	4.52	0.138
746	K 3-76	20 25 04.865	+33 34 50.70	–	0.539	0.2	3.76	5.1	12	–	–
747	K 3-78	20 45 22.710	+50 22 39.92	0.146	0.911	3.8	3.55	14.9	15	6.85	0.126
750	K 3-82	21 30 51.636	+50 00 06.96	–	0.951	24	4.73	35.6	30	2.49	0.29
751	K 3-83	21 35 43.877	+50 54 16.94	–	0.172	5	1.92	4.7	6.5	7.71	0.187
753	K 3-87	22 55 06.987	+56 42 31.14	–	0.181	6	2.45	10.6	4.5	7.91	0.23
755	K 3-90	01 24 58.628	+65 38 36.14	–	0.339	8.5	3.25	12.4	13.9	4.6	0.19
761	K 4-19	19 13 22.624	+03 25 00.30	–	0.708	–	3.33	–	–	–	–
762	K 4-28	19 30 16.668	+14 47 21.84	0.129	2.229	0.6	3.82	5	19	14.27	0.042
764	K 4-41	19 56 34.027	+32 22 12.96	–	0.93	3	3.58	11.5	15	7.59	0.11
765	K 4-47	04 20 45.157	+56 18 11.57	0.264	1.525	7.8	3.7	–	7.7	22.46	0.849
766	K 4-48	06 39 55.879	+11 06 30.69	–	0.707	2.2	3.11	11.8	14	8.86	0.095
770	K 4-57	22 48 34.363	+58 29 08.18	1.46	1.081	–	3.41	–	–	–	–
771	K 4-8	18 54 20.003	−08 47 33.17	–	0.229	–	2.91	3.1	–	–	–
773	KjPn 2	20 15 22.209	+40 34 44.76	0.093	0.661	–	3.36	7.3	–	–	–
781	LoTr 5	12 55 33.745	+25 53 30.60	0.137	–	10.6	–	–	5.6	8.69	0.447
798	MA 13	18 30 30.388	−07 27 38.29	0.182	–	–	–	28.7	–	–	–
800	MA 3	18 17 49.379	−06 48 21.55	–	0.564	–	3.19	6.3	–	–	–
801	MGP 1	16 48 48.548	−35 00 57.39	–	0.601	9	3.26	14.7	10.2	–	–
802	M 1-1	01 37 19.430	+50 28 11.50	–	0.433	4.5	2.92	14	8	7.27	0.159
803	M 1-11	07 11 16.693	−19 51 02.87	6.754	31.786	2.2	5.52	25.9	113	4.9	0.052
804	M 1-12	07 19 21.471	−21 43 55.46	1.03	5.606	1.8	4.21	21.9	41	7.13	0.062
805	M 1-13	07 21 14.952	−18 08 36.91	–	0.502	10	3.31	18.9	15	4.51	0.219
807	M 1-16	07 37 18.955	−09 38 49.67	0.195	1.148	3.6	3.67	31.3	31	5.71	0.1
808	M 1-17	07 40 22.206	−11 32 29.81	0.204	0.982	2.5	3.57	18.3	17	8.23	0.1
810	M 1-19	17 03 46.809	−33 29 43.75	–	1.881	2.8	3.8	23.2	20	–	–
811	M 1-2	01 58 49.675	+52 53 48.57	0.861	1.862	0.5	3.64	–	10	–	–
814	M 1-24	17 38 11.588	−19 37 37.64	0.243	3.627	<10	4.34	43.5	–	–	–
815	M 1-25	17 38 30.307	−22 08 38.88	0.237	–	3.2	–	39.9	57	4.93	0.076
816	M 1-26	17 45 57.653	−30 12 00.58	–	104.933	3.2	7.32	66	400	2.42	0.038
817	M 1-27	17 46 45.450	−33 08 35.06	0.446	–	8	–	64.9	63	3.74	0.145
818	M 1-29	17 50 18.003	−30 34 54.90	–	4.343	8.2	4.21	91.5	97	3.3	0.131
820	M 1-31	17 52 41.440	−22 21 56.83	0.435	5.727	2.3	4.23	28.8	60.5	–	–
821	M 1-32	17 56 19.980	−16 29 03.95	1.481	8.938	9	4.63	70.1	61	3.17	0.138
822	M 1-33	17 58 58.794	−15 32 14.79	0.495	4.194	4	4.03	49	60	4.63	0.09
823	M 1-34	18 01 22.193	−33 17 43.08	–	0.575	11.2	3.68	13.6	14.7	5.95	0.323
824	M 1-35	18 03 39.255	−26 43 33.47	0.514	3.572	<25	4.06	54	54	4.63	–
825	M 1-37	18 05 25.801	−28 22 04.19	0.208	3.508	2.5	4.06	10.9	15	8.44	0.102
826	M 1-38	18 06 05.765	−28 40 29.28	–	3.049	3.5	4.06	14.9	24	6.58	0.112
827	M 1-39	18 07 30.699	−13 28 47.61	0.692	–	4	–	58.2	100	3.92	0.076
828	M 1-4	03 41 43.428	+52 17 00.28	0.284	1.806	6	3.89	77.8	90	3.39	0.099
829	M 1-40	18 08 25.994	−22 16 53.25	1.187	11.344	4.5	4.75	163.3	208	2.83	0.062
831	M 1-42	18 11 05.028	−28 58 59.33	–	0.9	9	3.53	28.3	28.5	4.89	0.213
833	M 1-44	18 16 17.365	−27 04 32.47	0.336	0.841	4	3.37	9.4	9	9.24	0.179
834	M 1-45	18 23 07.984	−19 17 05.26	–	3.09	2.5	4.04	15.1	19	7.43	0.09
835	M 1-46	18 27 56.339	−15 32 54.43	0.327	–	11.5	–	78.1	81	2.58	0.144
838	M 1-5	05 46 50.000	+24 22 02.32	0.86	4.338	2.3	3.98	41.1	71	5.49	0.061
839	M 1-50	18 33 20.886	−18 16 36.86	0.285	2.153	5.6	3.95	35.4	50	4.12	0.112
841	M 1-52	18 33 58.542	−14 52 25.02	–	0.303	43.1	3.17	7.8	319	5.93	1.24
842	M 1-53	18 35 48.267	−17 36 08.71	0.126	1.422	6	4.16	19.6	8	3.93	0.114
843	M 1-54	18 36 08.357	−16 59 57.02	0.215	0.933	13	3.57	35.5	53	3.09	0.195
844	M 1-55	18 36 42.550	−21 48 59.09	1.613	0.475	<25	3.07	–	38	–	–
845	M 1-56	18 37 46.250	−17 05 46.55	0.195	2.641	1.5	3.84	14.6	22	9.48	0.069
846	M 1-57	18 40 20.248	−10 39 47.17	0.413	5.209	8	4.37	53.9	70	3.21	0.125
847	M 1-58	18 42 56.979	−11 06 53.10	0.229	–	6.4	–	37.7	60	3.69	0.114
848	M 1-59	18 43 20.178	−09 04 48.64	0.899	3.844	4.8	4.03	90.1	108	3.54	0.082
849	M 1-6	06 35 45.140	−00 05 37.37	1.139	5.895	3	4.25	54.4	86	4.7	0.068
851	M 1-61	18 45 55.072	−14 27 37.93	–	13.886	1.8	4.81	32.5	97	5.59	0.049
852	M 1-62	18 50 26.030	−22 34 22.54	–	0.23	1.5	2.39	13.5	12.8	–	–
855	M 1-65	18 56 33.639	+10 52 10.05	–	1.665	4	3.79	21	23	5.94	0.115
856	M 1-66	18 58 26.247	−01 03 45.70	0.215	–	2.7	–	45.7	59	5.39	0.071
857	M 1-67	19 11 30.881	+16 51 38.21	0.955	–	120.4	–	217.6	250	0.69	0.403
858	M 1-69	19 13 53.961	+03 37 41.90	0.23	1.813	–	3.85	31.4	–	–	–
859	M 1-7	06 37 20.955	+24 00 35.38	–	0.422	11	3.18	18.5	13	4.5	0.24
860	M 1-71	19 36 26.927	+19 42 23.99	1.507	15.253	3	4.89	83.8	204	–	–
861	M 1-72	19 41 33.975	+17 45 17.71	0.547	6.554	0.7	4.25	5.3	30	12.54	0.043
862	M 1-73	19 41 09.323	+14 56 59.37	0.16	3.83	6	4.27	47.7	43	4.17	0.121
863	M 1-74	19 42 18.874	+15 09 08.16	0.292	3.285	1	3.99	7.9	29	10.15	0.049
864	M 1-75	20 04 44.086	+31 27 24.42	0.187	0.739	14	3.81	36.5	26.2	3.32	0.225
865	M 1-77	21 19 07.360	+46 18 47.24	1.874	6.154	8	5.23	29.4	25	4.29	0.166
866	M 1-78	21 20 44.809	+51 53 27.88	19.514	226.731	6	8.41	363.5	1103.9	1.62	0.047
868	M 1-8	06 53 33.795	+03 08 26.96	–	0.303	18.4	2.92	16.3	23	3.06	0.273
869	M 1-80	22 56 19.806	+57 09 20.68	–	0.336	8	2.96	17.9	25	4.29	0.166
870	M 1-9	07 05 19.204	+02 46 59.16	0.113	0.941	2.3	3.34	22.4	27	7.22	0.081
873	M 2-12	17 24 01.451	−25 59 23.16	–	2.228	4.4	3.85	10.3	12.9	–	–
874	M 2-13	17 28 34.188	−13 26 20.82	–	0.888	1.5	3.35	9.7	13	10.68	0.078
876	M 2-15	17 46 54.449	−16 17 24.80	–	0.87	7.4	3.64	18.7	12.5	5.37	0.193
877	M 2-16	17 52 34.362	−32 45 51.10	–	1.38	2.5	3.56	20.4	24.8	5.86	0.071
878	M 2-17	17 52 04.896	−17 36 05.23	0.107	–	8	–	10.6	10	5.57	0.216
879	M 2-18	17 53 37.844	−32 58 47.93	–	1.349	1.5	3.69	11.1	17	9.4	0.068
880	M 2-19	17 53 45.619	−29 43 46.34	0.182	0.52	7.5	3.27	10.5	14	7.4	0.269
881	M 2-2	04 13 15.045	+56 56 58.08	0.31	1.828	6.5	4.57	52	54	3.66	0.115
882	M 2-20	17 54 25.422	−29 36 08.20	0.127	1.934	16.4	3.83	22.2	3.2	–	–
883	M 2-21	17 58 09.565	−29 44 20.08	0.305	0.789	3	3.42	20.3	23	7.01	0.102
884	M 2-22	17 58 32.634	−33 28 36.60	–	0.49	5.2	2.92	9.1	6.5	9.87	0.249

TABLE 1 (CONTINUED)

KN	NAME	R.A. (2000)	DEC (2000)	F (9 μm)	F (18 μm)	θ	MN_18	F(1.4 GHz)	F(5 GHz)	DIST	DIAM
		H:M:S	D:M:S	Jy	Jy	arcsec	arcsec	mJy	mJy	kpc	pc
885	M 2-23	18 01 42.610	−28 25 43.90	–	6.155	8.8	3.98	4.2	41	8.38	0.358
886	M 2-24	18 02 02.881	−34 27 47.07	–	3.19	6.8	3.94	3.2	3	11.79	0.389
888	M 2-26	18 03 11.844	−26 58 30.23	–	0.398	7	2.76	7.9	5	9.43	0.32
889	M 2-27	18 03 52.588	−31 17 46.54	–	3.369	3.8	4	22.5	50	5.65	0.104
890	M 2-28	18 05 02.695	−30 58 17.39	–	0.508	5.3	3.22	11.3	10	8.39	0.216
891	M 2-29	18 06 40.862	−26 54 55.95	–	1.179	<5	4.08	9.4	8	9.98	–
892	M 2-30	18 12 34.414	−27 58 11.59	0.131	0.924	3.5	3.4	13.9	14	8.1	0.137
893	M 2-31	18 13 16.026	−25 30 04.97	0.223	1.653	4	3.66	39.6	51	4.91	0.095
894	M 2-32	18 14 50.617	−32 36 55.21	–	0.585	<10	3.29	9.5	–	–	–
895	M 2-33	18 15 06.534	−30 15 32.89	–	1.138	5	3.77	11.9	12	8.52	0.207
898	M 2-36	18 17 41.418	−29 08 19.59	0.218	–	6.8	–	22.6	13	6.99	0.23
900	M 2-38	18 19 25.162	−26 35 19.92	–	0.522	8	3.2	7.5	8	8.13	0.315
901	M 2-39	18 22 01.148	−24 10 40.18	0.211	0.802	3.2	3.37	7.2	8	10.21	0.158
902	M 2-4	17 01 06.231	−34 49 38.58	0.194	2.996	2	3.87	24.5	32	7.15	0.069
903	M 2-40	18 21 23.851	−06 01 55.79	–	3.62	5.5	4.19	45.5	33	4.67	0.125
905	M 2-42	18 22 32.020	−24 09 28.40	–	0.455	3.9	3.08	9.6	14	7.83	0.148
906	M 2-43	18 26 40.048	−02 42 57.63	9.659	32.6	1.5	5.68	20.4	237	5	0.036
907	M 2-44	18 37 36.908	−03 05 55.96	0.385	2.105	8	3.89	48.3	54	3.45	0.134
908	M 2-45	18 39 21.837	−04 19 50.90	0.76	6.161	6.4	4.28	107	154	2.64	0.082
909	M 2-46	18 46 34.620	−08 28 01.85	0.111	0.455	4.4	3.12	13.1	12	6.48	0.138
910	M 2-47	19 13 34.559	+04 38 04.45	0.18	2.89	6	4.04	38.3	45	4.12	0.12
911	M 2-48	19 50 28.543	+25 54 30.21	–	0.376	4	2.79	16.9	19	7	0.136
912	M 2-49	21 43 17.624	+50 25 14.57	0.408	1.202	2.5	3.5	28.2	35	6.47	0.078
913	M 2-5	17 02 19.069	−33 10 05.01	0.202	–	5	–	14.1	12	7.69	0.186
914	M 2-50	21 57 41.814	+51 41 39.01	–	0.183	4.6	2.45	8.2	6.5	8.07	0.18
916	M 2-52	22 20 30.745	+57 36 21.62	–	0.133	13.5	2.39	14.9	14	3.97	0.26
917	M 2-53	22 32 17.720	+56 10 26.12	–	0.291	18	2.74	14.6	11	3.64	0.318
918	M 2-54	22 51 38.923	+51 50 42.50	0.22	6.06	–	4.19	5.4	8	14.61	–
920	M 2-6	17 04 18.326	−30 53 28.71	–	0.751	2	3.15	13.6	17	–	–
922	M 2-8	17 05 30.673	−32 32 08.30	0.231	0.921	4	3.5	16.2	18	7.27	0.141
923	M 2-9	17 05 37.952	−10 08 34.58	38.07	73.255	17.5	6.93	37.1	36	3.01	0.255
924	M 3-1	07 02 49.980	−31 35 31.50	–	0.21	11.2	2.71	25.7	24	3.78	0.205
925	M 3-10	17 27 20.152	−28 27 51.15	0.311	2.611	3.1	3.81	35.2	29	6.33	0.095
926	M 3-12	17 36 22.634	−21 31 12.22	–	0.616	7.5	3.01	11.2	12.5	6.98	0.254
927	M 3-13	17 41 36.594	−22 13 02.46	0.862	1.893	<7	3.73	–	–	–	–
928	M 3-14	17 44 20.598	−34 06 40.59	0.344	1.89	4	3.91	22.6	30	6.47	0.125
930	M 3-17	17 56 25.640	−31 04 16.82	–	1.075	<5	3.43	10	12	9	–
931	M 3-19	17 58 19.337	−30 00 39.32	–	0.8	7	3.5	7.9	7.4	8.62	0.293
933	M 3-20	17 59 19.318	−28 13 48.05	0.091	–	4	–	16.2	40	5.3	0.103
934	M 3-21	18 02 32.324	−36 39 12.24	0.265	2.617	<5	3.92	15.6	30	5.57	–
935	M 3-22	18 02 19.238	−30 14 25.38	–	0.451	6.4	3.15	10.1	8.7	8.45	0.262
936	M 3-23	18 07 06.148	−30 34 16.96	0.231	1.245	11.5	3.85	30	28	4.58	0.255
937	M 3-24	18 07 53.914	−25 24 02.71	–	0.887	<25	3.4	17.4	–	–	–
938	M 3-25	18 15 16.967	−10 10 09.47	0.831	–	1.5	–	25	76	6.89	0.05
939	M 3-26	18 16 11.405	−27 14 57.46	–	0.479	7	2.96	8.1	8	8.4	0.285
940	M 3-27	18 27 48.273	+14 29 06.06	0.21	0.996	1	3.55	–	53.2	8.55	0.041
941	M 3-28	18 32 41.288	−10 05 50.03	–	1.446	9	5.11	–	33	4.87	0.212
945	M 3-31	18 44 01.767	−19 54 52.52	–	1.205	<10	3.44	–	9	14.79	–
946	M 3-32	18 44 43.127	−25 21 33.85	0.159	0.705	7.5	3.27	12.2	12	7.06	0.257
947	M 3-33	18 48 12.131	−25 28 52.39	–	0.47	6	3.32	9.8	7.5	8.94	0.26
948	M 3-34	19 27 01.897	−06 35 04.63	0.154	1.764	8	3.91	29.6	29	4.12	0.16
949	M 3-35	20 21 03.769	+32 29 23.86	3.437	16.454	1.5	4.97	29.5	140	5.62	0.041
950	M 3-36	17 12 39.152	−25 43 37.39	–	0.577	3.2	3.22	4.9	3.5	13.92	0.216
953	M 3-39	17 21 11.505	−27 11 38.13	1.177	–	19	–	279.4	280	1.7	0.157
956	M 3-41	17 25 59.784	−29 21 50.15	–	1.007	<25	3.35	11.3	75	4.15	–
958	M 3-43	17 50 24.297	−29 25 18.70	–	2.05	3.8	3.64	–	27.2	6.2	0.114
959	M 3-44	17 51 18.894	−30 23 52.99	0.342	6.899	4.2	4.35	24.3	35	–	–
960	M 3-45	17 52 05.927	−30 05 13.81	–	0.614	3.5	3	20.4	24.3	–	–
965	M 3-5	08 02 28.932	−27 41 55.44	–	0.286	7	2.91	11	10	5.9	0.2
969	M 3-53	18 24 07.890	−11 06 42.08	0.233	1.24	–	3.61	19.5	–	–	–
970	M 3-54	18 33 03.745	−13 44 19.95	–	0.422	5.6	3.01	8.6	8	6.92	0.188
972	M 3-6	08 40 40.205	−32 22 33.22	0.407	5.983	11	4.95	77.4	75	2.74	0.146
973	M 3-7	17 24 34.429	−29 24 19.47	0.096	1.553	5	3.08	32.9	28	5.41	0.131
974	M 3-8	17 24 52.152	−28 05 54.61	0.297	–	3.2	–	18	20	7.45	0.116
975	M 3-9	17 25 43.364	−26 11 55.47	0.364	2.22	16	3.81	37.3	35	3.88	0.301
976	M 4-10	18 34 13.821	−13 12 24.57	–	1.92	1.2	3.81	12.1	33	9.04	0.053
979	M 4-17	20 09 01.927	+43 43 43.54	–	0.447	–	3.36	20	–	–	–
980	M 4-18	04 25 50.831	+60 07 12.72	1.687	6.346	3.75	4.22	18.5	22	6.37	0.116
981	M 4-2	07 28 53.808	−35 45 13.92	–	0.481	6	3.25	24.2	19	5.26	0.153
983	M 4-4	17 28 50.344	−30 07 44.47	0.088	–	–	–	13.9	9.8	–	–
985	M 4-7	17 51 44.663	−31 36 00.18	–	0.775	5.7	3.18	38	33	5.2	0.144
986	M 4-8	18 12 09.587	−10 42 58.30	0.117	2.155	1.4	3.67	10.7	19	10.21	0.069
989	MaC 1-11	18 14 50.890	−22 43 55.43	–	0.399	–	3.01	12.2	–	–	–
990	MaC 1-13	18 28 35.242	−08 43 22.82	–	0.683	–	3.5	30.4	–	–	–
1000	MeWe 1-7	16 47 57.070	−50 42 48.32	–	0.356	–	3.3	–	–	–	–
1003	Me 1-1	19 39 09.813	+15 56 48.13	0.45	0.931	4.7	3.46	36	45.1	4.58	0.104
1004	Me 2-1	15 22 19.274	−23 37 31.34	–	0.93	7	3.55	33.6	30	4.32	0.147
1005	Me 2-2	22 31 43.686	+47 48 03.96	0.606	2.556	1.2	3.85	16	40	8.56	0.05
1006	MyCn 18	13 39 35.116	−67 22 51.45	0.862	10.869	12.6	4.66	–	106	3.23	0.197
1007	My 60	10 31 33.390	−55 20 50.87	0.244	1.646	7.6	4.29	–	60	3.47	0.128
1009	Mz 2	16 14 32.433	−54 57 03.76	–	1.763	23	5.5	–	75	2	0.223
1010	Mz 3	16 17 13.392	−51 59 10.31	55.324	267.948	25.4	8.95	–	649	1.03	0.127
1014	NGC 1535	04 14 15.762	−12 44 22.03	1.037	5.562	18.4	8.8	167.8	160	1.77	0.158
1015	NGC 2022	05 42 06.229	+09 05 10.75	0.371	3.789	19.4	6.04	92.3	91	2.02	0.19
1017	NGC 2346	07 09 22.547	−00 48 22.98	0.505	0.595	54.6	3.64	37.6	86	2.07	0.548
1019	NGC 2392	07 29 10.768	+20 54 42.44	0.476	4.368	44.8	6.48	279.9	251	1.44	0.313

TABLE 1 (CONTINUED)

KN	NAME	R.A. (2000)	DEC (2000)	F (9 μm)	F (18 μm)	θ	MN_18	F(1.4 GHz)	F(5 GHz)	DIST	DIAM
		H:M:S	D:M:S	Jy	Jy	arcsec	arcsec	mJy	mJy	kpc	pc
1021	NGC 2452	07 47 26.248	−27 20 07.16	0.288	1.798	18.8	4.71	56	57	2.31	0.211
1024	NGC 2792	09 12 26.596	−42 25 39.90	0.399	3.618	13	5.13	–	116	1.26	0.079
1026	NGC 2867	09 21 25.337	−58 18 40.69	1.312	7.277	16	4.98	–	252	1.69	0.131
1028	NGC 3132	10 07 01.771	−40 26 11.11	0.883	3.437	45	8.18	–	230	1.5	0.327
1029	NGC 3195	10 09 20.910	−80 51 30.73	–	0.933	40	5.07	–	35	1.96	0.38
1030	NGC 3211	10 17 50.549	−62 40 14.57	0.286	2.113	16	4.52	–	228	1.7	0.132
1031	NGC 3242	10 24 46.138	−18 38 32.26	3.211	19.833	37.2	8.87	757.7	860	0.94	0.17
1034	NGC 3918	11 50 17.730	−57 10 56.90	2.747	27.613	18.8	6.14	–	859	1.17	0.107
1035	NGC 40	00 13 01.023	+72 31 19.07	–	54.443	36.4	9.48	510.3	460	0.98	0.173
1037	NGC 4361	12 24 30.754	−18 47 05.51	–	4.061	81	9.86	159.9	207	0.74	0.291
1039	NGC 5307	13 51 03.273	−51 12 20.62	0.26	2.349	12.6	4.41	–	95	2.42	0.148
1040	NGC 5315	13 53 56.972	−66 30 50.96	3.477	34.483	6	5.93	–	442	2.14	0.062
1042	NGC 5882	15 16 49.941	−45 38 58.60	2.331	17.353	14	5.78	–	334	1.74	0.118
1048	NGC 6210	16 44 29.521	+23 47 59.55	1.429	13.331	16.2	5.64	297.8	311	1.55	0.122
1050	NGC 6309	17 14 04.322	−12 54 37.71	–	6.375	17	5.63	131.5	151	2.35	0.194
1051	NGC 6326	17 20 46.301	−51 45 15.33	0.248	1.149	12	4.03	–	70	2.71	0.158
1053	NGC 6369	17 29 20.443	−23 45 34.22	7.301	43.871	28	8.47	1825	2002	0.75	0.102
1054	NGC 6439	17 48 19.797	−16 28 44.21	0.37	–	5	–	51.5	55	4.64	0.112
1056	NGC 6537	18 05 13.059	−19 50 34.86	4.099	26.593	4.7	5.63	427.5	640	1.77	0.04
1057	NGC 6543	17 58 33.409	+66 37 58.79	5.539	57.323	18.8	7.39	771.5	850	1.12	0.102
1059	NGC 6565	18 11 52.470	−28 10 42.27	–	1.057	9.2	3.88	47	37	4.36	0.194
1060	NGC 6567	18 13 45.136	−19 04 33.67	1.778	4.466	8.8	4.19	163	168	2.4	0.102
1061	NGC 6572	18 12 06.404	+06 51 12.17	9.597	93.442	10	7.06	557.5	1374	1.06	0.051
1062	NGC 6578	18 16 16.517	−20 27 02.67	1.357	–	8.6	–	158.2	170	2.31	0.096
1063	NGC 6620	18 22 54.186	−26 49 17.00	0.146	0.802	5	3.43	17.1	20.5	6.42	0.156
1064	NGC 6629	18 25 42.449	−23 12 10.59	0.799	–	15	–	257.8	275	1.84	0.134
1065	NGC 6644	18 32 34.641	−25 07 44.00	–	5.547	2.8	5.22	64.3	97	4.09	0.056
1067	NGC 6741	19 02 37.088	−00 26 56.97	0.682	4.923	8	4.25	131.9	230	2.32	0.09
1068	NGC 6751	19 05 55.560	−05 59 32.92	1.398	11.455	21	5.54	55.1	63	2.18	0.222
1071	NGC 6778	19 18 24.939	−01 35 47.41	0.463	1.644	15.8	4.39	64.6	55	2.54	0.195
1073	NGC 6790	19 22 56.965	+01 30 46.45	6.636	21.477	1.8	5.22	52.6	290	4.1	0.036
1074	NGC 6803	19 31 16.490	+10 03 21.88	0.603	5.242	5	4.15	68.9	114	3.26	0.079
1076	NGC 6807	19 34 33.543	+05 41 02.58	0.22	2.85	0.8	3.94	8	29	11.18	0.043
1077	NGC 6818	19 43 57.844	−14 09 11.91	0.851	6.01	18.2	5.55	290.2	300	1.47	0.13
1078	NGC 6826	19 44 48.161	+50 31 30.33	2.539	24.006	25.4	8.75	414.4	385	1.2	0.148
1083	NGC 6879	20 10 26.682	+16 55 21.30	0.111	0.831	5	3.59	23.1	18	5.78	0.14
1084	NGC 6881	20 10 52.464	+37 24 41.18	0.972	9.369	2.6	4.5	70.4	120	4.48	0.056
1085	NGC 6884	20 10 23.669	+46 27 39.54	0.743	6.356	5.3	4.46	152.4	200	2.7	0.069
1086	NGC 6886	20 12 42.813	+19 59 22.65	0.543	4.595	5.5	4.24	77.6	108	2.94	0.078
1087	NGC 6891	20 15 08.838	+12 42 15.63	0.345	4.865	10.2	5.14	110.8	105	2.35	0.116
1089	NGC 6905	20 22 22.940	+20 06 16.80	–	2.166	40.4	6.79	66.7	52	1.62	0.317
1091	NGC 7009	21 04 10.877	−11 21 48.25	5.275	31.698	28.2	7.24	682	750	1.09	0.149
1093	NGC 7027	21 07 01.696	+42 14 09.50	173.674	977.249	12.5	9.36	1362.4	5200	0.64	0.039
1098	NGC 7354	22 40 19.940	+61 17 08.10	2.748	15.223	20	6.85	581	579	1.19	0.115
1099	NGC 7662	23 25 53.968	+42 32 05.04	2.377	15.165	20	6.74	611.5	631	1.17	0.113
1100	Na 1	17 12 51.900	−03 16 00.13	0.083	0.569	8	3.37	23	22.5	4.2	0.163
1105	PB 1	07 02 46.764	−13 42 34.65	–	0.639	–	3.92	11.9	18	–	–
1106	PB 10	19 28 14.391	+12 19 36.17	0.322	2.045	8	3.94	50.4	50	3.53	0.137
1107	PB 2	08 20 40.188	−46 22 58.82	0.164	0.562	3	3.18	–	40	5.75	0.084
1108	PB 3	08 54 18.323	−50 32 22.34	0.256	1.635	7	3.84	–	70	3.4	0.115
1109	PB 4	09 15 07.747	−54 52 43.78	0.243	1.444	11.2	4.12	–	71	2.81	0.153
1110	PB 5	09 16 09.613	−45 28 42.79	3.014	11.328	5	4.71	–	107	–	–
1111	PB 6	10 13 15.949	−50 19 59.28	0.33	3.205	11	4.18	–	30	3.55	0.189
1112	PB 8	11 33 17.717	−57 06 14.00	0.16	2.536	5	4.06	–	27	5.15	0.125
1113	PB 9	19 27 44.814	+10 24 20.82	0.103	1.029	7	3.74	33.1	40	3.57	0.121
1114	PC 11	16 37 42.697	−55 42 26.49	1.164	5.76	5	4.03	–	11	–	–
1115	PC 12	16 43 53.781	−18 57 11.89	–	1.994	2.2	3.8	14.8	19	8.6	0.092
1117	PC 14	17 06 14.767	−52 30 00.40	0.136	0.809	7	3.64	–	30	4.32	0.147
1118	PC 17	17 35 41.677	−46 59 48.54	–	1.063	5	3.58	–	14.7	6.12	0.148
1120	PC 20	18 43 03.456	−00 16 37.02	0.212	1.123	–	3.59	27.3	–	–	–
1122	PC 22	19 42 03.514	+13 50 37.33	–	0.458	–	3.73	9.2	–	–	–
1123	PC 23	19 51 52.770	+32 59 17.48	0.053	0.691	2.2	3.27	10	21	8.06	0.086
1124	PC 24	20 19 38.133	+27 00 11.23	0.184	0.953	5	3.52	17.1	18	5.78	0.14
1127	PM 1-188	17 54 21.100	−15 55 51.78	6.838	4.779	–	3.92	–	–	–	–
1128	PM 1-276	19 02 17.857	+10 17 34.49	–	1.065	–	4.78	15.3	–	–	–
1129	PM 1-295	19 19 18.760	+17 11 48.09	–	2.02	–	5.32	13.9	–	–	–
1130	PM 1-310	19 38 52.135	+25 05 32.63	0.4	–	–	–	–	–	–	–
1132	PM 1-89	15 19 08.724	−53 09 50.05	0.584	6.983	–	4.53	–	–	–	–
1136	Pe 1-1	10 38 27.607	−56 47 06.40	0.846	8.744	3	4.48	–	125.3	4.16	0.061
1137	Pe 1-11	18 01 42.767	−33 15 26.30	–	0.779	9	3.51	10.9	8	7.9	0.345
1141	Pe 1-15	18 46 24.485	−07 14 34.57	0.079	0.722	5	3.49	8.3	8	7.4	0.179
1142	Pe 1-16	18 47 32.251	−06 54 03.52	–	0.555	–	3.33	14.2	–	–	–
1144	Pe 1-18	18 48 46.454	−05 56 07.71	0.486	–	1.1	–	6.6	42	8.44	0.045
1145	Pe 1-19	18 49 44.643	−07 01 35.03	–	0.366	3.9	3.15	4.8	6	8.42	0.158
1146	Pe 1-2	10 39 32.690	−57 06 13.70	0.269	2.818	–	4.1	–	–	–	–
1147	Pe 1-20	18 57 17.351	−05 59 51.79	–	0.191	8.4	2.51	5.1	29.4	4.52	0.183
1148	Pe 1-21	18 57 49.642	−05 27 39.73	–	0.396	8.6	2.81	6.3	30	3.95	0.165
1151	Pe 1-7	16 30 25.852	−46 02 51.10	2.801	23.646	5	5.27	–	117	–	–
1152	Pe 1-8	17 06 22.558	−44 13 09.96	–	2.47	–	5.23	–	–	–	–
1158	Pe 2-14	18 29 59.545	−19 40 37.74	–	0.527	–	3.13	3.7	–	–	–
1160	Pe 2-4	09 30 48.402	−53 09 59.33	0.11	0.663	–	3.34	–	–	–	–
1162	Pe 2-7	10 41 19.574	−56 09 16.34	0.043	0.511	–	3.18	–	–	–	–
1163	Pe 2-8	15 23 42.860	−57 09 25.02	6.342	39.225	1.6	5.99	–	100	5.83	0.045
1167	SaSt 1-1	08 31 42.877	−27 45 31.70	–	1.819	–	3.77	–	0.3	–	–
1168	SaSt 2-12	17 03 02.870	−53 55 54.16	0.175	1.161	–	3.59	–	–	–	–
1169	SaSt 2-3	07 48 03.683	−14 07 40.40	–	0.151	–	2	4	1.4	–	–

TABLE 1 (CONTINUED)

KN	NAME	R.A. (2000)	DEC (2000)	F (9 μm)	F (18 μm)	θ	MN_18	F(1.4 GHz)	F(5 GHz)	DIST	DIAM
		H:M:S	D:M:S	Jy	Jy	arcsec	arcsec	mJy	mJy	kpc	pc
1173	Sa 1-5	17 11 27.372	−47 25 01.58	–	0.364	–	2.4	–	–	–	–
1175	Sa 1-8	18 50 44.312	−13 31 02.18	–	1.15	5.6	3.8	13.5	11	6.33	0.172
1178	Sa 2-237	17 44 42.282	−15 45 11.45	0.703	2.588	–	4	5.4	–	–	–
1179	Sa 3-134	18 29 19.823	−15 07 39.97	0.083	0.927	–	3.54	2.7	–	–	–
1185	ShWi 2-5	18 03 53.660	−29 51 21.89	0.468	0.8	–	3.16	–	–	–	–
1191	Sn 1	16 21 04.421	−00 16 10.54	–	0.426	3	2.95	10.4	7	9.42	0.137
1193	Sp 3	18 07 15.793	−51 01 10.41	–	1.411	35.6	5.04	–	61	1.75	0.302
1196	StWr 4-10	16 02 13.042	−41 33 35.94	–	0.373	–	2.85	–	–	–	–
1198	Ste 2-1	10 11 57.662	−52 38 17.09	–	0.257	–	2.91	–	–	–	–
1201	SwSt 1	18 16 12.237	−30 52 08.71	9.268	52.915	1.3	6.25	26.7	216	3.79	0.024
1203	Tc 1	17 45 35.298	−46 05 23.81	1.197	5.695	15	5.81	–	801	1.39	0.101
1207	Te 1580	17 43 39.442	−25 36 42.51	–	0.658	–	3.35	11.3	–	–	–
1208	Te 2022	17 42 42.541	−29 51 34.65	–	46.919	–	9.09	–	–	–	–
1209	Te 2111	17 48 28.465	−24 41 25.07	–	0.627	–	3.32	20.7	–	–	–
1212	Th 2-A	13 22 33.854	−63 21 00.96	0.457	1.866	23	5.33	–	60	2.07	0.231
1214	Th 3-10	17 24 40.846	−30 51 59.47	0.153	1.635	2	3.5	21.6	29.5	7.11	0.069
1216	Th 3-12	17 25 06.093	−29 45 16.87	–	0.825	1.8	3.34	2.6	3.5	–	–
1217	Th 3-13	17 25 19.341	−30 40 41.79	–	4.774	2	3.99	7.4	14.3	–	–
1218	Th 3-14	17 25 44.060	−26 57 47.69	0.122	2.248	1.4	3.8	5.8	4	–	–
1221	Th 3-19	17 28 41.787	−28 27 19.32	–	0.967	2	3.4	9.9	4.2	14.64	0.142
1222	Th 3-23	17 30 21.340	−29 10 12.57	–	0.847	–	3.18	46.2	–	–	–
1224	Th 3-25	17 30 46.716	−27 05 59.12	–	0.841	2	3.4	14.9	18	8.77	0.085
1226	Th 3-27	17 35 58.467	−24 25 29.15	–	1.729	3.2	3.69	14.4	13.5	–	–
1228	Th 3-32	17 35 15.533	−28 07 01.70	–	1.842	–	3.73	10.2	–	–	–
1229	Th 3-33	17 35 48.123	−27 43 20.38	–	2.064	–	4.01	4.2	–	–	–
1230	Th 3-35	17 38 42.168	−28 42 45.33	0.259	2.482	–	3.8	10.7	–	–	–
1232	Th 3-55	17 30 58.838	−31 01 05.73	–	1.201	–	3.65	9.8	6.1	–	–
1234	Th 4-1	17 46 20.804	−20 13 48.08	0.227	–	<10	–	–	–	–	–
1235	Th 4-10	17 57 06.599	−18 06 43.43	–	0.562	–	2.94	4.3	–	–	–
1238	Th 4-3	17 48 37.390	−22 16 48.79	–	1.015	–	3.53	2.7	–	–	–
1239	Th 4-6	17 50 57.220	−18 46 48.13	–	0.332	–	2.81	5.9	6.1	–	–
1240	Th 4-7	17 52 22.569	−21 51 13.43	–	0.276	7	2.89	8.8	18.4	–	–
1241	Th 4-9	17 56 00.589	−19 29 26.60	0.595	1.13	–	3.41	3.1	–	–	–
1244	V-V 3-5	18 36 32.291	−19 19 28.01	0.152	0.693	–	3.67	11.6	10	–	–
1250	VBe 3	15 52 59.209	−56 24 27.19	–	0.196	–	2.44	–	–	–	–
1251	VY 2-1	18 27 59.603	−26 06 48.29	–	2.003	3.7	3.81	32.4	37	–	–
1252	Vd 1-1	16 42 33.429	−38 54 31.83	0.149	–	<10	–	6.8	–	–	–
1253	Vd 1-2	16 46 45.141	−38 36 58.10	0.253	4.186	–	3.98	2.7	–	–	–
1255	Vd 1-4	16 50 25.324	−39 08 18.87	0.253	0.556	–	3.09	4.2	–	–	–
1256	Vd 1-5	16 51 33.575	−40 02 56.01	–	0.139	–	2.62	3.7	–	–	–
1257	Vd 1-6	16 54 27.327	−38 44 11.23	–	0.643	–	3.21	11.2	–	–	–
1259	Ve 26	08 43 28.087	−46 06 39.72	1.509	13.141	–	4.86	–	–	–	–
1260	Vo 1	06 59 26.405	−79 38 47.20	17.523	47.264	–	6.18	–	–	–	–
1261	Vo 2	08 16 10.000	−39 51 50.67	0.145	1.134	–	3.69	60.9	–	–	–
1263	Vo 4	13 53 23.072	−60 33 47.40	–	0.849	–	3.61	–	–	–	–
1264	Vy 1-1	00 18 42.167	+53 52 20.03	0.133	0.761	6	3.66	19.8	28.9	5.34	0.155
1265	Vy 1-2	17 54 22.994	+27 59 57.99	0.105	0.786	4.6	3.3	11.1	–	–	–
1266	Vy 1-4	18 54 01.899	−06 26 19.81	–	1.182	4.5	3.9	19.7	22	6.01	0.131
1267	Vy 2-2	19 24 22.229	+09 53 56.66	7.85	56.233	0.6	6.47	5.9	50	9.82	0.029
1268	Vy 2-3	23 22 57.952	+46 53 58.24	–	0.38	4.6	3.29	6.5	3	9.95	0.222
1272	WeSb 4	18 50 40.302	−01 03 11.16	–	0.566	–	3.71	4.3	–	–	–
1287	WhMe 1	19 14 59.755	+17 22 46.01	7.89	13.232	–	4.79	–	–	–	–
1291	Wray 16-128	13 24 21.922	−57 31 19.29	–	0.898	–	4.08	–	–	–	–
1293	Wray 16-199	16 00 22.002	−48 15 35.29	–	0.974	–	3.49	–	–	–	–
1298	Wray 16-286	17 33 00.666	−36 43 52.54	–	3.591	–	3.87	10.7	–	–	–
1303	Wray 16-93	11 30 48.339	−59 17 04.63	–	0.248	–	2.86	–	–	–	–
1306	Wray 17-18	08 23 53.825	−45 31 10.70	–	0.311	–	2.88	–	–	–	–
1311	Y-C 2-5	08 10 41.628	−20 31 32.16	–	0.176	–	2.55	7.1	4.5	–	–

The longer wave FIS identifications are listed in Table 2, where apart from the Kerber et al. (2003) number, and PNe names and coordinates (Columns 1–4), we include photometry at 65, 90, 140 and 160 μm (Columns 5–8). The data have been assigned four levels of quality FQUAL, where FQUAL = 0 corresponds to "non-detections"; FQUAL = 1 implies that the source was not confirmed; FQUAL = 2 is for sources which are confirmed, but for which fluxes are unreliable; and FQUAL = 3 is for high quality fluxes, where the source is confirmed and the flux is reliable. We list sources for which at least one of the four channels has a FQUAL value of 3, and for these cases, include all of the fluxes corresponding to FQUAL = 1–3. As an example, the detection at 90 μm may have been assigned a FQUAL value of 3, but FQUAL factors for the other three channels (65, 140 and 160 μm) may be as low as 1. However, although this photometric listing is relatively complete, and provides more and less reliable results, we have used only FQUAL = 3 fluxes for the analysis below. The FQUAL values for the 65, 90, 140 and 160 μm channels are consecutively indicated in Column 9, whilst the remaining columns define the radio fluxes, distances and diameters described above.

The noise in these results again derives from absolute uncertainties in the fluxes, and relative errors deriving from a variety of instrumental causes, in-

TABLE 2

GALACTIC PNE IDENTIFIED IN THE AKARI FIS CATALOGUE

KN	NAME	R.A. (2000)	DEC (2000)	F (65 μm)	F (90 μm)	F (140 μm)	F (160 μm)	QUAL	DIAM	F (1.4 GHz)	F(5 GHz)	DIST	DIAM
		H:M:S	D:M:S)	Jy	Jy	Jy	Jy		arcsec	mJy	mJy	kpc	pc
1	000.6+08.8	17 14 09.788	−23 31 53.41	1.04	1.86	1.987	2.565	1311	–	10.7	–	–	–
3	008.1+08.2	17 33 35.332	−17 41 16.23	1.046	1.678	0.757	2.497	1311	–	7.5	–	–	–
6	050.6+19.7	18 08 20.083	+24 10 43.26	2.136	1.05	0.462	–	1311	–	–	–	–	–
7	099.3−01.9	22 04 12.301	+53 04 01.36	10.186	8.225	2.369	1.474	3311	–	–	–	–	–
10	341.4−09.0	17 35 02.502	−49 26 26.38	46.648	22.854	5.621	5.089	3331	–	–	–	–	–
11	A 12	06 02 20.045	+09 39 14.09	2.902	3.487	2.301	2.519	1311	37	38.3	36	2.04	0.37
18	A 2	00 45 34.678	+57 57 34.88	–	0.672	0.008	0.334	1311	30.9	7.6	2.3	4.68	0.7
21	A 23	07 43 17.984	−34 45 15.64	–	0.964	0.067	0.835	1311	54	4.2	6.8	2.74	0.72
23	A 26	08 09 01.644	−32 40 24.91	0.253	1.234	1.051	3.25	1311	40	22.5	2.4	4.11	0.8
27	A 30	08 46 53.514	+17 52 45.47	89.781	56.794	26.965	21.707	3333	4.47	–	2.3	2.55	0.06
35	A 40	16 48 34.515	−21 00 50.67	1.165	1.264	2.47	0.438	1311	34	4.5	2	10.2	1.68
41	A 46	18 31 18.290	+26 56 12.86	0.826	0.95	1.52	0.955	1321	63.4	–	5	2.74	0.84
44	A 49	18 53 28.292	−06 28 46.83	0.499	1.17	2.701	–	1311	45	–	–	–	–
47	A 52	19 04 32.342	+17 57 07.13	0.767	1.299	–	–	1311	–	3.4	–	–	–
48	A 53	19 06 45.910	+06 23 52.47	11.713	10.097	19.476	–	3331	31	33.6	85.7	1.68	0.25
50	A 55	19 10 25.768	−02 20 23.46	0.944	2.171	1.047	0.451	1311	54	10.8	6	2.98	0.78
52	A 57	19 17 05.733	+25 37 33.41	0.179	0.415	0.24	–	1311	36.9	2.2	–	–	–
53	A 58	19 18 20.476	+01 46 59.62	26.646	20.791	6.876	3.949	3331	–	–	–	–	–
54	A 59	19 18 40.003	+19 34 32.95	0.467	1.613	2.13	0.899	1311	86.7	13.7	18	1.69	0.71
56	A 60	19 19 17.819	−12 14 36.78	0.209	0.455	0.214	–	1311	74	–	11	2.07	0.74
59	A 63	19 42 10.372	+17 05 14.52	0.532	1.765	1.095	0.782	1311	40	4.5	–	–	–
63	A 68	20 00 10.607	+21 42 55.43	0.636	1.132	–	0.537	1311	–	–	–	–	–
67	A 71	20 32 24.243	+47 21 02.83	–	0.943	1.042	0.91	1311	158	–	82.8	0.84	0.64
69	A 73	20 56 27.032	+57 26 03.05	0.452	1.309	1.011	0.272	1311	73.2	11	7.4	2.31	0.82
71	A 75	21 26 23.540	+62 53 31.83	0.977	2.389	1.605	2.082	1311	56	19.3	17	2.04	0.55
75	A 8	05 06 38.378	+39 08 10.77	–	0.371	–	–	1311	60	4.3	25.6	1.78	0.52
77	A 82	23 45 47.814	+57 03 59.22	0.249	0.755	2.635	1.16	1311	81	7.6	5.3	2.41	0.95
83	Al 2-E	17 30 14.398	−27 30 19.41	1.227	2.023	–	0.022	1311	–	14.7	–	–	–
91	Al 2-Q	17 53 25.040	−29 17 08.73	0.179	3.261	5.271	1.104	1311	–	2.3	–	–	–
94	Ap 1-12	18 11 35.088	−28 22 37.02	8.231	6.48	1.255	1.526	3311	12	6.6	18.7	5.34	0.31
95	Ap 2-1	18 58 10.459	+01 36 57.15	873.272	609.29	793.279	958.062	3333	40	195	320.4	1.13	0.22
97	BV 5-1	00 20 00.450	+62 59 03.16	1.283	1.029	1.138	2.259	1311	41.6	10.6	17.7	4.05	0.82
99	BV 5-3	01 53 03.432	+56 24 17.11	1.01	0.622	0.576	1.718	1311	–	2.7	–	–	–
102	Bl 2-1	22 20 16.638	+58 14 16.59	2.659	2.965	–	1.066	1311	1.6	21.6	54	6.94	0.05
105	Bl 3-15	17 52 35.947	−29 06 38.97	3.78	3.21	3.346	5.144	1311	–	–	–	–	–
106	Bl B	17 36 59.836	−29 40 08.93	5.691	5.45	6.249	2.798	1311	–	8.9	–	–	–
118	CTS 1	18 06 59.785	−08 55 32.80	4.706	4.048	0.471	1.589	3311	–	24	–	–	–
119	Cn 1-1	15 51 15.936	−48 44 58.67	13.214	10.516	4.745	0.806	3331	–	–	10	–	–
120	Cn 1-3	17 26 12.392	−44 11 24.52	3.458	3.029	–	–	3311	–	–	–	–	–
122	Cn 1-5	18 29 11.653	−31 29 59.21	6.379	6.339	2.788	–	3311	7	51	44	4.43	0.15
123	Cn 2-1	17 54 32.978	−34 22 20.84	2.975	2.954	–	0.611	3311	2.2	25.2	49	6.17	0.07
124	Cn 3-1	18 17 34.133	+10 09 03.99	7.298	5.991	1.936	2.188	3311	4.5	59.5	75	4	0.09
127	Dd 1	20 08 43.080	+42 30 11.19	0.819	1.087	–	–	1311	–	–	6	–	–
133	DuRe 1	12 45 51.211	−64 09 38.08	8.398	6.469	11.267	6.274	1331	–	–	–	–	–
138	ESO 040-11	13 34 14.128	−75 46 31.33	1.049	0.991	1.758	–	1311	–	–	–	–	–
150	Fg 1	11 28 36.205	−52 56 04.01	5.624	10.809	6.454	4.621	3331	16	–	55	2.02	0.16
151	Fg 2	17 39 19.847	−44 09 37.14	3.506	2.488	0.622	0.477	1311	–	–	–	–	–
152	Fg 3	18 00 11.819	−38 49 52.73	14.692	11.152	4.286	3.226	3331	2	42	107	–	–
156	G001.6−05.9	18 13 15.842	−30 25 58.49	–	0.428	0.472	0.942	1311	–	–	–	–	–
158	G002.5+05.1	17 32 12.788	−24 04 59.56	15.981	11.822	3.348	1.594	3311	–	–	–	–	–
163	G009.3+05.7	17 45 14.155	−17 56 46.57	56.19	40.015	15.844	12.064	3333	–	–	–	–	–
164	G010.2+07.5	17 41 00.035	−16 18 12.50	1.362	0.956	–	1.539	1311	–	–	–	–	–
165	G011.1−07.9	18 40 19.914	−22 54 29.23	0.841	1.638	0.297	0.189	1311	–	–	–	–	–
168	G013.1−13.2	19 04 43.548	−23 26 08.82	21.108	13.815	4.63	2.404	3331	–	–	–	–	–
171	G014.4−06.1	18 39 40.056	−19 14 12.04	1.014	1.202	1.2	–	1311	–	–	–	–	–
175	G017.0+11.1	17 42 14.430	−08 43 18.61	5.365	5.666	1.605	0.349	3311	–	23.4	–	–	–
179	G019.2−04.4	18 42 24.770	−14 15 11.81	2.374	2.789	0.666	1.03	1311	–	7.3	–	–	–
181	G022.0−04.3	18 47 03.954	−11 41 11.74	8.676	8.306	2.024	1.337	3311	–	8.4	–	–	–
185	G034.5−11.7	19 36 17.531	−03 53 25.26	3.814	2.615	3.426	0.975	3311	–	8.8	–	–	–
186	G038.4+01.8	18 54 54.139	+05 48 11.29	–	2.998	–	–	1311	–	20.5	–	–	–
188	G039.1−02.2	19 10 53.284	+04 27 28.50	1.248	2.49	–	–	1311	–	11	–	–	–
191	G044.1+01.5	19 06 32.146	+10 43 23.93	1.413	3.034	4.193	–	1311	–	19.4	–	–	–
193	G047.2+01.7	19 11 35.828	+13 31 11.58	5.784	4.889	–	–	3311	–	–	–	–	–
202	G069.2+01.2	20 00 41.998	+32 27 41.23	1.094	1.588	–	–	1311	–	17	–	–	–
204	G076.6−05.7	20 48 16.627	+34 27 24.36	8.115	7.002	2.067	–	3311	–	–	–	–	–
207	G095.0−05.5	21 56 32.945	+47 36 13.40	0.858	0.472	–	–	1311	–	–	–	–	–
211	G124.0+02.9	01 02 24.488	+65 46 32.81	2.184	2.741	4.239	3.567	1311	–	7.4	–	–	–
221	G222.8−04.2	06 54 13.406	−10 45 38.27	1.878	1.168	0.744	0.631	1311	–	2.7	–	–	–
226	G255.3−03.6	08 06 28.339	−38 53 23.93	1.622	1.085	0.289	1.12	1311	–	2.8	–	–	–
228	G260.1+00.2	08 37 24.599	−40 38 07.46	4.072	4.911	2.082	0.131	3311	–	–	–	–	–
229	G270.1−02.9	08 59 02.971	−50 23 39.68	1.001	1.265		–	1311	–	–	–	–	–
231	G277.1−01.5	09 37 51.861	−54 27 08.59	1.247	1.106	–	–	1311	–	–	–	–	–
232	G279.1−00.4	09 53 27.058	−54 52 39.60	1.616	2.185	2.079	0.076	1311	–	–	–	–	–
234	G282.6−00.4	10 13 19.673	−56 55 32.24	3.692	3.317	6.231	1.671	1311	–	–	–	–	–
235	G285.1−02.7	10 19 32.466	−60 13 29.41	77.86	58.749	36.452	16.57	3333	–	–	–	–	–
236	G290.7+00.2	11 10 25.122	−60 15 36.85	10.823	13.328	28.365	19.063	3333	–	–	–	–	–
241	G308.5−03.5	13 46 25.712	−65 46 24.26	1.892	1.935	0.503	0.551	1311	–	–	–	–	–
246	G316.2+00.8	14 38 19.980	−59 11 46.12	17.965	12.604	7.104	2.124	3311	–	–	–	–	–
248	G326.4+01.0	15 19 43.867	−48 59 54.65	0.844	2.367	–	0.838	1311	–	–	–	–	–
251	G328.4−02.8	16 09 20.143	−55 36 09.84	10.647	9.904	5.721	6.032	3311	–	–	–	–	–
253	G331.3−12.1	17 16 21.107	−59 29 23.35	2.504	1.926	0.895	1.7	3311	–	–	–	–	–
264	G347.9−06.0	17 40 03.329	−42 24 05.58	1.674	1.07	–	0.135	1311	–	–	–	–	–
267	G351.5−06.5	17 52 09.386	−39 32 14.52	1.246	2.017	0.941	0.884	1311	–	–	–	–	–

TABLE 2 (CONTINUED)

KN	NAME	R.A. (2000)	DEC (2000)	F (65 μm)	F (90 μm)	F (140 μm)	F (160 μm)	QUAL	DIAM	F (1.4 GHz)	F(5 GHz)	DIST	DIAM
		H:M:S	D:M:S)	Jy	Jy	Jy	Jy		arcsec	mJy	mJy	kpc	pc
270	G352.6−04.9	17 47 52.679	−37 48 03.10	0.685	0.733	–	1.812	1311	–	3.7	–	–	–
275	G353.6−03.6	17 44 35.434	−36 14 01.67	0.631	1.004	1.947	1.427	1311	–	–	–	–	–
294	G356.8−03.0	17 50 10.734	−33 14 17.97	4.956	2.522	0.54	4.026	1311	–	4.2	–	–	–
299	G358.3−07.3	18 11 39.900	−34 00 21.99	–	0.701	–	0.763	1311	–	–	–	–	–
302	G358.7+05.1	17 22 43.615	−27 13 36.67	7.125	4.881	3.383	2.801	3311	–	–	–	–	–
307	G359.4−08.5	18 19 26.331	−33 37 04.86	0.298	0.974	–	0.672	1311	–	4.5	–	–	–
310	G000.5+01.9	17 39 31.219	−27 27 46.77	5.529	3.087	3.93	10.456	1311	–	6.8	–	–	–
323	G003.1+04.1	17 37 20.167	−24 03 27.84	1.6	1.494	0.414	0.727	1311	–	5.1	–	–	–
326	G003.6+04.9	17 35 31.198	−23 11 47.62	0.551	1.164	2.137	–	1311	–	4.6	–	–	–
332	G035.4+03.4	18 43 36.599	+03 46 39.24	5.368	5.503	3.326	0.518	3311	–	5.1	–	–	–
359	H 1-11	17 21 17.693	−22 18 35.32	3.175	2.96	2.676	–	3311	6	20.7	13	7.27	0.21
367	H 1-19	17 30 02.546	−27 59 17.54	5.167	4.576	–	1.333	3311	1.4	11.6	26	8.19	0.06
368	H 1-2	16 48 54.091	−35 47 09.01	6.754	7.334	3.178	5.698	3331	1	14.3	62	–	–
369	H 1-20	17 30 43.799	−28 04 06.68	3.73	3.436	–	–	3311	3.3	26.9	43.9	5.12	0.08
372	H 1-23	17 32 46.897	−30 00 15.07	5.346	2.646	1.913	0.27	1311	2.6	24.5	34.8	6.12	0.08
373	H 1-24	17 33 37.565	−21 46 24.78	2.864	4.191	1.34	0.725	1311	5	5.1	15	7.32	0.18
375	H 1-27	17 40 17.926	−22 19 17.64	4.632	4.237	2.276	1.683	3311	5.2	–	18	10.9	0.27
376	H 1-28	17 42 54.066	−39 36 24.04	0.741	1.613	0.91	0.82	1311	–	5.4	–	–	–
378	H 1-3	16 53 31.347	−42 39 23.45	6.802	6.116	14.597	–	1311	15.8	–	–	1.36	0.1
379	H 1-30	17 45 06.782	−38 08 49.48	0.047	2.454	2.628	1.4	1311	<5	7	81.3	5.21	–
380	H 1-31	17 45 32.104	−34 33 55.32	1.182	1.808	3.421	2.872	1311	0.7	6	16	11.8	0.04
385	H 1-36	17 49 48.172	−37 01 29.47	3.996	3.046	1.295	–	1311	0.8	11.8	50	–	–
390	H 1-40	17 55 36.049	−30 33 32.08	8.689	7.947	3.121	2.002	3311	3	8.1	31	7.84	0.11
391	H 1-41	17 57 19.145	−34 09 49.12	1.409	2.46	–	1.307	1311	9.6	16.6	12	6.6	0.31
392	H 1-42	17 57 25.169	−33 35 42.94	1.873	2.163	1.065	1.6	1311	5.8	34.5	40	4.82	0.14
394	H 1-44	17 58 10.641	−31 42 56.08	3.517	3.355	–	–	3311	<5	8	–	–	–
396	H 1-46	17 59 02.490	−32 21 43.42	2.175	1.824	1.577	–	3311	1.2	18.3	43	7.11	0.04
399	H 1-50	18 03 53.461	−32 41 42.15	2.527	1.911	0.001	–	3311	1.4	19.6	31	7.68	0.05
404	H 1-55	18 07 14.542	−29 41 24.51	2.607	2.827	4.162	1.519	1311	10	2.5	5.3	–	–
405	H 1-56	18 07 53.880	−29 44 34.26	1.409	1.586	1.4	–	1311	3	8.3	7.8	10.98	0.16
408	H 1-59	18 11 29.263	−27 46 15.69	1.006	1.115	0.501	–	1311	6	3.4	4.2	11.12	0.32
412	H 1-62	18 13 17.951	−32 19 42.74	4.164	3.569	–	2.715	3311	–	11.9	–	–	–
413	H 1-63	18 16 19.336	−30 07 35.98	1.399	0.981	–	1.129	1311	–	2.5	9	–	–
416	H 1-66	18 24 57.539	−25 41 55.76	1.68	2.448	2.442	4.279	1313	<10	10.4	6	9.5	–
417	H 1-67	18 25 04.976	−22 34 52.64	1.245	1.916	2.312	–	1311	6	12.2	11.9	7.51	0.22
418	H 1-7	17 10 27.389	−41 52 49.42	–	42.37	33.76	10.955	131	–	–	–	–	–
429	H 2-17	17 40 07.428	−24 25 42.57	3.915	2.947	1.795	–	3311	4	8.2	10	8.88	0.17
437	H 2-27	17 51 50.576	−33 47 35.59	2.026	4.543	5.283	3.193	1311	–	7.9	–	–	–
438	H 2-29	17 53 16.794	−32 40 38.56	0.841	1.959	1.309	0.054	1311	–	2.6	–	–	–
442	H 2-33	17 58 12.535	−31 08 05.99	1.633	2.283	–	–	1311	8	8.1	5	9.71	0.38
443	H 2-35	18 00 18.259	−34 27 39.29	0.161	0.981	2.435	0.421	1311	–	–	–	–	–
444	H 2-36	18 04 07.936	−31 39 13.70	0.939	1.627	1.844	1.4	1311	–	3.4	–	–	–
449	H 2-42	18 12 23.255	−26 32 54.02	1.024	1.992	0.43	3.923	1311	–	3.1	–	–	–
453	H 2-46	18 18 37.444	−31 54 45.42	0.751	0.772	–	2.136	1311	25	–	–	–	–
454	H 2-48	18 46 35.149	−23 26 48.24	3.332	2.115	1.08	–	3311	2	31.6	66	6.23	0.06
456	H 2-8	17 24 45.766	−21 33 35.80	–	0.443	2.309	–	1311	–	4.8	–	–	–
457	H 3-29	04 37 23.484	+25 02 40.94	2.391	1.128	–	3.097	1311	21	18.3	18	3.4	0.35
463	HaTr 13	19 08 02.149	+02 21 24.25	0.226	1.281	0.982	1.832	1311	–	3.6	–	–	–
464	HaTr 14	19 09 13.670	+07 05 44.86	1.974	1.872	–	–	1311	–	–	–	–	–
465	HaTr 2	15 30 18.542	−61 01 38.79	0.808	1.883	1.534	–	1311	–	–	–	–	–
467	HaTr 4	16 45 00.155	−51 12 19.83	0.422	1.93	3.937	3.937	1331	–	–	–	–	–
474	Hb 12	23 26 14.814	+58 10 54.65	28.818	19.707	6.499	3.075	3331	0.8	–	45	10.46	0.04
475	Hb 4	17 41 52.763	−24 42 08.07	13.541	14.269	0.952	1.287	3311	7.3	157.6	170	2.68	0.09
477	Hb 6	17 55 07.023	−21 44 39.98	20.768	14.246	6.261	2.636	1311	6	190.5	243	2.45	0.07
479	He 1-1	19 23 46.875	+21 06 38.60	1.896	2.307	–	–	1311	8	16	14	–	–
480	He 1-2	19 26 37.757	+21 09 27.04	4.268	3.83	3.69	2.034	3311	4.7	14.6	15	–	–
481	He 1-3	19 48 26.422	+22 08 37.62	3.687	3.402	–	–	1311	8	53.5	–	–	–
482	He 1-4	19 59 18.014	+31 54 39.14	2.196	3.218	–	–	3311	–	16.1	–	–	–
484	He 1-6	20 17 21.424	+25 21 46.78	–	0.59	0.228	–	1311	22.4	5	20.3	2.91	0.32
486	He 2-102	13 58 13.866	−58 54 31.78	3.526	5.212	–	0.187	3311	9	–	33	3.77	0.16
487	He 2-104	14 11 52.077	−51 26 24.18	5.304	5.412	2.607	1.568	3311	5	–	15	–	–
488	He 2-105	14 15 24.803	−74 12 46.61	2.007	2.755	0.431	0.625	1311	31	–	14	2.67	0.4
490	He 2-108	14 18 08.889	−52 10 39.76	11.056	11.255	2.98	–	3311	11	–	32	3.49	0.19
491	He 2-109	14 20 48.916	−55 27 59.21	0.507	0.868	1.644	1.676	1311	7.4	–	15.8	6.41	0.23
492	He 2-11	08 37 08.445	−39 25 08.09	14.232	29.419	9.803	8.864	3333	65	343.6	444.6	0.77	0.24
494	He 2-112	14 40 30.924	−52 34 56.66	5.436	5.861	2.376	1.855	3311	14.6	–	82	2.36	0.17
495	He 2-113	14 59 53.523	−54 18 07.20	146.924	75.968	29.685	20.859	3333	–	–	115	–	–
496	He 2-114	15 04 08.800	−60 53 18.78	2.378	3.831	2.893	13.696	1331	36.6	–	11	2.8	0.5
497	He 2-115	15 05 16.775	−55 11 10.39	9.04	7.229	3.019	0.869	3311	3	–	156	3.91	0.06
499	He 2-117	15 05 59.193	−55 59 16.53	30.411	20.756	7.71	–	3331	5	–	267	2.69	0.07
503	He 2-123	15 22 19.360	−54 08 12.77	13.454	14.537	6.106	5.808	3331	4.6	–	110	3.59	0.08
504	He 2-125	15 23 36.326	−53 51 27.95	2.858	3.458	1.854	0.569	1311	3	–	20.4	6.96	0.1
505	He 2-128	15 25 07.841	−51 19 42.29	1.343	1.317	–	2.54	1311	5	–	40	–	–
506	He 2-129	15 25 32.677	−52 50 37.96	1.332	1.958	0.083	1.087	1311	1.6	–	35	7.85	0.06
507	He 2-131	15 37 11.210	−71 54 52.89	52.897	32.153	10.413	6.777	3331	6	–	325	2.2	0.06
508	He 2-132	15 38 01.182	−58 44 42.07	5.143	6.911	3.164	–	3311	17.8	–	25	3.02	0.26
509	He 2-133	15 41 58.788	−56 36 25.72	19.455	12.659	2.857	3.351	3311	<10	–	210	3.18	–
510	He 2-136	15 52 10.666	−62 30 46.94	–	1.052	–	–	1311	10	–	23	–	–
511	He 2-138	15 56 01.694	−66 09 09.23	37.174	27.055	8.317	5.173	3333	7	–	76	3.61	0.12
512	He 2-140	15 58 08.063	−55 41 50.13	11.771	8.42	–	0.219	1311	2.6	–	80	5.03	0.06
513	He 2-141	15 59 08.762	−58 23 53.15	2.406	2.797	0.987	1.007	3311	13.8	–	51	2.77	0.19
514	He 2-142	15 59 57.608	−55 55 32.89	8.916	8.153	1.037	0.116	1311	3.6	–	65	4.75	0.08
519	He 2-149	16 14 24.266	−54 47 38.82	–	1.02	–	–	1311	3	–	10	8.52	0.12
520	He 2-15	08 53 30.701	−40 03 42.08	8.855	13.475	7.766	8.121	3331	23.8	94.5	105	1.92	0.22
521	He 2-151	16 15 42.269	−59 54 00.96	4.698	3.035	–	–	3311	5	–	10	–	–
522	He 2-152	16 15 20.031	−49 13 20.76	59.168	34.701	25.057	26.453	1333	11	–	196	2.09	0.11

TABLE 2 (CONTINUED)

KN	NAME	R.A. (2000)	DEC (2000)	F (65 μm)	F (90 μm)	F (140 μm)	F (160 μm)	QUAL	DIAM	F (1.4 GHz)	F(5 GHz)	DIST	DIAM
		H:M:S	D:M:S)	Jy	Jy	Jy	Jy		arcsec	mJy	mJy	kpc	pc
524	He 2-155	16 19 23.101	−42 15 35.98	3.768	6.096	1.291	–	3311	14.6	–	70	2.47	0.17
525	He 2-157	16 22 14.264	−53 40 54.09	2.612	2.42	–	0.963	1311	<5	–	30	6.24	–
526	He 2-158	16 23 30.605	−58 19 22.64	1.124	0.807	–	0.634	1311	2	–	2.7	14.71	0.14
528	He 2-161	16 24 37.786	−53 22 34.14	6.164	4.563	1.665	–	1311	10	–	32	3.64	0.18
530	He 2-163	16 29 31.333	−59 09 25.08	0.548	0.936	–	–	1311	<25	–	3.4	5.08	–
531	He 2-164	16 29 53.255	−53 23 15.37	4.289	4.731	4.26	5.638	1311	16	–	97	2.17	0.17
532	He 2-165	16 30 00.057	−54 09 28.00	1.498	2.651	2.271	5.82	1311	50	–	15.9	2.2	0.53
534	He 2-170	16 35 21.170	−53 50 11.11	1.035	1.091	–	–	1311	5	–	15	–	–
536	He 2-175	16 39 28.112	−36 34 16.41	8.23	8.479	3.012	1.863	3331	6.6	19.2	26.8	4.58	0.15
537	He 2-18	09 08 40.050	−53 19 13.91	0.712	1.44	0.206	0.118	1311	11	–	–	–	–
538	He 2-182	16 54 35.167	−64 14 28.43	0.723	0.97	0.501	–	1311	10	–	62	–	–
539	He 2-185	17 01 17.254	−70 06 03.35	0.31	0.532	0.323	–	1311	10	–	18	–	–
540	He 2-186	16 59 36.064	−51 42 06.46	1.573	1.378	0.342	–	1311	3	–	21	6.9	0.1
541	He 2-187	17 01 36.976	−50 22 57.49	0.606	2.288	1.562	1.152	1311	6	–	–	–	–
545	He 2-25	09 18 01.308	−54 39 29.01	1.808	1.355	1.19	0.091	1311	4.4	–	827.9	2.07	0.04
546	He 2-250	17 34 54.710	−26 35 56.92	2.625	3.212	–	0.965	3311	5	15.3	15	7.01	0.17
549	He 2-28	09 22 06.825	−54 09 38.60	1.481	1.19	0.504	0.84	1311	10	–	20	4.15	0.2
551	He 2-306	17 56 33.706	−43 03 18.90	2.165	1.648	0.535	–	1311	–	–	–	–	–
553	He 2-34	09 41 13.997	−49 22 47.18	1.043	0.693	1.428	–	1311	<10	–	–	–	–
554	He 2-35	09 41 37.504	−49 57 58.71	1.402	1.463	–	–	1311	5	–	20	5.61	0.14
555	He 2-36	09 43 25.538	−57 16 55.44	3.776	5.187	1.768	1.416	3311	22	–	90	3.1	0.33
556	He 2-37	09 47 24.987	−48 58 11.96	0.111	1.566	–	–	1311	23	–	22.6	2.8	0.31
557	He 2-39	10 03 49.164	−60 43 48.26	0.69	0.666	–	1.18	1311	–	–	–	–	–
561	He 2-428	19 13 05.239	+15 46 39.80	2.444	3.763	0.304	–	1311	8	26.7	7	6.16	0.24
562	He 2-429	19 13 38.422	+14 59 19.21	5.302	5.489	1.651	–	3311	4.2	58.5	64.9	4.33	0.09
563	He 2-430	19 14 04.197	+17 31 32.92	4.256	4.174	1.445	0.975	3311	1.7	18.2	40	7.36	0.06
564	He 2-432	19 23 24.821	+21 08 00.50	1.213	1.211	0.805	1.393	1311	2.3	21.3	32	6.88	0.08
565	He 2-434	19 33 49.420	−74 32 58.66	2.155	0.77	0.869	–	1311	10	–	–	–	–
567	He 2-437	19 32 57.657	+26 52 43.35	8.747	9.473	6.01	3.948	3331	–	6.6	–	–	–
568	He 2-440	19 38 08.403	+25 15 40.98	2.7	2.87	0.518	0.509	3311	2.2	26.4	43	6.45	0.07
570	He 2-447	19 45 22.164	+21 20 04.03	4.171	4.547	6.443	4.375	1131	1.2	22.9	60	7.63	0.04
571	He 2-459	20 13 57.898	+29 33 55.94	35.529	24.038	8.141	5.802	3331	1.3	13.9	64	7.24	0.05
572	He 2-47	10 23 09.143	−60 32 42.21	23.166	16.144	9.242	4.43	3331	5	–	170	–	–
575	He 2-50	10 34 19.002	−53 41 03.75	1.386	1.491	1.105	–	1311	<25	–	11.3	4.54	–
576	He 2-51	10 35 45.821	−64 19 11.74	1.019	1.942	2.329	2.343	1311	9	–	57	3.23	0.14
577	He 2-55	10 48 43.168	−56 03 10.21	0.961	1.151	0.498	0.539	1311	<25	–	–	–	–
581	He 2-64	11 27 24.259	−57 17 58.99	0.779	0.495	2.263	0.248	1311	–	–	–	–	–
582	He 2-67	11 28 47.369	−60 06 37.28	3.437	4.045	1.748	1.044	3311	5	–	41	–	–
583	He 2-68	11 31 45.427	−65 58 13.67	1.823	1.576	0.778	0.445	1311	10	–	34	–	–
584	He 2-7	08 11 31.890	−48 43 16.71	1.741	2.074	0.648	–	1311	44.6	–	47	2.91	0.63
586	He 2-71	11 39 11.198	−68 52 09.14	0.973	0.816	1.06	1.173	1311	5	–	12	–	–
588	He 2-73	11 48 38.191	−65 08 37.33	4.998	4.438	2.214	–	3311	4	–	76	4.23	0.08
589	He 2-76	12 08 25.433	−64 12 09.32	–	3.741	1.738	4.622	1311	–	–	–	–	–
590	He 2-78	12 09 10.196	−58 42 37.44	0.664	0.842	1.869	1.298	1311	–	–	–	–	–
591	He 2-81	12 23 01.237	−64 01 45.96	5.655	4.455	–	–	1311	<25	–	–	–	–
593	He 2-83	12 28 43.997	−62 05 35.05	13.117	8.492	1.805	2.953	3311	–	–	–	–	–
594	He 2-84	12 28 46.822	−63 44 37.22	–	3.755	6.61	9.376	1311	–	–	–	–	–
596	He 2-86	12 30 30.426	−64 52 05.58	18.48	14.073	3.369	–	3311	3.6	–	125	3.85	0.07
598	He 2-9	08 28 27.988	−39 23 40.27	5.928	4.829	0.147	1.568	3311	4.4	135.6	194.8	3.11	0.07
599	He 2-90	13 09 36.252	−61 19 35.96	12.683	9.68	7.373	11.11	1311	10	–	25	–	–
600	He 2-96	13 42 36.150	−61 22 29.18	18.266	13.075	5.562	3.139	3311	–	–	–	–	–
601	He 2-97	13 45 22.394	−71 28 56.13	1.942	1.843	–	–	1311	5	–	30	–	–
602	He 2-99	13 52 30.683	−66 23 26.49	8.545	7.715	3.001	2.34	3311	17	–	18	3.4	0.28
603	He 3-1333	17 09 00.932	−56 54 48.25	174.846	94.412	34.594	29.428	1333	–	–	26	–	–
606	Hf 39	10 53 59.586	−60 26 44.31	28.91	22.101	13.034	10.185	3331	–	–	–	–	–
607	Hf 48	11 03 55.979	−60 36 04.57	2.802	2.693	–	7.749	1311	–	–	–	–	–
608	Hu 1-1	00 28 15.614	+55 57 54.71	2.45	2.793	3.616	3.719	1311	10	28	26	3.86	0.19
609	Hu 1-2	21 33 08.349	+39 38 09.57	2.478	2.558	2.059	1.414	3311	6.5	107	155	2.53	0.08
610	Hu 2-1	18 49 47.562	+20 50 39.46	4.192	3.208	2.134	–	3311	1.8	42.6	110	4.52	0.04
611	IC 1295	18 54 37.206	−08 49 39.08	0.714	2.886	2.997	0.009	1311	100	45.9	44	1.18	0.57
612	IC 1297	19 17 23.459	−39 36 46.40	3.558	4.067	0.836	–	3311	7	59.4	68.9	3.75	0.13
613	IC 1454	22 42 24.997	+80 26 31.96	0.582	0.57	–	–	1311	34	3.3	1.3	5.29	0.87
614	IC 1747	01 57 35.896	+63 19 19.36	5.61	5.495	0.416	4.799	3311	13	85.8	124	2.23	0.14
615	IC 2003	03 56 21.984	+33 52 30.59	2.384	2.129	–	–	1311	10	54.8	30	3.89	0.19
616	IC 2149	05 56 23.908	+46 06 17.32	8.351	7.08	3.29	1.772	3331	8.4	177	280	2.03	0.08
617	IC 2165	06 21 42.775	−12 59 13.96	4.002	3.607	–	–	1311	9	180	188	2.47	0.11
618	IC 2448	09 07 06.261	−69 56 30.74	3.367	3.231	0.917	0.015	3311	10	–	73	3.41	0.17
619	IC 2501	09 38 47.213	−60 05 30.92	10.743	9.401	2.776	0.924	3331	2	–	261	2.09	0.02
620	IC 2553	10 09 20.856	−62 36 48.40	10.367	9.642	3.572	2.955	3311	9	–	92	2.85	0.12
621	IC 2621	11 00 20.111	−65 14 57.77	16.66	13.745	6.657	2.474	3331	5	–	195	2.94	0.07
622	IC 289	03 10 19.273	+61 19 00.91	7.28	8.816	1.371	0.208	3311	36.8	152	170	1.18	0.21
623	IC 351	03 47 33.143	+35 02 48.50	0.94	1.23	1.56	1.662	1311	7	31.9	27	4.45	0.15
624	IC 3568	12 33 06.834	+82 33 50.29	4.75	4.54	2.027	–	3311	18	94.1	95	2.47	0.22
626	IC 4191	13 08 47.343	−67 38 37.67	14.074	12.272	3.336	0.74	3331	14	–	172	1.95	0.13
627	IC 4406	14 22 26.278	−44 09 04.35	18.454	21.94	16.635	15.527	3333	20	–	110	1.5	0.15
628	IC 4593	16 11 44.545	+12 04 17.06	13.84	11.52	3.349	1.929	3311	12.8	90.6	92	2.42	0.15
629	IC 4634	17 01 33.572	−21 49 32.77	8.034	6.439	2.37	–	3311	5.5	116	100	3.47	0.09
630	IC 4637	17 05 10.506	−40 53 08.44	9.044	4.84	31.528	6.032	1331	18.6	–	132.5	2.29	0.21
631	IC 4642	17 11 45.025	−55 24 01.47	5.784	5.526	2.109	1.953	3311	16.6	–	60	2.52	0.2
633	IC 4673	18 03 18.408	−27 06 22.61	9.902	9.916	6.94	6.241	1311	16	53.4	62	3.12	0.24
634	IC 4699	18 18 32.024	−45 59 01.70	0.68	1.065	–	–	1311	5	–	20	4.91	0.12
636	IC 4846	19 16 28.220	−09 02 36.57	2.221	1.882	0.336	0.547	1311	2.9	38.7	43	5.72	0.08
637	IC 4997	20 20 08.741	+16 43 53.71	6.372	4.577	1.158	2.358	3311	2	30.1	127	5.45	0.05
638	IC 5117	21 32 31.027	+44 35 48.53	13.535	11.489	3.659	0.543	3111	1.5	34.1	210	5.01	0.04
639	IC 5217	22 23 55.725	+50 58 00.43	3.748	3.111	1.901	0.711	3311	6.5	50.4	163	2.71	0.09
640	IC 972	14 04 25.863	−17 13 40.84	0.633	0.604	0.214	0.676	1311	47	3.9	6.8	2.87	0.65

TABLE 2 (CONTINUED)

KN	NAME	R.A. (2000)	DEC (2000)	F (65 μm)	F (90 μm)	F (140 μm)	F (160 μm)	QUAL	DIAM	F (1.4 GHz)	F(5 GHz)	DIST	DIAM
		H:M:S	D:M:S)	Jy	Jy	Jy	Jy		arcsec	mJy	mJy	kpc	pc
644	J 900	06 25 57.275	+17 47 27.19	5.565	4.194	2.942	1.558	3311	6	107.8	100	3.29	0.1
651	KFL 13	18 12 44.988	−25 44 23.85	0.222	1.359	–	1.112	1311	–	4	3.5	–	–
652	KFL 14	18 13 01.106	−29 25 15.59	0.088	0.977	0.676	–	1311	–	–	1.5	–	–
660	KFL 9	18 07 19.381	−31 42 56.95	–	0.838	–	–	1311	–	2.8	3.1	–	–
666	K 1-14	17 42 36.757	+21 27 02.06	0.454	0.708	0.813	0.763	1311	47	–	–	–	–
669	K 1-17	19 03 37.362	+19 21 22.60	0.61	1.071	0.621	2.994	1311	45	4.6	–	–	–
672	K 1-21	08 04 14.193	−34 16 07.32	0.272	0.796	–	–	1311	29	6.5	5	3.88	0.55
681	K 2-16	16 44 49.050	−28 04 04.56	22.836	17.837	4.856	1.122	3331	–	–	–	–	–
684	K 2-5	17 54 26.179	−12 48 35.95	0.181	0.551	2.464	2.452	1311	24.6	4	3	–	–
686	K 3-1	18 23 21.721	+03 36 27.78	0.22	0.637	0.399	4.204	1311	5	5.4	5	8.31	0.2
687	K 3-11	18 41 07.311	−08 55 58.97	8.769	4.539	1.898	14.47	3111	3	14.5	17	7.33	0.11
693	K 3-18	19 00 34.829	−02 11 57.62	4.782	4.264	–	–	3311	3.5	–	11	13.98	0.23
695	K 3-2	18 25 00.576	−01 30 52.64	2.934	1.956	–	–	3311	2.8	25.9	31	6.37	0.09
696	K 3-20	19 02 10.154	−01 48 45.31	1.358	1.085	0.791	–	1311	–	6.3	–	–	–
697	K 3-21	19 02 40.327	+14 28 50.36	0.15	0.373	–	0.189	1311	–	–	–	–	–
699	K 3-24	19 12 05.820	+15 09 04.47	1.402	1.896	1.19	1.693	1311	6.2	8.5	–	–	–
700	K 3-26	19 14 39.178	+00 13 36.29	1.422	1.442	–	–	1311	–	6.4	0.5	–	–
702	K 3-29	19 15 30.561	+14 03 49.83	5.471	5.005	–	–	1311	1	13.9	65	8.07	0.04
703	K 3-3	18 27 09.338	+01 14 26.88	5.058	7.101	1.615	2.432	3311	10	35.9	34	3.43	0.17
704	K 3-30	19 16 27.691	+05 13 19.47	0.539	1.423	4.218	1.382	1311	3.3	12.1	23	6.46	0.1
705	K 3-31	19 19 02.666	+19 02 20.85	1.665	1.718	–	–	1311	1.5	16.8	39	7.83	0.06
708	K 3-35	19 27 44.036	+21 30 03.83	37.657	19.471	4.673	0.634	3311	1.7	14.5	60	6.56	0.05
709	K 3-36	19 32 39.557	+07 27 51.57	0.342	1.393	1.147	2.954	1311	–	3.1	0.2	–	–
710	K 3-37	19 33 46.749	+24 32 27.09	0.797	0.821	0.198	1.414	1311	2.5	14.4	17	7.93	0.1
711	K 3-38	19 35 18.354	+17 13 00.71	3.674	4.207	4.376	5.177	3311	5	28.7	31	5.09	0.12
712	K 3-39	19 35 54.469	+24 54 48.20	3.351	2.565	0.402	1.241	3311	1	3.6	11	13.35	0.06
713	K 3-4	18 31 00.227	+02 25 27.35	3.694	2.055	4.661	0.696	1311	21	17	21	–	–
714	K 3-40	19 36 21.828	+23 39 47.93	3.452	3.892	–	–	3311	4	17.1	20	6.18	0.12
717	K 3-43	19 40 25.908	+18 49 14.20	0.482	0.69	0.122	–	1311	3	4.8	0.4	–	–
720	K 3-49	19 54 00.702	+33 22 12.95	1.097	1.077	–	–	1311	–	5.5	7	34.5	–
721	K 3-5	18 31 45.833	+04 05 09.12	1.543	1.481	2.463	2.296	1311	10	6.7	3	7.11	0.34
723	K 3-52	20 03 11.435	+30 32 34.15	35.941	24.008	10.002	8.825	3331	0.7	16.9	65	9.42	0.03
724	K 3-53	20 03 22.475	+27 00 54.73	5.133	4.756	0.601	–	3311	0.9	10	69	9.27	0.04
726	K 3-55	20 06 56.210	+32 16 33.60	5.551	7.453	7.527	6.486	1311	8.2	86.6	90	2.96	0.12
728	K 3-57	20 12 47.679	+34 20 32.52	2.474	3.289	1.827	–	1311	6.3	46.8	60	3.72	0.11
729	K 3-58	20 21 58.324	+29 59 22.15	2.219	3.014	2.792	1.481	1311	4.8	5.4	–	–	–
730	K 3-6	18 33 17.490	+00 11 47.19	5.499	4.908	4.12	2.52	3311	0.7	10.4	55	10.2	0.03
732	K 3-61	21 30 00.710	+54 27 27.45	1.973	1.628	–	0.663	1311	6	16.6	14	5.73	0.17
733	K 3-62	21 31 50.203	+52 33 51.64	4.669	3.505	–	–	3311	2.5	59.5	115	4.62	0.06
734	K 3-63	21 39 11.976	+55 46 03.94	0.395	1.098	1.335	–	1311	7	8.5	29	–	–
735	K 3-64	04 13 27.255	+51 51 00.92	–	0.392	0.082	0.596	1311	–	–	–	–	–
737	K 3-66	04 36 37.243	+33 39 29.87	1.272	0.594	0.104	0.766	1311	2.1	15.4	18	8.42	0.09
738	K 3-67	04 39 47.905	+36 45 42.85	1.832	1.82	–	–	1311	2.2	33.3	42	6.49	0.07
740	K 3-69	05 41 22.147	+39 15 08.09	1.857	2.087	2.649	–	3311	0.5	2.9	0.4	13.87	0.03
741	K 3-7	18 34 13.601	−02 27 36.41	4.976	4.56	–	–	1311	6.3	29.5	30	4.52	0.14
742	K 3-70	05 58 45.350	+25 18 43.86	1.236	1.558	2.457	–	1311	1.6	4.4	6	–	–
746	K 3-76	20 25 04.865	+33 34 50.70	2.488	2.112	–	3.736	1311	0.2	5.1	12	–	–
747	K 3-78	20 45 22.710	+50 22 39.92	1.991	2.624	0.09	1.142	1311	3.8	14.9	15	6.85	0.13
750	K 3-82	21 30 51.636	+50 00 06.96	2.461	3.525	2.515	1.426	3311	24	35.6	30	2.49	0.29
751	K 3-83	21 35 43.877	+50 54 16.94	1.27	1.835	–	–	1311	5	4.7	6.5	7.71	0.19
752	K 3-84	21 38 49.006	+46 00 27.81	0.705	0.608	0.535	–	1311	–	2.7	–	–	–
754	K 3-88	23 12 15.494	+64 39 17.73	0.599	0.948	–	0.494	1311	–	7.1	0.3	–	–
755	K 3-90	01 24 58.628	+65 38 36.14	1.083	0.569	–	–	1311	8.5	12.4	13.9	4.6	0.19
757	K 3-92	02 03 41.171	+64 57 37.88	0.237	0.527	–	0.724	1311	13	–	2	7.11	0.45
759	K 3-94	03 36 08.086	+60 03 46.29	0.364	1.022	1.299	0.377	1311	10	6.9	5.5	5.98	0.29
761	K 4-19	19 13 22.624	+03 25 00.30	2.142	1.463	0.425	–	3311	–	–	–	–	–
764	K 4-41	19 56 34.027	+32 22 12.96	2.439	2.5	0.831	0.145	3311	3	11.5	15	7.59	0.11
765	K 4-47	04 20 45.157	+56 18 11.57	5.138	5.585	3.408	1.143	1331	7.8	–	7.7	22.46	0.85
766	K 4-48	06 39 55.879	+11 06 30.69	3.627	3.673	0.833	–	3311	2.2	11.8	14	8.86	0.09
768	K 4-53	20 42 16.744	+37 40 25.58	3.45	5.024	0.89	0.592	3311	–	34.4	–	–	–
769	K 4-55	20 45 10.021	+44 39 14.58	0.211	1.688	–	–	1311	–	6.2	–	–	–
775	KjPn 6	22 49 02.175	+67 01 38.89	0.518	0.873	1.165	1.764	1311	–	8	–	–	–
779	LoTr 10	14 46 20.239	−61 13 35.37	4.579	2.985	2.254	2.351	1311	–	–	–	–	–
782	LoTr 7	14 15 24.025	−67 31 55.87	0.13	0.861	1.249	1.025	1311	–	–	–	–	–
787	Lo 11	16 03 22.211	−36 00 53.73	0.205	1.758	1.073	–	1311	–	2.7	3.5	–	–
790	Lo 16	17 35 41.798	−40 11 26.20	3.656	10.988	4.495	10.058	3311	–	89.9	–	–	–
797	Lo 9	15 42 13.340	−47 40 46.33	0.121	0.63	–	0.09	1311	–	–	–	–	–
798	MA 13	18 30 30.388	−07 27 38.29	10.933	5.667	–	–	3311	–	28.7	–	–	–
799	MA 2	18 15 13.391	−06 57 12.20	1.006	1.304	0.076	0.792	1311	–	7.4	–	–	–
802	M 1-1	01 37 19.430	+50 28 11.50	0.993	0.51	–	1.437	1311	4.5	14	8	7.27	0.16
803	M 1-11	07 11 16.693	−19 51 02.87	18.8	15.084	3.463	1.214	3311	2.2	25.9	113	4.9	0.05
804	M 1-12	07 19 21.471	−21 43 55.46	3.723	2.383	1.515	–	3311	1.8	21.9	41	7.13	0.06
805	M 1-13	07 21 14.952	−18 08 36.91	2.662	4.368	3.749	–	1311	10	18.9	15	4.51	0.22
806	M 1-14	07 27 56.510	−20 13 22.89	2.101	1.844	1.666	0.876	3311	4.7	59.1	60	4.23	0.1
807	M 1-16	07 37 18.955	−09 38 49.67	8.731	7.022	7.089	6.625	3331	3.6	31.3	31	5.71	0.1
808	M 1-17	07 40 22.206	−11 32 29.81	3.93	3.522	2.095	3.194	3311	2.5	18.3	17	8.23	0.1
811	M 1-2	01 58 49.675	+52 53 48.57	1.513	1.075	0.416	0.094	1311	0.5	–	10	–	–
812	M 1-22	17 35 10.239	−18 34 20.41	2.072	1.918	–	2.497	1311	6	7.4	3.5	11.92	0.35
813	M 1-23	17 37 22.003	−18 46 41.87	2.195	3.146	2.712	–	1311	–	14.1	–	–	–
814	M 1-24	17 38 11.588	−19 37 37.64	7.928	7.466	0.478	0.707	3311	<10	43.5	–	–	–
815	M 1-25	17 38 30.307	−22 08 38.88	6.244	6.016	0.689	–	3311	3.2	39.9	57	4.93	0.08
819	M 1-30	17 52 58.946	−34 38 22.99	5.714	5.292	–	–	3311	3.5	23.4	31	5.9	0.1
822	M 1-33	17 58 58.794	−15 32 14.79	6.185	7.632	–	3.584	3311	4	49	60	4.63	0.09
823	M 1-34	18 01 22.193	−33 17 43.08	2.006	3.779	1.363	7.131	1311	11.2	13.6	14.7	5.95	0.32
826	M 1-38	18 06 05.765	−28 40 29.28	–	3.022	–	–	1311	3.5	14.9	24	6.58	0.11
828	M 1-4	03 41 43.428	+52 17 00.28	2.201	2.263	–	–	3311	6	77.8	90	3.39	0.1

TABLE 2 (CONTINUED)

KN	NAME	R.A. (2000)	DEC (2000)	F (65 μm)	F (90 μm)	F (140 μm)	F (160 μm)	QUAL	DIAM	F (1.4 GHz)	F(5 GHz)	DIST	DIAM
		H:M:S	D:M:S)	Jy	Jy	Jy	Jy		arcsec	mJy	mJy	kpc	pc
829	M 1-40	18 08 25.994	−22 16 53.25	44.078	20.96	–	7.625	3311	4.5	163.3	208	2.83	0.06
831	M 1-42	18 11 05.028	−28 58 59.33	5.007	7.279	8.013	4.503	3331	9	28.3	28.5	4.89	0.21
833	M 1-44	18 16 17.365	−27 04 32.47	5.194	5.412	6.768	2.805	1131	4	9.4	9	9.24	0.18
835	M 1-46	18 27 56.339	−15 32 54.43	19.466	12.055	3.57	4.934	3311	11.5	78.1	81	2.58	0.14
836	M 1-47	18 29 11.154	−21 46 53.43	1.007	1.099	–	–	1311	5.5	11.7	14	5.95	0.16
837	M 1-48	18 29 29.991	−19 05 44.58	1.291	2.036	2.169	1.771	1311	4.8	5	6	7.57	0.18
838	M 1-5	05 46 50.000	+24 22 02.32	2.046	1.733	0.522	–	1311	2.3	41.1	71	5.49	0.06
839	M 1-50	18 33 20.886	−18 16 36.86	2.416	3.361	0.749	0.299	1311	5.6	35.4	50	4.12	0.11
842	M 1-53	18 35 48.267	−17 36 08.71	3.355	4.38	4.325	0.782	3331	6	19.6	8	3.93	0.11
843	M 1-54	18 36 08.357	−16 59 57.02	5.805	6.572	5.373	4.726	3331	13	35.5	53	3.09	0.19
845	M 1-56	18 37 46.250	−17 05 46.55	3.028	3.273	0.56	3.358	3311	1.5	14.6	22	9.48	0.07
847	M 1-58	18 42 56.979	−11 06 53.10	5.187	4.822	–	0.323	3311	6.4	37.7	60	3.69	0.11
849	M 1-6	06 35 45.140	−00 05 37.37	3.831	2.361	3.46	–	3111	3	54.4	86	4.7	0.07
850	M 1-60	18 43 38.107	−13 44 48.64	6.538	6.621	0.146	1.54	3311	2.5	35.1	48	5.81	0.07
851	M 1-61	18 45 55.072	−14 27 37.93	11.311	9.759	–	1.401	3311	1.8	32.5	97	5.59	0.05
853	M 1-63	18 51 30.935	−13 10 36.81	1.535	1.661	1.588	–	1311	4.2	8.4	10.2	7.32	0.15
854	M 1-64	18 50 02.090	+35 14 36.10	0.761	0.51	0.321	2.018	1311	17	4.3	2.4	6	0.49
855	M 1-65	18 56 33.639	+10 52 10.05	2.434	1.681	1.962	0.76	3311	4	21	23	5.94	0.12
856	M 1-66	18 58 26.247	−01 03 45.70	2.414	2.583	–	14.087	1311	2.7	45.7	59	5.39	0.07
857	M 1-67	19 11 30.881	+16 51 38.21	26.235	28.609	16.751	8.822	3333	120.4	217.6	250	0.69	0.4
858	M 1-69	19 13 53.961	+03 37 41.90	3.234	3.032	–	–	3311	–	31.4	–	–	–
859	M 1-7	06 37 20.955	+24 00 35.38	3.427	5.261	4.004	2.22	3331	11	18.5	13	4.5	0.24
860	M 1-71	19 36 26.927	+19 42 23.99	14.339	11.593	3.032	4.86	1311	3	83.8	204	–	–
861	M 1-72	19 41 33.975	+17 45 17.71	3.039	2.61	–	0.131	3311	0.7	5.3	30	12.54	0.04
862	M 1-73	19 41 09.323	+14 56 59.37	6.896	7.01	2.241	–	3311	6	47.7	43	4.17	0.12
863	M 1-74	19 42 18.874	+15 09 08.16	2.335	1.682	–	–	1311	1	7.9	29	10.15	0.05
865	M 1-77	21 19 07.360	+46 18 47.24	8.792	7.776	1.68	0.532	3311	8	29.4	25	4.29	0.17
866	M 1-78	21 20 44.809	+51 53 27.88	843.838	742.643	243.538	250.943	1133	6	363.5	1103.9	1.62	0.05
867	M 1-79	21 37 01.500	+48 56 02.62	1.384	3.435	2.012	1.02	1311	31	21.8	19	2.62	0.39
868	M 1-8	06 53 33.795	+03 08 26.96	2.242	3.569	2.483	0.837	3311	18.4	16.3	23	3.06	0.27
869	M 1-80	22 56 19.806	+57 09 20.68	0.845	0.859	–	–	1311	8	17.9	25	4.29	0.17
870	M 1-9	07 05 19.204	+02 46 59.16	1.085	0.68	–	0.802	1311	2.3	22.4	27	7.22	0.08
871	M 2-10	17 14 07.022	−31 19 42.59	3.438	3.612	–	0.79	3311	2.2	11.6	9.1	10.71	0.11
872	M 2-11	17 20 33.252	−29 00 38.66	0.775	1.457	1.927	1.417	1311	2.2	17.4	22	7.32	0.08
873	M 2-12	17 24 01.451	−25 59 23.16	3.449	2.817	–	1.752	3311	4.4	10.3	12.9	–	–
875	M 2-14	17 41 57.252	−24 11 15.64	7.255	7.444	0.303	–	3311	2.2	22.4	39.1	–	–
876	M 2-15	17 46 54.449	−16 17 24.80	2.663	3.981	0.105	–	3311	7.4	18.7	12.5	5.37	0.19
877	M 2-16	17 52 34.362	−32 45 51.10	1.819	4.33	0.702	–	1311	2.5	20.4	24.8	5.86	0.07
881	M 2-2	04 13 15.045	+56 56 58.08	3.482	3.28	–	0.761	3311	6.5	52	54	3.66	0.12
886	M 2-24	18 02 02.881	−34 27 47.07	3.003	3.345	0.489	0.747	3311	6.8	3.2	3	11.79	0.39
889	M 2-27	18 03 52.588	−31 17 46.54	5.258	5.361	1.533	–	3311	3.8	22.5	50	5.65	0.1
892	M 2-30	18 12 34.414	−27 58 11.59	1.596	2.289	3.75	2.127	1311	3.5	13.9	14	8.1	0.14
893	M 2-31	18 13 16.026	−25 30 04.97	3.561	3.598	–	0.951	3311	4	39.6	51	4.91	0.1
895	M 2-33	18 15 06.534	−30 15 32.89	1.963	1.768	2.255	0.189	1331	5	11.9	12	8.52	0.21
896	M 2-34	18 17 15.947	−23 58 54.51	1.342	2.897	–	–	1311	<25	4.8	–	–	–
897	M 2-35	18 17 37.195	−31 56 46.86	–	0.643	–	0.424	1311	–	–	–	–	–
898	M 2-36	18 17 41.418	−29 08 19.59	3.903	3.904	0.449	1.042	3311	6.8	22.6	13	6.99	0.23
899	M 2-37	18 18 38.352	−28 08 01.00	0.83	1.565	2.636	–	1331	–	–	–	–	–
901	M 2-39	18 22 01.148	−24 10 40.18	2.212	1.762	0.729	–	3311	3.2	7.2	8	10.21	0.16
902	M 2-4	17 01 06.231	−34 49 38.58	3.778	3.978	0.977	–	3311	2	24.5	32	7.15	0.07
903	M 2-40	18 21 23.851	−06 01 55.79	7.267	7.246	3.168	–	1311	5.5	45.5	33	4.67	0.12
904	M 2-41	18 22 34.379	−30 43 29.66	1.289	1	0.666	2.018	1311	–	3	–	–	–
905	M 2-42	18 22 32.020	−24 09 28.40	1.337	1.655	1.41	–	1311	3.9	9.6	14	7.83	0.15
906	M 2-43	18 26 40.048	−02 42 57.63	13.475	9.881	4.454	0.769	3331	1.5	20.4	237	5	0.04
907	M 2-44	18 37 36.908	−03 05 55.96	5.521	5.483	–	2.237	1311	8	48.3	54	3.45	0.13
909	M 2-46	18 46 34.620	−08 28 01.85	2.976	4.938	2.008	2.894	3311	4.4	13.1	12	6.48	0.14
910	M 2-47	19 13 34.559	+04 38 04.45	3.707	4.756	0.071	0.869	3311	6	38.3	45	4.12	0.12
913	M 2-5	17 02 19.069	−33 10 05.01	5.407	5.084	2.977	–	3311	5	14.1	12	7.69	0.19
914	M 2-50	21 57 41.814	+51 41 39.01	0.367	0.487	–	0.47	1311	4.6	8.2	6.5	8.07	0.18
915	M 2-51	22 16 03.890	+57 28 33.75	2.498	5.809	7.035	6.729	3331	39.2	27.2	40.6	1.88	0.36
917	M 2-53	22 32 17.720	+56 10 26.12	1.772	2.662	1.949	1.464	1311	18	14.6	11	3.64	0.32
918	M 2-54	22 51 38.923	+51 50 42.50	4.945	3.546	0.724	0.357	3311	–	5.4	8	14.61	–
919	M 2-55	23 31 52.708	+70 22 10.11	1.845	3.756	3.575	1.759	1331	41	25.4	19	2.31	0.46
921	M 2-7	17 05 13.729	−30 32 18.46	1.162	1.162	1.019	–	1311	<25	6	7	8.55	–
924	M 3-1	07 02 49.980	−31 35 31.50	0.68	1.457	0.27	1.05	1311	11.2	25.7	24	3.78	0.21
925	M 3-10	17 27 20.152	−28 27 51.15	2.65	2.658	–	2.107	1311	3.1	35.2	29	6.33	0.1
926	M 3-12	17 36 22.634	−21 31 12.22	2.522	2.64	0.961	0.396	3311	7.5	11.2	12.5	6.98	0.25
927	M 3-13	17 41 36.594	−22 13 02.46	1.684	1.432	–	–	1311	<7	–	–	–	–
933	M 3-20	17 59 19.318	−28 13 48.05	1.786	1.353	–	–	1311	4	16.2	40	5.3	0.1
934	M 3-21	18 02 32.324	−36 39 12.24	2.846	2.546	1.57	0.155	3311	<5	15.6	30	5.57	–
935	M 3-22	18 02 19.238	−30 14 25.38	1.334	1.319	0.941	0.998	1311	6.4	10.1	8.7	8.45	0.26
937	M 3-24	18 07 53.914	−25 24 02.71	5.998	3.891	0.071	–	3311	<25	17.4	–	–	–
938	M 3-25	18 15 16.967	−10 10 09.47	10.367	9.618	3.429	10.727	3311	1.5	25	76	6.89	0.05
940	M 3-27	18 27 48.273	+14 29 06.06	1.087	0.606	2.032	–	1311	1	–	53.2	8.55	0.04
942	M 3-29	18 39 25.772	−30 40 36.71	0.337	0.899	0.928	0.985	1311	8.2	7.6	18.7	5.86	0.23
943	M 3-3	07 26 34.228	−05 21 52.16	0.185	0.596	0.466	–	1311	12.2	–	5.6	5.46	0.32
944	M 3-30	18 41 14.938	−15 33 43.58	2.824	3.184	–	–	3311	17.2	8.5	7	3.97	0.33
946	M 3-32	18 44 43.127	−25 21 33.85	2.932	2.875	3.04	0.488	3311	7.5	12.2	12	7.06	0.26
947	M 3-33	18 48 12.131	−25 28 52.39	2.216	1.695	–	–	1311	6	9.8	7.5	8.94	0.26
948	M 3-34	19 27 01.897	−06 35 04.63	2.664	2.402	0.475	0.162	1311	8	29.6	29	4.12	0.16
949	M 3-35	20 21 03.769	+32 29 23.86	4.837	3.65	–	–	3311	1.5	29.5	140	5.62	0.04
950	M 3-36	17 12 39.152	−25 43 37.39	1.387	1.603	1.946	2.054	1311	3.2	4.9	3.5	13.92	0.22
952	M 3-38	17 21 04.459	−29 02 59.21	6.63	5.961	0.778	0.384	3311	1.8	7.6	21	8.29	0.07
953	M 3-39	17 21 11.505	−27 11 38.13	22.638	24.194	7.809	1.158	3331	19	279.4	280	1.7	0.16
954	M 3-4	07 55 11.398	−23 38 12.46	1.061	1.155	0.983	0.47	1311	13.5	6.3	2.4	6.58	0.43
955	M 3-40	17 22 28.272	−27 08 42.40	5.041	4.717	3.036	2.794	3331	2.6	15.6	17	8.22	0.1

TABLE 2 (CONTINUED)

KN	NAME	R.A. (2000)	DEC (2000)	F (65 μm)	F (90 μm)	F (140 μm)	F (160 μm)	QUAL	DIAM	F (1.4 GHz)	F(5 GHz)	DIST	DIAM
		H:M:S	D:M:S)	Jy	Jy	Jy	Jy		arcsec	mJy	mJy	kpc	pc
963	M 3-48	17 59 56.823	−31 54 27.46	0.104	0.419	–	–	1311	–	–	–	–	–
965	M 3-5	08 02 28.932	−27 41 55.44	2.259	2.633	1.385	–	1311	7	11	10	5.9	0.2
967	M 3-51	18 04 56.233	−32 54 01.23	0.509	0.945	–	1.502	1311	–	3.2	–	–	–
969	M 3-53	18 24 07.890	−11 06 42.08	3.979	5.123	7.331	–	1311	–	19.5	–	–	–
975	M 3-9	17 25 43.364	−26 11 55.47	7.307	9.022	3.599	–	3331	16	37.3	35	3.88	0.3
977	M 4-11	18 54 17.671	−10 05 14.49	1.644	3.396	2.079	0.429	1311	21.2	9.4	–	–	–
978	M 4-14	19 21 00.718	+07 36 52.37	3.094	3.937	5.787	2.183	3311	7.4	11.8	8	6.28	0.23
980	M 4-18	04 25 50.831	+60 07 12.72	3.41	1.863	0.355	1.565	3311	3.8	18.5	22	6.37	0.12
981	M 4-2	07 28 53.808	−35 45 13.92	0.899	0.632	2.254	–	1311	6	24.2	19	5.26	0.15
982	M 4-3	17 10 41.751	−27 08 43.75	1.276	1.264	2.359	3.21	1311	1.6	12.2	28	8.13	0.06
987	M 4-9	18 14 18.360	−04 59 21.30	4.308	8.57	5.261	2.096	3311	44.2	43.8	42	1.72	0.37
990	MaC 1-13	18 28 35.242	−08 43 22.82	8.671	8.271	7.573	3.768	1311	–	30.4	–	–	–
992	MaC 1-2	13 54 27.067	−64 59 36.14	1.084	1.416	–	0.051	1311	–	–	–	–	–
1000	MeWe 1-7	16 47 57.070	−50 42 48.32	3.531	2.735	4.566	1.965	1311	–	–	–	–	–
1001	MeWe 1-8	16 48 40.194	−51 09 20.26	–	1.503	0.576	2.963	1311	–	–	–	–	–
1004	Me 2-1	15 22 19.274	−23 37 31.34	0.842	1.197	–	0.115	1311	7	33.6	30	4.32	0.15
1005	Me 2-2	22 31 43.686	+47 48 03.96	0.965	0.625	0.607	1.937	1311	1.2	16	40	8.56	0.05
1006	MyCn 18	13 39 35.116	−67 22 51.45	17.17	17.185	6.808	6.315	3331	12.6	–	106	3.23	0.2
1007	My 60	10 31 33.390	−55 20 50.87	2.58	3.539	0.41	–	1311	7.6	–	60	3.47	0.13
1009	Mz 2	16 14 32.433	−54 57 03.76	6.386	7.386	2.8	0.136	3111	23	–	75	2	0.22
1012	NGC 1501	04 06 59.190	+60 55 14.34	5.662	12.013	2.975	1.373	3331	51.8	207.7	210	1.03	0.26
1013	NGC 1514	04 09 16.990	+30 46 33.43	0.779	7.38	3.384	4.231	1331	100.4	182.7	288	1.01	0.49
1014	NGC 1535	04 14 15.762	−12 44 22.03	8.439	11.349	2.444	1.103	1311	18.4	167.8	160	1.77	0.16
1015	NGC 2022	05 42 06.229	+09 05 10.75	4.676	5.515	2.809	–	3311	19.4	92.3	91	2.02	0.19
1017	NGC 2346	07 09 22.547	−00 48 22.98	5.761	9.003	10.585	7.978	3331	54.6	37.6	86	2.07	0.55
1018	NGC 2371/2	07 25 34.720	+29 29 25.63	5.715	6.803	4.715	1.4	3331	43.6	48.1	–	2.07	0.44
1019	NGC 2392	07 29 10.768	+20 54 42.44	14.76	18.032	8.169	3.25	3331	44.8	279.9	251	1.44	0.31
1021	NGC 2452	07 47 26.248	−27 20 07.16	3.586	5.514	4.19	–	3311	18.8	56	57	2.31	0.21
1023	NGC 2610	08 33 23.320	−16 08 57.67	1.063	1.386	0.912	0.768	1311	43	29.8	30	1.86	0.39
1024	NGC 2792	09 12 26.596	−42 25 39.90	5.685	6.392	1.133	0.652	3311	13	–	116	1.26	0.08
1025	NGC 2818	09 16 01.656	−36 37 38.76	1.665	2.485	2.807	2.324	1311	40	46.6	33	1.79	0.35
1026	NGC 2867	09 21 25.337	−58 18 40.69	11.091	10.774	2.804	2.917	3311	16	–	252	1.69	0.13
1027	NGC 2899	09 27 03.123	−56 06 21.22	2.701	5.13	5.775	4.372	1331	90	–	86	1.06	0.46
1028	NGC 3132	10 07 01.771	−40 26 11.11	26.899	38.62	23.599	18.285	3131	45	–	230	1.5	0.33
1029	NGC 3195	10 09 20.910	−80 51 30.73	3.459	6.441	3.46	1.028	3331	40	–	35	1.96	0.38
1030	NGC 3211	10 17 50.549	−62 40 14.57	4.017	4.506	2.28	0.502	3311	16	–	228	1.7	0.13
1031	NGC 3242	10 24 46.138	−18 38 32.26	33.512	38.693	7.971	6.4	3333	37.2	757.7	860	0.94	0.17
1033	NGC 3699	11 27 57.745	−59 57 27.71	3.54	7.862	5.69	3.722	3311	44.8	–	67	1.54	0.33
1034	NGC 3918	11 50 17.730	−57 10 56.90	34.408	28.325	7.27	3.945	3331	18.8	–	859	1.17	0.11
1035	NGC 40	00 13 01.023	+72 31 19.07	48.192	36.405	11.212	9.101	3333	36.4	510.3	460	0.98	0.17
1036	NGC 4071	12 04 14.815	−67 18 35.57	1.429	3.284	4.025	1.239	1331	63	–	26	1.73	0.53
1038	NGC 5189	13 33 32.974	−65 58 26.67	15.323	23.021	9.626	7.972	3331	140	–	455	0.55	0.37
1039	NGC 5307	13 51 03.273	−51 12 20.62	3.896	4.726	0.144	1.748	3311	12.6	–	95	2.42	0.15
1040	NGC 5315	13 53 56.972	−66 30 50.96	67.003	47.078	16.764	8.931	3331	6	–	442	2.14	0.06
1041	NGC 5873	15 12 51.052	−38 07 33.65	1.246	0.795	–	–	1311	7	45.5	48	4.23	0.14
1042	NGC 5882	15 16 49.941	−45 38 58.60	38.54	29.7	9.091	5.312	3331	14	–	334	1.74	0.12
1045	NGC 6058	16 04 26.597	+40 40 56.05	1.308	1.251	1.208	0.906	1311	26.4	7	10	3.34	0.43
1046	NGC 6072	16 12 58.079	−36 13 46.06	14.896	25.114	14.516	12.712	3311	70	138.5	164	0.98	0.33
1047	NGC 6153	16 31 30.825	−40 15 14.22	88.194	69.461	19.749	10.285	3331	24.6	–	477	1.17	0.14
1048	NGC 6210	16 44 29.521	+23 47 59.55	28.626	21.385	7.113	6.288	3331	16.2	297.8	311	1.55	0.12
1049	NGC 6302	17 13 44.211	−37 06 15.94	670.18	304.595	188.327	201.675	3333	45	1906.8	3034	0.52	0.11
1050	NGC 6309	17 14 04.322	−12 54 37.71	15.699	16.964	5.961	2.593	3331	17	131.5	151	2.35	0.19
1052	NGC 6337	17 22 15.658	−38 29 03.47	19.391	14.945	–	–	1311	47	45.9	103	1.33	0.3
1053	NGC 6369	17 29 20.443	−23 45 34.22	69.688	61.394	18.329	11.351	3333	28	1825	2002	0.75	0.1
1055	NGC 650-51	01 42 19.948	+51 34 31.15	2.536	7.243	4.019	2.1	1311	138.4	138.9	125	1.56	1.05
1057	NGC 6543	17 58 33.409	+66 37 58.79	117.286	71.842	21.65	13.89	3333	18.8	771.5	850	1.12	0.1
1058	NGC 6563	18 12 02.753	−33 52 07.14	8.647	13.865	10.414	3.326	3331	43	61	69	2.36	0.49
1060	NGC 6567	18 13 45.136	−19 04 33.67	2.308	3.04	1.306	–	1311	8.8	163	168	2.4	0.1
1061	NGC 6572	18 12 06.404	+06 51 12.17	78.382	45.439	13.059	9.839	3333	10	557.5	1374	1.06	0.05
1063	NGC 6620	18 22 54.186	−26 49 17.00	2.124	2.806	1.033	–	1311	5	17.1	20.5	6.42	0.16
1064	NGC 6629	18 25 42.449	−23 12 10.59	25.167	19.057	5.565	3.093	3331	15	257.8	275	1.84	0.13
1065	NGC 6644	18 32 34.641	−25 07 44.00	2.548	2.359	1.031	1.555	1311	2.8	64.3	97	4.09	0.06
1066	NGC 6720	18 53 35.079	+33 01 45.03	31.015	40.615	20.511	20.619	3333	69.2	420.8	360	1.13	0.38
1067	NGC 6741	19 02 37.088	−00 26 56.97	10.43	11.81	–	0.433	1311	8	131.9	230	2.32	0.09
1068	NGC 6751	19 05 55.560	−05 59 32.92	15.44	16.206	6.072	4.448	3331	21	55.1	63	2.18	0.22
1069	NGC 6765	19 11 06.465	+30 32 42.52	0.685	1.27	1.117	–	1311	38	10.1	17.7	2.41	0.44
1070	NGC 6772	19 14 36.373	−02 42 25.04	4.95	10.678	4.095	3.955	3331	90	77.4	73	1.11	0.48
1071	NGC 6778	19 18 24.939	−01 35 47.41	8.968	12.541	6.421	2.524	3311	15.8	64.6	55	2.54	0.19
1073	NGC 6790	19 22 56.965	+01 30 46.45	7.792	6.359	2.105	2.493	3331	1.8	52.6	290	4.1	0.04
1074	NGC 6803	19 31 16.490	+10 03 21.88	7.54	7.287	3.109	0.15	3311	5	68.9	114	3.26	0.08
1075	NGC 6804	19 31 35.175	+09 13 32.01	11.111	11.345	4.413	1.41	3331	31.4	112.7	135	1.32	0.2
1076	NGC 6807	19 34 33.543	+05 41 02.58	0.645	0.718	0.65	1.521	1311	0.8	8	29	11.18	0.04
1077	NGC 6818	19 43 57.844	−14 09 11.91	12.621	14.24	5.929	3.97	1311	18.2	290.2	300	1.47	0.13
1078	NGC 6826	19 44 48.161	+50 31 30.33	27.865	26.039	7.148	3.726	3331	25.4	414.4	385	1.2	0.15
1081	NGC 6852	20 00 39.213	+01 43 40.05	0.96	0.953	0.564	0.786	1311	28	10.4	20	2.66	0.36
1083	NGC 6879	20 10 26.682	+16 55 21.30	1.513	1.296	2.735	–	1311	5	23.1	18	5.78	0.14
1085	NGC 6884	20 10 23.669	+46 27 39.54	11.033	10.902	2.693	1.791	3311	5.3	152.4	200	2.7	0.07
1086	NGC 6886	20 12 42.813	+19 59 22.65	8.122	7.47	3.494	1.503	3331	5.5	77.6	108	2.94	0.08
1087	NGC 6891	20 15 08.838	+12 42 15.63	7.305	8.289	3.144	2.253	3311	10.2	110.8	105	2.35	0.12
1088	NGC 6894	20 16 23.965	+30 33 53.17	2.634	8.688	3.956	–	3311	44	66.1	61	1.44	0.31
1089	NGC 6905	20 22 22.940	+20 06 16.80	5.483	5.801	3.971	1.94	3331	40.4	66.7	52	1.62	0.32
1090	NGC 7008	21 00 32.503	+54 32 36.18	25.227	25.494	10.836	9.013	3333	90	263.3	217	1.31	0.57
1091	NGC 7009	21 04 10.877	−11 21 48.25	70.225	66.268	14.071	11.285	3333	28.2	682	750	1.09	0.15
1092	NGC 7026	21 06 18.209	+47 51 05.35	30.06	29.863	9.726	5.815	3331	15	260.5	260	1.91	0.14
1094	NGC 7048	21 14 15.224	+46 17 17.52	3.555	6.284	4.067	5.812	3311	65	45.6	37	1.5	0.47
1096	NGC 7139	21 46 08.586	+63 47 29.45	0.45	1.675	1.275	0.807	1311	76	29.8	28.9	1.56	0.57

TABLE 2 (CONTINUED)

KN	NAME	R.A. (2000)	DEC (2000)	F (65 μm)	F (90 μm)	F (140 μm)	F (160 μm)	QUAL	DIAM	F (1.4 GHz)	F(5 GHz)	DIST	DIAM
		H:M:S	D:M:S)	Jy	Jy	Jy	Jy		arcsec	mJy	mJy	kpc	pc
1098	NGC 7354	22 40 19.940	+61 17 08.10	33.268	30.543	9.496	4.222	3331	20	581	579	1.19	0.12
1099	NGC 7662	23 25 53.968	+42 32 05.04	22.148	21.669	6.041	4.011	3331	20	611.5	631	1.17	0.11
1100	Na 1	17 12 51.900	−03 16 00.13	1.755	2.016	0.027	–	1311	8	23	22.5	4.2	0.16
1104	PBOZ 34	18 05 25.509	−25 13 37.23	1.296	5.988	1.724	–	1311	–	20.8	52	–	–
1105	PB 1	07 02 46.764	−13 42 34.65	1.675	1.619	1.828	–	1311	–	11.9	18	–	–
1106	PB 10	19 28 14.391	+12 19 36.17	5.336	6.444	4.651	–	3311	8	50.4	50	3.53	0.14
1107	PB 2	08 20 40.188	−46 22 58.82	0.882	0.718	–	–	1311	3	–	40	5.75	0.08
1108	PB 3	08 54 18.323	−50 32 22.34	4.526	4.492	2.307	2.818	3311	7	–	70	3.4	0.12
1109	PB 4	09 15 07.747	−54 52 43.78	4.735	6.393	2.352	0.322	3311	11.2	–	71	2.81	0.15
1110	PB 5	09 16 09.613	−45 28 42.79	9.504	7.797	2.42	3.249	3331	5	–	107	–	–
1111	PB 6	10 13 15.949	−50 19 59.28	3.869	3.036	1.924	–	3311	11	–	30	3.55	0.19
1112	PB 8	11 33 17.717	−57 06 14.00	5.599	5.831	1.735	–	3311	5	–	27	5.15	0.12
1113	PB 9	19 27 44.814	+10 24 20.82	1.854	2.683	2.603	–	1311	7	33.1	40	3.57	0.12
1114	PC 11	16 37 42.697	−55 42 26.49	0.536	1.411	0.574	–	1311	5	–	11	–	–
1116	PC 13	16 50 17.108	−30 19 55.50	0.441	1.149	–	–	1311	–	6.6	–	–	–
1117	PC 14	17 06 14.767	−52 30 00.40	1.694	2.376	2.814	0.399	1331	7	–	30	4.32	0.15
1118	PC 17	17 35 41.677	−46 59 48.54	2.489	1.923	0.244	0.629	1311	5	–	14.7	6.12	0.15
1119	PC 19	18 24 44.524	+02 29 28.10	1.632	0.877	0.617	0.512	1311	2.8	22.4	25.3	6.75	0.09
1120	PC 20	18 43 03.456	−00 16 37.02	8.889	7.243	–	2.627	1311	–	27.3	–	–	–
1121	PC 21	18 45 35.215	−20 34 58.32	1.961	2.703	2.015	1.245	3311	13.4	11.2	–	–	–
1122	PC 22	19 42 03.514	+13 50 37.33	1.509	1.767	–	–	1311	–	9.2	–	–	–
1124	PC 24	20 19 38.133	+27 00 11.23	2.484	2.735	1.285	–	1311	5	17.1	18	5.78	0.14
1127	PM 1-188	17 54 21.100	−15 55 51.78	4.799	4.75	0.318	–	3311	–	–	–	–	–
1128	PM 1-276	19 02 17.857	+10 17 34.49	3.793	5.214	2.516	2.136	3311	–	15.3	–	–	–
1129	PM 1-295	19 19 18.760	+17 11 48.09	7.702	7.546	7.139	0.96	1311	–	13.9	–	–	–
1130	PM 1-310	19 38 52.135	+25 05 32.63	6.213	4.603	1.867	7.758	1311	–	–	–	–	–
1132	PM 1-89	15 19 08.724	−53 09 50.05	10.027	9.316	2.292	–	3311	–	–	–	–	–
1136	Pe 1-1	10 38 27.607	−56 47 06.40	8.965	8.009	7.825	3.319	3331	3	–	125.3	4.16	0.06
1137	Pe 1-11	18 01 42.767	−33 15 26.30	2.643	2.175	0.823	1.553	1311	9	10.9	8	7.9	0.34
1138	Pe 1-12	18 17 42.379	−28 17 13.80	–	0.476	0.66	0.797	1311	12	–	3.4	10.2	0.59
1139	Pe 1-13	18 34 51.659	−22 43 16.97	0.076	0.731	–	1.028	1311	7	4.4	3	8.29	0.28
1141	Pe 1-15	18 46 24.485	−07 14 34.57	2.534	2.029	–	–	3311	5	8.3	8	7.4	0.18
1142	Pe 1-16	18 47 32.251	−06 54 03.52	2.434	2.455	7.163	1.089	3311	–	14.2	–	–	–
1147	Pe 1-20	18 57 17.351	−05 59 51.79	0.354	0.931	0.129	0.342	1311	8.4	5.1	29.4	4.52	0.18
1148	Pe 1-21	18 57 49.642	−05 27 39.73	1.16	1.48	0.549	3.774	1311	8.6	6.3	30	3.95	0.16
1149	Pe 1-3	10 44 31.116	−61 39 38.47	1.051	2.368	3.299	3.222	1311	8	–	24	–	–
1150	Pe 1-6	16 23 54.309	−46 42 15.28	–	4.576	–	–	311	7.2	–	40	3.94	0.14
1151	Pe 1-7	16 30 25.852	−46 02 51.10	42.654	25.28	11.357	2.405	3311	5	–	117	–	–
1152	Pe 1-8	17 06 22.558	−44 13 09.96	6.277	8.943	6.223	0.763	1311	–	–	–	–	–
1160	Pe 2-4	09 30 48.402	−53 09 59.33	2.264	2.602	1.272	0.906	1311	–	–	–	–	–
1162	Pe 2-7	10 41 19.574	−56 09 16.34	1.045	1.399	2.067	0.005	1311	–	–	–	–	–
1167	SaSt 1-1	08 31 42.877	−27 45 31.70	1.739	1.157	1.544	1.723	1311	–	–	0.3	–	–
1170	SaSt 3-166	18 29 11.268	−17 27 12.90	1.586	2.059	0.665	4.097	1311	–	3.2	–	–	–
1171	SaWe 2	17 27 00.197	−27 40 35.11	0.562	2.44	1.572	–	1311	–	14.2	3	–	–
1175	Sa 1-8	18 50 44.312	−13 31 02.18	2.218	2.007	–	0.59	3111	5.6	13.5	11	6.33	0.17
1176	Sa 2-21	08 08 44.278	−19 14 03.13	0.069	0.763	1.683	0.197	1311	40	8.5	2.4	4.11	0.8
1177	Sa 2-230	17 42 02.007	−15 56 07.46	1.949	1.323	–	–	1311	–	4.9	3.8	–	–
1178	Sa 2-237	17 44 42.282	−15 45 11.45	9.836	9.483	–	5.196	1113	–	5.4	–	–	–
1182	Sa 4-1	17 13 50.356	+49 16 11.26	0.427	0.457	0.832	0.571	1311	–	–	–	–	–
1187	Sh 1-89	21 14 07.628	+47 46 22.17	1.096	2.718	0.395	2.673	1311	120	13.5	42.5	1.88	1.09
1191	Sn 1	16 21 04.421	−00 16 10.54	0.277	0.596	1.471	0.928	1311	3	10.4	7	9.42	0.14
1192	Sp 1	15 51 40.934	−51 31 28.39	4.179	8.354	4.189	4.004	1311	72	–	75	1.21	0.42
1193	Sp 3	18 07 15.793	−51 01 10.41	8.052	12.906	6.587	7.967	3333	35.6	–	61	1.75	0.3
1196	StWr 4-10	16 02 13.042	−41 33 35.94	0.041	0.394	–	0.523	1311	–	–	–	–	–
1197	St 3-1	07 06 50.888	−03 05 09.50	0.753	0.932	0.385	–	1311	–	7.5	–	–	–
1198	Ste 2-1	10 11 57.662	−52 38 17.09	–	0.499	–	–	1311	–	–	–	–	–
1201	SwSt 1	18 16 12.237	−30 52 08.71	17.294	13.034	–	0.315	3311	1.3	26.7	216	3.79	0.02
1203	Tc 1	17 45 35.298	−46 05 23.81	10.648	6.85	0.575	0.533	3311	15	–	801	1.39	0.1
1210	Te 2337	17 48 45.272	−26 43 28.80	10.8	8.5	19.643	–	3311	–	15.2	–	–	–
1212	Th 2-A	13 22 33.854	−63 21 00.96	4.078	5.185	–	3.694	1311	23	–	60	2.07	0.23
1216	Th 3-12	17 25 06.093	−29 45 16.87	3.613	4.512	–	–	3311	1.8	2.6	3.5	–	–
1217	Th 3-13	17 25 19.341	−30 40 41.79	8.348	2.537	–	–	3111	2	7.4	14.3	–	–
1218	Th 3-14	17 25 44.060	−26 57 47.69	2.922	2.598	1.308	–	3311	1.4	5.8	4	–	–
1224	Th 3-25	17 30 46.716	−27 05 59.12	0.043	1.042	0.528	2.846	1311	2	14.9	18	8.77	0.09
1225	Th 3-26	17 31 09.297	−28 14 50.42	2.632	2.337	–	–	1311	6.6	10.4	10	7.86	0.25
1226	Th 3-27	17 35 58.467	−24 25 29.15	4.357	5.395	2.905	–	3311	3.2	14.4	13.5	–	–
1228	Th 3-32	17 35 15.533	−28 07 01.70	3.982	3.019	–	1.552	1311	–	10.2	–	–	–
1235	Th 4-10	17 57 06.599	−18 06 43.43	1.819	2.087	–	–	1311	–	4.3	–	–	–
1236	Th 4-11	18 00 08.820	−17 40 43.33	1.832	2.515	2.449	–	1311	<5	–	0.2	–	–
1238	Th 4-3	17 48 37.390	−22 16 48.79	1.11	1.217	0.433	–	1311	–	2.7	–	–	–
1244	V-V 3-5	18 36 32.291	−19 19 28.01	1.906	3.073	0.72	2.982	3311	–	11.6	10	–	–
1246	VBRC 1	08 30 54.197	−38 18 06.98	1.648	3.486	1.496	3.464	1311	–	37.9	–	–	–
1248	VBRC 6	14 41 35.992	−56 15 13.74	0.778	1.629	2.02	1.714	1311	–	–	–	–	–
1251	VY 2-1	18 27 59.603	−26 06 48.29	4.039	4.763	2.109	–	3311	3.7	32.4	37	–	–
1259	Ve 26	08 43 28.087	−46 06 39.72	16.331	10.899	6.139	0.586	3331	–	–	–	–	–
1260	Vo 1	06 59 26.405	−79 38 47.20	33.47	21.452	5.513	4.417	3331	–	–	–	–	–
1261	Vo 2	08 16 10.000	−39 51 50.67	1.385	1.676	–	0.006	1311	–	60.9	–	–	–
1262	Vo 3	08 42 16.561	−40 44 10.57	38.376	49.309	57.133	57.844	3333	–	–	–	–	–
1264	Vy 1-1	00 18 42.167	+53 52 20.03	1.077	1.394	–	0.028	1311	6	19.8	28.9	5.34	0.16
1265	Vy 1-2	17 54 22.994	+27 59 57.99	1.704	1.184	0.697	–	1311	4.6	11.1	–	–	–
1266	Vy 1-4	18 54 01.899	−06 26 19.81	1.821	2.476	–	1.253	1311	4.5	19.7	22	6.01	0.13
1267	Vy 2-2	19 24 22.229	+09 53 56.66	31.892	23.912	4.713	4.645	3111	0.6	5.9	50	9.82	0.03
1268	Vy 2-3	23 22 57.952	+46 53 58.24	0.655	0.785	1.564	–	1311	4.6	6.5	3	9.95	0.22
1271	WeSb 3	18 06 00.766	+00 22 38.57	0.261	0.936	2.347	–	1311	–	13.1	–	–	–
1274	We 1-1	00 38 54.178	+66 23 48.63	0.362	1.02	1.167	0.138	1311	19	5.2	1.5	6.57	0.61
1281	We 1-7	18 44 06.233	−12 12 57.15	–	1.68	3.263	1.739	1311	–	5.3	–	–	–

TABLE 2 (CONTINUED)

KN	NAME	R.A. (2000)	DEC (2000)	F (65 μm)	F (90 μm)	F (140 μm)	F (160 μm)	QUAL	DIAM	F (1.4 GHz)	F(5 GHz)	DIST	DIAM
		H:M:S	D:M:S)	Jy	Jy	Jy	Jy		arcsec	mJy	mJy	kpc	pc
1282	We 1-9	20 09 04.958	+26 26 54.13	0.99	2.131	1.816	2.896	1311	–	9.9	–	–	–
1287	WhMe 1	19 14 59.755	+17 22 46.01	6.393	5.811	1.662	3.378	3311	–	–	–	–	–
1288	Wray 16-120	12 45 54.930	−60 20 17.45	1.296	1.393	0.901	1.815	1311	–	–	–	–	–
1289	Wray 16-121	12 48 30.564	−63 50 01.79	0.016	3.465	3.108	3.314	1311	–	–	–	–	–
1290	Wray 16-122	13 00 41.215	−56 53 40.19	0.147	0.809	–	2.081	1311	–	–	–	–	–
1291	Wray 16-128	13 24 21.922	−57 31 19.29	1.399	1.924	2.794	0.051	1311	–	–	–	–	–
1292	Wray 16-189	15 51 19.819	−48 26 06.93	0.808	1.757	0.916	1.617	1311	–	–	–	–	–
1293	Wray 16-199	16 00 22.002	−48 15 35.29	2.151	2.989	–	–	1311	–	–	–	–	–
1296	Wray 16-266	17 22 36.947	−52 46 34.45	0.491	0.823	0.737	2.13	1311	–	–	–	–	–
1301	Wray 16-411	18 26 41.781	−40 29 52.52	1.512	0.884	0.772	1.506	1311	–	–	–	–	–
1303	Wray 16-93	11 30 48.339	−59 17 04.63	0.487	0.94	0.995	–	1311	–	–	–	–	–
1306	Wray 17-18	08 23 53.825	−45 31 10.70	0.69	1.462	2.112	0	1311	–	–	–	–	–
1308	Wray 17-31	09 31 20.485	−56 17 39.39	0.343	0.881	0.225	–	1311	–	–	–	–	–
1309	Wray 17-40	10 06 59.570	−64 21 49.99	0.157	1.65	0.365	1.062	1311	–	–	–	–	–
1310	Wray 17-59	13 19 29.925	−66 09 07.25	0.381	1.348	–	0.099	1311	–	–	–	–	–
1311	Y-C 2-5	08 10 41.628	−20 31 32.16	0.287	0.541	–	–	1311	–	7.1	4.5	–	–

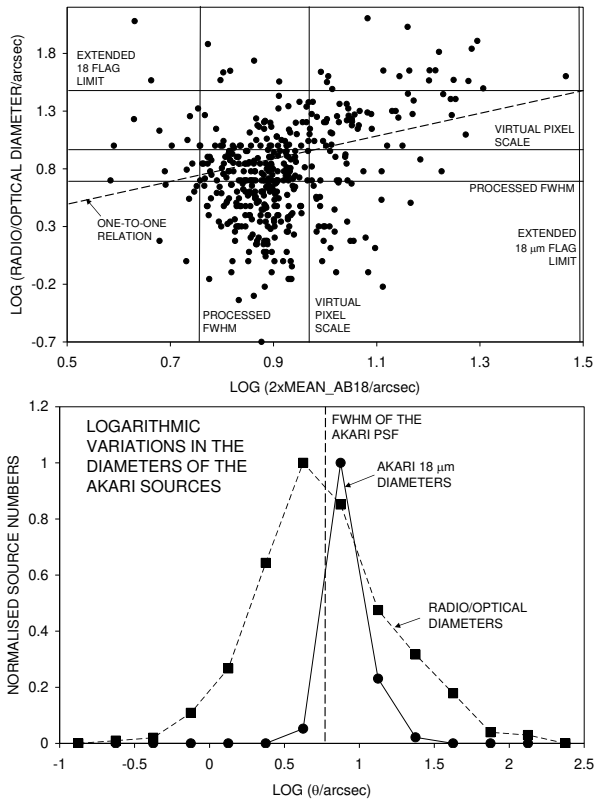

Fig. 2. Comparison between source diameters determined from radio and optical observations, and those determined through AKARI 18 μm observations (upper panel). We also indicate the diameter at which AKARI flags the sources as being extended ("Extended 18 μm Flag Limit"); the size of the virtual pixel scale; and the FWHM of the PSF (identified as the "Processed FWHM"). Although mean AKARI diameters are comparable to those for the optical/radio regime, it is clear that the range in θ is significantly smaller. This is illustrated in the lower panel, where we show distributions for the optical/radio and AKARI results.

cluding glitches, noise, residuals in the responsivity corrections and other anomalies. For the brighter AKARI sources, the absolute uncertainties are of order ∼15%, whilst relative errors are ∼10%, leading to total errors of ∼20% in all of the longer wave bands.

Of the sources listed in Tables 1 and 2, 415 PNe are common to both of the listings. Similarly, a total number of 857 PNe has been measured in this survey, corresponding to 79% of the sources listed in Kerber et al. (2003).

2.3. *Source Sizes in the AKARI Catalog*

We have noted, in § 2, that although virtual pixel sizes for the IRC results are of the order of 9-10 arcsec, the FWHM of the PSFs are ∼5.5–5.7 arcsec. Given that many PNe have dimensions exceeding these limits, it follows that AKARI should permit us to determine the angular dimensions for many of the detected PNe.

The AKARI IRC catalogue includes the flags EXTENDED09 and EXTENDED18, which are triggered when sources have radii >15.6 arcsec. None of the PNe in the present sample are flagged as being extended, even though a reasonable proportion (of order 13%) have radio/optical radii which are greater than these limits. The AKARI catalogue also provides mean radii of the sources at 9 and 18 μm, indicated by the parameters MEAN_AB09 and MEAN_AB18, although here again, the values appear quite different from those in previous studies. This disparity is most clearly to be seen in Figure 2, where we plot the AKARI parameter 2×MEAN_AB18 against the radio/optical diameters from Table 1. It is clear that there is little correlation between the two sets of parameters.

To understand what is happening more clearly, we first concentrate on the distribution of results with respect to the horizontal axis. It is apparent

that most of the sources have values 2×MEAN_AB18 which fall within a narrow range of radii $0.625 < \log(\theta/\mathrm{arcsec}) < 1.125$. The large majority of these are larger than the FWHM of the PSF. Where we now view the distribution of sources with respect to the vertical axis –that is, with respect to values of diameter taken from radio and optical observations– it becomes apparent that half of sources are smaller than the PSF, and that the distribution is very much broader than that of the AKARI results. This latter trend is also apparent in the lower panel of Figure 2, where we show normalized histograms of the AKARI and radio/optical results. Whilst the AKARI dimensions are sharply peaked close to $\theta = 7.5$ arcsec, the radio/optical data extend over a regime which is ∼60 times larger.

It is therefore clear that whilst the mean infrared sizes of the sources are similar to those in other wavelength regimes –the AKARI dimensions are ∼0.86 times as large as those determined through optical and radio observations– the level of agreement for individual sources is much less impressive. It is found that the infrared dimensions are mostly very much larger, or significantly less.

It is no surprise that there is a paucity of AKARI sources with dimensions less than the PSF – sources which are smaller than this limit would be unresolved. What is more surprising is that so many optically compact sources have substantially larger IR diameters, and that these are close to the size of the 18 μm PSF. One explanation for this may be that many smaller radio/optical sources correspond to younger PNe, in which the neutral envelopes are larger than the ionized regimes. Where a large fraction of the IR emission derives from these HI shells, then the dimensions of the sources will be correspondingly enhanced. On the other hand, it is possible that sources which are compact are prone to larger errors in their derived diameters, and that many of the MIR dimensions are significantly too large.

Similarly, it is possible that [OIV] λ25.87 μm and [NeV] λ24.316 μm are dominant in evolved PNe, leading to centralized emission, and smaller mean dimensions. A similar trend has been noted in MIPSGAL 24 μm mapping of PNe (Phillips & Márquez-Lugo 2011; Chu et al. 2009; Ueta 2006; Su et al. 2004, 2007), and this may explain the paucity of sources having larger angular diameters. Here again however, it is possible that weaker, more extended emission falls below the AKARI detection limits, and that this causes a significant reduction in the sizes of the PNe.

It is therefore clear that instrumental errors, and variations in the structures of the PNe are capable of explaining the disparities illustrated in Figure 2. Further analysis is required before these differences can be understood. Given the uncertainties in the veracity of the AKARI results, however, we shall be using radio/optical estimates of diameter in our investigation of evolutionary trends.

2.4. *Comparison of the AKARI and IRAS Photometric results*

We have finally undertaken a comparison between the AKARI photometry and corresponding IRAS results. The flux comparisons are provided in Figure 3, where all of the results have quality factors of 3. For this case, the IRAS PSC was interrogated using a search radius of 18 arcsec, comparable to the positional uncertainty for sources in this catalogue. This resulted in the detection of 573 nebulae with flux quality FQUAL = 3 in at least one of the photometric channels.

The IRAS photometry was undertaken at 12, 25, 60 and 100 μm; wavelengths which are slightly different from those quoted for the present results. It is not therefore possible to undertake a direct one-to-one comparison with the AKARI fluxes, although we are able to compare the closely adjacent channels at 9 and 12 μm, 18 and 25 μm, 65 and 60 μm, and 90 and 100 μm (Figure 3).

It is clear that whilst the fluxes are similar at 90 and 100 μm, the other comparisons show systematic differences in emission. For the most part, the IRAS fluxes are larger than those determined by the AKARI all-sky survey.

One possible explanation for these trends is that there is a calibration problem with the AKARI data, although this seems extremely improbable, and can almost certainly be discounted. The AKARI team has used a broad range of standard stars for the IRC calibration, for instance, including sources in the ecliptic polar regions and Large Magellanic Cloud. They have also used sources employed in calibrating the *Infrared Space Observatory* (*ISO*). There is a non-linear relation between input source fluxes and the AKARI signal; a function which is fitted using a second degree polynomial fit. When this correction is employed, it is clear that residual errors are small; there is certainly little evidence for the biases which are detected in the present work. Similar calibrations are used for the FIS results, where the AKARI team has used stellar, asteroidal, and planetary flux calibrators. Again, non-linear relations are detected between the source fluxes and measured signals, and

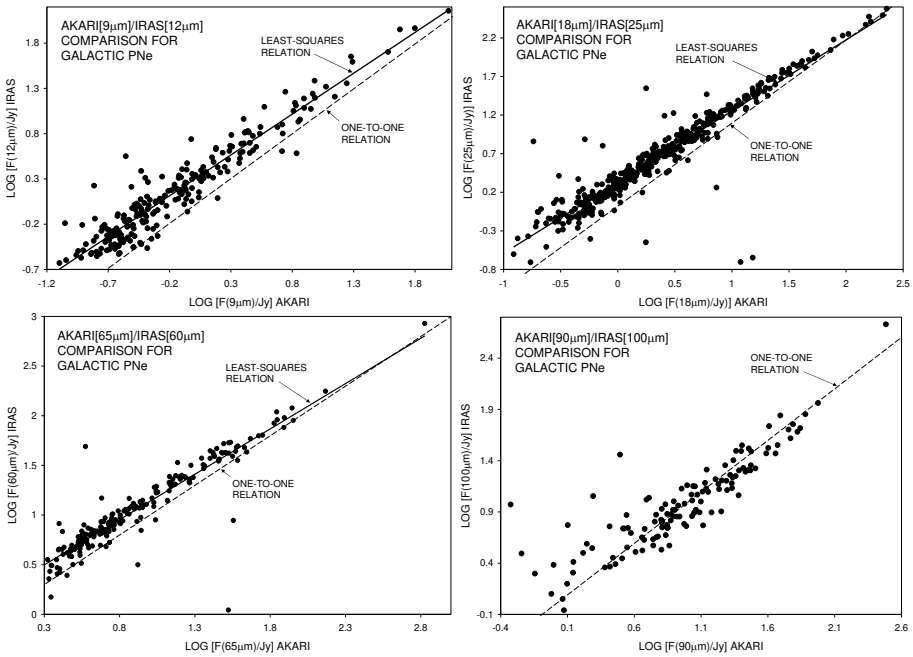

Fig. 3. Comparison of IRAS and AKARI photometric results, whence it is seen that there is a linear relation in all of the panels. However, there is also evidence for a systematic disparity between the trends. This may be partially attributable to differences in the wavelengths of observation, and the spectral gradients of the nebular SEDs.

these trends are subsequently corrected using logarithmic expressions.

We therefore believe that most of the difference can be attributed to the differing mean wavelengths of observation. Thus, where grain temperatures are of the order 110 K, and the grain emissivity function varies as $\epsilon \propto \lambda^{-\gamma}$, $\gamma \cong 1$, then one obtains flux differences similar to those noted in the 18 μm/24 μm panel. A somewhat higher temperature ($\sim$190 K) is required for the 12 μm/9 μm results; a value which is rather larger than is normally attributed to PNe dust continua. It is possible that these latter results are dominated by warmer components of emission, however, such as has been described in the analyses of 2MASS results (e.g., Phillips & Ramos-Larios 2005, 2006, 2007). It is also worth noting that emission at these shorter wavelengths occurs at the Wien limits of the dust continua, where flux levels tend to be lower. As a consequence, emission from lines and bands has a greater impact upon the results (see § 3.1 for a fuller description of these components), and may contribute to the discrepancies noted above.

Although this interpretation of the trends is plausible, and undoubtedly accounts for much of the disparity in the results, we note that flux differences are larger for fainter sources, and almost disappear where sources are brighter. One likely explanation for this trend arises from the fact that sources having larger apparent fluxes also have lower intrinsic radii. We determine that $F_\nu(18\ \mu\mathrm{m}) = 0.20(D/\mathrm{pc})^{-1.17}$, with a correlation coefficient $r \cong 0.51$. Given that sources with smaller diameters also tend to have higher grain temperatures (§ 3.2), this would imply that nebulae having higher fluxes $F_\nu(18\ \mu\mathrm{m})$ also have higher temperature continua. This, where it is the case, would lead to a narrowing of the flux differences.

3. EVOLUTIONARY TRENDS IN THE AKARI PHOTOMETRY

Previous analyses of *IRAS* photometry have suggested that the properties of nebular dust evolve with time. It has been suggested for instance that grain temperatures and dust/gas mass ratios both decrease as nebular radii increase. Similarly, it has been proposed that the masses and sizes of the grains decrease with radius (Pottasch et al. 1984; Lenzuni et al. 1989), although such an evolution has been discounted in the study of Stasinska & Szczerba (1999).

Such broad evolutionary trends are also apparent in the present AKARI spectral energy distributions (SEDs), examples of which are illustrated in Figure 4. In this case, the sources are ordered according to the channel of peak flux, and all of the fluxes have an FQUAL parameter of 3. Sources peaking

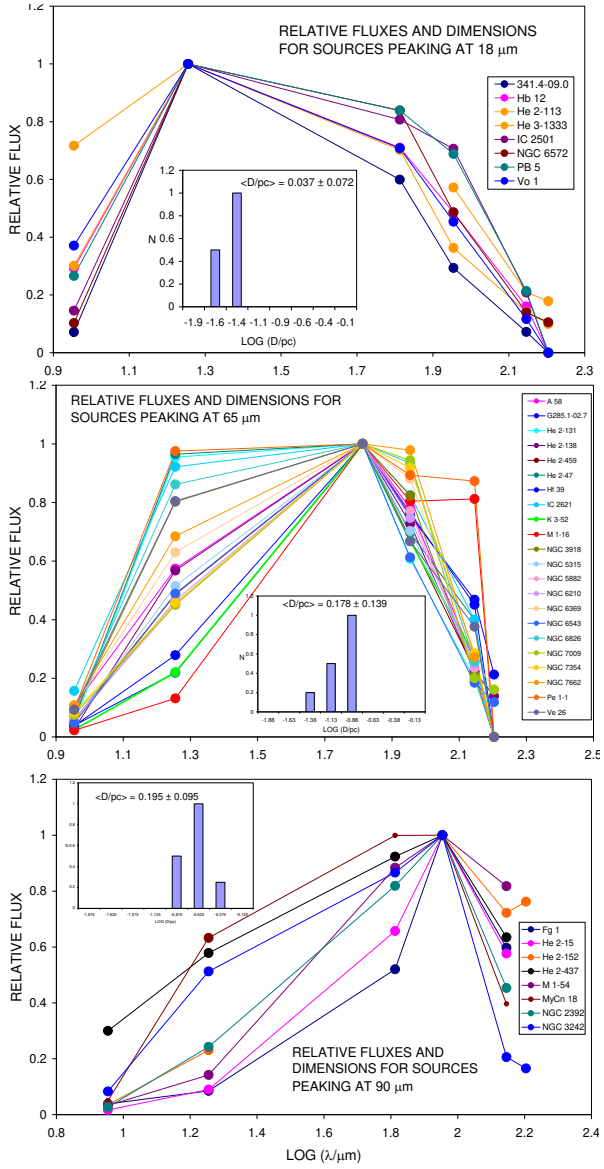

Fig. 4. An illustration of the variety of AKARI SEDs detected in the present analysis, where the sources are sorted with respect to the wavelength of peak emission. The sources in the top-most panel peak at 18 μm, whilst those in the middle and lower panels peak at 65 and 90 μm. There is therefore a cooling of the continua as one passes from the upper to the lower PNe. We have also included histograms and mean values of the nebular diameters D; where estimates for this parameter are taken from optical/radio observations. It is apparent that diameters are smaller for the upper SEDs, and shift to higher values for the lower SEDs. This trend is consistent with previous observations, and our later investigation of grain temperatures $T_{\rm GR}$. The color figure can be viewed online.

at 18 μm are shown in the upper panel, whilst those peaking at 65 and 90 μm are illustrated in the middle and lower graphs. We have also inserted histograms showing the distributions of sources with respect to intrinsic diameter, where the latter refers to the size of the ionized (radio/optical) emission envelope. It is clear that as the continua become cooler (i.e. the wavelength of peak FIR flux increases), so the sizes of the nebulae increase; precisely the trend which has been deduced from previous analyses of IRAS photometry. We shall consider this and further evolutionary trends in the following sections.

3.1. *Line and Band Contributions to the Nebular Fluxes*

FIR spectroscopy of PNe shows that most has continua dominated by emission from nebular grains, with temperatures $T_{\rm GR}$ of order $\sim$50–150 K. There is little doubt that these contribute the larger part of the emission in the present PNe, and we shall be assuming that this is the case for much of the analysis below. There are however several other bands and lines which are capable of affecting the results, and their contributions may be quite considerable. Thus for instance, the 9 μm IRC filter covers the regime of the PAH emission bands, and these are likely to contribute appreciable fluxes where C/O $>$ 1. Evidence for these bands has been noted from ISO and Spitzer spectroscopy (e.g., Ramos-Larios, Phillips, & Cuesta 2011; Ramos-Larios et al. 2011, in preparation; Cohen & Barlow 2005), and there is evidence that much of the emission arises from PDRs.

The 18 μm filter, by contrast, includes [OIV] λ25.87 μm, [NeV] λ24.316 μm, and the $\lambda\lambda$18.713 and 33.482 μm transitions of [SIII]; the 21 and 30 μm emission features; and broad components associated with crystalline and amorphous silicates. The former (21 and 30 μm) features are found in PNe with C/O $>$ 1, whilst silicates are formed in oxygen rich environments.

Perusal of *ISO*[1] pipeline spectra for 32 PNe reveals that a variety of other transitions affect the longer wave fluxes as well. These include [OIII] λ51.816 μm, [NII] λ57.317 μm, and [OI] λ63.184 μm (in the 65 and 90 μm channels); [OIII] λ88.355 μm (in the 90 μm channel); [NII] λ121.898 μm and [OI] λ145.526 μm (in the 140 μm and 160 μm channels); and [CII] λ157.741 μm (in the 160 μm passband).

Several of these transitions are strong, and may measurably affect the present results. Thus a de-

[1]Based on observations with ISO, an ESA project with instruments funded by ESA Member States (especially the PI countries: France, Germany, the Netherlands and the United Kingdom) and with the participation of ISAS and NASA.

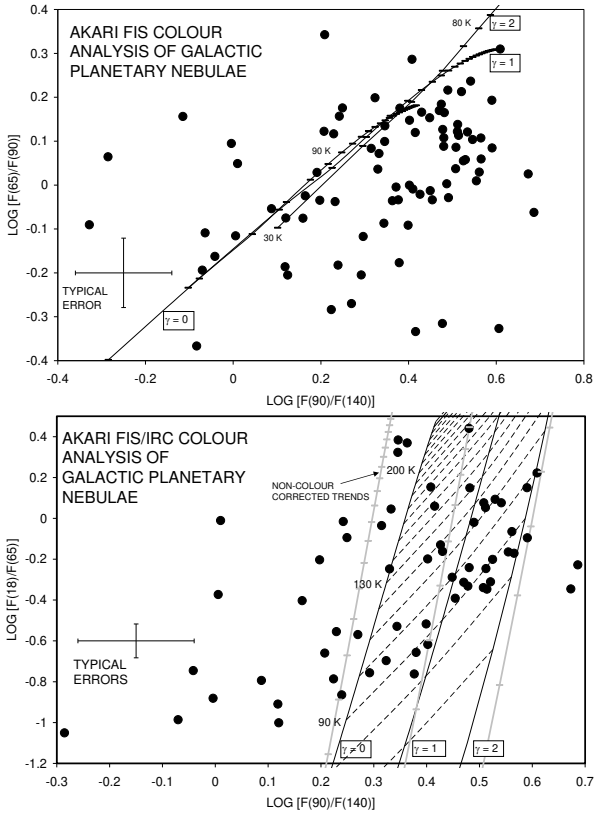

Fig. 5. Positions of PNe in the FIS/IRC colour-colour planes (filled circles), together with diagonal lines corresponding to colour-corrected grain emission loci. The temperatures of the grains are indicated by ticks and dashed lines, and represent increments of 10 K in $T_{\rm GR}$. Similarly, the diagonal loci correspond to emissivity exponents γ = 0, 1, and 2, as indicated in the panels. Finally, we have indicated the mean errors in the colours (error bars to the left-hand side), and the effects of not including colour corrections (the grey diagonal lines in the lower panel). Note that whilst a large fraction of PNe in the lower panel fall within the limits of the dust continuum loci, this is less the case in the upper panel, where most of the nebulae are positioned to the right. Some of these disparities are attributable to errors in the results, and to the contribution of line and band components.

tailed analysis of sources in which the continuum is clearly visible, and the S/N is reasonably high, suggests that [OIV] λ25.87 makes the largest average contribution to the 18 μm band ($\sim$20% of the dust continuum flux), whilst total line enhancement is of the order $\sim$40%. The line contributions to the other channels are less substantial, varying from $\sim$13% (at 65 μm), to $\sim$7% (90 μm), $\sim$0.4% (140 μm) and 4% (160 μm, where [CII] is strongest). Given the nature of the colour-colour mapping to be discussed in § 3.2, it is relevant to note that mean 18 μm/65 μm flux ratios would be increased by $\sim$22% (i.e. points would be shifted by $\sim$0.09 dex), whilst corrections to the other ratios are significantly less.

Finally, of the 32 PNe investigated in this present analysis, nine appear to have strong 30 μm features. These mostly fall between the IRC 18μm filter on the one hand, and the FIS 65 and 90 μm filters on the other. Their contributions to the AKARI photometry are therefore likely to be modest.

Some care must therefore be taken in interpreting the present photometry – a caveat that also applies to previous such analyses. Thus for instance, the analysis of Pottasch et al. (1984) is similar to that we shall be undertaking below, although the authors appear not to have taken account of colour corrections. Stasinska & Szczerba (1999) have attempted a more sophisticated analysis, in which photometry is corrected using SED evolutionary modeling. The authors ignore several important oxygen- and carbon-rich bands, however, whilst their assumptions of invariant abundances, identical nebular structures, a single grain emissivity function, and various other approximations, may lead to misleading results for many of their sample PNe.

3.2. *The AKARI Colour-Colour Planes, and Variation of Grain Temperatures*

The distribution of PNe within the AKARI colour planes is illustrated in Figure 5, where the upper panel shows trends with respect to the 65 μm/90 μm and 90 μm/140 μm flux ratios, and the lower panel represents the corresponding 18 μm/65 μm–90 μm/140 μm ratios. We also indicate the trends to be expected for smooth dust continua having emissivity exponents γ = 0, 1 and 2, and temperatures 30 K $< T_{\rm GR} <$ 270 K. The errors in the fluxes have been discussed in § 2.2, where it is noted that PNe with $F_\nu(18\mu{\rm m}) > 1$ Jy have S/Ns $\sim$15. Similar values apply for the FIS photometric results as well, where combined relative errors of $\sim$10%, and absolute errors of $\sim$15% lead to overall photometric uncertainties of $\sim$20%. We have used these estimates in determining the error bars in Figure 5.

A further correction relates to the broad widths (4.8–52.4 μm) of the AKARI filters, which necessitates a modification to the fluxes depending upon the nature of the SEDs. We have used the colour corrections of Shirahata et al. (2009) and Lorente et al. (2007) to modify the dust continuum trends in Figure 5, leading to shifts in the loci by as much as $\sim$0.1 dex. This leads to an overlapping of loci in

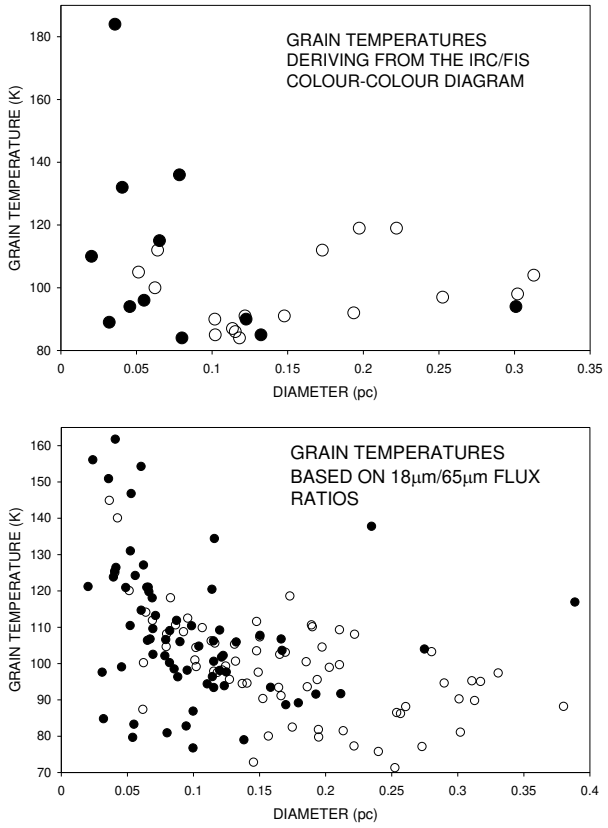

Fig. 6. The variation of grain temperatures as a function of nebular diameter, where we have evaluated $T_{\rm GR}$ using results in the lower panel of Figure 5 (upper panel). Notice how temperatures are larger for diameters < 0.05 pc, and fall within the range $T_{\rm GR} \sim 85-120$ K for larger shell diameters. Sources with angular sizes $\theta < 7$ arcsec are indicated by filled circles, and those having $\theta \geq 7$ arcsec are flagged using open circles. We also show temperatures calculated using 18 and 65 μm fluxes, and assuming an emissivity exponent $\gamma = 1$ (lower panel).

the FIS colour plane (upper panel), and a significant narrowing of the dust regime in the IRC/FIS colour plane (lower panel, where we show examples of the corrected and uncorrected loci).

Where the emission in PNe is dominated by grain continua, then the positions of the sources in Figure 5 will depend upon $T_{\rm GR}$ and γ. However, it is clear that the majority of nebulae in the upper panel fall well away from the dust emission trends. Some of this scatter is likely to be due to errors in the results, although it is interesting to note the bias in the ratios to larger values of 90 μm/140 μm. This is rather larger than would be expected from the *ISO* analysis described in § 3.1. Thus, whilst the shift could be explained in terms of an increase of 20% in the 90 μm flux, this would not be consistent with the smaller mean enhancements expected for ionic transitions in this regime (∼7%; see § 3.1). It would also fail to account for the higher levels of line contamination noted for the 65 μm band, which tend to push PNe to higher positions within this plane.

Similar problems occur for the 18–140 μm trends in the panel below, although in this case, many of the sources lie within the limits of the dust emission loci. We here assume that emission for these sources is dominated by dust continua, and use the positions of the nebulae to determine values for γ and $T_{\rm GR}$. The enhancement in 18 μm/65 μm ratios due to line emission (see § 3.1) may lead to increases in $T_{\rm GR}$ by ∼10–20 K – although see also our comments below concerning the partial detection of 18 μm fluxes.

The corresponding variation of $T_{\rm GR}$ with source diameter is illustrated in Figure 6 (upper panel), where filled circles correspond to sources having $\theta <$ 7 arcsec, and open circles are for nebulae which are larger. It is clear that dust temperatures are significantly higher where the sources have smaller physical dimensions, with $T_{\rm GR}$ approaching ∼180 K where D is less than ∼0.08 pc. By contrast, PNe having larger physical dimensions tend to have smaller values of $T_{\rm GR}$, and fall within a narrower range of values $T_{\rm GR} \sim 85 - 120$ K.

Stasinska & Szczerba (1999) have represented the variation of dust temperatures against Hβ surface brightnesses S(Hβ). The value of $T_{\rm GR}$ is determined using IRAS 25 and 60 μm fluxes, and by assuming that the emissivity exponents γ are uniformly equal to unity. This leads to qualitatively similar trends to those illustrated in the upper panel of Figure 6, although the nature of their procedure permits them to measure many more PNe. The authors find that temperatures are ∼60–100 K where $\log(\mathrm{S(H}\beta)/\mathrm{erg\ cm^{-2}\ s^{-1}\ sr^{-1}}) < -2$, and increase rapidly to higher S(Hβ).

A comparable analysis can be achieved using AKARI photometry at 18 and 65 μm, and where one adopts similar simplifying assumptions. The results are illustrated in Figure 6 (lower panel). It is again clear that there is a marked increase in temperatures for diameters < 0.07 pc; that temperatures are of order ∼70–110 K for larger nebulae; and that there is a significant overlap of values for angularly small and larger PNe. There is little evidence for the linear fall-off of temperatures noted by Pottasch et al. (1984).

Finally, we note that the FIS beams are relatively large, varying from 37 to 61 arcsec. Nevertheless, a small proportion of nebulae have diameters which are larger than these values. Given that the fluxes for

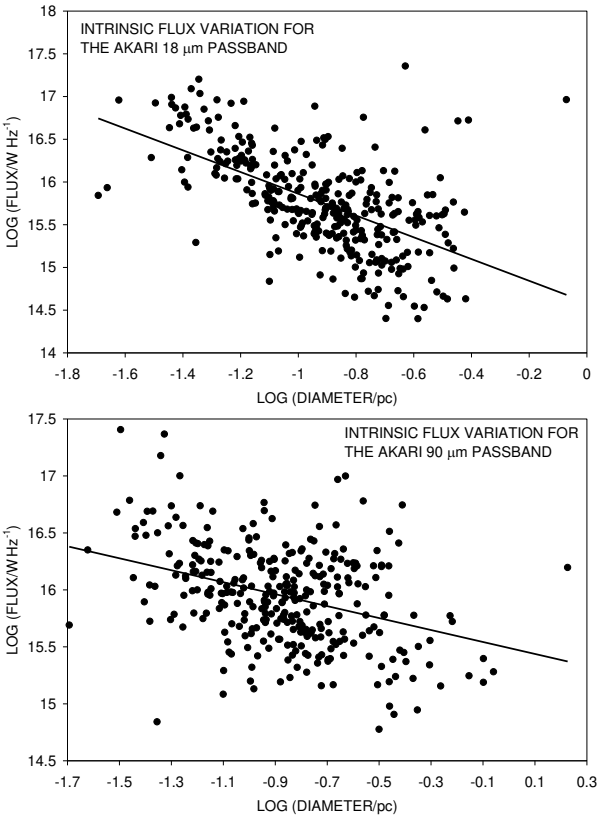

Fig. 7. The variation of the intrinsic 18 and 90 μm fluxes with nebular diameter. In both cases, there is a decrease of flux with increasing diameter, most clearly seen in the 18 μm trends. It is likely that most of this arises from systematic cooling of the IR continua.

these sources may be being only partially detected, we have excluded such nebulae from the present analyses. By contrast, the 18 μm beam sizes are very much smaller, and this may lead to a quite considerable short-fall in certain of the fluxes. This, where it is the case, would counteract the effects of line and band "contamination" noted in § 3.1. We note however that PNe having warmer dust continua tend to be smaller and unresolved (see Figure 6), and their fluxes and temperatures are therefore relatively secure. Similarly, sources having lower values of $T_{\rm GR}$ tend to be angularly large, and their shorter wave fluxes may be significantly too low. However, estimates of $T_{\rm GR}$ for such (lower) grain temperatures are relatively insensitive to uncertainties in the flux, and errors in the trends are likely to be modest. This is consistent with the variations noted in Figure 6, where we see little inconsistency between the estimated temperatures for large and smaller PNe (Figure 6).

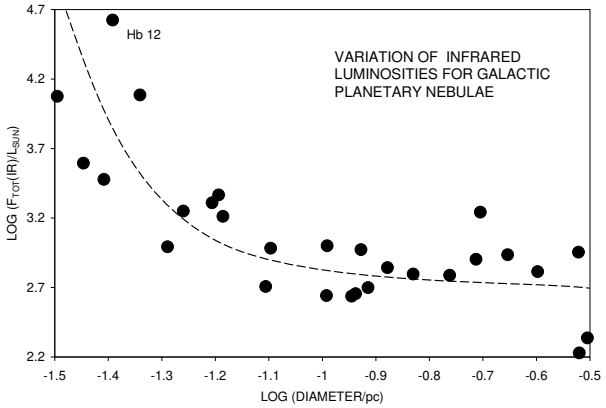

Fig. 8. Variation of total IR luminosity with nebular diameter. It is apparent that luminosities decline with expansion of the PNe, and have maximum values comparable to the luminosities of the central stars. This higher luminosity for the more compact sources suggests appreciable levels of dust opacity. The dashed curve represents an eye-fitting to the results.

3.3. *Variation of Nebular Fluxes and Luminosities with Nebular Evolution*

The emission characteristics of dust in PNe are expected to vary as the nebular envelopes evolve. Thus, expansion of the envelopes would be expected to lead to a reduction in stellar radiative flux densities, and decreases in the levels of direct grain heating. Similarly, the roles of changing stellar temperatures; absorption of Lyα radiation; and the transfer of grains from neutral to ionized regimes, will all be important in determining the energy budgets of the grains and, by extension, the temperature of the dust.

A trivial consequence of such evolution is noted in Figure 7, where we show the variation of intrinsic 18 and 90 μm fluxes as a function of source diameter. It would seem that both of the trends indicate a decrease of flux with D; a variation which may arise through a cooling of the dust continua, such as is noted in Figure 4.

An even more interesting trend is illustrated in Figure 8, where we have estimated total fluxes $F_{\rm TOT}$(IR) for sources within the dust emission regime of Figure 5 (lower panel). For this case, $F_{\rm TOT}$(IR) is determined using the values of γ and $T_{\rm GR}$ obtained from Figure 5; observed 90 μm fluxes; and the distances quoted in Table 1. It is again clear that luminosities decline with increasing nebular dimensions, and have values approaching $\approx 1.5 \times 10^4\ L_\odot$ where $D < 0.05$ pc – perhaps even larger ($\sim 4{\times}10^4\ L_\odot$) for Hb 12. Since this brightness

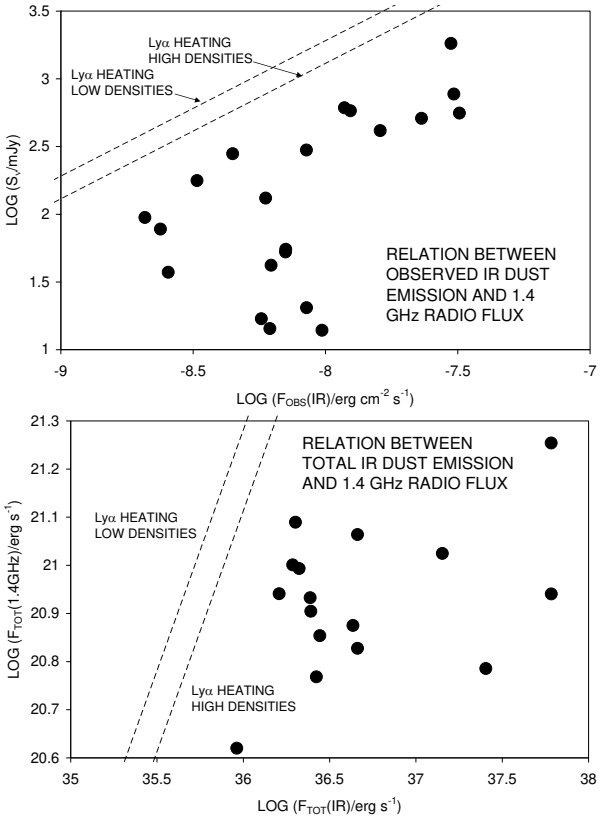

Fig. 9. A comparison between observed 1.4 GHz and integrated FIR fluxes (upper panel), and the intrinsic (distance corrected) counterparts of these fluxes (lower panel). The diagonal lines correspond to the trends where Lyα heating dominates the results, and represent low and high values of the nebular density. It is clear that Lyα heating represents ≤ 0.5 of the energy budget of the IR emitting grains.

is typical of the luminosities of PNe central stars, this suggests that a large fraction of the radiation is being absorbed by dust – a situation which would be consistent with the high levels of reddening observed in proto-planetary nebulae (PPNe).

It is finally interesting to adapt the analysis of Lyα heating of Pottasch et al. (1984) to the present AKARI results. The results of such a procedure are illustrated in Figure 9, where we show the relation between observed integrated IR and 1.4 GHz emission, and between intrinsic (distance corrected) IR and 1.4 GHz results (lower panel). The trends expected for Lyα heating are indicated by the dashed diagonal lines, determined for high and low density nebular regimes. It would appear that the infrared excess (IRE), corresponding to the ratio of the observed flux to Lyα heating, is of order > 2 for all of this present sample PNe. It is therefore clear that further heating of the grains is required over and above that expected by Lyα photons.

One would anticipate that values of the IRE would be largest where PNe are more compact, Lyα fluxes are smaller, and direct heating by the stellar radiation field is greatest. Subsequent nebular expansion would lead to further ionization of the shell; increased fluxes of Lyα photons; and the dilution of the stellar radiation field. Under these circumstances, the IRE would be expected to decline rather precipitously, and achieve minimum values of the order of unity.

To investigate whether some such evolution is actually occurring, we have determined FIR luminosities for a broad range of PNe. This involved using the 18 and 65 μm fluxes to determine $T_{\rm GR}$; assuming a grain emissivity exponent $\gamma = 1$; and employing 1.4 GHz fluxes to evaluate Lyα heating. We assume Lyα photon production rates relevant for lower density PNe, whilst the distances and sizes of the sources are taken from Tables 1 and 2. Under these circumstances, appropriate integration of the emission curves show that the luminosity of the source can be represented through

$$L = 3.11{\times}10^{13}\left[\frac{\mathrm{F}_\nu(90\ \mu m)}{\mathrm{Wm^{-2}Hz}}\right]\left[\frac{d}{\mathrm{kpc}}\right]^2\left[\sum_{i=0}^{4} a_i T_{\rm GR}^i\right]^{-1} L_\odot\,, \quad (1)$$

where d is source distance, the polynomial terms $[a_0, ..., a_4]$ are given by $[7.162 \times 10^{10}, -1.834 \times 10^9, 1.868{\times}10^7, -8.742{\times}10^4, 1.564{\times}10^2]$, and the expression is valid for temperatures $70 < T_{\rm GR}/\mathrm{K} < 160$. Similar expressions may be derived for differing values of γ.

Note that both here, and in the analysis of the results in Figure 5 (see above), we have used 90 μm fluxes to scale the results. This is advantageous for a variety of reasons. Not only are these results taken with the most sensitive of the FIS detectors –leading to larger numbers of PNe detections than in other channels– but this wavelength lies close to the continuum peak for most of the PNe SEDs. We have also assessed that levels of line contamination are likely to be modest (§ 3.1), although there is evidence that contaminants may be larger than is supposed (see § 3.2 and Figure 5). It is unlikely, however, that luminosities are very greatly in error, or that mean biases are greater than ∼0.1 dex.

The results of this analysis are illustrated in Figure 10, where the IRE is represented against nebular diameter. It is plain from this that some evolution does indeed appear to be occurring, with values of IRE approaching ∼50 for diameters < 0.07 pc. Al-

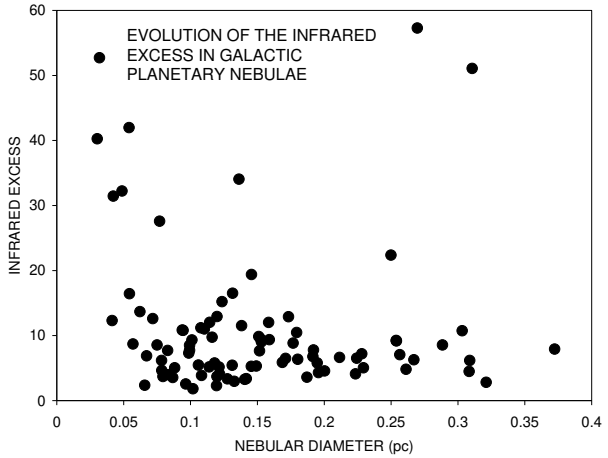

Fig. 10. Variation of the Infrared Excess in Galactic PNe. Notice the evolution in the IRE as nebular dimensions increase.

though the qualitative trend appears consistent with the analysis above, it is interesting to note that the IRE is still relatively large (≈5) even where nebulae are evolved – and that the minimum values are larger than found by Pottasch et al. (1984).

3.4. *Radio Infrared Flux Correlation*

It has been noted that the ratio of infrared to radio fluxes in extragalactic systems is reasonably constant, and invariable with redshift z. Appleton et al. (2004) have noted that the parameter $q_{70} = \log[S_\nu(70\ \mu\text{m})/S_\nu(20\text{cm})]$ is of order ∼2, whilst $q_{24} = \log[S_\nu(24\mu\text{m})/S_\nu(20\text{cm})]$ is ∼1. Cohen & Green (2001) have made a similar analysis for 21 Acker et al. (1992) PNe, using 8.3 μm fluxes taken from the Midcourse Science Experiment (MSX; Price et al. 2001). They derived MIR/radio ratios in the region of 12. However, a later analysis for ten MASH PNe (Parker et al. 2006; Miszalski et al. 2008) yielded a ratio of the order of ∼5 (Cohen et al. 2007). This difference between the less evolved Acker PNe, and more evolved MASH nebulae was attributed to an evolution in the properties of the sources – perhaps a reduction in PAH emission as fluorescent excitation decreased. This mechanism is only applicable, however, where C/O is greater than or close to unity.

A further investigation of this issue has also been undertaken by Zhang & Kwok (2009), using 8 and 24 μm photometry deriving from the GLIMPSE and MIPSGAL surveys. In this case, the authors note a linear relation between MIR and 1.4 GHz fluxes; a trend they interpret as indicating a constancy in the ratios q_{24} and q_8. It is also suggested that the scatter

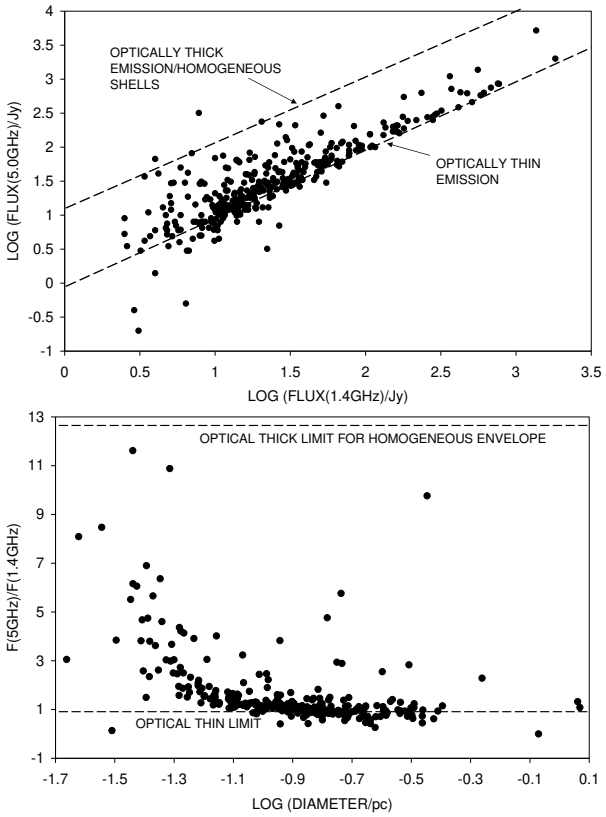

Fig. 11. The 1.4 and 5.0 GHz emission of the AKARI PNe, where we show a comparison between the fluxes (upper panel), and the evolution of the 5.0 GHz/1.4 GHz flux ratios (lower panel). The lower dashed line indicates the limit for optically thin sources, whilst the upper dashed line is for high opacity homogenous PNe. It is clear that most of the nebulae follow the locus for optically thin emission (upper panel), and that only a minority of sources are partially or totally optically thick. The evolution of the ratios (lower panel) indicates higher opacities where $D < 0.07$ pc.

in their figure is attributable to optical thickness at 1.4 GHz – a hypothesis which we will suggest, below, is unlikely to be the case.

We have investigated this question using the present AKARI photometric results, and 1.4 GHz measures deriving from Condon et al. (1998). It should be emphasized that whilst most PNe are likely to be optically thin at 5 GHz, a small proportion may have higher opacities. Thus, we have made a comparison between 5 and 1.4 GHz fluxes in Figure 11 based upon the data summarized in Tables 1 and 2. It is clear that the vast majority of sources follow the trend for optically thin emission (lower dashed line), although ∼20% fall between the optically thick and thin regimes (the former indicated

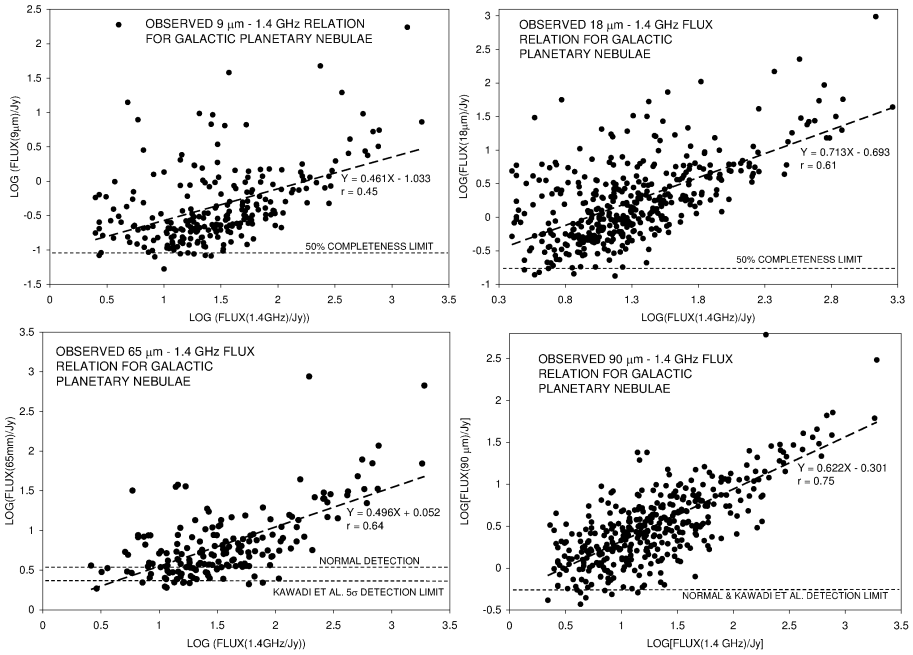

Fig. 12. The variation of infrared fluxes with respect to 1.4 GHz emission, where we illustrate the trends for four of the AKARI photometric channels. All of the results indicate linear trends. Note how the limiting AKARI and radio sensitivities restrict the numbers of observed sources, and appreciably modify the trends. Least-squares fits to the data are indicated using dashed lines, for which we indicate equations and correlation coefficients (r) within each of the panels.

by the upper line). It is therefore clear that whilst certain 5 GHz fluxes derive from partially or fully opaque regimes, the vast majority of 1.4 GHz results are optically thin - and yield fluxes proportional to the total masses of ionised gas.

Phillips (2007) has noted that higher 5 GHz/ 1.4 GHz ratios are confined to more compact sources, where density and emission measures are larger. This is also noted for the PNe investigated here (Figure 11, lower panel), where it is clear that higher 5 GHz opacities arise when diameters are < 0.07 pc; a range similar to that determined for higher values of $T_{\rm GR}$ (§ 3.2).

The variation of infrared emission with 1.4 GHz flux is illustrated in Figure 12, where it is clear that there is a linear relation between the two sets of data. Such trends are strongly affected by a variety of biases, however, and these greatly modify the perceived gradients. In the first place, distance-squared spreading of the fluxes would tend to lead to a one-to-one relation. It is also apparent that source numbers are truncated where $F_\nu(1.4\ {\rm GHz}) \leq 3$ Jy, corresponding to the sensitivity limit of the Condon et al. (1998) survey.

Even greater biases arise from the limiting sensitivities of the differing AKARI channels, however, and we have indicated these using horizontal dashed lines. We have included values corresponding to 50% source detection rates; a so-called "normal mode" detection limit quoted in the FIS Bright Source Catalogue (Yamamura et al. 2010); and the 5σ detection limit quoted by Kawada et al. (2007). Most of these limits are mutually consistent, and accord with the fall-offs in the numbers of PNe. The result, for the 9 and 65 μm results, is for an apparent flattening of the trends. It is apparent however that the 90 and 18 μm samples are significantly more complete, and trends are close to those expected for unbiased samples of PNe. We shall therefore be using these trends to assess variations in q_{18} and q_{90}.

We should finally add that detection limits at 140 and 160 μm are even higher, whilst PNe fluxes tend to be lower. This leads to extraordinarily strong truncations in the numbers of PNe, and we have excluded these results from the present analysis.

Distance corrected measures of the fluxes are illustrated in Figure 13. We note that the linear trends in Figure 12 have now largely disappeared, although the scatter between the nebulae is as large

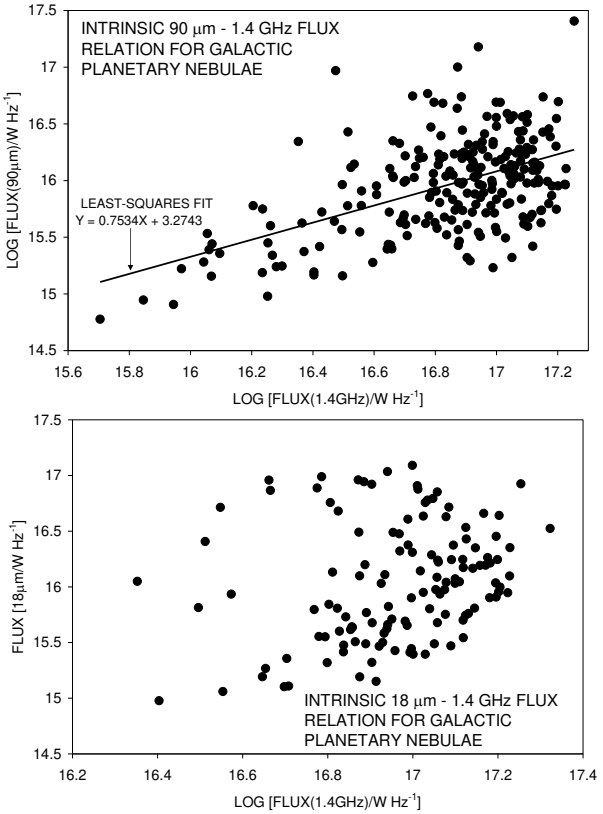

Fig. 13. The variation of intrinsic 18 and 90 μm emission with 1.4 GHz flux. There is still evidence for linearity in the 90 μm trends, although the 18 μm results appear to be random. We have indicated the equation and trend for the least-squares fit in the upper panel.

as before. There is still evidence for linearity between the 90 μm and 1.4 GHz results, although this is consistent with an approximate constancy of IR/radio flux ratios.

It would appear, apart from this, that there is little evidence for evolution or correlation – and certainly nothing like the invariance in q noted for extragalactic systems. The scatter in these planes is huge, and indicates variations of an order of magnitude or more. Most of this scatter likely to be intrinsic to the sources. The combined errors resulting from photometric errors (∼20%) and uncertainties in the distance (∼30%) are likely to be ∼60% for the 90 μm results, for instance – and probably somewhat less than that for the 18 μm trends. This is a factor ∼15 less than is observed in Figure 13.

Whilst it is therefore possible to obtain reasonable values of q for large ensembles of PNe, as has previously been undertaken by the authors cited above, there is little evidence that this parameter is invariant between PNe, or indicates any close relation between the mechanisms responsible for radio and IR emission. Whilst it is undoubtedly the case that UV radiation is stimulating the radio and infrared emission, there is little evidence for the levels of correlation noted in extragalactic systems.

4. CONCLUSIONS

The AKARI all-sky survey has resulted in photometry for 8.77×10^5 sources in the MIR, using the IRC at 9 and 18 μm, and 4.27×10^5 sources in the FIR using the FIS at 65–160 μm. We have interrogated this database to identify the counterparts of Galactic PNe, and undertaken an analysis of the resulting photometry.

Approximately 80% of the Kerber et al. (2003) sources were detected to quality levels FQUAL = 3, of which ∼ half were observed in both the FIR and MIR regimes. A comparison with photometry deriving from the IRAS survey shows that there are systematic differences between the two sets of flux, although much of the variation is attributable to differences in the wavelengths employed. We also note that the mean AKARI dimensions of the sources are similar to those at radio and optical wavelengths, although the distributions of diameters appear to be radically different. This may arise because of centrally concentrated fluxes due to [OIV] and [NeV], and/or high levels of dust emission in extended PDRs. It is also possible that limiting sensitivities and errors are biasing the distribution of AKARI results.

Analysis of the nebulae in the colour-colour planes suggests that many of the SEDs are consistent with dust continuum emission, although emission bands and ionic transitions also contribute to the results. We find evolutionary trends in grain temperatures similar to those measured in previous studies, with values approaching ∼160 K where nebulae are young ($D < 0.08$ pc), and $T_{\rm GR}$ ∼60–120 K where nebulae are more evolved.

Fluxes in the individual channels also show an evolution with nebular diameter, much of which may be attributed to cooling of the grains. However, we also note that total FIR emission declines with increasing nebular diameter, from a peak of $\approx 1.5 \times 10^4\ L_\odot$ where $D < 0.05$ pc, to values ∼600 $L_\odot$ in more evolved PNe. The high luminosities of less evolved sources suggest that dust opacities are appreciable. Although up to ∼0.5 of the grain heating may arise from absorption of Lyα photons, it seems likely that most of the energy budget depends upon absorption of the stellar radiation field. There is ev-

idence for an evolution in the IRE with expansion of the shells, consistent with the variations to be expected in stellar and Lyα heating.

Finally, it has been suggested that PNe may show a consistent IR/radio flux ratio similar to that determined in extragalactic systems, although with some possible evidence of evolution at $\sim$8 μm. Our present results fail to confirm this suggestion. It is plain that whatever the global values of the IR/radio ratio may be, they are highly variable between nebulae, and show little evidence for consistency.

This research is based on observations with AKARI, a JAXA project with the participation of ESA.

REFERENCES

Acker, A., Ochsenbein, F., Stenholm, B., Tylenda, R., Marcout, J., & Schohn, C. 1992, Strasbourg-ESO Catalogue of Galactic Planetary Nebulae (Garching: ESO)
Appleton, P. N., et al. 2004, ApJS, 154, 147
Cahn, J. B., & Kaler, J. B. 1971, ApJS, 22, 319
Chu, Y.-H., et al. 2009, AJ, 138, 691
Cohen, M., & Barlow, M. J. 2005, MNRAS, 362, 1199
Cohen, M., & Green, A. 2001, MNRAS, 325, 531
Cohen, M., et al. 2005, ApJ, 627, 446
Cohen, M., et al. 2007, ApJ, 669, 343
Condon, J. J., Cotton, W. D., Greisen, E. W., Yin, Q. F., Perley, R. A., Taylor, G. B., & Broderick, J. J. 1998, AJ, 115, 1693
Kataza, H., et al. 2010, AKARI/IRC ALL-Sky Survey Point Source Catalogue, Version 1.0 Release, Note Rev. 1, http://irsa.ipac.caltech.edu/data/AKARI/documentation/AKARI-IRC_PSC_V1_RN.pdf
Kawada, M., et al. 2007, PASJ, 59, 389
Kerber, F., Mignani, R. P., Guglielmetti, F., & Wicenec, A. 2003, A&A, 408, 1029
Lenzuni, P., Natta, A., & Panagia, N. 1989, ApJ, 345, 306
Lorente, R., Onaka, T., Ita, Y., Ohyama Y., Tanabe, T., & Pearson, C. 2007, Akari IRC Data User Manual, http://www.sciops.esa.int/SA/ASTROF/docs/IRC_IDUM_1.3.pdf
Miszalski, B., Parker, Q. A., Acker, A., Birkby, J. L., Frew, D. J., & Kovacevic, A. 2008, MNRAS, 384, 525
Murukami, H., et al. 2007, PASJ, 59, 369
Neugebauer, G., et al. 1984, ApJ, 278, L1
Onaka, T., et al. 2007, PASJ, 59, 401
Parker, Q. A., et al. 2006, MNRAS, 373, 79
Perek, L., & Kohoutek, L. 1967, Catalogue of Galactic Planetary Nebulae (Prague: Publishing House of Czechoslovak Academy of Sciences)
Phillips, J. P. 2004, MNRAS, 353, 589
_____. 2007, MNRAS, 378, 231
Phillips, J. P., & Márquez-Lugo, R. A. 2011, MNRAS, 410, 2257
_____. 2005, MNRAS, 364, 849
_____. 2006, MNRAS, 368, 1773
_____. 2007, AJ, 133, 347
_____. 2008, MNRAS, 383, 1029
Pottasch, S. R., et al. 1984, A&A, 138, 10
Price, S. D., Egan, M. P., Carey, S. J., Mizuno, D. R., & Kuchar, D. A. 2001, AJ, 121, 2819
Ramos-Larios, G., & Phillips, J. P. 2005, MNRAS, 357, 732
_____. 2008, MNRAS, 390, 1014
Ramos-Larios, G., Phillips, J. P., & Cuesta, L. C. 2011, MNRAS, 411, 1245
Shirahata, M., et al. 2009, PASJ, 61, 737
Siodmiak, N., & Tylenda, R. 2001, A&A, 373, 1032
Stasinska, G., & Szczerba, R. 1999, A&A, 352, 297
Su, K. Y. L., et al. 2007, ApJ, 657, L41
Su, K. Y. L., et al. 2004, ApJS, 154, 302
Tylenda, R., Siódmiak, N., Górny, S. K., Corradi, R. L. M., & Schwarz, H. E. 2003, A&A, 405, 627
Ueta, T. 2006, ApJ, 650, 228
Werner, M., et al. 2004, ApJS, 154, 1
Yamamura, I., Makiuti, S., Ikeda, N., Fukuda, Y., Oyabu, S., Koga, T., & White, G. J. 2010, AKARI/FIS All-Sky Survey Bright Source Catalogue Version 1.0, http://www.ir.isas.jaxa.jp/AKARI/Observation/PSC/Public
Zhang, C. Y. 1995, ApJS, 98, 659
Zhang, Y., & Kwok, S. 2009, ApJ, 706, 252

J. P. Phillips and R. A. Márquez-Lugo: Instituto de Astronomía y Meteorología, Av. Vallarta No. 2602, Col. Arcos Vallarta, C.P. 44130, Guadalajara, Jalisco, Mexico (jpp, alejmar@astro.iam.udg.mx).

Revista Mexicana de Astronomía y Astrofísica, **47**, 113–125 (2011)

MASS AND METAL EJECTION EFFICIENCY IN DISK GALAXIES DRIVEN BY YOUNG STELLAR CLUSTERS OF NUCLEAR STARBURST

A. Rodríguez-González,[1] A. Esquivel,[1] A. C. Raga,[1] and P. Colín[2]

Received 2010 August 26; accepted 2011 January 31

RESUMEN

Presentamos las eficiencias de pérdida de masa y metales obtenidas de modelos numéricos de vientos galácticos empujados por la energía depositada en brotes de formación estelar nucleares. Los brotes de formación estelar contienen cúmulos estelares jóvenes los cuales inyectan la energía suficiente para empujar parte del medio interestelar fuera de las galaxias. En algunos casos los vientos galácticos contienen una importante parte de los metales producidos por las nuevas generaciones estelares. Para estudiar las eficiencias de pérdida de masa y metales hemos desarrollado simulaciones numéricas 3D *N-Cuerpos/Smooth Particle Hydrodynamics* de vientos galácticos para los casos: adiabáticos y con pérdidas radiativas. Los modelos numéricos cubren una amplio intervalo de masas de los brotes de formación estelar (de $\sim 10^2$ a $\sim 10^7$ $M_\odot$) y de masas en las galaxias anfitrionas (de $\sim 6\times 10^6$ a $\sim 10^{11}$ $M_\odot$). Las regiones de formación estelar concentradas en el centro del potencial son una maquinaria importante para la pérdida y redistribución de masa y metales en este tipo de galaxias.

ABSTRACT

We present results from models of galactic winds driven by energy injected by nuclear starbursts. The total energy of the starburst is provided by young central stellar clusters and parts of the galactic interstellar medium are pushed out as part of the galactic wind (in some cases the galactic wind contains an important part of the metals produced in the new generation of stars). We have performed adiabatic and radiative 3D N-Body/Smooth Particle Hydrodynamics simulations of galactic winds using the GADGET-2 code. The numerical models cover a wide range of starburst (from $\sim 10^2$ to $\sim 10^7$ $M_\odot$) and galactic gas masses (from $\sim 6 \times 10^6$ to $\sim 10^{11}$ $M_\odot$). The concentrated central starburst regions are an efficient engine for producing the mass and metal loss in galaxies, and also for driving the metal redistribution in galaxies.

Key Words: galaxies: starburst — galaxies: star clusters: general — ISM: general — stars: winds, outflows

1. INTRODUCTION

A great amount of evidence, both observational and theoretical, indicates that galactic winds (GWs) are a necessary and very important ingredient of the evolution of galaxies and the inter-galactic medium. Their presence can explain, among other things, the very low metallicities found in dwarf galaxies, and the abundance of metals observed in the intracluster medium. Such outflows have been observed in galaxies of a variety of masses and at different redshifts (e.g., Martin 1999; Pettini et al. 2001; Veilleux, Cecil, & Bland-Hawthorn 2005). At the same time, different analytical and numerical models have been put forward to explain these outflows (e.g., Chevalier & Clegg 1985; Tomisaka & Ikeuchi 1988; Heckman, Armus, & Miley 1990; De Young & Heckman 1994; MacLow & Ferrara 1999; Strickland & Stevens 2000; Cantó, Raga, & Rodríguez 2000; Tenorio-Tagle, Silich, & Muñoz-Tuñón 2003; Fujita et al. 2004; Cooper et al. 2008; Fujita et al. 2009; Rodríguez-González, Raga, & Cantó 2009).

[1]Instituto de Ciencias Nucleares, Universidad Nacional Autónoma de México, Mexico.

[2]Centro de Radioastronomía y Astrofísica, Universidad Nacional Autónoma de México, Mexico.

Long ago, Lynds & Sandage (1963) found a large outflow in M82 and gave the first definition of a starburst (SB). They proposed that material was ejected from the nuclear regions as a consequence of a series of SN explosions. Since then, galaxies with concentrated central starbursts (M82, NGC 253, NGC 1569, to name a few) have been used to study the GW phenomenon.

Tenorio-Tagle & Muñoz-Tuñón (1998) showed the importance of the galactic potential component due to the cold dark matter halo in realistic models of GW, and concluded that the fate of the stellar wind and SNe material depends on the galactic properties and on the total energy injected by the SB. They showed that dwarf galaxies with an interstellar medium (ISM) with masses of the order of 10^9 $M_\odot$, retain their metals unless they undergo an extreme burst of star formation, much larger than those presently observed. On the other hand, MacLow & Ferrara (1999) explored both, analytically and numerically, the effects of stellar winds and SN explosions, in SBs with mechanical luminosities in the $\sim 10^{37}-10^{39}$ erg s^{-1} range on the ISM of dwarf galaxies with gas masses in the $\sim 10^6$ to 10^9 $M_\odot$ range. They distinguished between two possibilities of gas ejection: (a) A "blowout", which requires material be accelerated above the escape speed at a distance of about three times the scale height. (b) A "blow-away", in which virtually all the ISM is accelerated and lost to the galaxy. The blowout would happen preferably for flatter galaxies; rounder galaxies are more likely to be completely disrupted (blow-away) if enough energy is injected. Their conclusion was that dwarf galaxies in that mass range undergo blowout for moderate-to-high luminosity starbursts values ($L \sim 10^{38} - 10^{39}$ erg s^{-1}), whereas for galaxies with gas masses $M_g > 10^8$ $M_\odot$ and mechanical luminosity $L \sim 10^{37}$ erg s^{-1} the blowout was inhibited. They also found that in the lowest mass objects, blow-away occurs virtually independently of L.

Many authors have shown that in the nearest starburst galaxies GWs could form through the collective effect of many individual stellar cluster winds, which in turn are formed by the collective effect of many individual stellar winds. Perhaps the best studied starburst galaxy is M82, which has an extended, biconical filamentary structure in the optical (Shopbell & Bland-Hawthorn 1998; Ohyama et al. 2002). In M82, the super stellar clusters (SSCs) have Hα luminosities in the $(0.01-23)\times 10^{38}$ erg s^{-1} range (Melo et al. 2005). These authors compiled a catalog of 197 SSCs in M82 and 48 SSCs in NGC 253 (Melo 2005), with masses in the $10^4 < M/M_\odot < 10^6$ range (more recently, additional young star clusters in M82 have been reported by Smith et al. 2007 and Westmoquette et al. 2007). Other examples are NGC 1569 (Anders et al. 2004; Westmoquette, Smith, & Gallagher 2008) and M83 (Harris et al. 2001), with SSCs densities and masses similar to those of M82. Such an exceptional density of massive clusters (i.e. $\sim$620 kpc^{-2}, see also Anders et al. 2004; Melo et al. 2005; Melo 2005) is the best scenario to study powerful GWs driven by SSC winds originated in nuclear starburst regions.

Yet another interesting effect is when the material ejected from the SSCs winds does not abandon the galaxy. Tenorio-Tagle (1996) explored the effect of a non-uniform interstellar medium (density and temperature) in the cooling efficiencies within the giant cavities. In high density regions the cooling would be more effective and would produce a series of metal-rich cloudlets. Such cloudlets would fall back to the disk and produce local enhancements of metallicity. However, Recchi, Matteucci, & D'Ercole (2001) and Recchi et al. (2008) presented arguments against this scenario, pointing out that thermal conduction and hydrodynamical drag are likely to disrupt the condensations before they reach the disk, and thus the metals would be spread more or less uniformly throughout the galaxy.

In the present paper we study the effects of young stellar clusters in the nuclear starburst (SB) region on the ISM of dwarf disk-galaxies. In particular, we calculate the amount of enhanced metallicity material that will end up in the intergalactic medium (IGM) and/or in the outer regions of the galactic disk. The paper is organized as follows: in § 2 we describe the ingredients of the galactic models that we use. In § 3 we discuss the possible fate of the mass and metals in such galaxies. In § 4 we describe a series of 3D simulations of the interaction of SSCs with the galactic ISM. The results are presented in § 5, and our conclusions in § 6.

2. GALACTIC MODEL INGREDIENTS

Each galaxy in our study consists of a dark matter halo, and a rotationally supported disk of gas and stars. The models are constructed following the approach described in Springel, Di Matteo, & Hernquist (2005, see also Hernquist 1993 and Springel 2000). A near-equilibrium galaxy model is constructed, with a dark matter halo that follows a Hernquist (1990) profile, and a disk with exponential surface gas density. Then, using an iterative procedure, the vertical gas profile is determined self-

consistently for a particular effective equation of state.

2.1. *The halos*

We modeled the dark matter mass distribution with the Hernquist profile (Hernquist 1990),

$$\rho_h(r) = \frac{M_{\rm dm}}{2\pi}\frac{a}{r(r+a)^3}\,, \qquad (1)$$

where r is the radial distance, and $M_{\rm dm}$ is the dark matter mass. Two remarks can be made about the shape of this profile: (i) In the inner parts of the galaxy it agrees with the profile given by the Navarro, Frenk, & White (1996, henceforth NFW) fitting formula. (ii) Its faster than r^{-3} decline causes the total mass to converge, allowing the construction of isolated halos without the need of an *ad hoc* truncation. The a parameter is related to the scale radius r_s of the NFW profile by:

$$a = r_s\sqrt{2[\ln(1+c) - c/(1+c)]}\,, \qquad (2)$$

where $c = r_{200}/r_s$ is the concentration parameter, r_{200} is the radius at which the enclosed dark matter mean density is 200 times the critical value (where the critical density is $\rho_{\rm crit} = 3H^2/8\pi G$). We have set $c = 9$.

2.2. *The disk*

We modeled gas and star disk components with an exponential surface density profile (in the radial direction of the galactic disk, R) the scale of length being R_0,

$$\Sigma_g(R) = \frac{M_g}{2\pi R_0^2}\exp(-R/R_0)\,, \qquad (3)$$

$$\Sigma_*(R) = \frac{M_*}{2\pi R_0^2}\exp(-R/R_0)\,, \qquad (4)$$

so that the total mass of the disk is $M_d = (M_g + M_*) = m_d M_{\rm tot}$, where m_d is a dimensionless parameter (fixed in this work to $m_d = 0.041$), and $M_{\rm tot}$ is the total mass of the galaxy, incuding the dark matter halo (i.e. $M_{\rm tot} = M_d + M_h$, where M_h is the mass of the halo). The vertical mass distribution of the stars in the disk is specified by the profile of an isothermal slab with a constant scale height H. The 3D stellar density in the disk is hence given by,

$$\rho_*(R,z) = \frac{M_*}{4\pi\, H\, R_0^2}\,\mathrm{sech}^2\left(\frac{z}{2H}\right)\exp\left(-\frac{R}{R_0}\right)\,. \qquad (5)$$

In all models, H/R_0 was fixed to 0.2 whereas the relative content of gas in the disk (the rest of the disk mass is in stars) was set to 0.35. On the other hand, the disk spin fraction (the fraction of the total angular momentum in the disk), was set, as is customary, to the value of m_d. These values are typical of low-mass galaxies (e.g., Springel et al. 2005).

2.3. *Vertical structure of the gas disk*

The vertical structure of the disk at the beginning of the simulation is computed self-consistently with the halo and stellar disk components as follows. At $t = 0$ the gaseous disk has uniform temperature (fixed to 1000 K). Consider the vertical structure of the gas disk in hydrostatic equilibrium:

$$\frac{\partial\rho_g}{\partial z} = -\frac{\rho_g^2}{\gamma P}\frac{\partial\Phi_T}{\partial z}\,, \qquad (6)$$

where, $\Phi_T = \Phi_h + \Phi_d$ is the total gravitational potential (Φ_h and Φ_d are the halo and disk gravitational potentials, respectively). For a given Φ_T, the solution of this equation is constrained by the condition

$$\Sigma_g(R) = \int \rho_g(R,z)dz\,, \qquad (7)$$

where $\Sigma_g(R)$ is the gaseous surface mass density (see also equation 3). One can obtain the vertical distribution by integrating equation (6), with a central density value at the midplane ($z = 0$) and an effective equation of state of the form $P = P(\rho)$, see Springel et al. (2005). The starting value for the density is guessed, then adjusted in an iterative scheme until the desired surface density (equation 3) is recovered. This process is repeated for different radii to obtain an axisymmetric gas density distribution.

2.3.1. *Cooling*

For the non-adiabatic cases, we adopt the cooling functions computed in collisional ionization equilibrium (CIE) by Sutherland & Dopita (1993). The energy loss per unit mass of the gas is given by,

$$\left(\frac{du}{dt}\right)_{\rm cool} = -\frac{\Lambda_{\rm net}(\rho,T)}{\rho}\,. \qquad (8)$$

We must note that the cooling function we used in our models assumes solar abundances. However, the kind of galaxies treated in this paper should be less metallic and thus the cooling should be lower. For the less metallic galaxies the results would be shifted from our radiative models to the adiabatic ones.

3. THE FATE OF THE GAS INJECTED BY YOUNG STELLAR CLUSTERS

Depending on the total amount of kinetic energy injected by the SSCs two outcomes are possible: if the kinetic energy is larger than the gravitational potential of the galaxy, all material will escape and become part of the IGM; otherwise, the gas will return to the disk. If the material returns and reincorporates to the galaxy two things can happen: it can fall back close to the galactic center or far from it. Considering that GWs are confined to a cone, material that does not reach a high altitude will fall close to the galactic center, while gas that reaches a high altitude can fall back at large galactocentric radii.

3.1. *Mass loss measures*

In order to quantify the mass loss in numerical models one has to determine which material will be considered lost to the IGM. A natural estimation can be derived by comparing the velocity of a parcel of gas and the escape velocity at its current position. This has been done, for instance, in previous work by MacLow & Ferrara (1999) and D'Ercole & Brighenti (1999). This work, however, used Eulerian codes in which material that leaves the computational domain cannot be further analyzed, and therefore was automatically considered unbound. In reality, some of this material would return to the galaxy. Our models, that use the SPH (Smooth Particle Hydrodynamics) integration scheme, are not limited by the extent of the computational domain; thus, they were able to trace all the material for the duration of the simulation. We will consider the following more stringent criterion: only material that has left a cylindrical region of $R_{\rm max} = 20$ kpc and $|z_{\rm max}| = 20$ kpc (see also D'Ercole & Brighenti 1999) *and* has a velocity larger than the escape velocity at its current position will be considered effectively lost.

Mass loss in our models is thus carried out by first computing the total mass of unbound (ejected from the galaxy) gas $M_{\rm ej}$. To do this, we consider the total galaxy gravitational potential given by,

$$\Phi_T(r) = \Phi_h(r) + \Phi_d(r)\,, \tag{9}$$

where r is the distance to the center, and Φ_h and Φ_d are the dark matter halo and disk components, respectively. Gas particles outside the cilinder with velocity larger than the escape velocity

$$v_{\rm esc} = \sqrt{-2\Phi_T(r)} \tag{10}$$

are considered to be unbound. We define a 'total mass ejection efficiency' as the ratio of the mass ejected (unbound) to the total gas mass,

$$\xi_m \equiv \frac{M_{\rm ej}}{M_g}\,. \tag{11}$$

The mass ejection efficiency has two limiting cases: $\xi_m \to 0$ when all the galactic ISM is bound, and $\xi_m \to 1$ when all the galactic gas is expelled from the galaxy.

One can also define a "metal ejection efficiency" as

$$\xi_z \equiv \frac{M_{c,\rm ej}}{M_c}, \tag{12}$$

where M_c is the total mass injected by the SSCs, and $M_{c,\rm ej}$ the mass, also originated in the SSCs, that is unbound. The mass injected by a star cluster contains the metals produced in the lifetime of the massive stars, $t \sim$40 Myr. For that time-span, using the metal yields calculated by Meynet & Maeder (2002), Tenorio-Tagle et al. (2005) showed that the metallicity of the combined stellar winds remains at a value of $\sim$0.5 $Z_\odot$ from the start of the SB, up to a $t = 3$ Myr evolutionary time, and then rapidly grows to $\sim$15 $Z_\odot$ at $t \approx 7$ Myr, decreasing gradually to $\sim$3 $Z_\odot$ at $t \approx 20$ Myr.

The metal ejection efficiency has two limiting cases: $\xi_z \to 0$, when all the metallic gas injected by the nuclear starburst is kept in the galaxy disk, and $\xi_z \to 1$, when all the metallic gas processed in the burst is expelled from the galaxy. Galaxies with $\xi_z \to 1$ would be metal poor, while the IGM around them should be metal rich. On the other hand, metallic gas injected from the SBs region with $v_g < v_{\rm esc}$ is going to return to the galactic plane, and the ISM of such galaxies will be contaminated with the metals produced in the nuclear starburst.

3.2. *Disk contamination measures*

As mentioned above, bound gas ejected by the SSCs will return to the galactic disk, either close to the center if it never reached a high altitude, or spread to large galactocentric radii if it did. This mechanism is of course a continuum, and "high" or "low" altitude are just relative terms. To quantify the contamination of the disk by material originated in the SSCs we will consider as 'high altitude' a distance of at least 3 times the scale height of the disk, H.

One can define a new parameter, the fraction of bound gas (that is inside a cylinder of radius $R_{\rm max}$ and with velocity less than the escape velocity) that reaches at least an altitude of $3H$:

$$\chi_b \equiv \frac{M_{{\rm ej},3H}}{M_g}\,, \tag{13}$$

TABLE 1

THE GALACTIC MODELS

Galaxy model	M_g $M_\odot$	M_h $M_\odot$	$v_c(r_{200})$ km s^{-1}	H kpc	$N^a_{\rm ep}$	$N^r_{\rm ep}$
G1	6.2×10^6	4.3×10^8	12	0.044	335	478
G2	3.0×10^7	2.1×10^9	20.8	0.071	530	766
G3	7.0×10^7	4.9×10^9	27.7	0.094	473	573
G4	1.4×10^8	9.4×10^9	34.3	0.118	458	646
G5	2.1×10^8	1.4×10^{10}	39.4	0.135	453	681
G6	3.0×10^8	2.1×10^{10}	44.5	0.153	429	666
G7	4.7×10^8	3.2×10^{10}	51.9	0.178	379	655
G8	7.0×10^8	4.8×10^{10}	59.2	0.203	317	585
G9	1.1×10^9	7.3×10^{10}	68	0.233	255	434
G10	1.5×10^{10}	1.1×10^{11}	76.8	0.263	191	317

where $M_{\rm ej,3H}$ is the total bound mass (including the ISM and the material from the SSCs) that reaches an altitude $\geq 3H$. This mass will be reinserted into the galactic disk at different radii. However, since it includes material both from the SSCs (with high metallicity) and from the ISM around the SSCs (lower metallicity) it is not clear how much the metallicity of the disk will be enhanced by this mixture. For that reason we define the fraction of metallic bound gas that leaves the galactic disk and reaches an altitude between $3H$ and $z_{\rm max}$ as

$$\chi_{b,z} \equiv \frac{M_{c,3H}}{M_c}\,, \tag{14}$$

where $M_{c,3H}$ is the bound mass injected by the stellar cluster that reaches an altitude $3H \leq z \leq z_{\rm max}$, and M_c the total mass injected by the SSC wind. This gives a better measure of the amount of high metallicity material available to spread throughout the disk. Nevertheless, a detailed study of how it will be distributed in the disk is necessary for a complete disk contamination model, which is beyond the scope of this paper.

4. NUMERICAL SIMULATIONS

We have performed adiabatic and radiative 3D N-Body/SPH simulations that model the effect of a central compact starburst, in which mechanical energy is injected by stellar cluster winds, using GADGET-2[3]. All simulations were done with three types of particles: disk, halo, and gas particles, and, unless otherwise stated, each consist of 30000, 40000, and 30000 particles, respectively. Two separate simulations were run for each model, one adiabatic and a second one including radiative losses.

Most simulations (low-resolution simulations) use a timestep $\sim$1–3$\times10^5$ yr and a Plummer softening of 0.25 kpc, 0.5 kpc, and 0.25 kpc, for gas, halo, and disk particles, respectively. We ran a grid of models using different galaxy masses and starburst energies. The parameters of the models are described below.

4.1. *The host galaxies*

We constructed ten isolated galaxies as described in Springel (2000) and in § 2 of this paper. The galaxies are named G1 to G10; they have ISM masses in the range of $\sim5\times10^6 - 10^{10}$ $M_\odot$, similar to those used by MacLow & Ferrara (1999); the total masses are in the $\sim4\times10^8 - 1\times10^{12}$ $M_\odot$ range. The disk masses of the galaxies are given by $M_d = 0.041\,M_{\rm tot}$, and the total mass of the gas is 35% of the galactic visible mass in all of the models.

Table 1 shows the mass of the gas and the halo, the circular velocity at r_{200} and R_0 for all the galactic models.

4.2. *The starburst regions*

In order to reproduce the observed properties of starburst galaxies with young stellar clusters, including M82, NGC 253 and NGC 1569, we use a wide range of SBs masses. We should note that the numbers of these energetic stellar asociations in the host galaxies were detected at optical wavelengths (e.g.,

[3]GADGET-2 is a code for cosmological N-Body/SPH-simulation on serial workstations or massively parallel computers with distributed memory (Springel, Yoshida, & White 2001; Springel 2005).

TABLE 2

THE STARBURST MODELS

Starburst Model	E_c (erg)	$M_{\rm SB}$ ($M_\odot$)
S1	1×10^{52}	$\sim 5.5 \times 10^2$
S2	5×10^{52}	$\sim 2.75 \times 10^3$
S3	1×10^{53}	$\sim 5.5 \times 10^3$
S4	5×10^{53}	$\sim 2.75 \times 10^4$
S5	1×10^{54}	$\sim 5.5 \times 10^4$
S6	5×10^{54}	$\sim 2.75 \times 10^5$
S7	1×10^{55}	$\sim 5.5 \times 10^5$
S8	5×10^{55}	$\sim 2.75 \times 10^6$
S9	1×10^{56}	$\sim 5.5 \times 10^6$
S10	5×10^{56}	$\sim 2.75 \times 10^7$
S11	1×10^{57}	$\sim 5.5 \times 10^7$

for M82 see Melo et al. 2005; for NGC 1569 see Westmoquette et al. 2008). Since there is a high level of obscuration in the nuclear regions of M82, NGC 1569, and NGC 253, the real number of clusters would be larger. Melo et al. (2005) and Smith et al. (2007) have shown that in the nuclear SBs region of M82 the SSCs are confined to the central ∼200 pc of the galaxy.

We estimated the mass of the starburst using Starburst 99 models (Leitherer & Heckman 1995 and Leitherer et al. 1999[4]) with the appropriate mechanical energy and a Salpeter initial mass function (IMF) that includes stars between 1 and 100 $M_\odot$. In order to obtain a better estimation of the total starburst masses, we have calculated the mass of the stars between 0.1 and 1 $M_\odot$ using the Kroupa, Tout, & Gilmore (1993) IMF. We assumed that all of the energy produced in the SB lifetime is injected instantaneously, at a given time t_c, inside a spherical region of radius R_c at the center of the disk galaxy as thermal energy. At this time (corresponding to ∼10 orbital periods of the galactic disk at a radius of 150 pc), the gas in the central regions of the galaxy has already developed a clumpy structure. Actually, in the present version of the code we cannot consider the case of an injection that extends over a finite time period.

The total injected energy is obtained from

$$E_c = \int_0^{t_f} L_m(t) dt \,, \qquad (15)$$

where t_f is the typical SBs lifetime, and $L_m(t)$ the mechanical luminosity as a function of time. The most important contribution to the mechanical luminosity happens at ∼40 Myr (see also Leitherer et al. 1999) and after that time the mechanical luminosity decreases drastically, due to the fact that the most massive stars have died by then. Table 2 shows the total energy and the respective mass of all the starburst models (S1–S11).

[4]http://www.stsci.edu/science/starburst99/.

4.3. *The grid of models*

We computed a total of 220 numerical simulations of GWs produced by the nuclear starburst events, with different total masses of the galaxies G1–G10 (see Table 1), combined with different starburst energies S1–S11 (see Table 2), all adiabatic as well radiative (110 models each). The total energy injected by the starburst of the models S1–S11 was distributed in the gas particles inside a sphere of $R_c = 150$ pc at the center of each of the galactic models G1–G10.

We choose this size for the region in which the energy of the starburst is injected, because it is representative of the sizes of observed starbursts. For example, in M82 the starburst region has a $R_c \sim 175$ pc radius (Moorwood 1996), and in NGC 1569A the starburst hole has a $R_c \sim 100$ pc radius (Fujita et al. 2009). An exploration of the effects on our results of varying R_c is shown in § 6.

The number of energetic particles ($N^a_{\rm ep}$ and $N^r_{\rm ep}$, for the adiabatic and radiative cases, respectively) is related to the total number of particles of gas in the initial conditions. The energy per particle in the starburst region is $E_i = E_c/N_{\rm ep}$, the number of energetic points used in the galactic models, is shown in Table 1. All the cluster particles (the energetic particles) are tagged in order to estimate the fate of the metals produced during the starburst lifetime.

5. RESULTS

We have let the galaxy models evolve on their own for $t_c = 1.5 \times 10^7$ yr. At the time t_c, the total energy of the SB is injected in the center of the galaxy. MacLow & Ferrara (1999) injected the energy from the cluster in a continuous way over a period of 40 Myr. Given the fact that the flow induced by the cluster takes ∼0.5 Gyr to travel a distance of ∼10 kpc (i.e., the size of the galaxy), the differences that might result from releasing the cluster energy over ∼40 Myr=0.04 Gyr (rather than instantaneously) cannot be very important.

The ejection efficiencies were computed at $t =$ 1 Gyr in all our models. The values of the efficiencies reach a constant value of integration times of ∼0.2–0.5 Gyr and ∼0.4–0.7 Gyr for the adiabatic and radiative models (respectively).

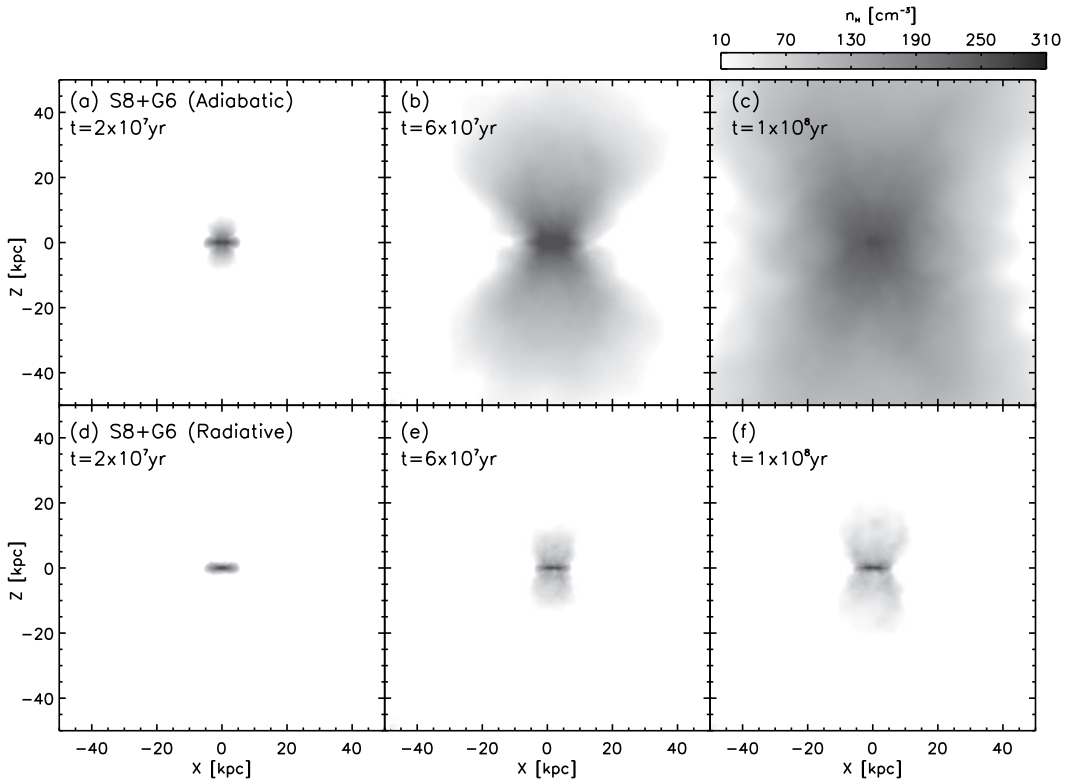

Fig. 1. Time sequence of cuts of number density in the xz-midplane ($y = 0$) for the model S8+G6 (see Tables 1 and 2). The integration times in years are given in the upper left corner of the frames. The top panels (a, b and c) are the adiabatic models, and the bottom panels are the radiative ones.

5.1. *Mass and metal ejection efficiencies*

Total mass and metal ejection efficiencies have been calculated using the definitions given in § 3. In particular, the kinetic and gravitational potential energies as a function of the radial distance r_i (with respect to the center of the potential) were computed for each gas particle. A particle i would escape the galactic gravitational potential if $v_i \geq v_{\rm esc} = \sqrt{-2\Phi_i}$, where v_i is the velocity and Φ_i the total potential at the position of the particle.

We also traced the high metallicity gas particles (injected by the SBs) and the low metallicity gas (galactic ISM gas). The high metallicity gas was tagged with a negative passive scalar, the ISM with a positive one. Therefore, ξ_z was calculated using the gas particles with a negative passive scalar, while ξ_m was calculated with all the gas particles (regardless of the sign of the passive scalar).

Figure 1 shows the temporal evolution of the ejected gas from a central starburst with properties that correspond to starburst model S8 at the center of galaxy model G6 (see Tables 1 and 2). The three timesteps shown are 2×10^7, 6×10^7 and 10^8 yr, for the adiabatic case –panels (a), (b) and (c), respectively–, and the radiative one –(d), (e) and (f), respectively. We can see the ejection of gas from the plane of the dwarf galaxy with a moderate ISM mass (3×10^8 $M_\odot$), produced by a central starburst that ejects a mass of 1.5×10^6 $M_\odot$. Such a SB corresponds to a region with ∼9000 massive stars, injecting a total energy during its lifetime of around 5×10^{55} erg (see the starburst models of Leitherer & Heckman 1995 and Leitherer et al. 1999). From the figure we see right away that the amount of gravitationally unbound gas is larger in the adiabatic than in the radiative case. However, in both cases an important part of the disk gas is pushed above the galactic plane, and in the radiative case a significant part of this gas is returned to the galactic disk.

For this model (S8+G6) the totality of the galaxy gas is pushed above $3H$; however, only 43% of the gas acquires enough energy to leave the galactic potential and become part of the IGM, while the remaining 57% would eventually return to the disk of the galaxy, since this ISM material is gravitationally bound. For the radiative case, the percentage of the

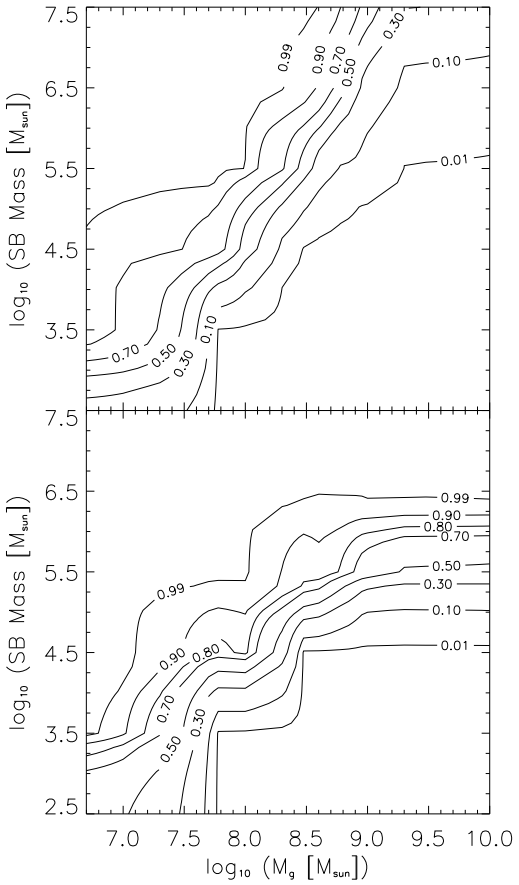

Fig. 2. Mass (ξ_m, top) and metal ejection efficiency (ξ_z, bottom) contours as a function of total mass of the gas and total starburst masses, for adiabatic models (top and bottom panel, respectively).

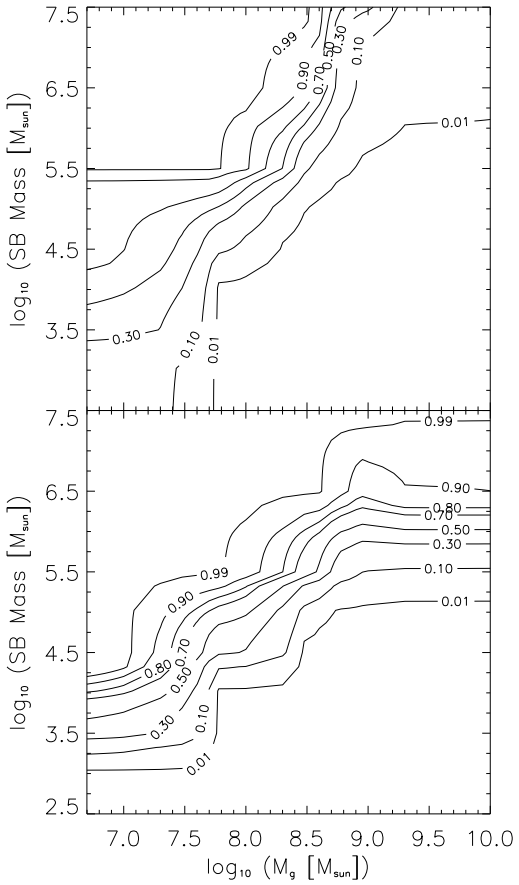

Fig. 3. Same as Figure 2, but for the radiative models.

gas that is gravitationally unbound is of 14%, while 4.7% of the ejected gas gets above $3H$ and returns to the galactic disk. On the other hand, in the adiabatic case 97% of the metallic gas ejected by the nuclear starburst escapes from the galactic gravitational potential. In other words, a galaxy with those parameters would be contaminated only with 5% of the metals produced in the massive SB. For the radiative S8+G6 model, 79% of the metals escape from the galaxy.

The mass ejection efficiencies are presented in Figures 2 and 3, for the adiabatic and the radiative model grids, respectively. In these figures, the abscissa sweeps the galactic models (G1–G10), and the ordinate sweeps the SB models (S1–S11).

Figure 2 shows isocontour maps of the mass ejection efficiency ξ_m (top panel) and the metal ejection efficiency ξ_z (bottom panel) for the adiabatic models as a function of the SB mass and the total gas mass of the galaxy. For the mass ejection efficiency (top panel) we plotted isocontours for $\xi_m = 0.01$, 0.10, 0.3, 0.5, 0.7, 0.9 and 0.99. In this figure, we can see that for the more massive galaxies (in which the gas mass is larger than 10^9 $M_\odot$) the fraction of unbound gas is less than $\sim$0.25, even for a rather large nuclear starburst. However, galaxies with an ISM of mass lower than 10^8 $M_\odot$ will lose virtually all of their gas if they undergo a nuclear starburst that injects more than 10^5 $M_\odot$.

From the $\xi_z = 0.01$, 0.10, 0.3, 0.5, 0.7, 0.8, 0.9 and 0.99 isocontours in the bottom panel one can see that most of the gas ejected from the cluster escapes the galaxy if the starburst mass is $> 10^{6.5}$ $M_\odot$. Also, most of the ejected gas escapes if the galaxy has a total gas mass $< 10^7$ $M_\odot$. On the other hand, for starburst masses $< 10^{4.5}$ $M_\odot$ and galactic gas masses $> 10^8$ $M_\odot$ most of the ejected metals are retained by the galaxy. From the bottom panel of Figure 2 we also see that a starburst with a mass $> 10^{5.5}$ $M_\odot$ will eject more than 50% of its wind into the IGM.

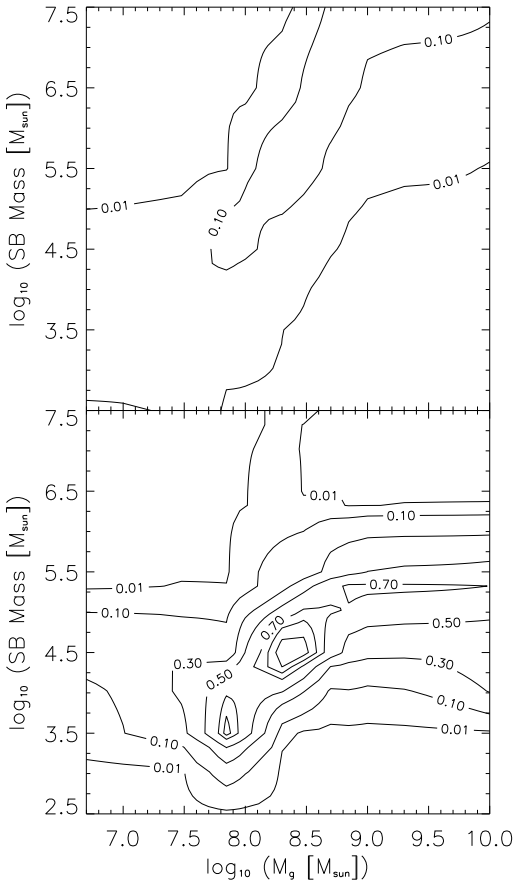

Fig. 4. Fractions of bound gas (χ_b, top) and bound metallic gas ($\chi_{b,z}$, bottom) that reach an altitude of at least $3H$, for the adiabatic models.

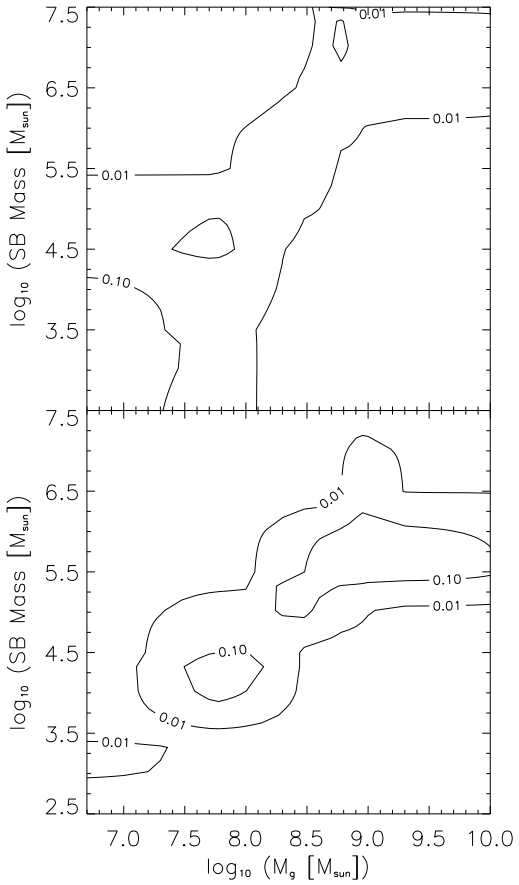

Fig. 5. Same as Figure 4, but for the radiative models.

Figure 3 shows the ξ_m (mass ejection) and ξ_z (metal ejection) efficiencies as a function of galactic gas mass and starburst mass computed from the radiative models. Both the ξ_m and ξ_z contour maps (top and bottom panels of Figure 3) are qualitatively similar to the ones computed from the adiabatic models (see Figure 2). Even though the detailed shapes of the contours vary, the main difference between the radiative and adiabatic cases is the following: in order to obtain similar ejection efficiencies, one needs a starburst mass larger by a factor of $\sim$2 in the radiative case.

5.2. *Material returned to the galactic disk*

Figure 4 shows the efficiencies of gas (χ_b, top panel) and metal mass ($\chi_{b,z}$, bottom panel) which reach at least 3 scale heights (H) above the disk but remain gravitationally bound, computed from the adiabatic models. Both panels show two low efficiency regions divided by a high efficiency ridge (which runs diagonally from low to high SB and galactic gas masses). In the high galactic mass/low SB mass region, the SB ejection mostly remains close to the galactic plane, and does not reach the required $3H$ height above the disk plane (in order to be counted in the χ_b and $\chi_{b,z}$ efficiencies). In the low galactic mass/high SB mass region, the SB ejection mostly escapes from the galaxy. From the $\chi_{b,z}$ distribution (bottom panel), we see that models with $M_g \sim 10^8 \rightarrow 10^9\ M_\odot$ and $M_{\rm SB} \sim 10^3 \rightarrow 10^5\ M_\odot$ are able to redistribute more than $\sim$50% of the ejected metals over the galactic ISM.

Figure 5 shows the χ_b (top panel) and $\chi_{b,z}$ (bottom panel) efficiencies computed from the radiative models. The efficiencies show the same qualitative behaviour (with two low efficiency regions separated by a high efficiency ridge) as the ones calculated from the adiabatic models. However, the maximum values of the efficiencies are lower. In the adiabatic case, the maximum values of the gas mass redistribution efficiency is of $\sim$20%, while a maximum value of only $\sim$10% is found for the radiative models. For the

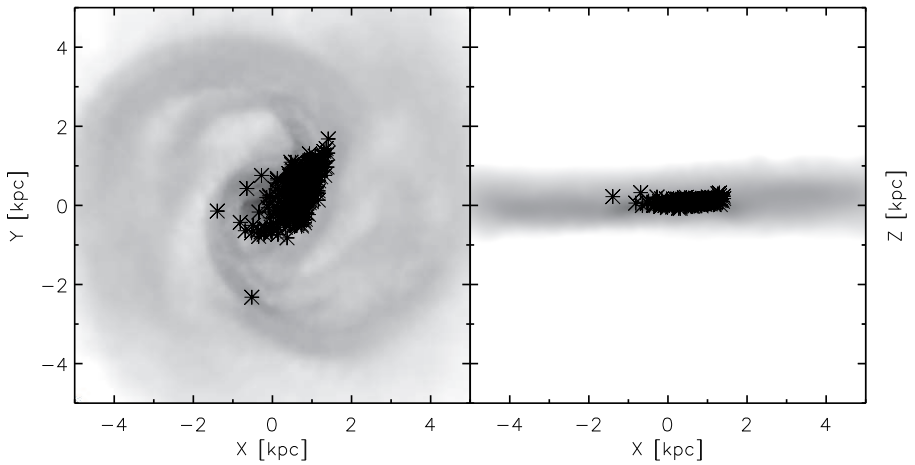

Fig. 6. Distribution of the SPH particles ejected by the central starburst for model S7+G9 after 1 Gyr. The inner region of the domain is shown, and the location of the SPH particles gives the spatial distribution of the metals that have been deposited back on the galactic disk. The left plot shows the distribution of positions projected onto the galactic disk, and the right plot shows the positions of the SPH particles projected onto a plane which includes the rotation axis of the galactic disk. The greyscale shows the distribution of the mass density on these two planes.

metal redistribution efficiency, values above ∼70% are obtained for the adiabatic models, while maximum values of only ∼20% are obtained from the radiative models.

In Figure 6, we show the distribution of metals that have fallen back onto the galactic disk from the starburst ejection of model S7+G9, after a 1 Gyr time evolution. The SPH particles corresponding to the collapsed material form a distribution with a height of ∼300 pc (about the initial scale height of the galactic disk), and with a radial extent of ∼2 kpc (see Figure 6), which is about twice the size of the initial scale of length (R_0) of the G9 galaxy (see Table 1). This is an illustration of the fact that in all of our models the infalling metals are redistributed over a large region of the galactic plane.

6. THE EFFECTS OF VARYING THE RADIUS OF THE INJECTION REGION AND THE RESOLUTION OF THE INITIAL STARBURST

In all of the models presented above, we have assumed that the energy from the starburst is injected in a spherical region of radius $R_c = 150$ pc (which is a representative value of the observed sizes of starburst regions, see § 4.3). In this section, we explore the effects on the ejection efficiencies of varying the value of R_c.

We focus on three of the starburst+host galaxy combinations which we have studied above (see Tables 1 and 2). We choose models S5+G3 (a small mass galaxy with an intermediate energy starburst, S10+G7 (an intermediate mass galaxy with a strong starburst) and S11+G9 (a high mass galaxy with a strong starburst). For these three models, we compute radiative simulations in which the starburst energies are injected in spheres of radii $R_c = 50$ to 150 pc (in 20 pc steps). The number of SPH particles within the spheres scales as the volume of the initial starburst (45 particles for $R_c = 50$ pc to 550 particles for $R_c = 150$ pc).

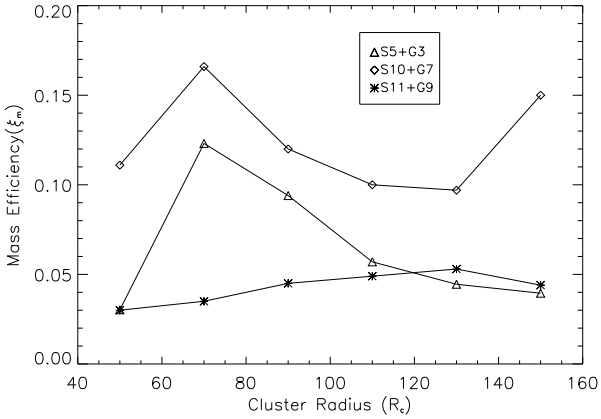

Fig. 7. The mass ejection efficiency ξ_m computed for models S5+G3, S10+G7 and S11+G9 as a function of the initial radius R_c of the starburst.

In Figure 7, we show the mass ejection efficiency ξ_m (see equation 11) computed for models S5+G3,

S10+G7 and S11+G9 as a function of the initial radius R_c of the starburst. We see that there is clear dependence of ξ_m on R_c, with differences by factors of $\sim$1.7 (for models S11+G9 and S10+G7), and over $\sim$3.5 for model S5+G3.

We should note that the models with the smaller energy injection regions (with $R_c = 50$ pc) have smaller mass ejection efficiencies than the models with larger energy injection regions (with $R_c = 70$ pc, see Figure 7). This is probably due to the fact that in the smaller volumes (covering the denser, inner region of the galaxy) the radiative cooling is stronger. In the models with even larger energy injection regions (with $R_c \geq 90$ pc, see Figure 7), the momentum per unit mass given to the galactic gas is lower, and therefore less material succeeds in escaping from the galactic potential. From these results, we conclude that in our intermediate and high mass galaxy models, variations of factors of $\sim$2 in the efficiencies are to be expected for starbursts (with the same energies) with initial radii in the $R_c = 50$ to 150 pc range.

We have also explored the effect of changing the total number of SPH particles in the simulations. We again choose models S5+G3, S10+G7 and S11+G9 (see above and Tables 1 and 2) as representative of our model grid, keeping a constant $R_c = 150$ pc initial radius for the starbursts, and we compute radiative simulations with more than one order of magintud more of gas, halo and disk particles (1500000, 2000000 and 1500000, respectively) than in the previous models (see § 4). In these new runs we have also changed the softening length to 50 pc, for all the components. In all the new models the mass ejection efficiency increases by a factor of the order of 2. For model S5+G3 this change is a factor of $\sim$1.5, while S10+G7 and S11+G9 suffer changes of factors of $\sim$2.21 and $\sim$1.6, respectively.

Therefore, we seem to obtain at least a partial convergence for the values of the ejection efficiencies in simulations with $\sim 10^6$ gas particles. However, the computing time necessary for these simulations is quite large ($\sim$30 times longer than for the 30000 gas particle models), so that our parameter study has been done at lower resolution.

7. DISCUSSION

MacLow & Ferrara (1999) computed radiative, axisymmetric simulations of the ejection of gas from galaxies due to central starbursts. Their models differ from ours in that the starburst energy is injected as a continuous source term during the 50 Myr of their simulations, while in our models the energy of the starburst is injected instantaneously at the beginning of the simulations.

If we convert their starburst mechanical luminosities into total energies (by multiplying the luminosities by 50 Myr), and use the relation between starburst energy and mass of Table 2, we can find correspondences between their models and ours. We then find that both the mass and metal ejection efficiencies computed by MacLow & Ferrara (1999) are generally consistent with the ones that we have computed, with typical differences of factors $\sim$3. We judge this to be a satisfying agreement given the differences between our models and the ones of MacLow & Ferrara (1999).

Interestingly, the highest SB mechanical energy/lower galactic mass model of MacLow & Ferrara (1999) approximately corresponds to our S5+G2 model (with $M_{\rm SB} = 3 \times 10^4\ M_\odot$ and $M_g = 3 \times 10^7\ M_\odot$). As can be seen in Figure 3, this model lies within the transition from low to high efficiency regimes. Therefore, the models of MacLow & Ferrara (1999) mostly missed the transition between low and high mass loss efficiencies which we are describing in the present paper.

D'Ercole & Brighenti (1999) computed a set of 5 models of galaxies with $M_g < 1.4 \times 10^8\ M_\odot$, similar to our galaxy models G1–G5, in which they inject energies in the range of our S6–S8 starbursts. Their "PEXT" model (see Table 2 of D'Ercole & Brighenti 1999) has parameters similar to our S8+G4 model (see Tables 1 and 2). The PEXT model has a $\xi_m = 0.31$ mass ejection efficiency, which is consistent with the $\xi_m = 0.45$ efficiency obtained from our S8+G5 model. D'Ercole & Brighenti (1999) have studied different possibilities (e.g., having galaxies with no rotation, or having fixed dark matter mass distributions) which have not been explored in our present work.

Fragile, Murray, & Lin (2004) computed mass and metal ejection efficiencies produced in galaxies with $10^9\ M_\odot$ (similar to our galaxy model G9) in which they inject energies in the range of our model S3-S7 starbursts. Their model 5 (see Table 1 of Fragile et al. 2004) has parameters similar to our S7+G9 model. Model 5 has a $\xi_m = 0.016$ mass ejection efficiency and $\xi_Z = 0.99$ metal ejection efficiency (see Table 2 of Fragile et al. 2004), which is consistent with the $\xi_m = 0.006$ and $\xi_Z = 0.805$ efficiencies of our model S7+G9. Fragile et al. (2004) have explored the metal ejection efficiencies for supernova events at different radial positions in the galactic disk. They find that a substantial fraction of the metals is retained in their off-center starburst mod-

els. These result shows that if we consider off-center galactic starbursts, the mass and metal ejection efficiencies will be substantially lower than the ones that we have computed in our present paper.

It is worth mentioning that the strong winds produced by the combination of individual stellar winds and SNe explosions not only produce the GWs, but have important consequences on the star formation history of their host galaxy as well. They are the most efficient way to redistribute metals to the ISM (and/or the IGM). This produces a feedback mechanism that facilitates the gravitational collapse of the ISM to form stars. The material with higher metallicity cools more efficiently, and it therefore forms high density condensations on shorter timescales than the metal poor gas (Scannapiecco et al. 2005; Sutherland & Dopita 1993). At the same time, the energy feedback from these strong winds can heat and disrupt cold gas clouds, thus inhibiting star formation.

Observations and theory suggest (e.g., Larson 1974; White & Rees 1978; White & Frenk 1991) that large outflows should be able to develop in small systems because of their shallower potential wells. This is because, according to hierarchical galaxy formation scenarios, large systems are formed by the aggregation of smaller ones. Thus, the energy feedback from strong winds should have a more important effect for systems in the early stages of formation.

Our models provide quantitative predictions of the amount of metals which are ejected into the IGM and which are redistributed within the host galaxy. These predictions could be used in a direct way for computing models of the star formation history of the host galaxy, and could also be included in models of the history of galaxy formation.

8. CONCLUSIONS

We computed 220 numerical simulations of GWs produced by nuclear starburst energy injected inside a spherical region (of radius R_c) at the center of the disk galaxy. We used different total masses of the galaxies G1–G10, combined with different starburst energies S1–S11, all adiabatic as well as radiative (110 models each). We have performed adiabatic and radiative 3D N-Body/SPH simulations of GW models using GADGET-2. The radiative models have been calculated using a solar metallicity cooling function. Finally, the adiabatic models were calculated in order to obtain the maximum possible value of the mass and metal ejection effciency in our models of galactic winds, and do not necessarily correspond to real cases of starbursts in galaxies.

From the grid of models we obtained the mass and metal ejection efficiencies as a function of the mass of the gas in the galaxy and the total mass of the nuclear starburst.

In the same way, we computed the efficiencies of gas and metal mass that reaches at least $3H$ above the disk but remains gravitationally bound for both the adiabatic and radiative regimes. We present these efficiencies as a function of the mass of interstellar medium in the galaxies versus total mass of the nuclear starburst.

We show that for compact starburst regions (e.g., inside the SSC) with masses larger than 10^6 $M_\odot$ in the adiabatic case, the metal injected by the nuclear starburst is expelled to the IGM (at least 90% of this gas). We show that in galaxies with gas masses between 10^7 to 10^{10} $M_\odot$ and with a massive nuclear starbursts the available metals are freed from the gravitational potential of the galaxy. In the radiative case the critical SB mass at which total loss of metals occurs is around 2 or 3 times larger than in the adiabiatic one.

In addition, we have calculated the efficiency of the metal redistribution in the disk of galaxies. We find that the metal redistribution is more efficient for intermediate and low mass starburst masses ($< 10^{4.5}$ $M_\odot$) and galactic gas masses $> 10^8$ $M_\odot$ (for both the adiabatic and radiative cases).

In this paper we presented models in which we did not consider many elements that are likely to be important in starburst galaxies; among these are:

- clumpiness in the medium,
- the generation of new stars,
- a different fraction of gas in the galaxy disk,
- the effect of galactic mass loading (see Fujita et al. 2009).

Therefore, there is a large range of possibilities for future studies including differential and/or selective galactic winds (also, Pilyugin 1993 and Recchi et al. 2001, 2002).

Finally, in our paper we have presented a limited resolution study (in § 6). Our evaluation of the dependence of the computed efficiencies on resolution is limited to a range of ∼3 in resolution. This range is of course not very impressive, and questions remain as to the results that would be obtained at considerably higher resolutions (presently not possible, at least for calculating relatively extended grids of models). When such higher resolution models do

become available, one will probably find different numerical values for the efficiencies, but one would expect that the transition between low and high ejection efficiency systems (found in the present work) will be preserved.

We thank the anonymous referee for very relevant comments that resulted in a substantial revision of the original version of this paper. We thank Volker Springel (from the Univ. of Heidelberg) for helpful suggestions which we have been included in this paper. We acknowledge support from the Conacyt grants 61547, 101356 and 101975.

REFERENCES

Anders, P., de Grijs, R., Fritze-v. Alvensleben, U., & Bissantz, N. 2004, MNRAS, 347, 17
Cantó, J., Raga, A. C., & Rodríguez, L. F. 2000, ApJ, 536, 896
Chevalier, R. A., & Clegg, A. W. 1985, Nature, 317, 44
Cooper, J. L., Bicknell, G. V., Sutherland, R. S., & Bland-Hawthorn, J. 2008, ApJ, 674, 157
D'Ercole, A., & Brighenti, F. 1999, MNRAS, 309, 941
De Young, D. S., & Heckman, T. M. 1994, ApJ, 431, 598
Fragile, P. C., Murray, S. D., & Lin, D. N. C. 2004, ApJ, 617, 1077
Fujita, A., MacLow, M.-M., Ferrara, A., & Meiksin, A. 2004, ApJ, 613, 159
Fujita, A., Martin, C. L., MacLow, M.-M., New, K. C. B., & Weaver, R. 2009, ApJ, 698, 693
Harris, J., Calzetti, D., Gallagher, J. S., Conselice, C. J., & Smith, D. A. 2001, AJ, 122, 3046
Heckman, T. M., Armus, L., & Miley, G. K. 1990, ApJS, 74, 833
Kroupa, P., Tout, C. A., & Gilmore, G. 1993, MNRAS, 262, 545
Hernquist, L. 1990, ApJ, 356, 359
_____. 1993, ApJ, 409, 548
Larson, R. B. 1974, MNRAS, 169, 229
Leitherer, C., & Heckman, T. M. 1995, ApJS, 96, 9
Leitherer, C., et al. 1999, ApJS, 123, 3
Lynds, C. R., & Sandage, A. R. 1963, ApJ, 137, 1005
MacLow, M. M., & Ferrara, A. 1999, ApJ, 513, 142
Martin, C. L. 1999, ApJ, 513, 156
Melo, V. P. 2005, PhD Thesis, Instituto de Astrofísica de Canarias, Spain
Melo, V. P., Muñoz-Tuñón, C., Maíz-Apellániz, J., & Tenorio-Tagle, G. 2005, ApJ, 619, 270
Meynet, G., & Maeder, A. 2002, A&A, 390, 561
Moorwood, A. F. M. 1996, Space Sci. Rev., 77, 303
Navarro, J. F., Frenk, C. S., & White, S. D. M. 1996, ApJ, 462, 563 (NFW)
Ohyama, Y., et al. 2002, PASJ, 54, 891
Pettini, M., et al. 2001, ApJ, 554, 981
Pilyugin, L. S. 1993, A&A, 277, 42
Recchi, S., Matteucci, F., & D'Ercole, A. 2001, MNRAS, 322, 800
Recchi, S., Matteucci, F., D'Ercole, A., & Tosi, M. 2002, A&A, 384, 799
Recchi, S., Spitoni, E., Matteucci, F., & Lanfranchi, G. A. 2008, A&A, 489, 555
Rodríguez-González, A., Raga, A. C., & Cantó, J. 2009, A&A, 501, 411
Scannapieco, C., Tissera, P. B., White, S. D. M., & Springel, V. 2005, MNRAS, 364, 552
Shopbell, P. L., & Bland-Hawthorn, J. 1998, ApJ, 493, 129
Smith, L. J., et al. 2007, ApJ, 667, 145
Springel, V. 2000, MNRAS, 312, 859
_____. 2005, MNRAS, 364, 1105
Springel, V., Di Matteo, T., & Hernquist, L. 2005, 361, 776
Springel, V., Yoshida, N., & White, S. 2001, New Astron., 6, 79
Strickland, D., & Stevens, S. 2000, MNRAS, 314, 511
Sutherland, R. S., & Dopita, M. A. 1993, ApJS, 88, 253
Tenorio-Tagle, G. 1996, AJ, 111, 1641
Tenorio-Tagle, G., & Muñoz-Tuñón, C. 1998, MNRAS, 293, 299
Tenorio-Tagle, G., Silich, S., & Muñoz-Tuñón, C. 2003, ApJ, 597, 279
Tenorio-Tagle, G., Silich, S., Rodríguez-González, A., & Muñoz-Tuñón, C. 2005, ApJ, 620, 217
Tomisaka, K., & Ikeuchi, S. 1988, ApJ, 330, 695
Veilleux, S., Cecil, G., & Bland-Hawthorn, J. 2005, ARA&A, 43, 769
Westmoquette, M. S., Exter, K. M., Smith, L. J., & Gallagher, J. S. 2007, MNRAS, 381, 894
Westmoquette, M. S., Smith, L. J., & Gallagher, J. S. 2008, MNRAS, 383, 864
White, S. D. M., & Frenk, C. S. 1991, MNRAS, 379, 52
White, S. D. M., & Rees, M. J. 1978, MNRAS, 183, 341

Alejandro Esquivel, Alejandro C. Raga, and Ary Rodríguez-González: Instituto de Ciencias Nucleares, Universidad Nacional Autónoma de México, Apdo. Postal 70-543, 04510 México, D. F., Mexico (esquivel, raga, ary@nucleares.unam.mx).
Pedro Colín: Centro de Radioastronomía y Astrofísica, Universidad Nacional Autónoma de México, Apdo. Postal 3-72, 58090 Morelia, Michoacán, Mexico (p.colin@crya.unam.mx).

Revista Mexicana de Astronomía y Astrofísica, **47**, 127–137 (2011)

THE USEFULNESS OF 2MASS JHK_S PHOTOMETRY FOR OPEN CLUSTER STUDIES

D. G. Turner

Department of Astronomy and Physics, Saint Mary's University, Halifax, Canada

Received 2010 September 23; accepted 2011 February 1

RESUMEN

Se utilizan datos en *JHK* para inferir el enrojecimiento y la distancia a cúmulos abiertos para los cuales son limitados los datos disponibles en el óptico. Se obtienen relaciones color-color y color-magnitud intrínsecos de la ZAMS con referencia a calibraciones existentes, estrellas estándar, tres cúmulos enrojecidos uniformemente: Stock 16, NGC 2362, y NGC 2281, y las enanas no-enrojecidas de las Hiadas. El método para inferir el enrojecimiento interestelar y la distancia a cúmulos abiertos escasamente poblados se aplica a Berkeley 44, Turner 1, y Collinder 419, cuyos resultados existentes están en conflicto con los inferidos a partir de los datos en *JHK*. Los últimos dos cúmulos son de especial interés: Turner 1 porque alberga a la Cefeida clásica con el período más largo de la Galaxia, y Collinder 419 porque yace en el complejo Cygnus X.

ABSTRACT

2MASS JHK_s data are used to infer the reddening and distance of open clusters for which limited optical data are available. Intrinsic ZAMS color-color and color-magnitude relations are derived with reference to existing calibrations, standard stars, three uniformly-reddened clusters: Stock 16, NGC 2362, and NGC 2281, and unreddened Hyades dwarfs. The method of inferring interstellar reddening and distance for sparsely-populated open clusters is applied to Berkeley 44, Turner 1, and Collinder 419, for which existing results conflict with those inferred from JHK_s data. The last two clusters are of special interest: Turner 1 because it hosts the Galaxy's longest-period classical Cepheid, and Collinder 419 because it lies in the Cygnus X complex.

Key Words: dust, extinction — Galaxy: open clusters and associations: general — Hertzsprung-Russell and C-M diagrams — methods: data analysis

1. INTRODUCTION

The introduction of CCD detectors to photometric studies of open clusters has led to significant improvements in the accuracy and precision of data for faint cluster stars observed previously via photoelectric or photographic techniques. The tradeoff is a low efficiency and associated steep wavelength dependence for such detectors in the blue-violet region, limiting photometric accuracy in the traditional ultraviolet filters: the Johnson system *U*-band and the Strömgren system *u*-band. Color corrections for observations in the ultraviolet become non-linear and multi-valued in that situation, particularly for hot stars that display a sizable Balmer discontinuity superposed on their continuum (see, for example, Moffat & Vogt 1977). Many recent open cluster studies have therefore been restricted to observations in the *BVRI* bands, or simply the *BVI* or *VRI* bands.

The intrinsic relations for OB stars and GK dwarfs in color-color diagrams restricted to such systems are nearly parallel to the reddening vectors for interstellar extinction (Caldwell et al. 1993), posing difficulties for establishing the reddening of cluster stars (see Carraro & Costa 2009). AF stars can be studied in such fashion (e.g., Turner et al. 2011), but that would limit photometric studies in *BVRI* to intermediate-age clusters with their main sequences consisting of unevolved $1 - 2\ M_\odot$ stars. Even in

such cases, an accurate knowledge of the interstellar reddening of member stars is essential for the reliable establishment of distance and age (Turner 1996), which means that the photometric study of many clusters may be limited by the nature of the filter bands employed for the observations. Some researchers studying intermediate-age and old clusters have therefore adopted an alternate approach to establish cluster intrinsic parameters, by identifying a putative red giant clump in cluster color-magnitude diagrams arising from the He-burning stage of low-mass red giants (Cannon 1970) and inferring the reddening, age, and distance of a cluster through optimized fitting of model isochrones to the data (e.g., Carraro, Vallenari, & Ortolani 1995; Carraro & Munari 2004).

There are two problems associated with such an approach. First, the dependence of the fitting technique on model isochrones may bias the results. Second, the most frequently encountered stars along most Galactic lines of sight tend to be K giants and A dwarfs (McCuskey 1965, 1970), which are also the most luminous members of intermediate-age open clusters. As noted by Burki & Maeder (1973), simulations of *UBV* photometry for unrelated stars lying in typical Galactic star fields can generate color-magnitude diagrams containing pseudo-main sequences similar to those of true open clusters. The presence of physically-unrelated A dwarfs and K giants along typical Galactic lines of sight may therefore generate features in open cluster color-magnitude diagrams, A dwarfs and G giants or FG dwarfs and K giants, in similar locations to those found in the color-magnitude diagrams of intermediate-age or old open clusters, respectively. The photometric properties of foreground or background stars in some open cluster fields could therefore be mistaken for the characteristics of an old open cluster color-magnitude diagram, thereby biasing studies of clusters tied to the red clump method.

An independent means of establishing cluster membership (e.g., star counts, proper motions, or radial velocities) and especially reddening for cluster stars is therefore essential for avoiding incorrect conclusions about cluster parameters. The ready availability of JHK_s photometry (Cutri et al. 2003) from the Two Micron All Sky Survey (2MASS, Skrutskie et al. 2006) for Galactic star fields offers one such means, since it addresses the primary parameter vital for open cluster studies: the amount of foreground reddening of cluster stars (e.g., Maciejewski, Mihov, & Georgiev 2009). Presented here are examples of star clusters, Berkeley 44, Turner 1, and Collinder 419, for which the method addresses potential incorrect choices of cluster parameters based solely on optical photometry.

2. JHK_S INTRINSIC RELATIONS

The effective wavelengths for the 2MASS JHK_s system, 1.235 μm, 1.662 μm, and 2.159 μm, respectively, are fairly close to those for the older *JK* system of Johnson (1968) and the *JHK* system studied by Koornneef (1983), and observations with the *JHK* and K_s filters are standardized in fairly similar fashion. The main source of difficulty is likely to be the presence of atmospheric absoprtion features within the same photometric bands (Milone & Young 2005, 2008), which reduces the precision of repeated observations. K_s-band observations, and possibly *H*-band observations, of stars are also suceptible to emission from circumstellar dust. Is it possible that the intrinsic *VJK* and *VJHK* colors for main-sequence stars derived by Johnson (1966, 1968) and Koornneef (1983), respectively, are also applicable to the 2MASS JHK_s system? Such a possibility can be tested from available 2MASS observations of standard stars and stars in open clusters of known reddening.

Intrinsic JHK_s colors for main-sequence stars were initially derived here as follows. The relationships of Johnson (1966, 1968) and Koornneef (1983) for intrinsic *V–J*, *V–H*, and *V–K* colors as functions of $(B–V)_0$ were tabulated and plotted, as in Figure 1 (upper), including estimates for *V–H* color from the intrinsic colors of Johnson (1966, 1968) using his tabulated values for *V–J* and *V–K* interpolated according to the effective wavelengths of the filters. Least squares fits to the data then established polynomial relationships between the colors.

The derived relationships were then tested using 2MASS data and *BV* observations for 19 reasonably bright, nearby and unreddened, photometric and spectroscopic dwarf standards, stars with unsaturated observations in the Ursa Major and Hyades clusters, which are both unreddened, and stars in the young cluster NGC 2244 corrected for differential reddening within the Rosette Nebula (see Turner 1976a). NGC 2244 stars were used in order to tie down the hot end of the sequence; its member stars possess excellent photometry on the *UBV* system (Johnson 1962) and lie in a region of well-established reddening law (Turner 1976a). Reddening corrections for early-type stars were applied using *UBV* colors and the relations $E(J–H) = 0.295\ E(B–V)$, $E(H–K_s) = 0.49\ E(J–H)$, and $A_V = 2.427\ E(J-H)$ for $R = A_V/E(B-V) = 3.05$, derived from van de

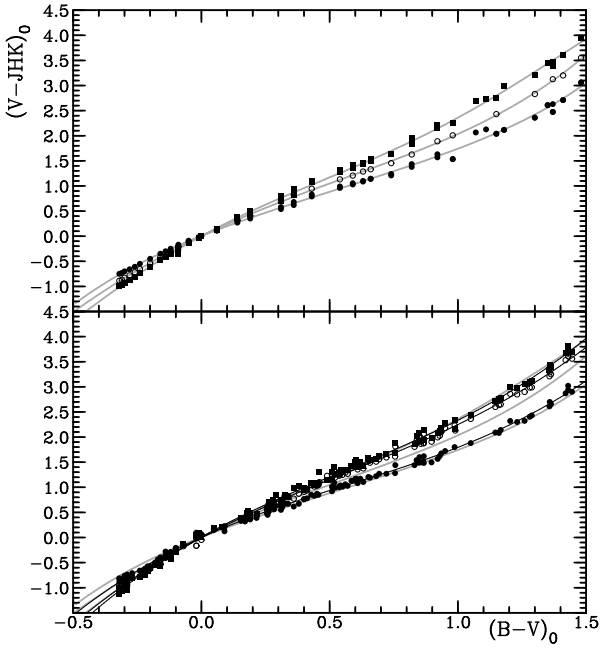

Fig. 1. Intrinsic $(V–K)_0$ (filled squares), $(V–H)_0$ (open circles), and $(V–J)_0$ (filled circles) colors for main-sequence stars are plotted as functions of intrinsic $(B–V)_0$ color from Johnson (1968) and Koornneef (1983) in the upper portion of the diagram. The adopted relations from least squares fits are denoted by gray curves. The lower diagram plots observed data for photometric standards and standard stars using the same symbols as above. Solid curves denote best fits to the data, and differ from the predicted relations (gray curves).

Hulst's reddening curve No. 15 (see Johnson 1966). In addition, the observations for Hyades stars were supplemented by data from Carney (1982) in order to reduce the photometric scatter typical of 2MASS observations. The results are plotted in the lower panel of Figure 1.

The observational trends of $V–J$, $V–H$, and $V–K_s$ are fairly similar to the predicted trends seen in the upper panel of Figure 1, but with noticeable offsets, particularly in $V–H$. The adopted intrinsic relations were therefore established from polynomial fits to the observational data rather than from the predicted relations, with the results tabulated in Table 1 for zero-age main sequence (ZAMS) stars. The derived polynomial relationships of Figure 1 were used to derive intrinsic $J–H$ and $H–K$ colors for main-sequence stars as a function of intrinsic broad band color index $(B–V)_0$, and the ZAMS calibration was that of Turner (1976b, 1979).

The intrinsic relationship for 2MASS colors in Table 1 is similar to the intrinsic color-color relation for dwarf stars in the UBV system, displaying a noticeable "kink" near spectral type A0. 2MASS J magnitudes sample the Brackett continuum in hot stars, while H and K_s magnitudes sample the Pfund continuum, so $J–H$ color should provide a measure of the Pfund discontinuity in hot stars, much like $U–B$ color provides a measure of the Balmer discontinuity. Similarly, $H–K_s$ color should provide a measure of stellar temperature, much like $B–V$ color does in the UBV system. For cool stars all colors should closely track changes in the slope of the black body continuum in the far infrared. Interstellar reddening affects JHK_s colors much less than it does UBV colors, but the effects of circumstellar emission are often more important in the far infrared than in the visible region. A UBV color-color diagram plots $U–B$ versus $B–V$, for which a plot of $J–H$ versus $H–K_s$ would be the closest approximation. It appears, however, that $J–H$ colors may display a greater precision than $H–K_s$ colors in 2MASS photometry, so the diagnostic tool used here to establish reddening for cluster stars is a 2MASS color-color diagram in which $H–K_s$ is plotted versus $J–H$.

The intrinsic relations were tested further using the three clusters used for the calibration and three additional clusters that lie in fields of uniform interstellar reddening: Stock 16 (Turner 1985a), NGC 2362 (Johnson & Morgan 1953; Johnson 1957; Johnson et al. 1961), and NGC 2281 (Pesch 1961), which are reddened by $E(B–V) = 0.49$, 0.11, and 0.11, respectively (see Turner 1996; Johnson et al. 1961). Obvious unreddened stars in the same fields were also included in the samples. Figure 2 plots 2MASS colors for stars in the core regions of Stock 16, NGC 2362, and NGC 2281 with cited magnitude uncertainties of less than ± 0.05, corrected for their known reddening or lack of reddening for suspected foreground stars, along with similar data for Hyades and Ursa Major cluster stars and dereddened data for stars in NGC 2244. Data for the Ursa Major cluster include 11 stars with observations of uncertain quality (bright stars with saturated photometry and blended stars). The lower right portion of Figure 2 displays the data for all clusters, except for UMa stars of poor quality, combined using running 20-point means as a function of $J–H$ color. The last step was made as a means of reducing the photometric scatter in both colors.

The intrinsic relation of Table 1 appears to be confirmed by stars in the open clusters of Figure 2, although there is clearly additional scatter in the observations of individual stars that cannot be attributed to differential reddening. In three of the

TABLE 1

EMPIRICAL JHK_S CALIBRATION FOR ZAMS STARS

J–H	H–K_s	M_J	J–H	H–K_s	M_J	J–H	H–K_s	M_J	J–H	H–K_s	M_J	J–H	H–K_s	M_J
−0.129	−0.107	−2.393	0.024	0.023	1.748	0.148	0.042	3.035	0.253	0.058	4.513	0.391	0.083	5.438
−0.125	−0.104	−2.021	0.028	0.026	1.779	0.151	0.042	3.088	0.256	0.058	4.546	0.396	0.084	5.455
−0.121	−0.100	−1.749	0.032	0.027	1.810	0.154	0.043	3.142	0.259	0.059	4.568	0.400	0.085	5.481
−0.117	−0.097	−1.506	0.036	0.027	1.841	0.157	0.043	3.196	0.262	0.059	4.591	0.405	0.085	5.507
−0.113	−0.094	−1.303	0.039	0.027	1.873	0.160	0.043	3.239	0.265	0.060	4.623	0.409	0.086	5.533
−0.109	−0.090	−1.130	0.043	0.028	1.904	0.162	0.044	3.293	0.268	0.061	4.646	0.414	0.087	5.559
−0.105	−0.087	−0.976	0.047	0.028	1.926	0.165	0.044	3.337	0.272	0.061	4.668	0.419	0.088	5.584
−0.101	−0.083	−0.832	0.051	0.029	1.957	0.168	0.045	3.390	0.275	0.062	4.690	0.424	0.089	5.609
−0.097	−0.080	−0.678	0.054	0.029	1.979	0.171	0.045	3.434	0.278	0.062	4.722	0.428	0.090	5.633
−0.093	−0.076	−0.533	0.058	0.030	2.001	0.173	0.045	3.478	0.282	0.063	4.744	0.433	0.091	5.658
−0.088	−0.072	−0.388	0.062	0.030	2.023	0.176	0.046	3.521	0.285	0.063	4.776	0.438	0.092	5.681
−0.084	−0.069	−0.233	0.065	0.031	2.045	0.179	0.046	3.565	0.288	0.064	4.808	0.443	0.093	5.705
−0.080	−0.065	−0.088	0.069	0.031	2.068	0.182	0.047	3.609	0.292	0.065	4.840	0.448	0.094	5.728
−0.119	−0.045	−2.279	0.021	0.024	1.732	0.188	0.052	2.982	0.365	0.069	4.468	0.536	0.107	5.370
−0.116	−0.042	−1.912	0.026	0.025	1.761	0.193	0.052	3.035	0.370	0.070	4.500	0.540	0.108	5.386
−0.112	−0.040	−1.644	0.030	0.026	1.790	0.198	0.053	3.089	0.375	0.070	4.523	0.544	0.110	5.411
−0.109	−0.037	−1.405	0.034	0.028	1.819	0.202	0.053	3.143	0.379	0.071	4.545	0.549	0.111	5.437
−0.106	−0.035	−1.206	0.038	0.029	1.848	0.207	0.054	3.186	0.384	0.072	4.578	0.553	0.113	5.462
−0.102	−0.032	−1.037	0.043	0.030	1.878	0.212	0.054	3.240	0.389	0.072	4.600	0.557	0.115	5.486
−0.099	−0.030	−0.887	0.047	0.031	1.898	0.217	0.055	3.284	0.394	0.073	4.622	0.562	0.117	5.511
−0.095	−0.027	−0.748	0.051	0.032	1.927	0.221	0.055	3.338	0.398	0.074	4.644	0.566	0.118	5.535
−0.092	−0.025	−0.597	0.056	0.033	1.948	0.226	0.055	3.382	0.403	0.074	4.676	0.570	0.120	5.558
−0.088	−0.023	−0.457	0.060	0.034	1.968	0.231	0.056	3.426	0.408	0.075	4.697	0.574	0.122	5.582
−0.085	−0.020	−0.316	0.064	0.034	1.988	0.236	0.056	3.470	0.412	0.076	4.729	0.579	0.124	5.605
−0.081	−0.018	−0.164	0.069	0.035	2.009	0.240	0.057	3.514	0.417	0.077	4.760	0.583	0.126	5.628
−0.077	−0.016	−0.023	0.073	0.036	2.030	0.245	0.057	3.558	0.422	0.078	4.792	0.587	0.128	5.650
−0.074	−0.014	0.109	0.078	0.037	2.061	0.250	0.058	3.602	0.427	0.078	4.823	0.591	0.130	5.673
−0.070	−0.012	0.231	0.082	0.038	2.072	0.255	0.058	3.646	0.431	0.079	4.854	0.595	0.132	5.694
−0.066	−0.010	0.344	0.087	0.039	2.093	0.260	0.058	3.690	0.436	0.080	4.884	0.599	0.135	5.716
−0.063	−0.008	0.447	0.091	0.039	2.114	0.264	0.059	3.724	0.441	0.081	4.915	0.603	0.137	5.737
−0.059	−0.006	0.550	0.096	0.040	2.146	0.269	0.059	3.768	0.445	0.082	4.945	0.608	0.139	5.758
−0.055	−0.004	0.654	0.100	0.041	2.178	0.274	0.060	3.802	0.450	0.083	4.976	0.612	0.141	5.779
−0.051	−0.002	0.757	0.105	0.042	2.200	0.279	0.060	3.846	0.454	0.084	5.006	0.616	0.144	5.799
−0.047	−0.001	0.852	0.109	0.042	2.232	0.283	0.061	3.880	0.459	0.085	5.026	0.620	0.146	5.819
−0.044	0.001	0.946	0.114	0.043	2.254	0.288	0.061	3.923	0.464	0.086	5.045	0.624	0.149	5.838
−0.040	0.003	1.041	0.118	0.044	2.286	0.293	0.061	3.957	0.468	0.087	5.065	0.628	0.151	5.857
−0.036	0.005	1.116	0.123	0.044	2.328	0.298	0.062	3.991	0.473	0.088	5.084	0.631	0.154	5.876
−0.032	0.006	1.201	0.127	0.045	2.361	0.303	0.062	4.035	0.477	0.089	5.103	0.635	0.156	5.895
−0.028	0.008	1.266	0.132	0.046	2.393	0.308	0.063	4.069	0.482	0.090	5.122	0.639	0.159	5.913
−0.024	0.009	1.342	0.137	0.046	2.426	0.312	0.063	4.102	0.487	0.091	5.140	0.643	0.162	5.930
−0.020	0.011	1.408	0.141	0.047	2.469	0.317	0.064	4.136	0.491	0.093	5.159	0.647	0.164	5.948
−0.016	0.012	1.465	0.146	0.047	2.502	0.322	0.064	4.169	0.496	0.094	5.177	0.651	0.167	5.965
−0.012	0.014	1.521	0.151	0.048	2.555	0.327	0.065	4.203	0.500	0.095	5.195	0.655	0.170	5.981
−0.008	0.015	1.558	0.155	0.048	2.598	0.332	0.065	4.236	0.505	0.096	5.213	0.658	0.173	5.997
−0.004	0.017	1.585	0.160	0.049	2.651	0.336	0.066	4.270	0.509	0.098	5.240	0.662	0.176	6.013
0.000	0.018	1.612	0.165	0.049	2.704	0.341	0.066	4.303	0.514	0.099	5.258	0.666	0.179	6.028
0.005	0.019	1.640	0.169	0.050	2.748	0.346	0.067	4.336	0.518	0.101	5.285	···	···	···
0.009	0.021	1.658	0.174	0.050	2.811	0.351	0.067	4.379	0.523	0.102	5.301	···	···	···
0.013	0.022	1.676	0.179	0.051	2.874	0.355	0.068	4.412	0.527	0.103	5.328	···	···	···
0.017	0.023	1.704	0.183	0.051	2.928	0.360	0.069	4.445	0.531	0.105	5.344	···	···	···

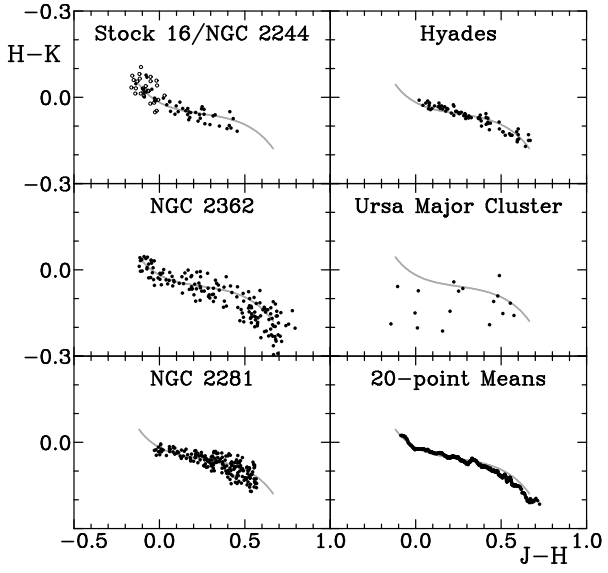

Fig. 2. Unreddened JHK_s colors (left) for stars in Stock 16 and NGC 2244 (top), NGC 2362 (middle), and NGC 2281 (bottom), and (right) for stars in the Hyades (top), and the Ursa Major cluster (middle) relative to the intrinsic relation for ZAMS stars (gray curves). The lower right diagram shows the data for stars in all clusters, except for saturated UMa stars, combined using running 20-point means.

four reddened clusters the *UBV* colors display *no* differential reddening, so it is unlikely to appear in the JHK_s colors unless there is some unforeseen component, such as circumstellar emission, affecting the observations. A pronounced "extra" scatter for B-type stars may have such an origin, given the evidence for circumstellar dust associated with some rapidly-rotating late B-type stars (Turner 1993), but it is unlikely that similar effects extend to the remaining cluster stars. It is more reasonable to attribute the scatter to intrinsic uncertainties in the precision of the JHK_s magnitude estimates, which appear to be larger than the cited values and also larger than what is attainable from iris photometry of photographic plates (Turner & Welch 1989). The tendency toward larger scatter for the coolest stars of NGC 2362 and NGC 2281 may be a problem with membership selection.

An earlier calibration similar to that of Table 1 was derived using stars in Stock 16, NGC 2362, and NGC 2251, with polynomial and linear fits made to combined running 20-point means for the data. Some of the features of the earlier calibration (see Turner et al. 2008, 2009) can be seen in the lower right portion of Figure 2, namely the pronounced "kink" near spectral type A0 in the mean data. But the data also match the new curved relationship very well.

For Hyades stars the JHK_s observations represent a combination of both 2MASS data and data from Carney (1982), as noted. The colors from both data sets display a scatter similar to that for Stock 16 and NGC 2244 members, but it is much reduced when the data are averaged together. There remains a sizeable residual scatter that is slightly larger than the cited uncertainties in the observations. Perhaps it represents an observational limitation for ground-based observations in the infrared imposed by variable atmospheric water vapour content (e.g., Milone & Young 2005, 2008). The scatter is greatly reduced in the 20-point running means, which is consistent with a problem that is tied to the precision of the observations. Otherwise, the intrinsic relation of Table 1 appears to be confirmed.

The colors for cluster stars in Figure 2 agree closely with the derived intrinsic relation, in most cases displaying only random scatter about it. If there were an extra reddening component of, say, 0.01 to 0.02 in *E(J–H)* for the stars, the centroids for the data would display a noticeable offset from the intrinsic relation. Thus, despite large scatter in the colors for stars in many open clusters, it is possible to derive an observational reddening for the stars from a color-color diagram by eye, with uncertainties of no more than ±0.01 to ±0.02 in *E(J–H)*, provided that the scatter in such cases is random in nature. Likewise, distance moduli derived from observational *J* versus *J–H* color-magnitude diagrams can be derived by eye with uncertainties typically no larger than ±0.1 to ±0.2. Such conclusions are confirmed by tests on the many open clusters studied to date (see, for example, Turner et al. 2008, 2009).

3. OTHER OPEN CLUSTERS

As noted above, the intrinsic relations of Table 1 have been tested successfully previously (Turner et al. 2008, 2009), but three clusters of uncertain properties were selected for further testing here: Berkeley 44, Turner 1, and Collinder 419. All three clusters possess limited published optical observations, and provide good examples of where 2MASS observations may help to clarify previous conclusions about cluster properties.

3.1. *Berkeley 44*

The sparse northern hemisphere cluster Berkeley 44 (Figure 3) has been identified as an old group by Carraro, Subramaniam, & Janes (2006), although

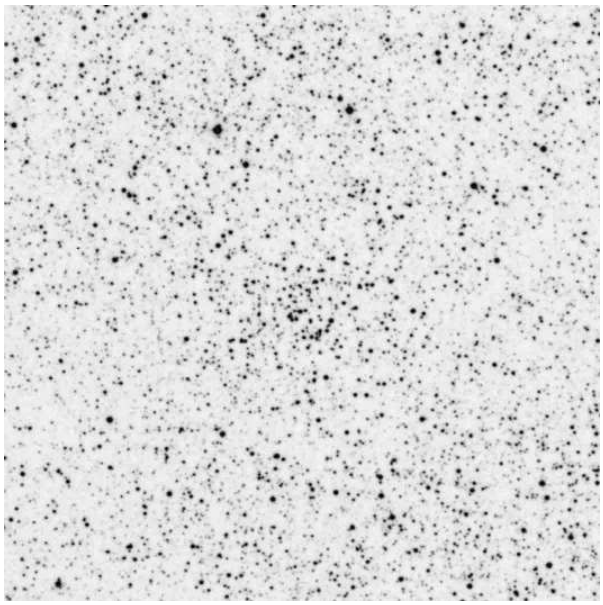

Fig. 3. The $15' \times 15'$ field of Berkeley 44 from the Palomar Observatory Sky Survey red image of the field. The image is centered on 2000 co-ordinates: 19:17:16, +19:33:00, the cluster center identified visually.

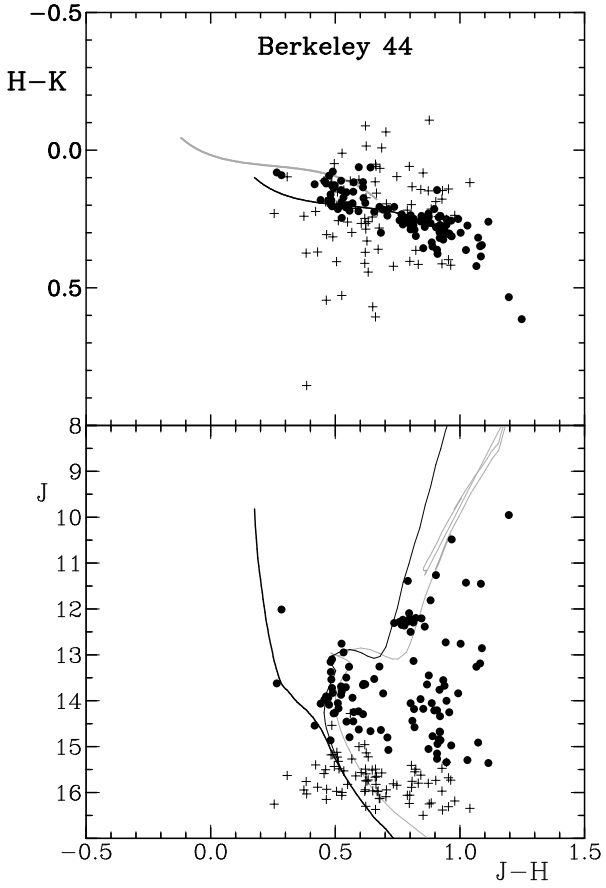

Fig. 4. JHK_s photometry for stars within $2'$ of the center of Berkeley 44 with magnitude uncertainties smaller than ± 0.05 (points) as well as with larger uncertainties (plus signs). The intrinsic color-color relation is depicted in gray (upper), while the intrinsic relations for $E(J–H) = 0.295$ ($E(B–V) = 1.00$) and $J–M_J = 12.1$ ($V_0–M_V = 11.38$) are shown as black lines. The thin black curve is an isochrone for $\log t = 9.3$ adapted from Meynet et al. (1993), the thin gray curve an isochrone of identical age from Bonatto et al. (2004).

with some question about its reality because of ambiguities in the star counts and the similarity of its color-magnitude diagram to that of stars in the surrounding reference field. The published co-ordinates for the cluster by Dias et al. (2002) and Carraro et al. (2006) do not match the optical density peak visible on the Palomar Observatory Sky Survey, and an alternate cluster center (Figure 3) was adopted here. The group lies more than 3° from the Galactic plane, so contamination by foreground early-type stars should be relatively low. However, the extreme faintness of cluster stars makes it necessary to consider both high quality and low quality 2MASS data for the field, with uncertainties of $\pm 0^{\rm m}.05$ representing the demarcation.

The 2MASS JHK_s data for Berkeley 44 (Figure 4) confirm that it is an old open cluster. The cluster color-color diagram is devoid of early-type stars lying within $2'$ of the adopted cluster center, most cluster members being cooler late-type stars. A few stars of inferred spectral types G and K appear to be essentially unreddened, with most stars of spectral types F or later reddened by similar amounts. The cluster color-magnitude diagram reveals a well-defined clump of red giants at $J \simeq 12.2$ with implied spectral types of early K, so the identification of this cluster as an old cluster is confirmed. The optimum fit by eye to the JHK_s observations yields a reddening of $E(J–H) = 0.295 \pm 0.02$ ($E(B–V) = 1.00 \pm 0.07$) and a distance modulus of $J–M_J = 12.1 \pm 0.1$ ($V_0 - M_V = 11.38 \pm 0.24$), corresponding to a distance of $d = 1.89 \pm 0.21$ kpc. The uncertainty in the intrinsic distance modulus includes the uncertainty in interstellar extinction towards the cluster. The ZAMS fit is tied to low quality JHK_s observations at the faint end, so may be less well-established than the formal uncertainty suggests, although the implied distance agrees closely with the value of 1.8 kpc derived by Carraro et al. (2006). The implied cluster reddening is significantly smaller than the value of $E(B–V) = 1.40 \pm 0.10$ obtained by Carraro et al. (2006), which in any case is

inconsistent with the 2MASS data unless one adopts an extreme fit to the very reddest stars.

Berkeley 44 main-sequence members have intrinsic *J–H* colors of ∼0.15 or redder, indicating stars of earliest spectral type ∼F0, corresponding to turnoffs for intermediate-age clusters of age $\sim 10^9$ yrs. A variety of model isochrones near $\log t \simeq 9$ were therefore tested in the cluster color-magnitude diagram (Figure 4), with the optimum fit produced by an isochrone of $\log t = 9.3$, as shown, corresponding to a cluster age of ∼2 Gyr. The procedure involved use of the M_V versus *B–V* isochrones published by Meynet, Mermilliod, & Maeder (1993), adapted to the M_J versus *J–H* system with our empirical link between the *UBV* and 2MASS systems. An isochrone of the same age from Bonatto, Bica, & Girardi (2004) is also plotted in Figure 4, but deviates systematically in *J–H* from the Meynet et al. (1993) isochrone, suggesting a possible problem in the conversion from $\log T_{\rm eff}$ to *J–H* with the Padova isochrones used by Bonatto et al. (2004). A problem arises with stars in the red giant clump, since they are not replicated well by either set of evolutionary models used for the isochrones. Yet their colors are consistent with the adopted cluster reddening. Berkeley 44 is indeed an old open cluster, but inferences about its parameters derived using the larger reddening estimated by Carraro et al. (2006) differ from those inferred from 2MASS observations.

3.2. *Turner 1*

The sparse cluster designated as Turner 1 (Figure 5) surrounding the long-period Cepheid S Vul was discovered during the preparation of finder charts for Galactic Cepheids (Turner 1985b), and was subsequently studied on the basis of photoelectric and photographic *UBV* photometry by Turner, Leonard, & Madore (1986).

UBV photometry for stars in Turner 1 yielded a cluster distance of 643 ± 25 pc and a reddening of $E(B–V) = 0.48 \pm 0.02$ for what appeared to be an old group of G-type dwarfs with a putative red giant branch, although there was also evidence for more heavily reddened B-type stars in the same field (Turner et al. 1986). The limited *UBV* data implied that Turner 1 lay foreground to the Cepheid S Vul, which is projected near its center, although no further tests were made, spectroscopic observations being restricted by the faintness of cluster stars. It was noted, however, that the putative reddened G-dwarf sequence identified from *UBV* colors might be contaminated by more heavily reddened B dwarfs.

2MASS JHK_s data provide new insights into the earlier results. It is possible to detect a sparse group of G dwarfs (with rather large photometric scatter) and a putative late-K giant branch in the data, with similar parameters to the *UBV* study (Figure 6). But many of the stars in the field, and most of the stars within 11′ of the adopted cluster center, appear instead to be reddened B-type and A-type stars (Figure 7). A best fit by eye to the JHK_s observations for the former yields a reddening of $E(J–H) = 0.15 \pm 0.02$ ($E(B–V) = 0.51 \pm 0.07$) and a distance modulus of $J\text{-}M_J = 9.7 \pm 0.1$ ($V_0–M_V = 9.34 \pm 0.24$), corresponding to a distance of $d = 0.74 \pm 0.08$ kpc, values that are reasonably consistent with those obtained for the cluster from *UBV* photometry. The model isochrone from Meynet et al. (1993) that best fits the observations has $\log t = 9.8$, implying a cluster age of ∼6 Gyr, although the red giants are displaced redward of that isochrone, much like in the case for Berkeley 44 red giant clump stars. Conceivably a refined empirical calibration of 2MASS intrinsic colors that includes a separate relation for red giant stars could eliminate the problem. There appear to be large numbers of M dwarfs lying along the line of sight to the cluster.

The implied best fit by eye to the JHK_s observations for the group of reddened B-type stars yields a reddening of $E(J\text{-}H) = 0.30 \pm 0.02$ ($E(B\text{-}$

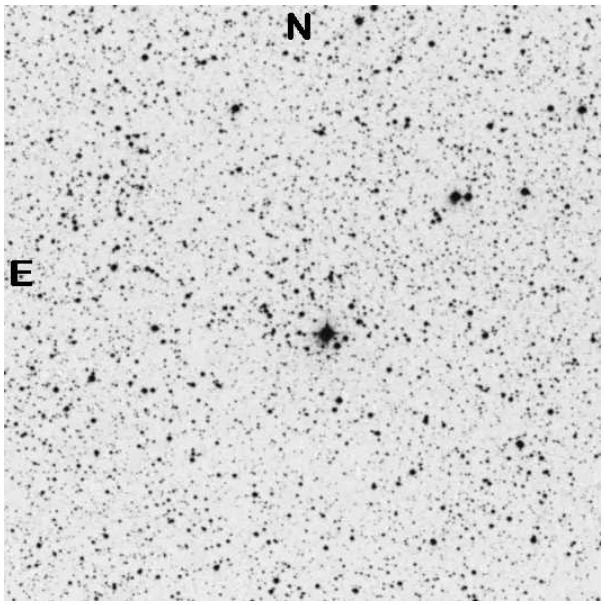

Fig. 5. The 15′ × 15′ field of Turner 1 from the Palomar Observatory Sky Survey red image of the field. The image is centered on 2000 co-ordinates: 19:48:26.5, +27:17:59, the cluster center identified from star counts (Turner 1985b). S Vul is the bright star near the center of the image.

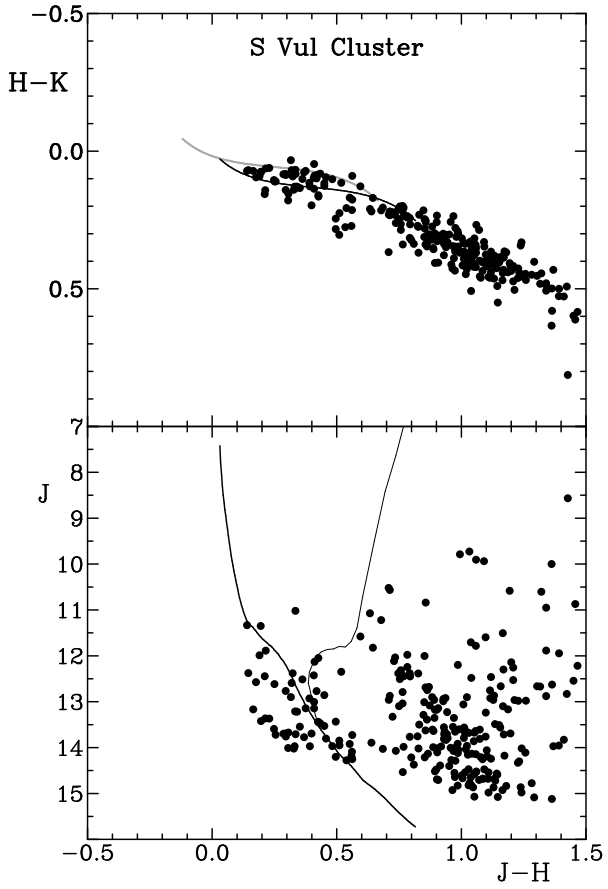

Fig. 6. JHK_s photometry for stars within $4'$ of the center of Turner 1 with magnitude uncertainties smaller than ±0.05. The intrinsic color-color relation is depicted in gray, while the intrinsic relations for $E(J–H) = 0.15$ ($E(B–V) = 0.51$) and $J–M_J = 9.7$ ($V_0–M_V = 9.34$) are shown as black lines. The thin black curve is an isochrone for $\log t = 9.8$ adapted from Meynet et al. (1993).

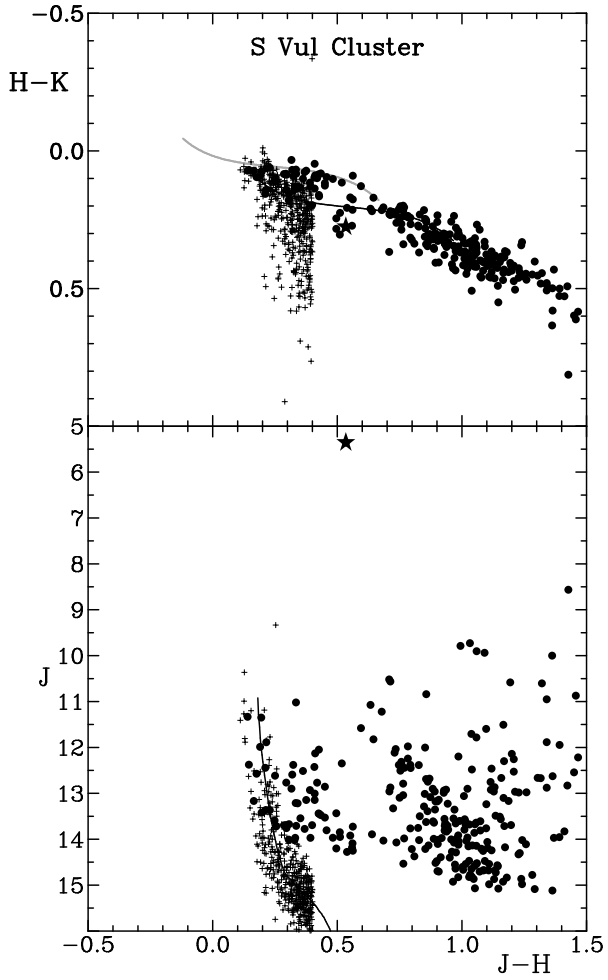

Fig. 7. The same as Figure 6 but for $E(J–H) = 0.29$ ($E(B–V) = 1.02$) and $J–M_J = 13.2$ ($V_0–M_V = 12.47$), shown as black lines. Small plus signs denote additional stars within $11'$ of the cluster center inferred to be B-type and A-type stars, with no restriction on photometric uncertainties. The star symbol corresponds to the Cepheid S Vul.

$V) = 1.02 \pm 0.07$) and a distance modulus of $J–M_J = 13.2 \pm 0.2$ ($V_0–M_V = 12.47 \pm 0.29$), corresponding to a distance of $d = 3.12 \pm 0.42$ kpc. Similar values were used by Turner (2010) with an earlier version of the 2MASS calibration to establish very reasonable estimates for the reddening and luminosity of the 68^d Cepheid S Vulpeculae as a possible cluster member.

S Vul is represented by the star symbol in Figure 7. In the present instance the results imply intrinsic parameters of $(\langle B\rangle - \langle V\rangle)_0 = 0.87 \pm 0.07$ and $\langle M_V\rangle = -6.86 \pm 0.29$ for the Cepheid, close to what would be predicted empirically (see Turner 2010). The angular brackets denote intensity means. Spectroscopic observations are essential for confirming the picture implied by the 2MASS observations, since star counts for stars identified photometrically as B dwarfs display only a marginal concentration towards the cluster core. It appears that the main concentration of stars in Turner 1 corresponds to the old, sparse, foreground cluster identified in Figure 6, with contamination by a young group of background B-dwarfs located along the same line of sight.

3.3. *Collinder 419*

Collinder 419 is a sparse group of stars (Figure 8) of small angular diameter ($40'.5$ according to Collinder 1931) associated with the massive O9 V((n)) double star HD 193322 (Walborn 1972). Collinder estimated a distance of 1470 pc for the

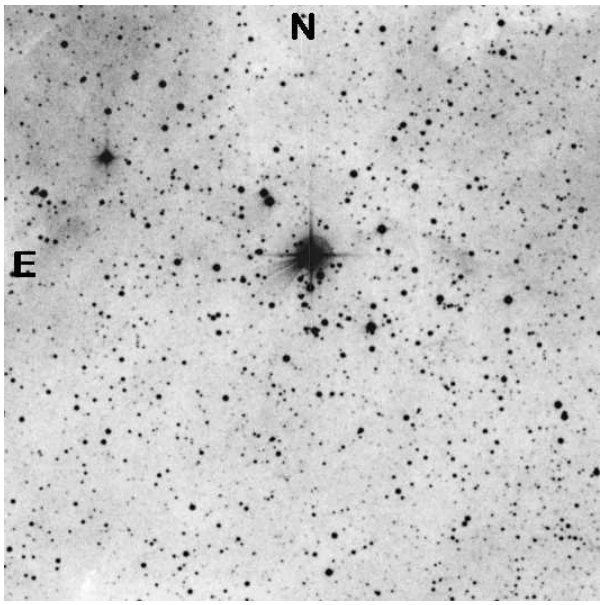

Fig. 8. The $15' \times 15'$ field of Collinder 419 from the Palomar Observatory Sky Survey red image of the field. The image is centered on 2000 co-ordinates: 20:18:08, +40:42:42, the adopted cluster center. HD 193322 is the bright star north of the center of the image.

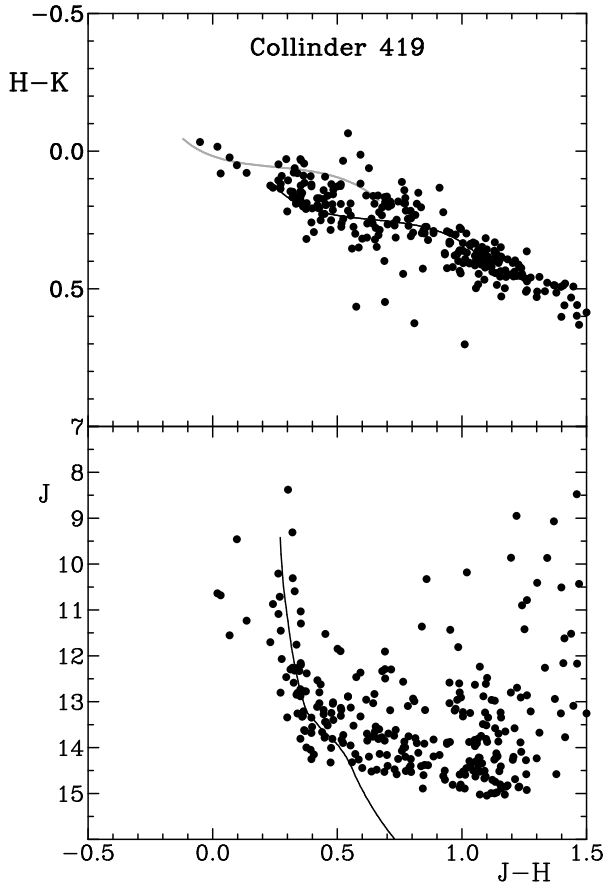

Fig. 9. JHK_s photometry for stars within $5'$ of the adopted center for Collinder 419 with uncertainties smaller than ±0.05. The intrinsic color-color relation is depicted in gray, while the intrinsic relations for *E(J–H)* = 0.39 (*E(B–V)* = 1.32) and *J–M*$_J$ = 11.7 (V_0–M_V = 10.75) are shown as black lines.

group from its angular diameter, while Gies et al. (2010) used astrometric and photometric data from the UCAC3 catalogue for bright stars in the field to derive a distance of $d = 741 \pm 36$ pc, with a reddening of $E(B–V) = 0.37 \pm 0.05$. Included as a possible member of the group was the M3 III star IRAS 20161+4035.

The cluster does not stand out well at optical wavelengths, but we were able to detect a slight density enhancement visually and estimate a crude center of symmetry at 2000 co-ordinates: 20:18:08, +40:42:42, close to the coordinates estimated by Collinder. The cluster also appears as a set of reddened B-type stars in available 2MASS JHK_s photometry for stars lying within $5'$ of that center of symmetry (Figure 9), reasonably consistent with Collinder's inferred dimensions. A best fit by eye to the JHK_s data yields a reddening of $E(J–H) = 0.39 \pm 0.02$ ($E(B–V) = 1.32 \pm 0.07$), significantly larger than the value estimated by Gies et al. (2010), a distance modulus of $J–M_J = 11.7 \pm 0.2$ ($V_0–M_V = 10.75 \pm 0.28$), and an inferred distance of $d = 1.42 \pm 0.18$ kpc, which is also larger than the Gies et al. (2010) value, although consistent with a location within the young complex of stars and H II regions (including Berkeley 87, Turner et al. 2010) associated with the Cygnus X region at ~ 1.2 kpc. In this case the 2MASS data provide a more solid basis for the reality of the group than the UCAC3 data, although they do not address the possible membership of HD 193322.

The cluster does not show up as a significant density enhacement from star counts, and it is conceivable that Collinder 419 represents merely a clump in one of the many OB associations seen along the direction of the Cygnus arm.

4. DISCUSSION

Table 2 summarizes the results of the present study of four open clusters using 2MASS observations. Most of the inferred parameters for the clusters differ from published results tied to optical photometry, although those for Turner 1b were considered as an alternate possibility in the study by

TABLE 2

DEDUCED PARAMETERS FOR CLUSTERS ANALYZED BY JHK_S PHOTOMETRY

Cluster	$E(J–H)$	$E(B–V)$	$J–M_J$	$V_0–M_V$	d (kpc)
Berkeley 44	0.295 ± 0.02	1.00 ± 0.07	12.1 ± 0.1	11.38 ± 0.24	1.89 ± 0.21
Turner 1a	0.15 ± 0.02	0.51 ± 0.07	9.7 ± 0.2	9.34 ± 0.29	0.74 ± 0.08
Turner 1b	0.29 ± 0.02	1.02 ± 0.07	13.2 ± 0.2	12.47 ± 0.29	3.12 ± 0.42
Collinder 419	0.39 ± 0.02	1.32 ± 0.07	11.7 ± 0.2	10.75 ± 0.28	1.42 ± 0.18

Turner et al. (1986). In each case the optical photometry was limited by the faintness of cluster members arising from large interstellar reddening, which is where JHK_s photometry has advantages over optical band photometry. The point to emphasize, however, is that JHK_s observations of cluster stars often provide relatively complete samples that can be used to infer reasonably accurate estimates for the all-important interstellar reddening toward the cluster, in most cases in more straightforward manner than what is often used for optical band $BVRI$ observations. Once the reddening is known, ZAMS fitting, or isochrone fitting in some cases, can then be used to derive the distance to the cluster. That is true despite the relatively low intrinsic precision of existing 2MASS data for most Galactic fields.

This publication makes use of data products from the Two Micron All Sky Survey, which is a joint project of the University of Massachusetts and the Infrared Processing and Analysis Center/California Institute of Technology, funded by the National Aeronautics and Space Administration and the National Science Foundation.

REFERENCES

Bonatto, C., Bica, E., & Girardi, L. 2004, A&A, 415, 571
Burki, G., & Maeder, A. 1973, A&A, 25, 71
Caldwell, J. A. R., Cousins, A. W. J., Ahlers, C. C., van Wamelen, P., & Maritz, E. J. 1993, South African Astron. Obs. Circ., 15, 1
Cannon, R. D. 1970, MNRAS, 150, 111
Carney, B. W. 1982, AJ, 87, 1527
Carraro, G., & Costa, E. 2009, A&A, 493, 71
Carraro, G., & Munari, U. 2004, MNRAS, 347, 625
Carraro, G., Subramaniam, A., & Janes, K. A. 2006, MNRAS, 371, 1301
Carraro, G., Vallenari, A., & Ortolani, S. 1995, A&A, 300, 128
Collinder, P. 1931, Ann. Obs. Lund, 2, 1
Cutri, R. M., et al. 2003, The IRSA 2MASS All-Sky Point Source Catalog of Point Sources, NASA/IPAC Infrared Science Archive
Dias, W. S., Alessi, B. S., Moitinho, A., & Lépine, J. R. D. 2002, A&A, 389, 871
Gies, D. R., et al. 2010, BAAS, 42, 566
Johnson, H. L. 1957, ApJ, 126, 121
_____. 1962, ApJ, 136, 1135
_____. 1966, ARA&A, 4, 193
_____. 1968, in Nebulae and Interstellar Matter, ed. B. L. Middlehurst & L. H. Aller (Chicago: Univ. Chicago Press), 167
Johnson, H. L., Hoag, A. A., Micthell, R. I., & Hallam, K. L. 1961, Lowell Obs. Bull., 5, 133
Johnson, H. L., & Morgan, W. W. 1953, ApJ, 117, 313
Koornneef, J. 1983, A&A, 128, 84
Maciejewski, G., Mihov, B., & Georgiev, Ts. 2009, Astron. Nachr., 330, 851
McCuskey, S. W. 1965, in Galactic Structure, ed. A. Blaauw & M. Schmidt (Chicago: Univ. Chicago Press), 1
_____. 1970, in IAU Symp. 38, The Spiral Structure of our Galaxy, ed. W. Becker & G. I. Kontopoulos (Dordrecht: Reidel), 189
Meynet, G., Mermilliod, J.-C., & Maeder, A. 1993, A&AS, 98, 477
Milone, E. F., & Young, A. T. 2005, PASP, 117, 485
_____. 2008, J. Am. Ass. Variable Star Obs., 36, 110
Moffat, A. F. J., & Vogt, N. 1977, PASP, 89, 323
Pesch, P. 1961, ApJ, 134, 602
Skrutskie, M. F., et al. 2006, AJ, 131, 1163
Turner, D. G. 1976a, ApJ, 210, 65
_____. 1976b, AJ, 81, 97
_____. 1979, PASP, 91, 642
_____. 1985a, ApJ, 292, 148
_____. 1985b, JRASC, 79, 175
_____. 1993, A&AS, 97, 755
_____. 1996, in ASP Conf. Ser. 90, The Origins, Evolution, and Destinies of Binary Stars in Clusters, ed. E. F. Milone & J.-C. Mermilliod (San Francisco: ASP), 443
_____. 2010, Ap&SS, 326, 219
Turner, D. G., Kovtyukh, V. V., Majaess, D. J., Lane, D. J., & Moncrieff, K. E., 2009, Astron. Nachr., 330, 807

Turner, D. G., Leonard, P. J. T., & Madore, B. F. 1986, JRASC, 80, 166
Turner, D. G., MacLellan, R. F., Henden, A. A., & Berdnikov, L. N., 2011, Acta Astron., submitted
Turner, D. G., Majaess, D. J., Lane, D. J., & Balam, D. D., 2010, BAAS, 42, 566
Turner, D. G., & Welch, G. A. 1989, PASP, 101, 1038
Turner, D. G., et al. 2008, MNRAS, 388, 444
Walborn, N. R. 1972, AJ, 77, 312

D. G. Turner: Department of Astronomy and Physics, Saint Mary's University, Halifax, Nova Scotia, B3H 3C3, Canada (turner@ap.smu.ca).

Revista Mexicana de Astronomía y Astrofísica, **47**, 139–158 (2011)

H II REGIONS AND PROTOSOLAR ABUNDANCES IN GALACTIC CHEMICAL EVOLUTION

L. Carigi and M. Peimbert

Instituto de Astronomía, Universidad Nacional Autónoma de México, Mexico

Received 2010 November 18; accepted 2011 February 3

RESUMEN

Presentamos modelos de evolución química del disco galáctico con diferentes rendimientos dependientes de Z. Encontramos que una tasa moderada de pérdida de masa en estrellas masivas de metalicidad solar produce un excelente ajuste con los gradientes de C/H y C/O del disco de la Galaxia. El mejor modelo reproduce: las abundancias de H, He, C y O derivadas de líneas de recombinación en M17, las abundancias protosolares y las relaciones C/O-O/H, C/Fe-Fe/H y O/Fe-Fe/H derivadas de estrellas de la vecindad solar. La concordancia del modelo con las abundancias protosolares implica que el Sol se originó a una distancia galactocéntrica similar a la actual. El modelo para $r = 3$ kpc implica que una fracción de las estrellas en la dirección del bulbo se formó en el disco interno. Nuestro modelo reproduce la relación C/O-O/H derivada de regiones H II extragalácticas en galaxias espirales.

ABSTRACT

We present chemical evolution models of the Galactic disk with different Z-dependent yields. We find that a moderate mass loss rate for massive stars of solar metallicity produces an excellent fit to the observed C/H and C/O gradients of the Galactic disk. The best model also fits: the H, He, C, and O abundances derived from recombination lines of M17, the protosolar abundances, and the C/O-O/H, C/Fe-Fe/H, and O/Fe-Fe/H relations derived from solar vicinity stars. The agreement of the model with the protosolar abundances implies that the Sun originated at a Galactocentric distance similar to the one it has now. Our model for $r = 3$ kpc implies that a fraction of the stars in the direction of the bulge formed in the inner disc. We obtain a good agreement between our model and the C/O versus O/H relationship derived from extragalactic H II regions in spiral galaxies.

Key Words: galaxies: abundances — galaxies: evolution — Galaxy: bulge — H II regions — ISM: abundances — Sun: abundances

1. INTRODUCTION

The comparison of detailed Galactic chemical evolution models, GCE models, with accurate abundance determinations of stars and gaseous nebulae provides a powerful tool to test the chemical evolution models and the accuracy of observational abundance determinations of stars of different ages and of H II regions located at different galactocentric distances.

In this paper we will compare our models with stellar and H II region abundances to test if the H II region abundances derived from recombination lines agree with the stellar abundances, in particular with the protosolar abundances that correspond to those present in the interstellar medium 4.5 Gyr ago. Also, our GCE models can be used to constrain the C yields for massive stars. The C yield is not well known and we will vary it to obtain the best fit between our GCE models and the observational data.

Carigi & Peimbert (2008, hereinafter Paper I) presented chemical evolution models of the Galactic disk for two sets of stellar yields that provided good fits to: (a) the O/H and C/H gradients (slope and absolute value) derived from H II regions based on recombination lines (Esteban et al. 2005) and includ-

ing the dust contribution (Esteban et al. 1998), and (b) the $\Delta Y/\Delta Z$ value derived from the Galactic H II region M17, and the primordial helium abundance, Y_p obtained from metal-poor extragalactic H II regions (Peimbert, Luridiana, & Peimbert 2007). In Paper I, based on our GCE models and combined with the constraints available, we were not able to discriminate between the stellar evolution models assuming high wind yields for massive stars, HWY, and those assuming low wind yields for massive stars, LWY.

Previous works has focused on the test of stellar yields using GCE models constrained by chemical gradients obtained by different methods, gradients that in general show similar slopes but a considerable spread in the absolute O/H ratios, e.g., Prantzos, Vangioni-Flam, & Chauveau (1994); Carigi (1996); Chiappini, Matteucci, & Meynet (2003a); Romano et al. (2010). To test the stellar yields it is necessary to have good absolute abundance values of stars and H II regions. To determine the O/H abundances of H II regions in irregular and spiral galaxies many methods have been used in the literature. Most of them have been based on fitting photoionized models to observations or on the determination of the electron temperature, T, from the 4363/5007 [O III] ratio directly from observations. A comparison of many of the different methods used has been made by Kewley & Ellison (2008). They find that the O/H differences derived by different methods between two given H II regions amount to 0.10–0.15 dex. On the other hand for all the methods the absolute difference for a given H II region is considerably larger, reaching values of 0.7 dex for extreme cases (see Figure 2 in their paper and the associated discussion). Most of the differences among the various calibrations are due to the temperature distribution inside the nebulae. In this paper we will use only abundances of H II regions based on recombination lines of H, He, C, and O. These lines depend weakly on the electron temperature; they are roughly proportional to $1/T$, therefore the relative abundances among these four elements are practically independent of the electron temperature.

There are two frequently used methods to derive C and O gaseous abundances from H II regions: (a) the most popular one, based on collisionally excited lines (or forbidden lines) and the $T(4363/5007)$ temperatures (the FL method) and (b) the one based on C and O recombination lines (the RL method). The RL method produces gaseous O and C abundances higher by about 0.15 to 0.35 dex than the FL method. The RL method is almost independent of the electron temperature, while the FL method is strongly dependent on the electron temperature. It is possible to increase the FL abundances under the assumption of temperature inhomogeneities to reach agreement with the RL values. The temperature distribution can be characterized by the average temperature, T_0, and the mean square temperature variation, t^2 (e.g., Peimbert 1967; Peimbert, Peimbert, & Luridiana 2002). The t^2 values needed to reach agreement between the RL and the FL abundances are in the 0.02 to 0.05 range, while the photoionization models predict typically t^2 values in the 0.003 to 0.01 range. This discrepancy needs to be sorted out (e.g., Peimbert & Peimbert 2011, and references therein).

Paper I is controversial because the C/H and O/H gaseous abundances of the H II regions have been derived from recombination lines (that is equivalent to the use of $t^2 \neq 0.000$ and forbidden C and O lines) and the assumption that 20% of the O atoms and 25% of the C atoms are trapped in dust grains (0.08 dex and 0.10 dex respectively). These assumptions increase the O/H ratio by about 0.25 to 0.45 dex relative to the gaseous abundances derived from $T(4363/5007)$, the forbidden O and C lines, and the assumption that $t^2 = 0.00$.

Due to the controversial nature of the H II region abundances used in Paper I and noting that we were not able to discriminate between the two sets of stellar yields adopted, we decided to test our GCE models further by including additional observational constrains: (a) the Asplund et al. (2009) protosolar abundances that provide us with the O/H, C/H, Fe/H, and $\Delta Y/\Delta O$ in the interstellar medium 4.5 Gyr ago; (b) the C/H, O/H, and Fe/H by Bensby & Feltzing (2006) for young F and G stars of the solar vicinity; (c) the O/H, C/H, and He/H derived from B stars by Przybilla, Nieva, & Butler (2008); and (d) throughout this paper for all the H II regions we will use abundances derived from recombination lines, and to obtain the total abundances we will increase the gaseous abundances by 0.10 dex in C and 0.12 dex in O to take into account the fraction of atoms trapped in dust grains, except for the metal-poor irregular galaxies for which we will use an 0.10 dex depletion for O (Esteban et al. 1998; Mesa-Delgado et al. 2009; Peimbert & Peimbert 2010).

We also decided to compare our best models with the C/O versus O/H results derived by Esteban et al. (2002, 2009) from bright H II regions in nearby spiral galaxies based on recombination lines, and to make a preliminary discussion of a comparison between our models for $r = 3$ kpc and the stars in the direction of

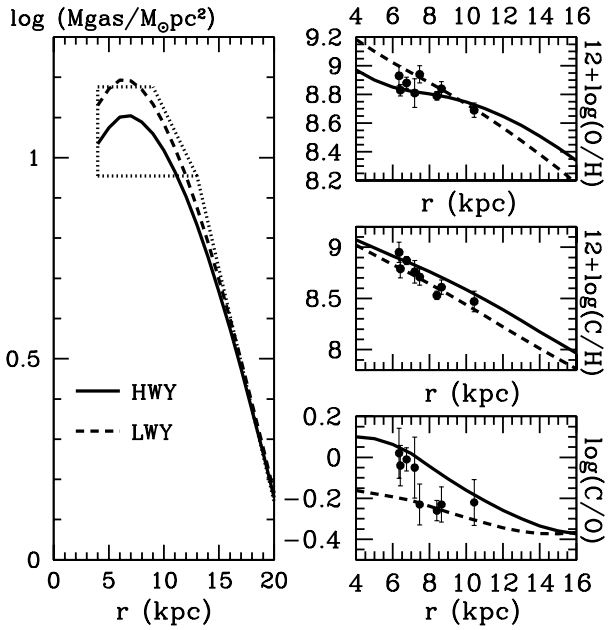

Fig. 1. Present-day radial distribution of: gas surface mass density (left panel), and ISM abundance ratios (right panels). Predictions of our chemical evolution models for the Galactic disk at the present time: HWY (continuous lines), LWY (dashed lines). Observational data: *area enclosed by dotted lines*: average gas surface density distribution by Kalberla & Kerp (2009), *filled circles*: H II regions, gas (García-Rojas & Esteban 2007) plus dust values (see text).

the Galactic bulge obtained by Bensby et al. (2010b) and Zoccali et al. (2008).

The symbols C, O, X, Y, and Z represent carbon, oxygen, hydrogen, helium, and heavy element abundances by unit mass respectively; while C/H, O/H, Fe/H, C/O, C/Fe, and O/Fe represent the abundance ratios by number.

In § 2 we discuss the general properties of the chemical evolution models. We consider infall models for the Galaxy with two sets of stellar yields, the HWY and the LWY. In § 3 we show the prediction of the current abundance gradients for the interstellar medium (ISM) of the Galactic disk and compare them with Galactic H II region abundances derived from recombination lines that include the dust correction. In addition we present for the solar vicinity the chemical history of the ISM and compare it with the chemical abundances of stars of different ages; we define the solar vicinity as a cylinder perpendicular to the Galactic plane, centered on the Sun, with a radius of 0.5 kpc, that extends into the halo to include the stars in the cylinder. In § 4 we compare our chemical evolution models with the protosolar chemical abundances and with those of the H II region M17. Based on the comparison between the observations and the models we present in § 5 a new Galactic chemical evolution model, with intermediate mass loss due to interstellar winds, IWY, that produces considerably better agreement with the observations. In § 6 we compare the IWY model with additional observations, those provided by extragalactic H II regions in spiral galaxies, and those provided by stars in the direction of the Galactic bulge. The conclusions are presented in § 7. A preliminary account of some of the results included in this paper was presented elsewhere (Peimbert et al. 2010).

2. CHEMICAL EVOLUTION MODELS WITH HIGH AND LOW WIND YIELDS

We present chemical evolution models for the Galactic disk. The models have been built to reproduce the present gas mass distribution, (see Figure 1, left panel) and the present-day O/H values for H II regions in the Galaxy for $6 < r(\mathrm{kpc}) < 11$, (see Figure 1, upper right panel) listed by García-Rojas & Esteban (2007). In what follows we describe in detail the characteristics of the models.

(i) In the models the halo and the disk are projected onto a single disk component of negligible width and with azimuthal symmetry; therefore all functions depend only on the galactocentric distance r and on the time t.

(ii) The models focus on $r \geq 4$ kpc; therefore, the physical processes associated with the Galactic bar are not considered.

(iii) The models are based on the standard chemical evolution equations originally written by Tinsley (1980) and widely used to date. See e.g., Pagel (2009), Matteucci (2001), and Prantzos (2008).

(iv) The age of the models is 13 Gyr, the time elapsed since the beginning of the formation of the Galaxy.

(v) The models are built based on an inside-out scenario with infalls that assume primordial abundances $Y_p = 0.2477$, $Z = 0.00$ (Peimbert et al. 2007). The adopted double infall rate is similar to that presented by Chiappini, Matteucci, & Gratton (1997), as a function of r and t, and is given by $\mathrm{IR}(r,t) = A(r)e^{-t/\tau_{\mathrm{halo}}} + B(r)e^{-(t-1\mathrm{Gyr})/\tau_{\mathrm{disk}}}$, where the halo formed in the first Gyr with a timescale $\tau_{\mathrm{halo}} = 0.5$ Gyr, and the disk started forming immediately after with longer timescales that depend on r, $\tau_{\mathrm{disk}} = (8 \times r/r_{\odot} - 2)$ Gyr. We adopt 8 kpc for the Galactocentric distance of the solar vicinity, $r_{\odot}$. The variables $A(r) = 10\ M_{\odot}\ \mathrm{pc}^{-2} \times e^{-[r(\mathrm{kpc})-r_{\odot}]/3.5\ \mathrm{kpc}}$

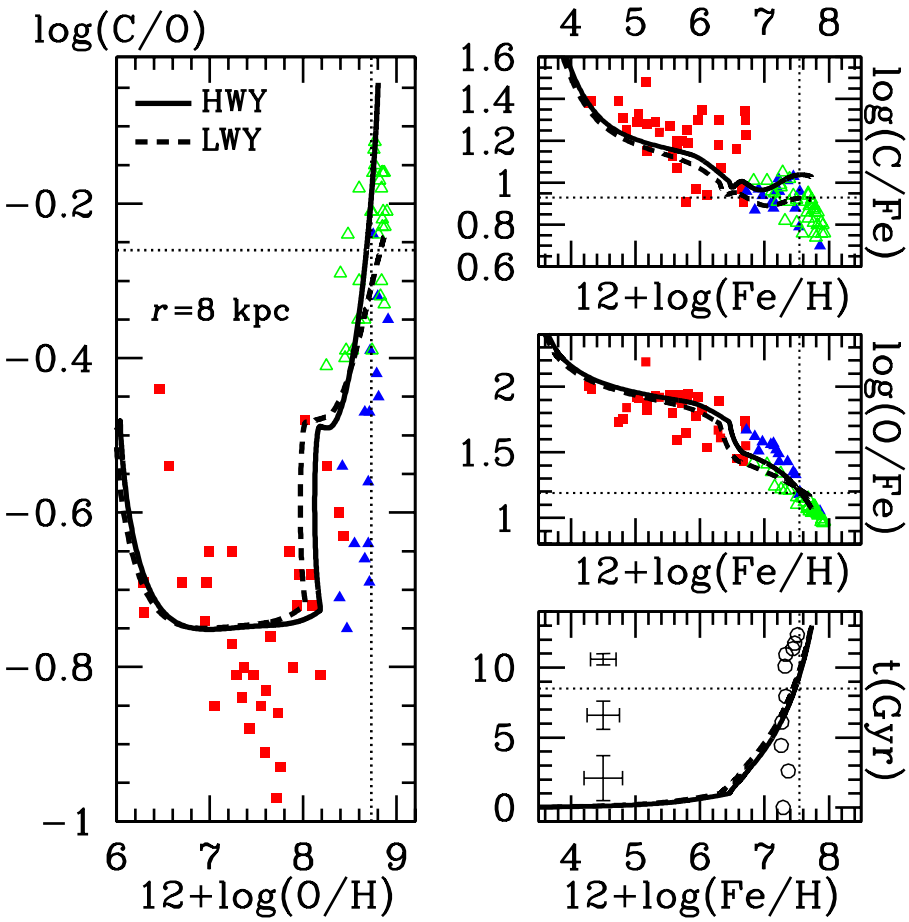

Fig. 2. Chemical evolution models for the solar vicinity (r = 8 kpc): HWY (continuous lines), LWY (dashed lines). The left panel shows the C/O evolution with O/H. The right panels show the evolution of C/Fe and O/Fe with Fe/H, and the Fe/H-time relation. Filled red squares: halo dwarf stars from Akerman et al. (2004). Filled blue and empty green triangles: thick-disk and thin-disk dwarf-stars from Bensby & Feltzing (2006). Dotted lines: protosolar values from Asplund et al. (2009). Open circles: mean ages and Fe/H values of disk stars with better determined ages from Nordström et al. (2004). Horizontal bars: internal dispersions in Fe/H shown by the sample. Vertical bars: age average errors. The color figure can be viewed online.

and $B(r) = 40\ M_\odot\ \mathrm{pc}^{-2} \times e^{-[r(\mathrm{kpc})-r_\odot]/3.5\ \mathrm{kpc}}$ are chosen to match the present-day mass density of the halo and disk components in the solar vicinity, which amount to 0.5 and 49.5 $M_\odot\ \mathrm{pc}^{-2}$, respectively, where the mass lost by the stars and the halo gas have been incorporated into the disk. Moreover, with the $A(r)$ and $B(r)$ variables the models reproduce the radial profile of the total mass in the Galaxy, $M_{\mathrm{tot}}(r) = 50\ M_\odot\ \mathrm{pc}^{-2} \times e^{-[r(\mathrm{kpc})-r_\odot]/3.5\ \mathrm{kpc}}$ (Fenner & Gibson 2003).

(vi) The models assume the initial mass function (IMF) proposed by Kroupa, Tout, & Gilmore (1993), in the mass range given by 0.08–80.0 $M_\odot$ for $Z > 10^{-5}$, and in the 9.0–80.0 $M_\odot$ mass range for $Z < 10^{-5}$. We consider that Population III does not include objects with less than 9.0 $M_\odot$ and that the change from Pop III to Pop II.5 occurs at $10^{-3.5} Z_\odot$ (Akerman et al. 2004; Bromm & Larson 2004).

(vii) The models include a star formation rate that depends on time and galactocentric distance, $\mathrm{SFR}(r,t) = \nu M_{\mathrm{gas}}^{1.4}(r,t)\ (M_{\mathrm{gas}}+M_{\mathrm{stars}})^{0.4}(r,t)$, taken from Matteucci et al. (1989) and Matteucci & Chiappini (1999), where ν is a constant in time and space. This SFR formula considers the feedback between gas and stars. In our models ν is chosen in order to reproduce the present-day radial distribution of gas surface mass density. We adopted ν values of 0.019 and 0.013 for the HWY and the LWY models, respectively. We assumed a ν value 5 times higher during the halo formation than that adopted for the

disk. These ν values combined with the adopted infall rate reproduce the chemical abundances shown by halo and disk stars (see Figure 2).

(viii) The only difference between the HWY and the LWY sets is the assumed mass-loss rate due to stellar winds by massive stars with $Z = 0.02$, see Figure 1 of Carigi & Peimbert (2008). All stellar yields are metal-dependent. We interpolate and extrapolate linearly the yields by mass and metallicity.

The HWY set includes:

(A) For massive stars (MS), those with $8 < m/M_{\odot} < 80$, the yields by: (a) Hirschi (2007) for $Z = 10^{-8}$ (with rotation velocity between 500 and 800 km s^{-1}, depending on stellar mass); (b) Meynet & Maeder (2002) for $Z = 10^{-5}$ and $Z = 0.004$ (with rotation velocity = 300 km s^{-1}); (c) Maeder (1992) for $Z = 0.02$ (high mass-loss rate with no rotation); (d) Since Fe is a chemical element used as observational constraint in most of the chemical evolution models and the Fe yield is not computed by Hirschi (2007), Meynet & Maeder (2002), and Maeder (1992), we adopt Woosley & Weaver (1995) values only for the Fe yields (Models B, for 12 to 30 $M_{\odot}$; Models C, for 35 to 40 $M_{\odot}$; while for $m > 40$ $M_{\odot}$, we extrapolate the $m = 40$ $M_{\odot}$ Fe yields, following Carigi & Hernández 2008). Our models, which include the Fe yields and the O yields by Meynet & Maeder (2002), can reproduce the O/Fe-Fe/H trend of the halo stars (see Figure 2).

(B) For low and intermediate mass stars (LIMS), those with $0.8 \leq m/M_{\odot} \leq 8$, we used the yields by Marigo, Bressan, & Chiosi (1996, 1998) and Portinari, Chiosi, & Bressan (1998) for the $Z = 0.004$ to $Z = 0.02$ range.

(C) For Type Ia SNe we have used the yields by Thielemann, Nomoto, & Hashimoto (1993) in the the SNIa formulation of Greggio & Renzini (1983). A fraction, Abin, of the binary stars of LIMS with a total mass between 3 and 16 $M_{\odot}$ are progenitors of SNIa. We assumed Abin = 0.066 for HWY model, while Abin = 0.094 for LWY models. These fractions are needed to reproduce the age-[Fe/H] relation of the disk stars, the O/Fe-Fe/H relation of the disk stars of the solar vicinity, and the protosolar Fe/H value for each model (see Figure 2).

In the LWY set we have updated the yields of massive stars only for $Z = 0.02$ assuming the yields by Hirschi, Meynet, & Maeder (2005) with rotation velocity = 300 km s^{-1}. The rest of the stellar yields are those included in the high wind set.

(ix) For MS the models include the stellar lifetimes given by Hirschi (2007), Meynet & Maeder (2002), and Hirschi et al. (2005), while for LIMS include the main sequence lifetimes from Schaller et al. (1992).

(x) Due to its deep potential well the models do not consider any type of outflows from the Galaxy. In addition, we disregard outflows of C and O rich material from SNe, because of the small C/O ratios observed in H II regions. See Carigi et al. (1995) and Carigi, Colín, & Peimbert (1999).

(xi) We do not include radial flows of gas or stars.

Since the solar vicinity and the Galactic disk contain stars and H II regions of a broad range of metallicities, our galaxy is a proper laboratory to study the $\Delta Y/\Delta O$ and $\Delta C/\Delta O$ behavior at high Z values and to test observationally the predictions of the HWY and the LWY models. Furthermore, the main elements affected by the winds of massive stars are He, C, and O; therefore, a careful comparison of the abundances predicted by the chemical evolution models with the observed values will allow us to constrain the mass loss rate and consequently the yields of massive stars.

3. THE GALACTIC H II REGION GRADIENTS AND THE CHEMICAL HISTORY OF THE SOLAR VICINITY

In Figure 1 we show the present-day radial distribution of the gaseous mass and the O/H, C/H, and C/O gradients in the Galactic disk predicted by the HWY and LWY models.

For Figure 1 we have chosen observational constraints that represent the current gas mass and the abundances of the Galactic disk. We have taken the average surface density as a function of the Galactic radius derived from H I shown by Kalberla & Kerp (2009) in their Figure 5. We have assumed the abundance ratios of the gas component determined from H II regions based on recombination lines by García-Rojas & Esteban (2007) corrected for dust depletion. It should be noted that the H II regions used by García-Rojas & Esteban (2007) are high density young objects that do not contain WR stars; consequently they have not been polluted by the evolution of their ionizing stars and their O/H and C/H values are representative of the present value of the Galactic interstellar medium.

Based on Figure 1, it can be noted that both models successfully reproduce the current radial distribution of gas surface mass density and the C/H and O/H gradients at the one σ level but neither of them reproduce the C/O gradient for all Galactocentric distances. The HWY model fits the C/O values of H II regions for $r < 7.3$ kpc, while the LWY model does so for $7.5 < r(\mathrm{kpc}) < 9$.

In the literature there are chemical abundance determinations from recombination lines of Galactic H II regions only for $6 < r(\mathrm{kpc}) < 11$. At present, the evidence for the flattening of the Galactic gradients is not conclusive: Vílchez & Esteban (1996) based on H II regions found a flat O/H gradient for $r > 14$ kpc, while more recent work based on Cepheids did not confirm this result, see Mattsson (2010). Additional observations of high quality obtained with the same method are needed to establish the behavior of the gradients for $r > 11$ kpc. With an inside-out scenario without dynamical effects it is difficult to reproduce a possible flattening of the O/H gradient, see Mattsson (2010). Cescutti et al. (2007) in an inside-out scenario reproduce the flattening of radial gradients shown by Cepheids for $r > 7$ kpc assuming a constant surface density for the halo. In our models this is equivalent to adopting a constant $A(r)$, which means that the volumetric density of the halo increases towards the outer parts of the Galaxy, a density distribution that we consider unlikely. According to Roskar et al. (2008) and Sánchez-Blázquez et al. (2009), the flattening is a consequence of stellar migration and of a break in the star formation rate at large radii. A third possibility is that the formation of the Galaxy had a modest stellar formation episode previous to the inside-out scenario. Support for this idea comes from the increase of the average age of the stars at large galactocentric distances (Vlajić, Bland-Hawthorn, & Freeman 2011, and references therein).

In Figure 2 we show the evolution of C/O-O/H, C/Fe-Fe/H, O/Fe-Fe/H, and time-Fe/H relations, predicted by the HWY and LWY models for $r = 8$ kpc. The time vs Fe/H plot is a representation equivalent to the known age-Z relation of the solar vicinity.

For Figure 2 we have chosen observational constraints that represent the chemical history of the solar vicinity. We have taken dwarf stars of the Galactic halo by Akerman et al. (2004), as representative of the first Gyr of the evolution, and dwarf stars of the Galactic thick and thin disk by Bensby & Feltzing (2006), as representative of the last 12 Gyr of the evolution. Also in Figure 2 we show the mean ages and Fe/H values of disk stars with better determined ages presented by Nordström et al. (2004) in the lower part of their Figure 28. Moreover, we have assumed the protosolar abundances by Asplund et al. (2009) as representative of $t = 8.5$ Gyr.

We converted the chemical abundances determined by Bensby & Feltzing (2006) to abundance ratios by number assuming their own solar abundances, see their paper for references. Also, we normalized the stellar ages by Nordström et al. (2004) to the age of the model (13.0 Gyr).

Based on Figure 2, it can be noted that both models produce a reasonable fit to the C/O-O/H, C/Fe-Fe/H, and O/Fe-Fe/H trends in the solar vicinity. From the C/O-O/H and C/Fe-Fe/H relations it can be seen that the HWY model predicts more C than observed in metal rich disk stars, while the LWY model predicts less than the HWY. Alternatively, both models predict a C/Fe plateau for Fe/H higher than solar, while metal rich stars of the thin disk show a C/Fe decrease. This observed trend could be explained if massive stars of $Z > Z_{\odot}$ are less efficient in producing C than massive stars of solar metallicity. Stellar yields of MS and LIMS for $Z > Z_{\odot}$ are needed to obtain a complete picture of the evolution at high Z (Carigi 2008).

Cescutti et al. (2009) and Romano et al. (2010) focused on the C/O-O/H relation shown by thin disk stars of the solar vicinity and found that the C/O rise at high O/H values can be explained partially with metallicity-dependent stellar winds in massive stars (Maeder 1992; Meynet & Maeder 2002). This result is in agreement with our previous conclusions (Carigi 1994, 1996, 2000; Carigi et al. 2005, and Paper I), and with those by Prantzos et al. (1994).

The fit of our models to the time-Fe/H relation shown by disk stars of the solar vicinity is reasonable for $4 < t(\mathrm{Gyr}) < 13$, but our models cannot reproduce the mean behavior of older stars of the Galactic disk. Probably the reason is that some of these stars originated closer to the center of the Galaxy and migrated outwards, or belonged to satellite galaxies with different chemical histories that were captured by our galaxy. Most of the stars of the sample have ages lower than 9 Gyr, corresponding to $t > 4$ Gyr, and the internal dispersion in Fe/H of old disk stars is higher than that of young stars. Both models fit the Fe/H values of the halo stars with ages between 12 and 13 Gyr in the $t < 1$ Gyr range.

The main difference between the HWY and the LWY sets is due to the stellar yields assumed for massive stars at $Z = 0.02$. The HWY assume a relatively high mass-loss rate for massive stars with $Z = 0.02$ (yields by Maeder 1992), while the LWY assume a relatively low mass-loss rate for massive stars with the same Z (yields by Hirschi et al. 2005). Since the mass loss rate is proportional to the stellar metallicity, the efficiency of this rate increases with metallicity and becomes important at $Z \sim Z_{\odot}$. According to Hirschi et al. (2005) mass loss rates are a key ingredient for the yields of massive stars and the

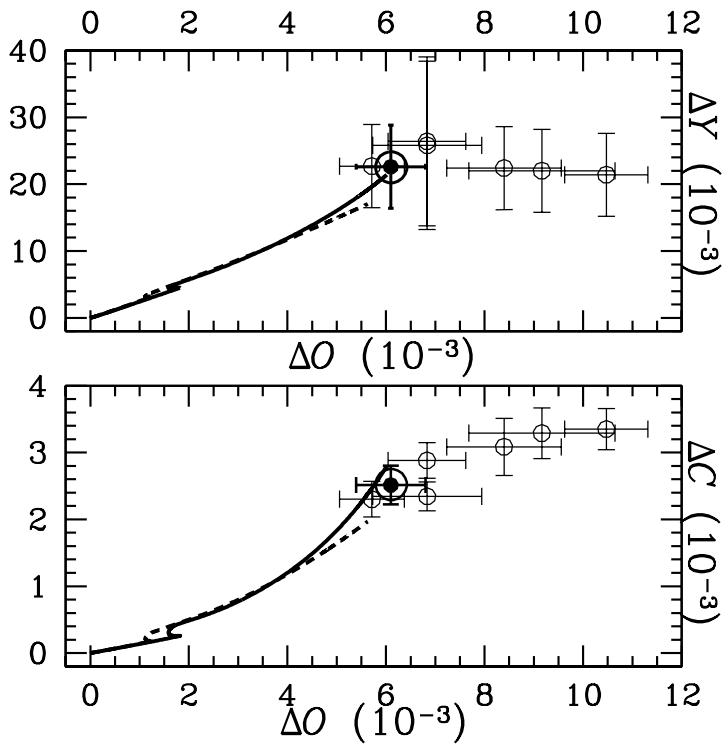

Fig. 3. ΔY vs ΔO (upper panel) and ΔC vs ΔO (lower panel) for the solar vicinity ($r = 8$ kpc). Evolution from $t = 0$ ($\Delta Y = \Delta C = \Delta O = 0$) to 8.5 Gyr (Sun-formation time) predicted by models that assume HWY (continuous lines), and LWY (dashed lines). $\odot$: Protosolar values by Asplund et al. (2009). Open circles: Protosolar values from photospheric data by different authors compiled by Asplund et al. (2009, Table 4) and corrected for gravitational settling (Asplund et al. 2009).

rates assumed by them are 2–3 smaller than those of Maeder (1992). This difference between a high and a low mass-loss rate produces opposite differences in the C and O yields. These differences occur in the pre-SN and in the SN phases. In the pre-SN phase massive stars are able to process He into C, and their stellar winds take away a lot of new C. Since the O production occurs deeper than the C production, the wind contribution to the O yield is much smaller than that to the C yield; consequently C constitutes the largest fraction of heavy elements ejected during the wind phases. While in the SN phase the contribution to the C and O total yields depends mainly on the mass of the CO core, a small fraction of C in the CO core remains unmodified and is ejected during the explosion. Alternatively the O production by the SNe is proportional to an important fraction of the mass of this core; consequently, O constitutes the largest fraction of heavy elements ejected during the SN stage. Therefore, when the initial stellar metallicity is higher, the mass loss rate is higher, the C yield is higher, the CO core is less massive, and consequently the O yield is smaller.

4. THE PROTOSOLAR AND THE PRESENT SOLAR VICINITY ABUNDANCES

To compare GCE models of Y, C, and O with observations we need to use the best abundance determinations available for these elements. We consider that the two most accurate Galactic Y, C, and O determinations are the protosolar values (Asplund et al. 2009) and the M17 H II region values (Paper I).

4.1. *Protosolar abundances*

In order to study the time-agreement with the protosolar values, we show in Figure 3 the predicted evolution of ΔY vs ΔO and ΔC vs ΔO from 0 to 8.5 Gyr (the Sun-formation time). The ΔY value for Figure 3 (and throughout this paper) is given by $\Delta Y = Y - Y_p$, where Y_p is the primordial He abundance, which amounts to 0.2477 (Peimbert et al. 2007). In this figure $\Delta O = O$, and $\Delta C = C$ because at the time of the primordial nucleosynthesis O and C are not produced. For $t = 0$ the models start at ΔY, ΔO, and ΔC equal to zero, and in this figure the evolution of the models stops at $t = 8.5$ Gyr, the time the Sun was formed. Also,

in this figure we present some of the most popular Y, C, and O protosolar abundances published in the last 21 years. These photospheric solar abundances were obtained by Anders & Grevesse (1989), Grevesse & Noels (1993), Grevesse & Sauval (1998), Lodders (2003), Asplund, Grevesse, & Sauval (2005), and Lodders, Palme, & Gail (2009); these abundances were compiled by Asplund et al. (2009) in their Table 4. To obtain the protosolar abundances of the heavy elements, the photospheric abundances were increased by 0.04 dex, which takes into account the effect of gravitational settling. We used the protosolar X values shown in Table 4 by Asplund et al. (2009) to change the abundances by number to abundances by mass.

From Figure 3 it can be noted that: (a) the HWY model fits very well the Y and O protosolar values, while the predicted C is about 1σ higher than observed. (b) The LWY model matches the Y and O protosolar values within 1σ, but the predicted C is about 2σ lower than observed. (c) The solar abundances predicted by our models are in much better agreement with the recent He, C, and O protosolar values determined by Asplund et al. (2009) than with the previous ones compiled by them. (d) The He protosolar abundance determinations have remained almost constant over the years, while the C and O ones have decreased.

4.2. ΔY *vs* ΔO *evolution compared with M17 and young B stars of the solar vicinity*

In Figure 4 we present the evolution of ΔY versus ΔO. The models presented in this figure for r equal to 6.75, 8, and 17 kpc correspond to the 0 to 13 Gyr range. The data should be compared with the end point of the evolution of the corresponding evolutionary track. In Figures 4, 5 and 7 the evolutionary tracks and the related observational data have the same color.

Since there are no good abundance determinations for the outer parts of the Galactic disk, we test our models with data of irregular galaxies. Therefore, in Figure 4 we show the ΔY and ΔO values of the metal poor extragalactic H II regions determined by Peimbert et al. (2007). Specifically, we compare our 17 kpc track with NGC 2366, because it contains one of the brightest H II regions of nearby galaxies. The gaseous O abundances of the metal poor H II regions were increased by 0.10 dex to include the fraction of O atoms embedded in dust grains inside the H II regions (Peimbert & Peimbert 2010). From that figure it can be noticed that the predicted chemical evolution of the Galaxy for large Galactocentric radii ($r > 17$ kpc) at $t = 13$ Gyr behaves like that of irregular galaxies at the present time.

In Figure 4 we also present the abundances of B stars of the solar vicinity derived by Przybilla et al. (2008). We have adopted the Orion X value shown in Carigi, Colín, & Peimbert (2006) for converting Xi/H (the abundance ratio by number of any i element) of B stars to Xi by mass. The ΔY abundance derived from B stars is in good agreement with the HWY and LWY models for $r = 8$ kpc. On the other hand, the ΔO value is about 1.5σ and about 4.5σ smaller than the values predicted by the HWY and LWY models, respectively. The O/H values derived by Simón-Díaz (2010) for the B stars of the Orion star forming region are in good agreement with the Przybilla et al. (2008) determinations.

We decided to include as observational constraints the O and He abundances of the H II region M17. This object has the best He abundance determination available because its degree of ionization is very high and the correction for neutral helium, which is always indirect, is the smallest one of the well observed Galactic H II regions (see Paper I). We show in Figure 4 two sets of ΔO values, one derived from O recombination lines, and the other derived from the O forbidden lines under the assumption that $t^2 = 0.00$.

The point with the highest ΔY and ΔO values of the HWY model at 6.75 kpc presented in Figure 4 (the point at $t = 13$ Gyr) should be compared with the two M17 values. The ΔY model value is in good agreement with the two M17 values. The ΔO value for $t^2 = 0.00$ is more than 5σ smaller than the model prediction, while the $t^2 \neq 0.00$ point is less than 2σ higher than the ΔO model prediction. For the LWY model the predicted ΔY value is in good agreement with the two M17 values; but the ΔO value of the $t^2 = 0.00$ point is 12σ smaller than the model prediction, while the ΔO value of the $t^2 \neq 0.00$ point is less than 2σ smaller than the model prediction. Based on this comparison we conclude that it is possible to get an excellent agreement with the $t^2 \neq 0.00$ ΔO value using a model with yields intermediate between the HWY and the LWY models, but that it is not possible to find a reasonable model to fit the ΔO value derived assuming $t^2 = 0.00$.

Since the HWY and the LWY models fit the protosolar values and produce a reasonable fit to the observed M17 ΔO and ΔY values, we conclude that the protosolar values in the context of Galactic chemical evolution provide a strong consistency check to the O recombination abundances derived from H II regions, and are in disagreement with the O abun-

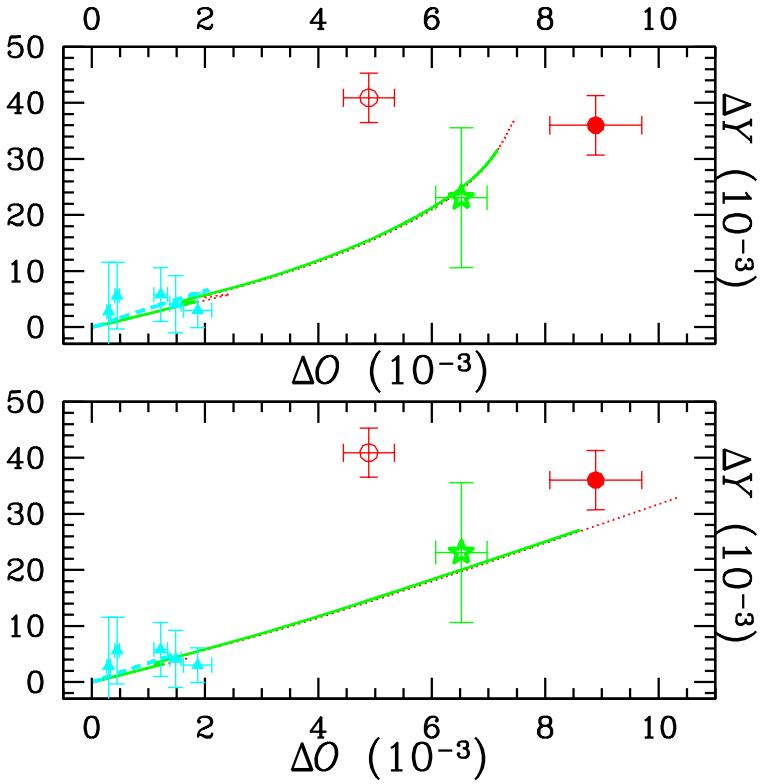

Fig. 4. Evolution of ΔY vs ΔO. The HWY model is shown in the upper panel and the LWY model in the lower panel. Chemical evolution tracks from 0 ($\Delta Y = \Delta O = 0$) to 13 Gyr (present time) for $r = 6.75$, 8, and 17 kpc (dotted-red, solid-green, and dashed-cyan lines, respectively). The three tracks in each panel partially overlap, from top to back they lie as follows: 17 kpc, 8 kpc, and 6.75 kpc. The values for the H II regions and the B stars correspond to 13 Gyr. The M17 H II region at $r = 6.75$ kpc is represented by a filled circle for $t^2 = 0.036$ (RL) and by an open circle for $t^2 = 0.00$ (FL). The solar vicinity B stars value by Przybilla et al. (2008) is represented by a star. The extragalactic low metallicity H II regions are represented by filled triangles for $t^2 \neq 0.00$ (FL) (Peimbert et al. 2007). A $Y_p = 0.2477$ is adopted (Peimbert et al. 2007). The color figure can be viewed online.

dances derived from forbidden lines under the assumption that $t^2 = 0.00$. Additional support for this result is provided by Simón-Díaz & Stasińska (2011) who, based on a study of 13 B-type stars of the Orion star forming region OB1, find that the stellar O/H abundances agree much better with the Orion H II region abundance derived from recombination lines than with that derived from collisionally excited lines.

4.3. *ΔC vs ΔO evolution compared with H II regions, and young B, F, and G stars of the solar vicinity*

In what follows we will discuss the ΔC and ΔO observational values adopted from the literature and we will compare them with the HWY and LWY model predictions. In Figure 5 we show the 0–13 Gyr evolution of the ΔC-ΔO relation for $r = 7$, 8, and 17 kpc.

The O/H ratio of the LWY model for $r = 17$ kpc and $t = 13$ Gyr corresponds to the O/H value of NGC 2363, the extragalactic metal-poor H II region best suited for our purpose. This model is in good agreement with the C/O observed ratio. Similarly the O/H ratio of the HWY model for $r = 17$ kpc and $t = 13$ Gyr corresponds to the O/H value of NGC 2363. This model is also in good agreement with the C/O observed ratio. The ΔO gas and dust values for NGC 2363 are those presented in Figure 4, while the ΔC value includes gas (Esteban et al. 2009) and dust components. We have considered the Y and O/Z values from Peimbert et al. (2007) to calculate X for NGC 2363 and to change the abundances by number to abundances by mass.

For $r \sim 8$ kpc and $t = 13$ Gyr there are several reliable C and O abundance determinations for the solar vicinity. To compare our models with observations we chose: (a) the average C/H and O/H values

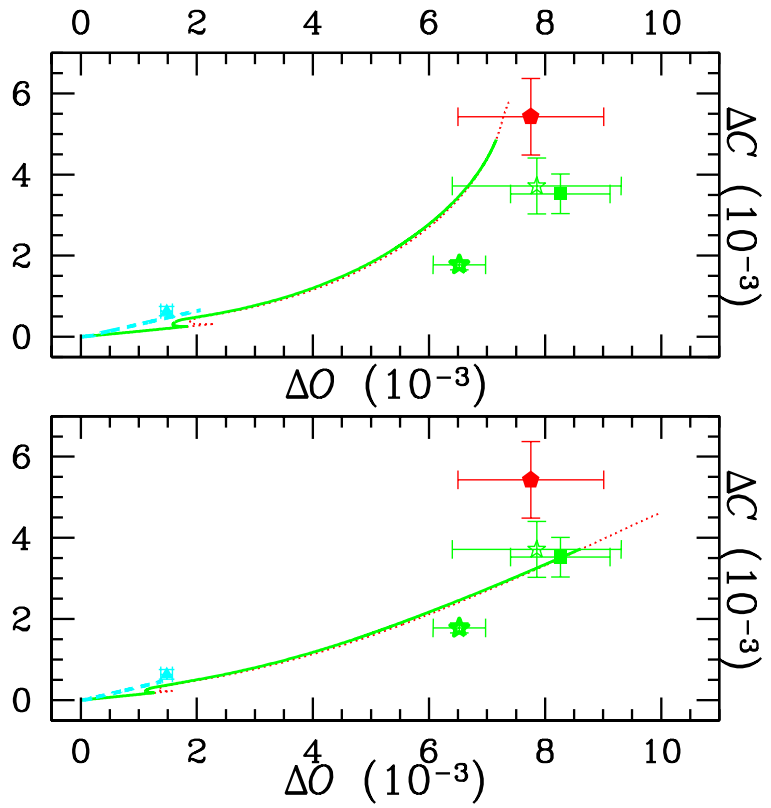

Fig. 5. ΔC vs ΔO diagram. The dotted red line represents the chemical evolution track from 0 ($\Delta C = \Delta O = 0$) to 13 Gyr (present time) for $r = 7$ kpc, the other lines as in Figure 4. A description of the symbols follows. Filled pentagon: Average values of the M17 and M20 H II regions at $r = 6.75$ and 7.19 kpc, respectively. Empty star: Average values of young F-G dwarf stars of the solar vicinity, $r \sim 8$ kpc, from Bensby & Feltzing (2006) (see text). Filled square: Average values of NGC 3576 and Orion H II regions at $r = 7.46$ and 8.40 kpc. Filled star: Average value of B stars by Przybilla et al. (2008). Filled triangle: NGC 2363 H II region in a very metal-poor irregular galaxy (see text). The color figure can be viewed online.

of NGC 3576 and Orion H II regions at $r = 7.46$ and 8.40 kpc, and the correction for the fractions of C and O embedded in dust grains; (b) the young F and G dwarf stars studied by Bensby & Feltzing (2006); (c) the average C and O values of B stars by Przybilla et al. (2008).

In Figure 5 we compare our models with the average ΔC and ΔO values of NGC 3576 and Orion, and find a reasonable agreement. To convert the Xi/H values by number to Xi by mass we adopted the X(Orion) value shown by Carigi et al. (2006).

Bensby & Feltzing (2006) studied 51 F and G dwarf stars of the solar vicinity, 35 belonging to the thin disk and 16 to the thick disk. To compare the abundances predicted by our models with those of the youngest stars presumably recently formed, it is necessary to select the youngest subset of the thin disk stars. The metal richest stars are expected to be the youngest ones. We made three subsets of the metal richest stars of the thin disk containing 4, 8, and 16 objects respectively, and obtained 12+log(O/H) average values of 8.87, 8.84, and 8.83 respectively, and 12+log(C/H) average values of 8.63, 8.64, and 8.59 respectively. In Figure 5 we present the subset of 8 stars as representative of the present day ISM, where we have adopted the X(Orion) by mass (Carigi et al. 2006) for converting Xi/H to Xi by mass. The agreement is very good. As we saw above, the other two subsets of F and G stars produce similar C/H and O/H values, also in good agreement with our models.

To convert the C and O abundances by number to abundances by mass of the B stars by Przybilla et al. (2008) we have taken the Orion X value shown in Carigi et al. (2006). From Figure 5 it can be seen that the ΔC value derived for the B stars is many sigma smaller than that predicted by the HWY and the LWY models. Moreover, it is also considerably

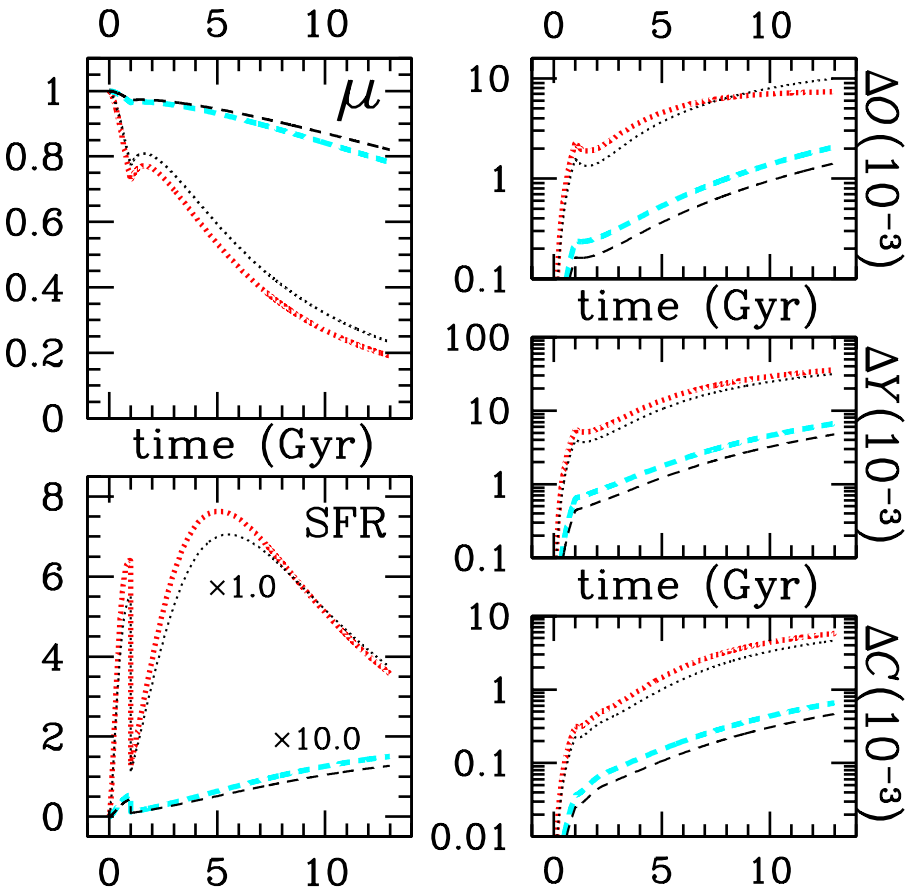

Fig. 6. Evolution of $M_{\rm gas}/M_{\rm tot} = \mu$, star formation rate, ΔO, ΔY, and ΔC for $r = 7$ kpc (dotted lines) and $r = 17$ kpc (dashed lines), assuming HWY (thick tracks) or LWY (thin tracks). Star formation history is in $M_\odot$ pc^{-2} Gyr^{-1} units and the SFR for $r = 17$ kpc has been multiplied by 10.

smaller then the values derived from the F-G dwarf stars and the average of NGC 3576 and the Orion nebula. Maybe part of the reason for the smaller C abundance in the B stars can be due to rotational mixing (e.g., Meynet & Maeder 2000; Fierro & Georgiev 2008). The B stars ΔO value is about 1.5σ and about 4.5σ smaller than the predicted HWY and LWY model values, respectively. Furthermore, the B stars ΔO value is in fair agreement with the F-G dwarf value and about 1.5σ smaller than the the average value of NGC 3576 and Orion. These differences between the B stars and the other objects of the solar vicinity should be studied further.

For $r = 7$ kpc and $t = 13$ Gyr we took the average of the abundances of the M17 and M20 H II regions as the observational constraint; the C/H and O/H gaseous values were obtained from García-Rojas & Esteban (2007) and Paper I, using recombination lines of C and O. We have adopted the M17 X value obtained in Paper I to convert the abundances by number of M17 and M20 to abundances by mass. Unfortunately, there are no observational data representative of the chemical past at $r = 7$ kpc.

The HWY model fits very well the current C and O values for $r = 7$ kpc and marginally the present-day O for $r = 8$ kpc, but does not explain the current C value for $r = 8$ kpc. Alternatively the LWY model fits quite well both the C and O values for the solar vicinity, but predicts a higher O abundance for $r = 7$ kpc.

In Figures 4 and 5 the evolutionary tracks partially overlap: for a given ΔO value the ΔY and ΔC values of the two different tracks are almost the same, but the time is very different. In Figure 6 we present the evolution of ΔO, ΔY, and ΔC as a function of time to appreciate the differences between the 7 kpc and the 17 kpc tracks. It is important to present the behavior of $\mu = M_{\rm gas}/M_{\rm tot}$ because it drives the O evolution. For example, the 17 kpc track reaches a ΔO value of about 2×10^{-3}

at 13 Gyr, while the 7 kpc track reaches this value at less than 1 Gyr, whereas the same ΔO value for both tracks occurs at a similar μ value. The small differences in ΔO, ΔY, and ΔC at a given μ value come from: (a) the delay in the C and He enrichment of the ISM due to LIMS, (b) the shape of the SFR, and (c) the differences between the HWY and LWY. In Figure 6 we also present the SFR behavior. It can be seen that for $r = 7$ kpc the SFR is not only different in shape to the one at $r = 17$ kpc but it is from one to two orders of magnitude higher.

From the HWY model it has been found that about half of ΔY and ΔC have been formed by LIMS and half by MS, (see Figure 3 of Carigi et al. 2005, and Figure 6 of Paper I), while most of the ΔO has been formed by MS. LIMS produce a very small amount of O according to yields by different authors (see Figure 7 of Karakas & Lattanzio 2007). In this paper we are using the yields by Marigo and collaborators (1996, 1998). For the LWY model the fractions of ΔY and ΔC due to MS are similar but smaller than for the HWY model. The similar fraction of C and He produced by MS and LIMS is also responsible for the behavior in Figures 4 and 5, where it can be seen that the $\Delta Y/\Delta O$ and the $\Delta C/\Delta O$ relations are similar for the HWY model and for the LWY model for $\Delta O < 5 \times 10^{-3}$.

5. INTERMEDIATE WIND YIELDS

From Figures 1–5 we conclude that the HWY and LWY models are in very good agreement with some of the data, but for other data the agreement is only fair. To improve the agreement with the observations, we suggest the use of intermediate wind yields (IWY) for the computation of the chemical evolution models. We define the IWY as the average of HWY and LWY.

In Figure 7 we present the chemical abundance predictions derived from the IWY model for the most critical observations. In particular, we stress the remarkable fit of the model with the observed values for: (a) the present-day ($t = 13$ Gyr) C/O gradient in the $6 < r(\mathrm{kpc}) < 11$ range with the gradient derived from Galactic H II regions; (b) the $t = 13$ Gyr and $r = 7$ kpc ΔY, and ΔO values with those of M17; (c) the $t = 13$ Gyr and $r = 7$ kpc ΔC, and ΔO values with the average of the M17 and M20 values; (d) the $t = 13$ Gyr and $r = 8$ kpc ΔC, and ΔO values with the average values for NGC 3576, and Orion, and for young F and G stars of the solar vicinity; (e) the $t = 8.5$ Gyr and $r = 8$ kpc ΔY, ΔC, and ΔO values with the protosolar values.

The fits presented in Figure 7 imply that the effects of migration have not been very important in the chemical history of the Galaxy. A similar conclusion on the migration effects for the solar vicinity has been found by Navarro et al. (2011) based on the kinematic properties and the metallicity of thin disk stars.

6. POSSIBLE IMPLICATIONS FOR OTHER SYSTEMS

In is important to study how general is the chemical evolution model derived for the disk of the Galaxy, and to explore its relationship with other spiral galaxies and the transition region between the disk and the bulge of the Galaxy. In what follows we present a preliminary discussion of these two topics.

6.1. *Other spiral galaxies*

Since the IWY model successfully reproduces the He, C, and O abundances in the Galactic disk and in the solar vicinity, we want to extend our study to other spiral galaxies with abundances determined by recombination lines in H II regions.

In Table 1 we collect the gaseous abundances of eight extragalactic H II regions belonging to four spiral galaxies: M31, M33, M101, and NGC 2403 (Esteban et al. 2002, 2009). We have included dust corrections identical to those considered for Galactic H II regions. Consequently, these data are consistent with the Galactic data used in our previous figures (e.g., Figure 7). In Table 1 we show the name and type of the host galaxy, and the name and the galactocentric distance of each extragalactic H II region.

In Figure 8 we show the present-day C/O and O/H values for $r = 4, 5, ..., 15, 16$ kpc (from right to left) predicted by the IWY model of the Galactic disk and the extragalactic H II regions values shown in Table 1.

We notice that in the C/O-O/H relation presented in Figure 8: (a) the spiral galaxy disks have a behavior similar to that of the Milky Way disk; (b) all the extragalactic H II regions of the sample are well reproduced by IWY models; and (c) we see the effect of the Z dependent yields for $12+\log(\mathrm{O/H}) > 8.4$. More determinations of the O/H and C/H ratios in extragalactic H II regions with $12+\log(\mathrm{O/H})$ values < 8.4 and > 8.8 are needed to further test the yields.

Since the general C/O-O/H trend of the extragalactic H II regions can be addressed using the results of the GCE model, we suggest that the four extragalactic spiral galaxies have a similar IMF, no selective outflows, and probably an inside-out formation scenario like our galaxy.

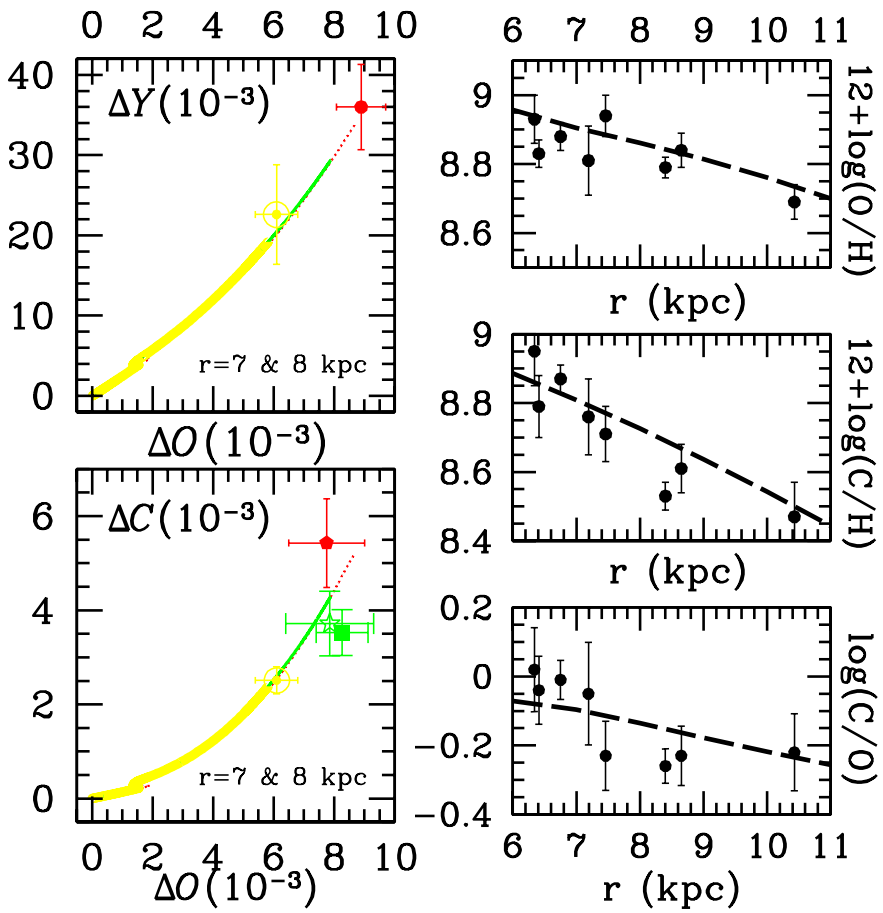

Fig. 7. Chemical evolution model assuming IWY=(HWY+LWY)/2.0. The left panels show the 0–13 Gyr evolution of ΔY vs ΔO and of ΔC vs ΔO for $r = 7$ kpc (dotted red lines) and $r = 8$ kpc (thin solid green line), data as in Figures 4 and 5; the thick yellow lines show the evolution from 0 to 8.5 Gyr for $r = 8$ kpc, data as in Figure 3. The right panels show the present-day ISM abundance ratios as a function of Galactocentric distance, data as in Figure 1. The color figure can be viewed online.

TABLE 1

EXTRAGALACTIC H II REGIONS

Host Galaxy	Type of Galaxy	Object	r (kpc)	12+log(O/H)[a]	12+log(C/H)[a]	log(C/O)[a]
M 101	ScdI	H1013	5.50	8.85 ± 0.09	8.67 ± 0.12	−0.08± 0.15
		NGC 5461	9.84	8.61 ± 0.06	8.30 ± 0.20	−0.21± 0.22
		NGC 5447	16.21	8.64 ± 0.06	8.20 ± 0.12	−0.34± 0.14
		NGC 5471	23.45	8.35 ± 0.15	7.79 ± 0.19	−0.46± 0.24
M 33	ScdII-III	NGC 595	2.87	8.81 ± 0.05	8.63 ± 0.12	−0.18± 0.13
		NGC 604	4.11	8.72 ± 0.03	8.40 ± 0.11	−0.22± 0.12
M 31	SbI-II	K932	16.0	8.74 ± 0.03	8.49 ± 0.13	−0.18± 0.14
NGC 2403	ScdIII	VS44	2.77	8.73 ± 0.04	8.32 ± 0.18	−0.31± 0.19

[a]Gaseous value plus dust correction.

TABLE 2

ABUNDANCE GRADIENTS NORMALIZED TO R_0[a]

Galaxy	R_0(kpc)[b]	12+log(O/H)	12+log(C/H)	log(C/O)
M101	28.95	$-0.492 \times (r/R_0)+8.84$	$-1.32 \times (r/R_0)+8.99$	$-0.65 \times (r/R_0)+0.03$
M33	6.83	$-0.492 \times (r/R_0)+9.00$	$-0.72 \times (r/R_0)+8.93$	$-0.22 \times (r/R_0)-0.10$
MW	11.25	$-0.495 \times (r/R_0)+9.16$	$-1.16 \times (r/R_0)+9.50$	$-0.65 \times (r/R_0)+0.34$

[a] R_0 = galactic photometric radius to 25 mag per square second.

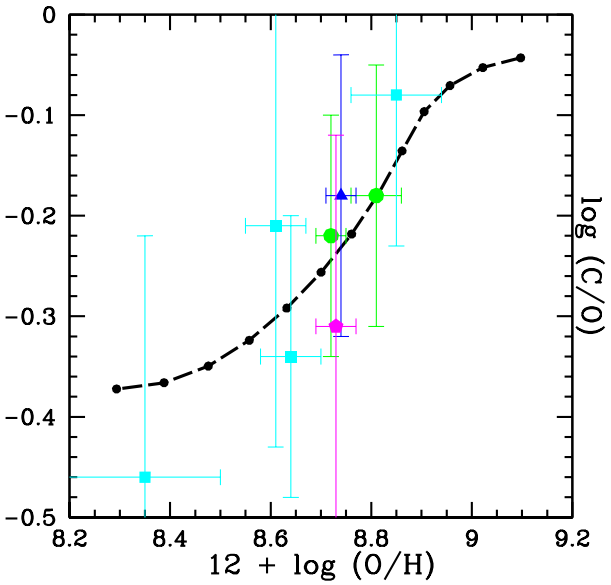

Fig. 8. C/O-O/H values at 13 Gyr predicted by IWY model (long-dashed lines). Small black circles: model predictions at different Galactocentric distances, from 4 kpc (right) to 16 kpc (left). Observed abundances ratios of extragalactic H II regions in spiral galaxies: cyan squares: M101, big green circles: M33, blue triangle: M31, and magenta pentagon: NGC 2403. The color figure can be viewed online.

It should be clear that Figure 8 does not correspond to models of the four spiral galaxies, and that the r values correspond to our galaxy and not to the other galaxies.

In Table 2 we present some galactic information for M33, M101, and the Milky Way, the only galaxies with determinations of chemical gradients based on recombination lines. Specifically, we show the galactic photometric radius to 25 mag per square second (R_0) and the chemical gradients normalized to R_0 corrected for dust depletion (Esteban et al. 2002, 2005, 2009). The MW R_0 was taken from de Vaucouleurs & Pence (1978).

In Figure 9 we show the O/H, C/O, and C/O values as a function of r normalized to R_0 for the eight extragalactic and the eight Galactic H II regions presented in Figures 8 and 7, respectively. Moreover we display the chemical gradients shown in Table 2.

From Figure 9, it can be noted that: (i) the O/H slope for the three galaxies is the same within the errors, which suggests that for a given galaxy the O/H gradient normalized to R_0 is a more meaningful representation than the standard gradient; (ii) the O/H gradients extend from $r/R_0 \sim 0.2$ to $r/R_0 \sim 1.0$; (iii) the O/H ratio at a given r/R_0 differs by a constant among M33, M101 and the MW; and (iv) for 12+log(O/H)$\sim$8.8 the slopes of the C/H and C/O gradients become steeper.

The parallel behavior of the O/H gradients when they are plotted relative to r/R_0 is remarkable, suggesting that the main mechanisms involved in the formation and evolution of spiral galaxies are similar.

The slope of the O/H gradients is similar, but the O/H absolute value at a given r/R_0 is different for each galaxy. In particular the MW shows an O/H ratio 0.24 dex higher than the average of M33 and M101 at a given r/R_0. Considering that the MW is an Sbc galaxy and M33 and M101 are Scd galaxies, this result probably implies that the earlier the type of a galaxy the higher the O/H value at a given r/R_0. This result might be due to the fact that the earlier the bulk of star formation occurs, the fainter the stellar luminosity at a given O/H value and consequently the higher the O/H value at a given R_0 value. More high accuracy determinations of O gradients in spiral galaxies are needed to test this result.

From Figures 8 and 9 it follows that we need: (i) to increase the r/R_0 coverage, mainly for smaller galactocentric distances, with abundance determinations of high accuracy; (ii) to increase the sample by including spiral galaxies of different types; and (iii) to make specific models for each galaxy. All this is

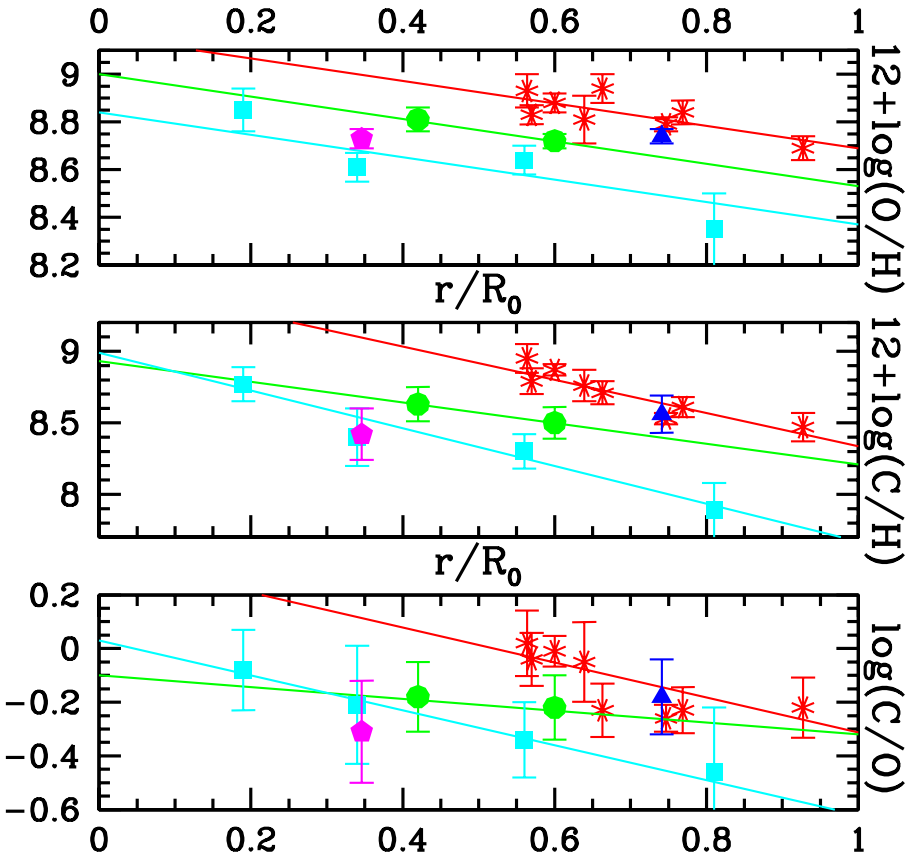

Fig. 9. Chemical abundance ratios of H II regions normalized to galactic photometric radius (R_0) for each galaxy (see Tables 1 and 2). Milky Way: red asterisks (see Figure 7). Others spiral galaxies: symbols as Figure 8. Lines represent the Galactic disk gradients of M101, M33, and the Milky Way. The color figure can be viewed online.

necessary in order to sort out possible differences in the galactic formation and evolution relative to that of the Galaxy and to understand the peculiar behavior of metal-rich stars and H II regions, see Carigi (2008), as well as to test stellar yields for $Z > Z_{\odot}$.

The present paper only includes specific models for our galaxy. We now present a preliminary discussion on the probable relevance of our results to the study of other spiral galaxies. It is beyond the scope of this paper to produce models for other galaxies and therefore to present a detailed comparison with the results derived by other authors, e.g., Chiappini, Romano, & Matteucci (2003b); Mollá & Díaz (2005); Renda et al. (2005); Yin et al. (2009); Marcon-Uchida, Matteucci, & Costa (2010); Magrini et al. (2010), using different sets of data. In future papers we plan to present detailed models for M31 (Meneses-Goytia, Carigi, & García-Rojas 2011) and M33 (Robles-Valdez, Carigi, & Bruzual 2011, in preparation).

6.2. *The transition region between the inner disk and the Galactic bulge*

A fraction of the stars observed in the direction of the Galactic center might have been formed in the true bulge and another fraction in the inner Galactic disk. Therefore we considered interesting to compare our IWY model for the innermost part of the disc with the abundances for these stars.

Since the inside-out model adopted as the Galactic formation scenario in this paper diverges for $r = 2$ kpc (see § 2), we obtained the chemical evolution of the innermost ring of the Galactic disk that our GCE model is able to consider, $r = 3 \pm 0.5$ kpc (with a 1 kpc width). The Galaxy at this radius formed efficiently: during the first Gyr the halo formed with a collapse time-scale of 0.5 Gyr and then the disk formed with a formation time scale of 1.0 Gyr. At the end of the evolution ($t = 13$ Gyr) the gaseous mass amounts to 7% of the baryonic mass inside the $r = 3 \pm 0.5$ kpc ring.

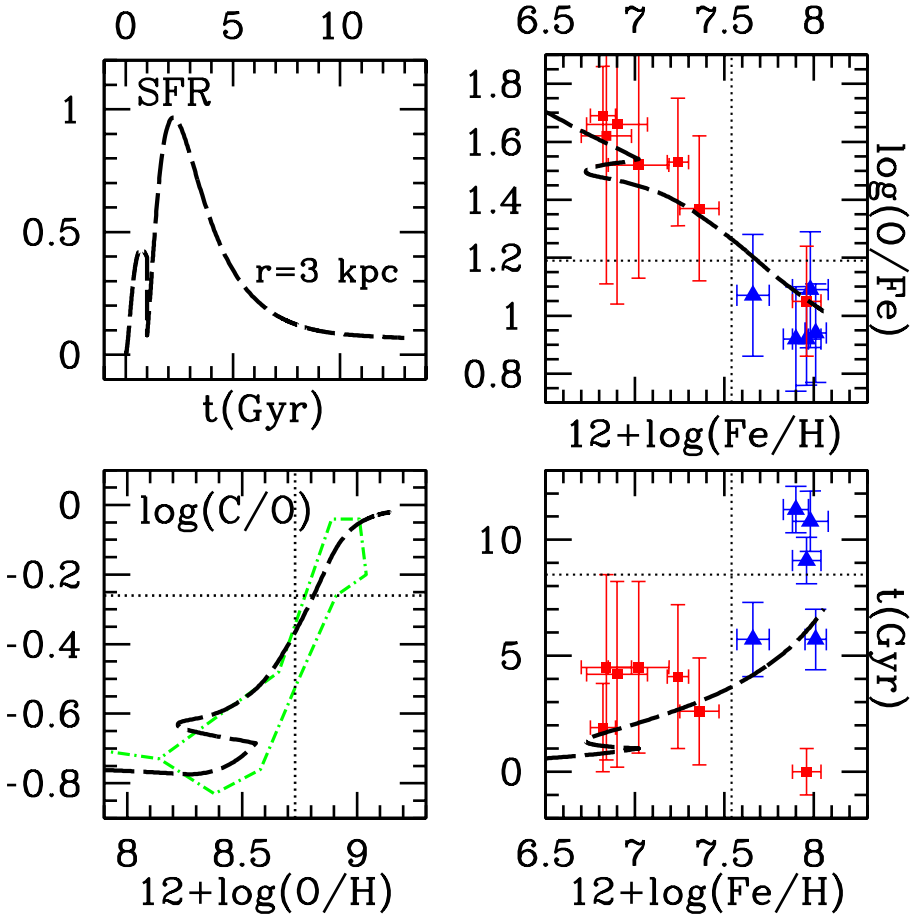

Fig. 10. Evolution for $r = 3$ kpc predicted by the IWY model (long-dashed black lines). Star formation history normalized to 70 $M_{\odot}$ pc^{-2} Gyr^{-1}. C/O-O/H, O/Fe-Fe/H, and time-Fe/H relations from 0 to 7 Gyr. Area enclosed by dot-short-dashed-green lines: Galactic bulge red giant stars presented by Cescutti et al. (2009). Filled symbols: microlensed dwarf and subgiant stars in the Galactic bulge from Bensby et al. (2010b), red squares: old stars with mean age of 9.8 ± 4.0 Gyr, blue triangles: young stars with mean age of 4.5 ± 1.6 Gyr. Ages were normalized to the age of the models (13 Gyr.) Dotted lines: protosolar values from Asplund et al. (2009). The color figure can be viewed online.

In Figure 10 we show the C/O-O/H, O/Fe-Fe/H, and Fe/H evolution obtained with the IWY model between 0 and 7 Gyr. We include the evolution from 0 to 7 Gyr and exclude the 7–13 Gyr range because at 7 Gyr the model reaches the highest Fe/H value shown by the stellar data. Moreover, in the excluded range the SFR is very low and the probability of forming stars younger than 6 Gyr (in the 7 to 13 Gyr range) is negligible.

In Figure 10 (C/O-O/H panel) we show also the area covered by the data of Cescutti et al. (2009). These authors collected [C/O] and [O/H] ratios for the Galactic bulge red giants determined by Fulbright, McWilliam, & Rich (2007) and Meléndez et al. (2008), and used the observed data to obtain the initial stellar C/H and O/H values relative to the solar abundances due to Asplund et al. (2005). In order to convert the Cescutti et al. (2009) data to abundances by number we used, only in this figure, the solar abundances by Asplund et al. (2005). For the other figures, we assumed the protosolar abundances by Asplund et al. (2009).

A description of the model in the C/O-O/H panel of Figure 10 follows. During the halo formation, the IWY model predicts an increase of 12+log(O/H) to 8.6 dex and an increase of 12+log(C/O) to −0.7 dex. After the halo formation finishes, at $t = 1$ Gyr, the O/H ratio decreases due to the dilution produced by the enormous amount of primordial gas that is accreted to form the disk. Later on, this accretion causes a rapid SFR increase, producing an O/H increase. The C/O rise from −0.7 dex to −0.5 dex

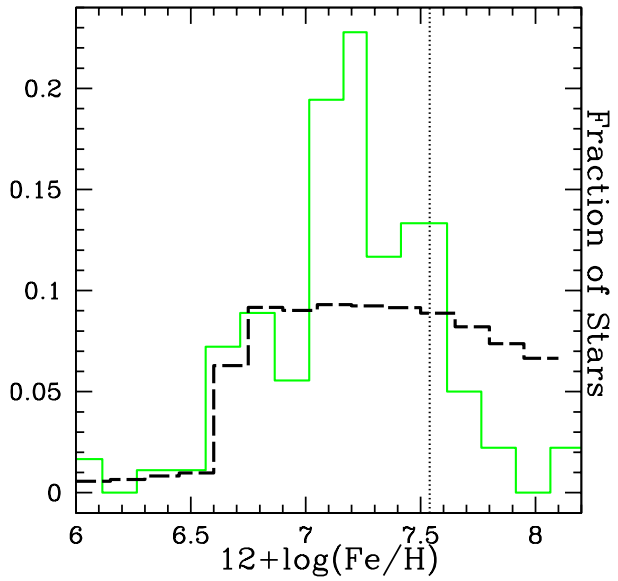

Fig. 11. Iron distribution function. Predictions for $r = 3$ kpc model that assume IWY (long-dashed black line) until 7 Gyr. Observed distribution for the outermost fields ($b = -12$) along the bulge minor axis by Zoccali et al. (2008) (continuous green line). Dotted line: protosolar Fe/H value from Asplund et al. (2009). The color figure can be viewed online.

is due mainly to LIMS, while the C/O rise from -0.5 dex to 0.0 dex is due to both massive stars and LIMS.

In Figure 10 (O/Fe-Fe/H and time-Fe/H panels), we included the chemical abundances determined by Bensby et al. (2010b) in microlensed dwarf and subgiant stars of the Galactic bulge. In order to convert the data of Bensby et al. (2010b) to abundances by number, we used their solar abundances. The stellar ages were normalized to the age of the model ($t = 13.0$ Gyr).

Our model at $r = 3$ kpc successfully reproduces the O/Fe-Fe/H obtained by Bensby et al. (2010b), but the time-Fe/H relation is only partially reproduced. Our model explains all old-metal-poor stars and two young stars, but not the oldest metal-rich star in their sample (see the square at 12+log(Fe/H)$\sim$7.9) which behaves like a common bulge star, see Ballero et al. (2007). The youngest and more metal-rich stars would be disk stars that formed at $r < 3$ kpc.

Since Fe is produced by massive stars and binary systems of LIMS, to a first approximation Fe behaves like C, which is produced by MS and single LIMS, see for example Akerman et al. (2004), and the C/O-O/H discussion presented above can be used to explain the O/Fe-Fe/H and time-Fe/H panels of Figure 10.

Bensby et al. (2010a) have studied red giant stars in the inner Galactic disc and find that the abundance trends of the inner disc agree very well with those of the nearby thick disc, and also with those of the Galactic bulge. Based on the stellar results of the thick and thin disks of the solar vicinity, of the inner Galactic disc, and of the Galactic bulge (Bensby & Feltzing 2006; Bensby et al. 2010a,b), they suggest that the bulge and the disk have had similar chemical histories. Moreover, Alves-Brito et al. (2010) also suggest that the bulge and local thick disk stars formed over similar timescales with similar star formation rates and initial mass functions.

Cescutti et al. (2009) present a Galactic bulge model, computed by Ballero et al. (2007), in which, in order to reproduce the total stellar mass, the iron distribution function, and the α/Fe-Fe/H relations (all constraints obtained from giant stars) they assume: a formation time scale of $\sim$0.1 Gyr, as well as a star formation efficiency one order of magnitude higher and an IMF flatter for $m > 1\ M_{\odot}$ than those considered in our models. This model, with a SFR as long as 0.5 Gyr, cannot explain the ages of the youngest bulge dwarfs found by Bensby et al. (2010b).

Note that, if we focus only on the C/O-O/H and O/Fe-Fe/H relations determined in dwarf stars of the Galactic bulge, we cannot distinguish between a scenario with a very rapid infall, efficient star formation, and a high relative formation of massive stars –that by Cescutti et al. (2009)– and another scenario with an order of magnitude less rapid infall, an order of magnitude less efficient star formation, and a lower relative formation of massive stars – the one presented in this paper.

Nevertheless, if we focus on the age-Fe/H relation shown by bulge dwarf stars, our model, with an extended bulge formation time and therefore an extended star formation history, produces a better fit to the data than that by Cescutti et al. (2009).

In Figure 11 we show the iron distribution function predicted by the IWY model for $r = 3$ kpc in the Galactic disk from 0 to 7 Gyr. Since there are no good abundance determinations for the inner parts of the Galactic disk, we compare our model with the 104 stars that belong to the outermost field along the bulge minor axis at $b = -12$, see lower panel of Figure 14 by Zoccali et al. (2008). We have used $12+\log(\mathrm{Fe/H})_{\odot} = 7.50$ to convert the [Fe/H] values of the Zoccali et al. (2008) sample to Fe/H abun-

dances by number. From that figure, we can say that a non-negligible fraction of the stars in the direction of the bulge might belong to the inner disk. Moreover, about the bulge sample we note that: (i) for 12+log(Fe/H) < 7 the contamination of the thick disk is high, (ii) for $7 < 12 + \log(\mathrm{Fe/H}) < 8$ the contamination of the thin disk is lower and the true bulge stars dominate, and (iii) for 12+log(Fe/H) > 8 the contribution of the metal-rich stars of the thin disk is important.

Note that in Figure 11 we are using only the outermost 104 stars of the total of 800 stars located in the direction of the bulge, and the results of our model for $r = 3$ kpc. On the other hand Cescutti & Matteucci (2011) show that their bulge model (the same as Cescutti et al. 2009) follows the constraint provided by the 800 stars very well using a Salpeter IMF. The model by Cescutti and Matteucci predicts a smaller number of stars for [Fe/H] values higher than solar, probably indicating that the bulge sample has been contaminated by innermost disk stars.

From the previous discussion it follows that the Galactic bulge is a complex structure that should be studied further (e.g., Zoccali 2010).

7. CONCLUSIONS

We have constructed models with three different sets of yields that differ only on their Z dependence at solar metallicities for massive stars: HWY, IWY, and LWY. The HWY and the LWY have been used before by us, while in this paper we introduce the IWY, that are given by (HWY + LWY)/2. We find that the IWY Galactic chemical evolution models produce better fits to the observational data than either the HWY or the LWY models.

We present a Galactic chemical evolution model based on the IWY for the disk of the Galaxy that is able to fit: (a) the C/O vs O/H, C/Fe vs Fe/H, O/Fe vs Fe/H, and Fe/H vs t relations derived from halo and disk stars of different ages in the solar vicinity, (b) the O/H, C/H, and C/O abundance gradients (slopes and absolute values) derived from Galactic H II regions, (c) the He/H, C/H, O/H, Fe/H protosolar abundances, and (d) the He/H and O/H values of the Galactic H II region M17.

We find that in general about half of the freshly made helium is produced by massive stars and half by LIMS, and that a similar situation prevails for carbon, while most of the oxygen is produced by massive stars. The agreement of the He/O and C/O ratios between the model and the protosolar abundances implies that the Sun formed from a well mixed ISM.

We note that the agreement of our model with the protosolar abundances and the Sun-formation time supports the idea that the Sun originated at a Galactocentric distance similar to that of the solar vicinity.

We show that chemical evolution models for the Galactic disk are able to reproduce the observed ΔY and ΔO protosolar values and the ΔY and ΔO values derived for M17 based on H, He and O recombination lines, but not the M17 ΔY and ΔO values derived from $T(4363/5007)$ and O collisionally excited lines under the assumption of $t^2 = 0.00$. This result provides a consistency check in favor of the presence of large temperature variations in H II regions and on the method based on the H, He, C and O recombination lines to derive abundances in H II regions.

We obtain that the IWY chemical evolution model of the Galactic disk for the present time, in the Galactocentric range $6 < r(\mathrm{kpc}) < 11$, produces a reasonable fit to the O/H vs C/O relationship derived from H II regions of nearby spiral galaxies. The yields predict an increase of the C/O ratio with O/H starting from 12+log(O/H)$\sim$8.4 which is observed in our Galaxy and in nearby galaxies. The O/H vs C/O relationship might imply that spiral galaxies have a similar IMF, no selective outflows, and probably a formation scenario similar to that of our galaxy.

We find a remarkable parallelism of the O/H gradients for M33, M101, and the Galaxy when they are plotted with respect to r/R_0 (R_0 is the galactic photometric radius to 25 mag per square second), suggesting some common mechanisms in the formation and evolution of spiral galaxies. The O/H ratio at a given r/R_0 differs by a constant among M33, M101 and the MW. The MW shows a 0.24 dex higher O/H ratio than the average of M33 and M101 at a given r/R_0.

We also find that the results for our model at $r = 3$ kpc can explain: (a) the C/O-O/H and O/Fe-Fe/H relations, and (b) partially the Fe/H-time relation and the Fe distribution function derived from stellar observations in the direction of the Galactic bulge. We find that stars belonging to the thin and thick discs make a significant contribution to these relations.

Future work to advance in this subject requires: (a) further studies of the Galactic bulge to be able to quantify the stellar contributions due to the inner disk and the true bulge; (b) to increase the H II regions r/R_0 coverage, mainly for the smaller galactocentric distances, with high accuracy C/H and O/H abundance determinations; (c) to increase the sam-

ple of spiral galaxies of different types with O/H gradients of high accuracy; and (d) to make specific models for each galaxy. All this is required to sort out possible differences in the galactic formation and evolution of other galaxies relative to that of the Galaxy.

We thank Jorge García-Rojas and César Esteban for useful discussions. We are also grateful to the anonymous referee for a careful reading of the manuscript and many excellent suggestions. This work was partly supported by the Conacyt grants 60354 and 129753.

REFERENCES

Alves-Brito, A., Meléndez, J., Asplund, M., Ramírez, I., & Yong, D. 2010, A&A, 513, 35
Akerman, C. J., Carigi, L., Nissen, P. E., Pettini, M., & Asplund, M. 2004, A&A, 414, 931
Anders, E., & Grevesse, N. 1989, Geochim. Cosmochim. Acta, 53, 197
Asplund, M., Grevesse, N., & Sauval, A. J. 2005, in Cosmic ASP Conf. Ser. 336, Abundances as Records of Stellar Evolution and Nucleosynthesis, ed. T. G. Barnes & F. N. Bash (San Francisco: ASP), 25
Asplund, M., Grevesse, N., Sauval, A. J., & Scott, P. 2009, ARA&A, 47, 481
Ballero, S. K., Matteucci, F., Origlia, L., & Rich, R. M. 2007, A&A, 467, 123
Bensby, T., Alves-Brito, A., Oey, M. S., Yong, D., & Meléndez, J. 2010a, A&A, 516, L13
Bensby, T., & Feltzing, S. 2006, MNRAS, 367, 1181
Bensby, T., et al. 2010b, A&A, 512, A41
Bromm, B., & Larson, R. V. 2004 ARA&A, 42, 79
Carigi, L. 1994, ApJ, 424, 181
_____. 1996, RevMexAA, 32, 179
_____. 2000, RevMexAA, 36, 171
_____. 2008, in The Metal-Rich Universe, ed. G. Israelian & G. Meynet (Cambridge: Cambridge Univ. Press), 415
Carigi, L., Colín, P., & Peimbert, M. 1999, ApJ, 514, 787
_____. 2006, ApJ, 644, 924
Carigi, L., Colín, P., Peimbert, M., & Sarmiento, A. 1995, ApJ, 445, 98
Carigi, L., & Hernández, X. 2008, MNRAS, 390, 582
Carigi, L., & Peimbert, M. 2008, RevMexAA, 44, 341 (Paper I)
Carigi, L., Peimbert, M., Esteban, C., & García-Rojas, J. 2005, ApJ, 623, 213
Cescutti, G., & Matteucci, F. 2011, A&A, 525, A126
Cescutti, G., Matteucci, F., Francois, P., & Chiappini, C. 2007, A&A, 462, 943
Cescutti, G., Matteucci, F., McWilliam, A., & Chiappini, C. 2009, A&A, 505, 605
Chiappini, C., Matteucci, F., & Gratton R. 1997, ApJ, 477, 765
Chiappini, C., Matteucci, F., & Meynet, G. 2003a, A&A, 410, 257
Chiappini, C., Romano, D., & Matteucci, F. 2003b, MNRAS, 339, 63
de Vaucouleurs, G., & Pence, W. D. 1978, AJ, 83, 1163
Esteban, C., Bresolin, F., Peimbert, M., García-Rojas, J., Peimbert, A., & Mesa-Delgado, A. 2009, ApJ, 700, 654
Esteban, C., García-Rojas, J., Peimbert, M., Peimbert, A., Ruiz, M. T., Rodríguez, M., & Carigi, L. 2005, ApJ, 618, L95
Esteban, C., Peimbert, M., Torres-Peimbert, S., & Escalante, V. 1998, MNRAS, 295, 401
Esteban, C., Peimbert, M., Torres-Peimbert, S., & Rodríguez, M. 2002, ApJ, 581, 241
Fenner, Y., & Gibson, B. K. 2003, PASA, 20, 189
Fierro, C. L., & Georgiev, L. 2008, RevMexAA, 44, 213
Fulbright, J. P., McWilliam, A., & Rich, R. M. 2007, ApJ, 661, 1152
García-Rojas, J., & Esteban, C. 2007, ApJ, 670, 457
Greggio, L., & Renzini, A. 1983, A&A, 118, 217
Grevesse, N., & Noels, A. 1993, in Origin and Evolution of the Elements, ed. N. Prantzos, E. Vangioni-Flam, & M. Cassé (Cambridge: Cambridge Univ. Press), 15
Grevesse, N., & Sauval, A. J. 1998, Space Sci. Rev., 85, 161
Hirschi, R. 2007, A&A, 461, 571
Hirschi, R., Meynet, G., & Maeder, A. 2005, A&A, 433, 1013
Kalberla, P. M. W., & Kerp, J. 2009, ARA&A, 47, 27
Karakas, A., & Lattanzio, J. C. 2007, PASA, 24, 103
Kewley, L. J., & Ellison, S. L. 2008, ApJ, 681, 1183
Kroupa, P., Tout, C. A., & Gilmore, G. 1993, MNRAS, 262, 545
Lodders, K. 2003, ApJ, 591, 1220
Lodders, K., Palme, H., & Gail, H.-P. 2009, in The Landolt-Börnstein, New Series, Vol. VI/4b, ed. J. E. Trümper (Berlin: Springer-Verlag), 560
Maeder, A. 1992, A&A, 264, 105
Magrini, L., Stanghellini, L., Corbelli, E., Galli, D., & Villaver, E. 2010, A&A, 512, 63
Marcon-Uchida, M. M., Matteucci, F., & Costa, R. D. D. 2010, A&A, 520, 35
Marigo, P., Bressan, A., & Chiosi, C. 1996, A&A, 313, 545
_____. 1998, A&A, 331, 564
Matteucci, F. 2001, Astrophysics and Space Science Library, Vol. 253, The Chemical Evolution of the Galaxy (Dordrecht: Kluwer), 293
Matteucci, F., & Chiappini, C. 1999, in Chemical Evolution from Zero to High Redshift, ed. J. R. Walsh & M. R. Rosa (Berlin: Springer-Verlag), 83
Matteucci, F., Franco, J., Francois, P., & Treyer, M. 1989, RevMexAA, 18, 145
Mattsson, L. 2010, A&A, 515, 68
Meléndez, J., et al. 2008, A&A, 484, L21
Meneses-Goytia, S., Carigi, L., & García-Rojas, J. 2011, Astrobiology, submitted

Mesa-Delgado, A., et al. 2009, MNRAS, 395, 855
Meynet, G., & Maeder, A. 2000, A&A, 361, 101
_____. 2002, A&A, 390, 561
Mollá, M., & Díaz, A. I. 2005, MNRAS, 358, 521
Navarro, J. F., Abadi, M. G., Venn, K. A., Freeman, K. C., & Anguiano, B. 2011, MNRAS, in press (arXiv:1009.0020)
Nordström, B, et al. 2004, A&A, 418, 989
Pagel, B. E. J. 2009, Nucleosynthesis and Chemical Evolution of Galaxies (Cambridge: Cambridge Univ. Press)
Peimbert, A., & Peimbert, M. 2010, ApJ, 724, 791
Peimbert, A., Peimbert, M., & Luridiana, V. 2002, ApJ, 565, 668
Peimbert, M. 1967, ApJ, 150, 825
Peimbert, M., Luridiana, V., & Peimbert, A. 2007, ApJ, 666, 636
Peimbert, M., & Peimbert, A. 2011, RevMexAA (SC), in press (arXiv:0912.3781)
Peimbert, M., Peimbert, A., Carigi, L., & Luridiana, V. 2010, in IAU Symp. 268, Light Elements in the Universe, ed. C. Charbonnel, M. Tosi, F. Primas, & C. Chiappini (Cambridge: Cambridge Univ. Press), 91
Portinari, L., Chiosi, C., & Bressan, A. 1998, A&A, 334, 505
Prantzos, N. 2008, EAS Publications Series, 32, 311 (arXiv:0709.0833)
Prantzos, N., Vangioni-Flam, E., & Chauveau, S. 1994, A&A, 285, 132
Przybilla, N., Nieva, M. F., & Butler, K. 2008, ApJ, 688, L103
Renda, A., Kawata, D., Fenner, Y., & Gibson, B. K. 2005, MNRAS, 356, 1071
Romano, D., Karakas, A. I., Tosi, M., & Matteucci, F. 2010, A&A, 522, 32
Roskar, R., Debattista, V. P., Stinson, G. S., Quinn, T. R., Tobias Kaufmann, T., & Wadsley, J. 2008, ApJ, 675, L65
Sánchez-Blázquez, P., Courty, S., Gibson, B. K., & Brook, C. B. 2009, MNRAS, 398, 591
Schaller, G., Schaerer, D., Meynet, G., & Maeder, A. 1992, A&AS, 96, 269
Simón-Díaz, S. 2010, A&A, 510, A22
Simón-Díaz, S., & Stasińska, G. 2011, A&A, 526, A48
Thielemann, F. K., Nomoto, K., & Hashimoto, M. 1993, in Origin and Evolution of the Elements, ed. N. Prantzos, et al.(Cambridge: Cambridge Univ. Press), 297
Tinsley, B. M. 1980, Fundam. Cosmic Phys., 5, 287
Vílchez, J. M., & Esteban, C. 1996, MNRAS, 280, 720
Vlajić, M., Bland-Hawthorn, J., & Freeman, K. C. 2011, ApJ, in press (arXiv:1101.0607)
Woosley, S. E., & Weaver, T. A. 1995, ApJS, 101, 181
Yin, J., Hou, L. K., Prantzos, T. A., Boissier, S., Chang, R. X., Shen, S. Y., & Zhangh, B. 2009 A&A, 505, 497
Zoccali, M. 2010, in IAU Symp. 265, Chemical Abundances in the Universe: Connecting First Stars to Planets, ed. K. Cunha, M. Spite, & B. Barbuy (Cambridge: Cambridge Univ. Press), 271
Zoccali, M., et al. 2008, A&A, 86, 177

Leticia Carigi and Manuel Peimbert: Instituto de Astronomía, Universidad Nacional Autónoma de México, Apdo. Postal 70-264, México 04510, D.F., Mexico (carigi, peimbert@astroscu.unam.mx).

Revista Mexicana de Astronomía y Astrofísica, **47**, 159–171 (2011)

TEMPERATURE, BRIGHTNESS AND SPECTRAL INDEX OF THE CYGNUS RADIO LOOP

V. Borka Jovanović[1] and D. Urošević[2]

Received 2010 October 18; accepted 2011 February 10

RESUMEN

Se presenta el brillo estimado del remanente de supernova del Velo del Cisne en 2720, 1420, 820, 408 y 34.5 MHz. Mediante el método que hemos desarrollado anteriormente para anillos grandes, utilizamos las observaciones de radioemisión en el continuo para calcular las temperaturas de brillo medias y los brillos superficiales del Velo del Cisne en las frecuencias mencionadas. Estimamos el espectro de las temperaturas medias versus frecuencia entre las cinco frecuencias y obtenemos el índice espectral del Velo del Cisne. Nuestros resultados muestran que el Velo evoluciona en un medio de baja densidad, y que la energía inicial de la explosión de supernova fue relativamente baja. Confirmamos el origen no-térmico de la radiación del anillo del Cisne y mostramos que nuestro método es aplicable a la mayoría de los remanentes de supernova.

ABSTRACT

The estimated brightness of the Cygnus loop supernova remnant (SNR) at 2720, 1420, 820, 408 and 34.5 MHz is presented. The observations of the continuum radio emission are used to calculate the mean brightness temperatures and surface brightnesses of this loop at the five frequencies in a wide spectral range, using the method we have previously developed for large radio loops. The spectrum for mean temperatures versus frequency between the five frequencies is estimated and the spectral index of the Cygnus loop is obtained. Also, from our results it can be concluded that the Cygnus loop evolves in a low density environment and that the initial energy of the supernova explosion was relatively low. The results obtained confirm the non-thermal origin of the Cygnus radio loop and show that our method is applicable to almost all remnants.

Key Words: ISM: supernova remnants — radiation mechanisms: non-thermal — radio continuum: general — surveys

1. INTRODUCTION

In our investigation, we are supposing the radio loops to be evolved supernova remnants (SNRs). Supernova remnants represent shells of approximately spherical shape which are spreading, and depending of the interstellar matter density, they change their shape. We can see only parts of these spherical contours which represent radio spurs, i.e., areas of more intense emission in the sky, spur-like and of huge dimensions. Radio loops consist of several spurs lying approximately on the same small circle of the celestial sphere. Their material probably expands inside of bubbles of low density. Bubbles are made by former SNR explosions or by strong stellar winds (Salter 1983; McKee & Ostriker 1977, and references therein). The radio emission from SNRs is generally understood to be synchrotron emission from relativistic electrons moving in the magnetic field.

A star in the constellation of Cygnus exploded and its remnant is the Cygnus loop. It is classified as a mid-aged SNR of type S, is located below (but near the plane of) the Galactic equator, and is less than 1 kpc away from us. It is listed in Green's catalogue of SNRs as G74.0-8.5 (Green 2004, 2006, 2009). As shown in Green (1984), this remnant has decelerated considerably by its interaction with the surrounding interstellar medium.

[1]Vinča Institute of Nuclear Sciences, University of Belgrade, Serbia.
[2]Faculty of Mathematics, University of Belgrade, Serbia.

Leahy, Roger, & Ballantyne (1997) presented high resolution 1420 MHz total intensity and polarization maps of the Cygnus loop and derived rotation measures. Aschenbach & Leahy (1999) made a comparison between the radio and X-ray emission from supernova remnants. The X-ray emission traces the hot gas behind the shock front, while the radio emission comes from the relativistic electron population emitting synchrotron radiation in the ambient magnetic field. They found that there are significant differences in the distribution of X-ray and radio brightness in the Cygnus loop. Also, significant temperature variations, seen along the rim and in the bright filaments interior to the rim, indicated that the Cygnus loop was caused by a supernova exploding in a cavity.

Uyaniker et al. (2002) suggested that the Cygnus loop may consist of two overlapping remnants. Substantial differences between the northern and southern part as well as in their emission characteristics have been observed (Uyaniker et al. 2004; Patnaude et al. 2002). Some authors proposed that the Cygnus loop consists of two likely interacting SNRs: G74.3-8.4 and G72.9-9.0 (Uyaniker et al. 2002; Leahy 2002). In Sun et al. (2006), from 4800 MHz observations, it is explained that the polarization maps (the difference in the polarization characteristic between the northern and southern part) support previous ideas that the Cygnus loop may consist of two SNRs. Besides, several compact radio sources are located within the boundary of the remnant. The main characteristics of the Cygnus loop in different spectral bands are: (a) in the radio band it is shell, brightest to the north-east, with fainter breakout regions to the south, with spectral variations; (b) in the optical it is a large filamentary loop, brightest to the north-east, not well defined to the south and west; (c) it is a shell in soft X-rays (see e.g., Green 2006).

Some radio maps which include this remnant are the following: the map by Kundu & Becker (1972) at 4940 MHz, Keen et al. (1973) at 2695 MHz, Uyaniker et al. (2004) at 2675 MHz, Leahy et al. (1997) at 1420 MHz, Dickel & Willis (1980) at 610 MHz, Green (1984) at 408 MHz. We found observations of the continuum radio emission at 2720 MHz (Reif et al. 1987), 1420 MHz (Reich & Reich 1986), 820 MHz (Berkhuijsen 1972), 408 MHz (Haslam et al. 1982) and 34.5 MHz (Dwarakanath & Udaya Shankar 1990), in electronic form and used them in this paper.

In our previous paper (Borka Jovanović & Urošević 2009a) we only calculated the temperatures and brightnesses at three frequencies. In this paper we expand the scope of our investigation to: brightness temperatures and surface brightnesses at five frequencies, as well as spectrum, $T-T$ graphs, radio spectral indices, an estimation of environment density and the initial energy of supernova explosion, and the flux density spectrum.

In our calculations, we used brightness temperatures over the whole area of the loop, so the mean temperature we estimated refers to the northern and southern parts together. In this research the average brightness temperatures and surface brightnesses of the Cygnus radio loop are calculated at the five frequencies: 2720, 1420, 820, 408 and 34.5 MHz. Then we study how these results compare with previous results (Roger et al. 1999; Reich, Zhang, & Fürst 2003; Uyaniker et al. 2004) and with current theories of SNR evolution. These theories predict that loops are non-thermal sources which are spreading inside the hot, low density bubbles made by former supernova explosions or by strong stellar winds (see Salter 1983; McKee & Ostriker 1977, and references therein).

Our aim is also to apply the method for the determination of the brightness temperature given in Borka (2007) which was developed for large radio loops, and to show that it is rather efficient in the case of much smaller radio loops, e.g., the Cygnus loop. We also check whether the results obtained using this method agree with the method of $T-T$ graphs and with results obtained with other methods. Our method is quite simple because we are using brightness temperature isolines to define borders of the Cygnus loop at the wide range of frequencies ($\nu_{\max}/\nu_{\min} = 2720\,\mathrm{MHz}/34.5\,\mathrm{MHz} \approx 79$). Other authors use different square or rectangular areas to determine the area of the loop and to calculate spectral indices, the brightness temperature and the flux of the loop (Uyaniker et al. 2004, page 917, and Leahy & Roger 1998, page 786). Also, we calculate the flux from the Cygnus loop and compare our results with results of other authors in different frequency ranges.

2. ANALYSIS

2.1. *Data*

We used the following radio-continuum surveys as the basic source of data in this paper: at 2720 MHz (Reif et al. 1987), 1420 MHz (Reich & Reich 1986), 820 MHz (Berkhuijsen 1972), 408 MHz (Haslam et al. 1982) and 34.5 MHz (Dwarakanath & Udaya Shankar 1990). These surveys are available in electronic form, in Flexible Image Transport Sys-

tem (FITS) data format[3]. This online survey sampler of the *Max-Planck-Institut für Radioastronomie* (MPIfR) near Bonn, Germany, allows users to pick a region of the sky and obtain images and data at different frequencies. The 2720-MHz Stockert survey has an angular resolution of 0°.35, the 1420-MHz Stockert survey (Reich & Reich 1986) 0°.59, the 820-MHz Dwingeloo survey (Berkhuijsen 1972) 1°.2, the 408-MHz all-sky survey (Haslam et al. 1982) 0°.85, and the 34.5-MHz Gauribidanur survey (Dwarakanath & Udaya Shankar 1990) 0°.7. The corresponding observations are given at the following rates (measured data) for both l and b: 1°/8 at 2720 MHz, 1°/4 at 1420 MHz, 1°/2 at 820 MHz, 1°/3 at 408 MHz and 1°/5 at 34.5 MHz. The effective sensitivities are about 5 mK T_b (T_b is an average brightness temperature), 50 mK, 0.20 K, 1.0 K and about 700 K, respectively.

FITS data format stores the multidimensional arrays and 2-dimensional tables containing rows and columns of scientific data sets. We extracted observed brightness temperatures from this data format into ASCII data files, and afterwards, using our programs in C and FORTRAN, we obtained the results presented in this paper.

2.2. *Method*

As there is a great influence of background radiation over the Cygnus loop area, it is very difficult to determine its area precisely. The area of this loop is enclosed with brightness temperature contours. The maps of a region in Cygnus, in new Galactic coordinates (l, b), with contours of the brightness temperatures T_b are plotted in Figures 1–5. In these figures, among all the brightness temperature contours, the most important are the outer contour and inner one, which represent the loop borders. The outer one (which corresponds to the minimum temperature of the loop) separates loop and background, while the inner one (corresponding to the maximum temperature) separates the loop and some superposed source. The interval of Galactic longitude of this loop is l=[76.5°, 71.5°], and of latitude it is b=[−10.5°, −7°]. We used the same method of calculation as given in Borka (2007) for Galactic radio loops I–VI, Borka, Milogradov-Turin, & Urošević (2008) for Loops V and VI and in Borka Jovanović & Urošević 2009b for the Monoceros loop. Our aim is to apply our method, which we developed for main Galactic loops I-VI and described in Borka (2007) and Borka et al. (2008), to smaller remnants and to show that it is applicable to almost all remnants. To confirm that our method works well, we also provide the area maps of Cygnus at the five frequencies (Figures 1–5) and some examples of the temperature profiles at 2720 MHz (Figure 6). In Figure 6 it should be noticed that the bottom panel shows only back-

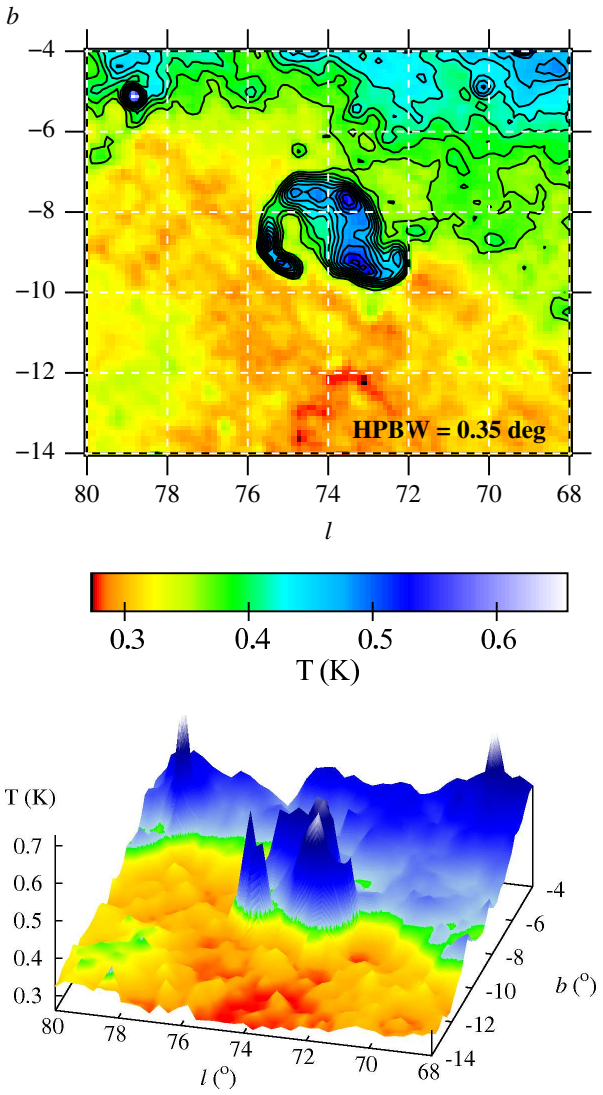

Fig. 1. Top: the 2720 MHz map of a region in Cygnus, in new Galactic coordinates (l, b), showing contours of brightness temperature. This radio loop has position: l = [76.5°, 71.5°]; b = [−10.5°, −7°]. The HPBW (Half Power Beam Width) for this frequency is 0°.35. The contours plotted represent the temperatures $T_{\rm min}$ and $T_{\rm max}$ from Table 1 and nine contours in between. The contours are plotted every 0.265 K, starting from the lowest temperature of 0.395 K and up to 0.66 K. The corresponding temperature scale is given (in K). Bottom: the 2720 MHz area map of Cygnus. The color figure can be viewed online.

[3]Available at the site `http://www.mpifr-bonn.mpg.de/survey.html`.

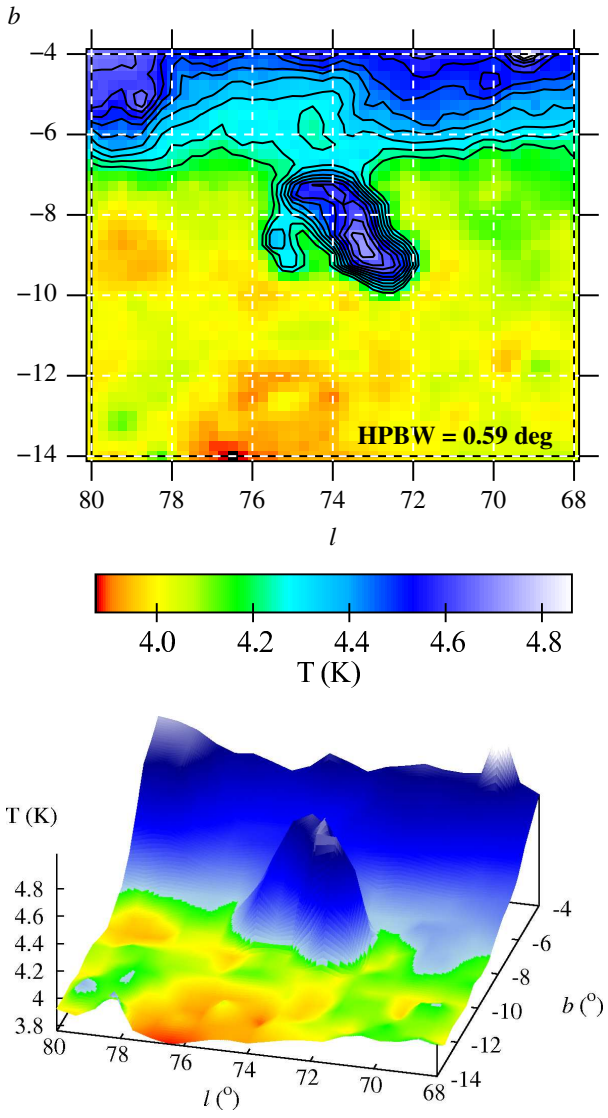

Fig. 2. The same as Figure 1, but for 1420 MHz. The HPBW for this frequency is 0°.59. The contours are plotted every 0.07 K, starting from the lowest temperature of 4.2 K and up to 4.9 K. The color figure can be viewed online.

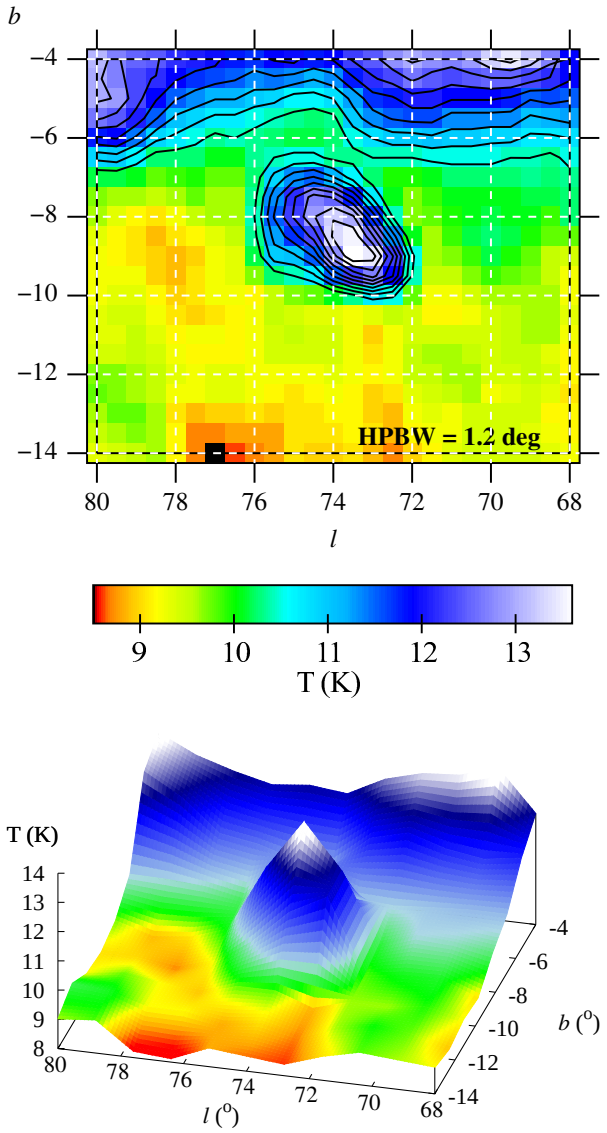

Fig. 3. The same as Figure 1, but for 820 MHz. The HPBW is 1°.2. The contours are plotted every 0.39 K, starting from the lowest temperature of 10.1 K and up to 14 K. The color figure can be viewed online.

ground radiation (not including the loop), where for $b = -10°$ the brightness temperature is not higher than 0.38 K. It is in agreement with the temperature intervals given in the first row of Table 1, where we posit 0.395 K for the minimum temperature of the loop with background, at 2720 MHz.

The mean temperatures and surface brightnesses of this radio loop are computed using data taken from radio-continuum surveys at 2720, 1420, 820, 408 and 34.5 MHz. We have subtracted the background radiation in order to derive the mean brightness temperature of the SNR alone. First, the temperature of the loop plus background was determined. For every bin in the survey we have some value for temperature $T_{\rm sum}$. We take all bins within the loop border and obtain the average temperature $<T_{\rm sum}>$ of the loop plus background. Then, the background alone near the loop was estimated. We determine the temperature of the background near the outer border of the loop (average value from all data near the outer border of the loop) and that is taken as the background temperature $T_{\rm back}$. And finally, the difference of these values is calculated to obtain the average temperature of the loop at

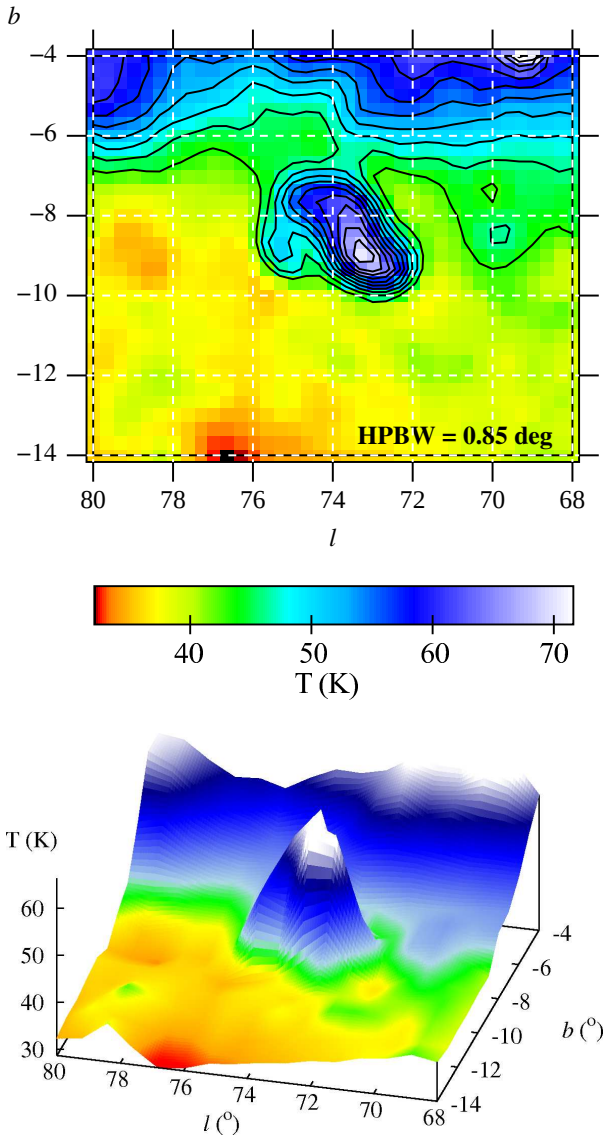

Fig. 4. The same as Figure 1, but for 408 MHz. The HPBW is 0°.85. The contours are plotted every 3.1 K, starting from the lowest temperature of 41 K and up to 72 K. The color figure can be viewed online.

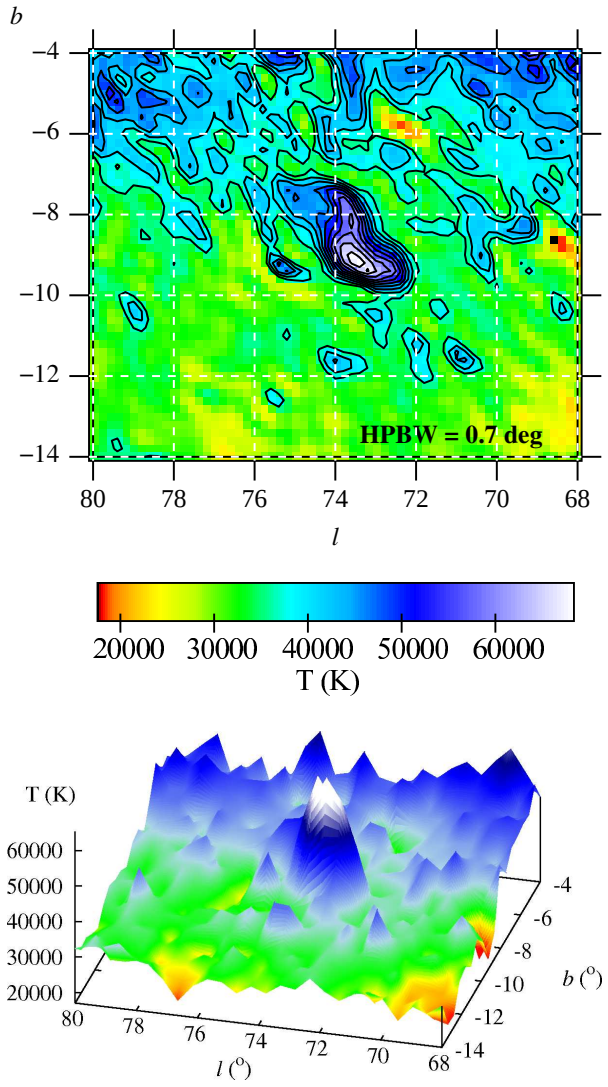

Fig. 5. The same as Figure 1, but for 34.5 MHz. The HPBW is 0°.7. The contours are plotted every 3550 K, starting from the lowest temperature of 34500 K and up to 70000 K. The color figure can be viewed online.

each frequency: average temperature of the loop is $<T_{\rm sum}> - T_{\rm back}$. The areas over which an average brightness temperature is determined at each of the five frequencies are taken to be as similar as possible within the limits of the measurement accuracy. $T_{\rm min}$ in Table 1 means the lower temperature limit between the background and the loop, and $T_{\rm max}$ means the upper temperature limit of the loop. So we used all measured values between $T_{\rm min}$ and $T_{\rm max}$, inside the corresponding regions of l and b, to calculate the brightness temperature of the loop including the background. The mean brightness temperature for the loop is found by subtracting the mean value of the background brightness temperature from the mean value of the brightness temperature over the area of the loop.

After deriving the mean brightness temperatures $T_{{\rm b},\nu}$, we have converted these values into surface brightness Σ_ν by:

$$\Sigma_\nu = \left(2k\nu^2/c^2\right) T_{{\rm b},\nu}\,, \qquad (1)$$

where k is the Boltzmann constant and c the speed of light. Results are given in Table 1.

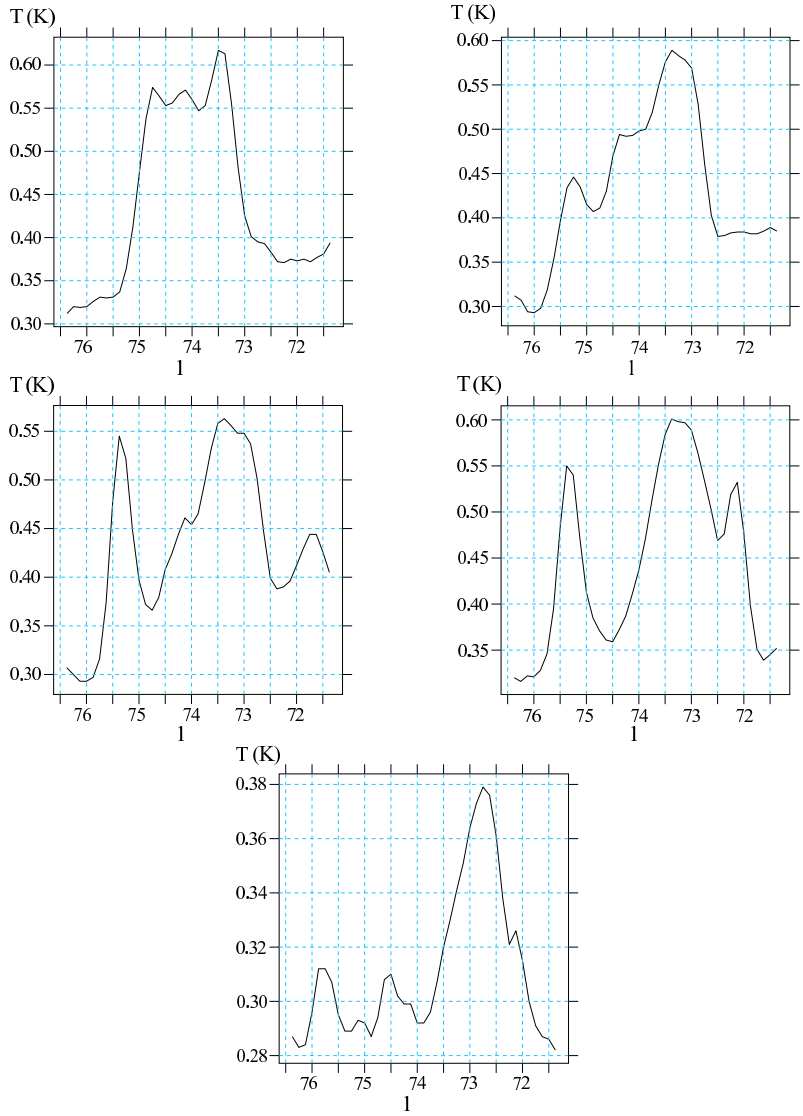

Fig. 6. Temperature profiles at 2720 MHz for Galactic longitude from 76°.5 to 71°.5 and for the following values of Galactic latitude: $b = -7°.5$ (top left), $b = -8°$ (top right), $b = -8°.5$ (middle left), $b = -9°$ (middle right) and $b = -10°$ (bottom). Temperatures are given in K, and Galactic longitudes in degrees. Notice that the bottom figure shows the temperature profile at a latitude which lies outside (but close enough to) the loop, and from that profile we can see what is the highest temperature of the background at $b = -10°$, at 2720 MHz (not of the loop with background).

3. RESULTS

The radio continuum maps are used for determining the area of the Cygnus loop and for deriving brightness temperatures over it. At each of the five frequencies, the areas are determined to be as similar as possible within the limits of measurement accuracy. There are still some differences between these areas and we think that the major causes of differing borders between the five frequencies are small random and systematic errors in the data. The surface brightnesses of SNRs must be above the sensitivity limit of the observations, and must be clearly distinguishable from the Galactic background emission (Green 1991). As it is very difficult to resolve the fainter parts of the loop from the background, they are not taken into account. For evaluation of the brightness temperatures over the area of the loop we had to take into account background radiation (see Webster 1974). Borders enclosing the spurs are defined to separate the spur and its background. For the method of calculation see also Borka (2007), Borka et al. (2008) and Borka Jovanović & Urošević

TABLE 1

TEMPERATURES AND BRIGHTNESSES OF THE CYGNUS RADIO LOOP AT 2720, 1420, 820, 408 AND 34.5 MHz

Frequency (MHz)	Temperature limits $T_{\rm min}$, $T_{\rm max}$ (K)	Temperature (K)	Brightness [10^{-22} W/(m^2 Hz Sr)]
2720	0.395, 0.66	0.160 ± 0.005	3.64 ± 0.12
1420	4.2, 4.9	0.49 ± 0.05	3.04 ± 0.30
820	10.1, 14.0	2.30 ± 0.20	4.75 ± 0.40
408	41, 72	15.3 ± 1.0	7.83 ± 0.50
34.5	34500, 70000	13960 ± 700	50.97 ± 2.56

TABLE 2

SPECTRAL INDICES FOR CYGNUS LOOP FROM $T-T$ PLOTS, BETWEEN 2720, 1420, 820, 408 AND 34.5 MHz

Frequency (MHz)	2720	1420	820	408	34.5
2720	···	1.52 ± 0.35	1.96 ± 0.53	2.35 ± 0.26	2.57 ± 0.23
1420	2.22 ± 0.76	···	2.27 ± 0.64	2.60 ± 0.28	2.67 ± 0.25
820	2.64 ± 0.61	3.10 ± 0.64	···	2.82 ± 0.31	2.82 ± 0.10
408	2.67 ± 0.26	2.79 ± 0.28	3.10 ± 0.31	···	2.78 ± 0.15
34.5	2.86 ± 0.23	2.95 ± 0.25	2.92 ± 0.10	2.94 ± 0.15	···

(2009b). As mentioned in these papers, if the value of $T_{\rm min}$ is changed by a small amount, the brightness contours become significantly different. If $T_{\rm min}$ is too small, the area of the spur becomes confused with the background and it becomes obvious that the border has been incorrectly chosen.

The results are given in Tables 1, 2 and 3. $T_{\rm min}$, given in the second column of Table 1, is the lower temperature limit, while $T_{\rm max}$ is the upper temperature of the loop and it is also the upper temperature limit (because there are no other superposed sources). These temperature limits enable us to distinguish the loop from the background. Then we derived the surface brightnesses using equation (1) for each frequency.

The values for the brightnesses in units of 10^{-22} W/ (m^2 Hz Sr) can be compared with results for the flux densities in Jy. The flux densities can be transformed into brightnesses or vice versa, taking into account that the frequencies have to be the same. Knowing the loop size Ω, the flux densities S_ν given in Jy can be transformed to brightnesses given in 10^{-22} W/(m^2 Hz Sr) by:

$$\Sigma_\nu = S_\nu \times 10^{-26}/\Omega\,. \qquad (2)$$

TABLE 3

BRIGHTNESS OF CYGNUS RADIO LOOP REDUCED TO 1000 MHz[a]

Frequency (MHz)	Brightness at 1000 MHz (10^{-22} W/(m^2 Hz Sr))
2720	7.05 ± 0.86
1420	3.84 ± 0.52
820	4.17 ± 0.29
408	4.33 ± 0.07
34.5	5.52 ± 1.40

[a]Using spectral index derived in this paper: $\beta_5 = 2.66 \pm 0.09$ (from the spectrum of all five frequencies 2720, 1420, 820, 408 and 34.5 MHz).

By use of the spectral indices, the brightnesses can be reduced to 1000 MHz according to the relation:

$$\Sigma_{1000} = \Sigma_\nu (1000/\nu)^{(2-\beta)}\,, \qquad (3)$$

where the temperature spectral index $\beta = \alpha + 2$, and α is the spectral index defined by $S_\nu \propto \nu^{-\alpha}$.

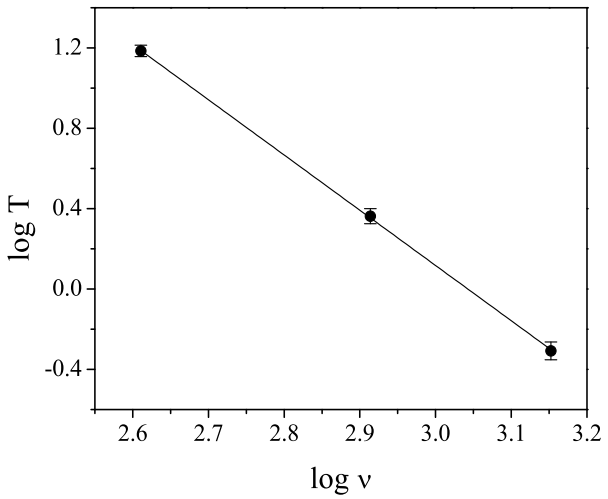

Fig. 7. Cygnus loop spectrum: temperature versus frequency, for three measurements (at 408, 820 and 1420 MHz).

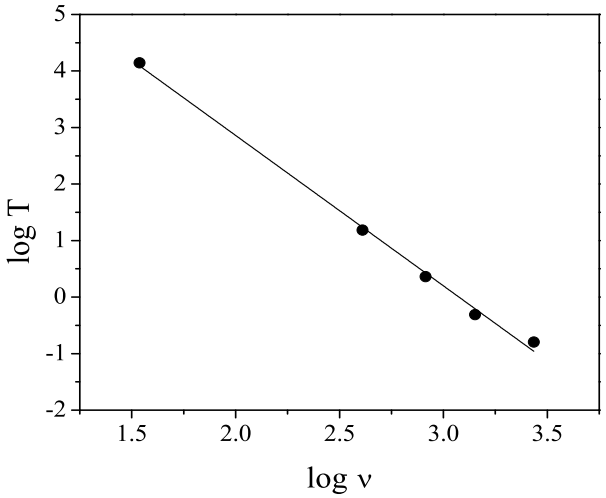

Fig. 8. Cygnus loop spectrum: temperature versus frequency, for five measurements (at 34.5, 408, 820, 1420 and 2720 MHz).

3.1. *Spectrum*

The spectrum was generated using mean temperatures at five different frequencies. The best-fit straight line spectrum enables the calculation of the spectral index as the negative value of the line's direction coefficient. In Figure 7 we show the spectrum for the three middle frequencies: 1420, 820 and 408 MHz because they are very well fitted with a straight line (see Figure 7). Frequencies 2720 and 34.5 MHz, lie on the very high and very low ends of the spectrum, as presented in Figure 8. If for the calculation of the spectral index we take only three frequencies 1420, 820 and 408 MHz, the result would be $\beta_3 = 2.76 \pm 0.03$. From a linear fit to all five frequencies 2720, 1420, 820, 408 and 34.5 MHz, we obtain $\beta_5 = 2.66 \pm 0.09$. It is a steeper spectral index in comparison to the average value for Galactic SNRs $\beta = 2.5$ (in Green's catalogue (Green 2009) the adopted value for the spectral index is not given because of its variability). The Cygnus loop is relatively old SNR. The shock wave has to be weak for evolved SNRs. The steeper spectral indices of SNRs should be expected for the smaller shock wave velocities. This is a result obtained from the diffuse particle acceleration theory (Bell 1978a,b). Additionally, the Cygnus loop probably expands in a low density environment. It looks like the large Galactic radio loops – evolved SNRs with steep spectral indices, immersed in a low density environment (see Borka 2007; Borka et al. 2008, and references therein).

The values we obtain, $\beta_3 = 2.76 \pm 0.03$ (from three frequencies), $\beta_5 = 2.66 \pm 0.09$ (from all five frequencies), are greater than 2.2 and confirm the non-thermal origin of the Cygnus loop emission. From Figure 8 it can be noticed that a linear fit is quite satisfactory. The value for the brightness temperature spectral index of the Cygnus loop is rather steep. This is at the high end of the spectral index distribution for SNRs as suggested in Clark & Caswell (1976).

3.2. $T - T$ *plot*

The measured data have different resolutions for different frequencies (see § 2.1), and therefore in order to obtain $T - T$ plots the data were retabulated: the higher resolution maps are convolved to the resolution of the lowest resolution map. In this way, we convolved data at 2720, 1420, 408 and 34.5 MHz to $0^\circ.5 \times 0^\circ.5$ resolution, which is the sampling rate of the 820 MHz survey. These retabulated data are presented in Figure 9 for the following frequencies: 2720 MHz (top left), 1420 MHz (top right), 820 MHz (middle left), 408 MHz (middle right) and 34.5 MHz (bottom). Then, for each frequency pair we used only the common points [with the same (l, b)] which belong to the loop area at both frequencies. In this way, we reduced the loop area to the same area for different frequencies. The obtained $T - T$ plots for five pairs of frequencies enabled the calculation of the spectral indices. We calculated two β values for each of these pairs: between 2720–1420, 2720–820, 2720–408, 2720–34.5, 1420–820, 1420–408, 1420–34.5, 820–408, 820–34.5 and 408–34.5 MHz. They are presented in Table 2.

For each of the ten frequency pairs, by interchanging the dependent and independent variables we obtained two β values for each pair and the mean value of these results is adopted as the radio spectral index, as suggested in Uyaniker et al. (2004). Regarding only three frequencies (because their spectrum lies on straight line, see Figure 7) 1420, 820 and 408 MHz, the average value of spectral index from $T-T$ is $<\beta_{TT}>_3 = 2.78 \pm 0.41$. Taking into account all five frequencies, we get $<\beta_{TT}>_5 = 2.63 \pm 0.30$. It can be noticed that, as expected, this value agrees well with the corresponding value obtained from the spectrum (see Uyaniker et al. 2004).

Then we calculated the mean value of the spectral index: regarding spectrum and $T-T$ graphs. Between 1420, 820 and 408 MHz we obtained $<\beta>_3 = 2.77 \pm 0.22$, and between 2720, 1420, 820, 408 and 34.5 MHz we obtained $<\beta>_5 = 2.64 \pm 0.20$.

4. DISCUSSION

The spectral index variations with position of more spatial features within the Cygnus loop can be found in the paper by Leahy (1999). He studied radio spectral indices by the $T-T$ plot method between 2695, 1420 and 408 MHz and found that the bright radio filaments all show negative curvature (steeper at higher frequency), and that regions dominated by diffuse emission show positive curvature (flatter at higher frequency).

It can be noticed that the mean value of spectral index for the Cygnus loop is a little higher then the corresponding value obtained from the literature (see Uyaniker et al. 2004 or Leahy & Rogers 1998). The reason for this is the different areas used for data of the Cygnus loop in these papers. In both papers they used square areas (see page 917 from Uyaniker et al. 2004, and page 786 from Leahy & Roger 1998). In these square areas they took into account parts of the Cygnus loop and parts of the background radiation near the loop (these parts we do not take into account). We take in account only higher intensity regions from these areas (see Figures 1–5).

In order to compare our values for the brightnesses with results for the fluxes given in other papers, we transform their calculated fluxes into brightnesses at 1000 MHz. Knowing the loop size Ω we reduce the flux densities given in Jy to brightnesses given in $10^{-22}\,\mathrm{W/(m^2\ Hz\ Sr)}$ by means of equation (2) and then, using the spectral indices, the brightnesses are extrapolated to 1000 MHz according to relation (3).

In our previous paper (Borka Jovanović & Urošević 2009a) we transformed the flux densities for the Cygnus Loop given in Roger et al. (1999) at 22 MHz ($S_\nu = 1378$ Jy) and Reich et al. (2003) at 863 MHz ($S_\nu = 184$ Jy) into Σ_{1000} using the loop size $\Omega = 240' \times 170'$ from Reich et al. (2003) and the spectral index $\beta = 2.49$ from Trushkin (2002). We obtained that the values from Borka Jovanović & Urošević (2009a) agree with previous data. In this paper, we use our derived value for the spectral index $\beta_5 = 2.66 \pm 0.09$, and obtain even better agreement. From the flux densities given in the paper mentioned, we calculated the following values for radiation intensities: $\Sigma_{1000} = 3.22 \times 10^{-22}\,\mathrm{W/(m^2\ Hz\ Sr)}$ from the flux given in Roger et al. (1999) and $\Sigma_{1000} = 4.84 \times 10^{-22}\,\mathrm{W/(m^2\ Hz\ Sr)}$ from the flux given in Reich et al. (2003).

Using our calculated β_5 and applying relation (3) to our calculated values of Σ_ν at 2720, 1420, 820, 408 and 34.5 MHz, for Σ_{1000} we obtain the values given in Table 3. Absolute errors for brightnesses at 1000 MHz are calculated in this way: $\Delta\Sigma_{1000} = (\Sigma_{1000}/\Sigma_{\nu 1})\,(\Delta\Sigma_{\nu 1} + \Sigma_{\nu 1} \cdot \ln(\nu_1/1000) \cdot \Delta\beta)$, where ν_1 takes values 2720, 1420, 820, 408 and 34.5 MHz.

Information about variations of the brightness and the spectrum over the radio image is presented by Leahy & Roger (1998) and by Uyaniker et al. (2002). The average values reduce the information imprinted in variations of brightness and spectrum over the radio image but give us other interesting information, like the explosion energy, the surface brightness and the distance to the Cygnus radio loop.

With regard to the loop borders in Figures 1–5, we derived the loop area at each frequency, as well as the corresponding angular radii (see Table 4). An angular radius is obtained in this way: our derived loop area, when approximated with a circle of the same area, gives the possibility of determining the angular radius as $\theta = \sqrt{\Omega/\pi}$. These areas can be compared to the areas calculated by other authors, e.g., $9(^\circ)^2.80$ at 1420 MHz (Leahy 2002) and $11(^\circ)^2.33$ at 863 MHz (Reich et al. 2003). When their areas are recalculated into angular radii in the way we described, the result are: $1^\circ.77$ at 1420 MHz (Leahy 2002) and $1^\circ.90$ at 863 MHz (Reich et al. 2003). It can be noticed that we obtained somewhat smaller values, but it has to be taken into account that other authors estimated only the rectangular map size while we estimated the loop size (inside its contour borders) exactly.

The relation between surface brightness (Σ) and diameter (D) for supernova remnants (SNRs) –so-called the $\Sigma - D$ relation– is appropriate for the description of the radio brightness evolution of these sources. The empirical relations should be used

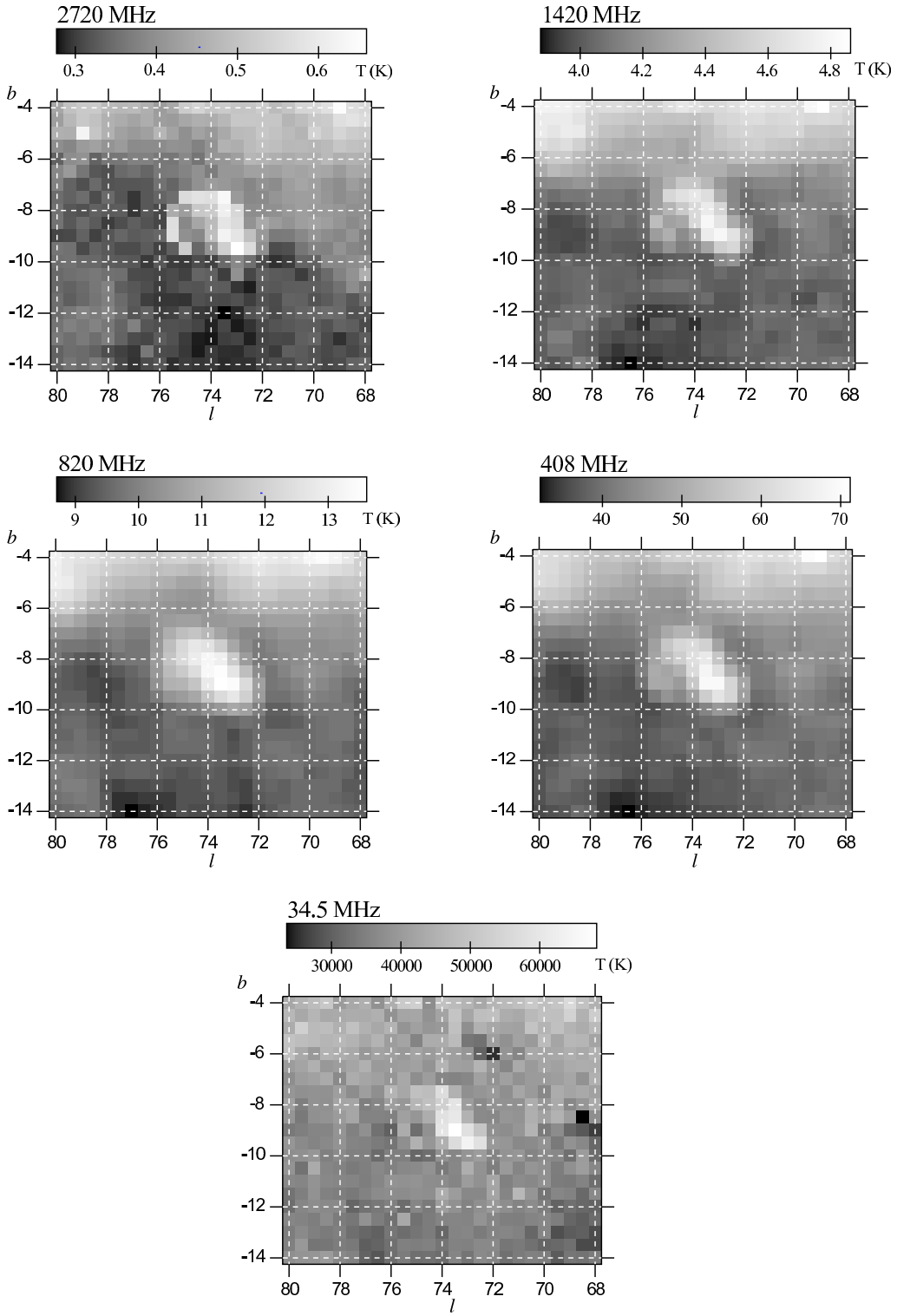

Fig. 9. The data retabulated to $0^\circ.5 \times 0^\circ.5$ resolution, for the following frequencies: 2720 MHz (top left), 1420 MHz (top right), 820 MHz (middle left), 408 MHz (middle right) and 34.5 MHz (bottom). The HPBWs for these frequencies are $0^\circ.35$, $0^\circ.59$, $1^\circ.2$, $0^\circ.85$ and $0^\circ.7$, respectively. The gray scales of temperatures are also given.

TABLE 4

THE CYGNUS LOOP AREAS Ω AND ANGULAR RADII θ AT THE FIVE FREQUENCIES

Frequency (MHz)	Ω [(°)^2]	θ (°)
2720	7.52	1.547
1420	8.64	1.658
820	9.46	1.735
408	9.88	1.773
34.5	8.44	1.639

with caution because of the limited usefulness due to selection effects (see Green 2009; Urošević 2010, and references therein). The updated theoretical relations were derived by Duric & Seaquist (1986), based on the Bell (1978a,b) diffuse shock particle acceleration theory, and by Berezhko & Völk (2004) based on the non-linear kinetic theory of the diffuse shock acceleration mechanism. The $\Sigma - D$ diagram at 1 GHz with the theoretically derived evolutionary tracks taken from Berezhko & Völk (2004) and with our value for the Cygnus loop superposed, is shown in Figure 10. To superpose the Cygnus position, we used the following results of our calculations: the mean value of the brightnesses at 1 GHz and the diameter, calculated as $D = 2r \sin\bar{\theta}$, where $\bar{\theta} = 1°.67$ is the mean angular radius for all five frequencies. The distance $r = 0.44$ kpc is taken from Green's (2009) catalogue of SNRs. So we added this point to the diagram: (D, Σ) = (25.7 pc, 4.98×10^{-22} W/(m^2 Hz Sr)). From its position in this diagram it can be concluded that the Cygnus loop evolves in the low density environment and the initial energy of the supernova (SN) explosion was relatively low (see Figure 10).

4.1. *Flux density spectrum*

On the basis of the values for brightnesses given in the fourth column of Table 1 and our calculated values for the loop size Ω (Table 4), we derived flux values in Jy. The calculated flux densities are given in Table 5. As the Cygnus loop is well studied SNR, it is possible to perform a multi-frequency spectral study. In Figure 11 we present a summary of some results obtained from other papers and from our study. Our results are labeled with asterisks. In this figure, we have seventeen results for the flux density values S_ν of Cygnus loop derived in several papers (values are given in Table 3 of Uyaniker et al. (2004) and five results from our paper.

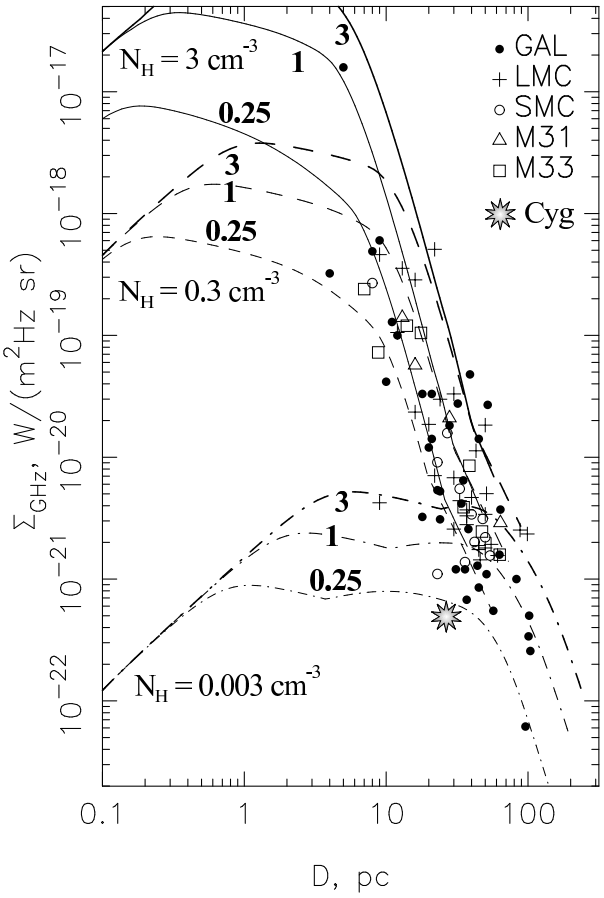

Fig. 10. The surface brightness versus diameter diagram from Berezhko & Völk (2004), with the value for Cygnus loop added. Three different densities for the interstellar matter (ISM) ($N_{\rm H}$ = 3, 0.3 and 0.003 cm^{-3}) are presented, plus three values for the (SN) explosion energy ($E_{\rm SN} = 0.25$, 1 and 3×10^{51} erg).

It can be seen from Figure 11 that our added flux values fit very well among other fluxes, which shows the correctness of our method, and also that we determined the loop area and its brightness well.

TABLE 5

FLUX DENSITIES (Jy) THAT WE CALCULATED AT THE FIVE FREQUENCIES

Frequency (MHz)	Flux density (Jy)
2720	83.37±2.60
1420	80.05±8.13
820	139.35±12.10
408	235.44±15.36
34.5	1309.04±65.65

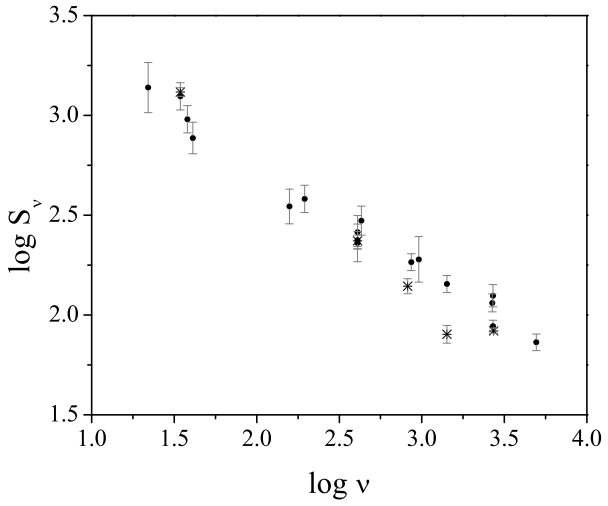

Fig. 11. Spectrum of Cygnus Loop: flux versus frequency for additional different frequencies, obtained from all available flux density values (values are given in Table 3 in Uyaniker et al. 2004) and from values calculated in this paper. We identify our values by asterisks.

5. CONCLUSIONS

The main result is to use a method for determining the brightness temperature given in Borka (2007) which is developed for large radio loops, and to show here that this method is applicable for much smaller loops, e.g., the Cygnus loop. We check the method by applying it to the Cygnus radio loop over a wide range of frequencies. It is in good agreement with the method of $T-T$ graphs and with results obtained with other methods. This method is quite simple because we use a brightness temperature isoline to define the border of the Cygnus loop. Other authors are using different square or rectangular areas to determine the area of the loop and to calculate spectral indices, brightness temperatures and the flux density of the loop (Uyaniker et al. 2004, page 917, and Leahy & Roger 1998, page 786). Also, we calculate the flux for the Cygnus loop and compare our results with those of other authors in different ranges of frequencies. We show that our results are in good agrement with other work.

We estimate the temperatures and brightness of the Cygnus loop SNR on the basis of observations of the continuum radio emission at the frequencies: 2720, 1420, 820, 408 and 34.5 MHz (this paper and Borka Jovanović & Urošević (2009a). The sensitivity of the brightness temperatures are: 5 mK for 2720 MHz, 50 mK for 1420 MHz, 0.2 K for 820 MHz, 1.0 K for 408 MHz and about 700 K $T_{\rm b}$ for 34.5 MHz. At a frequency of 2720 MHz the measurements are the most precise (they have the smallest relative errors) so positions of the brightness temperature contours of the loop are the most realistic for this frequency.

The borders between the five frequencies are somewhat different for this SNR, probably due to small, random and systematic errors in the calibrated data. Also, we suppose that there are uncertainties of about $(2 \times \Delta T)$ 10 mK for 2720 MHz, 100 mK for 1420 MHz, 0.4 K for 820 MHz, 2.0 K for 408 MHz and about 1400 K $T_{\rm b}$ for 34.5 MHz, in the border due to measurement errors, and there is a tiny difference in the absorption of radio emission in the interstellar medium at different wavelengths (Pacholczyk 1970).

We determine the average brightness temperature for the Cygnus radio loop region, after subtraction of a background level. Our values (when all reduced to 1000 MHz for comparison) are in good agreement with the earlier results. We present the radio continuum spectrum of the Cygnus loop using average brightness temperatures at five different frequencies. As can be seen from Figures 7 and 8, the linear fit provides a reliable spectral index. We present the $T-T$ plots which also enable the calculation of spectral index.

Also, from our results it can be concluded that the Cygnus loop evolves in a low density environment and that the initial energy of SN explosion was relatively low. This can be read off after superposing the position of this loop onto a theoretical $\Sigma-D$ diagram from Berezhko & Völk (2004), which was derived from non-linear kinetic theory of diffuse shock acceleration mechanism.

We show that our method for defining a loop border and for determining the values of temperature and brightness, which was developeded for main Galactic loops I-VI, could be applicable to all SNRs.

The authors are grateful to the referee whose suggestions substantially improved the paper. This research is supported by the Ministry of Science of the Republic of Serbia through project No. 176005.

REFERENCES

Aschenbach, B., & Leahy, D. A. 1999, A&A, 341, 602
Bell, A. R. 1978a, MNRAS, 182, 147
_____. 1978b, MNRAS, 182, 443
Berezhko, E. G., & Völk, H. J. 2004, A&A, 427, 525
Berkhuijsen, E. M. 1972, A&AS, 5, 263
Borka, V. 2007, MNRAS, 376, 634
Borka, V., Milogradov-Turin, J., & Urošević, D. 2008, Astron. Nachr., 329, 397

Borka Jovanović, V., & Urošević, D. 2009a, Publ. Astron. Obs. Belgrade, 86, 101
_____. 2009b, Astron. Nachr., 330, 741
Clark, D. H., & Caswell, J. L. 1976, MNRAS, 174, 267
Dickel, J. R., & Willis, A. G. 1980, A&A, 85, 55
Duric, N., & Seaquist, E. R. 1986, ApJ, 301, 308
Dwarakanath, K. S., & Udaya Shankar, N. 1990, J. Astrophys. Astron., 11, 323
Green, D. A. 1984, MNRAS, 211, 433
_____. 1991, PASP, 103, 209
_____. 2004, Bull. Astron. Soc. India, 32, 335
_____. 2006, A Catalogue of Galactic Supernova Remnants (2006 April version) (Cambridge: Cavendish Laboratory)
_____. 2009, Bull. Astron. Soc. India, 37, 45
Haslam, C. G. T., Salter, C. J., Stoffel, H., & Wilson, W. E. 1982, A&AS, 47, 1
Keen, N. J., Wilson, W. E., Haslam, C. G. T., Graham, D. A., & Thomasson, P. 1973, A&A, 28, 197
Kundu, M. R., & Becker, R. H. 1972, AJ, 77, 459
Leahy, D. A. 1999, ASP Conf. Ser. 168, New Perspectives on the Interstellar Medium, ed. A. R. Taylor, T. L. Landecker, & G. Joncas (San Francisco: ASP), 437
_____. 2002, AJ, 123, 2689
Leahy, D. A., & Roger, R. S. 1998, ApJ, 505, 784
Leahy, D. A., Roger, R. S., & Ballantyne, D. 1997, AJ, 114, 2081
McKee, C. F., & Ostriker, J. P. 1977, ApJ, 218, 148
Pacholczyk, A. G. 1970, Radio Astrophysics. Nonthermal Processes in Galactic and Extragalactic Sources (San Francisco: Freeman)
Patnaude, D. J., Fesen, R. A., Raymond, J. C., Levenson, N. A., Graham, J. R., & Wallace, D. J. 2002, AJ, 124, 2118
Reich, P., & Reich, W. 1986 A&AS, 63, 205
Reich, W., Zhang, X., & Fürst, E. 2003, A&A, 408, 961
Reif, K., Reich, W., Steffen, P., Müller, P., & Weiland, H. 1987, Mitt. Astron. Ges., 70, 419
Roger, R. S., Costain, C. H., Landecker, T. L., & Swerdlyk, C. M. 1999, A&AS, 137, 7
Salter, C. J. 1983, Bull. Astron. Soc. India, 11, 1
Sun, X. H., Reich, W., Han, J. L., Reich, P., & Wielebinski, R. 2006, A&A, 447, 937
Trushkin, S. A. 2002, CATS Database-Astrophysical CATalogs Support System, SNRs Spectra Request Form, `http://www.sao.ru/cats/snr_spectra.html`
Urošević, D., Vukotić, B, Arbutina, B., & Sarevska, M. 2010, ApJ, 719, 950
Uyaniker, B., Reich, W., Yar, A., & Fürst, E. 2004, A&A, 426, 909
Uyaniker, B., Reich, W., Yar, A., Kothes, R., & Fürst, E. 2002, A&A, 389, L61
Webster, A. S. 1974, MNRAS, 166, 355

V. Borka Jovanović: Atomic Physics Laboratory (040), Vinča Institute of Nuclear Sciences, University of Belgrade, P.O. Box 522, 11001 Belgrade, Serbia (vborka@vinca.rs)
D. Urošević: Department of Astronomy, Faculty of Mathematics, University of Belgrade, Studentski trg 16, 11000 Belgrade, Serbia (dejanu@matf.bg.ac.rs).

Revista Mexicana de Astronomía y Astrofísica, **47**, 173–184 (2011)

A VARIANT OF THE TITIUS-BODE LAW

J. Daniel Flores-Gutiérrez[1] and Carlos García-Guerra[2]

Received 2010 June 28; accepted 2011 February 15

RESUMEN

En el estudio de la distribución geométrica de los planetas invariablemente se menciona la ley de Titius Bode como un intento de clasificar *grosso modo* sus distancias heliocétricas mediante una sucesión de números enteros. Con el descubrimiento de un gran número de objetos planetarios ahora se sustenta, en cierta medida, el principio básico de dicha ley al través de la determinación de más elementos orbitales. Abordamos brevemente una clasificación de los parámetros orbitales utilizando la constante de proporcionalidad de Kepler y discutimos el problema de la aplicación de la ley TB a sistemas extrasolares. También analizamos las funciones propuestas por diversos autores las cuales reproducen las distancias heliocéntricas de los planetas, y efectuamos una comparación con la variante a la ley Titius Bode que proponemos aquí.

ABSTRACT

The study of the geometric distribution of the planets invariably mentions the Titius Bode law as an attempt to classify their heliocentric distances through a succession of integer numbers. With the discovery of more planetary objects better support is given to the basic principle of the law through their orbital parameters. We briefly refer to a classification of orbital parameters using Kepler's proportionality parameter and discuss the problem of applying the TB Law to extrasolar systems. We also review work by various authors who have proposed functions which reproduce with some degree of certainty the planetary heliocentric distances, and we compare them to our variant of the Titius-Bode Law.

Key Words: planets and satellites: formation — planets and satellites: general — solar system: general

1. INTRODUCTION

In the late eighteenth century Johann Daniel Tietz proposed a numerical sequence with which he tried to reproduce the heliocentric distances of the planets, and which was included in the compendium *Contemplation of the Nature* written by Charles Bonnet in 1764. In 1772 the famous German astronomer Johann Bode included Titius' ideas (*Latin conversion of Tietz*) in his texts on astronomy. According to Titius' scheme, the mathematical formulation is written in terms of the parameter N given by the integers 0, 3, 6, 12, 24, 48, 96 and 192 according to the order of the planets Mercury, Venus, Earth, Mars, Jupiter, Saturn and Uranus.

In terms of powers of two (2^n), the orbital parameters are determined by the equation $R_n = 4 + 3 \cdot 2^n$ where $N = -\infty, 0, 1, 2, 3, ...$, also in the order of the planets (Nieto 1970) or as proposed most recently $R_n = 0.4 + 0.3 \cdot 2^{n-2}$ with $n = 1, 2, 3, ...$ (Holton & Brush 2001). An interesting historical analysis of the progression was presented by Jaki (1972). Many discussions have arisen around the Titius-Bode model like those of Ovenden (1972, 1975) who analyzed the evolution of the circular and elliptical orbits and found that a Titius-Bode planetary distribution is a distribution of least interaction action between the planets, as well as how they evolve numerically into a resonant system from arbitrary initial conditions of position and velocity. Nieto (1970, 1975) made a detailed study of the Titius-Bode Law, and Horedt, Pop, & Ruck (1977) described a numerical application of the generalized Titius law for more than nine

[1]Instituto de Astronomía, Universidad Nacional Autónoma de México, Mexico.

[2]Facultad de Arquitectura, Universidad Nacional Autónoma de México, Mexico.

TABLE 1

EMPIRICAL SERIES REPRODUCING THE HELIOCENTRIC DISTANCES OF THE PLANETS

MODIFIED TITIUS BODE LAW										
This Paper		This paper								
Body	TB	TBmod			a	T	a_p	T_p	Δa_n	ΔT_n
	N	X	X'	N'	AU	Year	AU	Year	%	%
Mercury	0	0	0	0	0.4	0.253	0.387	0.251	3.4	0.8
Venus	3	0	3	3	0.7	0.586	0.723	0.615	−3.2	−4.8
Earth	6	3	3	6	1.0	1.000	1.000	1.000	0.0	0.0
Mars	12	6	6	12	1.6	2.024	1.523	1.881	5.0	7.6
Ceres	24	12	12	24	2.8	4.685	2.765	4.600	1.2	1.9
Jupiter	48	24	24	48	5.2	11.858	5.202	11.862	−0.1	−0.0
Saturn	96	48	48	96	10.0	31.623	9.510	29.458	5.2	7.3
Uranus	192	96	96	192	19.6	86.773	19.25	84.013	1.8	3.3
Neptune		192	96	288	29.2	157.788	30.19	164.749	−3.3	−4.2
Pluto		288	96	384	38.8	241.684	39.50	247.492	−1.8	−2.3

TB is the original succession N defining the Titius-Bode law. TBmod is the modified TB law by means of the empirical succession X and X' and $N' = X + X'$. In Columns a and T we give the semi-major axes of orbits of the planets calculated by the TBmod model $(N' + 4)/10$ and the period computed by the way of the Third Law of Kepler, respectively. In Columns a_p and T_p we present the astronomical values of the observed orbital parameters. In the last two columns we give the determination of the error between the computed heliocentric distances and the astronomical ones Δa and ΔT, where the values tending to zero indicate a good degree of certainty.

planetary objects. Patton (1988) obtained the TB Law for Lagrange multipliers and applied it with acceptable results to eleven large asteroids. Through the approach of Monte Carlo, Lynch (2003) concluded that it is not possible to assure that the Titius-Bode Law explains the distribution of planets and satellites and Chang (2008) found that the distribution of the ratio of rotational periods in the 55 Cnc system is apparently inconsistent with that derived from the Titius-Bode Law. More recently Kotliarov (2009) has presented an interesting discussion of the Butusov model and proposed a generating function for the distribution of the planets.

2. MODIFIED TITIUS-BODE LAW

We propose a modification to the Titius-Bode Law (TBmod) by combining the sequences X (0, 0, 3, 6, 12, 24, 48, 96, 192, 288, 384, 576, 960, 1728) and X' (0, 3, 3, 6, 12, 24, 48, 96, 96, 96, 192, 384, 768, 1536), which were derived empirically by García Guerra (2005). The sum of the sequences $N' = X + X'$ reproduces one by one the terms of the succession of Titius-Bode (TB) from Mercury to Pluto, including the approach to the asteroid Ceres and other distant planetary objects. The semi-major axes of the planets are derived from the modified TB formulation $a = (N' + 4)/10$ which shows the curvilinear distribution of distances for each one of them (Figure 1). We presented the exponential function fit $r = e^{0.6122x-2.8176}$, $R^2 = 0.9990$ obtained from the interpolation ($r = Ae^{x/t}$) and we compared it with the semi-major axes of major planetary bodies and other small objects, among them Ceto, Eris, Sedna and the distant object SQ372.

In Table 1 we display the orbital parameters a and T calculated with the TBmod model, and the data for a_p and T_p (Astronomical Almanac 2010); in the columns $\Delta a = (a_n - a_p)/a_p$ (Kotliarov 2008) and $\Delta T = (T_n - T_p)/T_p$ we give the proportionality ratios between the calculated and observed values to measure the degree of certainty, which is considered acceptable if their values are close to zero. In our case these TBmod ratios have values of less than 5% and 8% respectively. One of our goals is to determine some kind of mathematical expression that would represent the general TBmod behavior, and to compare it with tendencies that show the different models deduced from the TB law summarized in Table 2.

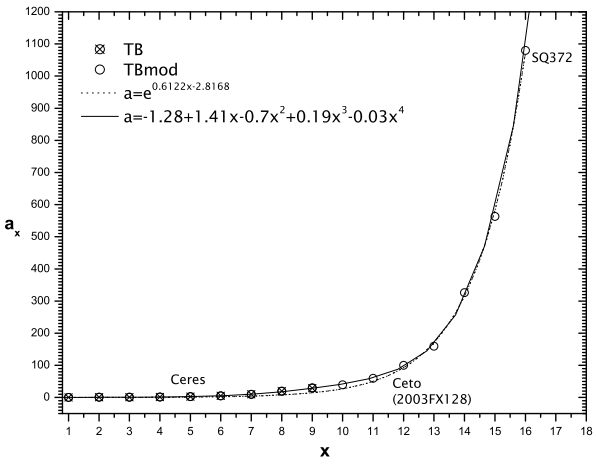

Fig. 1. Distribution of the semi-major axes of the planets and some small objects, given by the original and modified Titius-Bode Law, TB and TBmod respectively. We also present two interpolations that summarize the combination with an exponential function ($r = Ae^{x/t}$) and a seventh order polynomial (we only display the five first terms of the series), showing interpolated fits from Neptune to the interior region of the Kuiper Band.

Given the sequence of N' integer numbers; we carry out a setup of numerical operations in order to construct a function 2^n, which leads us to write this sequence like multiples of the common factor $3 \cdot 2^5$ whose first value $N' = 0$ for $n = 1$ (Mercury) we took into account in the discussion even though it does not exactly reproduce value the 0.387 of Mercury (Table 1). The resulting equations are:

$$r_n = 0.4 + 9.6 \cdot 2^{n-7}\,, \qquad n \leq 8 \qquad (1)$$

$$r_n = 29.2\,, \qquad n = 9 \qquad (2)$$

$$r_n = 29.2 + 9.6 \cdot \Sigma_{i=10}^{n}\ 2^{i-10}. \quad n \geq 10 \qquad (3)$$

If we arrange the elements $n = 9$ and $n \geq 9$ we realize that they constitute the total sum of the geometric progression given by $(2^{n-9} - 1)$, so that eventually we obtain the modified TBmod model, governed by two generic intervals of arithmetic and geometric progressions, respectively

$$r_n = 0.4 + 9.6 \cdot 2^{n-7}\,, \qquad n \leq 8 \qquad (4)$$

$$r_n = 19.6 + 9.6 \cdot 2^{n-9}\,, \qquad n \geq 9 \qquad (5)$$

Among the distributions of planetary bodies shown in Table 1 we observed that they present tendencies in the internal region of the Solar System including the TBmod distribution (Figure 2), although some of them diverge for the outer planets and even more so for distant objects. Note that all the models have difficulty in reproducing the parameters of Mercury, so that historically it has been necessary to postulate special conditions for this planet; we shall see how to avoid this problem.

TABLE 2

SOME MODELS THAT FIT THE TITIUS-BODE LAW

Titius-Bode Model	Reference
$r_n = 0.3 + 0.3 \cdot 2^n$	Wurm (1803)[a]
$n = -1, 0, 1, 2, ..., 6$	
$r_n = 0.2792 \cdot 1.53^n$	Armellini (1921)[a]
$n = 1, 2, 3, ..., 11$	
$r_n = 0.4 + 0.0075 \cdot 2^n$	Nicolini (1957)[a]
$n = -1, 0, 1, 2, ..., 6$	
$r_n = 0.2792 \cdot 1.52^n$	Munini & Armellini (1978)[a]
$n = 1, 2, 3, ..., 11$	
$r_n = 0.283 \cdot 1.52^n$	Badolati (1982)
$n = 1, 2, ...$	
$r_n = 0.4 + 0.3 \cdot 2^{(n-2)}$	Holton & Brush (2001)
$n = -\infty, 0, 1, 2, ..., 9$	
$r_n = e^{0.53074n - 1.51937}$	Ortiz et al. (2007)
$n = 0, 1, 2, 3, 4, ...$	
$r_n = e^{0.5894n - 1.65026}$	Poveda & Lara (2008)
$n = -\infty, 0, 1, 2, ..., 9$	
$r_n = e^{0.53707n - 1.661}$	Pankovic & Radakovic (2009)
$n = -1, 0, 1, 2, ..., 6$	

[a]As cited by Badolati 1982.

The actual distribution of the planets is contained in the TBmod curvilinear path, which coincides with the values of observed semi-major axes. We have chosen the logarithmic scale to better visualize the linear trace of the other six models. The Armellini and Bodolati model does not reproduce the distribution of planetary objects beyond Jupiter. The Nicolini and Holton & Brush models match the TBmod up to Uranus, as the Nicolini model is only for the planets. The Armellini and Bodolati models show values a_n that are very close. The case of the models of Wurm (not shown in Figure 2) falls short of all values Δa_n. In Ortiz et al. (2007), Poveda & Lara (2008), and Pankovic & Radakovic (2009) we observe that their traces exhibit a certain parallelism and proximity between the distribution of planetary objects. Finally, these cases including TBmod are those that best approximate the actual distribution of planetary objects. Of course the TBmod proposal shows the best approximation to the above mentioned distribution.

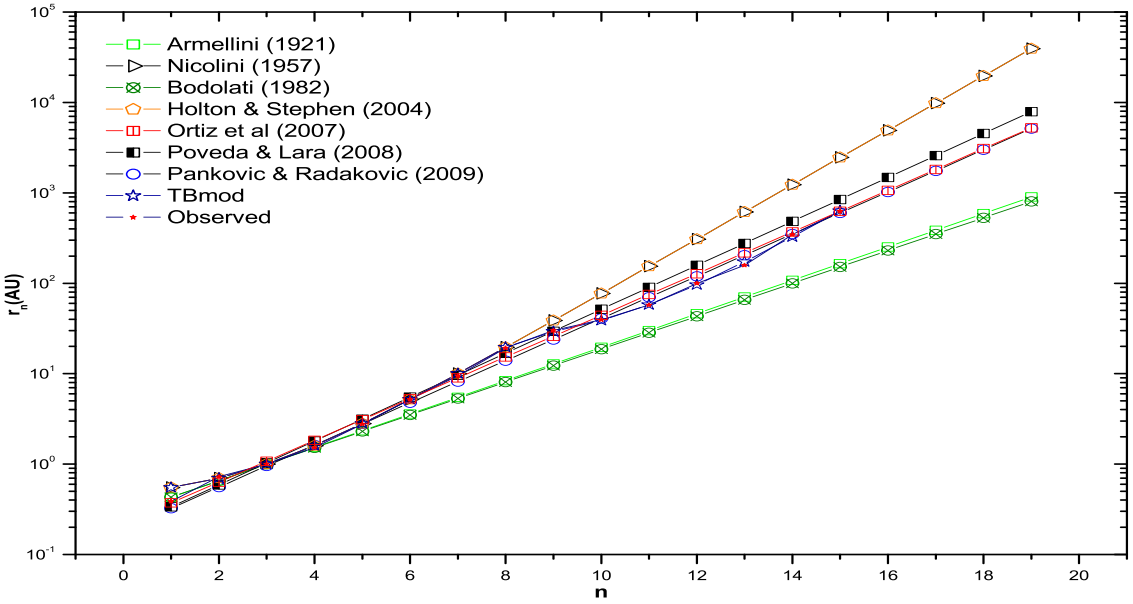

Fig. 2. Titius-Bode models of several authors including the TBmod variant proposed in this work. It is to be noted that the models are distributed above or below the real TB distribution of planets and the TBmod curvilinear path, which coincides with the values of the observed semi-major axes. We have chosen the logarithmic scale to better visualize the linear trace of the other six models. The color figure can be viewed online.

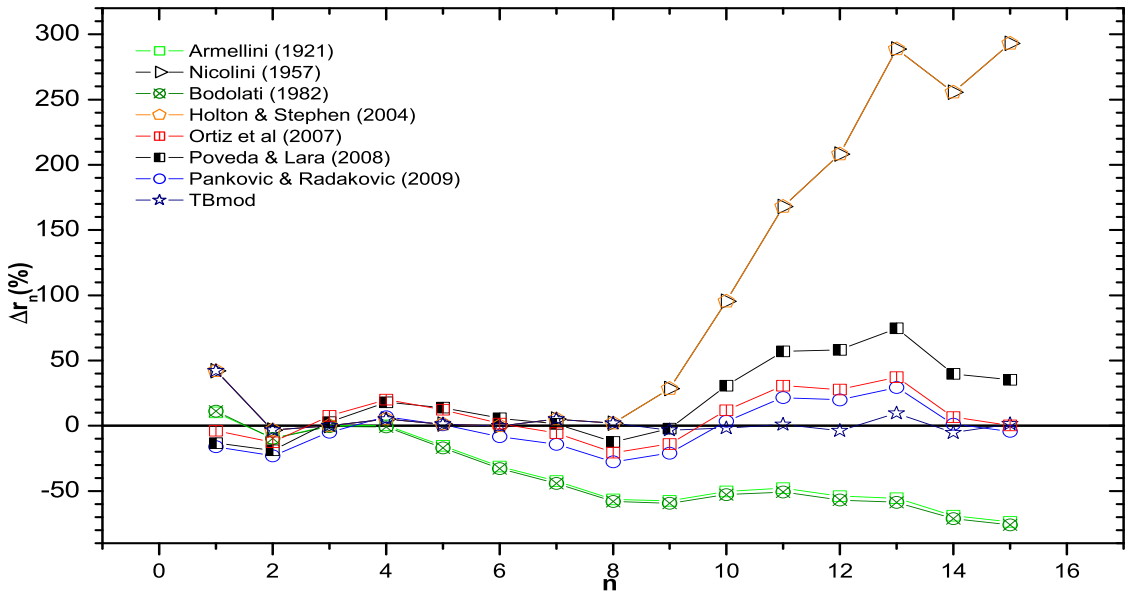

Fig. 3. The degree of certainty of the TB models proposed by various authors in terms of the ratio $\Delta a = (a_n - a_p)/a_p$. The color figure can be viewed online.

3. DEGREE OF CERTAINTY OF TBMOD

We realize that the modified TBmod model acceptably reproduces the orbital parameters a_n. We have examined the degree of certainty of the model through the differences between the calculated parameters (a_n, T_n) and those observed (a_p, T_p) by the ratio $\Delta a = (a_n - a_p)/a_p$, and similarly by calculating the ratio $\Delta T = (T_n - T_p)/T_p$, where the periods are the parameters obtained from Kepler's

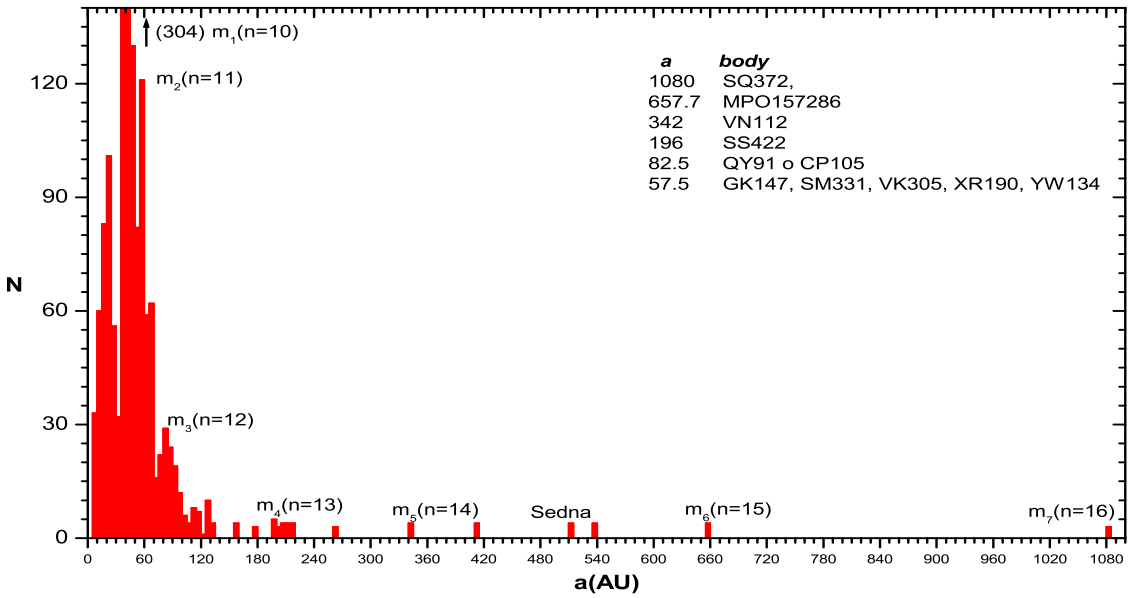

Fig. 4. Regions of accumulation in the Solar System of the small planetary bodies (taken from IAU Minor Planets Center: Observable Distant Minor Planets Orbital Elements). We observe that several of the small objects of the Solar System, like Eris, 2006HQ or Sedna, cannot be associated to the Titius-Bode Law. The color figure can be viewed online.

Third Law. If we apply this procedure to each of the models in Table 1 we will have an overview of the degree of certainty that the models possess as a whole.

The fit in Figure 3 shows the ratio between the values calculated for each model and the observed parameters. We can see that there are certain similarities up to the planet Saturn. However, there are divergences when we approach the outer regions of the Solar System. Note that the trace shows the smallest difference with the data for planetary objects due to the lower percentages of up to 10%. In this figure it is easy to identify the problem arising in all the models when reproducing the parameters of the planet Mercury; therefore it is normally avoided with an *ad hoc* number applied to this planet.

Another aspect that we want to emphasize is the fact that when general models are proposed what is implicitly done is to change the pattern of the sequence of integers for that of real numbers given by continuous functions $T = f(r)$. Thus, any Solar System object in principle will also fulfill this function and also the TB Law.

Given the large number of solar bodies now known we noticed that they fall on the semi-major axis distribution, although we know small objects like Eris, 2006HQ or Sedna that cannot be associated to the integers succession of the Titius-Bode Law. In the case of Ceres, which has historically been associated with the fifth place in the TB Law, we must say that we now know of the existence of a large number of other, smaller, planetary bodies whose orbital parameters are closer to the fifth place in Titius Bode's law.

With the intention of identifying the regions of the major accumulation of small planetary objects, we set ourselves the task of assembling the information (Figure 4) of IAU Minor Planets Center (Observable Distant Minor Planets Orbital Elements). We compare their semi-major axis accumulation points with the values corresponding to every integer n of the TBmod succession. The result indicates to us that only seven regions (m_1, m_2, m_3, m_4, m_5, m_6 and m_7) can be associated with some integer 10, 11, 12 (2002TC30), 13 (Ceto), 14, 15 and 16 respectively, which makes us see the generic representation of the Titius Bode Law.

Another aspect that we want to review is whether the distribution of planets in our Solar System could be compared with that of extrasolar systems (often very different from ours), and so we enquired whether the TB model could be applied to such planetary systems.

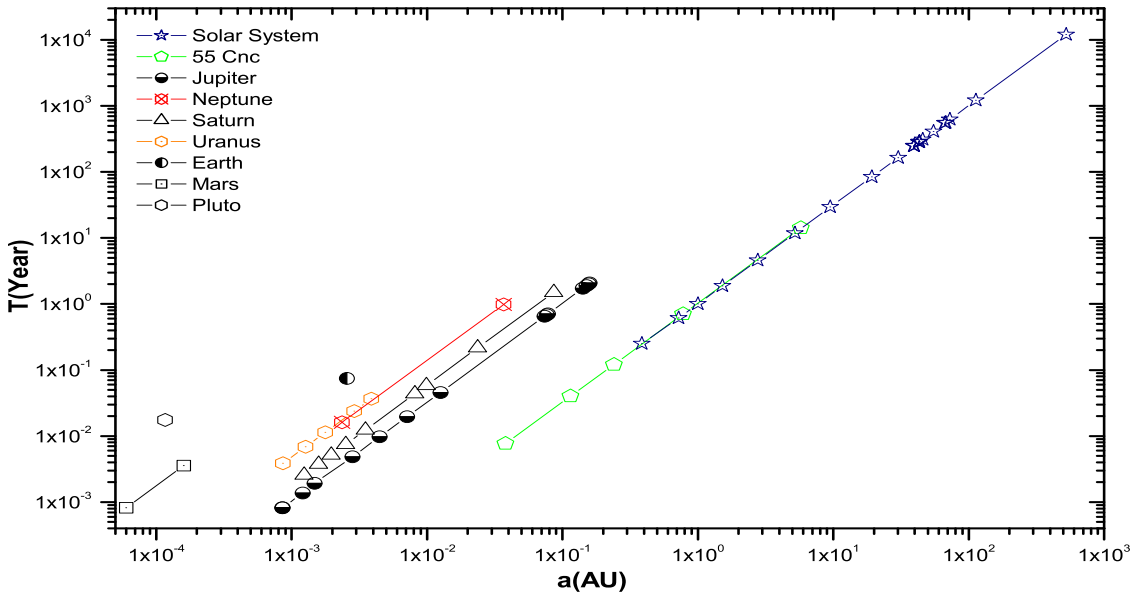

Fig. 5. Classification of planets and satellites. It shows the ranking of the Solar System and 55 Cnc, and satellite systems of planets. It is easy to see that 55Cnc and the Solar System are coincident because the masses of the central body are similar, but they differ clearly for the satellites. The color figure can be viewed online.

4. SYSTEMS OF SATELLITES AND EXOPLANETS

In the interpretation of the Titius-Bode Law a perennial concern has existed about its application to satellite systems that orbit the planets of our Solar System and, more recently, to planetary systems orbiting other stars such as υ And, 55 Cnc, 61 Vir, HD69830, HD181433, Gliese 876 and G1581 (data from Schneider 2010[3]). Of course, we must recognize the importance of characterizing the orbital period of the planetary objects under study by applying Kepler's Third Law $a^3/T^2 = K$, where $K = \pi^2 G(M + m)$ is called the Proportionality Kepler Parameter (Tables 3 and 4); we must have a clear idea that a self-gravitating system is characterized by means of its central mass and that this acts like a main factor of classification. This way, we observe in the fifth column that the values of $K[\mathrm{m^3\ s^{-2}}]$ are different for every self-gravitating system. Certainly this behavior is also estimated in the sixth column; the values of the ratio $a^3/T^2 = [\mathrm{AU^3\ yr^{-2}}]$ are of the order of one for our self-gravitating Solar System and 55Cnc, since both satisfy Kepler's proportionality. Finally, we must say that if the dimensionless ratio $(a^2/T^3)/K$ has fluctuations close to one, then the parameters T, a, M and m are well-established.

Thus, also the systems of satellites of the planets are characterized in a unique way, although the constants of proportionality they obey have very small values (Figure 5); the extrasolar planets system possesses specific values of the above mentioned constant that differ or not from that of our Solar System, so much as mass of the star differs from the mass of the sun (Figure 6).

Now assume that the planetary systems 61 Vir and 55 Cnc obey our TBmod model. To reproduce the values of their semi-major axes, it is necessary to take the negative part of the integer numbers. We chose the values -2, -1, 0, 1 therefore obtaining TBmod values 0.01, 0.1, 0.2 and 0.3 respectively, among which it is easy to find the values of the semi-major axes of the planets of 55 Cnc and 61 Vir (Figure 7). Note that the objects 55Cnc(f) and 55Cnc(d) correspond to the planets Venus and Jupiter, respectively, and 61Vir(d) to a place between Mercury and Venus. This leads us to reassess the general functions proposed here for the Solar System, since the two equations do not allow us to calculate semi-major axes of less than 0.4. In order to avoid this problem we note that with the equation (4) we can determine these small values, and the remaining ones by means of

[3]http://exoplanet.eu/catalog-all.php.

TABLE 3

ORBITAL PARAMETERS OF SEVERAL PLANETARY OBJECTS AND THE SATELLITE SYSTEMS OF THE PLANETS

		Object	a AU	T yr	m kg	K $m^3\ s^{-2}$	a^3/T^2 $AU^3\ yr^{-2}$	$a^3/T^2/K$
Sun	$M = 1.9891 \cdot 10^{30}$ kg							
		Mercury	0.387	0.251	$3.302 \cdot 10^{23}$	$3.120' \cdot 10^{18}$	0.9201	0.9273
		Venus	0.723	0.615	$4.869 \cdot 10^{24}$	$3.390 \cdot 10^{18}$	1.0006	1.0084
		Earth	1.000	1.000	$5.974 \cdot 10^{24}$	$3.390 \cdot 10^{18}$	1.0000	1.0078
		Mars	1.524	1.881	$6.419 \cdot 10^{23}$	$3.390 \cdot 10^{18}$	1.0005	1.0083
		Ceres	2.765	4.599	$9.500 \cdot 10^{20}$	$3.390 \cdot 10^{18}$	1.0000	1.0078
		Jupiter	5.203	11.862	$1.899 \cdot 10^{27}$	$3.390 \cdot 10^{18}$	1.0010	1.0079
		Saturn	9.509	29.458	$5.685 \cdot 10^{26}$	$3.360 \cdot 10^{18}$	0.9909	0.9984
		Uranus	19.251	84.013	$8.685 \cdot 10^{25}$	$3.430 \cdot 10^{18}$	1.0109	1.0187
		Neptune	30.188	164.749	$1.024 \cdot 10^{26}$	$3.440 \cdot 10^{18}$	1.0136	1.0215
		Pluto	39.499	248.430	$1.300 \cdot 10^{22}$	$3.380 \cdot 10^{18}$	0.9985	1.0063
		2002 TC302	55.096	410.620	$1.800 \cdot 10^{21}$	$3.360 \cdot 10^{18}$	0.9919	0.9997
		Eris	67.668	557.000	$1.700 \cdot 10^{22}$	$3.380 \cdot 10^{18}$	0.9987	1.0065
		2007 UK126	72.814	623.870	$7.100 \cdot 10^{20}$	$3.360 \cdot 10^{18}$	0.9919	0.9996
		2005 QU182	113.278	1210.530	$1.200 \cdot 10^{21}$	$3.360 \cdot 10^{18}$	0.9919	0.9997
		Sedna	524.453	12059.06	$7.200 \cdot 10^{21}$	$3.360 \cdot 10^{18}$	0.9920	0.9997
Jupiter	$M = 1.8990 \cdot 10^{27}$ kg							
		Metis	0.0009	0.0010	$9.4900 \cdot 10^{16}$	$3.2102 \cdot 10^{15}$	$9.210 \cdot 10^{-4}$	0.97240
		Adrasthea	0.0009	0.0010	$1.9000 \cdot 10^{16}$	$3.2102 \cdot 10^{15}$	$9.428' \cdot 10^{-4}$	0.99540
		Amalthea	0.0012	0.0010	$7.2200 \cdot 10^{18}$	$3.2102 \cdot 10^{15}$	$9.375 \cdot 10^{-4}$	0.98980
		Tebe	0.0015	0.0020	$7.6000 \cdot 10^{17}$	$3.2102 \cdot 10^{15}$	$8.707 \cdot 10^{-4}$	0.91920
		Io	0.0028	0.0050	$8.9400 \cdot 10^{22}$	$3.2103 \cdot 10^{15}$	$9.464 \cdot 10^{-4}$	0.99910
		Europa	0.0045	0.0100	$4.8000 \cdot 10^{22}$	$3.2102 \cdot 10^{15}$	$9.465 \cdot 10^{-4}$	0.99920
		Ganymmede	0.0071	0.0200	$1.4820 \cdot 10^{23}$	$3.2104 \cdot 10^{15}$	$9.470 \cdot 10^{-4}$	0.99970
		Callisto	0.0126	0.0460	$1.0760 \cdot 10^{23}$	$3.2103 \cdot 10^{15}$	$9.470 \cdot 10^{-4}$	0.99980
		Leda	0.0740	0.6540	$5.7000 \cdot 10^{15}$	$3.2102 \cdot 10^{15}$	$9.472 \cdot 10^{-4}$	1.00000
		Himalia	0.0765	0.6860	$9.4900 \cdot 10^{18}$	$3.2102 \cdot 10^{15}$	$9.523 \cdot 10^{-3}$	1.00530
		Lisisthea	0.0781	0.7100	$7.6000 \cdot 10^{16}$	$3.2102 \cdot 10^{15}$	$9.471 \cdot 10^{-4}$	0.99990
		Elara	0.0783	0.7110	$7.6000 \cdot 10^{17}$	$3.2102 \cdot 10^{15}$	$9.476 \cdot 10^{-4}$	1.00040
		Ananque	0.1413	1.7280	$3.8000 \cdot 10^{16}$	$3.2102 \cdot 10^{15}$	$9.459 \cdot 10^{-4}$	0.99860
		Carme	0.1507	1.8950	$9.4900 \cdot 10^{16}$	$3.2102 \cdot 10^{15}$	$9.528 \cdot 10^{-3}$	1.00590
		Pasiphae	0.1567	2.0120	$1.9000 \cdot 10^{17}$	$3.2102 \cdot 10^{15}$	$9.495 \cdot 10^{-4}$	1.00250
		Sinophe	0.1580	2.0750	$7.6000 \cdot 10^{16}$	$3.2102 \cdot 10^{15}$	$9.158 \cdot 10^{-4}$	0.96680
Saturn	$M = 5.97 \cdot 10^{26}$ kg							
		Mimas	0.0012	0.0030	$3.7500 \cdot 10^{19}$	$1.0100 \cdot 10^{15}$	$3.00 \cdot 10^{-4}$	0.95350
		Enceladus	0.0016	0.0040	$1.0800 \cdot 10^{20}$	$1.0100 \cdot 10^{15}$	$3.00 \cdot 10^{-4}$	0.95170
		Tethys	0.0020	0.0050	$1.0240 \cdot 10^{20}$	$1.0100 \cdot 10^{15}$	$3.00 \cdot 10^{-4}$	0.95170
		Dione	0.0025	0.0070	$1.0950 \cdot 10^{21}$	$1.0100 \cdot 10^{15}$	$3.00 \cdot 10^{-4}$	0.95170
		Rhea	0.0035	0.0120	$2.3060 \cdot 10^{21}$	$1.0100 \cdot 10^{15}$	$3.00 \cdot 10^{-4}$	0.95150
		Titan	0.0082	0.0440	$1.3450 \cdot 10^{23}$	$1.0100 \cdot 10^{15}$	$3.00 \cdot 10^{-4}$	0.95140
		Hiperion	0.0099	0.0580	$1.7100 \cdot 10^{19}$	$1.0100 \cdot 10^{15}$	$3.00 \cdot 10^{-4}$	0.94960
		Iapetus	0.0237	0.2170	$1.8800 \cdot 10^{21}$	$1.0100 \cdot 10^{15}$	$3.00 \cdot 10^{-4}$	0.94990
		Febe	0.0864	1.5070	$3.9800 \cdot 10^{17}$	$1.0100 \cdot 10^{15}$	$3.00 \cdot 10^{-4}$	0.95090
Uranus	$M = 8.69 \cdot 10^{25}$ kg							
		Miranda	0.0009	0.0040	$6.5900 \cdot 10^{19}$	$1.4700 \cdot 10^{14}$	$4.2800 \cdot 10^{-5}$	0.99000
		Ariel	0.0013	0.0070	$1.3500 \cdot 10^{21}$	$1.4700 \cdot 10^{14}$	$4.3300 \cdot 10^{-5}$	1.00000
		Umbriel	0.0018	0.0110	$1.2000 \cdot 10^{21}$	$1.4700 \cdot 10^{14}$	$4.3300 \cdot 10^{-5}$	1.00000
		Titania	0.0029	0.0240	$3.5000 \cdot 10^{21}$	$1.4700 \cdot 10^{14}$	$4.3300 \cdot 10^{-5}$	1.00000
		Oberon	0.0039	0.0370	$3.0140 \cdot 10^{21}$	$1.4700 \cdot 10^{14}$	$4.3300 \cdot 10^{-5}$	1.00000
Neptune	$M = 1.03 \cdot 10^{26}$ kg							
		Triton	0.0024	0.0160	$1.34 \cdot 10^{23}$	$1.7400 \cdot 10^{14}$	$5.04 \cdot 10^{-5}$	0.98000
		Nereida	0.0368	0.9860	$2.06 \cdot 10^{19}$	$1.7400 \cdot 10^{14}$	$5.10 \cdot 10^{-5}$	1.00000
Earth	$M = 5.97 \cdot 10^{24}$ kg							
		Luna	0.0026	0.0750	$7.3480 \cdot 10^{22}$	$1.0200 \cdot 10^{13}$	$3.0100 \cdot 10^{-6}$	1.00000
Mars	$M = 6.42 \cdot 10^{23}$ kg							
		Fobos	0.0001	0.0010	$9.6300 \cdot 10^{15}$	$1.0900 \cdot 10^{12}$	$3.2000 \cdot 10^{-7}$	1.00000
		Deimos	0.0002	0.0040	$1.9300 \cdot 10^{15}$	$1.0900 \cdot 10^{12}$	$3.2000 \cdot 10^{-7}$	1.01000
Pluto	$M = 1.30 \cdot 10^{22}$ kg							
		Charon	0.0001	1.5200	$0.0170 \cdot 10^{21}$	$2.4500 \cdot 10^{10}$	$5.2000 \cdot 10^{-9}$	0.72000

In the first, second, third, and fourth columns, the names of the bodies, the major semi-axes, their periods and their respective masses, are given. In the fifth and the sixth columns the values of the proportionality parameter of Kepler for each body, and the quotient are given, and finally, in the seventh column we give the quotient of these parameters of proportionality whose value is very near to one.

TABLE 4

ORBITAL PARAMETERS OF THE EXOPLANETARY SYSTEM GLIESE 876, G1581, υ AND, 55 CNC, HD160691, HD69830 AND 61 VIR

Object	M kg		a AU	T yr	m kg	K $m^3\ s^{-2}$	$a^3\ T^{-2}$ $AU^3\ yr^{-2}$	$a^3\ T^{-2}/K$
υ And	$2.525 \cdot 10^{30}$ kg							
		1	0.059	0.01	$1.3100 \cdot 10^{27}$	$4.27 \cdot 10^{18}$	1.29	1.02
		2	0.822	0.65	$22.0036 \cdot 10^{27}$	$4.31 \cdot 10^{18}$	1.31	1.03
		3	2.550	3.57	$19.5356 \cdot 10^{27}$	$4.30 \cdot 10^{18}$	1.30	1.03
55Cnc	$1.97 \cdot 10^{30}$ kg							
		1	0.038	0.01	$0.0456 \cdot 10^{27}$	$3.36 \cdot 10^{18}$	0.92	0.93
		2	0.115	0.04	$1.5644 \cdot 10^{27}$	$3.36 \cdot 10^{18}$	0.95	0.95
		3	0.240	0.12	$0.3209 \cdot 10^{27}$	$3.36 \cdot 10^{18}$	0.94	0.95
		4	0.781	0.71	$0.2734 \cdot 10^{27}$	$3.36 \cdot 10^{18}$	0.94	0.95
		5	5.770	14.29	$7.2808 \cdot 10^{27}$	$3.37 \cdot 10^{18}$	0.94	0.95
61 Vir	$1.8890 \cdot 10^{30}$ kg							
		1	0.050	0.01	$0.0304 \cdot 10^{27}$	$3.19 \cdot 10^{18}$	0.95	1.01
		2	0.218	0.10	$0.1088 \cdot 10^{27}$	$3.19 \cdot 10^{18}$	0.95	1.01
		3	0.476	0.34	$0.1367 \cdot 10^{27}$	$3.19 \cdot 10^{18}$	0.95	1.01
HD69830	$1.71 \cdot 10^{30}$ kg							
		1	0.079	0.02	$0.0627 \cdot 10^{27}$	$2.89 \cdot 10^{18}$	0.86	1.01
		2	0.186	0.09	$0.0721 \cdot 10^{27}$	$2.89 \cdot 10^{18}$	0.86	1.01
		3	0.630	0.54	$0.1101 \cdot 10^{27}$	$2.89 \cdot 10^{18}$	0.86	1.01
HD181433	$1.55 \cdot 10^{30}$ kg							
		1	0.080	0.03	$0.0452 \cdot 10^{27}$	$2.62 \cdot 10^{18}$	0.78	1.00
		2	1.760	2.63	$1.2150 \cdot 10^{27}$	$2.62 \cdot 10^{18}$	0.79	1.01
		3	3.000	5.95	$1.0252 \cdot 10^{27}$	$2.62 \cdot 10^{18}$	0.76	0.99
Gliese876	$1.55 \cdot 10^{29}$ kg							
		1	0.021	0.01	$0.0399 \cdot 10^{27}$	$1.12 \cdot 10^{18}$	0.32	0.97
		2	0.130	0.08	$1.3559 \cdot 10^{27}$	$1.13 \cdot 10^{18}$	0.32	0.97
		3	0.208	0.17	$4.3202 \cdot 10^{27}$	$1.13 \cdot 10^{18}$	0.32	0.97
		4	0.334	0.34	$0.0873 \cdot 10^{27}$	$1.12 \cdot 10^{18}$	0.32	0.97
G1581	$6.16 \cdot 10^{29}$ kg							
		1	0.030	0.01	$0.0116 \cdot 10^{27}$	$1.04 \cdot 10^{18}$	0.36	1.18
		2	0.041	0.01	$0.0934 \cdot 10^{27}$	$1.04 \cdot 10^{18}$	0.32	1.04
		3	0.070	0.04	$0.0320 \cdot 10^{27}$	$1.04 \cdot 10^{18}$	0.27	0.89
		4	0.220	0.18	$0.0424 \cdot 10^{27}$	$1.04 \cdot 10^{18}$	0.32	1.04

In the Columns 1 to 5, the names of the bodies, the mass of the star, the major semi-axes, their periods and the planet masses, are given. In Columns 6 and 7 the values of the proportionality parameter of Kepler for each body, and the quotient are given, and finally, in Column 8 we give the quotient of these parameters of proportionality, whose value is very close to one.

the following equations (TBF):

$$r_n = 0.008 + 9.6 \cdot 2^{n-6}\,, \qquad -4 \le n < 2 \qquad (6)$$

$$r_n = 0.4 \quad + 9.6 \cdot 2^{n-7}\,, \qquad 2 \le n < 9 \qquad (7)$$

$$r_n = 19.6 \ + 9.6 \cdot 2^{n-9}\,. \qquad n \ge 9 \qquad (8)$$

Now we present the distribution of the objects that induces each of the equations (6–8) in order to discern their tendencies and to display the intervals that are valid in each (the values of χ^2 for each interval are 0.002, 0.241 and 0.379 respectively). It is obvious that there are three regions bound by the intersection of the equations (6) and (7), and equations (7) and (8) (Figure 8) and whose approximate values are found to be $(n_1, r_1) = (2.5,\ 0.8\ \text{AU})$ and $(n_2,\ r_2) = (8.4,\ 26.5\ \text{AU})$, respectively. This suggests that these three intervals delimit the regions between the Sun and Venus, inside the region of the hypothetical vulcanoid objects that contains Mercury, between Major Solar Bodies but without Mercury, and finally from Neptune to the regions of the outer Solar System, into which we have included the accumulation points (m_1, m_2, m_3, m_4, m_5, m_6 and m_7).

Taking equations (6–8) we have determined the values of the semi-major axes and have fitted exponential functions (values of R^2 as 0.9999, 0.9971 and 0.9999 respectively):

$$r = e^{0.63413x - 1.81942}\,, \qquad x < 2 \qquad (9)$$

$$r = e^{0.67115x - 2.38121}\,, \qquad 2 \le x < 9 \qquad (10)$$

$$r = e^{0.68879x - 3.89173}\,. \qquad x \ge 9 \qquad (11)$$

Since equation (9) represents the vulcanoid objects we wish to compare it with the semi-major axes

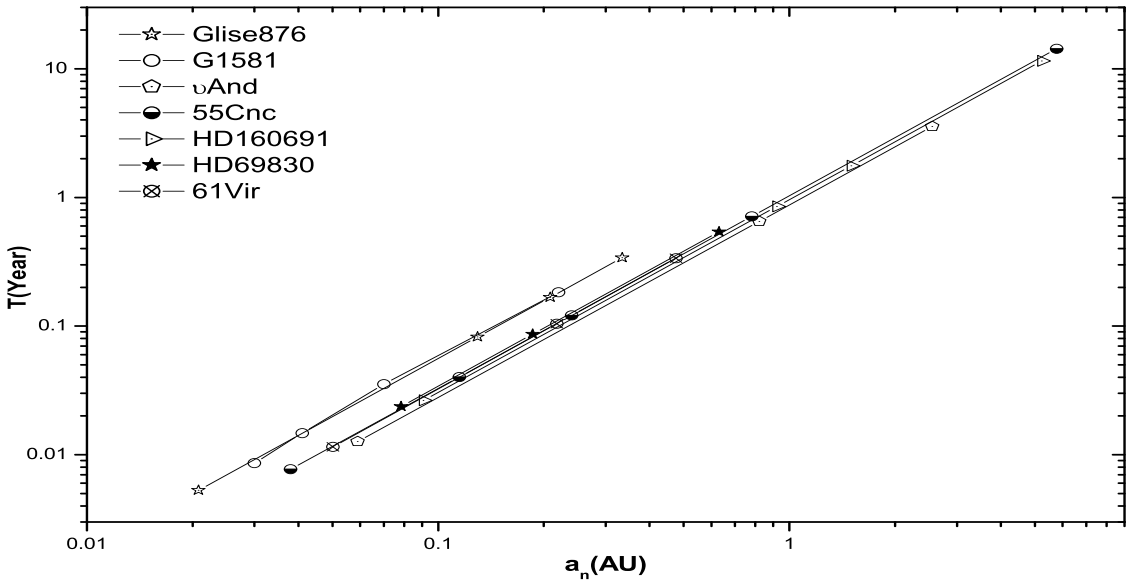

Fig. 6. Orbital parameters of the exoplanetary system. Observe that the systems whose central masses are similar to that of the Sun are υ And, 55 Cnc, 61 Vir, HD 69830 and HD 181433, and differ from those of Gliese 876 and Gliese 1581.

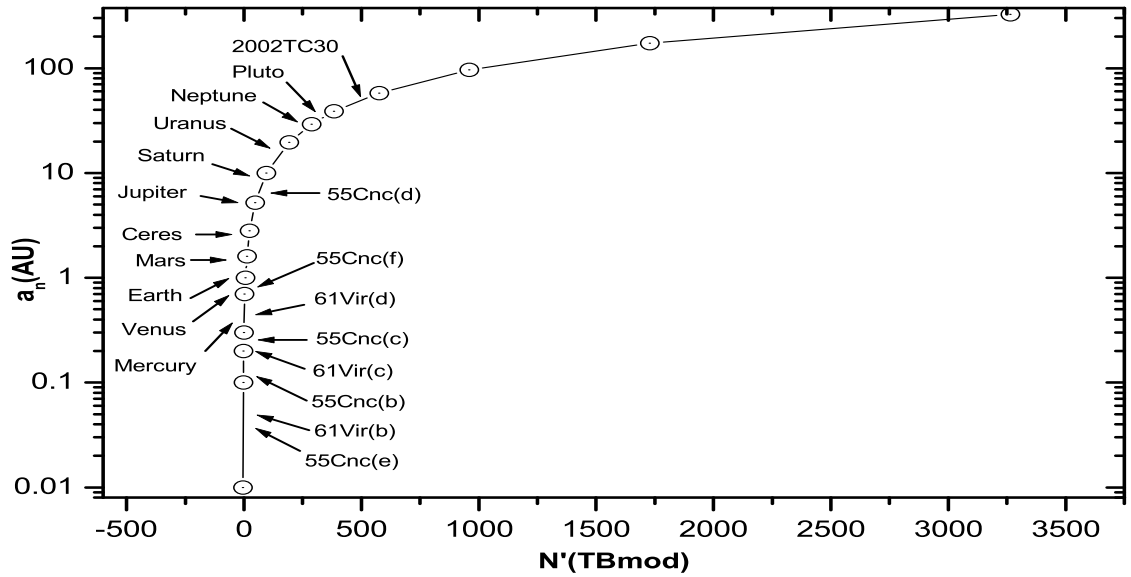

Fig. 7. Distribution of exoplanets of 55Cnc and 61Vir. As the central mass of both systems is similar to that of the Sun, we will assume that they satisfy the equations we have called TBF. We include the members of the Solar System with the purpose of comparing the extrasolar objects with those familiar to us. On the abscissa axis we give the heliocentric distances of the planetary objects according to the order of the integer succession TB law.

of the exoplanets (Schneider 2010)[4] known until now. We have found that some accumulation points correspond to certain elements of TBF (Figure 9). Nevertheless, it is not possible to represent the totality of them. Another interesting aspect is the concentration of vulcanoid objects around $n = -2$. Perhaps it is due to the existence of the protoplanetary wall near a central mass recently analyzed (Calvet, D'Alessio, & Woolum 2005), whose radius of subli-

[4]http://exoplanet.eu/catalog-all.php.

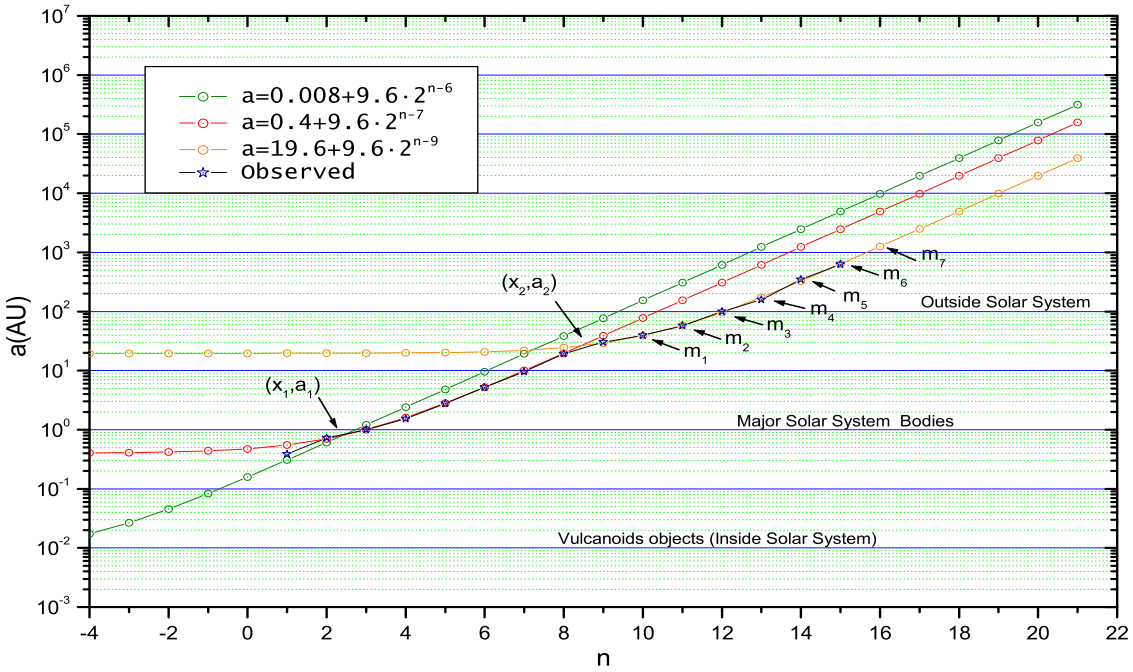

Fig. 8. Distribution of the planetary objects in three regions defined by the intersections of the functions The intersection of the first two, assuming them as continuous functions, defines the point $(n1,\ a1) = (2.5,\ 0.8$ AU), and the intersection of the second and the third ones gives the points $(n2,\ a2) = (8.4,\ 26.5$ AU). Through these points the three regions of the Solar System are defined and it is possible to apply them to extrasolar systems with central masses similar to those of the Sun, 55 Cnc and 61 Vir. We include the accumulation points (m_1, m_2, m_3, m_4, m_5, m_6 and m_7).The color figure can be viewed online.

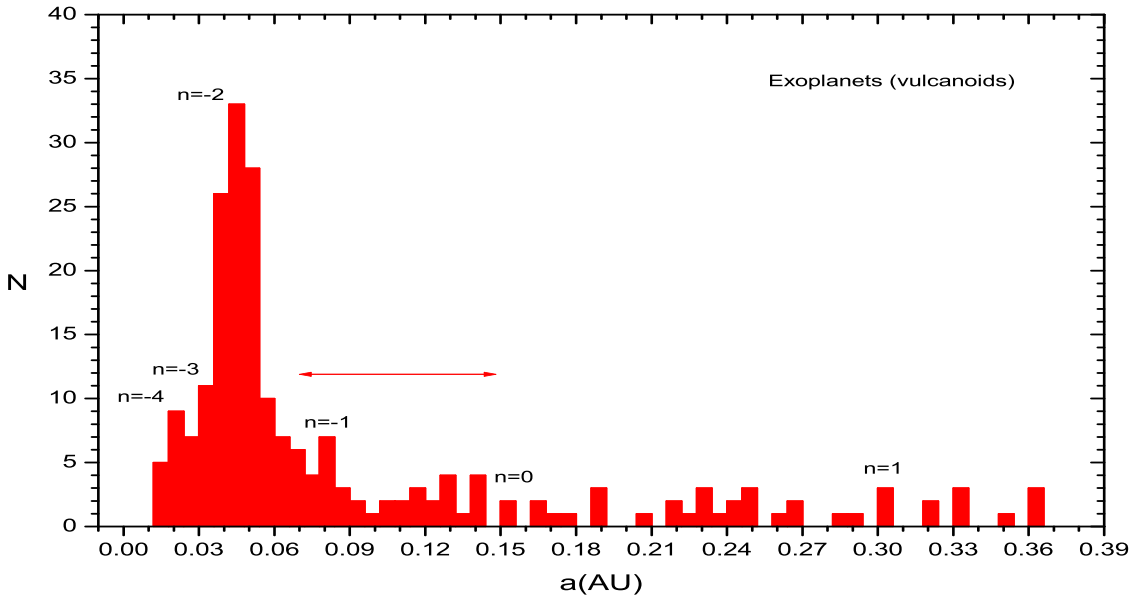

Fig. 9. Exoplanets with semi-major axes less 0.39 AU. The color figure can be viewed online.

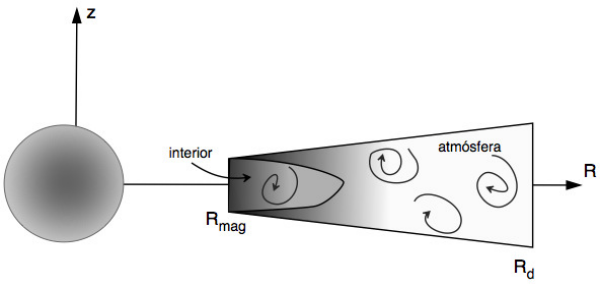

Fig. 10. A simplified distribution of a protostellar turbulent disk model to give an idea of how annular regions can form in such a disk.

mation we identify with the red color line between 0.07 and 0.15 AU.

Perhaps the origin of these regions can be found in the early formative stages of the protoplanetary disk dominated by turbulent forces that led to the formation of ring band regions (annular regions). With time, these regions evolved, and were confined into bands by the presolar material. The planets would have been formed as a result of the agglomeration of small particles into larger ones. A hydrodynamic vision has been included in the recent model of Adame (2010), who describes a turbulent protostellar disk (Figure 10) with central small masses. Here we can see certain criteria for the formation of annular regions; for example, it is possible to consider that the origin of the TBF distribution arises from a stationary wave system, according to the initial conditions, the mass of the central body being the main parameter.

5. FINAL COMMENTS AND CONCLUSIONS

We have studied the general structure of the Solar System through the Titius-Bode Law, which we have applied to the exoplanets system. It has lead to us to consider that the TBF distribution of planetary objects (equations (6–11) occurs in three great groups: Inner Solar System bodies, Major Solar System bodies and Outer Solar System bodies. For the case of Mercury ($n = 1$) we improved the determination of the semi-major axis. The order of the major objects agrees well with the integer TBF sequence, including the accumulation region ($n = 5$) represented by Ceres or the asteroid belt. In the outer Solar System, where objects with very eccentric orbits are located, we observed that the TBF integers are associated mainly to regions of accumulation of small agglomerations with values $n = 15$ or 16, and to the abundant concentrations of small objects for $n = 10$, 11 or 12.

If we consider solely those systems with central masses similar to the Sun, i.e., 55 Cnc, 61 Vir and HD69830, we can assign to certain objects values n of TBF (vulcanoids and major objects) according to equations (6–8) and Table 4. For example, 55Cnc(1) with $n = -2$, 61Vir(1) with $n = -2$, HD69830(1) with $n = -1$, and HD69830(2) with $n = 0$.

With the set of equations (equations 6–11) we can see the general orbital behavior of Solar System bodies, which appears to contain the final status of the presolar cloud processes from the stage of protoplanetary disk to planet formation. Of course, any theory would have to include other phenomena, such as migration of planets (Masset 2008), or magnetohydrodynamic phenomena that may have occurred in our Solar System. In this context, when we think about the distribution of planets in the Solar System, we are actually considering the primitive physical conditions which dominated the presolar cloud which created regions of the protoplanetary ring from which the planets were created after a process of accretion of the particles that formed these protoplanetary rings.

We have speculated that the TBF distribution arose from a stationary wave system in the presolar cloud where it induced the formation of certain annular regions, simultaneously generating turbulent accretion phenomena. On the other hand, we imagine that these conditions differ from other protoplanetary environments where the distribution and size of such rings would be subject to different chemical composition, shape, distribution and laws of accretion of the solid bodies.

We thank the referee for useful comments which improved our presentation.

REFERENCES

Adame, L. 2010, PhD Thesis, Universidad Nacional Autónoma de México, Mexico

Badolati, E. 1982, Moon and the Planets, 26, 339

Calvet, N., D'Alessio, P. D., & Woolum, D. S. 2005, in ASP Conf. Ser. 341, Chondrites and the Protoplanetary Disk, ed. A. N. Krot, E. R. D. Scott, & B. Reipurth (San Francisco: ASP), 353

Chang, H. Y. 2008, J. Astron. Space Sci., 25, 239

García Guerra, C. 2005, Distancias Planetarias (Mexico: SEP; Registro Público de Derechos de Autor 03-2005-081713522000-01, 25 agosto 2005)

Holton, G. J., & Brush, S. G. 2001, Physics, the Human Adventure: from Copernicus to Einstein and Beyond (3rd ed.; New Brunswick, N. J.: Rutgers Univ. Press)

Horedt, G. P., Pop, P., & Ruck, H. 1977, Celest. Mech., 16, 209

Jaki, S. L. 1972, Am. J. Phys., 40, 1014
Kotliarov, I. 2008, MNRAS, 390, 1411
_____. 2009, arXiv:0807.0757v1
Lynch, P. 2003, MNRAS, 341, 1174
Masset, F. S. 2008, in IAU Symp. 249, Exoplanets: Detection, Formation and Dynamics, ed. Y.-S. Sun, S. Ferraz-Mello, & J.-L. Zhou (Cambridge: Cambridge Univ. Press), 331
Nieto, M. M. 1970, A&A, 8, 105
_____. 1975, Icarus, 25, 171
Ortiz, J. L., Moreno, F., Molina, A., Santos Sanz, P., & Gutiérrez, P. J. 2007, MNRAS, 379, 1222
Ovenden, M. W. 1972, Nature, 239, 508
_____. 1975, Vistas Astron., 18, 473
Patton, J. M. 1988, Celest. Mech., 44, 365
Pankovick, V., & Radakovick, A. 2009, arXiv:0903.1732v1
Poveda, A., & Lara, P. 2008, RevMexAA, 44, 243

J. Daniel Flores-Gutiérrez: Instituto de Astronomía, Universidad Nacional Autónoma de México, Apdo. Postal 70-264, 04510 México, D. F., Mexico (daniel@astro.unam.mx).
Carlos García-Guerra: Facultad de Arquitectura, Universidad Nacional Autónoma de México, Mexico (carlosgg2000@hotmail.com).

Revista Mexicana de Astronomía y Astrofísica, **47**, 185–192 (2011)

uvby − *β* PHOTOELECTRIC PHOTOMETRY OF THE OPEN CLUSTERS NGC 1647 AND NGC 1778

C. A. Guerrero,[1] J. H. Peña,[1] and J. P. Sareyan[2]

Received 2010 October 21; accepted 2011 February 15

RESUMEN

Se presenta fotometría $uvby - \beta$ de 35 estrellas en la dirección del cúmulo abierto NGC 1647 y de 16 estrellas del cúmulo NGC 1778. Del análisis de los datos obtenidos para NGC 1647 se ha determinado un enrojecimiento $E(b-y) = 0.32 \pm 0.02$ mag y un módulo de distancia de $V_0 - M_V = 8.75 \pm 0.09$ correspondiente a una distancia $d = 564 \pm 106$ pc; asimismo, se han encontrado las estrellas miembros y se ha determinado un valor numérico para la edad del cúmulo de log edad (en años) $= 7.98 \pm 0.23$. A partir del análisis de los datos obtenidos para NGC 1778, se concluye que no es posible determinar si hay un cúmulo en esa dirección, pues las distancias encontradas para las estrellas observadas son muy diferentes.

ABSTRACT

We present photometry $uvby - \beta$ for 35 stars in the direction of the open cluster NGC 1647 and for 16 stars in the direction of the cluster NGC 1778. From the analysis of the data obtained for NGC 1647 we determine a mean reddening of $E(b-y) = 0.32 \pm 0.02$ mag and a distance modulus of $V_0 - M_V = 8.75 \pm 0.09$ corresponding to a distance $d = 564 \pm 106$ pc; also, we find the cluster member stars and a numerical value of log age (in years) $= 7.89 \pm 0.23$. From the analysis of data obtained for NGC 1778, we conclude that it is not possible to determine whether there is a cluster in that direction, because the distances found for the observed stars are very different.

Key Words: open clusters and associations: individual (NGC 1647, NGC 1778) — techniques: photometric

1. INTRODUCTION

Galactic open clusters are ensembles of stars with low concentration and irregular shape, gravitationally-bound systems formed at the same time from the same original cloud. They represent examples of stars of comparable age and intrinsic chemical composition and are important in the study of stellar evolution and star formation. As a consequence, the problem of determining the cluster member stars is very important. For this, it is necessary to know the distance, reddening and absolute magnitude of each star.

The present work studies two open clusters, NGC 1647 and NGC 1778, using Strömgren photometry ($uvby - \beta$) to determine their parameters: reddening, distance modulus and age. The results will be compared with those obtained from the Johnson photometry taken from the literature.

Based on the individual distances of the stars, we will determine whether they belong to the cluster. There are other important physical characteristics in the study of stellar evolution to characterize a star cluster namely temperature and surface gravity of the stars. Using them we can determine the clusters' age (Meynet, Mermilliod, & Maeder 1993).

NGC 1647 is situated beyond the Taurus dark cloud complex, only a few degrees from the Hyades cluster. The center equatorial coordinates are $\alpha(2000) = 4^h46^m8^s.45$ and $\delta(2000) = +19°04'37''$. The diameter of the cluster is about $45'$ and it is a relatively rich cluster that has not been studied by $uvby - \beta$ photometry. Other authors have reported physical parameters (Table 1): Hoag & Applequist (1965) observed 65 stars and reported a distance $d = 549$ pc, a reddening $E(B-V) = 0.30$ and

[1]Instituto de Astronomía, Universidad Nacional Autónoma de México, Mexico.

[2]Lesia, Observatoire de Paris-Meudon and Observatoire de la Cote d'Azur, France.

TABLE 1

COMPARISON OF PARAMETERS, NGC 1647

Parameter	Paunzen[a]	Hoag[b]	Turner[c]	Hebb[d]	Zdanavičius[e]	Guerrero[f]
$E(B-V)$	0.370	0.30	0.29	0.37	0.35	0.35
$V_0 - M_V$	9.81	8.7	8.67	8.7	8.42	8.75
d (pc)	540	549	542	550	555	564
log age	8.158	–	8.27	8.3	8.1	7.98

[a]Paunzen & Mermilliod (2007). [b]Hoag & Applequist (1965). [c]Turner (1992). [d]Hebb et al. (2004). [e]Zdanavičius et al. (2005). [f]This paper.

TABLE 2

COMPARISON OF PARAMETERS, NGC 1778

Parameter	Paunzen[a]	Hoag[b]	Barbon[c]	Joshi[d]	Pandey[e]	Xin[f]
$E(B-V)$	0.33 6	0.34	0.33	0.34	0.23	0.23
$V_0 - M_V$	11.88	10.7	11.11	10.3	10.2	11.53
d (pc)	1469	1380	1670	1062	1100	2023
log age	8.155	–	–	8.2	11.3	11.8

[a]Paunzen & Mermilliod (2007). [b]Hoag & Applequist (1965). [c]Barbon & Hassan (1973). [d]Joshi et al. (1975). [e]Pandey (1998). [f]Xin et al. (2007).

a distance modulus $V_0 - M_V = 8.7$. Using Johnson photometry Turner (1992) observed 45 stars, reported a distance $d = 542 \pm 4$ pc, and measured a reddening $E(B-V) = 0.29 \pm 0.01$, a distance modulus $V_0 - M_V = 8.67 \pm 0.02$ and an age log age = 8.27 years. Hebb, Wyse, & Gilmore (2004) with 53 stars determined a distance $d = 550$ pc, a reddening $E(B-V) = 0.37$, a distance modulus $V_0 - M_V = 8.7$ and an age log age = 8.3 years. Using the Vilnius seven-color photometric system, Zdanavičius et al. (2005) published a study of 252 stars and reported a distance $d = 555 \pm 74$ pc, a reddening $E(B-V) = 0.35 \pm 0.01$, a distance modulus $V_0 - M_V = 8.42 \pm 0.02$ and an age log age = 8.1 years.

NGC 1778 lies in the direction of the Perseus arm; the coordinates for its center are: $\alpha(2000) = 5^h08^m04^s.56$ and $\delta(2000) = +37°01'24''$. The diameter of the cluster is about $10'$ and it is a very poorly populated, faint cluster, which has no previously observed $uvby-\beta$ photometry. Other authors have reported physical parameters (Table 2): Hoag & Applequist (1965) observed 10 stars and reported a distance $d = 1380$ pc, a reddening $E(B-V) = 0.34$ and a distance modulus of $V_0 - M_V = 10.7$, using Johnson photometry. In 1973, Barbon & Hassan observed 14 stars and reported a distance $d = 1670$ pc, a reddening $E(B-V) = 0.33$ and a distance modulus $V_0 - M_V = 11.11$. Joshi, Sagar, & Pandey (1975) observed 85 stars and reported a reddening $E(B-V) = 0.34$, a distance $d = 1062$ pc, a distance modulus $V_0 - M_V = 10.13$ and an age log age = 8.2 years. Pandey (1998) observed 16 stars and reported a distance $d = 1100$ pc, a distance modulus $V_0 - M_V = 10.2$ and an age log age = 11.3 years. Xin, Deng, & Han (2007) using 15 stars determined a distance $d = 2023$ pc, a reddening $E(B-V) = 0.23$, a distance modulus $V_0 - M_V = 11.53$ and an age log age = 11.18 years.

2. OBSERVATIONS

Observations were made at the Observatorio Astronómico Nacional, San Pedro Mártir, Mexico, with the 1.5 m telescope and a Strömgren spectrophotometer. The observing run consisted of five nights from 22 to 26 in October 2007. We chose to observe all the brightest stars up to magnitude 13 (close to the limit of the telescope-photometer system), according to the chart of Paunzen & Mermilliod (2007, WEBDA, magnitude limit 13).

In order to be able to transform the data into the $uvby-\beta$ absolute system, a set of photometric standards was observed along with the program stars.

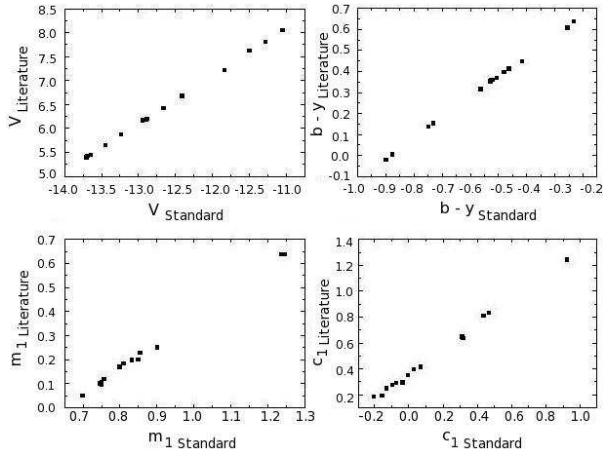

Fig. 1. Sample of the transformation correlations between instrumental and standard values for a group of standard stars for the October, 2007 season.

2.1. *Data acquisition*

Each measurement consisted of five ten-second integrations for each star. The obtained values of the standard stars and for all the observed bright stars are the average of these measurements. A ten-second integration of the sky was subtracted from the *uvby* filters and from the N and W filters that define Hβ. Individual uncertainties were determined by calculating the standard deviations of the fluxes in each filter for each star. The precision of each measurement is a function of both the brightness and the spectral type of each star, but we tried to observe them long enough to obtain a sufficient number of source counts to ensure a signal/noise ratio $N/\sqrt{(N)}$ close to a 0.01 mag accuracy.

Seasonal errors were evaluated through the diferences (calculated minus reported) of the magnitude and colors for the standard stars. Ten to fifteen standard stars were observed each night. Emphasis is made on the large range in the magnitude and color values of the standard stars (see Figure 1).

2.2. *Data reduction*

Standard data reduction procedures have been done with the numerical package NABAPHOT (Arellano Ferro & Parrao 1988). The chosen system was that defined by the standard values of Olsen (1983), and we also took some bright standard stars from the Astronomical Almanac (2006). The transformation equations (1–5) are those given by Crawford & Barnes (1970) and by Crawford & Mander (1966); in these equations D, F, H and L are the slope coefficients for $(b-y)$, m_1, c_1 and β, respectively. B, J and I are the color term coefficients of V, m_1 and c_1. The errors are calculated through the standard stars observed, evaluating the differences in magnitude and colors between the derived values and those of the literature. These differences for V, $(b-y)$, m_1, c_1 and β are ±0.010, ±0.006, ±0.007, ±0.021 and ±0.004 respectively, providing a numerical estimation of our uncertainties when transforming into the standard system.

$$V = 19.096 + 1.000(b-y) + y_{\rm obs}, \quad (1)$$

$$(b-y) = -0.002 + 0.867(b-y)_{\rm obs}, \quad (2)$$

$$m_1 = 0.981 + 0.001(m_1)_{\rm obs} + 0.375(b-y), \quad (3)$$

$$c_1 = -0.648 + 1.044(c_1)_{\rm obs} + 0.042(b-y), \quad (4)$$

$$\mathrm{H}\beta = 2.978 + 1.237(\mathrm{H}\beta)_{\rm obs}. \quad (5)$$

Table 3 lists the photometric values of the observed stars of NGC 1647 and Table 4 the values of the NGC 1778 stars, ordered by decreasing β values. Column 1 reports the WEBDA ID of the stars as listed by Paunzen & Mermilliod (2007), Columns 2 to 5 the Strömgren values V, $(b-y)$, m_1, and c_1 respectively; Column 6, the β value, Columns 7 and 8, the reddening-free indexes $[m_1]$ and $[c_1]$ (independent of interstellar extinction) derived from the observations. Column 9 lists the spectral types reported by Paunzen & Mermilliod (2007), and Column 10 the photometric spectral type obtained from the diagram $[c_1]-[m_1]$.

3. METHODOLOGY

When studying a cluster it is important to establish membership of its star on a star-by-star basis, taking advantage of the Strömgren photometry, with the calibrations made by Nissen (1988) based on the calibrations by Crawford (1975, 1979) for the A and F stars and by Shobbrook (1984) for early type stars. In the present study the determination of physical parameters, such as the effective temperature and surface gravity, has been done through the measured Strömgren photometric data in the standard system, once corrected for interstellar extinction. Theoretical $uvby-\beta$ indexes, such as those of Lester, Gray, & Kurucz (1986, hereinafter LGK86), allowed us to directly compare our photometry with that obtained theoretically. LGK86 calculated grids for stellar atmospheres for G, F, A, B and O stars in a temperature range from 5500 K up to 50000 K; they also calculated $\log g$ and $T_{\rm eff}$ as a function of the Strömgren indexes. The determination was done in the $(b-y)$ versus β diagram and in the $[c_1]$ versus β diagram (Figure 2).

The evaluation of reddening was done by establishing to which spectral class each star belongs:

TABLE 3

$uvby-\beta$ PHOTOELECTRIC PHOTOMETRY OF NGC 1647

WEBDA	V	$b-y$	m_1	c_1	$[m_1]$	$[c_1]$	β	MK	ST
2	7.465	0.996	0.510	0.245	0.828	0.045	2.893	K0	late
10	11.052	0.398	0.035	0.979	0.162	0.899	2.892	B7.5IV	B9
68	10.150	0.361	0.117	0.995	0.232	0.922	2.889		A3
71	10.671	0.312	0.054	0.941	0.153	0.878	2.864	A0	B9
34	10.593	0.257	0.061	0.900	0.143	0.848	2.851	B9	B9
42	9.667	0.246	0.077	0.912	0.155	0.862	2.850	B9.5IV	B9
29	10.674	0.259	0.062	0.967	0.144	0.915	2.838	A0 IV	B9
49	10.048	0.290	0.083	0.945	0.175	0.887	2.832	B8	B8
31	10.264	0.219	0.082	0.905	0.152	0.861	2.794	B8	B9
48	10.402	0.247	0.075	0.825	0.154	0.775	2.778	A0	B8
5	10.220	0.358	0.056	0.660	0.170	0.588	2.774	A0	B6
37	8.864	0.246	0.040	0.651	0.118	0.601	2.774	B9.5IV	B5
57	9.985	0.333	0.041	0.691	0.147	0.624	2.772	A0	B5
70	10.466	0.288	0.062	0.707	0.154	0.649	2.767	B9	B6
419	9.811	0.197	0.047	0.629	0.110	0.589	2.756		B4
51	9.943	0.303	0.080	0.766	0.177	0.705	2.753	B9 IV	B7
99	10.059	0.327	0.044	0.794	0.148	0.728	2.753	B9 IV	B7
54	10.075	0.290	0.053	0.654	0.145	0.596	2.746	A0 V	B5
22	9.067	0.199	0.042	0.739	0.105	0.699	2.742	B9 II	B6
59	9.698	0.400	0.008	0.773	0.136	0.693	2.738	A0	B7
3	10.026	0.290	0.055	0.656	0.147	0.598	2.736	B7.5IV	B4
94	9.667	0.216	0.047	0.666	0.116	0.622	2.726	B9 III	B5
55	10.246	0.341	0.040	0.632	0.149	0.563	2.724	B7 V	B4
66	10.246	0.350	0.017	0.913	0.129	0.843	2.721	B8	B8
233	10.136	0.254	0.092	0.571	0.173	0.520	2.708		B4
102	9.307	0.281	0.026	0.770	0.115	0.713	2.702	B9 III	B6
45	8.860	0.248	0.039	0.645	0.118	0.595	2.700	B7.5IV	B4
44	9.213	0.231	0.033	0.769	0.106	0.722	2.697	B8 IV	B8
15	8.561	0.304	0.020	0.644	0.117	0.583	2.620	B8 III	B4
65	9.561	0.364	0.153	0.34	0.269	0.267	2.611	G0	late
105	8.391	1.048	0.556	0.214	0.891	0.004	2.585	K2	late
1	5.963	0.727	0.694	0.280	0.926	0.134	2.562	K0	late
84	8.779	1.084	0.840	0.088	1.186	−0.128	2.553	K5	late
16	9.480	0.496	0.232	0.449	0.39	0.349	2.548	K0 V	late

early (B or early A) or late (late A or F) types; the later-class stars (later than G) were not considered in the analysis since no reddening determination calibration has yet been developed for such MS stars. Further analyses were done considering the numerical criteria of Lindroos (1980) for Strömgren photometry.

4. RESULTS

The application of the above mentioned numerical packages gave the results listed in Table 5 for NGC 1647 and Table 6 for NGC 1778. The following values are listed: the WEBDA identificator, the reddening, $E(b-y)$, the reddening-free indexes (in decreasing β values), the absolute magnitude, the distance modulus, the distance (in parsecs), the effective temperature and the surface gravity. When histograms of the distances are drawn (Figure 3a), one can see that 24 of the 35 observed stars in NGC 1647 lie around a distance of 564 pc corresponding to a distance modulus of 8.75 ± 0.09. However, when the histogram of distances to the stars is plotted for

TABLE 4

$uvby-\beta$ PHOTOELECTRIC PHOTOMETRY OF NGC 1778

WEBDA	V	$b-y$	m_1	c_1	$[m_1]$	$[c_1]$	β	MK	ST
46	13.014	0.570	0.150	0.380	0.330	0.270	2.830		late
33	10.975	0.250	0.020	0.950	0.100	0.900	2.828	A0	B9
36	11.527	0.240	0.050	0.720	0.120	0.680	2.764		B6
8	11.794	0.250	−0.086	0.750	0.280	0.700	2.753		late
5	11.150	0.240	0.010	0.710	0.090	0.660	2.744	B9.5IV	B5
39	11.681	−0.200	0.320	0.810	0.250	0.850	2.740	B7 IV-V	A3
41	11.964	0.250	0.010	0.620	0.090	0.570	2.740		B4
32	10.283	0.240	−0.010	0.640	0.070	0.590	2.729	B6 III-IV	B3
3	10.190	0.480	0.110	0.600	0.270	0.500	2.699	B6 IV	late
141	11.285	0.230	−0.065	0.530	0.070	0.490	2.671		B2
7	11.810	0.280	−0.030	0.840	0.060	0.780	2.664	B6 IV-V	B6
31	10.197	0.270	−0.020	0.840	0.070	0.780	2.623	B9 III	B6
37	11.599	0.470	0.150	0.360	0.300	0.260	2.617		late
140	9.638	0.280	−0.040	0.630	0.050	0.570	2.614	A0	B3
2	10.104	0.860	0.370	0.360	0.640	0.190	2.585	G8 III	late
34	11.437	1.000	0.560	0.310	0.880	0.110	2.579		late

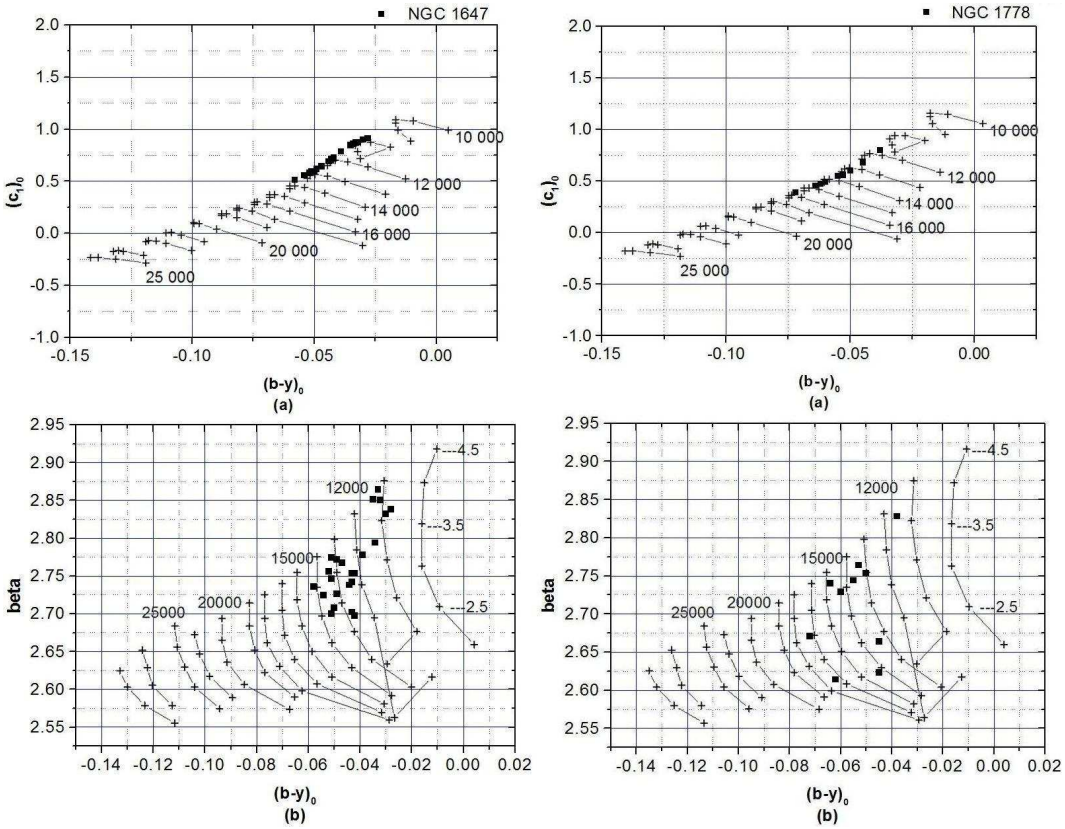

Fig. 2. Left panels (a) LGK86 isotherms for NGC 1647. (b) LGK86 isogravities for NGC 1647. Right panels (a) LGK86 isotherms for NGC 1778. (b) LGK86 isogravities for NGC 1778.

TABLE 5

REDDENING AND UNREDDENED PARAMETERS OF NGC 1647

WEBDA	$E(b-y)$	$(b-y)_0$	$(m_1)_0$	$(c_1)_0$	Hβ	V_0	M_V	DM	dist (pc)	$T_{\rm eff}$ (K)	$\log g$	membership
94	0.428	−0.030	0.163	0.898	2.892	9.21	1.23	7.98	395	11000	4.0	n
71	0.343	−0.033	0.162	0.870	2.864	9.20	0.98	8.22	440	11000	4.5	y
34	0.292	−0.035	0.148	0.845	2.851	9.34	0.86	8.48	496	11000	4.5	y
42	0.284	−0.032	0.162	0.874	2.850	9.04	0.84	8.21	438	11000	4.5	y
29	0.287	−0.028	0.148	0.912	2.838	9.44	0.68	8.76	564	11000	4.0	y
49	0.325	−0.030	0.181	0.900	2.832	8.65	0.62	8.03	404	11000	4.0	y
31	0.253	−0.034	0.158	0.857	2.794	9.18	0.18	9.00	632	11000	3.5	y
48	0.293	−0.039	0.164	0.784	2.778	9.14	0.02	9.12	667	12000	3.5	y
5	0.417	−0.051	0.170	0.594	2.774	8.46	0.07	8.39	476	13000	4.0	y
37	0.341	−0.051	0.157	0.591	2.774	8.56	0.07	8.50	501	13000	4.0	y
57	0.382	−0.049	0.155	0.618	2.772	8.34	0.04	8.31	459	13000	4.0	y
70	0.335	−0.047	0.162	0.643	2.767	9.03	−0.04	9.06	649	12000	4.0	y
419	0.248	−0.052	0.123	0.580	2.756	8.75	−0.16	8.91	605	13000	4.0	y
51	0.350	−0.043	0.186	0.712	2.753	8.44	−0.29	8.72	556	12000	3.0	y
99	0.369	−0.042	0.155	0.724	2.753	8.47	−0.30	8.77	567	12000	3.5	y
54	0.341	−0.051	0.155	0.589	2.746	8.61	−0.31	8.92	607	13000	3.5	y
22	0.240	−0.043	0.118	0.700	2.742	8.64	−0.45	9.10	659	12000	3.5	y
59	0.444	−0.044	0.141	0.689	2.738	7.80	−0.51	8.31	458	12000	3.5	y
3	0.311	−0.058	0.185	0.512	2.736	8.80	−0.43	9.23	701	14000	4.0	n
15	0.265	−0.049	0.126	0.616	2.726	8.53	−0.64	9.17	682	13000	3.5	y
55	0.395	−0.054	0.158	0.557	2.724	8.55	−0.63	9.18	686	13000	3.5	y
66	0.385	−0.035	0.133	0.84	2.721	8.59	−1.06	9.65	851	13000	3.0	n
233	0.296	−0.050	0.129	0.595	2.708	7.59	−0.95	8.54	511	13000	3.0	y
102	0.324	−0.043	0.123	0.708	2.702	7.91	−1.24	9.16	678	12000	3.0	y
45	0.299	−0.051	0.129	0.588	2.700	7.57	−1.10	8.68	544	13000	3.0	y
44	0.273	−0.042	0.115	0.717	2.697	8.04	−1.38	9.41	763	12000	3.0	n
10	0.356	−0.052	0.127	0.576	2.620	7.05	−3.63	10.68	1365	13000	3.0	n

TABLE 6

REDDENING AND UNREDDENED PARAMETERS OF NGC 1778

WEBDA	$E(b-y)$	$(b-y)_0$	$(m_1)_0$	$(c_1)_0$	Hβ	V_0	M_V	DM	dist (pc)	$T_{\rm eff}$ (K)	$\log g$
33	0.231	−0.038	0.017	0.797	2.828	9.85	0.64	9.21	695	11000	4.0
36	0.218	−0.053	0.036	0.560	2.764	10.44	−0.06	10.49	1256	13000	4.0
8	0.242	−0.050	−0.013	0.600	2.753	10.39	−0.21	10.60	1317	13000	3.5
5	0.223	−0.055	0.003	0.547	2.744	10.05	−0.32	10.38	1189	14000	3.5
41	0.238	−0.064	0.004	0.453	2.740	10.79	−0.38	11.17	1716	15000	3.5
32	0.243	−0.060	−0.007	0.490	2.729	9.10	−0.53	9.63	845	14000	3.0
141	0.263	−0.072	0.014	0.388	2.671	10.16	−1.53	11.70	2184	16000	3.0
7	0.270	−0.045	−0.028	0.676	2.664	10.29	−2.19	12.48	3137	12000	2.5
31	0.261	−0.045	−0.012	0.680	2.623	8.94	−3.88	12.83	3677	12000	2.0
140	0.286	−0.062	−0.016	0.472	2.614	8.24	−3.54	11.79	2275	14000	2.5
39	0.449	−0.041	0.273	0.835	2.740	14.43	−0.66	15.09	1043	14000	2.5
3	0.555	−0.078	0.255	0.341	2.699	7.66	−1.02	8.68	545	13000	30
37	0.502	−0.101	0.234	0.147	2.617	9.28	−2.86	12.14	2678	12000	2.5
2	0.836	−0.102	0.506	0.141	2.585	6.40	−4.08	10.48	1247	13000	3.5
34	1.044	−0.118	0.829	−0.041	2.579	7.43	−4.47	11.90	2394	11000	3.0

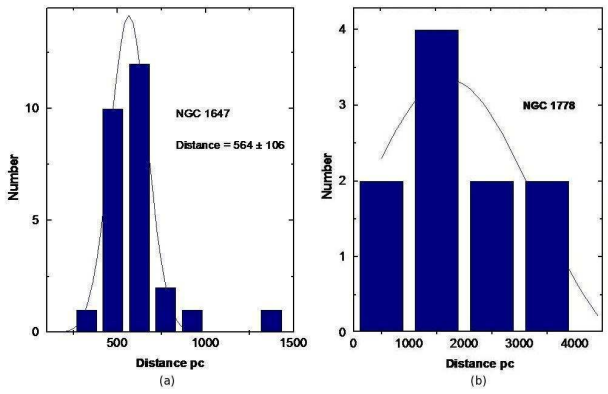

Fig. 3. Histogram of the distances for the stars in the direction of (a) NGC 1647 and (b) NGC 1778. The thin line is a Gaussian fit to the data.

NGC 1778 (Figure 3b), it is not possible to identify a cluster in that direction. We compared the distances obtained photometrically with those derived from studies of proper motions and Hipparcos (1997). However, only two stars in NGC 1647 were observed by Hipparcos; the first star is NGC 1647 15 (HIP 22122), with a parallax 1.66 mas, equivalent to a distance of 602 pc. This distance is consistent, within the error, with 682 pc, a distance that we determined photometrically. The second star observed by Hipparcos is NGC 1647 94 (HIP 22185), with a parallax 3.52 mas, equivalent to a distance 284 pc. This distance is smaller than that determined with photometry (395 pc). However, is still closer than the rest of the stars. For NGC 1647, stars which are members of the cluster are listed un the last column of Table 5; the criterion for those stars is a one sigma deviation from the average.

Once the membership is established, the age can be estimated by first calculating the effective temperature of the hottest stars. These temperatures are determined by plotting the location of such stars on the theoretical grids of LGK86, after evaluating the unreddened colors (Figure 2) for a solar chemical composition. We have considered this metallicity because, although no metallicity has been reported for NGC 1647, the cluster is located within 1.5 kpc from the Sun, i.e., at galactocentric distances where no substantial radial metallicity gradient has been detected (see e.g., Andrievsky et al. 2002). Thus, we can adopt the solar abundance of heavy elements for the cluster and neglect metallicity corrections.

Star 3 is the star with the highest temperature, but based on the distance, we concluded that it does not belong to the cluster. The next hottest star is star 55 because, even though there are several stars with effective temperature of 13000 K, that star has the most negative value of $(b-y)_0$. Hence, given the calibrations of Meynet et al. (1993) for open clusters, a log age of 7.98 ± 0.23 (i.e. 9.54×10^7 yr) is found from the relation $\log \text{age (yr)} = -3.6 \log T_{\rm eff} + 22.956$, which is valid in the range $[3.98, 4.25]$ of $\log T_{\rm eff}$ (with a precision of 3×10^{-3}).

In the case of NGC 1778, Hipparcos (1997) also observed only two stars in the cluster. The first star is NGC 1772 5 (HIP 23904), which has a negative parallax, -0.59 mas, because the true parallax is smaller than the error. The second star is NGC 1778 2 (HIP 23894), which has a parallax of 2.84 mas, equivalent to a distance of 352 pc, very different from 1247 pc, the distance that we determined. In Table 5 we can see that there is a wide spread in the distances determined by different authors, but Joshi et al. (1975) propose that the difference is due to the fact that they used a revised value of 6.1 for the reddening coefficient R for NGC 1778 (Johnson 1968) because R varies significantly with longitude and galactic extinction in the region $100^\circ < l < 220^\circ$. This value differs from the usually accepted value of $R = 3$, but NGC 1778 has galactic coordinates $l = 168^\circ.88$ and $b = -2^\circ.00$.

5. CONCLUSIONS

New $uvby-\beta$ photoelectric photometry has been acquired for 35 stars of the open cluster NGC 1647 and 16 stars of the open cluster NGC 1778. For NGC 1647, unreddened indexes in the LGK86 grids allowed us to determine the effective temperature of the hottest star as 13000 K. We found a mean distance to the cluster of 564 ± 106 pc, which corresponds to a distance modulus of 8.75 ± 0.09 and a reddening $E(b-y) = 0.32 \pm 0.02$, which, through the relation $E(b-y) = 0.9E(B-V)$, gives a color excess of $E(B-V) = 0.35$ mag. These results are in good agreement with the parameters reported by other authors (Table 1).

In the case of NGC 1778, we were unable to determine whether a cluster in that direction exists or not. NGC 1778 observations include only 16 bright stars and, due to observing limitations, have not reached the cluster MS which is fainter. The determined distance to the stars represented in the histogram (Figure 3b) does not show any clustering of stars. Consequently, we do not have statistically significant data to derive any conclusion regarding this cluster, but based on an earlier and deeper photometric study, it is clear that NGC 1778 is an open star cluster.

We would like to thank the staff of the OAN-SPM for their assistance in securing the observations. Proofreading was done by J. Miller. One of us, Guerrero, C. A., would like to thank S. S. Gil for fruitful discussions. This work was partially supported by PAPIIT IN108106 and PAPIIT IN114309. This research has made use of the Simbad databases operated at CDS, Strasbourg, France; NASA ADS Astronomy Query Form and the WEBDA database, operated at the Institute for Astronomy of the University of Vienna.

REFERENCES

Andrievsky, S. M., Bersier, D., Kovtyukh, V. V., Luck, R. E., Maciel, W. J., Lépine, J. R. D., Beletsky, Yu. V. 2002, A&A, 384, 140
Arellano Ferro, A., & Parrao, L. 1988, Reporte Técnico, 57 (Mexico: IA-UNAM)
Barbon, R., & Hassan, S. M. 1973, A&AS, 10, 1
Crawford, D. L. 1975, AJ, 80, 955
_____. 1979, AJ, 84, 1858
Crawford, D. L., & Barnes, J. V. 1970, AJ, 75, 978
Crawford, D. L., & Mander, J. 1966, AJ, 71, 114
Hebb, L., Wyse, F. G. R., & Gilmore, G. 2004, AJ, 128, 2881
ESA 1997, Hipparcos and Tycho Catalogues, ESA SP-1200 (Noordwijk: ESA)
Hoag, A., & Applequist, N. L. 1965, ApJS, 12, 215
Johnson, H. L. 1968, in Nebulae and Interstellar Matter, ed. B. M. Middlehurst & L. H. Aller (Chicago: University of Chicago), 167
Joshi, U. C., Sagar, R., & Pandey, P. 1975, Pramana, 4, 160
Lester, J. B., Gray, R. O., & Kurucz, R. I. 1986, ApJ, 61, 509 (LGK86)
Lindroos, K. P. 1980, Stockholms Obs. Rep., 17, 68
Meynet, G., Mermilliod, J. C., & Maeder, A. 1993, A&AS, 98, 477
Nissen, P. 1988, A&A, 199, 146
Olsen, E. H. 1983, A&AS, 54, 55
Pandey, A. K. 1998, Bull. Astron. Soc. India, 26, 539
Paunzen, E., & Mermilliod, J. C. 2007, WEBDA, A Site Devoted to Stellar Clusters in the Galaxy and the Magellanic Clouds (Vienna: Institute of Astronomy of the University of Vienna), http://www.univie.ac.at/webda/
Shobbrook, R. R. 1984, MNRAS, 211, 659
Turner, D. G. 1992, AJ, 104, 1865
Xin, Y., Deng, L., & Han, Z. W. 2007, ApJ, 660, 319
Zdanavičius, J., et al. 2005, Baltic Astron., 14, 179

C. A. Guerrero and J. H. Peña: Instituto de Astronomía, Universidad Nacional Autónoma de México, Apdo. Postal 70-264, 04510, México, D. F., Mexico (cguerrero, jhpena@astro.unam.mx)
J. P. Sareyan: Lesia, Observatoire de Paris-Meudon and Observatoire de la Cote d'Azur, France (jean-pierre.sareyan@obspm.fr).

Revista Mexicana de Astronomía y Astrofísica, **47**, 193–193 (2011)

ERRATUM

Received 2011 February 12; accepted 2011 February 15

In the paper entitled: Compact radio sources in the vicinity of the ultracompact HII region G78.4+2.6 by C. Neria, Y. Gómez, and L. F. Rodríguez , that was published in RevMexAA, Vol. 46, No. 2, pp. 253-262, October 2010, please disregard Equations A14 and A16. The correct Equations A14 and A16 are as follows.

$$S \gg \frac{S_1}{2\pi(x_1/\theta)} \tag{A14}$$

$$S \gg \left[\frac{\theta}{\theta_S}\right]^2 \frac{S_1}{2\pi(x_1/\theta)} \tag{A16}$$

AUTHOR INDEX

Avila, R. Recalibrated turbulence profiles at San Pedro Mártir. *R. Avila, L. Sánchez, I. Cruz-González, E. Carrasco, & V. M. Castaño.* 75

Borka Jovanović, V. Temperature, brightness and spectral index of the Cygnus radio loop. *V. Borka Jovanović & D. Urošević.* 159

Carigi, L. H II Regions and the Protosolar Helium, Carbon, and Oxygen Abundances in the Context of Galactic Chemical Evolution. *L. Carigi & M. Peimbert.* 139

Carrasco, E. Recalibrated turbulence profiles at San Pedro Mártir. *R. Avila, L. Sánchez, I. Cruz-González, E. Carrasco, & V. M. Castaño.* 75

Castaño, V. M. Recalibrated turbulence profiles at San Pedro Mártir. *R. Avila, L. Sánchez, I. Cruz-González, E. Carrasco, & V. M. Castaño.* 75

Cavichia, O. Planetary nebulae in the inner Milky Way II: the Bulge-Disk transition. *O. Cavichia, R. D. D. Costa, & W. J. Maciel.* 49

Colín, P. Mass and metal ejection efficiency in disk galaxies driven by young stellar clusters of nuclear starburst. *A. Rodríguez-González, A. Esquivel, A. C. Raga, & P. Colín.* 113

Costa, R. D. D. Planetary nebulae in the inner Milky Way II: the Bulge-Disk transition. *O. Cavichia, R. D. D. Costa, & W. J. Maciel.* 49

Cruz-González, I. Recalibrated turbulence profiles at San Pedro Mártir. *R. Avila, L. Sánchez, I. Cruz-González, E. Carrasco, & V. M. Castaño.* 75

Esquivel, A. Mass and metal ejection efficiency in disk galaxies driven by young stellar clusters of nuclear starburst. *A. Rodríguez-González, A. Esquivel, A. C. Raga, & P. Colín.* 113

Flores-Gutiérrez, J. D. A variant of the Titius-Bode Law. *J. D. Flores-Gutiérrez & C. García-Guerra.* 173

Gómez, Y. ERRATUM. *C. Neria, Y. Gómez, & L. F. Rodríguez.* 193

García-Guerra, C. A variant of the Titius-Bode Law. *J. D. Flores-Gutiérrez & C. García-Guerra.* 173

Guerrero, C. A. $uvby - \beta$ Photoelectric Photometry of the Open Clusters NGC 1647 and NGC 1778. *C. A. Guerrero, J. H. Peña, & J. P. Sareyan.* 185

Hiriart, D. *UBVR* polarimetry of high-galactic latitude carbon stars. *J. M. López & D. Hiriart.* 63

López, J. M. *UBVR* polarimetry of high-galactic latitude carbon stars. *J. M. López & D. Hiriart.* 63

Márquez-Lugo, R. A. Mid- and Far-Infrared Photometry of Galactic Planetary Nebulae with the AKARI All-Sky Survey. *J. P. Phillips & R. A. Márquez-Lugo.* 83

Maciel, W. J. Planetary nebulae in the inner Milky Way II: the Bulge-Disk transition. *O. Cavichia, R. D. D. Costa, & W. J. Maciel.* 49

Neria, C. ERRATUM. *C. Neria, Y. Gómez, & L. F. Rodríguez.* 193

Peña, J. H. $uvby - \beta$ Photoelectric Photometry of the Open Clusters NGC 1647 and NGC 1778. *C. A. Guerrero, J. H. Peña, & J. P. Sareyan.* 185

Peimbert, M. H II Regions and the Protosolar Helium, Carbon, and Oxygen Abundances in the Context of Galactic Chemical Evolution. *L. Carigi & M. Peimbert.* 139

Phillips, J. P. Mid- and Far-Infrared Photometry of Galactic Planetary Nebulae with the AKARI All-Sky Survey. *J. P. Phillips & R. A. Márquez-Lugo.* 83

Phillips, J. P. Mid-Infrared Observations of Planetary Nebulae detected in the GLIMPSE 3D Survey. *J. A. Quino-Mendoza, J. P. Phillips, & G. Ramos-Larios.* 31

Quino-Mendoza, J. A. Mid-Infrared Observations of Planetary Nebulae detected in the GLIMPSE 3D Survey. *J. A. Quino-Mendoza, J. P. Phillips, & G. Ramos-Larios.* 31

Raga, A. C. Mass and metal ejection efficiency in disk galaxies driven by young stellar clusters of nuclear starburst. *A. Rodríguez-González, A. Esquivel, A. C. Raga, & P. Colín.* 113

Ramos-Larios, G. Mid-Infrared Observations of Planetary Nebulae detected in the GLIMPSE 3D Survey. *J. A. Quino-Mendoza, J. P. Phillips, & G. Ramos-Larios.* 31

Rodríguez, L. F. ERRATUM. *C. Neria, Y. Gómez, & L. F. Rodríguez.* 193

Rodríguez-González, A. Mass and metal ejection efficiency in disk galaxies driven by young stellar clusters of nuclear starburst. *A. Rodríguez-González, A. Esquivel, A. C. Raga, & P. Colín.* 113

Sánchez, L. Recalibrated turbulence profiles at San Pedro Mártir. *R. Avila, L. Sánchez, I. Cruz-González, E. Carrasco, & V. M. Castaño.* 75

Sánchez-Salcedo, F. J. The Parker instability in axisymmetric filaments: final equilibria with longitudinal magnetic field. *F. J. Sánchez-Salcedo & A. Santillán.* 15

Saffe, C. FUNDPAR: A program for Deriving Fundamental Parameters from Equivalent Widths. *C. Saffe.* 3

Santillán, A. The Parker instability in axisymmetric filaments: final equilibria with longitudinal magnetic field. *F. J. Sánchez-Salcedo & A. Santillán.* 15

Sareyan, J. P. $uvby - \beta$ Photoelectric Photometry of the Open Clusters NGC 1647 and NGC 1778. *C. A. Guerrero, J. H. Peña, & J. P. Sareyan.* 185

Turner, D. G. The usefulness of 2MASS $JHK_{\rm s}$ photometry for open cluster studies. *D. G. Turner.* 127

Urošević, D. Temperature, brightness and spectral index of the Cygnus radio loop. *V. Borka Jovanović & D. Urošević.* 159